



Synthesis of Reactive Polyurethane Adhesives and Studying the Effect of Ketonic Resins

Nesrin Köken^{1*}  , Serdar Aydın²  

^{1*}Istanbul Technical University, Faculty of Science, Department of Chemistry, 34469-Maslak, Istanbul, Turkey

² Istanbul Technical University, Graduate School of Science, Engineering and Technology, Polymer Science and Technology Department, 34469-Maslak, Istanbul, Turkey

Abstract: In this study, the effects of cyclohexanone formaldehyde ketonic resin (CFR) with different montmorillonite (MM) content (from 0,5 to 3 wt%) on the viscosity, initial adhesion strength, and temperature resistance of polyurethane one-component adhesives were investigated. *In situ* MM modified cyclohexanone formaldehyde resin (MM-CFR) was used as polyol into formulation with a specified weight ratio (rate of 10% by weight of polyether polyol). One-shot technique was used for synthesis. CFR with varying montmorillonite (MM) content were incorporated blank polyurethane was synthesized using polyether polyol and polymeric 4,4'-methylene diphenyl diisocyanate (p-MDI). In experimental studies, the ratio of the isocyanate groups (NCO) to the hydroxyl group (OH) was 4.84. Reaction completion was followed by FTIR spectroscopy. Chloroparaffin was used as a plasticizer to adjust the viscosity and to reduce the fragile structure of the product. The NCO % values of the synthesized adhesive PU were measured by titration. When TGA data were examined, it was found that the heat resistance of the product increased with the addition of CFR and MM-CFR. As a result, it has been determined that the adhesion properties and thermal resistance were improved with the use of ketonic resins in one component reactive adhesives.

Keywords: Polyurethane, ketonic resin, cyclohexanone-formaldehyde resin, adhesive, montmorillonite

Submitted: December 11, 2018. **Accepted:** October 03, 2019.

Cite this: Köken N, Aydın S. Synthesis of Reactive Polyurethane Adhesives and Studying the Effect of Ketonic Resins. JOTCSA. 2020;7(1):1-10.

DOI: <https://doi.org/10.18596/jotcsa.495458>.

***Corresponding author. E-mail:** nesrin@itu.edu.tr.

INTRODUCTION

Polyurethanes were developed by Otto Bayer in 1937, and became a success story that is now a billion-dollar business (1). They are produced as elastomers, foams, coatings, adhesives fibers, synthetic leathers and others. The polyurethane industry has shown significant growth over the last twenty years, this being particularly the case with adhesives. There are many different types of PU adhesives with increasing demand being due to the versatility of PU chemistry and the unique properties of polyurethanes (2, 3). These

normally consist of polyol (polyester or polyether type), isocyanate and other additives. The properties of the polyurethane adhesives depend on the stoichiometric proportions and the types of isocyanates and polyols used. Nowadays, availability of different types of polyols in commercial sizes enables polyurethane adhesives which meet customer requirements (4-5). Typically, adhesives are grouped according to their chemistry (6), with formaldehyde (F) based adhesives representing the most important group. As reaction partners of formaldehyde, urea (UF), melamine (MF), phenol (PF), resorcinol

(RF) and mixtures thereof (e.g. MUF, PRF) are involved. Besides formaldehyde-based polymers, adhesives using highly reactive isocyanates are applied in wood industry, e.g. polymeric diphenylmethane diisocyanate (pMDI), emulsion polymer isocyanates (EPI), or polyurethane (PUR) adhesives. The performance of a wood adhesive system is dependent on a wide range of variables, such as the surface smoothness of wood substrate, temperature, pH, presence of wood extractives, and the amount of debris present which are related to the environment such as the level and rate of a change in both temperature and relative humidity (7). Adhesives based on urea formaldehyde and phenol formaldehyde are the major adhesives used for bonding wood, but some of these adhesives are very sensitive to hydrolysis, and stress scission (8–9).

The oldest types of one-component PU adhesives were based upon di- or triisocyanates that cured by reacting with active hydrogens on the surface of the substrate or moisture present in the air or substrate. One-component reactive polyurethane adhesives are prepared by reaction between monomeric or polymeric isocyanates and polyols (10). These systems offer the advantage of being one-package systems. Moisture cure systems are available based on isocyanates. The atmospheric moisture hydrolyzes isocyanate to generate the primary amines which immediately react with the isocyanate groups to give urea linkages. The urea linkage is more stable and more moisture resistant than the urethane linkage (11-12). One-component polyurethane adhesives have been come popular on the European market for the bonding of load-bearing timber components such as glued laminated timber products, finger-joints and I-beams. Their main advantages are a colorless glueline, easy application of a one-component adhesives and fast hardening within one to three hours without heat application (13-14). The one-component reactive polyurethane adhesives subject to study are widely used especially in the furniture sector. One of the most important parameters affecting the productivity of the furniture producers is that the parts joined by bonding are waiting for long time and cannot be subjected to any processing during this period. In this case, the productivity of the production decreases. Ketonic resins are used as a resin in the ink and paint sector in an intensive adhesion. Many successful products that use ketonic resins in this direction are commercially and

domestically available (15-16). However, their use in polyurethane adhesives has not been the subject to date due to the fact that ketonic resins are more difficult to access than polyols and the costs associated therewith are high.

Montmorillonite (MM) a layered silicate used widely to prepare polymer-clay nanocomposites, consists of two external silica tetrahedral sheets and a central octahedral sheet of alumina. The layers with high aspect ratio (about 1 nm thickness and 100 nm width and length) are stacked via weak dipolar force and form interlayer galleries which are generally occupied by cations (for example Na^+ , Ca^{2+} , Li^+) which can be easily substituted with organic cations via ion exchange reaction in water. The special structures of MM play important roles in improving mechanical, thermal and diffuse barrier properties of polymer-layered silicate nanocomposites (17–18).

The aim of this work is to use CFR and montmorillonite modified cyclohexanone formaldehyde resin as polyol for polyurethane one component adhesives. PU adhesives synthesized were monitored with their physical, mechanical, thermal and spectroscopic properties. When TGA data were examined, it was found that the heat resistance of the product increased with the addition of CFR and MM-CFR. As a result, it has been determined that the adhesion properties and thermal resistance were improved with the use of ketonic resins in one component reactive adhesives.

MATERIALS AND METHODS

Materials and Instrumentation

A commercially available polymeric methylene diphenylene isocyanate (p-MDI) with a product name Wannate® PM-200 and a polyether polyol with a commercial name Caradol ED56-200 (Shell Chemicals) were used as received from the commercial suppliers. The polyol is a polyoxypropylene glycol with 2,000 MW and OHv 56. p-MDI is a dark brown liquid with a functionality between 2.6-2.7 containing some higher functionality isocyanates. The NCO % of the p-MDI is between 30.5-32.0. The viscosity of p-MDI is 150-250 mPa.s at 25°C which means that the material is liquid at room temperature. The chemical structure of p-MDI is shown in Figure 1.

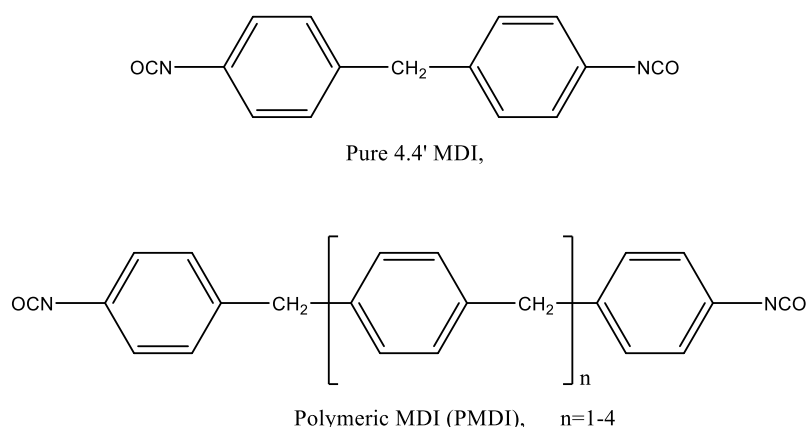


Figure 1: The chemical structure of MDI and p- MDI

Cyclohexanone- formaldehyde ketonic resin (CFR) and montmorillonite (MM) were used and the basic structure of the ketonic resin is shown in Figure 2.

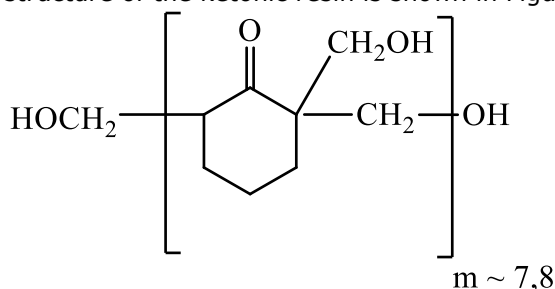


Figure 2: Cyclohexanone formaldehyde resin (CFR).

Montmorillonite is known as a clay and it is a 2:1 clay which means that it has two tetrahedral sheets of silica sandwiching a central octahedral sheet of alumina.

The chloroparaffin used in the synthesis is tris-(2-chloroisopropyl) phosphate (TCPP) with a commercial name Fyrol-PCF available from ICI Industrial Products. The basic structure of the TCPP is shown in Figure 3.

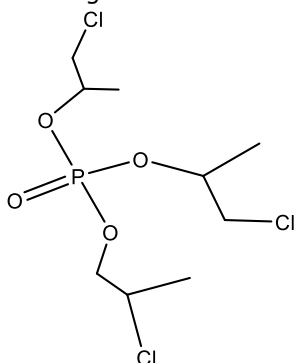


Figure 3: Structure of Tris-(2-chloroisopropyl) phosphate (TCPP).

The viscosity of the raw material is 65 mPa.s and the chlorine content is 32.5 %. The water content of the material is below 0.07 %. 2,2'-dimorpholino diethyl ether (DMDEE) was used as a catalyst.

Fourier transform infrared (FTIR) spectra were performed to follow the reaction completion with

Bruker Tensor-27. FT-IR was also used for incoming quality control of the raw materials including p-MDI, polyol and chloroparaffin. TGA/DSC-1 from Mettler Toledo was used to determine the heat stability of samples. In order to prepare TGA samples were dried at 100 °C for 3 h. A 5 mg powder sample of the product was subjected to TGA analysis, and heated at linear heating rate of 10 °C/min.

The flow behavior and the viscosities of the samples were measured with rheometer MCR-102 from Anton Paar. Shear Rate is changed from 1 to 100 rpm and the viscosity is measured at 25 °C. Spindle: PP25, plate-plate was used.

The NCO % of the pre-polymers were measured according to EN-ISO 11909 with an automatic titrator. The model of the automatic titrator is T-50 from Mettler Toledo. Test specimens are prepared according to EN 204:2001 and tested with a static force testing equipment with model DVT.G21 from Devotrans. Shear strength of samples were also measured after 1 h to see the build-up of adhesion performance depend on time.

Synthesis of One Component Polyurethane Adhesives

Polyurethane adhesives are synthesized with one-shot technique. One-shot technique is the addition of all raw materials at once and letting reaction to completion. NCO % is kept between 15-18 for a good shelf life and it is required to make calculations to achieve pre-determined NCO %.

Calculations

It is required to calculate the amount of polyol and isocyanate to be reacted to be able to obtain the chemically stoichiometric equivalents. By changing the isocyanate index the theoretical stoichiometric amount of isocyanate can be adjusted depending on the desired polyurethane structure (2, 13).

Experiments were carried out with constant NCO/OH ratio. NCO/OH ratio is 5.38 for

comparison samples and of 4.84 for experiments carried out. In the case of reactive polyurethane adhesives, excess isocyanate isocyanate (NCO/OH is well above 4) is preferred, in order to ensure the presence of reactive -NCO groups at the pre-polymer ends. The final NCO % was expected to be 16.24 for comparison samples and vary for the experiments depend on the OHv of CFR and MM-CFR.

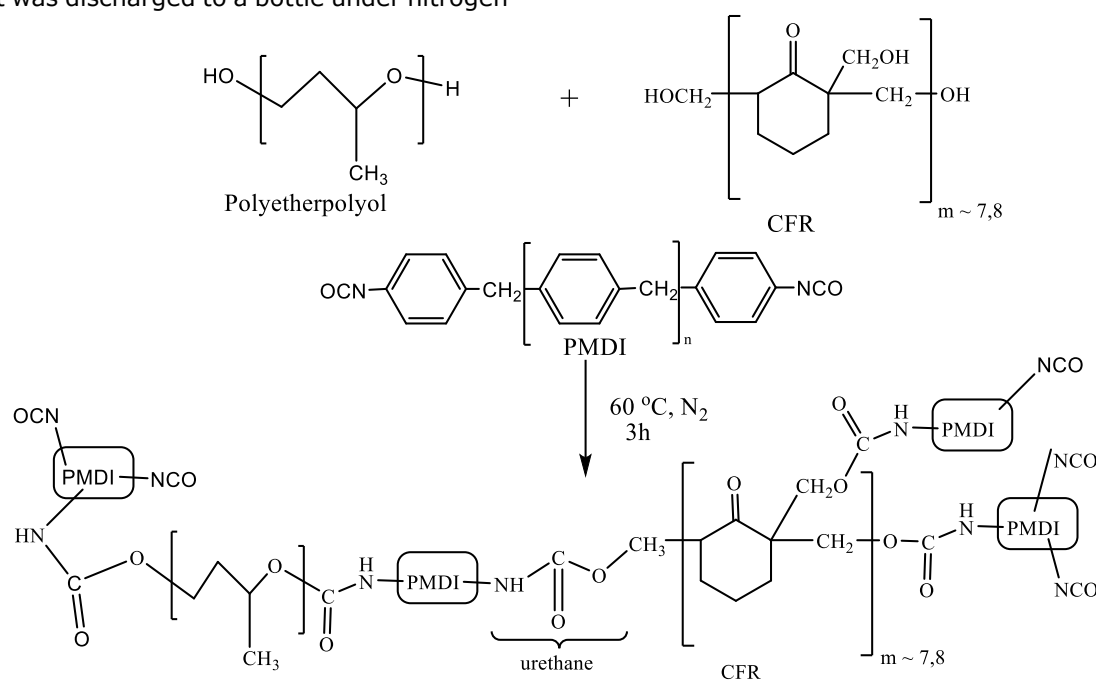
Synthesis of blanks PU samples

Polyether polyol (39.80 g) was introduced into reaction vessel at room temperature and the temperature was raised to 60°C under inert atmosphere. p-MDI (55.10 g) was added than and the reaction carried out for 3 h at the temperature of 60-65 °C. Completion of reaction was followed by FT-IR. There is a characteristic peak at 3400 cm^{-1} corresponding to OH group of polyols. The peak disappears with the completion of reaction. NCO groups of isocyanate reacts with OH groups of polyols to form urethane linkage. There are no more OH groups left as excess of isocyanate is used and all OH groups are consumed. System was cooled down to 40 °C to add the catalyst (DMDEE) (0.30 g) and the product was discharged to a bottle under nitrogen

to carry the tests. If chloroform used in PU prepolymer than it is added together with polyol to the reaction vessel.

Synthesis of PU adhesives with ketonic resins

CFR /or MM-CFR (3.98 g) was added with chloroform into the reaction vessel at room temperature. Chloroform is used to dissolve the CFR and/or MM-CFR because it does not melt even over 100 °C without solvent. Polyether polyol (35.82 g) was charged as second ingredient, then the temperature was raised to 65 °C to remove water under vacuum. The system was kept at 65 °C under vacuum for 1 h until the water trapped was removed from the system. The next step is the addition of p-MDI (55.10 g) for the polymerization and the reaction was continued for 3h. Completion of reaction was followed by FT-IR. System was cooled down to 40 °C to add the catalyst (0.30 g) and the product was discharged to a bottle under nitrogen to carry the tests. Chloroform (CHCl_3) was stripped-off from the adhesives synthesized by using vacuum before adding catalyst. Formation of PU-CFR is shown in Scheme 1.



Scheme 1: Formation reaction of PU-CFR.

RESULTS AND DISCUSSION

Cyclohexanone-formaldehyde ketonic resin (CFR) and Montmorillonite containing Cyclohexanone-formaldehyde ketonic resin (MM-CFR) were synthesized in this study. Polyether polyol and polymeric 4,4'-methylene diphenyl diisocyanate (p-MDI) were used only to synthesize the polyurethane pre-polymer/adhesive blanks for comparison of results. CFR and MM-CFR at a rate of 10% by weight of polyether polyol were used in the synthesis. In the case of reactive polyurethane adhesives, excess isocyanate

isocyanate (NCO/OH is well above 4) is preferred, in order to ensure the presence of reactive -NCO groups at the pre-polymer ends (19). In parallel with the reduction of the amount of polyether polyol used, the ratio of isocyanate groups (NCO) to hydroxyl groups (OH) was 5.38 (CFR and MM-CFR ketonic resins were not involved in calculation). Chloroform was used as a solvent in trials using ketonic resins. Chloroform was used as a solvent and removed by heat and vacuum after the reaction. The ratio of the isocyanate group (NCO) to the hydroxyl group (OH) for the two different blank samples synthesized for this

study (4.84). In the first case, chloroparaffin (TCPP) was used as a plasticizer in the first 6 synthesis to adjust the viscosity and to reduce the fragile structure of the products. The amount of montmorillonite used in the synthesis of polyurethane adhesive and other parameters are shown in Table 1. The NCO % values of the synthesized PU adhesives decreased with the use of CFR and MM-CFR. It has been found that the NCO % value tends to decrease with the increase in the amount of MM in the CFR. The NCO % value of the adhesives synthesized in the absence of chloroparaffin are higher as seen in Table 1. It is known that chloroparaffin contains certain amount of water inside and if it is not removed than it will react with NCO groups of isocyanates. Sample PU1-CFR has a lower NCO % than PU Blank-1 which results that OHv of CFR is higher than the polyether polyol used. It is expected from NCO % to increase with increasing MM concentration but the opposite was observed. This could be explained as the OH groups that

montmorillonite has and water trapped inside was not able to strip-off under vacuum reacted with isocyanate groups. Trapped water inside montmorillonite could be the major reason instead of OH groups available.

In order to characterize the chemical structure of CFR; MM (pristine clay), MM-CFR1, MM-CFR2, MM-CFR3 and MM-CFR4 samples were analyzed with FT-IR (Figure 3). Characteristic peaks of cyclohexanone formaldehyde resin appear at 3400 cm^{-1} , 2920 cm^{-1} , 1700 cm^{-1} and 1450 cm^{-1} . In this study, these characteristic peaks were observed at 3399 cm^{-1} , 2925 cm^{-1} , 1699 cm^{-1} , and 1445 cm^{-1} . These peaks respectively attributed to hydroxy methyl groups, aliphatic -CH_2 , carbonyl C=O , and -CH_2 methylene bridges. Also, between $970\text{-}1200\text{ cm}^{-1}$ three main peaks were observed which belongs to the C-O stretch between methylene bridges and cyclohexanone ring.

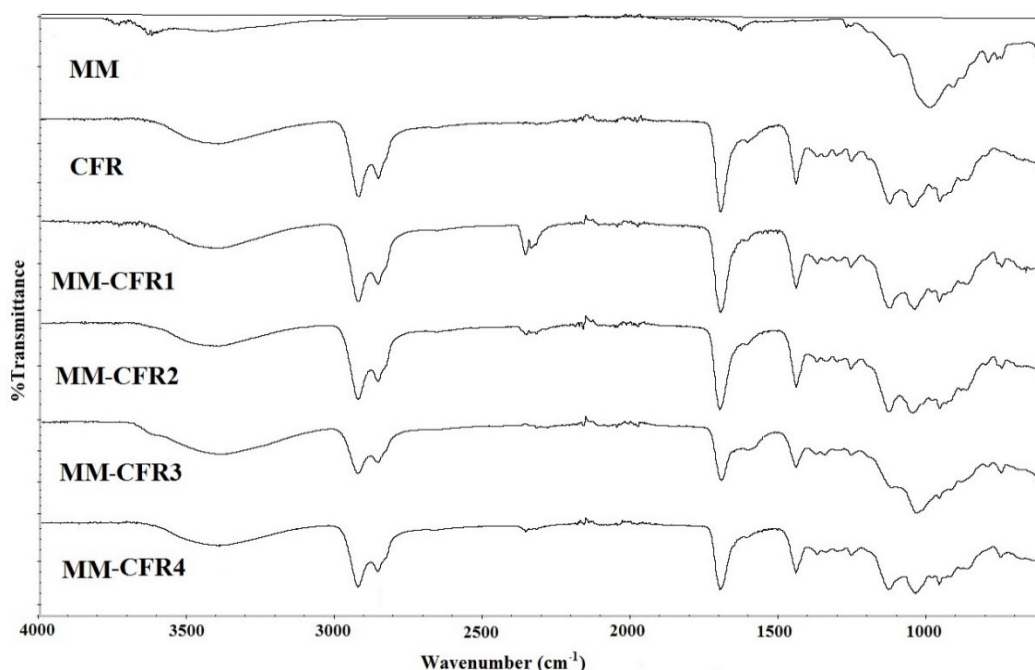


Figure 3: FTIR spectrum of pristine clay (MM), CFR and MM-CFRs.

Table 1: The amount of montmorillonite used in the synthesis of polyurethane adhesive and other parameters. ($T=65\text{ }^{\circ}\text{C}$).

Sample Code	Ketonic	Resin	MM (w %)	Chloroform (Solvent)	Chloroparaffin (Plasticizer)	NCO %
PU1-Blank	-	-	-	-	+	15.463
PU1-CFR	-	CFR	-	+	+	14.646
PU1-MMCFR1	-	MMCFR1	0.5	+	+	14.272
PU1-MMCFR2	-	MMCFR2	1.0	+	+	14.729
PU1-MMCFR3	-	MMCFR3	1.5	+	+	14.210
PU1-MMCFR4	-	MMCFR4	3.0	+	+	13.559
PU2-Blank	-	-	-	-	-	16.336
PU2-CFR-2	-	CFR	-	+	-	15.328
PU2-MMCFR1	-	MMCFR1	0.5	+	-	15.166
PU2-MMCFR2	-	MMCFR2	1.0	+	-	15.745

Each experiment was controlled with FT-IR to ensure the completion of reaction. FT-IR

spectrum of polyol (Caradol ED 56-200) and PUMM-CFR2 were shown in Figure 4. The peak at

3428 cm^{-1} is due to stretching vibrations of $-\text{OH}$ groups of polyol and CFR. Aliphatic C-H vibrations are seen as peaks at 2800-2950 cm^{-1} . The functional $-\text{C}=\text{O}$ group of cyclohexanone appears at 1700 cm^{-1} . Broad OH peak of polyol must be lost and new urethane linkage should be formed if the reaction was completed. The stretching absorption of $-\text{C}-\text{N}$ 1405 cm^{-1} and the band 1701

cm^{-1} confirm the presence of R-O-CO-N groups. The absorption bands around 2274 cm^{-1} show the presences of terminal NCO groups in PU. The bands around 1217 cm^{-1} and 1067 cm^{-1} are due to P=O and P-O-C stretching frequencies respectively. Furthermore, the C-Cl stretching was seen at about 755 cm^{-1} .

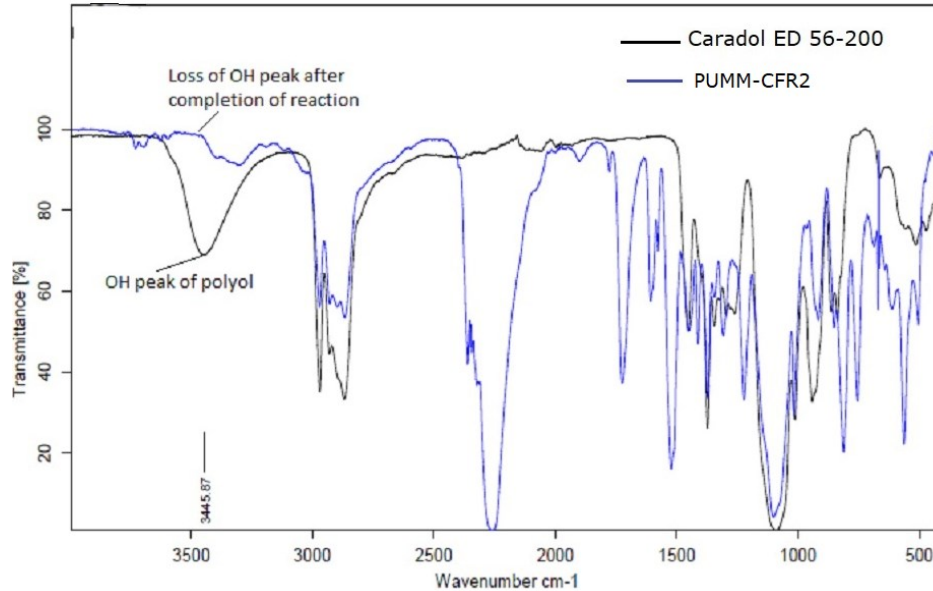


Figure 4: FT-IR spectrum of polyol (Caradol ED 56-200) and PU1-MMCFR2.

All PU adhesive synthesized with and without cyclohexanone-formaldehyde resins (CFR) containing different montmorillonite concentration show Newtonian flow properties. The viscosity of adhesives does not change with

varying shear rate as can be seen from Figure 5. Montmorillonite is a kind of filler which may give thixotropic behavior to materials but the amount used in CFR was not high so it didn't have any effect to change the flow properties of adhesives.

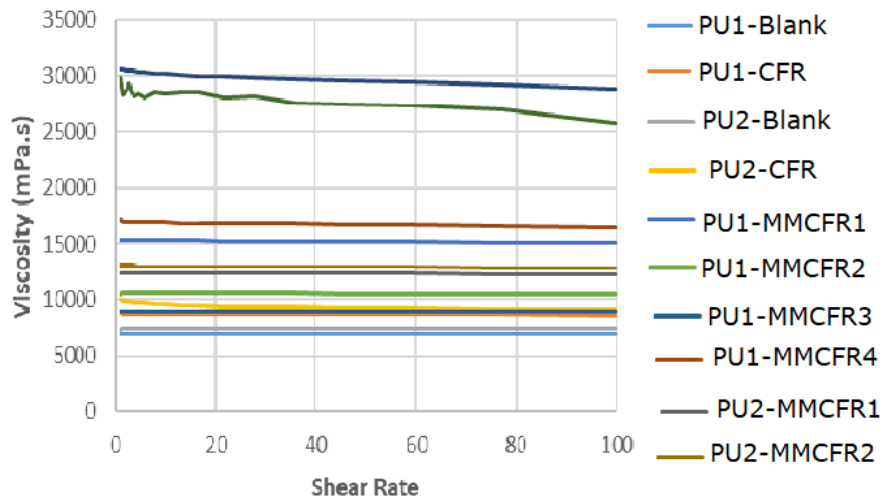


Figure 5: Viscosity (mPa.s) – Shear Rate (1/s) chart.

It was observed that the viscosity of the products increase in parallel with the increase of the MM content and CFR. This can be explained with OHv of CFR and also the increasing amount of montmorillonite content in CFR. Increasing amount of montmorillonite supports viscosity raise dramatically even used in small portions. Viscosity of adhesives increase from $\sim 7,000$ mPa.s to $\sim 30,000$ mPa.s without chloroparaffin (Figure 6). But the highest viscosity dropped

down to $\sim 17,000$ mPa.s which was still workable as an adhesive. The product viscosity remained at acceptable levels with incorporation of chloroparaffin.

Another reason of viscosity increase could be the water content of raw materials used. NCO groups of isocyanates would react with trace water in polyol mixture and it would cause NCO % to decrease which result an increase of viscosity.

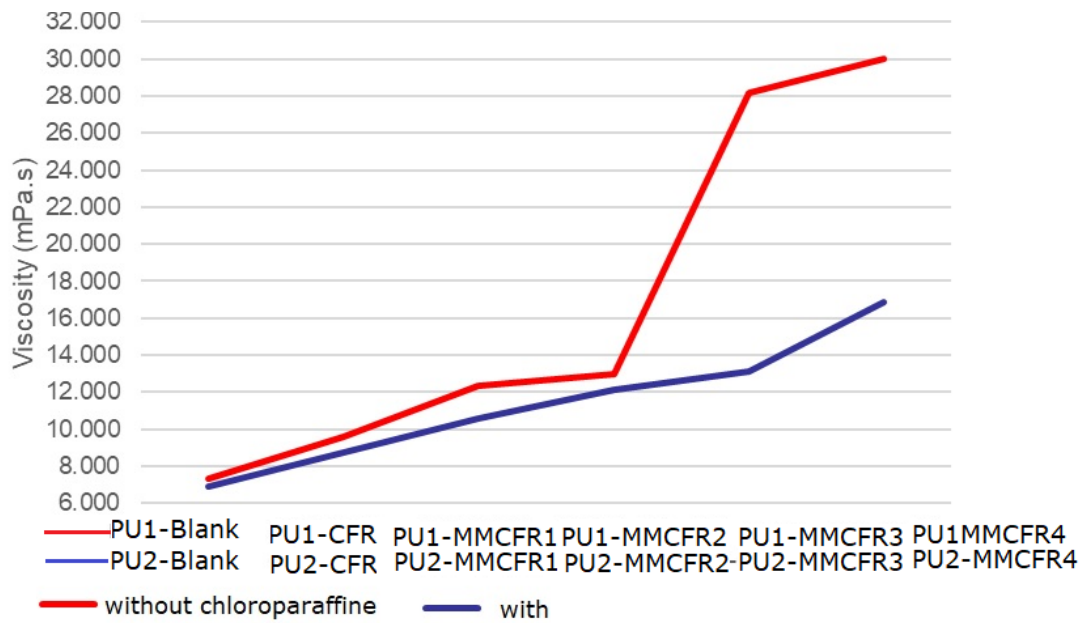


Figure 6: Viscosity change of adhesives with and without chloroparaffin.

Beach wood was used to measure the shear strength of adhesives. If adhesive layer detaches from the wood while loading to the equipment or any result could not be read from the equipment, it is considered "Fail". If fibers of the wood were come-off, after adhesive layer broken when stress applied at equipment than it is considered as "Wood Failure".

Blanks and adhesives prepared with PU-CFR and PU-MMCFR are far from showing any strength at time 10 min after bonding. Adhesives show raise in adhesion strength through time and datas can

be collected at time 20 min after bonding. PU1-CFR and PU2-CFR have higher shear strength than samples Pu Blank-1 and PU Blank-2 respectively at time 20 and 30 minutes after bonding. The results from Table 2 show us that PU-CFR and PU-MMCFR themselves have an influence on shear strength build-up through time. It was observed that the build-up of green strength and the final strength are both better than blank samples. After 24 h in other means 1440 minutes shear strength of each trial is high enough to result wood failure and there is not a significant difference.

Table 2: Shear Strength (kgf/cm²) at different intervals.

Sample No	10 min (kgf/cm ²)	20 min (kgf/cm ²)	30 min (kgf/cm ²)	1440 min (24h) (kgf/cm ²)
PU Blank-1		95.6	120.7	
PU1-CFR		105.8	155.3	
PU1-MMCFR1		Fail	148.0	
PU1-MMCFR2		125.7	184.0	
PU1-MMCFR3		150.5	237,4	
PU1-MMCFR4		164.3	202.5	Wood Failure
PU Blank-2	Fail	133.9	77.9	
PU2-CFR		Fail	177.0	
PU2-MMCFR1		123.1	150.4	
PU2-MMCFR2		165.3	178.1	
PU2-MMCFR3		238.3	236.7	
PU2-MMCFR4		245.7	243.5	

Decomposition temperature of polyurethane adhesives synthesized were investigated with TGA. PU Blank-1 has the lowest decomposition temperature where the sample PU1-MMCFR4 has the highest decomposition temperature as shown in Figure 7. When TGA data were examined, it was found that the heat resistance of the product increased with the addition of CFR and MM-CFR.

It is found from the graph that samples with PU-CFR and PU-MMCFR have a better high temperature resistance. The increase in the amount of MM in the CFR appears to have a positive effect on the results. In this case, the use of CFR and MM-CFR may be appropriate in applications where temperature resistance is required.

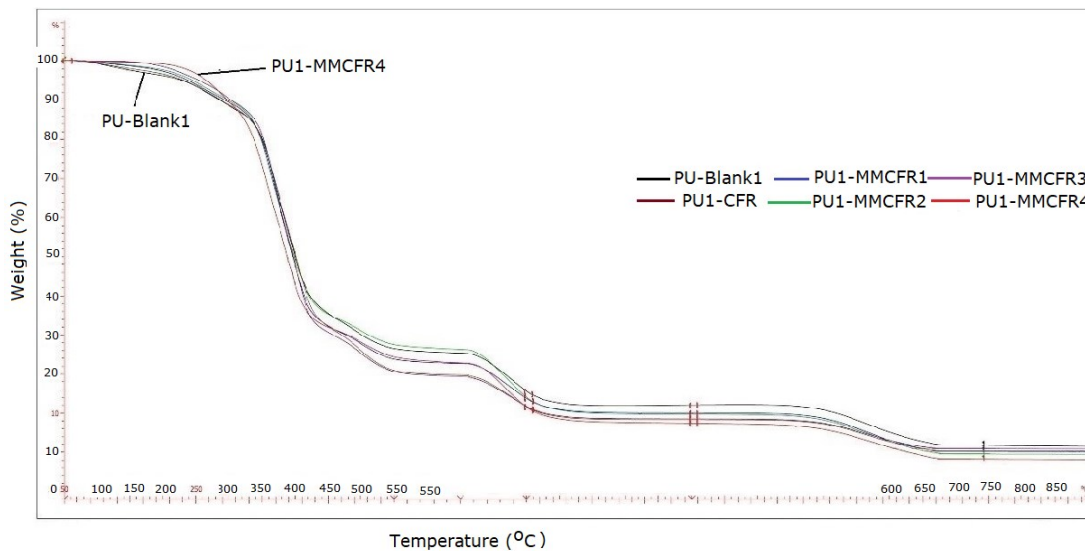


Figure 7: TGA thermograms for PU Blank-1, PU1-CFR, PU1-MMCFR1, PU1-MMCFR2, PU1-MMCFR3 and PU1-MMCFR4.

Similar results were observed for the samples synthesized without chloroparaffin. PU Blank-2 has the lowest decomposition temperature where

the PU2-MMCFR4 has the highest decomposition temperature as shown in Figure 8.

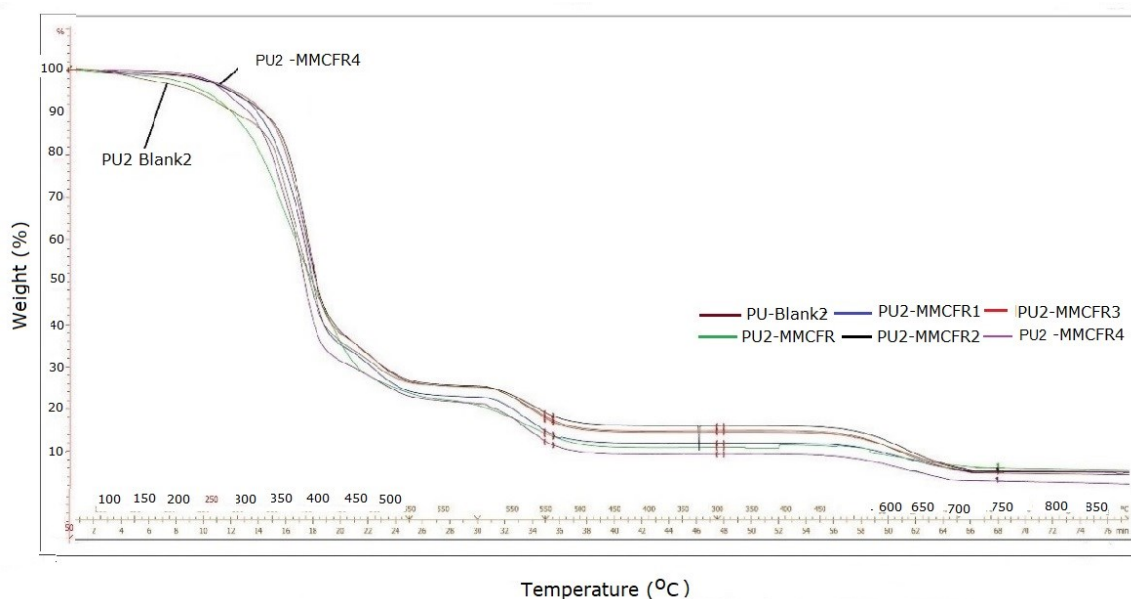


Figure 8: TGA thermograms for PU Blank-2, PU2-CFR and PU2-MMCFR1 to PU2-MMCFR4.

CONCLUSION

As a result of the study, it was observed that all products show Newtonian flow properties, so CFR does not have any effect on flow properties and the amount of montmorillonite is not high enough to give thixotropy. Viscosity increases with CFR and montmorillonite. Increasing viscosity value is also proportional with montmorillonite content in CFR. Viscosity increase is high enough not letting adhesives suitable for manual and machine applications. Chloroparaffin supports viscosity decrease without giving-up from other properties so it could be a good option to keep viscosity at certain value and letting to increase the montmorillonite content for better thermal and

shear strength build-up in short time properties.

Use of CFR and montmorillonite in PU adhesives support adhesion strength growth which is also called green strength. No force values could be read at time 10 minute after bonding and it was an adhesive failure. Force values could be read at time 20 minute after bonding and specimens prepared with CFR showed higher shear strength. Samples prepared with CFR and montmorillonite had higher shear strength compared to CFR only samples. Higher content of montmorillonite resulted higher shear strength. Shear strength after 24 h or 1440 minute could not be read because the wood specimens are all broken. It

can be judged that the adhesive and cohesive strength of adhesive are higher than the wood specimens' strength (13). Build-up of green strength can be also a result of lower free NCO content, so it might be the next step to keep free NCO content constant and change the amount of CFR and montmorillonite.

The NCO % values of the synthesized PU adhesives were visibly reduced by the use cyclohexanone- formaldehyde resin. It can be judged that the OHv of the CFR was higher. Higher OHv will result lower NCO % values of final product. Besides, NCO % was not expected to decrease with increasing MM amount in CFR. This can be explained by the water trapped in the MM and could not be removed by vacuum.

Samples with CFR showed higher thermal resistance and the highest thermal resistance was belong to the sample with highest montmorillonite content. This proves that thermal resistance increases with incorporation of CFR and montmorillonite.

Shear strength results show that the cyclohexanone formaldehyde ketonic resin and in situ modified montmorillonite – cyclohexanone formaldehy resins can be used as an important agent to increase the initial adhesion strength or build-up of green strength for one component reactive polyurethane adhesives with better thermal resistance .

REFERENCES

1. Saunders J, Frisch K. Polyurethanes: Chemistry and technology. Part 1. New York: Interscience Publishers; 1962.
2. Meier-Westhues U. Polyurethanes: coatings, adhesives and sealants. Vincentz Network GmbH; 2007.
3. Randall D, Lee S. The polyurethanes book. Everberg, Belgium: Huntsman Polyurethanes; 2002.
4. da Silva ALD, Martín-Martínez JM, Bordado JCM. Influence of the free isocyanate content in the adhesive properties of reactive trifunctional polyether urethane quasi-prepolymers. International journal of adhesion and adhesives. 2006;26(5):355–62.

5. Clauß S, Dijkstra DJ, Gabriel J, Kläusler O, Matner M, Meckel W, et al. Influence of the chemical structure of PUR prepolymers on thermal stability. International journal of adhesion and adhesives. 2011;31(6):513–23.
6. Frihart C. Wood adhesion and adhesives. New York: CRC Press; 2005.
7. Crocombe A. A. Single lap joint geometry. In: Da Silva L, Öchsner A, editors. Modeling of adhesively bonded joints. Springer; 2008.
8. Dunky M. Urea-formaldehyde (UF) adhesive resins for wood. International Journal of Adhesion and Adhesives. 1998;18(2):95–107.
9. Pizzi A, Mittal K. Wood adhesives. CRC Press; 2011.
10. Poljanšek I, Fabjan E, Moderc D, Kukanja D. The effect of free isocyanate content on properties of one component urethane adhesive. International Journal of Adhesion and Adhesives. 2014;51:87–94.
11. Uyanik N, Yalçinkaya H, Kizilcan N. Poly (dimethyl siloxane)-containing five-block copolymers: effects of resin blocks. Surface Coatings International Part B: Coatings Transactions. 2001;84(4):309–16.
12. Gruenewaelder B, Schoetmer B, Haller W, Ness B, Single-Component Polyurethane Adhesive United States Patent US 7,259,207 B2 Aug. 21, 2007
13. Frangi A, Fontana M, Mischler A, Shear behavior of bond lines in glued laminated timber beams at high temperatures. Wood Sci Technol (2004) 38: 119–126
14. Richter K, Pizzi A, Despres. Thermal stability of Structural One- Component Polyurethane Adhesives for Wood-Structure-Property Relationship. Journal of Applied Polymer Science. 2006;102:5698–5707
15. Kızılcan N, Ustamehmetoğlu B. Chemical polymerization of pyrrole in the presence of ketone-formaldehyde resins. Journal of Applied Polymer Science. 2005;96(3):618–24.
16. Uhl FM, Davuluri SP, Wong S-C, Webster DC. Polymer films possessing

nanoreinforcements via organically modified layered silicate. Chemistry of materials. 2004;16(6):1135-42.

17. Chaiko DJ, Leyva AA. Thermal transitions and barrier properties of olefinic nanocomposites. Chemistry of materials. 2005;17(1):13-9.

18. Ionescu M. Chemistry and technology of polyols for polyurethanes. 2nd edition. Vol. 1. Shawbury, Shrewsbury, Shropshire, United Kingdom: Smithers Rapra; 2016.

19. F. Merger, G. Schleier and D. Schlotterbeck, Germ. Offen. DE 3,624,924(1988).



Characterization of a Bentonite and Its Permanent Aqueous Suspension

Fatma Eda Özgülven¹  , Abdullah Devrim Pekdemir¹  , Müşerref Önal^{2,*}  ,
Yüksel Sarıkaya²  

¹Graduate School of Natural and Applied Sciences, Ankara University, Ankara, Turkey

²Department of Chemistry, Faculty of Science, Ankara University, Ankara, Turkey

Abstract: A bentonite sample taken from Reşadiye (Tokat/Turkey) deposit was mixed with distilled water. The formed permanent aqueous suspension was separated by decantation from the flocculated solid fraction. The deflocculated mass percent of the bentonite was evaluated almost 60% by weighing. The bentonite and its permanently suspended solid fraction are examined by using X-ray diffraction, chemical, thermal, cation exchange, and particle size analyses. Mineralogy and chemical composition of the samples were discussed with respect to the experimental results. A sodium-rich aluminum, iron, and magnesium smectite was determined as the major clay mineral in the bentonite and also illite as minor one. Clinoptilolite, plagioclase, quartz, opal-CT, calcite, magnesite, and dolomite are the nonclay minerals found in the bentonite as impurities. The suspension contains large amount sodium-rich smectite and plagioclase whereas lesser opal-CT. Particle size of the bentonite and deflocculated fraction was found to be lesser than 11 μm and 2 μm , respectively.

Keywords: Bentonite, Cation exchange capacity, Mineralogy, Smectite, Suspension.

Submitted: March 05, 2019. **Accepted:** October 03, 2019.

Cite this: Özgülven F, Pekdemir A, Önal M, Sarıkaya Y. Characterization of a Bentonite and Its Permanent Aqueous Suspension. JOTCSA. 2020;7(1):11-8.

DOI: <https://doi.org/10.18596/jotcsa.535937>.

***Corresponding author. E-mail:** onal@science.ankara.edu.tr. Tel.: +90 312 21267 20 / 1173.
Fax: +90 312 2232395.

INTRODUCTION

Natural sedimentary rocks which contain a smectite to be major clay mineral is called as bentonite. Besides smectites, bentonites also include other clay and nonclay minerals as impurities with the different contents (1). Smectites are the ionic compounds but undissolved in water. Their multiatomic anions are hydrated and hydroxylated aluminum, iron, magnesium or lithium silicates. The corresponding monoatomic cations are Na^+ or Ca^{2+} as well as both of them and lesser amount K^+ . Clay minerals in smectite group were named according to their chemical composition such as montmorillonite, beidellite, nontronite, hectorite, and saponite (2).

Smectite anions formed from layers with the three sheets. Each layer has two silica tetrahedral (T) sheets bonded by oxygen bridges to a central alumina octahedral (O) sheet. Thus, smectites are called 2:1 (TOT) layered clay minerals (3). There are considerable substitution of Fe^{2+} , Mg^{2+} and Li^+ for Al^{3+} in the dioctahedral sheets and also less substitution of Al^{3+} for Si^{4+} in the tetrahedral sheets. Here, to have electrical neutrality, three Mg^{2+} or Fe^{2+} are needed instead of two Al^{3+} or Fe^{3+} . Smectites including more divalent or trivalent cations are distinguished as dioctahedral or trioctahedral.

The TOT (2:1) layers negatively charged depending on these ion exchanges. This negative

electrical charge is generally balanced by the Na^+ and Ca^{2+} cations diffused between the TOT layers and around their edges. These can be exchangeable with the many inorganic and organic cations. The minerals having Na^+ and Ca^{2+} ions as the major exchangeable cations are called sodium-rich smectite (NaS) and calcium-rich smectite (CaS), respectively. Generally, NaS has one water layer whereas CaS has two ones in the interlayer. NaS dispersed in water gives permanent suspension whereas CaS gives a temporary one (4-6). Natural rocks having NaS or CaS as major clay minerals are called sodium bentonite (NaB) or calcium bentonite (CaB), respectively. The equivalent amount of exchangeable cations in unit mass such as one kilogram of smectite or bentonite is defined to be cation exchange capacity (CEC). The high layer charge and cation exchange capacity, high nanoporosity and surface area, fine particle size and also swelling capacity, high viscosity and thixotropy of their aqueous suspension are the excellent physicochemical properties of the smectites as well as bentonites (7-10).

Natural and chemically modified bentonites are used either directly or as an industrial raw materials in a large number areas depending on the physicochemical properties (11-13). Some of the areas directly used are drilling mud, dam filler, foundry sand binder, pat litter, ceramic, crayons, cement, desiccants, and agricultural carriers (14). Some of the modified bentonite and their major clay mineral smectites are used as decolorization earth, catalyst, pillared clay, organoclay, and polymer-clay nanocomposites (15-17). They are also used as an additive to prepare paints, cosmetics, adhesives, emulsion stabilizers, animal feed bonds, and cleaning agents. Pure smectite minerals are rarely found in the nature. Therefore, they would be isolated from bentonites.

The usage area and economic value of bentonites change depending on the type, crystal structure, and physicochemical properties of their smectite as well as other clay and nonclay minerals. Beside smectite other clay minerals are harmless for human health whereas the crystalline silicas such as quartz, cristobalite, and tridymite as well as a zeolite mineral named erionite are harmful (18-20). Fly powder of these minerals of less than 5 μm particle size and 0.1% by mass in a bentonite would cause to an illness called as silicosis. Therefore, the aim of the present study is to characterize the minerals in a bentonite and its permanent aqueous suspensions.

MATERIAL AND METHODS

A light yellow-colored bentonite sample taken from Reşadiye (Tokat, Turkey) bed was used as

the main material in this study. A sample having the mass of 10 g was weighed from the bentonite powder which is previously dried at 100 °C for 2 hours. The sample was mixed with 0.5 L of distilled water in a beaker. The resulting heterogeneous mixture was stirred for one day and then left to stand. After one week, the permanent suspensions was removed by pulling with a pipette. This decantation process was repeated until it does not form any permanent suspension. The consecutive suspensions were accumulated in a beaker and heated until the water was removed. The formation of the permanent aqueous suspension indicated that the separated fraction contain a sodium-rich smectite as the major clay mineral. The Brunauer-Emmett-Teller (BET) specific surface area (S), specific nanopore volume (V) and nanopore size distribution of bentonite (BE) and also separated fraction (SF) were determined in an our previous study (21). According to this, S values for BE and SF are 27 and 43 m^2g^{-1} as well as V values 0.055 and 0.065 $\text{cm}^3 \text{g}^{-1}$, respectively.

The X-ray diffraction (XRD) patterns for the bentonite (BE) and separated fraction (SF) were recorded from random mounts prepared by glass slide method using a Rikagu D-Max 2200 Powder Diffractometer. It operates at 40 kV and 30 mA, using Ni filtered $\text{CuK}\alpha$ radiation having 0.15418 nm wavelength at a scanning speed of 2° 2 θ min^{-1} .

The BE and SF samples were digested in a furnace at 1000 °C for 2 h and weighed after cooling to the room temperature. The mass loss by this process was taken as loss on ignition (LOI). Chemical analysis of the samples were performed as the mass percent of metal oxides by using a Hitachi Z-2200 Atomic Absorption Spectrophotometer.

Cation exchange capacity for the BE and SF samples were determined by the methylene blue method (22). Aqueous suspensions of BE and SF were prepared by mixing 2 g of the sample and 300 mL of distilled water. The pH values of these suspensions were adjusted in the interval of 2.5 and 3.8 by using 0.05 M H_2SO_4 solution. The prepared suspensions were titrated with 0.01 M aqueous methylene blue solution. The end of the titration was determined by the blue coloration of the suspension on a filter paper.

Thermal gravimetric analysis (TG) and differential thermal analysis (DTA) plots of the BE and SF samples were recorded between 25 and 1400 °C with the heating rate 10 Kmin^{-1} and $\alpha\text{-Al}_2\text{O}_3$ was used as inert material.

Particle size distribution of the BE and SF samples in their aqueous suspensions were

determined by using a Mastersizer Instrument based on a light scattering technique. The content of the BE and SF samples are 0.0187 and 0.0071 as Vol. % in the suspensions, respectively.

RESULTS AND DISCUSSION

Mass fraction of the deflocculated solid

Mass of the SF was determined to be 6 g in the permanent aqueous suspension which is formed on the heterogeneous mixture of 10 g of BE and 0.5 L of distilled water. Accordingly, the mass fraction (χ) of SF in BE must be:

$$\chi = 6 \text{ g}/10 \text{ g} = 0.6 \quad (\text{Eq. 1})$$

Namely, the content of the SF in the BE is 60% by mass.

XRD- analyses

XRD pattern of the BE and SF are respectively given in Figures 1 and 2. Accordingly, major and minor clay minerals in bentonite are a sodium-rich smectite (NaS) and an illite (I), respectively (23). Illites are 2:1 layered minerals as well as smectites but they contain almost

unexchangeable K^+ cations between the layers instead of exchangeable Na^+ and Ca^{2+} . There are also clay minerals contained mixture of smectite and illite layers in different ratios. Nonclay minerals such as silica, carbonate, feldspar, and zeolite are found in the bentonite in various contents as impurities. Opal-A (OA: $SiO_2 \cdot nH_2O$), opal-CT (OCT: $SiO_2 \cdot nH_2O$), and quartz (Q: SiO_2) are the amorphous, paracrystalline and crystalline silica polymorphs, respectively. Calcite (C: $CaCO_3$), magnesite (M: $MgCO_3$), and dolomite (D: $CaCO_3 \cdot MgCO_3$) are the carbonate minerals. Clinoptilolite (Cln) is a zeolite that is the non-hydroxylated but hydrated silicate mineral. The chemical formula for the clinoptilolite is given nearly as $(Na,Ca)_{4-6}Al_6(Al,Si)_4Si_{29}O_{72} \cdot 24H_2O$. Plagioclase (PO) found in the bentonite is a feldspar that are the non-hydroxylated and non-hydrated silicate mineral. Plagioclase is a mixture of the albite ($NaAlSi_3O_8$) and anorthite ($CaAlSi_2O_8$) minerals. Its general chemical formula can be given in the following form $Na_xCa_yAl_{x+2y}Si_{3x+2y}O_8$ where $x+y=1$ and $0 \leq y \leq 1$. Plagioclase is a ceramic flux as well as other feldspars. Although their crystal structures are different the chemical composition of clay, feldspar and zeolite minerals are close to each other.

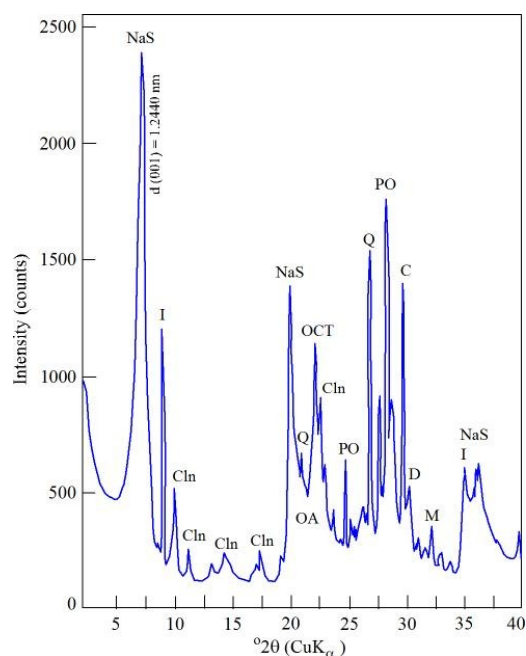


Figure 1. The XRD-pattern for the natural bentonite (NaS: Sodium smectite, I: Illite, Cln: Clinoptilolite, OA: Opal-A, OCT: Opal-CT, Q: Quartz, PO: Plagioclase, C: Calcite, D: Dolomite, M: Magnesite).

The SF contains feldspar and lesser opal-CT as the impurities. Evaluating of the XRD-reflection at $2\theta=28.2^\circ$ indicated that the feldspar is a plagioclase. The position (2θ) intensity (I) and full width at half maximum (FWHM) peak height

for the sodium smectite (NaS) and plagioclase (PO) minerals were evaluated and represented on the Figure 2. The type, abundance, and crystallite for a mineral are characterized by the position, intensity and width of the major XRD reflections.

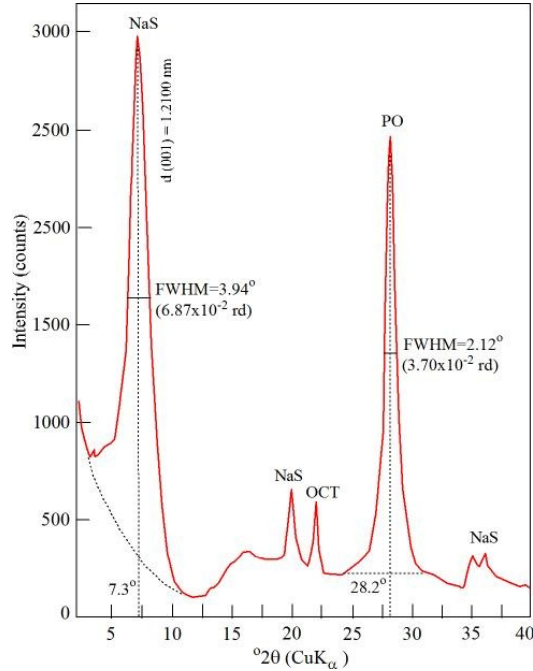


Figure 2. The XRD-pattern for a fraction (SF) of the natural bentonite (BE) that is permanently deflocculated in water (NaS: Sodium smectite, OCT: Opal-CT, PO: Plagioclase)

The XRD reflection at $2\theta=7.3^\circ$ is the most characteristic for sodium-rich smectite (NaS). This peak results from diffraction of X-rays with the wavelength $\lambda= 0.15418 \text{ nm}$ reflected by the successive 2:1 (TOT) layer surfaces ($n=1$).

Accordingly, the total thickness (d) of the TOT and a water layers located in the interlayer position is calculated from the Bragg equation in the following form:

$$d = \frac{n\lambda}{2 \sin \theta} = \frac{1(0.15418 \text{ nm})}{2 \sin (7.3/2)^\circ} = 1.21 \text{ nm} \quad (\text{Eq. 2})$$

Ideal value of the of d for NaS and CaS is 1.2 nm and 1.5 nm, respectively. For this reason, the clay minerals permanently separated in water is called sodium-rich smectite.

XRD reflection of NaS is evaluated to be 3.94° ($6.87 \times 10^{-2} \text{ rd}$) as indicated in Figure 1. The average size (23) of the smectite crystal in the direction perpendicular to the reflection surfaces is calculated from the Scherrer equation (24) in the following form:

Full width at half maximum (FWHM) peak height above background for the most characteristic

$$L = \frac{K \lambda}{FWHM \cos \theta} = \frac{10(0.15418 \text{ nm})}{(6.87 * 10^{-2} \text{ rd}) \cos(\frac{7.3}{2})^\circ} = 25.29 \text{ nm} \quad (\text{Eq. 3})$$

where $K=10$ is a constant when unit of wavelength is nm.

Similarly, the d and L parameters for the plagioclase (PO) were calculated given as follows:

$$d = \frac{n\lambda}{2 \sin \theta} = \frac{1(0.15418 \text{ nm})}{2 \sin (28.2/2)^\circ} = 0.32 \text{ nm} \quad (\text{Eq. 4})$$

$$L = \frac{K\lambda}{FWHM \cos \theta} = \frac{10(0.15418 \text{ nm})}{(3.70 \times 10^{-2} \text{ rd}) \cos(28.2/2)^\circ} = 42.98 \text{ nm} \quad (\text{Eq. 5})$$

where 2θ and FWHM values were taken from Figure 2. These are larger than those of smectite.

Chemical analysis

Chemical analyses of the BE and SF samples are given in Table 1 as mass percentages of the metal oxides. Since the chemical composition of smectites and other silicate minerals are close to each other there is no great significant change between the chemical analyses. However, the

greater percentages of Al_2O_3 , Fe_2O_3 and MgO in SF than those of BE are due to the spontaneous transfer of NaS and plagioclase into the aqueous suspension. The lesser percentages of CaO in SF revealed that the calcium-rich smectite, calcite, and dolomite minerals do not spontaneously deflocculated into water. Consequently, clay mineral in the suspension would be a sodium-rich aluminum, iron, and magnesium smectite.

Table 1. Chemical analysis of the bentonite (BE) and its permanently separated fraction (SF) in water.

Samples	SiO_2	Al_2O_3	Fe_2O_3	MgO	TiO_2	CaO	Na_2O	K_2O	IOL
BE	62.60	16.65	3.44	1.63	0.29	3.37	2.59	0.98	8.45
SF	61.97	19.73	4.74	2.40	0.22	0.91	2.58	0.38	7.08

Cation exchange capacity

The exchangeable cations of smectite minerals can be quantitatively displaced with the methylene blue cations (22). Cation exchange capacity of BE and SF were determined as 65 and 108 meq/100 g, respectively. Thus, the mass percent of SF in BE would be as follows:

$$x = \frac{65 \text{ meq}/100 \text{ g}}{108 \text{ meq}/100 \text{ g}} = 0.60 \quad (\text{Eq. 6})$$

This result revealed that the feldspar mineral found in SF has exchangeable cations such as Na^+ and Ca^{2+} as well as smectites. This value matched to the mass ratio determined by the weighing as the mentioned above.

Thermal analysis

The TG/DTA patterns for the BE and SF samples are respectively given in Figures 3 and 4. While the temperature is increasing in the range of 25 and 450 °C, the endothermic mass decreases are caused from the loss of the zeolitic as well as hydration water in the minerals. The endothermic mass decreases in the temperature interval of 450 and 750 °C are only due to the dehydroxylation of clay minerals. The mass loss for the BE and SF samples is evaluated from the TG curves as 5.3% and 4.4%, respectively. The exothermic peaks located between 900 and 1000 °C are due to the decomposition of the silicate minerals in the bentonite which are mentioned above. The endothermic peaks at almost 1200 °C are caused from the melting of the plagioclase which is a fluxing material for ceramic industry.

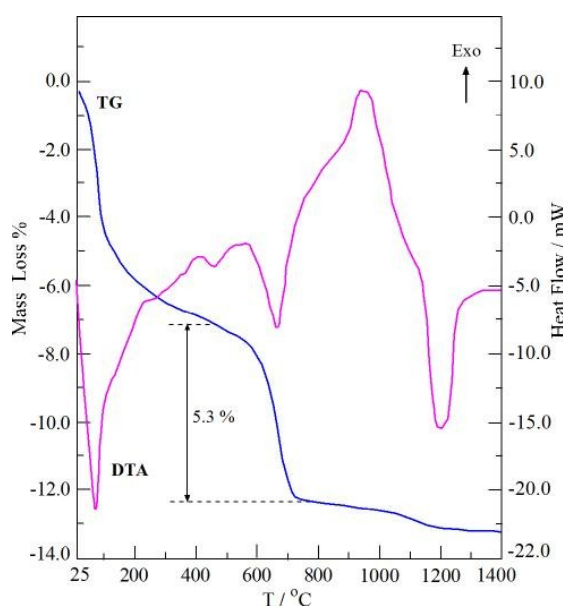


Figure 3. The TG/DTA curves for the natural bentonite (BE).

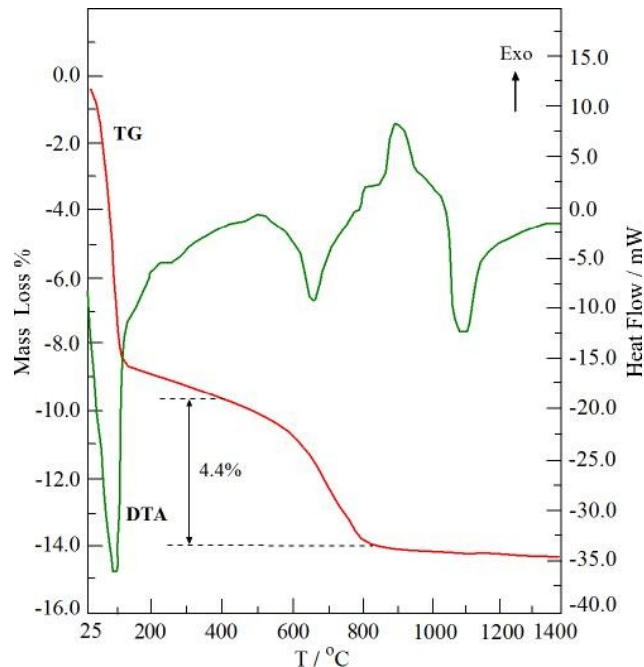


Figure 4. The TG/DTA curves for a fraction (SF) of the natural bentonite (BE) that is permanently deflocculated in water.

Particle size distribution

The particle size distribution curves of the BE and SF sample are given in Figures 5 and 6. Two peaks laying on the size interval lesser than 2 μm would be caused from the smectite and plagioclase which are spontaneously deflocculated in water. This result also showed that the particle size of quartz is larger than 2 μm. The third peak in Figure 5 is originated from other clay and nonclay particles that are

spontaneously flocculated fraction of the bentonite in a short time. Thus, the volume percent of the deflocculated particles was read from the cumulative particle size curve to be 0.60 as represented in Figure 5. This value is completely match with the mass percent found above. This equality revealed that the mean density of the BE and SF is almost equal each other.

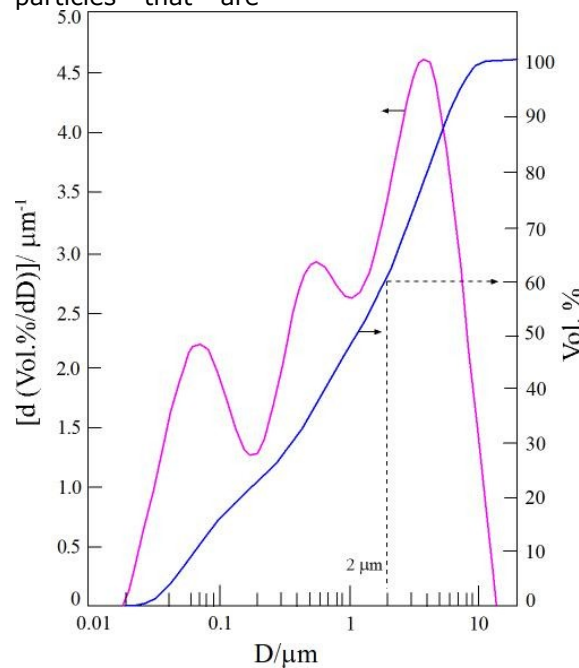


Figure 5. The cumulative and differential particle size distribution curves of the natural bentonite (BE).

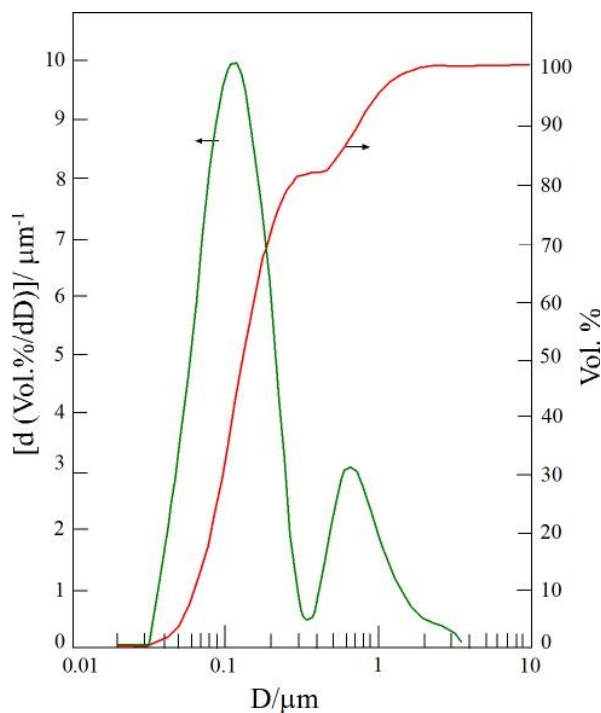


Figure 6. The cumulative and differential particle size distribution curves for a fraction (SF) of the natural bentonite (BE) that is permanently deflocculated in water.

CONCLUSION

The microsized particles of minerals formed from the agglomeration of their nanosized crystals. A bentonite and its fraction which is permanently deflocculated in water would be extensively investigated to obtain using areas and economic value. Mineralogy, chemical composition, and several physicochemical properties such as cation exchange capacity, thermal behavior, and particle size distribution of the samples should be discussed according to the possible uses. The evidence of the minerals such as quartz, cristobalite, tridymite, and erionite which are harmful for human health are ought to be precisely investigated. For example, there is quartz in the examined bentonite with the particle size larger than 2 μm , but it is not permanently deflocculated in water. So, this harmless fraction may be used to prepare organoclays, pillared clays, electrodes, and clay-polymer nanocomposites. On the other hand; drilling mud, foundry sand binder, and dam filler preparation are seen the possible uses areas of the natural bentonite. Because of the bentonite contains harmful quartz the workers must use dust masks.

ACKNOWLEDGMENTS

The authors thank to Research Foundation of Ankara University (Project No:17H0430010) for financial support to this work.

REFERENCES

1. Grim RE. The history of the development of clay mineralogy. *Clays and Clay Minerals*. 1988;36:97-101
2. Grim RE, Güven N. *Bentonites- Geology, Mineralogy, Properties and Uses*. Developments in Sedimentology, 24. Elsevier; New York, 1978.
3. Grim RE. *Clay Mineralogy*, McGraw-Hill; New York, 1968.
4. Bergman WE and Fisher HB. Bentonite suspensions. *Industrial and Engineering Chemistry*. 1950;42:1895-1900.
5. Luckham PL, Rossi S. The colloidal and rheological properties of bentonite suspensions. *Advanced in Colloid and Interface Science*. 1999;82:43-92.
6. Minase M, Kondo M, Onikato M, Kawamura K. The viscosity of suspensions of bentonite. *Clay Science*. 2006;12:125-130.
7. Rollins MB. Sealing properties of bentonite suspensions, *Clays and Clay Minerals*. 1969;16:415-423.
8. Zhu R, Chen Q, Zhou Q, Xi Y, Zhu J, He H. Adsorbates based on montmorillonite for contaminant removal from water: a review. *Applied Clay Science*. 2016;123: 239-258.

9. Uddin MK. A review on the adsorption of heavy metals by clay minerals, with special focus on the past decade. *Chemical Engineering Journal*. 2017;308:438-462.
10. Derakhshany E, Naghizadeh A. Optimization of humic acid removal by adsorption onto bentonite and montmorillonite nanoparticles. *Journal of Molecular Liquids*. 2018;259:76-81.
11. Noyan H, Önal M, Sarıkaya Y. The effect of heating on the surface area, porosity and surface acidity of a bentonite. *Clay and Clay Minerals*. 2006;54:375-381.
12. Noyan H, Önal M, Sarıkaya Y. The effect of sulphuric acid activation on the crystallinity, surface acidity, and bleaching power of a bentonite. *Food Chemistry*. 2007;105:156-163.
13. Komadel P. Acid activated clays: Materials in continuous demand. *Applied Clay Science*. 2016;131:84-99.
14. Murray HH. Traditional and new applications for kaolin, smectite, and palygorskite: a general overview. *Applied Clay Science*. 2000;17:207-221.
15. Çelik M, Önal M. Synthesis and characterization of poly(glycidyl methacrylate)/Na-montmorillonite nanocomposites. *Journal of Applied Polymer Science*. 2004;94:1532-1538.
16. Çelik M, Önal M. Polymethacrylamide/Na-montmorillonite nanocomposites synthesized by free-radical polymerization. *Material Letters*. 2006;60:48-52.
17. Silva SM, Sampaio KA, Ceriani R, Verhe R, Stevens C, De Greyt W, Meirelles JA. Effect of type of bleaching earth on the final color of refined palm oil. *LTW-Food Science and Technology*. 2014;59:1258-1264.
18. Elzea JM, Odom IE, Miles WJ. Distinguishing well ordered opal-CT and opal-C from high temperature cristobalite by X-ray diffraction. *Analytica Chimica Acta*. 1994;286:107-116.
19. Elzea JM, Rice SB. TEM and X-ray diffraction evidence for cristobalite and tridymite stacking sequences in opal. *Clays and Clay Minerals*. 1996;44:492-500.
20. Önal M, Kahraman S, Sarıkaya Y. Differentiation of α -cristobalite from opals in bentonites from Turkey. *Applied Clay Science*. 2007;35:25-30.
21. Önal M, Sarıkaya Y, Alemdaroğlu T, Bozdoğan İ. Isolation and characterization of a smectite as a micro-mesoporous material from a bentonite. *Turkish Journal of Chemistry*. 2003;27:683-693.
22. Yener N, Biçer C, Önal M, Sarıkaya Y. Simultaneous determination of cation exchange capacity and surface area of acid activated bentonite powders by methylene blue sorption. *Applied Surface Science*. 2012;258: 2534-2539.
23. Moore DM, Reynolds, Jr RC. X-ray diffraction and the Identification and Analysis of Clay Minerals. Oxford University Press; Oxford, 1997.
24. Patterson A. The Scherrer formula for X-ray particle size determination. *Physical Review*. 1939;56:978-982.



Synthesis and Spectroscopic Characterization of Protic Tris(2-Hydroxyethyl)-Ammonium Ionic Liquids

Hüseyin AKBAŞ^{1,*}  

¹Department of Chemistry, Tokat Gaziosmanpaşa University, 60250, Tokat, Turkey

Abstract: Protic ionic liquids (PILs) having tris(2-hydroxyethyl)ammonium (or triethanolammonium) as cations and methacrylate, dihydrogenborate, formate, and acetate as anions have been synthesized through stoichiometric neutralization reaction. PILs have been characterized by elemental analyses, FTIR, ¹H and ¹³C NMR spectroscopic methods. The viscosity of **PIL4** was measured using a cone-and-plate viscometer at ambient temperature. The viscosity value indicates that the fluidity of **PIL4** is 829 cP (the viscosity of water is 0.7977 cP at 30 °C).

Keywords: Protic ionic liquids, Spectroscopy, Synthesis, Triethanolammonium salts, Viscosity.

Submitted: August 28, 2019. **Accepted:** October 07, 2019.

Cite this:

DOI: <https://doi.org/10.18596/jotcsa.612396>.

***Corresponding author. E-mail:** huseyin.akbas@gop.edu.tr.

INTRODUCTION

In general, ionic liquids (ILs) are liquid at temperatures below 100 °C and those liquids can remain fluid in a wide temperature range (1). ILs have attracted intense interest in both academia and industry in recent years due to their impressive properties such as low volatility, high dissolution capacity, large electrochemical window, and high thermal and electrical conductivity (2-4). One of the most important properties of ILs is their environmentally friendly and non-hazardous nature due to negligible vapor pressures. Thus, ILs have recently been of great interest as green chemicals rather than conventional solvents (5).

PILs are obtained by proton transfer between a Brønsted acid and a Brønsted base (6). An equimolar amount of acid and base react together in a uniform or aqueous solution. In general, the rest of ILs can be classified as aprotic ILs (AILs), but there are some subclasses similar to PILs such as Brønsted acidic ILs, which are typically functionalized to have a proton

present on the anion. PILs have many applications as lubricants (7, 8), biologically active materials (9, 10), electrolytes (11-13), catalysts (14 15), etc.

Hydroxylammonium-based PILs have hydrogen bond donor properties that significantly increase their applications. Hydroxylammonium IL has been used to dissolve many insoluble polymers such as zein (an industrially important natural polymer), polyaniline and polypyrrole (16). The effect of the hydroxyl group on the dissolution with polar solvents in this type of IL was disclosed by determining the solvatochromic parameter (17). Nowadays, aqueous monoethanolamine has been used for the removal of CO₂ from natural gas in industrial processes due to serious environmental concerns about volatility, recovery and abrasiveness (18). Yuan et al. synthesized a series of hydroxylammonium ILs and determined the solubility of SO₂ at atmospheric pressure (19). Garaev et al. found that hydroxylammonium-based ILs with carboxylate anion are highly biodegradable and practically non-toxic (20).

Ahfad-Hosseini et al. developed a new method for the synthesis of celecoxib (a selective COX-2 inhibitor) with high yield and least environmental hazard using tris-(2-hydroxyethyl)ammonium acetate (II) as IL and evaluated the effect of IL concentration and reaction temperatures on the yield of celecoxib production (21). Furthermore, the physicochemical properties of hydroxylammonium-based ILs such as glass transition temperature, density, conductivity, sound velocity, viscosity and decomposition temperature at different temperatures have been studied intensively (22-25).

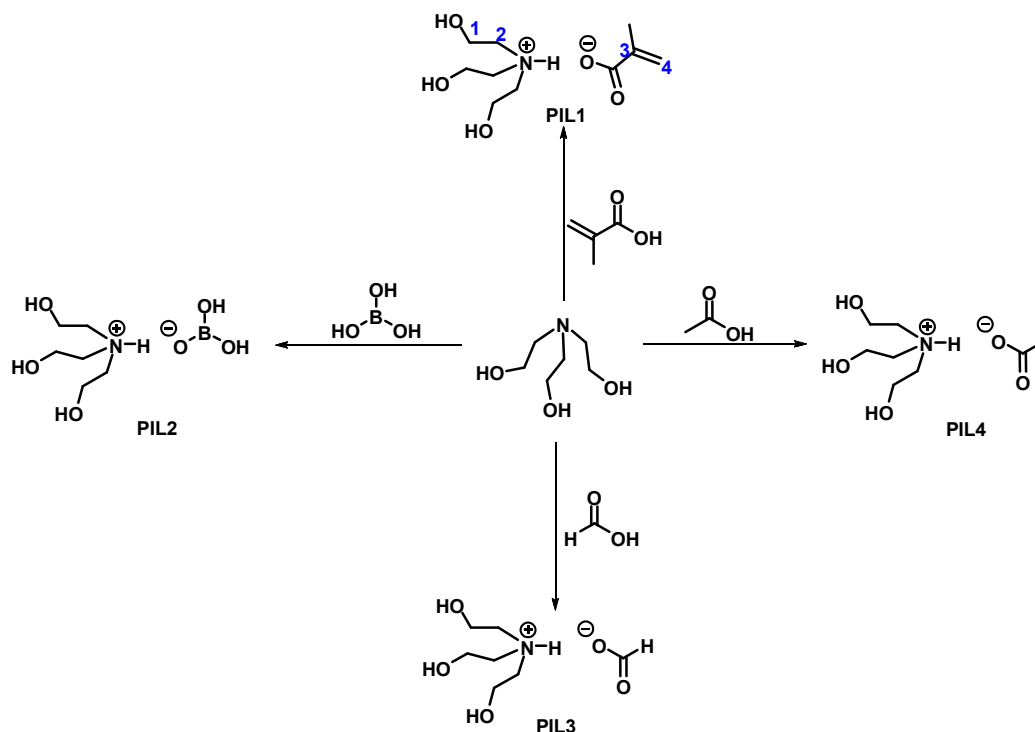
Herein, the PILs consisting of tris(2-hydroxyethyl)ammonium cation and anions of different inorganic or carboxylic acids have been obtained, and these are tris(2-hydroxyethyl)ammonium methacrylate (**PIL1**), tris(2-hydroxyethyl)ammonium dihydrogenborate (**PIL2**), tris(2-hydroxyethyl)ammonium formate (**PIL3**) and tris(2-hydroxyethyl)ammonium acetate (**PIL4**) (Scheme 1). The structure of the synthesized PILs was determined by elemental analysis, FTIR, ^1H and ^{13}C NMR techniques. The

viscosity has been measured at atmospheric pressure with ambient temperature.

EXPERIMENTAL

Material and Methods

Triethanolamine, methacrylic acid, boric acid, formic acid, and acetic acid were purchased from commercial sources and used without further purification. ^1H - and ^{13}C -NMR spectra of the PILs were measured using AC Bruker 400 MHz NMR spectrometer in Methanol- d_4 and D_2O at ambient temperature. FT-IR spectra were recorded on a Jasco FT-IR 4700 spectrometer in the range of 400-4000 cm^{-1} . Elemental analyses were recorded on a Elementar Vario Micro Cube elemental analyzer. The viscosity of **PIL4** was measured using a Brookfield DV2TRVCP Viscometer. The cone and plate method was used where the sample (0.5 mL) was placed between a 2 cm cone and a flat plate. The cone was made to rotate and the viscosity of the sample was measured.



Scheme 1. The scheme represents the PILs.

General procedure for the synthesis of PILs 1-4

The PILs were synthesized according to the previous literature (26). A mixture of triethanolamine (5.00 g, 33.51 mmol) and methacrylic acid (2.89 g, 33.51 mmol), boric acid (2.07 g, 33.51 mmol), formic acid (1.54 g, 33.51

mmol) or acetic acid (2.01 g, 33.51 mmol) is prepared in 1:1 molar ratio. Triethanolamine is placed in a two-necked 100 mL round-bottomed flask, which is fitted with a dropping funnel, and connected to a condenser. Methacrylic acid, boric acid, formic acid or acetic acid is placed in the dropping funnel, and added the acid dropwise to the diethylenetriamine in the flask. The reaction

is vigorous and the rate is controlled by regulating the addition of acid. The reaction should be complete in about 24 h. The PILs thus prepared was kept in a vacuum oven at 80 °C for 48 hours to remove excess moisture formed during the reaction. The dried solvent was sealed with laboratory parafilm to prevent any moisture contamination.

Synthesis of PIL1

Anal. Calc. for $C_6H_{16}NO_3^+(C_4H_5O_2^-)$ (%): C, 51.05; H, 9.00; N, 5.95 Found (%): C, 49.96; H, 8.98; N, 5.92. FTIR (cm^{-1}): $\hat{\nu}$ 3232 (O-H), 2922 (C-H aliph.asym.), 2876 (C-H aliph.sym.), 1644 (C=C), 1551, 1445 (COO⁻), 1062 (C-N). ¹H NMR (D₂O, ppm, numberings of protons are given in Scheme 1): 3.91 (t, 6H, ³J_{HH} = 4.7 Hz, **H₁**), 3.38 (t, 6H, ³J_{HH} = 4.7 Hz, **H₂**), 5.62; 5.31 (d, 2H, ²J_{HH} = 1.0 Hz, **H₄**), 1.84 (s, 3H, **CH₃**), 4.69-8.04 (m, 4H, HN⁺, OH). ¹³C NMR (D₂O, ppm, numberings of carbons are given in Scheme 1): 55.55 (**C₁**), 55.36 (**C₂**), 177.38 (C=O), 142.42 (**C₃**), 120.24 (**CH₃**), 18.92 (**C₄**).

Synthesis of PIL2

Anal. Calc. for $C_6H_{16}NO_3^+(BH_2O_3^-)$ (%): C, 34.15; H, 8.60; N, 5.12 Found (%): C, 34.23; H, 8.41; N, 5.18. FTIR (cm^{-1}): $\hat{\nu}$ 3270 (O-H), 2951 (C-H aliph.asym.), 2877 (C-H aliph.sym.), 1369 (B-O), 1065 (C-N). ¹H NMR (methanol-d₄, ppm, numberings of protons are given in Scheme 1): 3.88 (t, 6H, ³J_{HH} = 5.8 Hz, **H₁**), 3.21 (t, 6H, ³J_{HH} = 5.8 Hz, **H₂**), 3.61-8.06 (m, 6H, HN⁺, OH). ¹³C NMR (methanol-d₄, ppm, numberings of carbons are given in Scheme 1): 63.01 (**C₁**), 59.70 (**C₂**).

Synthesis of PIL3

Anal. Calc. for $C_6H_{16}NO_3^+(CHO_2^-)$ (%): C, 43.07; H, 8.78; N, 7.18 Found (%): C, 43.38; H, 8.96; N, 7.22. FTIR (cm^{-1}): $\hat{\nu}$ 3239 (O-H), 2935 (C-H aliph.asym.), 2876 (C-H aliph.sym.), 1588, 1439 (COO⁻), 1060 (C-N). ¹H NMR (methanol-d₄, ppm, numberings of protons are given in Scheme 1): 3.77 (t, 6H, ³J_{HH} = 5.3 Hz, **H₁**), 3.24 (t, 4H, ³J_{HH} = 5.3 Hz, **H₂**), 8.43 (s, 1H, **-H**), 4.77-7.99 (m, 4H, HN⁺, OH). ¹³C NMR (methanol-d₄, ppm, numberings of carbons are given in Scheme 1): 57.35 (**C₁**), 57.16 (**C₂**), 169.95 (C=O).

Synthesis of PIL4

Anal. Calc. for $C_6H_{16}NO_3^+(C_2H_3O_2^-)$ (%): C, 45.92; H, 9.15; N, 6.69 Found (%): C, 46.13; H, 8.91; N, 6.82. FTIR (cm^{-1}): $\hat{\nu}$ 3187 (O-H), 2924 (C-H aliph.asym.), 2864 (C-H aliph.sym.), 1563, 1397 (COO⁻), 1062 (C-N). ¹H NMR (methanol-d₄, ppm, numberings of protons are given in Scheme 1): 3.70 (t, 6H, ³J_{HH} = 5.4 Hz, **H₁**), 3.05 (t, 6H, ³J_{HH} =

5.4 Hz, **H₂**), 1.83 (s, 3H, **-CH₃**), 4.77-7.97 (m, 4H, HN⁺, OH). ¹³C NMR (methanol-d₄, ppm, numberings of carbons are given in Scheme 1): 58.31 (**C₁**), 57.49 (**C₂**), 23.14 (**CH₃**), 178.80 (C=O).

RESULTS AND DISCUSSION

Tris(2-hydroxyethyl)ammonium cation based PILs were synthesized by proton transfer between an equimolar amount of triethanolamine, and different acids such as methacrylic acid, boric acid, formic acid or acetic acid (Scheme 1). The triethanolamine and various acids have been selected based on their structural properties and availability. At room temperature, **PIL4** is liquid, while **PIL1-3** are quasi-solid state. All the PILs were soluble in polar protic solvents such as water, methanol, and ethanol. There are publications in which the triethanolamine salt (**PIL3** and **PIL4**) containing formic and acetic acid is indicated (20, 21, 27). However, only ¹H NMR (using DMSO as a solvent) and FT-IR (using a NaCl disk) spectroscopic techniques were used for structural characterization. A structural study based on NMR (¹H- and ¹³C-) spectroscopy of the prepared PILs was subsequently performed in concordance with FT-IR spectra and elemental analysis. Thus, these studies have confirmed the presence of protonated amine.

The chemical shifts, multiplicities and coupling constants of all PILs were determined by interpreting the ¹H and ¹³C NMR signals (Supplementary Material, Figures S1-8), and are presented in the "Experimental Section". The three PILs could easily be dissolved in methanol-d₄, except **PIL1**. For the triethanolammonium cation, the resonance signals of the CH₂ group protons (3.91-3.70 ppm for **H₁** and 3.38-3.05 ppm for **H₂**) in the ¹H NMR spectra of PILs are downfield-shifted compared to the original triethanolamine (3.46 ppm for **H₁** and 2.57 ppm for **H₂**) (28). The chemical shift does not exceed 0.8 ppm. The average coupling constant, ³J_{HH}, is 5.3 Hz. Both the OH and the NH resonances are relatively broad at 3.61-4.77 ppm and 7.97-8.06 ppm, respectively. Further, the carboxylic acid proton (-COOH) at about 8-12 ppm (29) was not observed in the ¹H NMR spectra of the **PIL1**, **PIL3** and **PIL4**. This may be indicative of the formation of PILs. ¹³C NMR chemical shifts of the triethanolammonium cation in the spectra of the studied PILs are in the range of 63.01-55.55 ppm for the neighboring the oxygen atom (**C₁**), while those of the protons adjacent to the nitrogen atom (**C₂**) are in the range of 59.70-55.36 ppm. On the other hand, the carbonyl carbon atoms (C=O) of the **PIL1**, **PIL3** and **PIL4** were

observed at 177.38, 169.95 and 178.80 ppm, respectively.

In tris(2-hydroxyethyl)-ammonium based PILs, the proton of the acid is located on the onium nitrogen atom (N^+H) in the cation and forms trifurcate hydrogen bonds with three hydroxyethyl groups resulting in the formation of the tricyclic protatran cation (30, 31). Therefore, these PILs are known as protatrans (Figure 1).

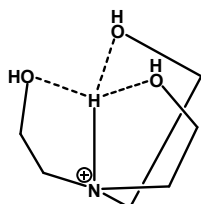


Figure 1. The structure of the tris(2-hydroxyethyl)-ammonium cation (protatran).

The results of the FT-IR analyses were very similar for all of the PILs. In the absorption IR spectra of the obtained PILs, a broad characteristic ammonium band of $\nu(N^+H)$ was observed in the range of 2400–3000 cm^{-1} (Figure S9). In the FT-IR spectrum of triethanolamine, the strong band at 3303 cm^{-1} corresponds to the stretching vibrations of the OH groups involved in intramolecular hydrogen bonds. The wide band of $\nu(OH)$ resulting from the high symmetry of the molecules of the PILs was found at about 3232 cm^{-1} . This band is due to the vibrations of the three hydroxy groups of the triethanolammonium cation in which oxygen atoms form intramolecular hydrogen bonds with the N^+H hydrogen atom (Figure 1). A higher strength hydrogen bond formed by the OH groups of the protatran cation with the carboxylic group of the

acid anion results in $\nu(OH)$ bands at low frequencies ($\sim 3153\text{ cm}^{-1}$) (32). This explanation disagrees with the FT-IR results of the PILs, the spectrum of which does not have this band. Protatran methylene CH_2 vibrations correspond to the bands at 2951–2864 cm^{-1} . The PILs show two strong absorption bands between 1563–1551 and 1445–1397 cm^{-1} , which are assigned to the asymmetric and symmetric stretching vibrations of the carboxylate ion, $\nu(COO^-)$, respectively, indicating clearly the PIL formation. At the same time, it was known that the degree and nature of interaction between the cation and anion in protatran is reflected in the frequencies of symmetric and asymmetric vibrations $\nu(COO^-)$ (33, 34). The difference between these values ($\Delta\nu$) is used as a criterion of the structure of the molecule. The value of $\Delta\nu > 200\text{ cm}^{-1}$ points to a significant asymmetry of the carboxylic group, while the value of $\Delta\nu < 200\text{ cm}^{-1}$ is indicative of its approximate symmetry (35). The molecule of **PIL1** is characterized by the vibration bands of the carboxylate anion at 1551 [$\nu_{as}(COO^-)$] and 1445 cm^{-1} [$\nu_s(COO^-)$]. The value of $\Delta\nu$ equal to 106 cm^{-1} points to a significant symmetry of the carboxylic group. It can be assumed that other **PIL3** (149 cm^{-1}) and **PIL4** (166 cm^{-1}) with $\Delta\nu < 200\text{ cm}^{-1}$ have the structure close to that of **PIL1**.

The viscosity of the **PIL4** which was liquid at ambient temperature was measured. Considering the fluidity of **PIL4**, CP52 type spindle was used to measure the viscosity of this PIL, and viscosity value was given in Table 1. Most PILs are viscous liquids, the viscosities being comparable to and greater than the viscosity of water (water's viscosity is 0.7977 cP at 30 °C) (36). Also, the viscosity of the **PIL4** is higher compared to the initial triethanolamine (404 cP at 30 °C) (37).

Table 1. Viscosity data of **PIL4**.

Code	Viscosity (cP)	Temperature (°C)	Speed (RPM)	Torque (%)	Spindle
PIL4	829	29	60	50.1	CP-52

CONCLUSION

Four triethanolammonium-based PILs which belongs to the class of protic alkanolammonium ionic liquids, have been synthesized by proton transfer reaction from carboxylic and inorganic acids to triethanolamine. These PILs show good solubility in polar solvents (water, alcohols, etc.). The PILs have been established by elemental analysis and 1H , ^{13}C NMR, FT-IR spectroscopic methods. It is shown that the obtained spectral characteristics confirm salt formation for all the studied compounds. The structure of PILs depends on the type and strength of hydrogen bonds between the triethanolammonium cation

(protatran) and carboxylate anion, which affects the frequencies of stretching vibrations of OH and COO^- groups.

ACKNOWLEDGMENTS

The author acknowledges to Professor Ahmet Karadağ for his helpful comments.

REFERENCES

1. Wasserscheid P, Keim W. Ionic liquids- new "solutions" for transition metal

- catalysis. *Angew. Chem. Int. Ed.* 2000;39:3772-89.
2. Chhotaray PK, Gardas RL. Thermophysical properties of ammonium and hydroxylammonium protic ionic liquids. *J. Chem. Thermodynamics* 2014;72:117-24.
 3. Marcinkowski Ł, Pena-Pereira F, Kloskowski A, Namiesnik J. Opportunities and shortcomings of ionic liquids in single-drop microextraction. *Trends in Analyt. Chem.* 2015;72:153-68.
 4. Oliveria MVS, Vidal BT, Melo CM, de Miranda RCM, Soares CMF, Coutinho JAP, Ventura SPM, Mattedi S, Lima AS. (Eco) toxicity and biodegradability of protic ionic liquids. *Chemosphere* 2016;147:460-6.
 5. Earle MJ, Seddon KR. Ionic liquids. Green solvents for the future. *Pure Appl. Chem.* 2000;72:1391-98.
 6. Austen CA, Ansari Y, Zhao Z. Ionic liquids: past, present and future. *Faraday Discuss.* 2012;154:9-27.
 7. Zhao Q, Zhao G, Zhang M, Wang X, Liu W. Tribological behavior of protic ionic liquids with dodecylamine salts of dialkyldithiocarbamate as additives in lithium complex grease. *Tribol. Lett.* 2012;48:133-44.
 8. Espinosa T, Sanes J, Jiménez A, Bermúdez M. Protic ammonium carboxylate ionic liquid lubricants of OFHC copper. *Wear* 2013;303:495-509.
 9. Akbaş H, Okumuş A, Karadağ A, Kılıç Z, Hökelek T, Koç LY, Açıık L, Aydın B, Türk M. Structural and thermal characterizations, antimicrobial and cytotoxic activities, and in vitro DNA binding of the phosphazanium salts. *J. Therm. Anal. Calorim.* 2016;123:1627-41.
 10. Akbaş H, Karadağ A, Aydın A, Destegül A, Kılıç Z. Synthesis, structural and thermal properties of the hexapyrrolidinocyclotriphosphazenes-based protic molten salts: Antiproliferative effects against HT29, HeLa, and C6 cancer cell lines. *J. Mol. Liq.* 2017;230: 482-95.
 11. Nakamotoa H, Watanabe M. Brønsted acid-base ionic liquids for fuel cell electrolytes. *Chem. Commun.* 2007;2539-41.
 12. Yasuda T, Watanabe M. Protic ionic liquids: fuel cell applications. *MRS Bulletin* 2013;38:560-66.
 13. Vogl T, Menne S, Kühnel R, Balducci A. The beneficial effect of protic ionic liquids on the lithium environment in electrolytes for battery applications. *J. Mater. Chem. A* 2014;2:8258-65.
 14. Akbari J, Heydari A, Ma'mani L, Hosseini SH. Protic ionic liquid [TMG][Ac] as an efficient, homogeneous and recyclable catalyst for Boc protection of amines. *Chimie C.R.* 2010;13:544-47.
 15. Xiao L, Su D, Yue C, Wu W. Protic ionic liquids: A highly efficient catalyst for synthesis of cyclic carbonate from carbon dioxide and epoxides. *J. CO₂ Utilization* 2014;6:1-6.
 16. Choi HM, Kwon I. Dissolution of zein using protic ionic liquids: N-(2-Hydroxyethyl) ammonium formate and N-(2-hydroxyethyl) ammonium acetate. *Ind. Eng. Chem. Res.* 2011;50:2452-54.
 17. Salari H, Harifi-Mood AR, Elahifard MR, Gholami MR. Solvatochromic probes absorbance behavior in mixtures of 2-hydroxy ethylammonium formate with methanol, ethylene glycol and glycerol. *J. Sol. Chem.* 2010;39:1509-19.
 18. Bara JE, Camper DE, Gin DL, Noble RD. Room-temperature ionic liquids and composite materials: platform technologies for CO₂ capture. *Acc. Chem. Res.* 2010;43:152-59.
 19. Yuan X, Zhang S, Liu J, Lu X. Solubilities of CO₂ in hydroxyl ammonium ionic liquids at elevated pressures. *Fluid Phase Equilibria* 2007;257:195-200.
 20. Garaev V, Kleperis J, Pavlovica S, Vaivars G. Properties of the Nafion membrane impregnated with hydroxyl ammonium based ionic liquids. *IOP Conf. Ser.: Mater. Sci. Eng.* 2012;38:012064.
 21. Ahfad-Hosseini HR, Bagheri H, Amidi S. Ionic liquid-assisted synthesis of celexocib using tris-(2-hydroxyethyl)ammonium acetate as an

- efficient and reusable catalyst. *IJPR* 2017;16:158-64.
22. Anouti M, Caillon-Caravanier M, Le Floch C, Lemordant D. Alkylammonium-based protic ionic liquids part I: preparation and physicochemical characterization. *J. Phys. Chem. B* 2008;112:9406-11.
23. Pinkert A, Ang KL, Marsh KN, Pang S. Density, viscosity and electrical conductivity of protic alkanolammonium ionic liquids. *Phys. Chem. Chem. Phys.*, 2011;13:5136-43.
24. Xu Y, Yao J, Wang C, Li H. Density, viscosity, and refractive index properties for the binary mixtures of n-butylammonium acetate ionic liquid + alkanols at several temperatures. *J. Chem. Eng. Data* 2012;57:298-308.
25. Kurnia KA, Wilfred CD, Murugesan T. Thermophysical properties of hydroxyl ammonium ionic liquids. *J. Chem. Thermodynamics* 2009;41:517-21.
26. Karadağ A, Destegül A. N-(2-hydroxyethyl)-ethylenediamine-based ionic liquids: Synthesis, structural characterization, thermal, dielectric and catalytic properties. *J. Mol. Liq.* 2013;177:369-75.
27. Yuan XL, Zhang SJ, Lu XM. Hydroxyl ammonium ionic liquids: synthesis, properties, and solubility of SO₂. *J. Chem. Eng. Data* 2007;52:596-99.
28. Gruzdev MS, Shmukler LE, Kudryakova NO, Kolker AM, Safonova LP. Synthesis and properties of triethanolamine-based salts with mineral and organic acids as protic ionic liquids. *J. Mol. Liq.* 2018;249:825-30.
29. Erdik E. Organik kimyada spektroskopik yöntemler (Turkish); Gazi Büro Kitabevi: Ankara, Turkey, 1993.
30. Fundamensky VS, Kochina TA, Kondratenko YA, Zolotarev AA, Vlasov YG, Ignatyev IS. Ionic liquids based on triethanolammonium salts of dicarboxylic acids (oxalic, malonic, succinic): crystal structure and cation-anion interaction. *J. Mol. Liq.* 2017;230:113-20.
31. Kondratenko Y, Kochina T, Fundamensky V, Ignatyev I, Panikorovskii T, Nyanikova G. Triethanolammonium salicylate-protic alkanolammonium ionic liquid. *J. Mol. Liq.* 2016;221:1218-24.
32. Gruzdev MS, Shmukler LE, Kudryakova NO, Kolker AM, Sergeeva YA, Safonova LP. Triethanolamine-based protic ionic liquids with various sulfonic acids: Synthesis and properties. *J. Mol. Liq.* 2017;242:838-44.
33. Deacon GB, Phillips RJ. Relationships between the carbon-oxygen stretching frequencies of carboxylato complexes and the type of carboxylate coordination. *Coord. Chem. Rev.* 1980;33:227-50.
34. Voronkov MG, Albanov AI, Aksamentova TN, Adamovich SN, Chipanina NN, Mirskov RG, Kochina TA, Vrazhnov DV, Litvinov MY. Tris(2-hydroxyethyl)ammonium salts: 2,8,9-Trihydroprotatranes. *Russ. J. Gen. Chem.* 2009;79:2339-46.
35. Kondratenko YA, Kochina TA, Fundamensky VS, Vlasov YG. Triethanolammonium salts of biologically active carboxylic acids. *Russ. J. Gen. Chem.* 2015;85:2710-14.
36. Gao L, Wan H, Han M, Guan G. Deep desulfurization of model oil by extraction with a low viscosity ionic liquid [BMIM]SCN. *Petrol. Sci. Tech.* 2014;32:1309-17.
37. DiGuilio RM, Lee RJ, Schaeffer ST, Brasher LL, Teja AS. Densities and viscosities of the ethanolamines. *J. Chem. Eng. Data* 1992;37:239-42.

Synthesis and Spectroscopic Characterization of Protic Tris(2-Hydroxyethyl)-Ammonium Ionic Liquids

Hüseyin AKBAŞ^{1,*}

¹Department of Chemistry, Tokat Gaziosmanpaşa University, 60250, Tokat, Turkey

*Corresponding author. E-mail:huseyin.akbas@gop.edu.tr

Supplementary Material

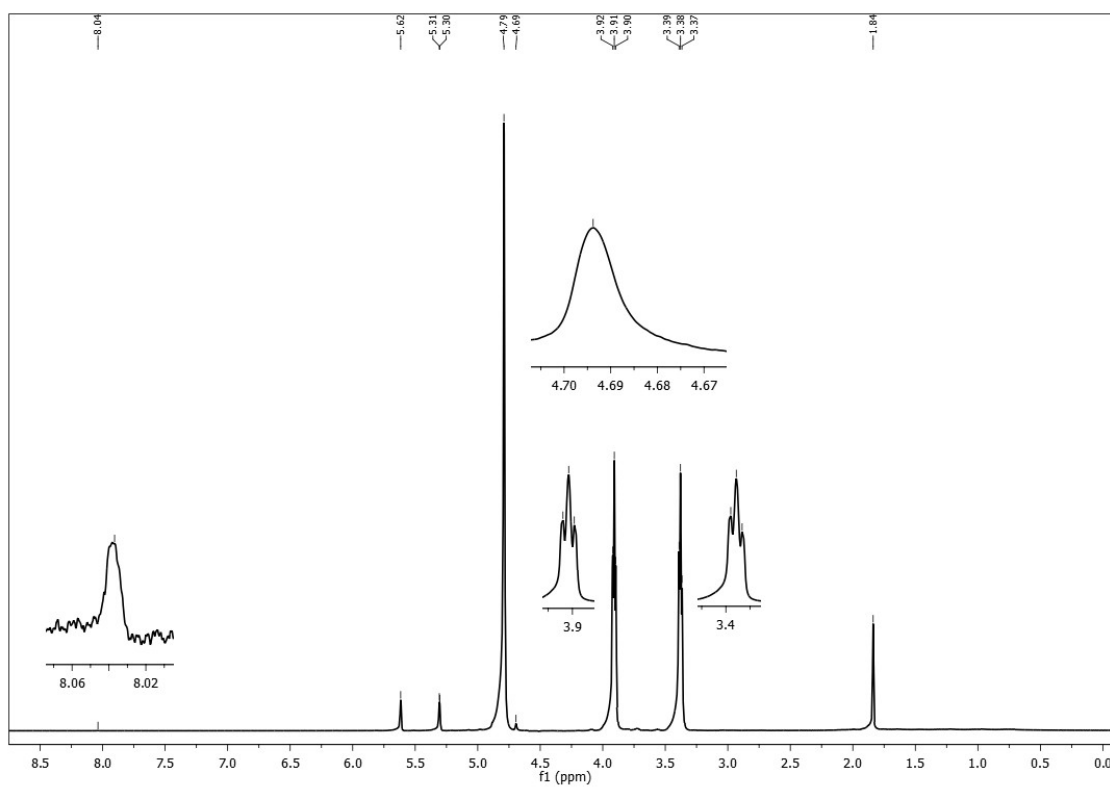


Figure S1. The ¹H NMR spectrum of **PIL1**.

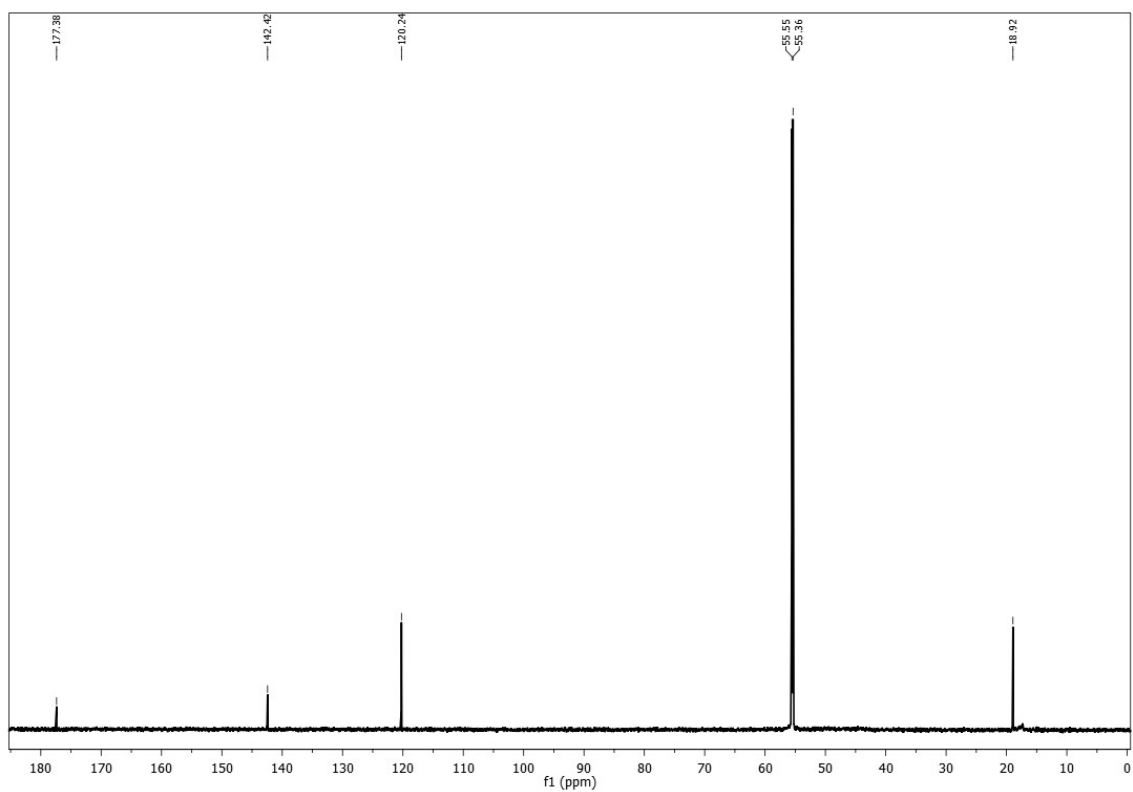


Figure S2. The ^{13}C NMR spectrum of **PIL1**.

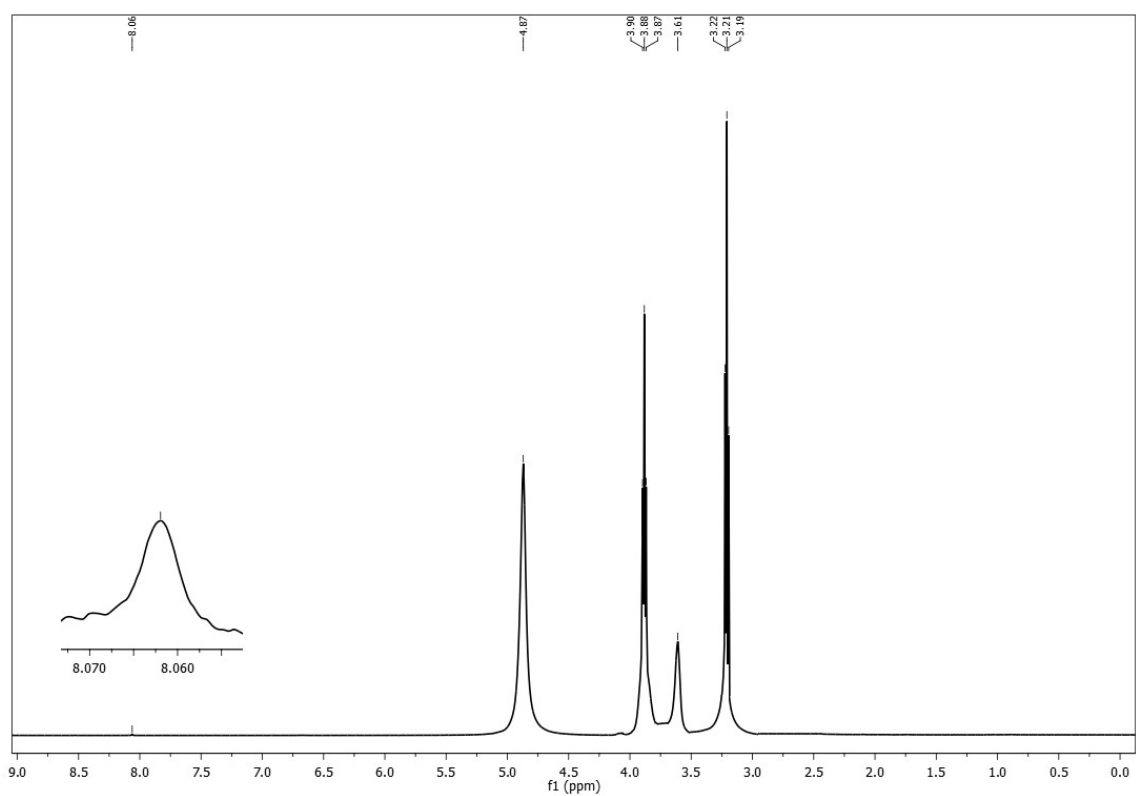


Figure S3. The ^1H NMR spectrum of **PIL2**.

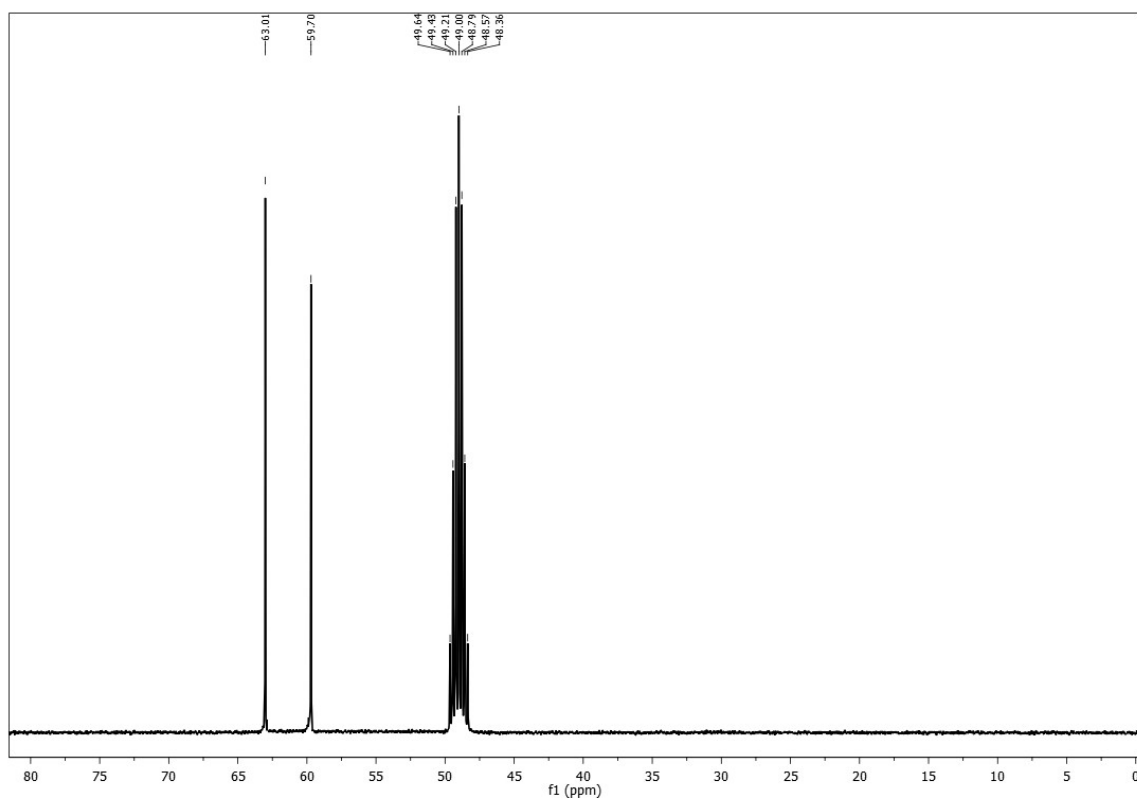


Figure S4. The ^{13}C NMR spectrum of **PIL2**.

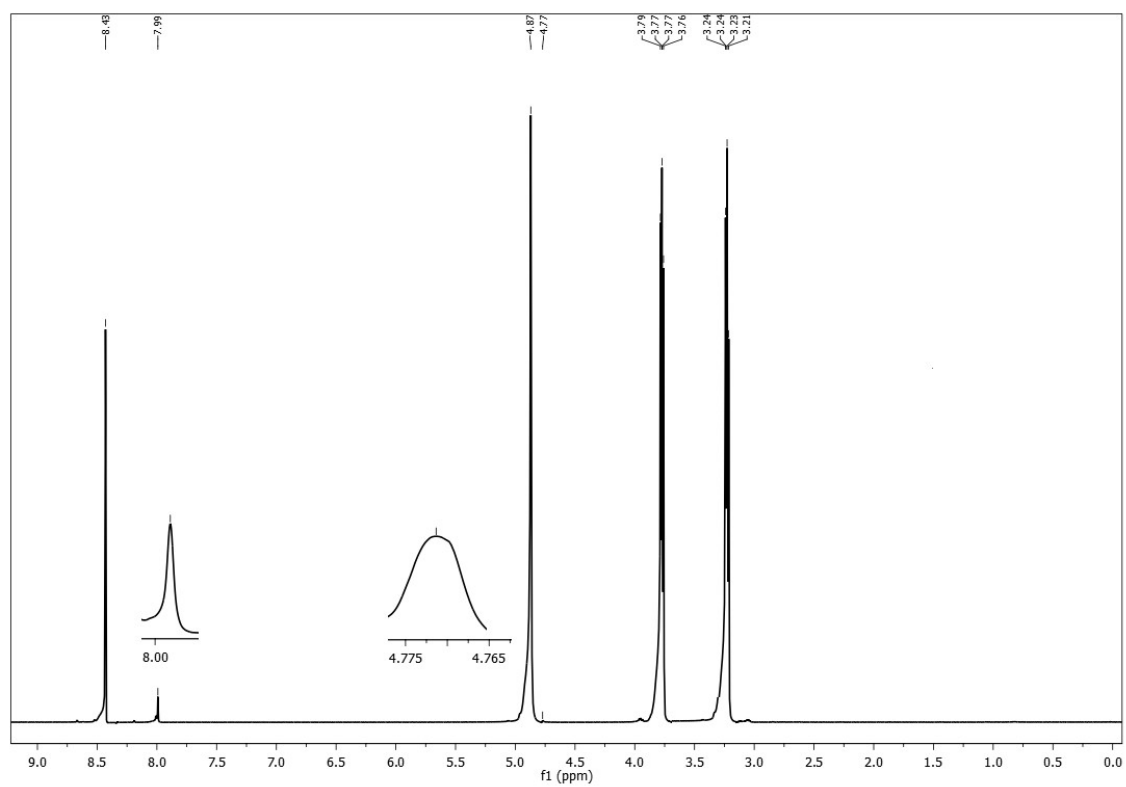


Figure S5. The ^1H NMR spectrum of **PIL3**.

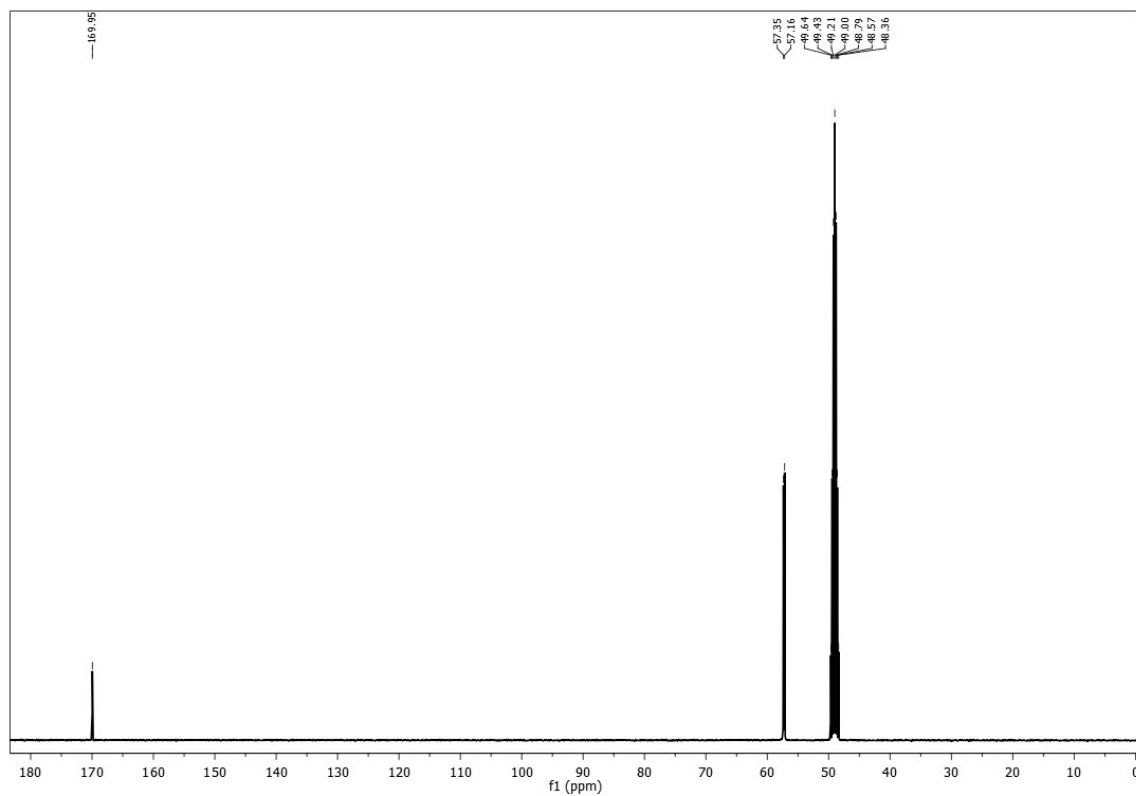


Figure S6. The ^{13}C NMR spectrum of **PIL3**.

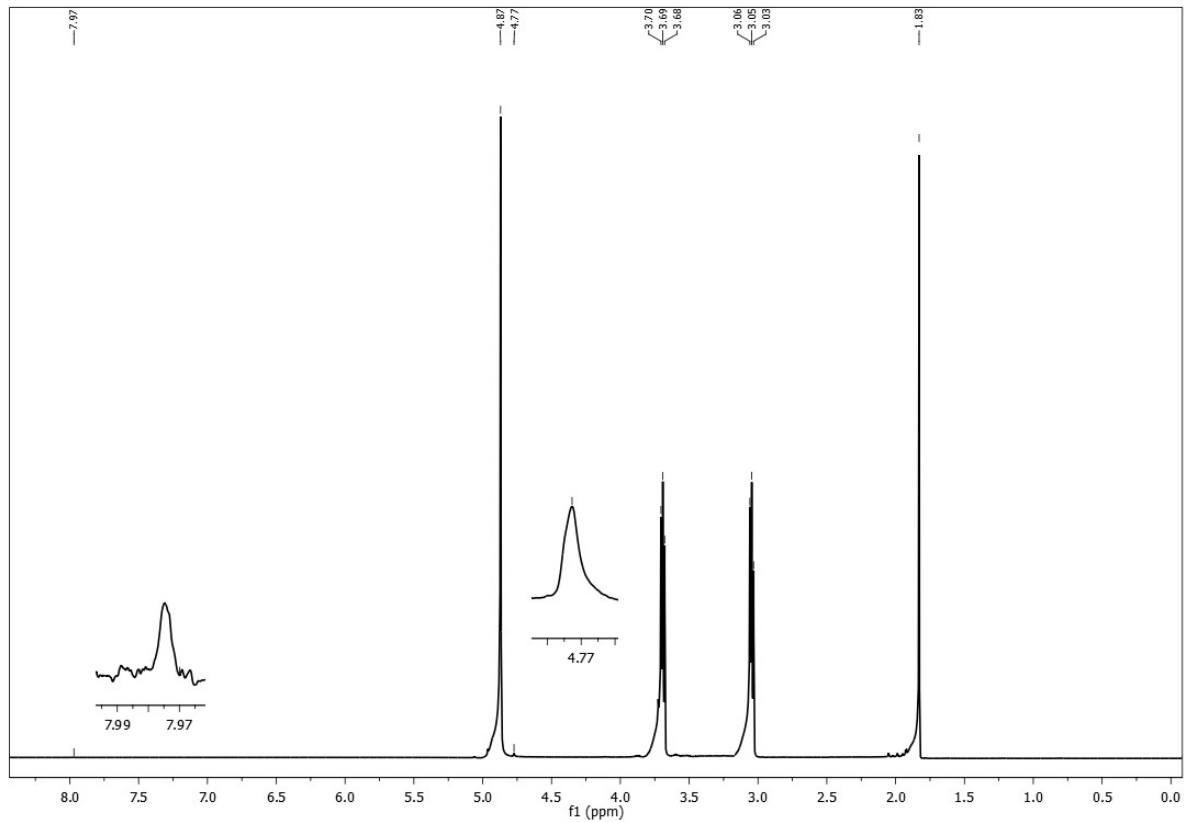


Figure S7. The ^1H NMR spectrum of **PIL4**.

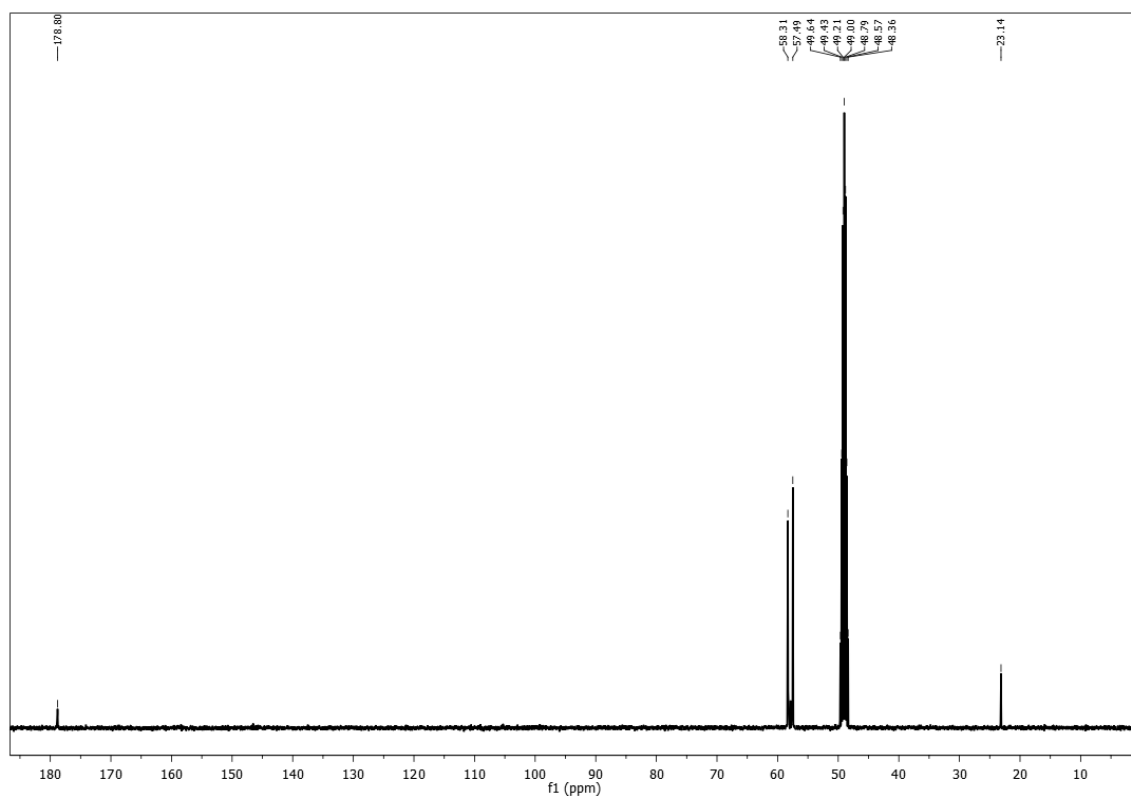


Figure S8. The ^1H NMR spectrum of **PIL4**.

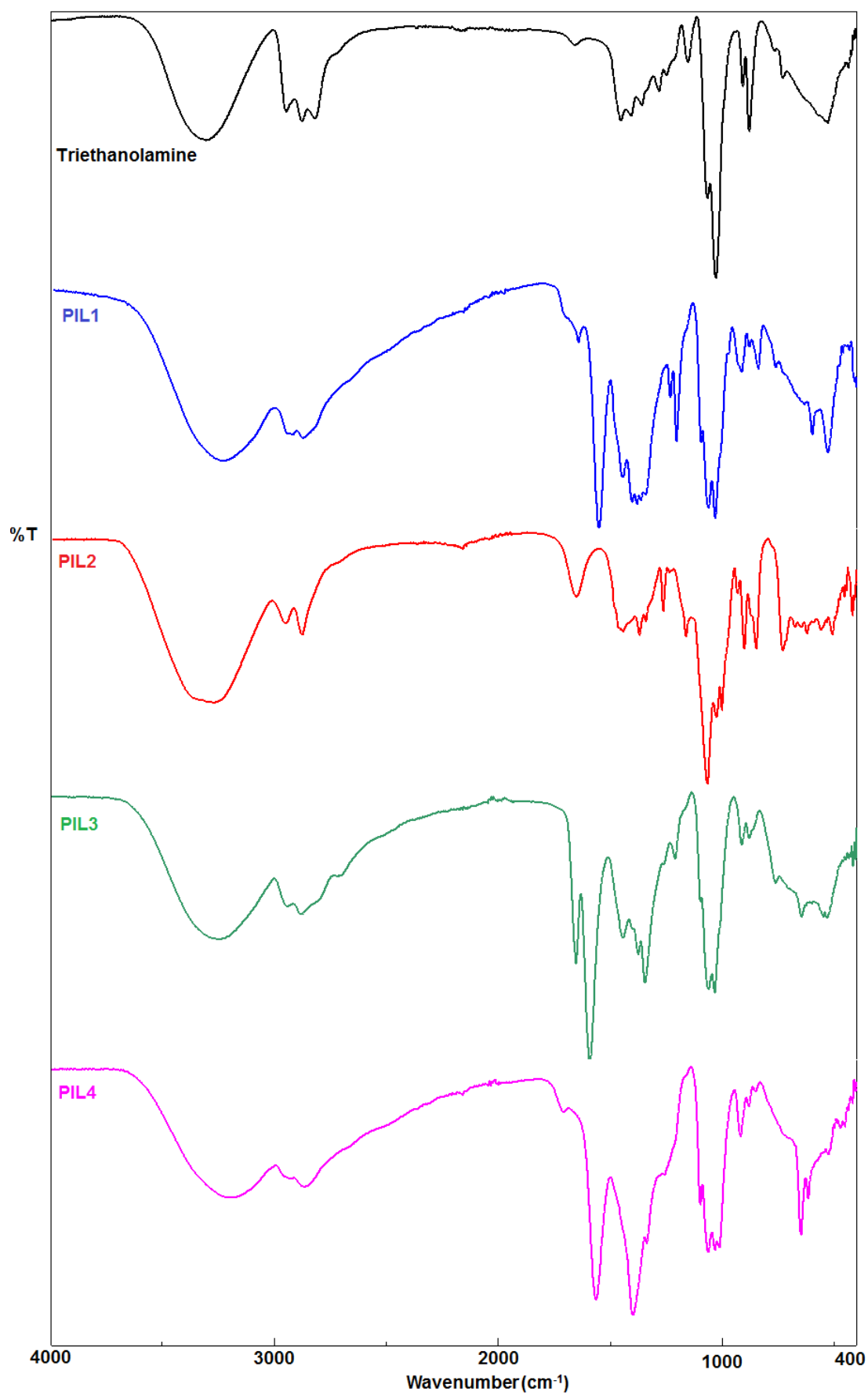


Figure S9. The FT-IR spectra of triethanolamine and PILs.



Microwave- and ultrasound-promoted greener synthesis of thiazolyl-pyrazoline derivatives and investigation of their biological activities

Arif MERMER^{1*}  

Department of Biotechnology, Hamidiye Institute of Health Sciences, University of Health Sciences, İstanbul, Turkey.

Abstract: Six thiazolyl-pyrazoline derivatives were synthesized starting from corresponding chalcone compounds for their antioxidant capacity and antiurease inhibitory activities. In addition to the conventional method, ultrasonic sonication and microwave irradiation methods which are environmental methods were used in the synthetic stage. Compound 2-(5-(3-bromophenyl)-3-phenyl-4,5-dihydro-1H-pyrazol-1-yl)-4-phenyl thiazole (5a) exhibited the most potent antiurease activity with IC_{50} of $2,28 \pm 0,02$, which was comparable to the positive control.

Keywords: Thiazole; Ultrasound Sonication; Microwave Irradiation; Antioxidant Capacity; Antiurease Inhibitor; ADME prediction.

Submitted: May 11, 2019. **Accepted:** October 10, 2019.

Cite this: Mermer A. Microwave- and ultrasound-promoted greener synthesis of thiazolyl-pyrazoline derivatives and investigation of their biological activities. JOTCSA. 2020;7(1):25–36.

DOI: <https://doi.org/10.18596/jotcsa.563286>.

Corresponding Author. E-mail: arfmermer@hotmail.com, Tel:+90506 462 2979.

INTRODUCTION

Thiazoles and their derivatives have taken continuing attention over the years because of their various biological activities such as anti-hypertensive, anti-inflammatory, analgesic, antimicrobial, anti-HIV, and herbicidal activity (1-5). Commercially available drugs such as blenoxane, bleomycine, and tiazofurin have a thiazole ring in their structure (6). In many studies, it has been seen that thiazole derivative compounds have tuberculostatic, antibacterial, antifungal, antiurease, and antioxidant activities (7-9). One of the important heterocyclic structure, pyrazoles have attracted the attention of organic chemists in recent years due to their wide biological activity properties. Compounds containing pyrazole nucleus are known to have analgesic, anti-inflammatory, antipyretic, antiarrhythmic, muscle relaxant, psychoanaleptic, anticonvulsant, hypotensive, antidiabetic and

antibacterial activities (10-16). The yield, which is one of the problems experienced in the field of synthetic organic chemistry, has an important place in modern drugs discovery. In organic reactions, the compounds should be quick and easy to synthesize, and the obtained compounds should be pure and easy to separate. From this perspective, organic chemists and researchers from many other scientific fields show a great deal of interest in the application of new methods and synthetic strategies. Compared to conventional method, microwave-assisted and ultrasonic sonicated synthesis have applied as advantageous methods for achieving these objectives (17-27).

Urease (urea amidohydrolase; E.C.3.5.1.5), a nickel-containing metalloenzyme, catalyzes the hydrolysis of urea to ammonia and carbon dioxide (28). Urease activity has been an important virulence factor in the pathogenesis of

many clinical conditions that are detrimental to human and animal health and agriculture. At the same time, urease is the main cause of the occurrence of pathogens induced by *Helicobacter pylori* and thus the colonization of the bacteria survives even at the low pH of the stomach. Therefore, these bacteria can cause gastric and peptic ulcers. (29). Many strategies based on urease inhibition are used for the treatment of infections caused by urease-producing bacteria. In this paper, we reported here the synthesis and biological activity screening studies of a series of thiazolyl-pyrazoline derivatives by using green chemistry techniques (Microwave irradiation and ultrasound sonication) and conventional method.

EXPERIMENTAL

All chemicals used in synthetic phase and biological activity assays were purchased from FlukaChemie AG Buchs (Switzerland). The Büchi B-540 apparatus was used to determine the melting points of the obtained compounds. The progress of reactions were followed by thin-layer chromatography (TLC) on silica gel 60F₂₅₄ aluminum sheets. Ethyl acetate:diethyl ether (1:1) and ethyl acetate:chloroform (2:1) were used as mobile phase and detection was performed using UV light. FT-IR spectra were recorded using a Perkin Elmer 1600 series FTIR spectrometer. ¹H NMR and ¹³C NMR spectra were registered in DMSO-d₆ on a Bruker Avance II 400 MHz NMR Spectrometer (400.13 MHz for ¹H and 100.62 MHz for ¹³C). The chemical shifts are given in ppm relative to Me₄Si as an internal reference, J values are given in Hz. Microwave and ultrasound mediated syntheses were carried out using monomode CEM-Discover microwave apparatus and Bandelin Sonorex Super RK102H ultrasonic bath, respectively. The Mass spectra were obtained on a Quattro LC-MS (70 eV) Instrument.

General method for the synthesis of compounds 3a,b

Method 1. Substituted benzaldehyde compounds (10 mmol) and acetophenone (10 mmol) were dissolved in 30 mL of ethanol. The mixture was stirred for several minutes at 10 °C until dissolved. Then 1 mL of a 40% aqueous potassium hydroxide solution was added slowly to the reaction flask with a self-equalizing addition funnel. The reaction solution was allowed to stir at room temperature for approximately 4-5 h. After completion of the reaction, a solid precipitate formed and filtered. The corresponding product was crystallized from ethanol.

Method 2. The solution of corresponding benzaldehyde (10 mmol) and acetophenone (10 mmol) in ethanol (5 mL) was irradiated 30 °C, 50 W for 35-40 min in closed vessel in the presence of 1 mL of a 40% aqueous potassium hydroxide solution. After completion of the reaction (the progress of the reaction was followed by TLC), a solid precipitate formed and filtered. The corresponding product was crystallized from ethanol.

Method 3. The solution of corresponding benzaldehyde (10 mmol) and acetophenone (10 mmol) in ethanol (5 mL) was sonicated in the presence of 1 mL of a 40% aqueous potassium hydroxide solution for 30-35 min. After completion of the reaction (the progress of the reaction was followed by TLC), a solid precipitate formed and filtered. The corresponding product was crystallized from ethanol.

(E)-3-(3-bromophenyl)-1-phenylprop-2-en-1-one (3a)

FT-IR(ν_{\max} , cm⁻¹): 3063, 1656, 1604, 1215. ¹H NMR (DMSO-d₆, δ ppm): 7.42 (t, 1H, J=16.0 Hz, arH), 7.58 (t, 2H, J=16.0 Hz, arH), 7.64 (d, 1H, J=8.0 Hz, arH), 7.68 (d, 1H, J=8.0 Hz, arH), 7.88 (d, 1H, J=4.0 Hz, CH), 8.03 (d, 1H, J=4.0 Hz, CH), 8.18 (s, 1H, arH), 8.21 (d, 2H, J=8.0 Hz, arH). ¹³C NMR (DMSO-d₆, δ ppm): arC: (126.86 (C), 128.74 (CH), 129.13 (2CH), 129.28 (2CH), 131.33 (CH), 133.81 (CH), 137.65 (C), 137.80 (C)), 124.02 (CH), 142.69 (CH), 189.53 (C=O). EI MS m/z (%): 287.17 ((M)⁺, 100), 289.19 ((M+2)⁺, 44).

(E)-3-(2-chloro-6-fluorophenyl)-1-phenylprop-2-en-1-one (3b)

FT-IR(ν_{\max} , cm⁻¹): 3090, 1664, 1598, 1270. ¹H NMR (DMSO-d₆, δ ppm): 7.42 (t, 1H, J=20.0 Hz, arH), 7.49-7.57 (m, 2H, arH), 7.60 (t, 2H, J=16.0 Hz, arH), 7.71 (t, 1H, J=16.0 Hz, arH), 7.83 (s, 1H, CH), 7.86 (s, 1H, CH), 8.06 (d, 2H, J=4.0 Hz, arH). ¹³C NMR (DMSO-d₆, δ ppm): arC: (116.05 (d, J=20.0 Hz, CH), 121.80 (d, J=15.0 Hz, C), 128.95 (2CH), 129.25 (d, J=12.0 Hz, CH), 129.49 (2CH), 132.68 (d, J=10.0 Hz, CH), 133.72 (CH), 134.04 (CH), 137.49 (C), 135.51 (C), 161.73 (d_{C-F}, J=253.0 Hz, C)), 126.82 (d, J=3.0 Hz, CH), 142.69 (CH), 189.78 (C=O). EI MS m/z (%): 261.70 ((M+1)⁺, 100).

General method for the synthesis of compounds 4a,b

Method 1. A mixture of chalcone derivatives (10 mmol), thiosemicarbazide (15 mmol), and KOH (10 mmol) was refluxed in ethanol (30 mL) for 6-7 h. After cooling, the solution was poured into ice-water and stirred for a few minutes. The

precipitate was filtered and crystallized from ethanol.

Method 2. A mixture of chalcone derivatives (10 mmol), thiosemicarbazide (15 mmol), and KOH (10 mmol) in ethanol (10 mL) was irradiated in a closed vessel at 100 W, 100 °C for 40-50 min. After cooling, the solution was poured into ice-water and stirred for a few minutes. The precipitate was filtered and crystallized from ethanol.

Method 3. A mixture of chalcone derivatives (10 mmol), thiosemicarbazide (15 mmol), and KOH (10 mmol) in ethanol (10 mL) was sonicated at 50 °C for 35 min. After cooling, the solution was poured into ice-water and stirred for a few minutes. The precipitate was filtered and crystallized from ethanol.

5-(3-bromophenyl)-3-phenyl-4,5-dihydro-1H-pyrazole-1-carbothioamide (4a)

FT-IR(u_{max} , cm^{-1}): 3482, 3343, 3063, 1564, 1470, 1341. 1H NMR (DMSO- d_6 , δ ppm): 3.20 (q, 1H, $J=20.0$ Hz), 3.91 (q, 1H, $J=32.0$ Hz), 5.94 (q, 1H, $J=12.0$ Hz, CH), 7.14 (d, 1H, $J=8.0$ Hz, arH), 7.30 (d, 2H, $J=4.0$ Hz, arH), 7.43-7.47 (m, 4H, arH), 7.89 (d, 2H, $J=8.0$ Hz, arH), 8.12 (bs, 2H, NH_2). ^{13}C NMR (DMSO- d_6 , δ ppm): 42.69 (CH_2), 62.82 (CH), arC: (122.14 (C), 124.88 (CH), 127.65 (2CH), 128.57 (CH), 129.16 (2CH), 130.29 (CH), 131.12 (CH), 131.22 (C), 131.33 (CH), 146.14 (C)), 155.46 (C=N), 176.14 (C=S). EI MS m/z (%): 300.22 (42), 361.29 (($M+1$) $^+$, 100).

5-(2-chloro-6-fluorophenyl)-3-phenyl-4,5-dihydro-1H-pyrazole-1-carbothioamide (4b)

FT-IR(u_{max} , cm^{-1}): 3255, 3084, 1583, 1473. 1H NMR (DMSO- d_6 , δ ppm): 3.25 (q, 1H, $J=20.0$ Hz), 3.99 (q, 1H, $J=28.0$ Hz), 6.17 (q, 1H, $J=16.0$ Hz, CH), 7.14-7.20 (m, 1H, arH), 7.31 (s, 2H, arH), 7.48 (s, 3H, arH), 7.88 (s, 2H, arH), 8.03 (s, 2H, NH_2). ^{13}C NMR (DMSO- d_6 , δ ppm): 43.20 (CH_2), 58.37 (CH), arC: (115.68 (CH), 125.78 (CH), 127.48 (2CH), 128.51 (d, $J=6.0$ Hz, C), 129.14 (2CH), 129.81 (d, $J=10.0$ Hz, CH), 130.90 (CH), 131.29 (C), 133.98 (d, $J=7.0$ Hz, C), 161.32 (d_{CF} , $J=248.0$ Hz, C)), 154.76 (C=N), 175.99 (C=S). EI MS m/z (%): 334.83 (60), 356.88 (($M+Na$) $^+$, 100).

General method for the synthesis of compounds 5a-f

Method 1. The mixture of corresponding compound (10 mmol) and substituted phenacyl halides (10 mmol) in ethanol (25 mL) was refluxed in 80 °C for 3-4 h. After completion of reaction, the solvent was evaporated under

reduced pressure and a solid appeared. The precipitate was filtered by washing cold water and crystallized from methylene chloride/ethanol (1:1).

Method 2. The mixture of corresponding compound (10 mmol) and substituted phenacyl halides (10 mmol) in ethanol (10 mL) was irradiated in monomode microwave reactor in closed vessel at 100 °C, 100 W for 20 min. After completion of reaction, the solvent was evaporated under reduced pressure and a solid appeared. The precipitate was filtered by washing cold water and crystallized from methylene chloride/ethanol (1:1).

Method 3. The mixture of corresponding compound (10 mmol) and substituted phenacyl halides (10 mmol) in ethanol (10 mL) was sonicated at 50°C for 15 min. After completion of reaction, the solvent was evaporated under reduced pressure and a solid was appeared. The precipitate was filtered by washing cold water and crystallized from methylene chloride/ethanol (1:1).

2-(5-(3-bromophenyl)-3-phenyl-4,5-dihydro-1H-pyrazol-1-yl)-4-phenylthiazole (5a)

FT-IR(u_{max} , cm^{-1}): 3107, 2916, 1617, 1532, 1318. 1H NMR (DMSO- d_6 , δ ppm): 3.46 (q, 1H, $J=24.0$ Hz), 4.06 (q, 1H, $J=32.0$ Hz), 5.67 (q, 1H, $J=20.0$ Hz, CH), 7.34 (t, 1H, $J=16.0$ Hz, arH), 7.41 (s, 1H, arH), 7.43 (s, 3H, arH), 7.49 (d, 5H, $J=4.0$ Hz, arH), 7.69 (s, 1H, CH), 7.74 (d, 2H, $J=8.0$ Hz, arH), 7.80 (d, 2H, $J=8.0$ Hz, arH). ^{13}C NMR (DMSO- d_6 , δ ppm): 42.69 (CH_2), 62.82 (CH), 105.87 (CH), arC: (122.07 (C), 126.21 (2CH), 126.98 (2CH), 127.65 (2CH), 128.99 (2CH), 129.31 (2CH), 130.58 (CH), 130.70 (CH), 130.96 (CH), 131.26 (C), 131.30 (CH), 132.48 (C), 133.72 (C), 144.63 (C)), 149.62 (C), 153.74 (C=N), 164.95 (thiazole C2). EI MS m/z (%): 304.39 (35), 384.46 (48), 461.41 (($M+1$) $^+$, 100).

2-(5-(3-bromophenyl)-3-phenyl-4,5-dihydro-1H-pyrazol-1-yl)-4-(4-chlorophenyl)thiazole (5b)

FT-IR(u_{max} , cm^{-1}): 3061, 2917, 1609, 1532, 1306. 1H NMR (DMSO- d_6 , δ ppm): 3.38 (q, 1H, $J=16.0$ Hz), 4.03 (q, 1H, $J=28.0$ Hz), 5.67 (q, 1H, $J=20.0$ Hz, CH), 6.91 (d, 2H, $J=8.0$ Hz, arH), 7.31 (d, 2H, $J=8.0$ Hz, arH), 7.45 (s, 1H, CH), 7.49 (d, 3H, $J=8.0$ Hz, arH), 7.64 (s, 2H, arH), 7.75 (d, 1H, $J=8.0$ Hz, arH), 7.81 (d, 3H, $J=8.0$ Hz, arH). ^{13}C NMR (DMSO- d_6 , δ ppm): 43.25 (CH_2), 64.27 (CH), 105.89 (CH), arC: (122.92 (C), 126.21 (CH), 126.98 (2CH), 127.66 (2CH),

128.99 (2CH), 129.30 (2CH), 130.58 (CH), 130.70 (CH), 130.95 (CH), 131.27 (C), 131.30 (CH), 132.47 (C), 133.73 (C), 144.63 (C)), 149.61 (C), 153.75 (C=N), 164.95 (thiazole C2). EI MS m/z (%): 246.76 (35), 332.45 (58), 495.88 ((M+1)⁺, 100).

2-(5-(3-bromophenyl)-3-phenyl-4,5-dihydro-1H-pyrazol-1-yl)-4-(2,4-dichlorophenyl)thiazole (5c)

FT-IR (ν_{\max} , cm^{-1}): 3069, 2919, 1625, 1518, 1358. ¹H NMR (DMSO- d_6 , δ ppm): 3.45 (q, 1H, J=24.0 Hz), 4.06 (q, 1H, J=28.0 Hz), 5.67 (q, 1H, J=20.0 Hz, CH), 7.28 (d, 1H, J=8.0 Hz, arH), 7.33-7.38 (m, 4H, arH), 7.50 (d, 4H, J=8.0 Hz, arH), 7.71 (d, 1H, J=4.0 Hz, arH), 7.74 (s, 1H, CH), 7.81 (d, 2H, J=8.0 Hz, arH). ¹³C NMR (DMSO- d_6 , δ ppm): 43.23 (CH₂), 64.35 (CH), 105.05 (CH), arC: (122.05 (C), 125.98 (CH), 126.22 (CH), 126.96 (CH), 128.05 (CH), 128.15 (C), 128.98 (2CH), 129.31 (2CH), 130.54 (CH), 130.75 (CH), 130.92 (CH), 131.29 (CH), 131.32 (C), 134.86 (C), 136.45 (C), 144.76 (C)), 150.87 (C), 153.55 (C=N), 164.83 (thiazole C2). EI MS m/z (%): 316.41 (30), 461.29 (64), 530.31 ((M+1)⁺, 100).

2-(5-(2-chloro-6-fluorophenyl)-3-phenyl-4,5-dihydro-1H-pyrazol-1-yl)-4-phenylthiazole (5d)

FT-IR (ν_{\max} , cm^{-1}): 3055, 2921, 1605, 1542, 1340. ¹H NMR (DMSO- d_6 , δ ppm): 3.51 (q, 1H, J=8.0 Hz), 4.05 (q, 1H, J=16.0 Hz), 6.18 (q, 1H, J=20.0 Hz, CH), 7.26 (d, 1H, J=8.0 Hz, arH), 7.33 (d, 4H, J=8.0 Hz, arH), 7.50 (d, 5H, J=8.0 Hz, arH), 7.70 (s, 1H, CH), 7.80 (d, 4H, J=8.0 Hz, arH). ¹³C NMR (DMSO- d_6 , δ ppm): 43.76 (CH₂), 60.21 (CH), 104.60 (CH), arC: (125.87 (2CH), 126.78 (2CH), 127.97 (2CH), 128.92 (2CH), 129.32 (2CH), 130.39 (CH), 130.84 (d, J=9.0 Hz, CH), 131.37 (2C), 134.88 (C), 136.39 (C), 161.88 (d_{C-F} , J=248.0 Hz, C)), 150.73 (C), 153.05 (C=N), 164.08 (thiazole C2). EI MS m/z (%): 434.94 ((M+1)⁺, 100), 456.95 ((M+Na)⁺, 57).

2-(5-(2-chloro-6-fluorophenyl)-3-phenyl-4,5-dihydro-1H-pyrazol-1-yl)-4-(4-chlorophenyl)thiazole (5e)

FT-IR (ν_{\max} , cm^{-1}): 3111, 2972, 1612, 1543, 1320. ¹H NMR (DMSO- d_6 , δ ppm): 3.52 (q, 1H, J=24.0 Hz), 4.06 (q, 1H, J=28.0 Hz), 6.17 (q, 1H, J=20.0 Hz, CH), 7.39 (d, 4H, J=8.0 Hz, arH), 7.42 (s, 1H, CH), 7.49 (s, 3H, arH), 7.74 (s, 2H, arH), 7.80 (d, 3H, J=4.0 Hz, arH). ¹³C NMR (DMSO- d_6 , δ ppm): 42.82 (CH₂), 60.02 (CH), 105.02 (CH), arC: (126.80 (2CH), 127.53 (2CH), 128.95 (2CH), 129.33 (2CH), 129.75 (C), 130.45 (2CH), 130.84 (CH), 130.94 (CH), 131.32 (C),

132.42 (C), 133.75 (C), 136.54 (C), 161.88 (d_{C-F} , J=249.0 Hz, C)), 149.47 (C), 153.27 (C=N), 164.16 (thiazole C2). EI MS m/z (%): 286.56 (37), 358.46 (58), 469.40 ((M+1)⁺, 100).

2-(5-(2-chloro-6-fluorophenyl)-3-phenyl-4,5-dihydro-1H-pyrazol-1-yl)-4-(2,4-dichlorophenyl)thiazole (5f)

FT-IR (ν_{\max} , cm^{-1}): 3084, 2918, 1621, 1557, 1306. ¹H NMR (DMSO- d_6 , δ ppm): 3.38 (q, 1H, J=24.0 Hz), 4.03 (q, 1H, J=28.0 Hz), 5.65 (q, 1H, J=16.0 Hz, CH), 6.92 (d, 2H, J=8.0 Hz, arH), 7.34 (d, 2H, J=8.0 Hz, arH), 7.39 (s, 1H, CH), 7.43 (d, 2H, J=8.0 Hz, arH), 7.49 (d, 2H, J=8.0 Hz, arH), 7.76 (d, 1H, J=8.0 Hz, arH), 7.80 (d, 2H, J=8.0 Hz, arH). ¹³C NMR (DMSO- d_6 , δ ppm): 43.46 (CH₂), 64.15 (CH), 105.50 (CH), arC: (126.87 (2CH), 127.66 (2CH), 128.45 (C), 128.49 (2CH), 129.00 (2CH), 129.31 (2CH), 130.45 (CH), 131.47 (C), 132.39 (C), 133.84 (C), 134.10 (C), 136.75 (C), 160.34 (d_{C-F} , J=243.0 Hz, C)), 149.69 (C), 153.44 (C=N), 164.87 (thiazole C2). EI MS m/z (%): 356.63 (36), 430.76 (51), 503.84 ((M+1)⁺, 100).

Antioxidant activity

Antioxidant activity studies: In the DPPH (2,2-diphenyl-1-picrylhydrazyl) radical scavenging activity method developed by Blois (33), freshly prepared 1mL methanolic DPPH solution and 100 μ L dissolved compound in DMSO were mixed. After mixing, the reaction content was incubated for 30 min at room temperature in the dark and was then measured at 520 nm. By drawing the graph of absorbance readings, the SC₅₀ value is calculated by determining the concentration of 50% of the total amount of DPPH radical.

FRAP (the ferric reducing ability of plasma) assay described by Benzie & Strain (34) with some modification was carried out to all synthesized compounds. According to this method, To 100 μ L of each sample was added 2.9 mL newly prepared FRAP reagent containing 300 mmol/L acetate buffer (pH 3.6), 10 mmol/L TPTZ (2,4,6-tripyridyl-s-triazine) and 20 mmol/L FeCl₃.6H₂O in proportions of 10:1:1 (v/v/v). The mixture was incubated for 30 min at 37 °C and measured at 593 nm. The values were expressed as μ mol of Trolox/g. CUPRAC (cupric ion reducing antioxidant capacity) was measured following the procedure described by Apak et al. (35) with some modification. Briefly, 100 μ L of each chemical solution was mixed with 900 mL bi-distilled water, 1 mL acetate buffer solution (1 mmol/L, pH: 7.0), 1 mL CuCl₂ (10 mmol/L) and 1 mL 7.5 mmol/L neocuproine to a final volume of 4 mL. The reaction mixture was then incubated in the dark for 30 min at room temperature, and

the absorbance of the reaction mixture was measured at 450 nm against a water blank. Trolox was used as the standard calibration curves, and the results were expressed as μmol Trolox equivalent per g.

In vitro antiurease inhibition assay (36)

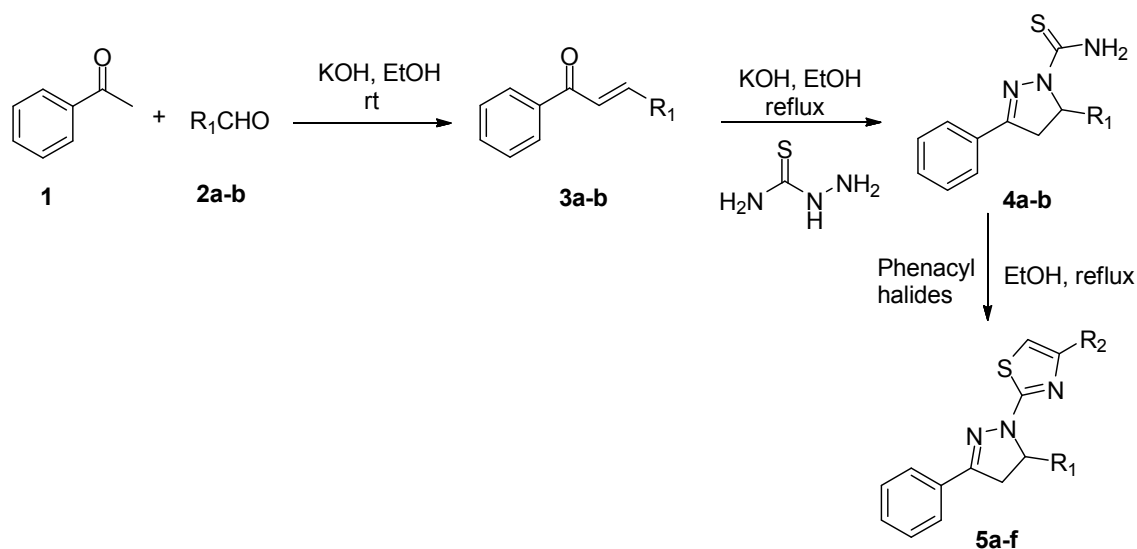
Reaction mixtures including 25 μL of Jack Bean urease, 55 μL of buffer (0.01 mol/L K_2HPO_4 , 1 mmol/L EDTA and 0.01 mol/L LiCl, pH 8.2) and 10 mmol/L urea were incubated with 5 μL of the test compounds at room temperature for 15 min in microtiter plates. The production of ammonia was measured following the indophenol method and was used to determine the urease inhibitory activity. The phenol reagent (45 μL , 1% w/v phenol and 0.005% w/v sodium nitroprusside) and alkali reagent (70 μL , 0.5% w/v sodium hydroxide and 0.1% v/v NaOCl) were added to each well. This mixture was incubated for 15 minutes more at 35 $^\circ\text{C}$ and optical density was measured at 625 nm against a blank solution including distilled water instead of enzyme. For

the determination of the IC_{50} value of the extracts, activity assays were conducted at five different extract concentration and dose-response curve was generated. Thiourea was used as standard inhibitor.

RESULTS AND DISCUSSION

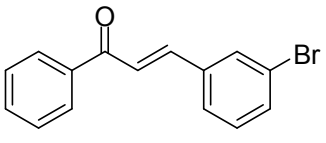
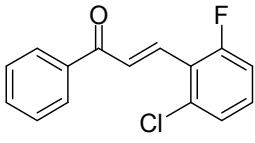
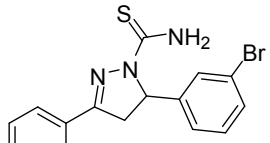
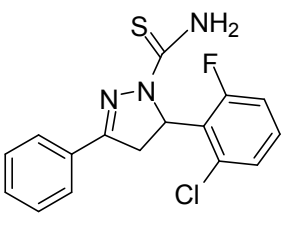
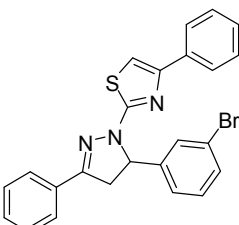
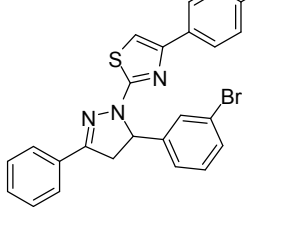
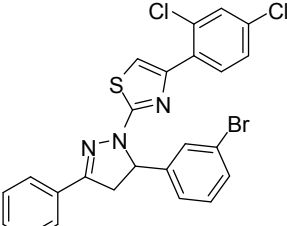
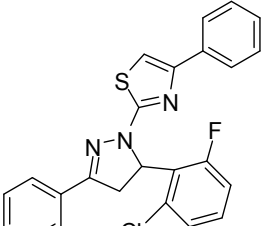
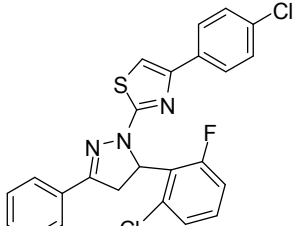
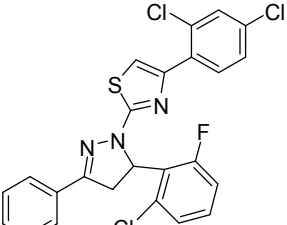
Chemistry

The synthesis of thiazole derivatives was demonstrated in Scheme 1. Acetophenone was treated with 3-bromobenzaldehyde and 2-chloro-6-fluorobenzaldehyde afforded substituted chalcones (**3a,b**) in excellent yields (92%, 88%), respectively. Pyrazoline derivatives (**4a,b**) were synthesized by the reaction between obtained chalcone compounds (**3a,b**) and thiosemicarbazide in basic medium via intermolecular cyclization. The final compounds (**5a-f**) were obtained by condensing with pyrazolinyl substituted thioamides (**4a,b**) and α -halo ketones.



Scheme 1. Synthesis of thiazoly-pyrazoline derivatives (**5a-f**).

Table 1. Molecular formula of all compounds.

 3a	 3b	 4a
 4b	 5a	 5b
 5c	 5d	 5e
 5f		

In the present study, all reactions were firstly performed by conventional method. Microwave irradiation and ultrasonic sonication methods which are greener techniques, were performed instead of conventional method due to lower yield, longer reaction times and too much solvent consumption. When applied the greener methods, MW and US, for synthesizing chalcone and thioamide derivatives (**3a,b** and **4a,b**), the reaction time decreased from 4-5 h to 35-40 min (for **3a,b**) and from 6-7 h to 35 min (for **4a,b**). Also, the reaction yields increased from 76-83% to 84-92% (Table 4). In order to obtain the final products, optimization studies were applied in microwave and ultrasound methods. To optimize reaction conditions in microwave irradiation method, 5a was selected and microwave (MW) irradiation was enforced at various power, temperature values and time (the progress of reaction was monitored by TLC) (Table 2). Microwave irradiation reduced the reaction time

from 3 h to 20 min when compared to conventional method. Another advantage of the microwave-irradiated optimization study is the increase in reaction yield. When Table 2 is examined, the yields of 76% for have increased to 83%.

After observing the yield increase in the microwave irradiation method, we decided to perform this study with ultrasonic sonication method, which was used in previous studies and obtained very good reaction yields (30). For optimization conditions in ultrasound method, again 5a was chosen, and US was implemented at different temperature and time. When the results were investigated, the best reaction yield was obtained in 50 °C 15 min with 89% (Table 3). When the three methods were compared, the lowest reaction time, the best reaction yield and the minimum solvent consumption were obtained in the ultrasonic method, so the synthesis of the

remaining compounds was also performed according to this method. **Table 2.** Optimization conditions of the reaction in Microwave Irradiation.

All of the compounds represented in Table 1 were characterized by spectroscopic methods (FT-IR, ^1H NMR, ^{13}C NMR and EI-MS). In FT-IR spectra of compounds 3a and 3b, a sharp peak at 1656-1664 cm^{-1} verified the presence of carbonyl group. The methylene protons were observed at 7.83-8.03 ppm in ^1H NMR spectrum and another evidence that supports the formation of structures is the carbon peaks of the carbonyl group in ^{13}C NMR at 189.53-189.78 ppm. FT-IR spectrum of pyrazoline derivative compounds formed by intramolecular cyclization of chalcone and thiosemicarbazide, the carbonyl peak was lost and amino stretching vibrations were observed. The CH_2 and CH protons observed in the ^1H NMR spectrum showed that the pyrazoline ring was formed. Also, the absence of carbonyl carbon in the ^{13}C NMR spectrum and the resonance of the pyrazoline CH_2 and CH carbons at the relevant sites supported the formation of the structure. $\text{C}=\text{N}$ stretching bands occurring at 1518-1625 cm^{-1} in the FT-IR spectrum of the thiazole derivatives (5a-f) and the disappearance of the amino group in the previous compounds proved the formation of structures. The CH protons in the thiazole ring resonated as a sharp

singlet between 7-8 ppm in the ^1H NMR spectrum. Meanwhile, the vicinal protons in pyrazole ring appeared in the region of 3.38-4.06 and 5.65-6.18 ppm. In ^{13}C NMR spectra, carbon atom of CH from thiazole ring occurred in 164.08-164.95 ppm. The appearance of (M), (M+1), (M+2) and/or (M+Na) ion peaks at corresponding m/z values confirming their molecular masses for all compounds in EI-MS spectrum.

Biological Activity

Antioxidant Capacity: DPPH, FRAP, and CUPRAC methods which are important for determination of antioxidant capacity (AC, $\mu\text{mol TE/g}$) of synthesized compounds were applied. When the results of all assays were examined, the best activity among all compounds showed compounds 5a and 5e. (Table 5). For DPPH radical scavenging assay, trolox was used as the standard and the results are given as SC_{50} value. According to DPPH method, all compounds showed low activity except for 5a and 5e that exhibited good activity with 1.15 ± 0.02 and 1.20 ± 0.04 SC_{50} values, respectively. On the other hand, 3a (789.13 ± 25.46 $\mu\text{mol TE/g}$) and 3b (864.68 ± 16.30 $\mu\text{mol TE/g}$) for CUPRAC, 3b (5.87 ± 0.03) for DPPH and 5f (428.62 ± 7.42 $\mu\text{mol TE/g}$) had the lowest AC values among the synthesized compounds.

Table 2. Optimization conditions of the reaction in Microwave Irradiation.

Entry	Solvent	Power (W)	Temp. ($^{\circ}\text{C}$)	Time (min)	Yield (%)
1	EtOH	100	50	5	76
2	EtOH	100	50	10	77
3	EtOH	100	100	10	81
4	EtOH	100	100	20	83
5	EtOH	100	100	30	80
6	EtOH	100	150	20	78

*Compound 5a was selected for optimization.

Table 3. Optimization conditions of the reaction in Ultrasound Sonication.

Entry	Solvent	Temp ($^{\circ}\text{C}$)	Time (min)	Yield (%)
1	EtOH	25	10	72
2	EtOH	25	15	74
3	EtOH	40	10	80
4	EtOH	40	15	85
5	EtOH	50	15	89
6	EtOH	50	20	86

*Compound 5a was selected for optimization.

Table 4. Time and yield data of compounds 3-5 using CM, MW and US methods.

Compd.	Time (min)			Yield (%)			mp (°C)
	CM ^a	MW ^b	US ^c	CM ^a	MW ^b	US ^c	
3a	240	35	30	83	89	92	79-81
3b	300	40	35	79	85	88	84-86
4a	360	40	30	76	81	84	199-200
4b	420	50	45	78	82	85	178-179
5a	180	20	15	76	83	89	162-164
5b	180	20	15	78	82	85	155-156
5c	180	20	15	79	84	90	149-150
5d	210	20	15	80	83	88	157-158
5e	210	20	15	78	81	86	150-152
5f	240	20	15	75	79	84	145-147

^aConventional Method, ^bMicrowave Irradiation Method, ^cUltrasound Sonication Method.

Table 5. Antioxidant capacity (AC) values and antiurease activity of synthesized compounds.

Compd.	FRAP (μmol TE/g)	DPPH SC ₅₀	CUPRAC (μmol TE/g)	Urease Inh. (IC ₅₀)
3a	465.42±6.12	5.16±0.02	789.13±25.46	13.55±0.02
3b	528.76±7.18	5.87±0.03	864.68±16.30	11.36±0.02
4a	496.37±6.21	5.36±0.04	986.42±12.66	9.89±0.02
4b	466.57±5.68	4.38±0.01	1001.64±6.96	8.74±0.02
5a	884.93±4.15	1.15±0.02	2274.28±18.54	2.28±0.02
5b	642.55±6.42	2.32±0.03	1286.63±8.23	7.12±0.02
5c	586.44±6.84	2.45±0.04	1558.74±5.10	6.56±0.02
5d	540.16±7.32	3.18±0.02	1440.14±10.56	6.48±0.02
5e	796.24±3.28	1.20±0.04	2145.45±15.43	3.36±0.02
5f	428.62±7.42	3.08±0.06	1232.28±16.12	6.82±0.02
Trolox		0.04±0.00		
Thiourea				12.02±0.06

Urease Inhibitory Activity: The obtained compounds were examined for their in vitro urease inhibitory activity against Jack bean urease. Among the synthesized compounds, the thiazolyl-pyrazoline derivatives 5a and 5e displayed excellent activity compared to the thiourea used as the standard drug. Other compounds showed good-moderate activity with different IC₅₀ values ranging from 6.48±0.02 to 11.36±0.02. Compound 3a exhibited less activity than thiourea (Table 5).

ADME Prediction: The prediction of ADME properties was implemented by a computational study. In this context, we have calculated molecular volume (MV), molecular weight (MW), logarithm of partition coefficient (miLog P), number of hydrogen bond acceptors (n-ON), number of hydrogen bond donors (n-OH/NH), topological polar surface area (TPSA), number of rotatable bonds (n-ROTB) and Lipinski's rule of five (31) using Molinspiration online property calculation toolkit (Molinspiration, 2015). % ABS was calculated by: %ABS=109-(0.345×TPSA)

(32). It was monitored that all compounds displayed an excellent % absorption (%ABS) ranging from 94.64% to 100%. All results are indicated in Table 6.

CONCLUSION

In this study, thiazolyl-pyrazoline derivatives were synthesized in comparison with the conventional method, microwave irradiation and ultrasonic sonication methods. Due to the long reaction time and low reaction yield in the conventional studies, green chemical techniques MW and US were used for synthesis. It was observed that the US method was more effective when compared to each other. While the reaction yield in MW method was between 79-89%, it was in US method between 84-92%. When the results were examined in terms of reaction time, the reaction was carried out in the US method in 5 minutes less than the MW method. Also, antioxidant capacity and antiurease inhibition studies of all compounds were investigated. According to the antioxidant capacity results, all

compounds except for **5a** and **5e**, showed low activity. For DPPH, **5a** and **5e** displayed good-moderate activity with SC50 values 1.15 ± 0.02 and 1.20 ± 0.04 , respectively when compared to used standard Trolox. Moreover, all compounds exhibited urease inhibition ranging from 1.15 ± 0.02 to 13.55 ± 0.02 when compared to standard drug, thiourea. And compounds 5a-f which may be regarded as new analogues of thiazolyl-pyrazoline derivatives showed good-moderate/excellent inhibitory effect with IC50 values. Especially 5a and 5e displayed excellent activity with the IC50 values 1.15 ± 0.02 and 1.20 ± 0.04 , respectively. Based on the biological activity results, it is concluded that these newly synthesized compounds can be regarded as new drug candidates displaying antioxidant and antiurease activity.

ACKNOWLEDGEMENT

I am very thankful to Prof. Dr. Neslihan DEMİRBAŞ and Ahmet DEMİRBAŞ for providing me laboratory facility and also thankful to Yakup ŞİRİN for investigation of biological studies.

REFERENCES

- Rostom SAF, El-Ashmawy IM, El Razik H.A.A, Badr MH, Ashour HMA. Design and synthesis of some thiazolyl and thiadiazolyl derivatives of antipyrine as potential non-acidic anti-inflammatory, analgesic and antimicrobial agents. *Bioorg Med Chem.* 2009; 17: 882-895.
- Al-Saadi MS, Faidallah HM, Rostom SAF. Synthesis and biological evaluation of some 2,4,5-trisubstituted thiazole derivatives as potential antimicrobial and anticancer agents. *Arch Pharm Chem Life Sci.* 2008; 341: 424-434.
- Li Z, Yang Q, Qian X. Novel thiazonaphthalimides as efficient antitumor and DNA photocleaving agents: Effects of intercalation, side chains, and substituent groups. *Bioorg Med Chem.* 2005; 13: 4864-4870.
- Li FY, Guo XF, Fan ZJ, Zhang YQ, Zong GN, Qian XL, Ma LY, Chen L, Zhu YJ, Tatiana K, Morzherin YY, Belskaya NP. Synthesis and biological activities of novel 2-amino-1,3-thiazole-4-carboxylic acid derivatives. *Chinese Chem Lett.* 2015; 26: 1315-1318.
- Tenórioa RP, Carvalho CS, Pessanha CS, de Lima JG, de Faria AR, Alves AJ, de Melo EJT, Góes AJS. Synthesis of thiosemicarbazone and 4-thiazolidinone derivatives and their in vitro anti-Toxoplasma gondii activity. *Bioorg Med Chem. Lett.* 2005; 15: 2575-2578.
- Milne GWA. *Ashgate Handbook of Antineoplastic Agents*, Gower, London, UK, 2000.
- Karthikeyan, MS. Synthesis, analgesic, anti-inflammatory and antimicrobial studies of 2,4-dichloro-5-fluorophenyl containing thiazolotriazoles. *Eur. J. Med. Chem.* 2009; 44: 827-33.
- Scherman WR, Dickson DE. 4-(5-Nitro-2-furyl)thiazoles^{1a}. *J Org Chem.* 1952; 27: 1351-1355.
- de Aquino TM, Liesen AP, da Silva REA, Lima VT, Carvalho CS, de Faria AR, de Araújo JM, de Lima JG, Alves AJ, de Melo EJT, Góes AJS. Synthesis, anti-Toxoplasma gondii and antimicrobial activities of benzaldehyde 4-phenyl-3-thiosemicarbazones and 2-((phenylmethylene)hydrazono)-4-oxo-3-phenyl-5-thiazolidineacetic acids. *Bioorg Med Chem.* 2008; 16: 446-456.
- Taha M, Ismail NH, Imran S, Wadood A, Rahim F, Khan KM, Riaz M. Hybrid benzothiazole analogs as antiurease agent: Synthesis and molecular docking studies. *Bioorg Chem.* 2016; 66: 80-87.
- Tuncbilek M, Altanlar N. Synthesis of New 3-(substituted phenacyl)-5-(3'-(4h-4-oxo-1-benzopyran-2-yl)-benzylidene)-2,4-thiazolidinediones and their antimicrobial activity. *Arch Pharm Chem Life Sci.* 2006; 339: 213-216.
- Parmar SS, Pandey BR, Dwivedi C, Harbison RD. Anticonvulsant activity and monoamine oxidase inhibitory properties of 1, 3, 5-trisubstituted pyrazolines. *J Pharm Sci.* 1974; 63: 1152-1155.
- Can OD, Ozkay UD, Kaplancıklı ZA, Ozturk Y. Effects of some 1,3,5-trisubstitued-2-pyrazoline derivatives on depression and anxiety parameters of mice. *Arch Pharm Research.* 2009; 32:1293-1299.
- Palaska E, Erol D, Demirdamar R. Synthesis and antidepressant activities of some 1,3,5-triphenyl-2-pyrazolines. *Eur J Med Chem.* 1996; 31: 43-47.
- Zitouni GT, Chevallet P, Kilic FS, Erol K. Synthesis of some thiazolyl-pyrazoline derivatives and preliminary investigation of their hypotensive activity. *Eur J Med Chem.* 2000; 35: 635-641.

16. Bondavalli F, Bruno O, Ranise A, Schenone F, Addonizio P, De Novellis V, Loffreda A, Marmo E. 3,5-Diphenyl-1H-pyrazole derivatives. I--Esters and N-substituted carbamates of 1-(2-hydroxyethyl)-3,5-diphenyl-1H-pyrazole and its 4-bromo derivative with depressant, antiarrhythmic, analgesic and other activities. *Farmacologia*. 1988; 43: 725-743.
17. Martins MAP, Pereira CMP, Beck P, Machado P, Moura S, Teixeira MV, Bonacorso HG, Zanatta N. Microwave-assisted synthesis of 5-trichloromethyl substituted 1-phenyl-1H-pyrazoles and 1, 2-dimethylpyrazolium chlorides. *Tetrahedron Lett.* 2003; 44: 6669-6672.
18. Kahveci B, Yilmaz F, Mentese E, Özil M, Karaoğlu ŞA. Microwave-Assisted Synthesis of Some Novel Benzimidazole Derivatives Containing Imine Function and Evaluation of Their Antimicrobial Activity. *J Heterocyclic Chem.* 2014; 51: 982-990.
19. Mentese E, Özil M, Karaoğlu ŞA, Kahveci B. Rapid and Efficient Microwave-Assisted Synthesis of Some New Triazol-3-one Derivatives. *J Heterocyclic Chem.* 2013; 50: 386-390.
20. Mermer A, Demirci S, Ozdemir SB, Demirbas A, Ulker S, Ayaz FA, Aksakal F, Demirbas N. Conventional and microwave irradiated synthesis, biological activity evaluation and molecular docking studies of highly substituted piperazine-azole hybrids. *Chinese Chem. Lett.* 2017; 28: 995-1005.
21. Cebeci YU, Demirbas N, Ozdemir SB, Bayrak H, Demirbas A, Aksakal F, Karaoğlu SA. Structure-Based Hybridization, Microwave Prompted Synthesis and Biological Evaluation of Novel 4-(2-Fluoro-4-Nitrophenyl)morpholine Derivatives. *Letters in Org. Chem.* 2018; 15: 940-959.
22. Gul, Hİ, Yamali C, Yesilyurt F, Sakagami H, Kucukoglu K, Gulcin I, Gul M, Supuran CT. Microwave-assisted synthesis and bioevaluation of new sulfonamides. *Journal of Enzyme Inhibition and Medicinal Chem.* 2017; 32: 369-374.
23. Koca M, Erturk AS, Umaz A. Microwave-assisted intermolecular aldol condensation: Efficient one-step synthesis of 3-acetyl isocoumarin and optimization of different reaction conditions. *Arab. J. Chem.* 2018; 11: 538-545.
24. Mermer A, Demirbas N, Demirbas A, Colak N, Ayaz FA, Alagumuthu M, Arumugam S. Synthesis, biological activity and structure activity relationship studies of novel conazole analogues via conventional, microwave and ultrasound mediated techniques. *Bioorg. Chem.* 2018; 81: 55-70.
25. Silva FAN, Galluzzi MP, Pizzuti L, Gressler V, Rivelli DP, Barros SBM, Pereira CMP. Ultrasound irradiation promoted large-scale preparation in aqueous media and antioxidant activity of azoles. *Lett Drug Des Discov.* 2009; 6: 323-326.
26. Pizzuti L, Martins PLG, Ribeiro BA, Quina FH, Pinto E, Flores AFC, Venzke D, Pereira CMP. Efficient sonochemical synthesis of novel 3, 5-diaryl-4, 5-dihydro-1H-pyrazole-1-carboximidamides. *Ultrason Sonochem.* 2010; 17: 34-37.
27. Duarte A, Cunico W, Pereira CMP, Flores AFC, Freitag RA, Siqueira GM. Ultrasound promoted synthesis of thioesters from 2-mercaptobenzoxa (thia) zoles. *Ultrason Sonochem.* 2010; 17: 281-283.
28. Holm L, Sander C. An evolutionary treasure: unification of a broad set of amidohydrolases related to urease. *Proteins.* 1997; 28: 72-82.
29. Mobley HL, Island MD, Hausinger RP. Molecular biology of microbial ureases. *Microbiol. Rev.* 1995; 59: 451-480.
30. Venzke D, Flores AFC, Quina F.H, Pizzuti L, Pereira CMP. Ultrasound promoted greener synthesis of 2-(3, 5-diaryl-4, 5-dihydro-1H-pyrazol-1-yl)-4-phenylthiazoles. *Ultrason Sonochem.* 2011; 18: 370-374.
31. Lipinski CA, Lombardo L, Dominy BW, Feeney P. Experimental and computational approaches to estimate solubility and permeability in drug discovery and development settings. *Adv Drug Deliv Rev.* 1997; 23: 3-25.
32. Zhao Y, Abraham MH, Lee J, Hersey A, Luscombe NC, Beck G, Sherborne B, Cooper I. Rate-limited steps of human oral absorption and QSAR studies. *Pharm Res.* 2002; 19: 1446-1457.
33. Blois MS. Antioxidant determinations by the use of a stable free radical. *Nature.* 1958; 181: 1199-1200.
34. Benzie IFF, Strain JJ. (2) Ferric reducing/antioxidant power assay: Direct measure of total antioxidant activity of biological fluids and modified version for simultaneous measurement of total antioxidant power and

ascorbic acid concentration. *Methods Enzymol.* 1999; 299: 15-27.

35. Apak R, Guclu K, Ozyurek M, Karademir SE. Novel total antioxidant capacity index for dietary polyphenols and vitamins C and E, using their cupric ion reducing capability in the presence of

neocuproine: CUPRAC method. *J Agric Food Chem.* 2004; 52: 7970-7981.

36. Weatherburn MW. Estimation of ammonia nitrogen by colorimetric method. *Anal Chem.* 1967; 39: 971-974.

Table 6. Pharmacokinetic parameters for good oral bioavailability of synthesized compound 3-5.

Compd.	% ABS	TPSA (A ²)	n-ROTB	MV	MW	miLog P	n-ON acceptors	n-OHND donors	N violations
	-	-	-	-	≤500	≤5	<10	<5	≤1
3a	103.11	17.07	3	219.74	287.16	4.60	1	0	0
3b	103.11	17.07	3	220.32	260.69	4.38	1	0	0
4a	94.64	41.62	3	271.32	360.28	4.16	3	2	0
4b	94.64	41.62	3	271.90	333.82	4.12	3	2	0
5a	99.17	28.49	4	361.54	460.40	6.77	3	0	1
5b	99.17	28.49	4	375.08	494.85	7.45	3	0	1
5c	99.17	28.49	4	388.61	529.29	8.05	3	0	2
5d	99.17	28.49	4	362.12	433.94	6.73	3	0	1
5e	99.17	28.49	4	375.66	468.38	7.41	3	0	1
5f	99.17	28.49	4	389.19	502.83	8.02	3	0	2

% ABS: percentage absorption, TPSA: topological polar surface area, n-ROTB: number of rotatable bonds, MV: molecular volume, MW: molecular weight, miLog P: logarithm of partition coefficient of compound between n-octanol and water, n-ON acceptors: number of hydrogen bond acceptors, n-OHND donors: number of hydrogen bond donors.



Evaluation of phytochemical contents and antioxidant activity of pomegranate flower

Zehra Tekin , F. Zehra Küçükbay* 

İnönü University, Faculty of Pharmacy, Department of Basic Pharmaceutical Sciences,
Malatya, Turkey

Abstract: Pomegranate is one of the most abundant fruits consumed in Turkey. This study aimed to determine the content of total phenolic, total flavonoid, and antioxidant activity of *Punica granatum* L. flower in different extracts. Antioxidant activities of different extracts were determined 2,2-diphenyl-1-picrylhydrazyl (DPPH•) radical scavenging, reducing power, and metal chelating methods. The results showed that the total phenolic content for the extracts ranged from 14.82 to 90.86 mg gallic acid equivalents (GAE) / g extract. The contents of flavonoids were found to range from 7.35 to 500.00 mg quercetin equivalents (QUE)/ g extract. All pomegranate flower extracts displayed remarkable antioxidant activity according to DPPH and reducing power assays. Especially the methanolic extract of pomegranate flower possesses significant scavenging activity against DPPH• (85.80 %), as well as the largest contents of flavonoids and phenolic compounds. The antioxidant capacity of the methanolic extract was also greater than those of BHT and α -tocopherol in DPPH and reducing power assays. The results demonstrated that the antioxidant activity of extracts of *Punica granatum* L. flower might, at least in part, have high content of flavonoids and other phenolics.

Keywords: Pomegranate flower, *Punica granatum* Linn., antioxidant activity, phenolic compounds.

Submitted: July 31, 2019. **Accepted:** October 11, 2019.

Cite this: Tekin Z, Küçükbay F. Evaluation of phytochemical contents and antioxidant activity of pomegranate flower. JOTCSA. 2020;7(1):37-42.

DOI: <https://doi.org/10.18596/jotcsa.628615>.

***Corresponding author. E-mail:** zehra.kucukbay@inonu.edu.tr.

INTRODUCTION

Punica granatum Linn. known as pomegranate is a member of the Punicaceae family. Pomegranate is a famous ancient fruit originating from the Middle East. Main producers and exporters in the world are Turkey, India, Iran, China, United States, Spain, South Africa, Peru, Chile, and Argentina (1). In Turkey, the annual production of pomegranate is 537.847 tons and it is cultivated in Adiyaman, Mersin, Antalya, Adana, Gaziantep, and Şanlıurfa (2).

Pomegranate possesses a broad array of pharmacological properties such as antioxidant (3), anti-inflammatory (4), anti-cancer (5,6), anti-parasitic (7), analgesic (8), antimicrobial (9), neuroprotective (10), antifungal (11), antiulcer (12), and antidiarrheal (13). The flowers of pomegranate have been ethnomedically used for their anti-cholinesterase, anti-hyperglycemic (14), anti-diabetic, anti-obesity (15), anti-bacterial, and antioxidant (16) effects. The constituents including gallic acid (17), ellagic acid, ethyl brevifolin-carboxylate, maslinic acid, ursolic acid, oleanolic acid, asiatic acid, sterol, daucosterol, punicaflavone, pelargonidin 3,5-

diglucoside and pelargonidin 3-glucoside (18) are responsible for the pharmacological effects of pomegranate flower extract.

The content of phytochemicals that contributes to the antioxidant effect of the pomegranate flowers located in Adiyaman is unknown and during pomegranate juice production, antioxidant-rich flowers of pomegranates are discarded. Moreover pomegranate flowers constitutes an inexpensive source for the extraction of phytochemicals that might be utilized in the pharmaceutical, cosmetic and food industries. Thus, the objective of this research is to evaluate the nutritional quality of pomegranate flowers, which constitute the pomegranate fruit juice industry wastes. Another aim is to evaluate whether total phenolic and flavonoid contents of pomegranate flowers are correlated with antioxidant activity.

MATERIAL AND METHODS

Chemicals

Ferric chloride and 2,2-diphenyl-1-picrylhydrazyl (DPPH), AlCl_3 , NaNO_2 , ethanol, and standard compounds, quercetin and alpha-tocopherol were purchased from Sigma Chemical Co. (Sigma-Aldrich GmbH, Steinheim, Germany). Butylated hydroxytoluene (BHT) and butylated hydroxyanisole (BHA) were obtained from Acros. Folin-Ciocalteu reagent, trichloroacetic acid, and methanol were purchased from Merck. All the other chemicals used were of analytical grade.

Plant material

Dried pomegranate flowers were bought from a local shop in Adiyaman, Turkey. The flowers were ground and then the powder was kept at 4 °C until the extraction process.

Preparation of Extract

The powdered flowers (10 g) were extracted with n-hexane (H), methanol (M), 1% acidified methanol (99% methanol, AME 1 and 70% methanol, AME 2) in a Soxhlet apparatus for 4 h. Extracts were concentrated using a rotary evaporator (40 °C) under vacuum and kept at 4 °C until analysis.

Determination of total phenolic content

The total contents of phenolic compounds were determined by the Folin-Ciocalteu method (19). The extracts were dissolved in methanol. 50 μL of samples were mixed with 450 μL deionized water, 250 μL of 1.0 N Folin reagent and 1250 μL of 7.5% Na_2CO_3 . The mixture was mixed in a vortex before allowed to rest for 120 minutes at room temperature and the absorbance was measured at 765 nm. The calibration curve was plotted by different concentration of gallic acid equivalents (in mg/g).

Determination of total flavonoid content

The overall flavonoid content of the *Punica granatum* L. flower extract was estimated using the aluminum chloride colorimetric method (20). 500 μL extract solution (1 mg/mL) was blended with 4500 μL of distilled water and 300 μL 5.0% NaNO_2 . Having waited for 5 min, 300 μL of AlCl_3 solution was added to the blend and allowed to stand for 6 min. Then, 2000 μL of 1.0 M NaOH was added and volume increased to 10 mL with distilled water. The absorbance of the mixture after it turned to pink was measured at 510 nm using UV/Vis spectrophotometer (Shimadzu UV-160). A calibration curve of standard reference was established using quercetin (range of concentration from 4 to 20 $\mu\text{g/mL}$) as standard reference plotted. Total flavonoid content was expressed as mg of quercetin equivalents g extract.

Determination of antioxidant activity by DPPH radical scavenging assay

The antioxidant activity of the *Punica granatum* L. flower extract was determined by the DPPH (2,2-diphenyl-1-picrylhydrazyl) free radical scavenging assay (21). 1 mL of 0.10 mM DPPH solution was mixed with 3 mL of extract solution at different concentration. (12.5-125 $\mu\text{g/mL}$). Vigorously shaken mixture was incubated in dark at room temperature 30 min. The absorbance was measured at 517 nm by a UV/Vis spectrophotometer. Butylated hydroxytoluene (BHT), butylated hydroxyanisole (BHA) and alpha-tocopherol were utilized as standards. Using the equation below, radical scavenging percentage was calculated :

$$\text{Radical scavenging activity (\%)} = \left[\frac{(A_{\text{Control}} - A_{\text{Sample}})}{A_{\text{Control}}} \right] \times 100 \quad (\text{Eq. 1})$$

A_{control} is the absorbance at the addition of ethanol instead of the extract/standard; A_{sample} is the absorbance at the addition of extract/standard.

Reducing power assay

The reducing power of different *Punica granatum* L. flower extracts was evaluated by the method of Oyaizu (22). 1 mL of the extract at different concentrations was mixed with 2.50 mL of phosphate buffer (0.20 mol/L, pH 6.60) and 2.50 mL 1.0% potassium ferricyanide and vortexed. The mixture was incubated at 50 °C for 20 minutes in a water bath. 2.50 mL of 10% trichloroacetic acid was then added to the mixture, and centrifuged at 6000 rpm for 10 minutes. 1.25 mL of supernatant was mixed with 1.25 mL of distilled water and 0.50 mL of 0.10% ferric chloride and mixed well. The absorbance of final solution was measured at 700 nm using a UV/Vis spectrophotometer. Higher absorbance of the reaction mixture meant higher reducing power.

Metal chelating activity

The chelation of ferrous ions of the studied extracts was observed according to the method as described by Dinis et al. (23). 50 µL of 2.0 mM FeCl₂ was mixed with 3750 µL of the extracts having different concentrations (12.5-125 µg/mL) and vortexed. After 10 min of incubation, the reaction was started by adding 200 µL of 5.0 mM ferrozine and the solution was incubated at room temperature for 20 min and then the absorbance of the solution was measured at 562 nm using a spectrophotometer. EDTA was utilized as a positive control. The percentage inhibition of Fe²⁺ - ferrozine complex was calculated by the following equation:

$$\text{Inhibition (\%)} = \frac{(\text{Abs}_{\text{control}} - \text{Abs}_{\text{sample}})}{\text{Abs}_{\text{control}}} * 100 \quad (\text{Eq. 2})$$

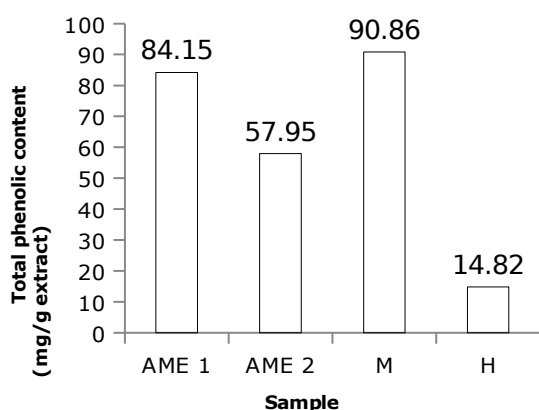


Figure 1. Total phenolic content as equivalent mg of gallic acid per g of AME 1, AME 2, M and H extracts of pomegranate flower.

A_{control} ; the absorbance at the addition of ethanol instead of the extract/standard, A_{sample} ; the absorbance at the addition of extract/standard.

RESULTS AND DISCUSSION

The yields of n-hexane, methanol, 1% acidified methanol (99% methanol and 70% methanol) extracts of the flower of *P. granatum* L. were 0.03%, 15.19%, 46.04% and 31.83%, respectively.

Total phenolic content

Total phenolic contents of the extracts of pomegranate flower determined by Folin-Ciocalteu method are presented as gallic acid equivalents (mg gallic acid/ g extract) in Figure 1. The amount of total phenolic contents in the determined extracts ranged from 14.82±0.01 to 90.86±0.01 mg GAE / g extract. The results showed that the highest total phenolic content was obtained in the methanolic extract, while the lowest was observed in the n-hexane extract. Eddebbagh et al.(24) found that the phenolic content of 80% methanolic extract of dried pomegranate flower is 90.73 mg GAE/ g of dry weight flowers. Abdolahi et al. (16) have found 28 mg GAE/ g dry weight in 70% ethanolic extract and Rashid and Shafi (25) have found 190.50 and 103.81 mg GAE/ g in methanolic and aqueous extracts in dried pomegranate flower. These differences in phenolic contents might be due to location, soil and climate.

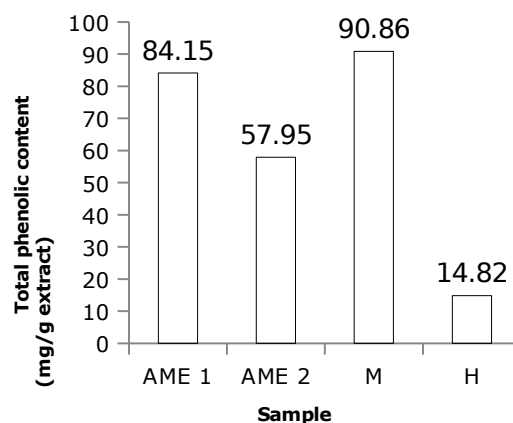


Figure 2. Total flavonoid content as equivalent mg of quercetin per g of AME 1, AME 2, M and H extracts of pomegranate flower.

Total flavonoid content

The total flavonoid contents in the determined extracts of pomegranate flowers are expressed in

terms of quercetin equivalent (mg quercetin/ g extract) in Figure 2. The flavonoid content was 350.74 ± 0.01 , 172.79 ± 0.02 , 500.00 ± 0.01 and 7.35 ± 0.01 mg QUE /g in AME 1, AME 2, M and H extracts, respectively. The results showed that the greatest total flavonoid content was obtained in the methanolic extract. Eddebbagh et

al. (24) have found 221.70 mg QUE/ g dry weight in 80% methanolic extract and Abdolahi et al. (16) have reported 64.38 ± 0.81 mg catechin equivalents per gram of dry weight in dried pomegranate flower. These differences might be related to solvent used and location.

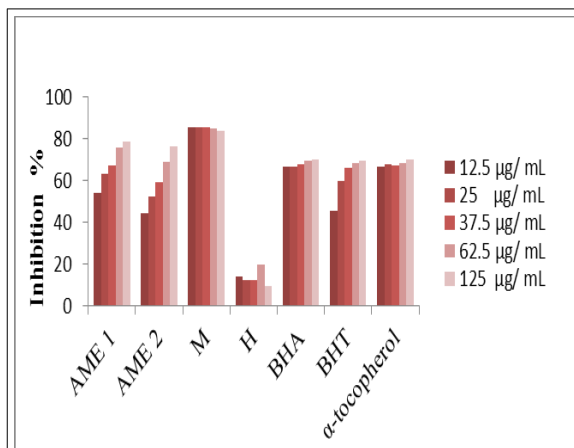


Figure 3. DPPH• radical scavenging activity(%) of AME 1, AME 2, M and H extracts of pomegranate flower.

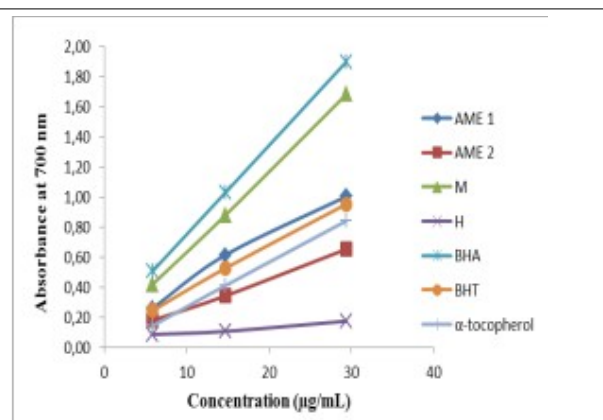


Figure 4. Reducing power activity(%) of AME 1, AME 2, M and H extracts of pomegranate flower.

DPPH radical scavenging activity

DPPH radical scavenging activity of the pomegranate flower extracts is summarized in Figure 3 and compared with the standard antioxidants such as BHA, BHT and α -tocopherol. The potential of different pomegranate flower extracts to scavenge free radical varied 54.12-78.54% in AME 1, 44.22-76.56% in AME 2, 83.82-85.80% in M and 9.57-19.80% in H. Among them, the methanolic extract exhibited the higher values of DPPH radical scavenging activity. Pomegranate flower extracts clearly showed that as the concentration got higher the antioxidant activity against DPPH radical in all extracts increased. Abdolahi et al. (16) have reported 91.04% inhibition at concentration of 100 $\mu\text{g/mL}$ pomegranate flower extract. On the other hand, Rashid and Shafi (25) have found 76.89% and 69.23% in methanolic and aqueous extract of flowers of pomegranate, respectively.

These differences can also be explained with soil and climate differences.

Reducing power activity

Reducing power activities of extracts are shown in Figure 4 with standard antioxidant compounds (BHA, BHT and α -tocopherol). The reducing power of the all extracts dose with the increase in concentration (Table 1). In addition, methanolic extract showed 2.93 times stronger antioxidant activity than that of α -tocopherol at an initial concentration of 5.88 $\mu\text{g/mL}$. In the literature, the reducing properties are usually related to the presence of reductones (reducing agents) which have been found to exert antioxidant ability to break the free radical chain by donating a hydrogen atom (26). So, the data gathered from the present study suggest that pomegranate flower might contain polyphenol which acts as reducing agents.

Table 1. Reducing power activity of AME 1, AME 2, M and H extracts of pomegranate flower.

Extracts/Standards	Reducing Power ($\mu\text{g/mL}$, 700 nm)		
	5.88	14.70	29.41
AME 1	0.260	0.613	1.004
AME 2	0.179	0.342	0.653
M	0.419	0.878	1.683
H	0.085	0.106	0.174
BHA	0.507	1.028	1.900
BHT	0.244	0.525	0.953
α -tocopherol	0.143	0.410	0.841

Metal chelating activity

Metal chelating activity of the pomegranate flower extracts and EDTA are presented in Table 2. n-Hexane extract possessed moderate metal

chelating activity whereas all the other extracts exhibited none. The highest metal chelating activity of 9.299% was determined in n-hexane extract.

Table 2. Metal chelating activity of AME 1, AME 2, M and H extracts of pomegranate flower.*ND; non-detected.

Extracts/ Standard	Inhibition, %				
	12.5 $\mu\text{g/mL}$	25 $\mu\text{g/mL}$	37.5 $\mu\text{g/mL}$	62.5 $\mu\text{g/mL}$	125 $\mu\text{g/mL}$
AME 1	*ND	ND	ND	ND	ND
AME 2	ND	ND	ND	ND	ND
M	ND	ND	ND	ND	ND
H	ND	0.104	1.149	1.985	9.299
EDTA	8.045	40.020	56.426	78.892	84.430

CONCLUSION

Our results show that the flowers of *P. granatum* may have health benefits when consumed. Our belief is that they display potential as a functional food or value-added ingredient for years to come. Also *P. granatum* flower might be considered a source of important antioxidant with bioactive properties to be explored for pharmaceutical applications. Further studies can be undertaken to investigate the effect of toxicity in these extracts.

REFERENCES

1. Kalaycıoğlu Z., Erim FB., Total phenolic contents, antioxidant activities, and bioactive ingredients of juices pomegranate cultivars worldwide, *Food Chemistry*, 2017; 221; 496-507.

2. TÜİK, Turkish Statistical Institute, 2019, <http://tuik.gov.tr>

3. Adhmi VM., Mukhtar H., Polyphenols from green tea and pomegranate for prevention prostate cancer, *Free Radic. Res.* 2006; 40; 1095-104.

4. Colombo E., Sangiovanni E., Dell'Agli M., A review on the anti-inflammatory activity of pomegranate in the gastrointestinal tract., *Evidence-Based Complementary and Alternative Medicine*, 2013; 1-12.

5. Lansky EP., Newman RA., *Punica granatum* (pomegranate) and its potential for prevention and treatment of inflammation and cancer, *Journal of Ethnopharmacology*, 2007; 109; 177-206.

6. Sharma P., McCless .F., Afaq F., Pomegranate for prevention and treatment of cancer: an update, *Molecules*, 2017; 22(1); 177.

7. Williams AR., Soelberg J., Jäger AK., Anthelmintic properties of traditional African and Caribbean medicinal plants: identification of extracts with potential activity against *Ascaris suum* in vitro, *Parasite*, 2016; 23(24);1-6.

8. Nadia Z., Aicha M., Sihem H., Abdelmalik B., In vivo analgesic activities and safety assesment of *Vitis*

- vinifera L and Punica granatum L fruits extracts, *Tropical Journal of Pharmaceutical Research*, 2017; 16(3); 553-61.
9. Bassiri-Jahromi S., Doostkam A., Comparative evaluation of bioactive compounds of various cultivars of pomegranate (*Punica granatum*) in different world regions, *AIMS Agriculture and Food*, 2019; 4(1); 41-55.
10. DaSilva NA., Nahar PP., Ma H., Eid A., Wei Z., Meschwitz S., Zawia NH., Slitt AL., Seeram NP., Pomegranate ellagitannin-gut microbial-derived metabolites, urolithins, inhibit neuroinflammation in vitro, *Nutritional Neuroscience*, 2019; 22(3); 185-95.
11. Sharayei P., Azarpazhooh E., Zomorodi S., Ramaswamy HS., Ultrasound assisted extraction of bioactive compounds from pomegranate (*Punica granatum* L.) peel, *LWT*, 2019; 101; 342-50.
12. Moghaddam G., Sharifzadeh M., Hassanzadeh G., Khanavi M., Dolatshahi F., Sadeghi N., Oveisi MR., Hajimahmoodi M., Anti-ulcerative potential of *Punica granatum* L. (Lythraceae) hydroalcohol fruit peel extract, *Tropical Journal of Pharmaceutical Research*, 2014; 13(7); 1093-7.
13. Zhao S-S., Ma D-X., Zhu Y., Zhao J-H., Zhang Y., Chen J-Q., Sheng Z-L., Antidiarrheal effect of bioactivity-guided fractions and bioactive components of pomegranate (*Punica granatum* L.) peels, *Neurogastroenterology & Motility*, 2018; 30(7); 1-10.
14. Bekir J., Cazaux S., Mars M., Bouajila J., In vitro anti-cholinesterase and anti-hyperglycemic activities of flowers extracts from seven pomegranate varieties, *Industrial Crops and Products*, 2016; 81; 176-9.
15. Wu S., Tian L., A new flavone glucoside together with known ellagitannins and flavones with anti-diabetic and anti-obesity activities from the flowers of pomegranate (*Punica granatum*), *Natural Product Research*, 2019; 33(2); 252-7.
16. Abdolahi N., Soltani A., Mirzaali A., Soltani S., Balakheyli H., Aghaei M., Antibacterial and antioxidant activities and phytochemical properties of *Punica granatum* flowers in Iran, *Iranian Journal of Science and Technology, Transactions A: Science*, 2018; 42; 1105-10.
17. Huang THW., Peng G., Kota BP., Li GQ., Yamahara J., Roufogalis BD., Li Y., Anti-diabetic action of *Punica granatum* flower extract: Activation of PPAR- γ and identification of an active component, *Toxicology and Applied Pharmacology*, 2005; 207(2); 160-9.
18. Bekir J., Mars M., Vicendo P., Ftterich A., Bouajila J., Chemical composition and antioxidant, anti-inflammatory and antiproliferation activities of pomegranate (*Punica granatum*) flowers, *Journal of Medicinal Food*, 2013; 16(6); 544-50.
19. Singleton VL., Rossi JA., Colorimetry of total phenolics with phosphomolybdic-phosphotungstic acid reagents, *American Journal of Enology and Viticulture*, 1965; 16; 144-58.
20. Zhishen J., Mengcheng T., Jianming W., The determination of flavonoid contents in mulberry and their scavenging effects on superoxide radicals, *Food Chemistry*, 1999; 64(4); 555-9.
21. Blois MS., Antioxidant determinations by the use of a stable free radical, *Nature*, 1958; 181; 1199-200.
22. Oyaizu M., Studies on product of browning reaction prepared from glucose amine, *Japanese Journal of Nutrition*, 1986; 44; 307-15.
23. Dinis TCP., Madeira VMC., Almeida LM., Action of phenolic derivatives (acetaminophen, salicylate, and 5-aminosalicylate) as inhibitors of membrane lipid peroxidation and as peroxy radical scavengers, *Archives of Biochemistry and Biophysics*, 1994; 315(1); 161-169.
24. Eddebbagh M., Messaoudi M., Abourriche A., Berrada M., Attaleb M, Benbacer L., Bennamara A., Correlation of the cytotoxic and antioxidant activities of Moroccan pomegranate (*Punica Granatum*) with phenolic and flavonoid contents, *Journal of Pharmacy and Pharmacology*, 2016; 4; 511-9.
25. Rashid M., Shafi S., Evaluation of in vitro antioxidant and anti-diabetic potential of Kashmiri pomegranate (*Punica granatum* Linn.) flower extract, *International Research Journal of Pharmacy*, 2018; 9(9); 117-24.
26. Elfellah W., Hannachi H., Tlili N., Yahia Y., Nasri N., Ferchichi A., Total phenolic contents and antioxidant activities of pomegranate peel, seed, leaf and flower, *Journal of Medicinal Plants Research*, 2012; 6; 4724-30.



Hydrothermal Synthesis and Crystal Structure of Zn(II) Coordination Polymer with Rigid 4,4'-azobispyridine

Figen Arslan Biçer  

Department of Chemistry, Karabük University, TR-78050 Karabük, Turkey

Abstract: The new metal complex with phenylsuccinic acid (H_2psa) and 4,4'-azobispyridine (4,4'-abpy), $\{[Zn(psa)(H_2O)_3(\mu-4,4'-abpy)](H_2O)\}_n$ (**I**), was synthesized by hydrothermal process. The structure of **I** has been characterized by IR spectra, elemental analysis, and single crystal X-ray diffraction. Single crystal X-ray analysis reveals that the psa ligand O-coordinated to the Zn(II) ion and distorted octahedral geometry of Zn(II) ion is completed by bridging 4,4'-abpy and three aqua ligands.

Keywords: Coordination polymers, 4,4'-azobispyridine, phenylsuccinic acid, Zn complexes.

Submitted: March 06, 2019. **Accepted:** October 11, 2019.

Cite this: Arslan Biçer F. Hydrothermal Synthesis and Crystal Structure of Zn(II) Coordination Polymer with Rigid 4,4'-azobispyridine. JOTCSA. 2020;7(1):43-8.

DOI: <https://doi.org/10.18596/jotcsa.536258>.

***Corresponding author. E-mail:** farslan@karabuk.edu.tr.

INTRODUCTION

Although it was stated that coordination polymers had emerged in 1960s, it has attracted attention via leading reports on the findings of the porous structures and associated functionalities since 1990s (1). Since the past decade, the interest in searching for the coordination polymers has aroused profoundly for the immediate increase in the publication ratio and number about them. Coordination polymers which are known as 1D, 2D and 3D are considered structurally interesting, especially 1D polymers have intriguing electrical, optical and magnetic properties (2). For 1D chains, self-assembly of metal ions that have specific directionality and functionality with organic ligands that have appropriate functional groups is relatively simple; however, this simplicity leads to corporate structural features at the metal centers or in the backbone of the bridging ligands (3). We have studied on the metal-phenylsuccinate-azobispyridine system, in which 4,4'-azobispyridine (4,4'-abpy) has a structure with a π conjugated system and two

coordinatively active nitrogen atoms in which pyridine nitrogens are more basic and are more accessible for polynuclear arrangements for steric reasons (4-12). Furthermore, azobispyridine complexes are used as electro-optical devices for reversible data storage, in indicators, therapeutic and drug delivery agents, and photochemical switches. Even if H_2psa displays coordination capabilities of the two carboxylate groups and an amazing phenyl ring side group, that is presumed to modulate and affect the orientation relationship (13), in fact there are still few studies on H_2psa . In addition, more interesting coordination polymers can be obtained through enforcing it as a configurationally asymmetric bridging ligand. The aim of this work was to prepare new coordination polymers of phenylsuccinate complexes of Zn(II) metal ion with 4,4'-azobispyridine by hydrothermally process, and to analyze their structural and spectroscopic characteristics using single crystal X-ray diffraction and IR technique.

EXPERIMENTAL

Materials and measurements

All chemicals used were of analytical reagent quality. The 4,4'-abpy ligand was synthesized by oxidation of the 4-aminopyridine with NaOCl according to literature (Kirpal-Reiter method) (15). Elemental analysis was performed by standard methods at IBTAM (İnönü University Scientific Research Centre). The IR spectrum was recorded on a Bruker Tensor 27 FT/IR spectrophotometer using KBr pellets and operating at 4000-400 cm^{-1} . The X-ray diffraction data of the complex were collected with a Bruker Kappa Apex2duo diffractometer. The structures were solved and refined by full-matrix least-squares techniques on F^2 by using the SHELXT-2015 program (16). The absorption corrections were done by the multiscan technique. All non-hydrogen atoms were refined anisotropically. All non-water hydrogen atoms were included in the refinement process by using a riding model.

Synthesis of the complex

$\text{Zn}(\text{Ac})_2 \cdot 2\text{H}_2\text{O}$ (24 mg, 0.11 mmol), phenylsuccinic acid (21 mg, 0.11 mmol) and 4,4'-abpy (20 mg, 0.11 mmol) were placed into 10 mL of distilled H_2O in a pyrex bottle. The bottle was sealed and heated in an oven at 120 $^\circ\text{C}$ for 72 h, and then cooled slowly to 25 $^\circ\text{C}$. Red blocks of **1** (33 mg, 58%) were isolated after washing with distilled water and acetone, and finally drying in air. Anal. Calc. for $\text{C}_{20}\text{H}_{24}\text{N}_4\text{O}_8\text{Zn}$: C, 46.75; H, 4.71; N, 10.90. Found: C, 47.09; H, 4.27; N, 10.12%. IR (cm^{-1}): 3505 (mb), 3433 (m), 3104 (w), 3053 (w), 2976 (w), 2911 (w), 1611 (s), 1583 (s), 1491

(m), 1423 (s), 1367 (s), 1226 (m), 1168 (m), 1051 (m), 1026 (m), 846 (s), 741 (m), 704 (m), 680 (s), 566 (m), 526 (w).

RESULT AND DISCUSSION

Vibrational Analysis

The elemental analysis results and selected IR data are consisted with assigned formulation. The observation of the IR spectrum of **1** was performed by considering the most important internal vibrations of carboxylate, phenyl and azo groups, and water molecules.

The bands of stretching vibrations $\nu(\text{O}-\text{H})$ were found at 3433 cm^{-1} for compound **1**, indicating that the water molecules exist within the structures. Because of the $\nu(\text{CH})$ vibrations of aromatic and aliphatic groups, the relatively weak bands are above and below 3000 cm^{-1} , respectively. The absorption bands of the carbonyl groups of **1** in which psa is O-coordinated (monodentate) are found out as strong bands at 1583 cm^{-1} and 1611 cm^{-1} respectively (14,17). It is considered that intra- and intermolecular hydrogen bonding interactions involving the carbonyl group shift this band to higher frequencies. The bands of symmetric $\nu_s(\text{COO})$ stretch was found at 1367 cm^{-1} for **1**. The values of $\Delta\nu[\nu_{\text{as}}(\text{COO}) - \nu_s(\text{COO})]$ in the the complex (more than 200) fall within the range for a vibrational mode associated with a monodentate ligand (18). The bands centered around 1423 cm^{-1} are assigned to the $\text{N}=\text{N}$ vibrations of the 4,4'-abpy ligand. $\text{C}=\text{N}$ vibrations of 4,4'-abpy appear at ca. 1583 cm^{-1} .

Crystal Structure

The crystal data, experimental details and refinement details of complex are given in Table 1. Selected bond distances, angles and hydrogen band geometries are listed in Tables 2-3, respectively.

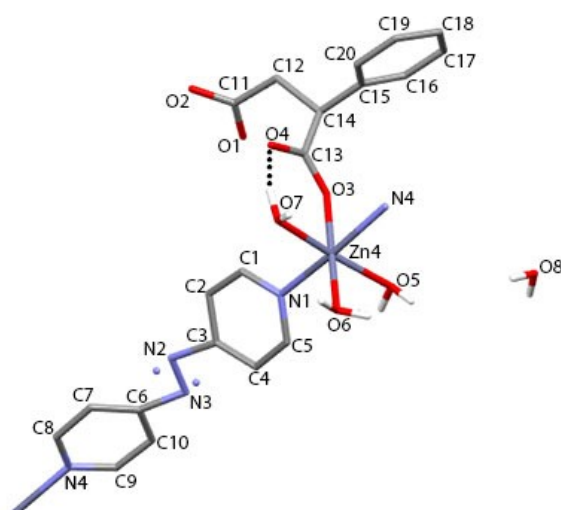


Figure 1. The crystal structure of **I** displaying the atom-labelling scheme.

Table 1. Crystal data and structure refinement parameters for complex **I**.

Crystal data	1
Empirical formula	C ₂₀ H ₂₄ N ₄ O ₈ Zn
Formula weight	513.83
Crystal system	Monoclinic
T (K)	100 (2)
λ (Å)	0.71073
Space group	P2 ₁ /n
a (Å)	12.676(4)
b (Å)	9.681(2)
c (Å)	19.455(6)
β (°)	108.716(9)
V (Å ³)	2261.3(11)
Z	4
D _c (g cm ⁻³)	1.5091
μ (mm ⁻¹)	1.14
Measured ref.	75543
Independent ref.	5634
θ Range (°)	0.963–1.00
Crystal size (mm)	0.15 × 0.11 × 0.1

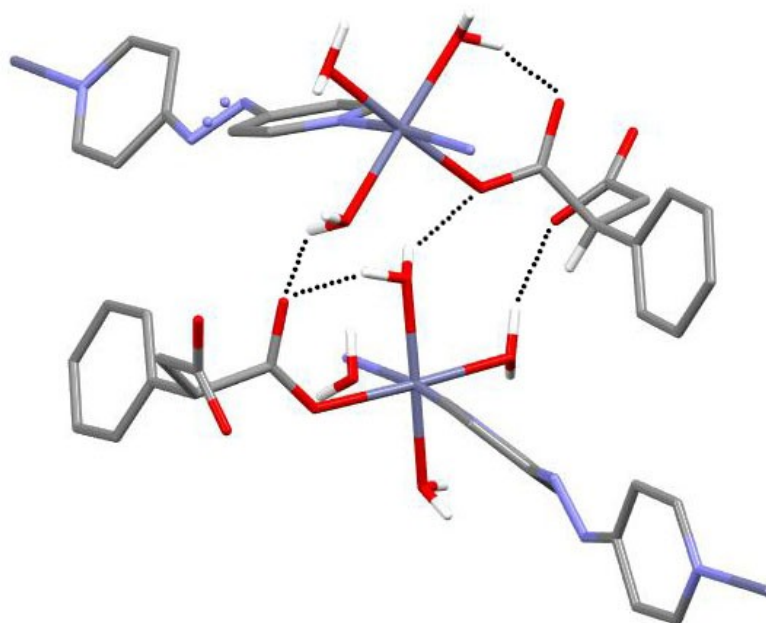
R_{int}	0.088
S	1.05
$R, R_w[I > 2\sigma(I)]$	0.067, 0.189
$\Delta\rho_{\text{max}}/\Delta\rho_{\text{min}} (\text{e}\text{\AA}^{-3})$	2.5, / -0.89

Table 2 Selected bond distances and angles for complex **I** (\AA , $^\circ$)

Bond distance	\AA	Bond distance	\AA
Zn4-O5	2.074	Zn4-O6	2.110
Zn4-N1	2.148	Zn4-O3	2.188
Bond angle	$^\circ$	Bond angle	$^\circ$
O5-Zn4-N1	95	O6-Zn4-N1	106
O7-Zn4-O3	92.6	O6-Zn4-O3	177.6
			6

According to the X-ray structural analysis, **I** crystallized in the monoclinic space group of $P2_1/n$. The asymmetric unit comprises of a Zn(II) atom, one half of the abpy, one PSA ligand as monodentate, three aqua ligands and one the lattice water molecule. (Figure 1.) The zinc settles with an octahedral geometry with

the PSA units and three aqua ligands on the equatorial plane and the axial sites are filled by two symmetry-related μ -abpy ligands ($\text{Zn-N} = 2.148(3) \text{ \AA}$) and subsequently, together with the the bridging abpy ligands, compose a one-dimensional coordination polymer. (Figure 2.).

**Figure 2.** Hydrogen-bonding for **I**

Contrary to expectations, PSA ligand is coordinated monodentate via carboxylate oxygen. The azo N atoms of 4,4'-azobispyridine was found to be distorted, probably due to unresolved disorder.

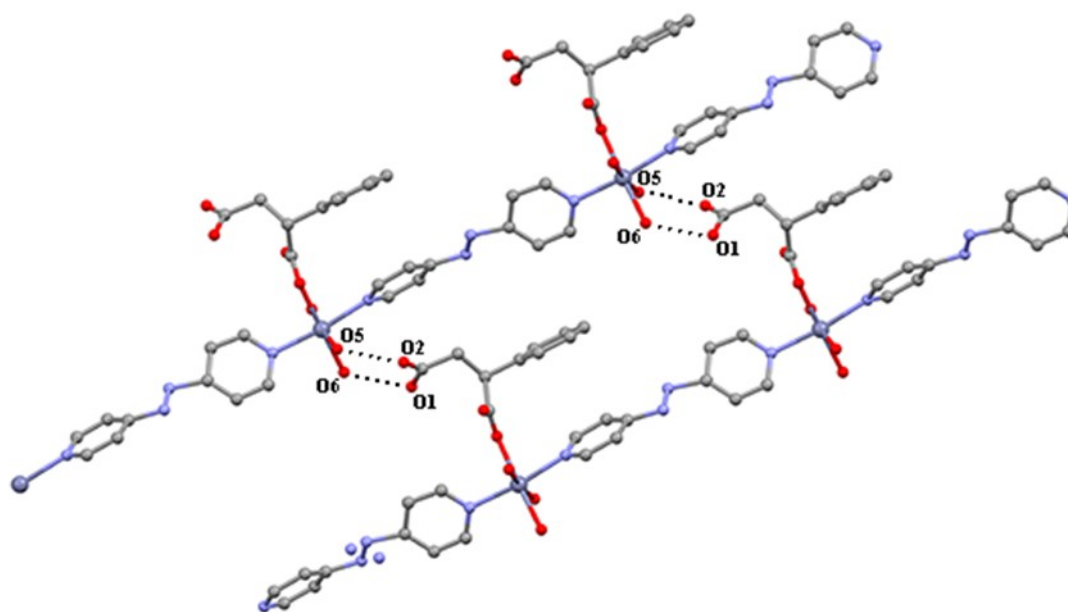
Table 3. Hydrogen-bond parameters for complex **I** (Å, °)

D-H...A	D-H	H...A	D...A	D-H...A
O5—H5A...O4	0.87	2.06	2.795(4)	141.4
O5—H5B...O2 ⁱ	0.87	1.87	2.649(5)	148.8
O7—H7A...O4 ⁱⁱ	0.87	1.82	2.628(4)	153.7
O6—H6A...O1 ⁱⁱⁱ	0.87	1.91	2.744(5)	160.4
O6—H6B...O1 ⁱ	0.87	1.95	2.815(5)	169.0
O8—H8B...O2 ⁱ	0.85	1.96	2.803(9)	172.5

Symmetry codes: (i) $-x+1, -y+1, -z+1$; (ii) $-x+1/2, y-1/2, -z+1/2$; (iii) $x, y-1, z$.

The crystals are stabilized by intra- and intermolecular hydrogen bonding. As shown in Figure 2, adjacent complex units are connected by O5—H5A...O4, O5—H5B...O2ⁱ, O6—H6A...O1ⁱⁱⁱ and O8—H8B...O2ⁱ hydrogen bonding between aqua and carboxy oxygen atom of phenylsuccinate

ligands. 1D coordinasyon polymer units are connected by O5—H5B...O2ⁱ and O6—H6B...O1ⁱ hydrogen bonds between aqua and carboxy oxygen atom of phenylsuccinate ligands (Figure 3).

**Figure 3.** View of the infinite 1D chain structure of **I**.

CONCLUSIONS

As a summary, the title coordination polymer, $\{[\text{Zn}(\text{psa})(\text{H}_2\text{O})_3(\mu\text{-}4,4'\text{-abpy})](\text{H}_2\text{O})\}_n$, has been hydrothermally prepared by utilizing phenylsuccinic acid and 4,4'-azobispyridine ligands. X-ray structural analysis and IR data display that the complex compose a one-dimensional coordination polymer together with the the bridging abpy ligands. It is examined that phenylsuccinate-azobispyridine system should be a good candidate to achieve the desired multifunctionalities in coordination polymer.

ACKNOWLEDGEMENTS

This work has been supported by Karabuk University, Scientific Research Unit (KBÜBAP-18-YL-060). Author is thankful to Prof. Dr. O. Z. Yeşilel, for crystallographic data analysis.

REFERENCES

1. Zhang J-P, and Chen X-M. Metal–Organic Frameworks for Second-Order Nonlinear Optics. *Struct Bond*. 2014; 157:1–26.

2. Leong WL, and Vittal JJ. One-Dimensional Coordination Polymers: Complexity and Diversity in Structures, Properties, and Applications. *Chem. Rev.* 2011; 111:688-764.
3. Janiak C, and Vieth JK. MOFs, MILs and more: concepts, properties and applications for porous coordination networks (PCNs). *New J. Chem.*, 2010; 34:2366-2388.
4. Li B, Liu H, Xu Y, Chen J, Wang H, Xu Z. Synthesis and crystal structure of two cobalt complexes: [Co₂(4,4'-azpy)₅(H₂O)₆][ClO₄]₄·(H₂O)₁₀·(4,4'-azpy)₄ with a novel two-dimensional large rectangle organic-inorganic hybrid network and one-dimensional chain complex {[Co(3,3'-azpy)(H₂O)₄][ClO₄]₂·[3,3'-azpy]₃}_n (4,4'-azpy, 4,4'-azobispyridine, 3,3'-azpy, 3,3'-azobispyridine). *J. Mol. Struct.* 2001; 597:21-30.
5. Dey R, Ghoshal D. Syntheses and characterization of two supramolecular self-assembled Mn(II) compounds using trans 4,4'-azobispyridine as a bridging ligand: Effect of n-n interactions in the formation of a solid-state structure. *Polyhedron.* 2012; 34:24-30.
6. Theilmann O, Saak W, Haase D, Beckhaus R. Reactions of Low-Valent Titanocene(II) Fragments with trans-4,4'-Azobispyridine (RN=NR, R = C₅H₄N): Formation of Tetranuclear Molecular Squares by trans-cis Isomerization. *Organometallics.* 2009; 28:2799-2807.
7. Arslan F. Synthesis, crystal structure and spectrothermal characterization of zinc(II) salicylato complex with 2,2'-azobispyridine, [Zn(Hsal)₂(H₂O)(abpy)]·H₂O. *Dyes and Pigments.* 2007; 75:521-525.
8. Zhuang Z, Cheng J, Wang X, Yin Y, Chen G, Zhao B, Zhang H, Zhang G. Spectroscopy of 4,4'-azopyridine by density functional theory and surface-enhanced Raman scattering. *J. Mol. Struct.* 2006; 794:77-82.
9. Noro S, Kitagawa S, Nakamura T, Wada T. Synthesis and Crystallographic Characterization of Low-Dimensional and Porous Coordination Compounds Capable of Supramolecular Aromatic Interaction Using the 4,4'-Azobis(pyridine) Ligand. *Inorg. Chem.* 2005; 44:3960-3971.
10. Zhuang Z, Shanga X, Wanga X, Ruana W, Zhaoa B. Density functional theory study on surface-enhanced Raman scattering of 4,4'-azopyridine on silver. *Spectrochim. Acta Part A.* 2009; 72:954-958.
11. Niu Y, Song Y, Hou H, Zhu Y. The syntheses, crystal structures and optical limiting effects of HgI₂ adduct polymers bridged by bipyridyl-based ligands. *Inorganica Chimica Acta.* 2003; 355:151-156.
12. Launay J, Tourrel-Pagis M, Lipskier J, Marvaud V, Joachim C. Control of intramolecular electron transfer by a chemical reaction. The 4,4'-azopyridine/1,2-bis(4-pyridyl)hydrazine system. *Inorg. Chem.* 1991; 30:1033-1038.
13. Thuery P. Uranyl-organic bilayer assemblies with flexible aromatic di-, tri- and tetracarboxylic acids. *CrystEngComm*, 2009, 11:1081-1088.
14. Hu S, Zhang P, Yu F-Y, Lin D-R, Chen M-X. Constructions of two photoluminescent 3D coordination polymers comprising of hydroxide-bridged cadmium chain and polynuclear cadmium macrocycle using phenylsuccinic acid. *J. Mol. Struct.* 2013; 1051:72-77.
15. Baldwin D A, Lever A B P, Parish R V. Complexes of 2,2'-azopyridine with iron(II), cobalt(II), nickel(II), copper(I), and copper(II). Infrared study. *Inorg. Chem.* 1969; 8(1):107-115.
16. Sheldrick G, SHELXT - Integrated space-group and crystal-structure determination *Acta Crystallogr. Sect. A.* 2015; 71:3-8
17. Gomez G E, Bernini M C, Brusau E V, Narda G E, Vega D, Kaczmarek A M, Van Deun R, Nazzarro M. Layered exfoliable crystalline materials based on Sm-, Eu- and Eu/Gd-2-phenylsuccinate frameworks. Crystal structure, topology and luminescence properties. *Dalton Trans.*, 2015; 44:3417-3429.
18. Wang J, Zhang Y, Liu X-Q, Xiao J, Zhou H, Yuan A-H. Two Zn(II) and Co(II) compounds with dicarboxylates and curved 4,4'-azopyridine ligands: Syntheses, crystal structures and gas sorption properties. *Microporous and Mesoporous Materials.* 2012; 159:100-104.



New Homodinuclear Alkyl- and Aryl- Dithiophosphonato Cd(II) and Hg(II) complexes: Syntheses and Characterizations

Ertuğrul Gazi Sağlam^{1*}, Elif Bulat¹, Nurcan Acar² and İbrahim Demirel¹

¹ University of Yozgat Bozok, Department of Chemistry, 66900, Yozgat, Turkey,

² University of Ankara, Department of Chemistry, 06100 Tandoğan, Ankara, Turkey

Abstract: New Cd(II) and Hg(II) complexes of five previously known dithiophosphonic acids ((*p*-MeO-C₆H₄)PS(SH)(OR), HLⁿ, (n= 1-5); R= 3-pentyl-, HL¹; R=1-phenyl-1-propyl-, HL²; R= 4-*tert*-butylbenzyl-, HL³; R= diphenylmethyl-, HL⁴; R= 4-*tert*-butylcyclohexyl-, HL⁵) were prepared and characterized. To do this, the dithiophosphonic acids involved were treated with stoichiometric amount of the corresponding metal salts in methyl alcohol. The complexes came of as powdery crystals and were recrystallized from chloroform. The pure complexes were characterized by using elemental analyses as well as mass-(ESI), FTIR-, Raman-, NMR- (¹H, ¹³C, ³¹P) spectroscopies.

Keywords: Dithiophosphonic Acid, Phosphonodithioic Acid, Dithiophosphonate Complexes, Lawesson's Reagent.

Submitted: May 15, 2019. **Accepted:** September 21, 2019.

Cite this: Sağlam E, Bulat E, Acar N, Demirel İ. New Homodinuclear Alkyl- and Aryl-Dithiophosphonato Cd(II) and Hg(II) complexes: Syntheses and Characterizations. JOTCSA. 2020;7(1):49-64.

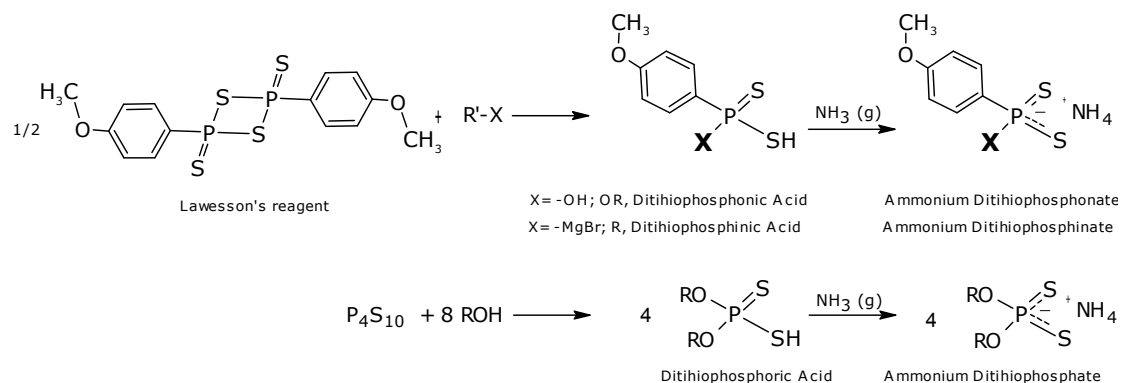
DOI: <https://doi.org/10.18596/jotcsa.565642>.

***Corresponding author. E-mail:** ertugrulgazi.saglam@bozok.edu.tr

INTRODUCTION

Dithiophosphate (phosphorodithioate, (RO)₂PS₂⁻), dithiophosphonate (phosphonodithioate, (R)(R'O)PS₂⁻) and dithiophosphinate (phosphinodithioate, (R)(R')PS₂⁻) type ligands are an important class of phosphorus-sulfur compounds and collectively named as phosphoro-1,1-dithiolates (1). The three types of compounds are synthesized through the reactions of either the so-called Lawesson's reagent (2) (LR, 2,4-bis(4-methoxyphenyl)-1,3-dithia-2,4-diphosphetane 2,4-disulfide), or the Berzelius' reagent (P₄S₁₀, tetraphosphorus pentasulfide) (3).

Dithiophosphates require the use of P₄S₁₀ and the corresponding alcohol as starting material (4) while the dithiophosphonates and dithiophosphinates are obtained by the reaction of LR with a nucleophilic agent, an alcohol for dithiophosphonates (5) and a carbo-anion for dithiophosphinates (6). The dithiophosphoric (DTP), dithiophosphonic (DTPOA) and dithiophosphinic (DTPA) acids themselves are either liquids or else, difficult to crystallize as they are hygroscopic. Besides, all these compounds have disagreeable odors, and they have been found to be suitable to convert to their ammonium salts (7), which are easy to crystallize. As an example, the synthesis of dithiophosphonic acid ammonium salts is given in Scheme 1.



Scheme 1. Synthesis reaction of phosphor-1,1-dithiolates.

The dithiophosphonate groups are typical, soft base type ligands and naturally prone to be coordinated to transition metal cations of relatively lower charges (8,9). Generally, the reaction of the proper metal salts with the corresponding ammonium dithiophosphonate in an organic solvent (8) to obtain complexes. Alternatively, a one-pot reaction starting with the corresponding LR which is categorized perthiophosphonic acid (PTFA), nucleophile and metal salt sometimes proves to be preferable (10).

The dithiophosphonate anions act as bidentate ligands, because the negative charge is delocalized over the two sulfur atoms (11).

The coordination topology of the complexes formed is related to the nature of the metal cation. Group 10 metals tend to form monomeric complexes of the general formula $[\text{M}(\text{DTPOA})_2]$ with square planar geometries (12), whereas Group 12 metals form dimeric complexes of the general formula $[\text{M}_2(\mu\text{-DTPOA})_2(\text{DTPOA})_2]$ and tetrahedral geometries. In these dimeric complexes, some of the sulfur atoms act as bridging ligands. As shown in Figure 1, the dimeric structure has an eight-membered ring comprising two metals, two phosphorus and four sulfur atoms (13).

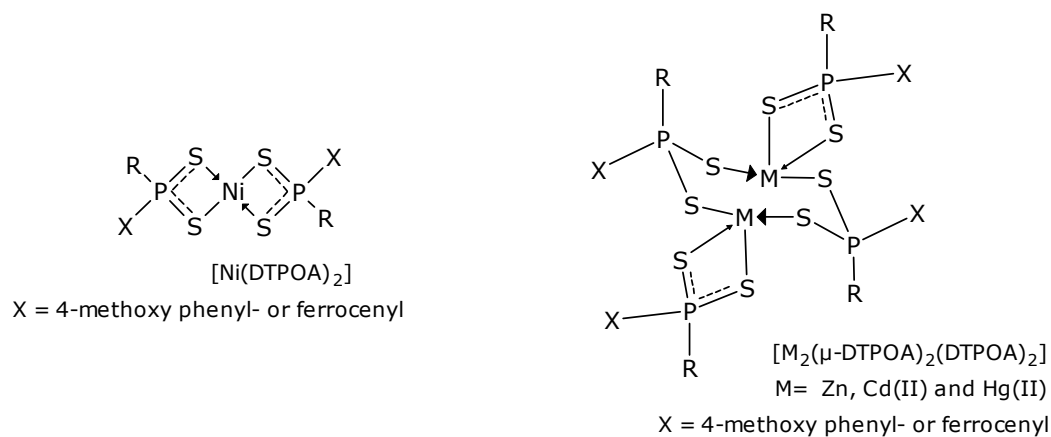


Figure 1. Structures of Group 10 and Group 12 DTPOA complexes.

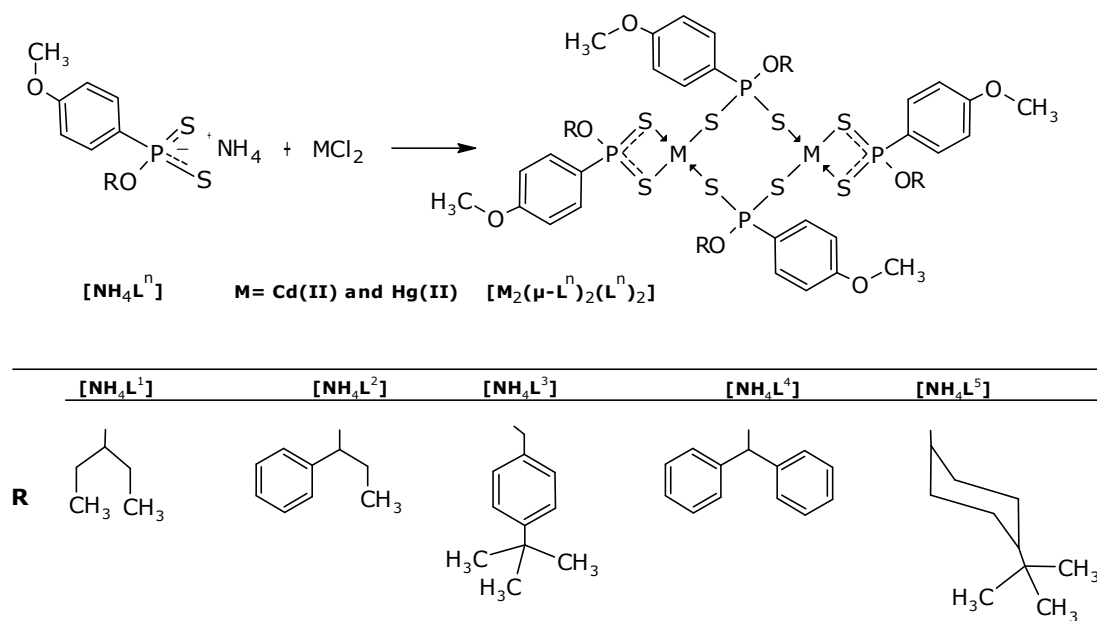
Due to their affinity to transition metals, lipophilic phosphorus-dithiolate ligands are designed to prepare stable metal chelates complexes that are extractable into nonpolar organic media. These ligands are used in the mining industry as flotation aids (14,15). Other applications that are DTPOA and their complexes including lubricants anti-wear additives (16,17) and agricultural pesticides (18) are also reported. Investigations are

also underway to design molecular complexes of radioactive transition metal cations to introduce into the human body for medical imaging (19-21). Some of tin DTPOA complexes are effective in chemotherapy (22) while some cadmium DTPOA complexes show antibacterial effect (23).

Among the transition metal-DTPOA complexes, the Ni(II)-DTPOAs are the most

extensively studied species (8,9) while studies on Cd(II)- and Hg(II)-DTPOAs are relatively scarce (13). Therefore, we have focused on the synthesis of Cd(II)- and Hg(II)-DTPOA complexes. In this study, we prepared the cadmium and mercury complexes of five, already known

dithiophosphonate ligands (24) and characterized them by using elemental analyses, mass spectroscopic (ESI), Infrared spectroscopic (FT-IR), Raman spectroscopic, $^1\text{H-NMR}$, $^{13}\text{C-NMR}$ ve $^{31}\text{P-NMR}$ data. The general reaction used for the synthesis is shown in Scheme 2.



Scheme 2. Synthesis reaction of cadmium(II) and mercury(II) dithiophosphonato complexes.

EXPERIMENTAL

Materials and instruments

Ethanol, $\text{CdCl}_2 \cdot \text{H}_2\text{O}$ and HgCl_2 were purchased from Sigma-Aldrich. Ammonium dithiophosphonates ($[\text{NH}_4\text{L}^n]$, $n = 1-5$) were synthesized as described in the literature (24).

Microanalyses were carried out using a LECO CHNS-932 CHNS-O elemental analyzer.

Melting points were measured by an Electrothermal 9200 melting point apparatus.

Vibrational spectra were recorded on a Perkin Elmer Spectrum Two Model FT-IR Spectrometer using the ATR method ($200\text{--}4000\text{ cm}^{-1}$) and are presented in cm^{-1} units. Raman spectra were run in the range $4000\text{--}100\text{ cm}^{-1}$, using a Renishaw in-Via Raman microscope, with a Peltier-cooled CCD detector (-70°C). The Raman microscope was equipped with a 50X objective. The excitation was carried out by the 785 lines of a diode laser.

The LC/MS spectra were obtained on a Waters Micromass ZQ connected to a Waters

Alliance HPLC (C-18 column), using an ESI(+) ionizer.

$^1\text{H-}$ (400 MHz), $^{13}\text{C-}$ (100 MHz) and $^{31}\text{P-NMR}$ (160 MHz) spectra were performed by using a Varian Mercury (Agilent) FT spectrometer in CDCl_3 . SiMe_4 was used for $^1\text{H-NMR}$ and $^{13}\text{C-NMR}$ while 85% H_3PO_4 was used for $^{31}\text{P-NMR}$ as chemical shift standards. Chemical shifts (δ) are reported in ppm.

Syntheses of compounds

General Procedure of $[\text{Cd}_2(\mu\text{-L}^n)_2(\text{L}^n)_2]$ and $[\text{Hg}_2(\mu\text{-L}^n)_2(\text{L}^n)_2]$

To an ethanolic solution of 4.70 mmoles of the $[\text{NH}_4\text{L}^n]$ of interest (1.45 g of $[\text{NH}_4\text{L}^1]$ and $[\text{NH}_4\text{L}^2]$; 1.68 g of $[\text{NH}_4\text{L}^3]$; 1.80 g of $[\text{NH}_4\text{L}^4]$ and 1.80 g of $[\text{NH}_4\text{L}^5]$) were added 2.35 mmol of metal(II) chloride (0.48 g of $\text{CdCl}_2 \cdot \text{H}_2\text{O}$; 0.64 g of HgCl_2) dissolved in 50-60 mL of ethanol. The solution was stirred at room temperature for 15 min. The white complex participated is filtered through filter paper and dried in a vacuum desiccator.

Bis-{bis-[O-3-pentyl-(4-methoxyphenyl)dithiophosphonato]cadmium(II)}, $[\text{Cd}_2(\mu\text{-L}^1)_2(\text{L}^1)_2]$
Yield: 0.25 g (71%). Yellow. m.p. $177\text{--}178^\circ\text{C}$, (decomposition). $^1\text{H NMR}$ (δ :ppm, CDCl_3): $\delta =$

0.94 (t, $^3J_{\text{HH}} = 7.5$ Hz, 24H, C8-H), 1.77 (m, 16H, C7-H), 4.8 (m, 4H, C6-H), 3.83 (s, 12H, OCH₃), 6.93 (A-part of AA'MM'X, $^4J_{\text{PH}} = 3.3$ Hz (J_{AX}), $N = 8.8$ Hz, 8H, *m*-H), 8.01 (M-part of AA'MM'X, $^3J_{\text{PH}} = 14.5$ Hz (J_{MX}), $N = 8.8$ Hz, 8H, *o*-H). ¹³C-NMR (CDCl₃): $\delta = 9.3$ (s, C8), 27.1 (d, $^3J_{\text{P-C}} = 4.0$ Hz, C7), 81.1 (d, $^2J_{\text{P-C}} = 8.2$ Hz, C6), 55.4 (s, CH₃O-), 113.5 (d, $^3J_{\text{P-C}} = 16.2$ Hz, C3), 132.2 (d, $^2J_{\text{P-C}} = 14.2$, C2) Hz, 132.2 (d, $J_{\text{P-C}} = 123.9$ Hz, C1) 162.3 (d, $^4J_{\text{PC}} = 3.3$, C4). ³¹P-NMR (CDCl₃): $\delta = 103.42$. LC/MS: m/z 1406.2 ([M+Na]⁺, 2%), 1093.1 ([M-L¹]⁺, 100%), 689.1 ([M/2]⁺, 29%). Anal. Calcd. for: C₄₈H₇₂Cd₂O₈P₄S₈ (1382.32g.mol⁻¹): C, 41.71; H, 5.25; S, 18.56; found: C, 41.82; H, 5.29; S, 18.79 %.

Bis-{bis-[O-1-phenyl-1-propyl-(4-methoxyphenyl)dithiophosphonato]cadmium(II)}, [Cd₂(μ -L²)₂(L²)₂]
Yield: 0.29 g (74%). White. m.p. 137-138°C, (decomposition). ¹H NMR (δ :ppm, CDCl₃): $\delta = 0.87$ (t, $^3J_{\text{HH}} = 7.4$ Hz, 12H, C8-H), 2.01 (m, 8H, diastereotopic protons, C7-H), 5.70 (m, 4H, C6-H), 3.80 (s, 12H, OCH₃), 6.93 (A-part of AA'MM'X, $^4J_{\text{PH}} = 3.2$ Hz (J_{AX}), $N = 8.8$ Hz, 8H, *m*-H), 7.28 (m, 20H, Ar-CH), 7.93 (M-part of AA'MM'X, $^3J_{\text{PH}} = 14.6$ Hz (J_{MX}), $N = 8.8$ Hz, 8H, *o*-H). ¹³C-NMR (CDCl₃): $\delta = 9.8$ (s, C8), 31.4 (d, $^3J_{\text{P-C}} = 5.4$ Hz, C7), 80.8 (d, $^2J_{\text{P-C}} = 7.3$ Hz, C6), 55.4 (s, CH₃O-), 113.5 (d, $^3J_{\text{P-C}} = 16.3$ Hz, C3), 126.9 (s, C12), 127.5 (s, C11), 128.1 (s, C10), 129.0 (d, $J_{\text{P-C}} = 122.7$ Hz, C1), 132.4, 140.9 (d, $^2J_{\text{P-C}} = 3.1$ Hz, C9), (d, $^2J_{\text{P-C}} = 14.4$ Hz, C2), 162.4 (d, $^4J_{\text{PC}} = 3.3$, C4). ³¹P-NMR (CDCl₃): $\delta = 104.58$. LC/MS: m/z 1597.3 ([M+Na]⁺, 29%), 1237.3 ([M-L²]⁺, 100%), 810.2 ([M/2]⁺, 36%). Anal. Calcd. for: C₆₄H₇₂Cd₂O₈P₄S₈ (1574.49 g.mol⁻¹): C, 48.82; H, 4.61; S, 16.29; found: C, 49.01; H, 4.67; S, 16.56 %.

Bis-{bis-[O-4-*tert*-butylbenzyl-(4-methoxyphenyl)dithiophosphonato]cadmium(II)}, [Cd₂(μ -L³)₂(L³)₂]
Yield: 0.32 g (80%). White. m.p. 189-200°C, (decomposition). ¹H NMR (δ :ppm, CDCl₃): $\delta = 1.32$ (s, 36H, C12), 5.34 (m, 8H, C6-H), 3.83 (s, 12H, OCH₃), 6.94 (A-part of AA'MM'X, $^4J_{\text{PH}} = 3.3$ Hz (J_{AX}), $N = 8.7$ Hz, 8H, *m*-H), 7.35 (m, 16H, Ar-CH), 8.00 (M-part of AA'MM'X, $^3J_{\text{PH}} = 14.5$ Hz (J_{MX}), $N = 8.7$ Hz, 8H, *o*-H). ¹³C-NMR (CDCl₃): $\delta = 31.3$ (s, C12), 34.6 (s, C11), 55.4 (s, CH₃O-), 67.6 (d, $^2J_{\text{P-C}} = 6.7$ Hz, C6), 113.7 (d, $^3J_{\text{P-C}} = 16.3$ Hz, C3), 125.3 (s, C9), 130.7 (s, C8), 132.5 (d, $^2J_{\text{P-C}} = 14.5$ Hz, C2), 128.4 (d, $J_{\text{P-C}} = 121.7$ Hz, C1), 133.1 (d, $^3J_{\text{P-C}} = 9.9$ Hz, C7), 151.2 (s, C10), 162.6 (d, $^4J_{\text{PC}} = 3.2$, C4). ³¹P-NMR (CDCl₃): $\delta = 106.20$. LC/MS: m/z 1687.90 ([M]⁺, 17%), 1321.4 ([M-L³]⁺, 100%), 843.4 ([M/2]⁺, 55%), 479.3

([CdL³]⁺, 36%). Anal. Calcd. for: C₇₂H₈₈Cd₂O₈P₄S₈ (1686.70 g.mol⁻¹): C, 51.27; H, 5.26; S, 15.21; found: C, 51.33; H, 5.29; S, 15.39 %.

Bis-{bis-[O-di-phenylmethyl-(4-methoxyphenyl)dithiophosphonato]cadmium(II)}, [Cd₂(μ -L⁴)₂(L⁴)₂]
Yield: 0.28 g (68%). White. m.p. 101-102°C, (decomposition). ¹H NMR (δ :ppm, CDCl₃): 7.28 (s, 40H, Ar-CH), 7.93 (A-part of AA'MM'X, $^4J_{\text{PH}} = 14.7$ Hz (J_{AX}), $N = 8.8$ Hz, 8H, *m*-H), 7.28 (m, 16H, Ar-CH), 6.93 (d, $^3J_{\text{PH}} = 16.4$ Hz 4H, C6H), 6.79 (M-part of AA'MM'X, $^3J_{\text{PH}} = 3.3$ Hz (J_{MX}), $N = 8.8$ Hz, 8H, *o*-H), 3.78 (s, 12H, OCH₃). ¹³C-NMR (CDCl₃): $\delta = 55.4$ (s, CH₃O-), 79.6 (d, $^2J_{\text{P-C}} = 6.9$, C6) Hz, 113.6 (d, $^3J_{\text{P-C}} = 16.1$ Hz, C3), 127.5 (s, C9), 127.6 (s, C10), 128.2 (s, C8), 129.6 (d, $J_{\text{P-C}} = 121.5$ Hz, C1), 132.3 (d, $^2J_{\text{P-C}} = 14.3$ Hz, C2), 141.0 (d, $^3J_{\text{P-C}} = 4.6$ Hz, C7), 162.4 (d, $^4J_{\text{PC}} = 3.3$ Hz, C4). ³¹P-NMR (CDCl₃): $\delta = 106.25$. LC/MS: m/z 1787.80 ([M+Na]⁺, 31%), 907.9 ([M/2+Na]⁺, 32%), 575.9 ([Cd₂P₃S₈]⁺, 100%). Anal. Calcd. for: C₈₀H₇₂Cd₂O₈P₄S₈ (1766.66 g.mol⁻¹): C, 54.39; H, 4.11; S, 14.52; found: C, 54.47; H, 4.14; S, 14.77 %.

Bis-{bis-[O-4-*tert*-butylcyclohexyl-(4-methoxyphenyl)dithiophosphonato]cadmium(II)}, [Cd₂(μ -L⁵)₂(L⁵)₂]
Yield: 0.32 g (78%). White. m.p. 115-116°C, (decomposition). ¹H NMR (δ :ppm, CDCl₃): $\delta = 0.82$ (m, 36H, C11-H), 0.96 (m, 4H, C9-H), 1.11 (m, 8H, C8'-H), 1.43 (m, 8H, C8-H), 1.74 (m, 8H, C7'-H), 2.25 (m, 8H, C7-H), 3.83 (m, 16H, C6-H overlapped with OCH₃), 6.92 (A-part of AA'MM'X, $^4J_{\text{PH}} = 3.3$ Hz (J_{AX}), $N = 8.8$ Hz, 8H, *m*-H), 7.99 (M-part of AA'MM'X, $^3J_{\text{PH}} = 14.5$ Hz (J_{MX}), $N = 8.8$ Hz, 8H, *o*-H). ¹³C-NMR (CDCl₃): $\delta = 25.7$ (s, C8), 27.6 (s, C11), 32.3 (s, C10), 46.9 (s, C9), 34.2 (s, C7), 78.1 (d, $^2J_{\text{P-C}} = 7.9$ Hz, C6), 55.4 (s, CH₃O-), 113.6 (d, $^3J_{\text{P-C}} = 16.1$ Hz, C3), 129.6 (d, $J_{\text{P-C}} = 121.5$ Hz, C1), 132.3 (d, $^2J_{\text{P-C}} = 14.3$ Hz, C2), 162.4 (d, $^4J_{\text{PC}} = 3.3$, C4). ³¹P-NMR (CDCl₃): $\delta = 102.65$. LC/MS: m/z 1679.1 ([M+Na]⁺, 28%), 1297.1 ([M-L⁵]⁺, 35%), 827.9 ([M/2]⁺, 32%), 512.8 ([Cd₂PS₈]⁺, 100%). Anal. Calcd. for: C₆₈H₁₀₄Cd₂O₈P₄S₈ (1654.79 g.mol⁻¹): C, 49.36; H, 6.33; S, 15.50; found: C, 49.52; H, 6.39; S, 15.71 %.

Bis-{bis-[O-3-pentyl-(4-methoxyphenyl)dithiophosphonato]mercury(I I)}, [Hg₂(μ -L¹)₂(L¹)₂]
Yield: 0.27 g (69%). White. m.p. 125-126°C, (decomposition). ¹H NMR (δ :ppm, CDCl₃): $\delta = 0.99$ (t, $^3J_{\text{HH}} = 7.5$ Hz, 24H, C8-H), 1.83 (m, 16H, C7-H), 4.8 (m, 4H, C6-H), 3.85 (s, 12H,

OCH₃), 6.96 (A-part of AA'MM'X, ⁴J_{PH} = 3.4 Hz (*J*_{AX}), *N* = 8.6 Hz, 8H, *m*-H), 8.6 (M-part of AA'MM'X, ³J_{PH} = 14.5 Hz (*J*_{MX}), *N* = 8.6 Hz, 8H, *o*-H). ¹³C-NMR (CDCl₃): δ = 9.4 (s, C8), 27.1 (s, C7), 81.4 (d, ²J_{PC} = 8.0 Hz, C6), 58.4 (s, CH₃O-), 113.7 (d, ³J_{P-C} = 16.3 Hz, C3), 131.9 (d, ²J_{P-C} = 14.0 Hz, C2) Hz, 130.1 (d, *J*_{P-C} = 126.6 Hz, C1) 162.4 (d, ⁴J_{PC} = 3.3, C4). ³¹P-NMR (CDCl₃): δ = 100.63. LC/MS: *m/z* 1581.8 ([M+Na]⁺, 100%), 1268.8 ([M-L¹]⁺, 35%), 803.0 ([M/2]⁺, 47%). Anal. Calcd. for: C₄₈H₇₂Hg₂O₈P₄S₈ (1558.68 g.mol⁻¹): C, 39.99; H, 4.66; S, 16.46; found: C, 40.13; H, 4.70; S, 16.59 %.

Bis-{bis-[O-1-phenyl-1-propyl-(4-methoxyphenyl)dithiophosphonato]mercury(I I)}, [Hg₂(μ-L²)₂(L²)₂]
Yield: 0.21 g (48%). White. m.p. 90-91°C, (decomposition). ¹H NMR (δ:ppm, CDCl₃): δ = 0.94 (t, ³J_{HH} = 7.4 Hz, 12H, C8-H), 2.03 (m, 8H, diastereotopic protons, C7-H), 5.84 (m, 4H, C6-H), 3.85 (s, 12H, OCH₃), 6.93 (A-part of AA'MM'X, ⁴J_{PH} = 3.4 Hz (*J*_{AX}), *N* = 8.9 Hz, 8H, *m*-H), 7.31 (m, 20H, Ar-CH), 7.93 (M-part of AA'MM'X, ³J_{PH} = 14.4 Hz (*J*_{MX}), *N* = 8.9 Hz, 8H, *o*-H). ¹³C-NMR (CDCl₃): δ = 9.8 (s, C8), 31.2 (s, C7), 55.4 (s, CH₃O-), 81.2 (s, C6), 113.7 (d, ³J_{P-C} = 16.3 Hz, C3), 127.1 (s, C12), 127.9 (s, C11), 128.4 (s, C10), 129.5 (d, *J*_{P-C} = 125.3 Hz, C1), 132.0 (d, ²J_{P-C} = 14.2 Hz, C2), 140.6 (d, ²J_{PC} = 3.0 Hz, C9), 162.5 (d, ⁴J_{PC} = 3.4, C4). ³¹P-NMR (CDCl₃): δ = 106.20. LC/MS: *m/z* 1413.3 ([M-L²]⁺, 32%), 339.2 ([L²]⁺, 28%), 233.0 ([HgS]⁺, 100%). Anal. Calcd. for: C₆₄H₇₂Hg₂O₈P₄S₈ (1750.85 g.mol⁻¹): C, 43.90; H, 4.14; S, 14.65; found: C, 43.97; H, 4.16; S, 14.77 %.

Bis-{bis-[O-4-*tert*-butylbenzyl-(4-methoxyphenyl)dithiophosphonato]mercury(I I)}, [Hg₂(μ-L³)₂(L³)₂]
Yield: 0.36 g (78%). White. m.p. 138-139°C, (decomposition). ¹H NMR (δ:ppm, CDCl₃): δ = 1.32 (s, 36H, C12), 5.4 (m, 8H, C6-H), 3.83 (s, 12H, OCH₃), 6.94 (A-part of AA'MM'X, ⁴J_{PH} = 3.3 Hz (*J*_{AX}), *N* = 8.7 Hz, 8H, *m*-H), 7.35 (m, 16H, Ar-CH), 8.00 (M-part of AA'MM'X, ³J_{PH} = 14.5 Hz (*J*_{MX}), *N* = 8.7 Hz, 8H, *o*-H). ¹³C-NMR (CDCl₃): δ = 30.9 (s, C12), 34.6 (s, C11), 55.4 (s, CH₃O-), 67.6 (d, ²J_{P-C} = 6.5 Hz, C6), 113.8 (d, ³J_{P-C} = 16.3 Hz, C3), 125.5 (s, C9), 128.1 (s, C8), 132.3 (d, ²J_{PC} = 14.3 Hz, C2), 129.3 (d, *J*_{P-C} = 124.2 Hz, C1), 133.0 (d, ³J_{P-C} = 9.8 Hz, C7), 151.4 (s, C10), 162.7 (d, ⁴J_{PC} = 3.3, C4). ³¹P-NMR (CDCl₃): δ = 103.94. LC/MS: *m/z* 1498.6 ([M-L³]⁺, 100%), 932.6 ([M/2]⁺, 20%). Anal. Calcd. for: C₇₂H₈₈Hg₂O₈P₄S₈ (1683.01 g.mol⁻¹): C, 46.42;

H, 4.76; S, 13.77; found: C, 46.57; H, 4.83; S, 13.97 %.

Bis-{bis-[O-di-phenylmethyl-(4-methoxyphenyl)dithiophosphonato]mercury (II)}, [Hg₂(μ-L⁴)₂(L⁴)₂]
Yield: 0.24 g (49%). White. m.p. 89-90°C, (decomposition). ¹H NMR (δ:ppm, CDCl₃): δ = 7.36 (s, 40H, Ar-CH), 7.92 (A-part of AA'MM'X, ⁴J_{PH} = 14.6 Hz (*J*_{AX}), *N* = 8.7 Hz, 8H, *m*-H), 7.28 (m, 16H, Ar-CH), 6.98 (d, 4H, C6 adjacent with Ar_{meta}), 6.92 (M-part of AA'MM'X, ³J_{PH} = 3.4 Hz (*J*_{MX}), *N* = 8.7 Hz, 8H, *o*-H adjacent with C6), 3.84 (s, 12H, OCH₃). ¹³C-NMR (CDCl₃): δ = 55.4 (s, CH₃O-), 80.1 (d, ²J_{P-C} = 6.4, C6) Hz, 113.7 (d, ³J_{P-C} = 16.4 Hz, C3), 127.6 (s, C9), 128.0 (s, C10), 128.5 (s, C8), 129.5 (d, *J*_{P-C} = 125.0 Hz, C1), 132.0 (d, ²J_{PC} = 14.3 Hz, C2), 140.6 (s, C7), 162.6 (d, ⁴J_{PC} = 3.3, C4). ³¹P-NMR (CDCl₃): δ = 102.22. LC/MS: *m/z* 1381.6 ([M-Hg⁴]+Na]⁺, 29%), 996.1 ([M/2+Na]⁺, 47%), 575.9 ([HgP₂S₄-O-CH₂(C₆H₄)₂]⁺, 100%). Anal. Calcd. for: C₈₀H₇₂Hg₂O₈P₄S₈ (1943.02 g.mol⁻¹): C, 49.45; H, 3.73; S, 13.20; found: C, 49.63; H, 3.78; S, 13.41 %.

Bis-{bis-[O-4-*tert*-butylcyclohexyl-(4-methoxyphenyl)dithiophosphonato]mercury (II)}, [Hg₂(μ-L⁵)₂(L⁵)₂]
Yield: 0.18 g (39%). White. m.p. 84-85°C, (decomposition). ¹H NMR (δ:ppm, CDCl₃): δ = 0.85 (m, 36H, C11-H), 1.01 (m, 4H, C9-H), 1.24 (m, 8H, C8'-H), 1.50 (m, 8H, C8-H), 1.82 (m, 8H, C7'-H), 2.34 (m, 8H, C7-H), 3.85 (m, 16H, C6-H overlapped with OCH₃), 7.00 (A-part of AA'MM'X, ⁴J_{PH} = 3.4 Hz (*J*_{AX}), *N* = 8.8 Hz, 8H, *m*-H), 8.04 (M-part of AA'MM'X, ³J_{PH} = 14.4 Hz (*J*_{MX}), *N* = 8.8 Hz, 8H, *o*-H). ¹³C-NMR (CDCl₃): δ = 25.7 (s, C8), 25.7 (s, C11), 32.3 (s, C10), 46.4 (s, C9), 34.2 (s, C7), 78.2 (s, C6), 55.4 (s, CH₃O-), 113.7 (d, ³J_{P-C} = 16.2 Hz, C3), 129.7 (d, *J*_{P-C} = 124.6 Hz, C1), 132.1 (d, ²J_{P-C} = 14.1 Hz, C2), 162.8 (s, C4). ³¹P-NMR (CDCl₃): δ = 101.05. LC/MS: *m/z* 1854.3 ([M+Na]⁺, 23%), 1268.8 ([M-L⁵]⁺, 31%), 350.9 ([HgS₄+Na]⁺, 100%). Anal. Calcd. for: C₆₈H₁₀₄Hg₂O₈P₄S₈ (1831.14 g.mol⁻¹): C, 44.60; H, 5.72; S, 14.01; found: C, 44.67; H, 5.74; S, 14.15 %.

RESULTS AND DISCUSSION

Spectroscopic studies

IR and Raman spectra

IR and Raman spectra are expected to bear evidence about the existence of PS and M-S bonds in the structures of the complexes. Indeed, ν(PS)_{asym} and ν(PS)_{sym} bands as well as a couple of bands another relating to the

coordination, namely, $\nu(\text{M-S})_{\text{asym}}$ and $\nu(\text{M-S})_{\text{sym}}$ are clearly visible in both the spectra as listed in Table 1.

Table 1: Selected IR and Raman (R) data (cm^{-1}) assignment of vibrational bands for the complexes.

Complex	$\nu(\text{Cd-S})_{\text{sym}}$		$\nu(\text{Cd-S})_{\text{asym}}$		$\nu(\text{PS})_{\text{sym}}$		$\nu(\text{PS})_{\text{asym}}$	
	IR	R	IR	R	IR	R	IR	R
$[\text{Cd}_2(\mu\text{-L}^1)_2(\text{L}^1)_2]$	286	288	340	341	539	552	660;64 7	664;63 5
$[\text{Cd}_2(\mu\text{-L}^2)_2(\text{L}^2)_2]$	283	285	362	366	536	542	676;64 8	680;63 5
$[\text{Cd}_2(\mu\text{-L}^3)_2(\text{L}^3)_2]$	293;30 8	292;30 7	393	393	543	550	661;64 6	666;63 5
$[\text{Cd}_2(\mu\text{-L}^4)_2(\text{L}^4)_2]$	295	292	347	347	555;51 7	564;52 3	620	618
$[\text{Cd}_2(\mu\text{-L}^5)_2(\text{L}^5)_2]$	267	289	294	414	582	540;52 4	663	664

Complex	$\nu(\text{Hg-S})_{\text{sym}}$		$\nu(\text{Hg-S})_{\text{asym}}$		$\nu(\text{PS})_{\text{sym}}$		$\nu(\text{PS})_{\text{asym}}$	
	IR	R	IR	R	IR	R	IR	R
$[\text{Hg}_2(\mu\text{-L}^1)_2(\text{L}^1)_2]$	389	311	386	310	555	541	629	633
$[\text{Hg}_2(\mu\text{-L}^2)_2(\text{L}^2)_2]$	335	330	363	350	563	569	637	619
$[\text{Hg}_2(\mu\text{-L}^3)_2(\text{L}^3)_2]$	363	363	394	389	544	547	645	641
$[\text{Hg}_2(\mu\text{-L}^4)_2(\text{L}^4)_2]$	382	378	417	407	547	547	622	619
$[\text{Hg}_2(\mu\text{-L}^5)_2(\text{L}^5)_2]$	356	357	389	389	579	582	627	629

Meanwhile, the N-H stretching signal does not exist in the vibrational spectra of the complexes, indicating that the ammonium salt is no longer present (24).

IR and Raman data reported for similar compounds agree well with the signals (24-29).

Mass Spectra

The main features of the mass spectra for the complexes are given in Table 2.

The natural abundance of cadmium and mercury, as well as sulfur isotopes, are reflected in the appearance of the peaks. Some mass peaks have the mass to charge values that are 23 units higher than the molecular mass, related to the leaving group. This discrepancy is suggested to have come from the Na^+ ions that may have detached from the buffer solution used in the ionizer.

The compounds $[\text{Cd}_2(\mu\text{-L}^1)_2(\text{L}^1)_2]$, $[\text{Cd}_2(\mu\text{-L}^2)_2(\text{L}^2)_2]$, $[\text{Cd}_2(\mu\text{-L}^3)_2(\text{L}^3)_2]$ and $[\text{Hg}_2(\mu\text{-L}^3)_2(\text{L}^3)_2]$ display mass signals corresponding to the molecule minus a single ligand but the disintegration patterns of the other six complexes do not appear to show any commentable feature. For these complexes, the molecular ion peaks are the sole usable information.

The molecular ion peaks corresponding to the dimeric $[\text{Cd}_2(\mu\text{-L}^n)_2(\text{L}^n)_2]$ complexes are relatively weak but visible anyway. On the other hand, Hg(II) complexes, except for $[\text{Hg}_2(\mu\text{-L}^1)_2(\text{L}^1)_2]$ and $[\text{Hg}_2(\mu\text{-L}^5)_2(\text{L}^5)_2]$ do not display any molecular ion peak at all. The molecular peak of $[\text{Hg}_2(\mu\text{-L}^1)_2(\text{L}^1)_2]$ is extraordinarily intense (the main peak actually). Mass spectral data reported for similar compounds agree well (30-33) with the signals we observed.

Table 2: MS spectral data for the complexes.

	[M] ⁺	m/z 100 % Intensity	Removing groups from [M] ⁺	
			[M-L ⁿ] ⁺	[M/2] ⁺
[Cd ₂ (μ-L ¹) ₂ (L ¹) ₂]	1406.2, [M+Na] ⁺ ; 2%	1093.1, [M-L ¹] ⁺ ; 100%		689.1, [M/2] ⁺ ; 29%
[Cd ₂ (μ-L ²) ₂ (L ²) ₂]	1597.3, [M+Na] ⁺ ; 29%	1237.3, [M-L ²] ⁺ ; 100%		810.2, [M/2] ⁺ ; 36%
[Cd ₂ (μ-L ³) ₂ (L ³) ₂]	1687.90, [M] ⁺ ; 17%	1321.4, [M-L ³] ⁺ ; 100%		843.4, [M/2] ⁺ ; 55%
[Cd ₂ (μ-L ⁴) ₂ (L ⁴) ₂]	1787.80, [M+Na] ⁺ ; 31%	575.9, [Cd ₂ P ₃ S ₈] ⁺ ; 100%	-	907.9, [M/2+Na] ⁺ ; 32%
[Cd ₂ (μ-L ⁵) ₂ (L ⁵) ₂]	1679.1, [M+Na] ⁺ ; 28%	512.8, [Cd ₂ PS ₈] ⁺ ; 100%	1297.1, [M-L ⁵] ⁺ ; 35%	827.9, [M/2] ⁺ ; 32%
[Hg ₂ (μ-L ¹) ₂ (L ¹) ₂]	1581.8, [M+Na] ⁺ ; 100%		1268.8, [M-L ¹] ⁺ ; 35%	803.0, [M/2] ⁺ ; 47%
[Hg ₂ (μ-L ²) ₂ (L ²) ₂]	-	233.0, [HgS] ⁺ ; 100%	1413.3, [M-L ²] ⁺ ; 32%	-
[Hg ₂ (μ-L ³) ₂ (L ³) ₂]	-	1498.6, [M-L ³] ⁺ ; 100%		932.6, [M/2] ⁺ ; 20%
[Hg ₂ (μ-L ⁴) ₂ (L ⁴) ₂]	-	575.9, [HgP ₂ S ₄ -O-CH ₂ (C ₆ H ₄) ₂] ⁺ ; 100%	-	996.1, [M/2+Na] ⁺ ; 47%
[Hg ₂ (μ-L ⁵) ₂ (L ⁵) ₂]	1854.3, [M+Na] ⁺ ; 23%	350.9, [HgS ₄ +Na] ⁺ ; 100%	1268.8, [M-L ⁵] ⁺ ; 31%	-

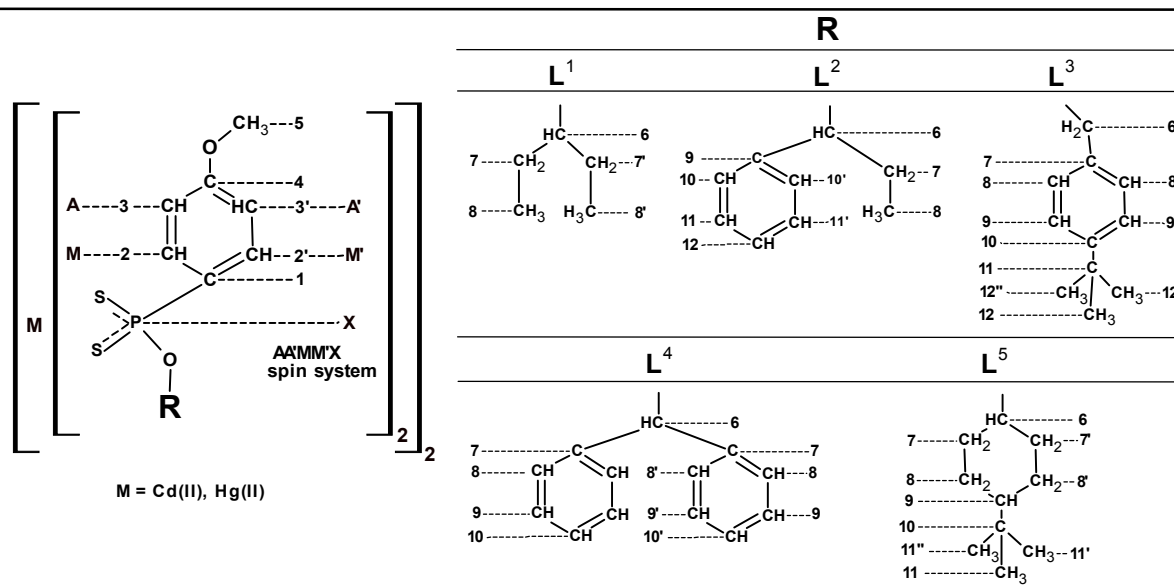


Figure 2. Numbering scheme for $[\text{Cd}_2(\mu\text{-L}^n)_2(\text{L}^n)_2]$ and $[\text{Hg}_2(\text{L}^n)_2(\text{L}^n)_2]$ complexes.

NMR Spectra

The numbering scheme for carbon atoms is given in Figure 2.

¹H-NMR spectra

The ¹H-NMR spectra of all the compounds display a signal corresponding to the anisole group protons, a doublet of two doublets; therefore these four protons constitute an AA'MM'X spin system in each compound.

In all the complexes the *ortho*-protons on the anisole ring are all split by ~14.5 Hz by the phosphorus atom. The four bond P-H splitting of the *meta*-protons on the same ring is ~3.3 Hz in the Cd(II)-DTPOAs ($\delta = 6.93$ ppm) and ~3.4 Hz in the Hg(II)-DTPOAs ($\delta = 6.93$ ppm) species.

On the ¹H-NMR spectra of the complexes containing L², the methylene protons on C7 show up as a diastereotopic couple as expected spectra.

The signals of some of the alkyl protons on the cyclohexyl group of L⁵ overlapped with each other in the spectra of $[\text{Cd}_2(\mu\text{-L}^5)_2(\text{L}^5)_2]$ and $[\text{Hg}_2(\mu\text{-L}^5)_2(\text{L}^5)_2]$. There are also overlaps between C6 protons and the phenyl protons of diphenylmethyl group of the complexes $[\text{Cd}_2(\mu\text{-L}^4)_2(\text{L}^4)_2]$ and $[\text{Hg}_2(\mu\text{-L}^4)_2(\text{L}^4)_2]$. The overall ¹H-NMR spectral data are given in Table 3.

Table 3: ¹H NMR spectral data for the complexes.

	[Cd₂(μ-L¹)₂(L¹)₂]	[Cd₂(μ-L²)₂(L²)₂]	[Cd₂(μ-L³)₂(L³)₂]	[Cd₂(μ-L⁴)₂(L⁴)₂]	[Cd₂(μ-L⁵)₂(L⁵)₂]
M part of AA'MM'X N = J _{AM} + J _{AM'}	Ar _{ortho} δ = 8.01 (8H) ³ J _{PH} = 14.5 (J _{MX}); N = 8.8	δ = 7.93 (8H) ³ J _{PH} = 14.6 (J _{MX}); N = 8.8	δ = 8.03 (8H) ³ J _{PH} = 14.6 (J _{MX}); N = 8.7	δ = 7.93 (8H) ³ J _{PH} = 14.7 (J _{MX}); N = 8.8	δ = 7.99 (8H) ³ J _{PH} = 14.5 (J _{MX}); N = 8.8
A part of AA'MM'X	Ar _{meta} δ = 6.93 (8H) ⁴ J _{PH} = 3.3 (J _{AX}); N = 8.8	δ = 6.93 (8H) ⁴ J _{PH} = 3.2 (J _{AX}); N = 8.8	δ = 6.91 (8H) ⁴ J _{PH} = 3.2 (J _{AX}); N = 8.7	δ = 6.79 (8H) ⁴ J _{PH} = 3.3 (J _{AX}); N = 8.8	δ = 6.92 (8H) ⁴ J _{PH} = 3.3 (J _{AX}); N = 8.8
OCH ₃	δ = 3.83 (s, 12H)	δ = 3.80 (s, 12H)	δ = 3.81 (s, 12H)	δ = 3.78 (s, 12H)	δ = 3.83 (s, 16H) overlapped with C6-H
C6-H	δ = 4.8 (m, 4H)	δ = 5.70 (m, 4H)	δ = 5.3 (d, 4H) ³ J _{PH} = 8.7	δ = 6.93 (d, 4H) ³ J _{PH} = 16.4	
C7-H	δ = 1.77 (m, 16H)	δ = 2.01 (m, 8H) diastereotopic protons	-	-	C7-H, δ = 2.25 ; (m, 8H) C7'-H, δ = 1.74 ; (m, 8H)
C8-H	δ = 0.94 (t, 24H) ³ J _{HH} = 7.5	δ = 0.87 (t, 12H) ³ J _{HH} = 7.4	-	-	C8-H, δ = 1.43 ; (m, 8H) C8'-H, δ = 1.11 ; (m, 8H)
C9-H	-	-	-	-	δ = 0.96 (m, 4H)
C11-H	-	-	-	-	δ = 0.82 ; (m, 36H)
C12H	-	-	δ = 1.31 ; (s, 36H)	-	-
Ar-CH	-	δ = 7.28 ; (m, 20H)	δ = 7.32 ; (m, 16H)	δ = 7.28 ; (m, 40H)	-

	$[\text{Hg}_2(\mu\text{-L}^1)_2(\text{L}^1)_2]$	$[\text{Hg}_2(\mu\text{-L}^2)_2(\text{L}^2)_2]$	$[\text{Hg}_2(\mu\text{-L}^3)_2(\text{L}^3)_2]$	$[\text{Hg}_2(\mu\text{-L}^4)_2(\text{L}^4)_2]$	$[\text{Hg}_2(\mu\text{-L}^5)_2(\text{L}^5)_2]$
Ar _{ortho} M part of AA'MM'X N= J _{AM} + J _{AM'}	$\delta = 8.6$ (4H) $^3J_{\text{PH}} = 14.5$ (J _{MX}); N= 8.6	$\delta = 7.95$ (4H) $^3J_{\text{PH}} = 14.5$ (J _{MX}); N= 8.9	$\delta = 8.00$ (8H) $^3J_{\text{PH}} = 14.5$ (J _{MX}); N= 8.7	$\delta = 7.92$ (8H) $^3J_{\text{PH}} = 14.6$ (J _{MX}); N= 8.7	$\delta = 8.04$ (8H) $^3J_{\text{PH}} = 14.4$ (J _{MX}); N= 8.8
Ar _{meta} A part of AA'MM'X	$\delta = 6.96$ (4H) $^4J_{\text{PH}} = 3.4$ (J _{AX}); N= 8.6	$\delta = 6.93$ (4H) $^4J_{\text{PH}} = 3.4$ (J _{AX}); N= 8.9	$\delta = 6.94$ (8H) $^4J_{\text{PH}} = 3.3$ (J _{AX}); N= 8.7	$\delta = 6.92$ (8H) $^4J_{\text{PH}} = 3.4$ (J _{AX}); N= 8.8, Ar-H _{ort.} (adjacent C-6H)	$\delta = 7.00$ (8H) $^4J_{\text{PH}} = 3.4$ (J _{AX}); N= 8.8
OCH ₃	$\delta = 3.85$ (s, 12H)	$\delta = 3.85$ (s, 12H)	$\delta = 3.83$ (s, 12H)	$\delta = 3.84$ (s, 12H)	
C6-H	$\delta = 4.8$ (m, 4H)	$\delta = 5.84$ (m, 8H)	$\delta = 5.4$ (d, 8H) $^3J_{\text{PH}} = 9.2$	$\delta = 6.98$ (d, 4H) $^3J_{\text{PH}} = 16.4$ (Ar _{meta} adjacent)	$\delta = 3.85$ (s, 16H) overlapped with C6-H
C7-H	$\delta = 1.83$ (m, 16H)	$\delta = 2.03$ (m, 8H) diastereotopic protons	-	-	C7-H, $\delta = 2.34$; (m, 4H) C7'-H, $\delta = 1.82$; (m, 4H) C8-H, $\delta = 1.50$; (m, 4H) C8'-H, $\delta = 1.24$; (m, 4H)
C8-H	$\delta = 0.99$ (t, 24H) $^3J_{\text{HH}} = 7.5$	$\delta = 0.94$ (t, 12H) $^3J_{\text{HH}} = 7.4$	-	-	
C9-H	-	-	-	-	$\delta = 1.01$ (m, 4H)
C11-H	-	-	-	-	$\delta = 0.85$; (m, 36H)
C12H	-	-	$\delta = 1.32$; (s, 36H)	-	-
Ar-CH	-	$\delta = 7.31$; (m, 20H)	$\delta = 7.35$; (m, 16H)	$\delta = 7.36$; (m, 40H)	-

(Chemical shifts (d) are reported in ppm. *J* values are reported in Hz. s: singlet; d:doublet; t:triplet dd:doublet of doublets; m:multiplet).

¹³C-NMR spectra

The proton-decoupled ¹³C-NMR spectra display a one-bond P-C coupling of about the same order of magnitude (114.2-123.9 Hz) in all the Cd(II) complexes. The same couplings are within even a narrower range (124.2-126.6 Hz) in the Hg(II) species. The C1 and C2 carbons appear at further downfield (by about ~7 ppm and ~2 ppm, respectively) in all the complexes compared to their position in the spectra of the corresponding ligands (2). The NMR signals of C8 on the spectra of [Cd₂(μ-L³)₂(L³)₂] and [Hg₂(μ-L³)₂(L³)₂] are situated between the two hands of the doublet corresponding to C1 (split into two by phosphorus). Similar overlap is observed between the signals C8, C9 and C10 of [Cd₂(μ-L⁴)₂(L⁴)₂] all of which falling between C1 signals.

¹³C-NMR data of all the complexes are presented in Table 4.

³¹P-NMR spectra

The chemical shift data for the proton-decoupled ³¹P-NMR spectra of the ten complexes are presented in Table 5.

For comparison, ³¹P-NMR chemical shift values are also given. All the compounds display a single ³¹P-NMR signal indicating that the compounds are somehow symmetrical in solution. This is also evident from the formula given in Scheme 2.

Table 5 indicates that there is no parallel relation between the chemical shifts of the ligands and of the complexes, but all lay within the narrow range, 100.63-107.17 ppm. This indicates that the chemical environment of the phosphorus atom those not undergo either geometrically or electronically to a drastic change during the complexation.

Other features of the NMR spectra (¹H-, ¹³C- and ³¹P-) are in a good agreement with the literature (24,31, 34-36).

Table 4: ^{13}C -NMR data for the complexes.

	$[\text{Cd}_2(\mu\text{-L}^1)_2(\text{L}^1)_2]$	$[\text{Cd}_2(\mu\text{-L}^2)_2(\text{L}^2)_2]$	$[\text{Cd}_2(\mu\text{-L}^3)_2(\text{L}^3)_2]$	$[\text{Cd}_2(\mu\text{-L}^4)_2(\text{L}^4)_2]$	$[\text{Cd}_2(\mu\text{-L}^5)_2(\text{L}^5)_2]$
C1	$\delta = 130.0$ (d) $J_{\text{PC}} = 123.9$	$\delta = 129.0$ (d) $J_{\text{PC}} = 122.7$	$\delta = 128.4$ (d) $J_{\text{PC}} = 121.7$	$\delta = 127.3$ (d) $J_{\text{PC}} = 114.2$	$\delta = 129.6$ (d) $J_{\text{PC}} = 121.5$
C2	$\delta = 132.2$ (d) $^2J_{\text{PC}} = 14.2$	$\delta = 132.4$ (d) $^2J_{\text{PC}} = 14.4$	$\delta = 132.5$ (d) $^2J_{\text{PC}} = 14.5$	$\delta = 132.4$ (d) $^2J_{\text{PC}} = 14.3$	$\delta = 132.3$ (d) $^2J_{\text{PC}} = 14.3$
C3	$\delta = 113.5$ (d) $^3J_{\text{PC}} = 16.2$	$\delta = 113.5$ (d) $^3J_{\text{PC}} = 16.3$	$\delta = 113.7$ (d) $^3J_{\text{PC}} = 16.3$	$\delta = 113.6$ (d) $^3J_{\text{PC}} = 16.4$	$\delta = 113.6$ (d) $^3J_{\text{PC}} = 16.1$
C4	$\delta = 162.3$ (d) $^4J_{\text{PC}} = 3.3$	$\delta = 162.4$ (d) $^4J_{\text{PC}} = 3.3$	$\delta = 162.6$ (d) $^4J_{\text{PC}} = 3.2$	$\delta = 162.4$ (d) $^4J_{\text{PC}} = 3.0$	$\delta = 162.4$ (d) $^4J_{\text{PC}} = 3.3$
C5	$\delta = 55.4$ (s)	$\delta = 55.4$ (s)	$\delta = 55.4$ (s)	$\delta = 55.4$ (s)	$\delta = 54.4$ (s)
C6	$\delta = 81.1$ (d), $^2J_{\text{PC}} = 8.2$	$\delta = 80.8$ (d) $^2J_{\text{PC}} = 7.3$	$\delta = 67.6$ (d) $^2J_{\text{PC}} = 6.7$	$\delta = 79.6$ (d) $^2J_{\text{PC}} = 6.9$	$\delta = 78.1$ (d) $^2J_{\text{PC}} = 7.9$
C7	$\delta = 27.1$ (d) $^3J_{\text{PC}} = 4.0$	$\delta = 31.4$ (d) $^3J_{\text{PC}} = 5.4$	$\delta = 133.1$ (d) $^3J_{\text{PC}} = 9.9$	$\delta = 141.0$ (d) $^3J_{\text{PC}} = 4.6$	$\delta = 34.2$ (d) $^3J_{\text{PC}} = 3.8$
C8	$\delta = 9.3$ (s)	$\delta = 9.8$ (s)	$\delta = 130.7$ (s)	$\delta = 128.2$ (s)	$\delta = 25.7$ (s)
C9	-	$\delta = 140.9$ (d) $^3J_{\text{PC}} = 3.1$	$\delta = 125.3$ (s)	$\delta = 127.5$ (s)	$\delta = 46.9$ (s)
C10	-	$\delta = 128.1$ (s)	$\delta = 151.2$ (s)	$\delta = 127.6$ (s)	$\delta = 32.3$ (s)
C11	-	$\delta = 127.5$ (s)	$\delta = 34.6$ (s)	-	$\delta = 27.6$ (s)
C12	-	$\delta = 126.9$ (s)	$\delta = 31.3$ (s)	-	-

	$[\text{Hg}_2(\mu\text{-L}^1)_2(\text{L}^1)_2]$	$[\text{Hg}_2(\mu\text{-L}^2)_2(\text{L}^2)_2]$	$[\text{Hg}_2(\mu\text{-L}^3)_2(\text{L}^3)_2]$	$[\text{Hg}_2(\mu\text{-L}^4)_2(\text{L}^4)_2]$	$[\text{Hg}_2(\mu\text{-L}^5)_2(\text{L}^5)_2]$
C1	$\delta = 130.1$ (d) $J_{\text{PC}} = 126.6$	$\delta = 129.5$ (d) $J_{\text{PC}} = 125.3$	$\delta = 129.3$ (d) $J_{\text{PC}} = 124.2$	$\delta = 129.5$ (d) $J_{\text{PC}} = 125.0$	$\delta = 129.7$ (d) $J_{\text{PC}} = 124.6$
C2	$\delta = 131.9$ (d) ${}^2J_{\text{PC}} = 14.0$	$\delta = 132.0$ (d) ${}^2J_{\text{PC}} = 14.2$	$\delta = 132.3$ (d) ${}^2J_{\text{PC}} = 14.3$	$\delta = 132.0$ (d) ${}^2J_{\text{PC}} = 14.3$	$\delta = 132.1$ (d) ${}^2J_{\text{PC}} = 14.1$
C3	$\delta = 113.7$ (d) ${}^3J_{\text{PC}} = 16.3$	$\delta = 113.7$ (d) ${}^3J_{\text{PC}} = 16.3$	$\delta = 113.8$ (d) ${}^3J_{\text{PC}} = 16.3$	$\delta = 113.7$ (d) ${}^3J_{\text{PC}} = 16.4$	$\delta = 113.7$ (d) ${}^3J_{\text{PC}} = 16.2$
C4	$\delta = 162.4$ (d) ${}^4J_{\text{PC}} = 3.3$	$\delta = 162.5$ (d) ${}^4J_{\text{PC}} = 3.4$	$\delta = 162.7$ (s) ${}^4J_{\text{PC}} = 3.3$	$\delta = 162.6$ (s) ${}^4J_{\text{PC}} = 3.3$	$\delta = 162.8$ (s)
C5	$\delta = 58.4$ (s)	$\delta = 55.4$ (s)	$\delta = 55.4$ (s)	$\delta = 55.4$ (s)	$\delta = 54.4$ (s)
C6	$\delta = 81.4$ (d) ${}^2J_{\text{PC}} = 8.0$	$\delta = 81.2$ (s)	$\delta = 67.6$ (s) ${}^2J_{\text{PC}} = 6.5$	$\delta = 80.1$ (s) ${}^2J_{\text{PC}} = 6.4$	$\delta = 78.2$ (s)
C7	$\delta = 27.1$ (s)	$\delta = 31.2$ (s)	$\delta = 133.0$ (d) ${}^3J_{\text{PC}} = 9.8$	$\delta = 140.6$ (s)	$\delta = 34.2$ (s)
C8	$\delta = 9.4$ (s)	$\delta = 9.8$ (s)	$\delta = 128.1$ (s)	$\delta = 128.5$ (s)	$\delta = 25.7$ (s)
C9	-	$\delta = 140.6$ (s) ${}^3J_{\text{PC}} = 3.0$	$\delta = 125.5$ (s)	$\delta = 127.6$ (s)	$\delta = 46.4$ (s)
C10	-	$\delta = 128.4$ (s)	$\delta = 151.4$ (s)	$\delta = 128.0$ (s)	$\delta = 32.3$ (s)
C11	-	$\delta = 127.9$ (s)	$\delta = 34.6$ (s)	-	$\delta = 27.6$ (s)
C12	-	$\delta = 127.1$ (s)	$\delta = 30.9$ (s)	-	-

(Chemical shifts (d) are reported in ppm. J values are reported in Hz. s: singlet; d:doublet; m: multiplet)

Table 5: ³¹P-NMR data relating to the complexes and the corresponding ligands.

	[NH ₄ L ¹]	[NH ₄ L ²]	[NH ₄ L ³]	[NH ₄ L ⁴]	[NH ₄ L ⁵]
δ , ppm	101.62	105.56	106.82	103.41	107.17
	[Cd ₂ (μ -L ¹) ₂ (L ¹) ₂]	[Cd ₂ (μ -L ²) ₂ (L ²) ₂]	[Cd ₂ (μ -L ³) ₂ (L ³) ₂]	[Cd ₂ (μ -L ⁴) ₂ (L ⁴) ₂]	[Cd ₂ (μ -L ⁵) ₂ (L ⁵) ₂]
δ , ppm	103.42	104.58	106.20	106.25	102.65
	[Hg ₂ (μ -L ¹) ₂ (L ¹) ₂]	[Hg ₂ (μ -L ²) ₂ (L ²) ₂]	[Hg ₂ (μ -L ³) ₂ (L ³) ₂]	[Hg ₂ (μ -L ⁴) ₂ (L ⁴) ₂]	[Hg ₂ (μ -L ⁵) ₂ (L ⁵) ₂]
δ , ppm	100.63	106.20	103.94	102.22	101.05

CONCLUSIONS

Five different dithiophosphonato ligands were synthesized and purified according to the procedure reported elsewhere (22). New Cd(II) and Hg(II) complexes were synthesized and characterized by elemental analyses and ¹H-NMR, ¹³C-NMR, ³¹P-NMR and MS.

Based on the MS data, all the complexes were found to be of dimeric structure. ³¹P-NMR data indicate that the complex molecules are symmetrical in solution. A comparative examination of the ³¹P-NMR data of the ligands and of the complexes show that the process of coordination has some influence on the electron delocalization within the aromatic ring attached the P atom, but also that the same process has of little strain on the environment of the phosphorus atom.

ACKNOWLEDGEMENTS

This study is supported by the Project Coordination Application and Research Center of Bozok University (BAP 6602b-FEN/18-221).

REFERENCES

- Haiduc I. 1,1-Dithiolato Ligands in Comprehensive Coordination Chemistry II Edited by McCleverty JA, Meyer TJ. 2004; 1: 349-76.
- Thomsen I, Clausen K, Scheibye S, Lawesson S-O. Thiation with 2,4-bis(4-Methoxyphenyl)-1,3,2,4-Dithiadiphosphetane 2,4-disulfide: N-methylthiopyrrolidone. Organic Syntheses, Coll. 1990; 7: 372.
- Ozturk T, Ertas E, Mert O. A Berzelius Reagent, Phosphorus Decasulfide (P₄S₁₀), in Organic Syntheses, Chem. Rev. 2010; 110(6): 3419-78.
- Kour M, Kumar S, Andotra S, Kour G, Singh G, Gupta VK, Rajni Kant R, Katoch M, Pandey S K.

Chromium(III) complexes of dimethyl diphenyl dithiophosphates: Synthesis, characterization, and antibacterial studies. Phosphorus, Sulfur Silicon Relat. Elem. 2017; 192(10): 1-5.

5. Diemert K, Kuchen W. Synthesis of Dithiophosphinic Acids by Nucleophilic Fission of Perthiophosphonic Anhydrides. Angew. Chem. Internat. Edit. 1971; 10(7): 508-9.

6. Aydemir C, Solak S, Acar Doğanlı G, Şensoy T, Arar D, Bozbeyoglu Mercan Dogan N, Lönnecke P, Hey-Hawkins E, Şekerçi M, Karakuş M, Synthesis, Characterization, and Antibacterial Activity of Dithiophosphonates and Amidodithiophosphonates. Phosphorus, Sulfur Silicon Relat. Elem. 2015; 190(3): 300-9.

7. Karakuş M, Lönnecke P, Hey-Hawkins E. Zwitterionic ferrocenyl dithiophosphonates: the molecular structure of [FcP(S)S(OCH₂CH₂NH₂Me)] [Fc=Fe(η^5 -C₅H₄)(η^5 -C₅H₅)]. Polyhedron, 2004; 23: 2281-84.

8. Van Zyl W E, Woollins J D. The coordination chemistry of dithiophosphonates: An emerging and versatile ligand class. Coord. Chem. Rev. 2013; 257: 718-73.

9. Haiduc I, Bryan Sowerby D. Stereochemical Aspects of Phosphor-1,1-Dithiolato Metal Complexes: Coordination Patterns, Molecular Structures and Supramolecular Associations in Dithiophosphinates and Related Compounds. Polyhedron 1995; 15(15): 2469-21.

10. Liu H-L, Mao H-Y, Chen X, Zhang H-Y, Hou H-W, Wu Q, Zhu Y, Ye B-X, Yuan L-J. Four novel sulfur-rich complexes: Syntheses, crystal structures of three nickel(II) and one cobalt(II) complex with derivatives of Lawesson's Reagent. Polyhedron. 2004; 23: 1799-4.

11. Van Zyl W.E. Dithiophosphonates and Related P/S-Type Ligands of Group 11 Metals: Comments Inorg. Chem. 2010; 31(1-2): 13-45.

12. Gray I P, Milton H L, Slawin A M Z, Woollins J. D. Synthesis and structure of [Fc(RO)PS₂]⁻ complexes. Dalton Trans. 2003; 3450-57.

13. Karakuş M, Yılmaz H, Bulak E, Lonnecke, P. Bis{ μ -[O-cyclopentyl(4-methoxyphenyl) dithiophosphonato]1 κ : S,2 κ : S-[O-cyclopentyl (4-methoxyphenyl) dithiophosphonato] 1 κ 2S,S } dizinc (II). *Appl. Organometal. Chem.* 2005; 19: 396-97.
14. Harrison PG, Begley MJ, Kikabhai T, Killer F. Zinc(II) Bis(O,O'-dialkyl dithiophosphates): Interaction with Small Nitrogen Bases. The Crystal and Molecular Structure of Hexakis(μ -O,O'-diethyl dithiophosphate)- μ -thio-tetra zinc, Zn₄[S₂P(OEt)₂]₆S. *Dalton Trans.* 1986; 925–28.
15. Guoxin T, Yongjun Z, Jingming X. Extraction of Am(III) and Ln(III) By Dialkyldithiophosphinic Acid with Different Alkyl Groups. *Solvent Extr. Ion Exch.* 2001; 19(6): 993–1005.
16. Yagishita K, Konishi S. Lubricating oil additive and lubricating oil composition. 2013; US 8,481,467.
17. Ziyatdinova GK, Budnikov GK, Samigullin AI, G Gabdullina T, Sofronov AV, Al'metkina LA, Nizamov IS, Cherkasov RA. Electrochemical Determination of Synthetic Antioxidants of Bisdithiophosphonic Acids. *J. Anal. Chem.* 2010; 65: 1273-79.
18. Cristau P, Dahmen P. Active compound combinations comprising carboxamide derivatives. 2017; US 9,801,374.
19. Bellande E, Comazzi V, Laine J, Lecayon M, Pasqualini R, Duatti A, Hoffschir D. Synthesis and Biodistribution of Nitrido Technetium-99m Radiopharmaceuticals with Dithiophosphinate Ligands: a Class of Brain Imaging Agents *Nucl. Med. and Biol.* 1995; 22(3): 315-20.
20. Pasqualini R, Bellande E, Comazzi V, Laine J. Radiopharmaceutical product having in particular a cerebral tropism comprising a nitro complex of a transition metal and method for preparing said product. 1996; US 5,496,929.
21. Pasqualini R, Comazzi V, Bellande E. Process for the preparation of nitride complexes of transition metals. 1995; US 5,399,339.
22. Feng W, Teo X-Y, Novera W, Ramanujulu PM, Lian D, Huan D, Moore PK, Deng L-W, Dymock BW. Discovery of New H₂S Releasing Phosphordithioates and 2,3-Dihydro-2-phenyl-2-sulfanylenebenzo[d][1,3,2]oxazaphospholes with Improved Antiproliferative Activity. *J. Med. Chem.* 2015; 58(16): 6456–80.
23. Banaei A, Saadat A, McArdle P, Mohammad Goli M, Crystal structure, antibacterial activity and nanoparticles of Cd(II) complex derived from dithiophosphonate ligand. *Phosphorus, Sulfur Silicon Relat. Elem.* 2018; 193(6): 369-74.
24. Sağlam EG, Bulat E, Zeyrek CT, Dal H, Hökelek T. Syntheses of and structural studies on some square planar dithiophosphonato Ni(II) complexes, octahedral pyridine derivatives thereof and X-ray crystallography, DFT and molecular docking studies of the latter. *J. Mol. Struc.* 2019; 1178: 112–25.
25. Casas JS, García-Tasende MS, Sánchez A, Sordo J, Castellano EE, Zukerman-Schpector J. Synthesis, crystal structure and spectroscopic properties of bis(diphenyldithiophosphinato)cadmium(II). *Inorg. Chim. Acta.* 1994; 219(1–2): 115-19.
26. Shi W, Shafaei-Fallah M, Anson CE, Rothenberger A. Metal thiophosphonates and related compounds: an emerging area of supramolecular coordination chemistry. *Dalton Trans.* 2006; 26: 3257-62.
27. Czernuszewicz R, Maslowsky, E Jr, Nakamoto K. Infrared and Raman Spectra of Bis(imidotetraphenyldithiodiphosphino-S,S') Complexes with Cu(II), Co(II) and Fe(II). *Inorg. Chim. Acta.* 1980; 40: 199-2.
28. Paddy JL, Lee NCJ, Waters DN, Trott W. Zinc Dialkyldithiophosphate Oxidation by Cumene Hydroperoxide: Kinetic Studies by Raman and ³¹P NMR Spectroscopy. *J. Tribology Trans.* 1990; 33(1): 15-20.
29. Larsson ML, Holmgren A. Reversible phase transition in Zn₂(O,O-di(cyclohexyl)dithiophosphate)₄, studied by Raman spectroscopy and compared with NMR results. *Vib. Spectro.* 2004; 34(2): 243-46.
30. Chakravarty M, Pailloux S, Ouizem S, Smith KA, Duesler EN, Paine RT, Williams NJ, Hancock RD. Synthesis and metal coordination chemistry of (phenyl)(pyridine-2-ylmethyl)phosphinodithioic acid. *Polyhedron* [2-C₅H₄N]CH₂P(S)(SH)(Ph). 2012; 33: 327-35.
31. Karakuş M, Yılmaz H. Synthesis and Characterization of Ni(II), Zn(II), and Cd(II) Complexes with Dithiophosphonate Derivatives. *Russ. J. Coord Chem* 2006; 32(6): 437–43.

Sağlam EG et al. JOTCSA. 2020; 7(1): 49-64.

RESEARCH ARTICLE

32. Keck H, Kuchen W. Massenspektrometrische Untersuchungen An Organophosphorverbindungen IV. Über den massenspektrometrischen Zerfall von Dithiophosphinsäuren. Phosphorus, Sulfur Silicon Relat. Elem. 1983; 14: 225-28.

33. Heinz S, Keck H, Kuchen W. Mass spectrometric studies of dithiophosphinato metal complexes. Org. Mass Spectrom. 1984; 19: 82-86.

34. Karakuş M, Yılmaz H, Özcan Y, S İde. Appl. Crystallographic report: Bis{ μ -[O-cyclopentyl (4-

methoxyphenyl) dithiophosphonato] $1\kappa:S,2\kappa$: S-[O-cyclopentyl(4-methoxyphenyl) dithiophosphonato]- $1\kappa^2S,S'$ }dicadmium(II). Organometal. Chem. 2004; 18: 141-42.

35. Ramirez RG, Toscano RA, Silverstru C, Haiduc I. Studies on inorganic tin diphenyldithiophosphinates. Crystal and molecular structure of CIS-dichlorobis(diphenyldithiophosphinato)tin(IV). Polyhedron 1996; 15(21): 3857-67.

36. Przychodzen W. New Products of Reaction of Lawesson's Reagent With Diols. Phosphorus, Sulfur Silicon Relat. Elem. 2004; 179: 1621-33.



Computational Screening of Covalent Organic Frameworks for Hydrogen Storage

Ezgi Gulcay¹   and İlknur Erucar^{2*}  

¹Ozyegin University, Faculty of Engineering, Department of Mechanical Engineering, 34794, Istanbul, Turkey.

²Ozyegin University, Faculty of Engineering, Department of Natural and Mathematical Sciences, 34794, Istanbul, Turkey.

Abstract: Covalent Organic Frameworks (COFs) have been considered as promising materials for gas storage applications due to their highly porous structures and tunable characteristics. In this work, high-throughput molecular simulations were performed to screen the recent Computation-Ready Experimental COF Database (CoRE-COF) for H₂ storage as a first time in the literature. Predictions for H₂ uptakes were first compared with the experimental data of several COFs. Motivated from the good agreement between simulations and experiments, we performed Grand Canonical Monte Carlo (GCMC) simulations to compute volumetric H₂ uptakes of 296 COFs at various temperatures and pressures and identified the best candidates which exhibit superior performance for H₂ storage. COFs outperformed several well-known MOFs such as HKUST-1, NU-125, NU-1000 series, NOTT-112 and UiO-67 at 100 bar/77 K adsorption and 5 bar/160 K desorption conditions. We also examined the effect of Feynman-Hibbs correction on simulated H₂ isotherms and H₂ working capacities of COFs to consider quantum effects at low temperatures. Results showed that the Feynman-Hibbs corrections do not affect the ranking of materials based on H₂ working capacities, but slightly affect the predictions of H₂ adsorption isotherms. We finally examined the structure-performance relations and showed that density and porosity are highly correlated with the volumetric H₂ working capacities of COFs. Results of this study will be highly useful in guiding future research and focusing experimental efforts on the best COF adsorbents identified in this study.

Keywords: Covalent organic frameworks, Molecular simulations, Hydrogen storage, Working capacity, Adsorption..

Submitted: May 15, 2019. **Accepted:** October 27, 2019.

Cite this: Gulcay E, Erucar, İ. Computational screening of covalent organic frameworks for hydrogen storage. JOTCSA. 2020; 7(1): 65–76.

DOI: <https://doi.org/10.18596/jotcsa.565460>.

Corresponding Author. E-mail: ilknur.erucar@ozyegin.edu.tr, **Tel:** +90 (216) 564-9297.

INTRODUCTION

Developing energy-efficient and safe hydrogen (H₂) storage systems has gained importance in transportation sector due to non-toxic and environmentally friendly products of H₂ compared to those of fossil fuels. Additionally, H₂ has almost triple energy density that of gasoline per

mass unit. Many companies including Honda, Toyota, Hyundai, and General Motors have been recently producing hydrogen-powered vehicles (1). Storing H₂ in vehicles is possible at room temperature and very high pressure (~700 bar). However, high pressure operating conditions bring safety issues to the attention of the manufacturers for the critical equipment design.

As alternative to the high-pressure H₂ storage systems, liquefaction at low temperature (77 K) has been also investigated for on-board H₂ storage. Recently, cryo-adsorption processes in which H₂ molecules are stored at 77 K and 100 bar and desorbed at 160 K and 5 bar using a porous material have been considered for automotive industry (2). H₂ molecules can be adsorbed at moderate temperatures and pressures within a porous adsorbent material due to the van der Waals interactions. Herein, the careful choice of an adsorbent material is important. A promising adsorbent should have high working capacity. Working capacity is defined as the gas amount that can be delivered when the storage pressure is decreased to a pre-determined desorption pressure (3). To have a high gas working capacity, adsorbents should have the maximum gas uptake at an adsorption pressure and the minimum gas uptake at a desorption pressure.

Many different adsorbent materials including activated carbons, (4) zeolites, (5) metal organic frameworks (MOFs) (6) and covalent organic frameworks (COFs) (7, 8) have been tested for efficient H₂ store systems. To evaluate H₂ storage capacities of these materials, ARPA-E (Advanced Research Projects Agency-Energy) target set by the U.S. Department of Energy (DOE) has been commonly used. The DOE target for on board H₂ storage systems was set to 4.5 wt%; 30 g/L for 2020 and 5.5 wt%; 40 g/L for 2025 and 6.5 wt %; 50 g/L as ultimate target (9). Among these adsorbent materials, MOFs constructed from metal ions and organic linkers via coordination bonds are potential candidates for H₂ storage due to their large surface areas and high pore volumes (10). For example, Gómez-Gualdrón et al. (2) investigated the isorecticular series of zirconium MOFs including NU-1101, NU-1102 and NU-1103 (NU: Northwestern University) and found that NU-1101 gives the highest measured volumetric H₂ uptake as 46.6 g/L (9.1 wt %), whereas NU-1103 gives the highest gravimetric H₂ uptake as with 12.6 wt% (43.2 g/L) at 77 K/100 bar adsorption and 160 K/5 bar desorption conditions based on the tank design criteria proposed by HSECoE, Hydrogen Storage Engineering Center of Excellence (11). Langmi et al. (12) reviewed H₂ uptakes in MOFs at both 77 K and 298 K and showed that MOFs provide total volumetric H₂ uptake in the range of 40-60 g/L (6-15 wt%) at 77 K whereas it decreases to less than 15 g/L (0.5-1 wt%) at 298 K. COFs as a sub class of MOFs have been also considered as promising adsorbents for H₂ storage. COFs are consisted of light elements including B (boron), C (carbon), N (nitrogen) and O (oxygen) and organic linkers which are covalently bonded. COFs exhibit large surface areas (711-1590

m²/g), high porosities (0.25-0.94) and large pore sizes (7.0×27.0 Å) (13). Furukawa et al. (14) examined the H₂ storage performances of seven COFs including COF-1, COF-5, COF-6, COF-8, COF-10, COF-102 and COF-103 at 77 K. They found that saturated H₂ uptakes of these COFs are in the range of 1.5 wt% to 7.2 wt%. Ding and Wang (15) summarized the H₂ uptakes of thirteen COFs and reported that COFs with larger surface areas exhibit higher H₂ uptake capacities. All these studies showed that developing novel adsorbents which have high storage and working capacity for H₂ at ambient conditions has been still a critical issue for practical applications.

Both MOFs and COFs can be synthesized using the reticular design concept which provides numerous materials with different chemical functionalities. Evaluating the performance of a large number of materials for H₂ storage using experimental methods is challenging due to time, cost, and equipment concerns. Therefore, molecular simulations play a very useful role for providing reliable gas adsorption data in a reasonable time. Many computational studies on H₂ uptake in MOFs were performed in the literature (16). Bucior et al. (1) performed a large-scale molecular simulation study to identify promising candidates for H₂ storage. Among 54,776 MOFs, 25 materials were reported to exceed the DOE 2025 volumetric system target (40 g/L). In a different study, Ahmed et al. (17) screened real and hypothetical MOFs (totally 500,000 MOFs) for H₂ adsorption up to 100 bar at 77 K. Among these halves million MOFs, NU-100 (also known as PCN-610, PCN for porous coordination network) surpassed the DOE's 2020 system level target (30 g/L) and gave H₂ uptake almost 35 g/L. They also investigated the relation between structural properties of MOFs and their performances and reported that porosity has positively correlated with the volumetric working capacity of MOFs. Six different COFs (COF-1, 5, 102, 103, 105 and 108) have also been tested for H₂ storage by Han et al. (7) due to their large surface areas (up to ~4000 m²/g) and low crystal densities (~0.2 g/cm³). Among these COFs, COF-108 gave the highest H₂ gravimetric uptake (~19 wt%) and COF-102 gave the maximum volumetric H₂ uptake (~40 g/L) at 77 K and 100 bar. In a recent study, Cao et al. (18) performed simulations of four different three-dimensional (3D) COFs (COF-102, 103, 105 and 108) and their lithium (Li)-doped counterparts for H₂ storage at 298 K up to 100 bar. Results showed that H₂ gravimetric uptake capacities of Li-doped COFs (COF-105 and COF-108) nearly doubled and both reached ~7 wt% at ambient temperature due to the favorable interactions between H₂ and Li atom. Assfour et al. (19) performed molecular simulations of eleven COFs for H₂ storage at 77 K and 298 K up to 100 bar.

Similar to study of Han et. al. (7), they found that COF-108 has the highest gravimetric H₂ uptake as 21 wt% and 4.17 wt% at 77 K and 100 bar and at 298 K and 100 bar, respectively. These results suggest that COFs can be promising materials for H₂ storage. Currently, 309 COFs were deposited in the Computation-Ready Experimental COF Database (CoRE-COF) (20) and to the best of our knowledge, there is no study in the literature which evaluates H₂ storage performances of COFs by using high-throughput molecular simulation techniques. Therefore, computational studies will be highly useful to identify the potential COF candidates for H₂ capture.

In this work, we screened the recent CoRE-COF database (20) for H₂ storage as a first time in the literature. We first compared our predictions with the available experimental data in the literature for H₂ uptake. We examined the effect of Feynman-Hibbs corrections on simulated H₂ isotherms in COFs. In many computational studies on H₂ storage, H₂ molecules are treated as classical molecules. However, at sufficiently low temperatures, quantum effects should be considered in simulations due to the low mass of H₂. We then performed Grand Canonical Monte Carlo (GCMC) simulations to compute volumetric H₂ uptakes of 296 COFs at three different operating conditions: (i) at 100 bar/77 K → 2 bar/77 K, (ii) at 100 bar/77 K → 5 bar/77 K, and (iii) at 100 bar/77 K → 5 bar/160 K. Reporting volumetric H₂ adsorption is crucial because it directly relates to the required volume of an on-board tank. We also investigated the effect of the Feynman-Hibbs correction on simulated H₂ working capacities of COFs and the ranking of the best materials. The best performing materials were then compared with the top performing MOFs which were previously identified in the literature. We finally examined the relations between structural properties of COFs such as pore sizes, densities, porosities and their H₂ working capacities to provide structure-performance relationships.

MATERIALS AND METHODS

Computational details

To validate our computational methodology, we first compared our predictions with the available experimental data of Furukawa et al. (14) for single-component H₂ adsorption. Adsorption isotherms of H₂ in four different COFs (COF-5, COF-6, COF-8 and COF-10) were computed at 77 K up to 80 bar to be consistent with the study of Furukawa et al. (14). We also computed saturated H₂ uptakes in several COFs reported in the literature by Li et al. (21) (ACOF-1), Stegbauer et al. (22) (ATFG-COF), Furukawa et

al. (14) (COF-1, COF-5, COF-6, COF-8, COF-10, COF-102, and COF-103), Li et al. (23) (COF-JLU2), Ge et al. (24) (COF-TpAzo), Neti et al. (25) (CoPc-PorDBA), Kaleeswaran et al. (26) (iPrTAPB-TFP, iPrTAPB-TFPB, TAPB-TFP, and TAPB-TFPB), Kang et al. (27) (NUS-3), Bhunia et al. (28) (PCTF-n, n=1-2), and Kahveci et al. (29) (TD-COF-5). All the crystal structures of COFs were taken from CoRE-COF database.(20) To compare our simulation results and experimental values, the absolute adsorbed gas amount (n_{abs}), which could not be directly measured, was converted to the excess adsorption (n_{ex}).⁽³⁾ The excess adsorption can be explained by the difference between the amount of the absolute adsorption, and also bulk gas in the adsorbed region and calculated from Equation 1:

$$n_{ex} = n_{abs} - V_p \cdot \rho_{bulk}(P, T) \quad (\text{Eq. 1})$$

Herein, n_{ex} is the excess adsorption, n_{abs} is the absolute adsorbed gas amount, V_p is the pore volume (cm³/g) and ρ_{bulk} represents the density of the gas in the bulk phase calculated with the Peng-Robinson equation of state at temperature (T) and pressure (P), respectively.

The crystal structures of 309 COFs were taken from the solvent-free CoRE-COF database (20). The largest cavity diameter (LCD), pore-limiting diameter (PLD), surface area (SA), density, pore volume (PV) and porosity (ϕ) were calculated by Zeo++ software (30). SA calculations were performed using nitrogen kinetic diameter as 1.86 Å and the trial number was set to 2000. For PV calculations, zero probe size was used, and the number of trials was set to 50,000. Among 309 COFs, 13 COFs have almost zero accessible SAs and these frameworks were excluded from further H₂ adsorption analysis.

Grand Canonical Monte Carlo (GCMC) simulations were performed to compute single-component H₂ adsorption in 296 COFs at various temperatures (77 K and 160 K) and pressures (2 bar, 5 bar and 100 bar) as implemented in RASPA software (31). Three different types of moves including translation, reinsertion, and swap of the molecule were considered in GCMC simulations. Rotation move was also applied in GCMC simulations for the three-site model of H₂. The Lorentz-Berthelot mixing rules were employed to calculate pair wise interactions. The Peng-Robinson equation of state was used to convert the pressure to the corresponding fugacity. Simulations were carried out for a total of 10⁴ cycles with 3000 cycles for the equilibration. Lennard-Jones (LJ) 12-6 and Coulombic potentials were used to model repulsion-dispersion forces, and electrostatic

interactions, respectively using Equation 2 as follows:

$$U_{ij(r)} = 4 \epsilon_{ij} \left(\left(\frac{\sigma_{ij}}{r} \right)^{12} - \left(\frac{\sigma_{ij}}{r} \right)^6 \right) + \frac{q_i q_j}{4 \pi \epsilon_0 r} \quad (\text{Eq. 2})$$

where U_{ij} represents the potential energy between atoms i and j , r is the separation distance from the center of one particle to the center of the other particle, ϵ_{ij} the well depth and σ_{ij} is the molecular length scale based on the particle diameter. In Equation 2 ϵ_0 , q_i and q_j show the electric constant, partial atomic charges of i and j , respectively. The cut-off radius for truncation was set to 12.8 Å. The simulation cell

lengths were increased to at least 25.6 Å along each dimension. To compute electrostatic interactions between gas molecules and the frameworks' atoms, the partial atomic charges of materials were estimated using the charge equilibration method as implemented in RASPA (31). Ewald's summation (32) was used for the long-range electrostatic calculations. H_2 molecules were modeled using two different models including a single-site model (33), and three-site linear molecule with two sites located at two atoms and the third one located at its center of mass (COM) (34). The interaction parameters of H_2 used in molecular simulations were given in Table 1.

Table 1: The interaction parameters and partial charges used for H_2 molecules.

Molecule	Site	$\epsilon/\text{kB (K)}$	$\sigma (\text{Å})$	$q(\text{e})$
H_2	Center of Mass (COM)	36.700	2.958	-0.936
	H	0.000	0.000	0.468
H_2	Single-site	34.200	2.960	0.000

The Feynman-Hibbs correction (35) given in Equation 3 was applied to include quantum effects at 77 K.

$$U_{FH(r)} = U_{LJ(r)} + U_{coul(r)} + \frac{\hbar^2}{24 \mu KT} \nabla^2 U_{LJ(r)} \quad (\text{Eq. 3})$$

In Equation 3, $U_{FH(r)}$ the potential energy calculated with the Feynman-Hibbs correction, $U_{LJ(r)}$ is the Lennard-Jones (LJ) R-X potential and $U_{coul(r)}$ is the Coulombic potential shown in Equation (2). \hbar is the Planck constant divided by 2π , μ is the reduced mass, K is the Boltzmann constant and T is the absolute temperature.

The potential parameters of COFs were taken from the Universal Force Field (UFF) (36). This force field was chosen based on the results of previous gas uptake predictions that gave a good agreement with experiments.(37)

H_2 working capacities (WC_{H_2}) were calculated for 296 COFs, which have $S_A > 0 \text{ m}^2/\text{g}$, using the following equation:

$$WC_{H_2} = N_{ads} - N_{des} \quad (\text{Eq. 4})$$

where, WC_{H_2} is the H_2 working capacity (g/L), N_{ads} is the adsorbed gas amount calculated at the adsorption pressure and N_{des} is the adsorbed gas amount (g/L) calculated at the desorption pressure.

RESULTS AND DISCUSSION

Comparisons of experiments with simulations:

Figure 1 shows the comparison of our predictions with the experimental measurements of COF-5, COF-6, COF-8 and COF-10 for single-component H_2 adsorption at 77 K. Simulations were performed by considering three different scenarios: all electrostatic interactions are on, H_2 - H_2 electrostatic interactions are on and all electrostatic interactions are off. For the first case (all electrostatic interactions are on), H_2 - H_2 electrostatic interactions using the Darkrim and Levesque potential and H_2 -framework electrostatic interactions were computed during GCMC simulations and the Feynman-Hibbs correction was added into the potential energy. For the second case (H_2 - H_2 electrostatic interactions are on), only H_2 - H_2 electrostatic interactions were considered using the Darkrim and Levesque potential (34) and the Feynman-Hibbs correction was applied during simulations. For the last case (all electrostatic interactions are off), a simple single-site LJ potential for H_2 was used and the Feynman-Hibbs correction was not applied in simulations. As shown in Figure 1, simulations performed using Feynman-Hibbs corrections agreed well with the experiments. Simulations performed using the single-site H_2 model overestimated H_2 uptake in all these COFs. For example, Furukawa et al. (14) measured 35.1 mg H_2 /g COF-5 at 80 bar and 77 K, we predicted H_2 uptake in COF-5 using the single-site model as 41.2 mg/g under the same

conditions. Results obtained from simulations with the Feynman–Hibbs corrections were found

to be similar. The predicted H₂ uptakes in COF-5 obtained

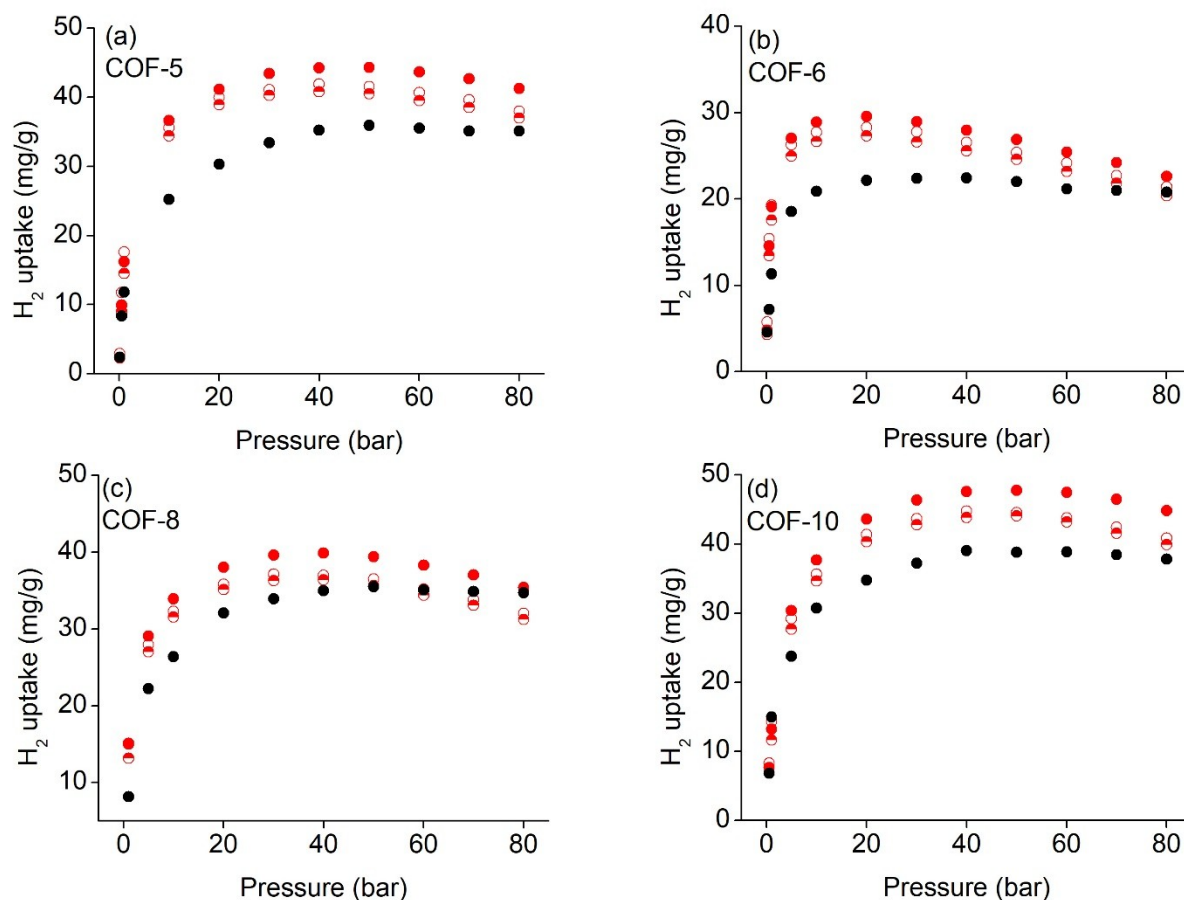


Figure 1: Comparison of our simulations with the experiments (14) for single-component H₂ adsorption in (a) COF-5, (b) COF-6, (c) COF-8 and (d) COF-10 at 77K. Open, half-closed and closed red spheres represent our predictions obtained from all electrostatic interactions were on, only H₂-H₂ electrostatic interactions were on, and all electrostatic interactions were off, respectively. Black spheres represent the experimental data measured by Furukawa et al. (14)

from the simulations with the Feynman–Hibbs corrections were found as 37.0 mg/g (H₂-H₂ electrostatic interactions are on) and 38.0 mg/g (all electrostatic interactions are on) at the same conditions. Results showed that instead of assigning partial charges of COFs which requires high computation cost, only H₂-H₂ electrostatic interactions may be considered to compute H₂ adsorption in COFs at cryogenic conditions in a reasonable time. Similar results were also found by Assfour et al. (19) who emphasized that coulombic interactions between H₂-H₂ molecules and COFs do not affect the H₂ uptake capacities of several COFs at both 77 K and 298 K.

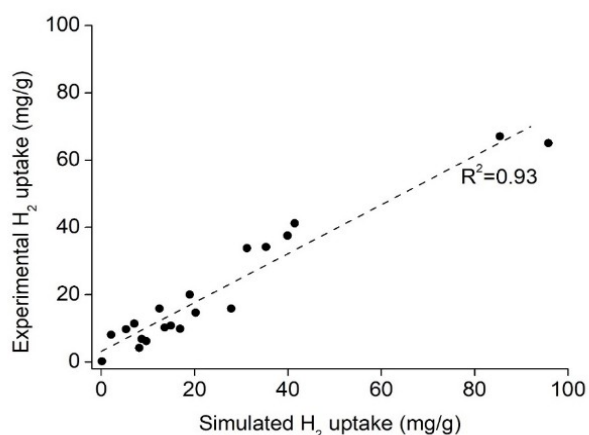
We also compared our predictions with the experiments for the saturated H₂ uptake capacities of 20 COFs in Figure 2. COFs' names together with the calculated and measured H₂ uptakes at the various temperatures and

pressures were given in Table 2. Among these COFs, only COF-102 and COF-103 are 3D and the remaining COFs are all 2D. Simulated H₂ uptakes were obtained from the GCMC simulations with the Feynman–Hibbs corrections using the Darkrim and Levesque potential for H₂ (only H₂-H₂ electrostatic interactions are on). The good agreement between simulations and experiments for saturated H₂ uptakes in these COFs was found. The large discrepancy was observed between simulated H₂ uptake and experimental measurements for only 3D COFs, COF-102 and COF-103. Simulations dramatically overestimated H₂ uptake in COF-102 and COF-103 which may be attributed to the remaining solvent molecules and defects inside these materials. Overall, motivated from the good agreement between our simulations and the experimental measurements, we further computed H₂ working capacities of 296 experimental COFs and discussed below.

Table 2: Data for comparison of simulations with the experiments for the saturated H₂ uptake capacities of 20 COFs.

COF Name	P (bar)	T (K)	Our data (mg/g)	Literature Data (mg/g)	Reference
ACOF-1 ^[1]	1	77	16.89	9.89	(21)
ATFG-COF ^[2]	30	308	2.14	8.12	(22)
COF-1	90	77	20.24	14.68	(14)
COF-5	90	77	35.30	34.19	(14)
COF-6	90	77	18.97	20.04	(14)
COF-8	80	77	31.23	33.85	(14)
COF-10	80	77	39.91	37.58	(14)
COF-102	90	77	85.41	67.07	(14)
COF-103	90	77	95.79	65.05	(14)
COF-JLU2 ^[3]	1	77	12.48	15.86	(23)
COF-TpAzo ^[4]	1	77	13.61	10.29	(24)
CoPc-PorDBA ^[5]	1	77	41.43	41.24	(25)
iPrTAPB-TFP ^[6]	1	77	7.09	11.42	(26)
iPrTAPB-TFPB ^[7]	1	77	8.15	4.18	(26)
TAPB-TFP	1	77	14.90	10.82	(26)
TAPB-TFPB	1	77	9.63	6.26	(26)
NUS-3 ^[8]	1	273	0.14	0.24	(27)
PCTF-1 ^[9]	0.25	77	5.31	9.75	(28)
PCTF-2	0.5	77	8.67	6.86	(28)
TD-COF-5 ^[10]	1	77	27.88	15.89	(29)

[1]ACOF: azine-based COF; [2]ATFG: 1,3,5-triformylphloroglucinol; [3]JLU: Jilin University; [4]TpAzo: triformylphloroglucinol 4,4'-azodianiline; [5]CoPc-PorDBA: cobalt-based phthalocyanine- porphyrin dehydrobenzoannulenes; [6]iPrTAPB-TFP: 1,3,5-tris(4- aminophenyl)benzene - 1,3,5-triformylphloroglucinol; [7] TFPB: 1,3,5-tris(4'-formylphenyl)benzene; [8]NUS: : National University of Singapore; [9]PCTF: porous covalent triazine-based organic frameworks [10]TD: triptycene-derived.

**Figure 2:** Comparison of experiments and our simulations for the saturated H₂ uptakes in different 20 COFs.

Effect of Feynman-Hibbs correction on simulated H₂ working capacities of COFs

Working capacity is a useful metric to evaluate adsorbents for gas separation applications. Classical LJ potential and a simple spherical H₂ model are commonly used in simulations to compute H₂ working capacities of adsorbents at 77 K in the literature. However, at low temperatures quantum effects can be important for small molecules. Therefore, the Feynman-Hibbs correction can be used to account quantum effects at low temperatures in simulations. In Figure 3, we compared H₂ working capacities of 296 COFs calculated at three different operating conditions (a) from 100 bar/77 K to 2 bar/77 K, (b) from 100 bar/77 K to 5 bar/77 K, and (c) from 100 bar/77 K to 5 bar/160 K based on their potential energies. Figure 3 shows that simulation results obtained from the simulations using the Feynman-Hibbs corrections were found

to be almost similar with the results obtained

There are obvious linear relationships between the results obtained from only LJ potential and the results obtained from LJ potential with Feynman-Hibbs corrections. We then examined the ranking of COFs based on H₂ working capacities calculated from only LJ potential and LJ potential with the Feynman-Hibbs corrections and estimated the Spearman's rank correlation coefficient (SRCC) ($-1 \leq SRCC \leq 1$). When SRCC is 1, there is a perfect correlation between two rankings. Table 3 shows the comparison of ranking of COFs based on volumetric H₂ working capacities calculated from GCMC simulations using different potentials. As shown in Table 3, the ranking of COFs is highly correlated, and the Feynman-Hibbs correction and adsorbate-adsorbent electrostatic interactions do not actually affect the ranking of materials. Therefore, we can conclude that predictions using only LJ potential with the single-site H₂ model can give quick and reliable information about the volumetric H₂ working capacities of COFs.

from the simulations using the single-site H₂ model at three different operating conditions.

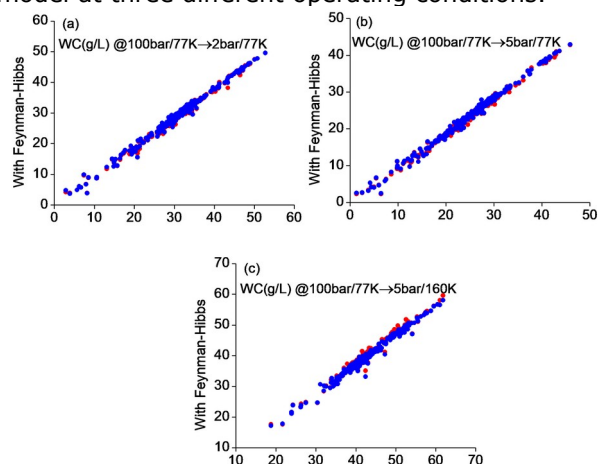


Figure 3: Comparison of H₂ WCs of 296 COFs calculated with the Lennard-Jones potential only (x-axis) and the Feynman-Hibbs corrections (y-axis). Red (blue) points represent our predictions obtained from all electrostatic interactions were on (only H₂-H₂ electrostatic interactions were on).

Table 3: Comparison of the ranking of COFs based on their volumetric H₂ working capacities.

Adsorption/desorption conditions	LJ vs LJ with the FH* (all electrostatic interactions)	LJ vs LJ with the FH (only H ₂ -H ₂ electrostatic interactions)
100 bar/77 K → 2 bar/77 K	0.96	0.97
100 bar/77 K → 5 bar/77 K	0.96	0.99
100 bar/77 K → 5 bar/160 K	0.99	0.98

*: Feynman-Hibbs correction

Evaluating the performance of COFs for H₂ storage:

We identified the top performing COFs for H₂ storage and ranked them based on their WCs computed from single-component GCMC simulations at 100 bar/77 K adsorption and 5 bar/77 K/160 K desorption conditions. Table 4 shows the top performing 10 COFs which exhibit the highest volumetric H₂ WCs (38.9-42.9 g/L) at 100 bar/77 K adsorption and 5 bar/77 K desorption conditions. The WCs here were obtained from the results of GCMC simulations

with the Feynman-Hibbs correction using the Darkrim and Levesque potential for H₂ (only H₂-H₂ electrostatic interactions are on).

The densities (porosities) of the top 10 COFs range from 0.16 g/cm³ to 0.24 g/cm³ (0.87-0.92). The top materials have all 3D structures except IISERP-COF3 which has 2D structure. COF-DL-229-3-fold has the highest H₂ WC (42.9 g/L) among 296 COFs which can be attributed to its high porosity (0.87) and large surface area (8462.g m²/g).

Table 4: Top performing 10 COFs ranked based on their H₂ WCs calculated at 100 bar/77 K adsorption and 5 bar/77 K desorption conditions.

COF	LCD-PLD (Å)	ρ (g/cm ³)	φ	WC (g/L)
COF-DL ^[1] 229-3-fold	10.72-10.15	0.24	0.87	42.92
PI ^[2] -COF-5-2P ^[3]	13.35-10.52	0.26	0.88	41.14
COF-DL229-2-fold	17.57-14.36	0.16	0.92	40.78
DL-COF-1-ctn	16.21-14.26	0.19	0.90	40.67
DL-COF-2-ctn	16.19-14.24	0.21	0.90	40.47
COF-105	18.80-16.12	0.18	0.91	39.63
DL-COF-1-bor	22.72-16.03	0.17	0.91	39.41
IISERP ^[4] -COF3	22.16-19.77	0.22	0.90	39.15
Ni-DBA ^[5] -3D-COF-ctn	20.96-17.60	0.17	0.92	39.04
DL-COF-2-bor	25.15-15.94	0.19	0.91	38.87

[1] DL: dual linkage; [2] PI: polyimide; [3] 2P: biphenyl-4,4'-dicarboxaldehyde; [4] IISERP: Indian Institute of Science Education and Research Pune; [5] DBA: dehydrobenzoannulenes.

It is also important to note that COF-DL-229-3-fold has smaller pore sizes ($10.72 \times 10.15 \text{ \AA}$) compared to the remaining 9 COFs which enhance H₂-COF interactions. Bucior et al. (1) also discussed that large-pored materials exhibit weak H₂-adsorbent interactions to bind H₂ molecules.

We also ranked 296 COFs based on their volumetric H₂ WCs calculated at 100 bar/77 K adsorption and 5 bar/160 K desorption conditions and listed in Table 5. Since adsorption is an exothermic process, when the desorption temperature increased from 77 K to 160 K, H₂ uptakes in COFs decreased as expected. Since H₂ WCs were calculated using the difference between H₂ uptake amounts at adsorption and

desorption pressures, volumetric H₂ WCs (52.7-58.0 g/L) were increased as shown in Table 5. COF-103 exhibited the highest volumetric H₂ WC as 58.0 g/L at 100 bar/77K adsorption and 5 bar/160 K desorption conditions. The top performing materials listed in Table 5 have higher densities ($0.24\text{-}0.47 \text{ g/cm}^3$) compared to the top candidates listed in Table 4 whereas they have narrower pore sizes and lower porosities than the latter. These materials also have 3D structures except ILCOF-1-AB. Among these 20 materials, COF-DL229-3fold is the common COF that exhibits high performance for H₂ capture at two different adsorption/desorption conditions. Results showed that different operating conditions should be considered in order to identify the best performing COFs for H₂ storage.

Table 5: Top performing 10 COFs ranked based on their H₂ WCs calculated at 100bar/77K adsorption and 5bar/160K desorption conditions

COF	LCD-PLD (Å)	ρ (g/cm ³)	φ	WC (g/L)
COF-103	9.68-8.50	0.39	0.80	58.04
ILCOF ^[1] -1-AB	11.09-9.41	0.34	0.82	56.71
COF-102	9.04-7.99	0.42	0.78	56.52
3D-Py ^[2] -COF-2P	13.47-12.29	0.28	0.85	56.06
BF ^[3] -COF-1	13.26-8.62	0.40	0.79	54.63
COF-DL229-3fold	10.72-10.15	0.24	0.87	54.13
BF-COF-2	13.28-7.58	0.47	0.78	53.87
3D-CuPor-COF	16.46-13.64	0.33	0.84	53.47
3D-Por ^[4] -COF	16.31-13.66	0.31	0.84	53.26
COF-DL229-5fold	11.25-11.20	0.37	0.80	52.73

[1] ILCOF: imine-linked; [2] Py: pyrene-based; [3] BF: base-functionalized; [4] Por: porphyrin.

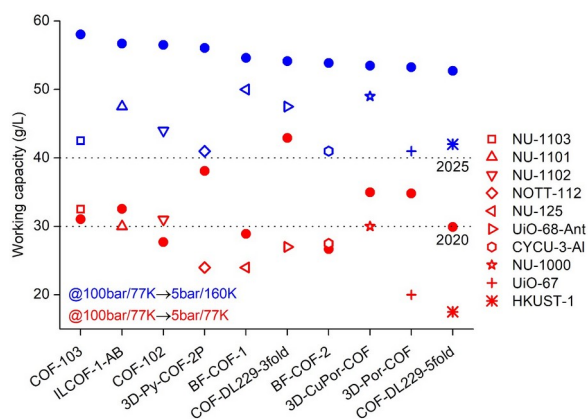


Figure 4: Comparison of volumetric H₂ WCs of the top performing 10 COFs (closed spheres) with those of the promising MOFs (open symbols) identified in the literature. (9)

Figure 4 shows the comparison of volumetric H₂ WCs of the top performing 10 COFs (listed in Table 5) studied under different temperature and pressure conditions with those of the best-performing MOFs at the same conditions. All

porous materials surpassed the DOE target for 2025 at 100 bar/77 K adsorption and 5 bar/160K desorption conditions. Among 10 COFs, only ILCOF-1-AB has 2D structure, the remaining COFs are all 3D. As shown in Figure 4, COFs also outperformed the top performing 10 MOFs including HKUST-1 (also known as Cu-BTC, BTC: benzene-1,3,5-tricarboxylate), NU-125, NU-1000, NU-1101, NU-1102,

NU-1103, NOTT-112 (NOTT: University of Nottingham), UiO-68-Ant (UiO: University of Oslo; Ant: anthracene), UiO-67 and CYCU-3-Al (CYCU: Chung-Yuan Christian University; Al: aluminum) at 100 bar/77 K adsorption and 5 bar/160 K desorption conditions. Among 10 COFs, COF-DL229-3-fold exhibited promising performance for H₂ storage at two different operating conditions, exceeding the DOE 2020 and 2025 targets. This can be attributed to optimal pore sizes ($10.72 \text{ \AA} \times 10.15 \text{ \AA}$) of COF-DL229-3-fold, its adequate porosity (0.87) and density (0.24 g/cm^3). Bobbitt et al. (37) also discussed that the materials, which have optimal porosity (~ 0.9) and pore sizes ($\sim 12 \text{ \AA}$), tend to

strongly bind with H₂ molecules, resulting in high H₂ uptake capacity.

As shown in Figure 4, NU-1103 (32.5 g/L) outperformed BF-COF-1, BF-COF-2, COF-102, COF-103, and COF-DL229-5-fold at 100 bar/77 K adsorption and 5 bar/77 K desorption conditions. This might be explained that NU-1103 has lower density (0.29 g/cm³) and higher porosity (0.88) than these 5 COFs, whose densities were around 0.4 g/cm³ and porosities ~0.80. Moreover, NU-1000, NU-1101 and NU-1102 have slightly higher porosities (~0.80) than BF-COF-1, BF-COF-2, and COF-102 (0.78), and these MOFs (~30.5 g/L) also outperformed 3 COFs at the same operating conditions. At 100 bar/77 K adsorption and 5 bar/77 K desorption conditions, BF-COF-2 gave almost similar H₂ WC with CYCU-3-Al due to their similar densities (~0.45 g/cm³). The other 4 COFs, namely as ILCOF-1-AB, 3D-Py-COF-2P, 3D-CuPor-COF, and 3D-Por-COF gave higher H₂ WCs than MOFs at two operating conditions. Overall, COFs can exceed the DOE 2020 and 2025 targets for on board H₂ storage.

Developing relationships between structural characteristics of materials and their performance for gas adsorption is important to better understand the behavior of materials and to synthesize promising candidates for desired applications. For this reason, we finally examined the structure-performance relationships for 296 COFs studied in this work. We investigated the relations between volumetric H₂ WCs of COFs and their structural properties including the LCD, PLD, SA, density (ρ), UV (Unit cell volume), PV, and porosity (ϕ) in Figure 5.

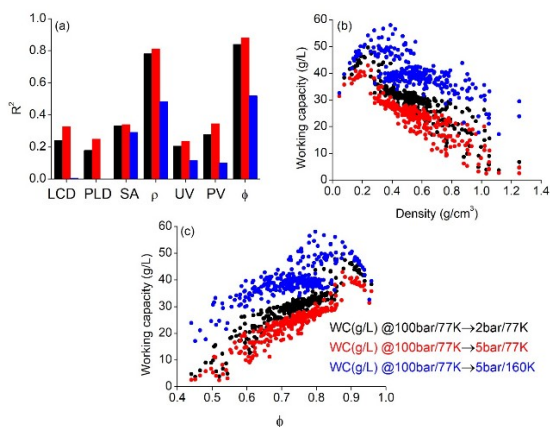


Figure 5: (a) R² values showing the relations between WC of H₂ (g/L) and several physical parameters. Relations between (b) density and H₂ working capacity (g/L), (c) porosity and H₂ working capacity (g/L).

As shown in Figure 5 (a), correlation coefficients (R²) were found to be higher than 0.8 for the relations between volumetric WCs and ρ , and ϕ of COFs for two operating conditions: at 100 bar/77 K for adsorption and at 2 bar/77 K (also 5 bar/77 K) for desorption. For the third case (from 100 bar/77 K to 5 bar/160 K), we did not observe a strong correlation (R² = 0.5) between volumetric H₂ WCs and ρ , and ϕ of COFs. Weak correlations between volumetric H₂ WCs of COFs and their LCDs, PLDs, SAs, UVs, PVs were observed for each three operational conditions as shown in Figure 5 (a).

Figure 5(b) shows the relationships between volumetric H₂ WCs of COFs and their densities (ranged from 0.05 to 1.25 g/cm³) at three operating conditions. H₂ WCs of COFs are negatively correlated with the density, especially $\rho > 0.3$ g/cm³, at these conditions. The materials which have densities in the range of 0.12 g/cm³ and 0.26 g/cm³ exhibited generally high H₂ WCs (32.4-54.1 g/L). For example, COF-DL229-3fold were found to have the highest H₂ WCs as 49.62 g/L (42.92 g/L) at 100 bar/77 K → 2 bar/77 K (at 100 bar/77K → 5 bar/77 K) due to its optimal density (0.24 g/cm³) and high porosity (0.87). In Figure 5(c), the linear relationships between H₂ WCs of COFs and their porosities (ranged from 0.44 to 0.96) can be seen. The materials which have high porosities (≥ 0.8) and quite low densities (0.2-0.4 g/cm³) generally exhibit high volumetric H₂ WCs.

For example, COF-103, which gave the maximum H₂ WC at 100 bar/77 K → 5 bar/160K, has high porosity (0.80) and quite low density (~0.4 g/cm³). On the other hand, COF-DL229-0-fold has the highest porosity (0.96), however exhibited an average performance for H₂ (~35 g/L) at three operating conditions due to its extremely low density (0.08 g/cm³) and very large pore sizes (24.6×31.9 Å). Results emphasized that volumetric H₂ storage in COFs can be negatively (positively) correlated with the densities (porosities) of COFs, like MOFs. It is also important to note that among 296 COFs, 257 COFs have 2D structures, and the remaining 39 COFs which commonly show high performance for H₂ storage are 3D.

CONCLUSIONS

In this work, H₂ storage performance of 296 COFs was assessed at various temperatures and pressures. Top 10 COFs, which gave the highest volumetric H₂ WCs were identified in different operating conditions. Effects of electrostatic interactions and the Feynman-Hibbs correction on the ranking of the top materials were examined and results showed that coulombic interactions

and the Feynman-Hibbs correction do not actually affect the ranking of COFs based on their H₂ WCs. Among 296 COFs, COF-DL229-3fold outperformed the ultimate DOE 2020 and DOE 2025 technical targets for on board H₂ storage. The COFs which have high porosities (≥ 0.8) and adequate densities (0.2-0.4 g/cm³) exhibited a promising performance in terms of volumetric H₂ storage. Results of this study will be helpful for future experimental and computational studies to design and synthesize novel COFs for H₂ capture.

REFERENCES

- Bucior BJ, Bobbitt NS, Islamoglu T, Goswami S, Gopalan A, Yildirim T, Farha OK, Bagheri N, Snurr RQ. Energy-based descriptors to rapidly predict hydrogen storage in metal-organic frameworks. *Molecular Systems Design & Engineering*. 2019;4(1):162-74.
- Gómez-Gualdrón DA, Wang TC, García-Holley P, Sawelewa RM, Argueta E, Snurr RQ, Hupp JT, Yildirim T, Farha OK. Understanding volumetric and gravimetric hydrogen adsorption trade-off in metal-organic frameworks. *ACS Applied Materials & Interfaces*. 2017;9(39):33419-28.
- Mason JA, Veenstra M, Long JR. Evaluating metal-organic frameworks for natural gas storage. *Chemical Science*. 2014;5(1):32-51.
- Stadie NP, Vajo JJ, Cumberland RW, Wilson AA, Ahn CC, Fultz B. Zeolite-templated carbon materials for high-pressure hydrogen storage. *Langmuir*. 2012;28(26):10057-63.
- Vitillo JG, Ricchiardi G, Spoto G, Zecchina A. Theoretical maximal storage of hydrogen in zeolitic frameworks. *Physical Chemistry Chemical Physics*. 2005;7(23):3948-54.
- Farha OK, Yazaydin AO, Eryazici I, Malliakas CD, Hauser BG, Kanatzidis MG, Nguyen ST, Snurr RQ, Hupp JT. De novo synthesis of a metal-organic framework material featuring ultrahigh surface area and gas storage capacities. *Nature Chemistry*. 2010;2(11):944-8.
- Han SS, Furukawa H, Yaghi OM, Goddard III WA. Covalent organic frameworks as exceptional hydrogen storage materials. *Journal of the American Chemical Society*. 2008;130(35):11580-1.
- Rabbani MG, Sekizkardes AK, Kahveci Z, Reich TE, Ding R, El-Kaderi HM. A 2D mesoporous imine-linked covalent organic framework for high pressure gas storage applications. *Chemistry—European Journal*. 2013;19(10):3324-8.
- García-Holley P, Schweitzer B, Islamoglu T, Liu Y, Lin L, Rodriguez S, Weston MH, Hupp JT, Gómez-Gualdrón DA, Yildirim T. Benchmark study of hydrogen storage in metal-organic frameworks under temperature and pressure swing conditions. *ACS Energy Letters*. 2018;3(3):748-54.
- Suh MP, Park HJ, Prasad TK, Lim D-W. Hydrogen storage in metal-organic frameworks. *Chemical Reviews*. 2011;112(2):782-835.
- Siegel D, Hardy B, Team H. Engineering an adsorbent-based hydrogen storage system: what have we learned 2015 [Available from: https://energy.gov/sites/prod/files/2015/02/f19/fcto_h2_storage_summit_siegel.pdf]
- Langmi HW, Ren J, North B, Mathe M, Bessa-rabov D. Hydrogen storage in metal-organic frameworks: a review. *Electrochimica Acta*. 2014;128:368-92.
- Gulcay E, Erucar I. Molecular simulations of COFs, IRMOFs and ZIFs for adsorption-based separation of carbon tetrachloride from air. *Journal of Molecular Graphics and Modelling*. 2019;86:84-94.
- Furukawa H, Yaghi OM. Storage of hydrogen, methane, and carbon dioxide in highly porous covalent organic frameworks for clean energy applications. *Journal of the American Chemical Society*. 2009;131(25):8875-83.
- Ding S-Y, Wang W. Covalent organic frameworks (COFs): from design to applications. *Chemical Society Reviews*. 2013;42(2):548-68.
- Basdogan Y, Keskin S. Simulation and modelling of MOFs for hydrogen storage. *CrystEngComm*. 2015;17(2):261-75.
- Ahmed A, Seth S, Purewal J, Wong-Foy AG, Veenstra M, Matzger AJ, Siegel DJ. Exceptional hydrogen storage achieved by screening nearly half a million metal-organic frameworks. *Nature Communications*. 2019;10(1):1568.
- Cao D, Lan J, Wang W, Smit B. Lithium-doped 3D covalent organic frameworks: high-capacity hydrogen storage materials. *Angewandte Chemie International Edition*. 2009;48(26):4730-3.
- Assfour B, Seifert G. Adsorption of hydrogen in covalent organic frameworks: comparison of simulations and experiments. *Microporous and Mesoporous Materials*. 2010;133(1-3):59-65.
- Tong M, Lan Y, Qin Z, Zhong C. Computation-ready, experimental covalent organic fra-

mework for methane delivery: screening and material design. *Journal of Physical Chemistry C*. 2018;122(24):13009-16.

21. Li Z, Feng X, Zou Y, Zhang Y, Xia H, Liu X, Mu Y. A 2D azine-linked covalent organic framework for gas storage applications. *Chemical Communications*. 2014;50(89):13825-8.

22. Stegbauer L, Hahn MW, Jentys A, Savasci GK, Ochsenfeld C, Lercher JA, Lotsch BV. Tunable water and CO₂ sorption properties in isostructural azine-based covalent organic frameworks through polarity engineering. *Chemistry of Materials*. 2015;27(23):7874-81.

23. Li Z, Zhi Y, Feng X, Ding X, Zou Y, Liu X, Mu Y. An azine-linked covalent organic framework: synthesis, characterization and efficient gas storage. *Chemistry–A European Journal*. 2015;21(34):12079-84.

24. Ge R, Hao D, Shi Q, Dong B, Leng W, Wang C, Gao Y. Target synthesis of an azo (N=N) based covalent organic framework with high CO₂-over-N₂ selectivity and benign gas storage capability. *Journal of Chemical & Engineering Data*. 2016;61(5):1904-9.

25. Neti VSPK, Wu X, Hosseini M, Bernal RA, Deng S, Echegoyen L. Synthesis of a phthalocyanine 2D covalent organic framework. *CrystEng-Comm*. 2013;15(36):7157-60.

26. Kaleeswaran D, Vishnoi P, Murugavel R. [3+3] Imine and β -ketoenamine tethered fluorescent covalent-organic frameworks for CO₂ uptake and nitroaromatic sensing. *Journal of Materials Chemistry C*. 2015;3(27):7159-71.

27. Kang Z, Peng Y, Qian Y, Yuan D, Addicoat MA, Heine T, Hu Z, Tee L, Guo Z, Zhao D. Mixed matrix membranes (MMMs) comprising exfoliated 2D covalent organic frameworks (COFs) for efficient CO₂ separation. *Chemistry of Materials*. 2016;28(5):1277-85.

28. Bhunia A, Vasylyeva V, Janiak C. From a supramolecular tetranitrile to a porous covalent triazine-based framework with high gas uptake capacities. *Chemical Communications*. 2013;49(38):3961-3.

29. Kahveci Z, Islamoglu T, Shar GA, Ding R, El-Kaderi HM. Targeted synthesis of a mesoporous triptycene-derived covalent organic framework. *CrystEngComm*. 2013;15(8):1524-7.

30. Willems TF, Rycroft CH, Kazi M, Meza JC, Haranczyk M. Algorithms and tools for high-throughput geometry-based analysis of crystalli-

ne porous materials. *Microporous and Mesoporous Materials*. 2012;149(1):134-41.

31. Dubbeldam D, Calero S, Ellis DE, Snurr RQ. RASPA: molecular simulation software for adsorption and diffusion in flexible nanoporous materials. *Molecular Simulation*. 2016;42(2):81-101.

32. Ewald PP. Die berechnung optischer und elektrostatischer gitterpotentiale. *Annalen der Physik*. 1921;369(3):253-87.

33. Buch V. Path integral simulations of mixed para-D₂ and ortho-D₂ clusters: The orientational effects. *Journal of Chemical Physics*. 1994;100(10):7610-29.

34. Darkrim F, Levesque D. Monte Carlo simulations of hydrogen adsorption in single-walled carbon nanotubes. *The Journal of Chemical Physics*. 1998;109(12):4981-4.

35. Feynman R, Hibbs A. *Quantum mechanics and path integrals*: McGraw-Hill, New York; 1965.

36. Rappé AK, Casewit CJ, Colwell K, Goddard III WA, Skiff WM. UFF, a full periodic table force field for molecular mechanics and molecular dynamics simulations. *Journal of the American Chemical Society*. 1992;114(25):10024-35.

37. Bobbitt NS, Chen J, Snurr RQ. High-throughput screening of metal-organic frameworks for hydrogen storage at cryogenic temperature. *Journal of Physical Chemistry C*. 2016;120(48):27328-41.



Density Functional Theory (DFT) Approach for Kinetic and Thermodynamic Study of Reaction Mechanism of Copper(II) Complex from 2-hydrazinyl-4,5-dihydro-1h-imidazole and anthracene-9-carbaldehyde

Shola Elijah Adeniji^{1*}  

¹ Chemistry Department, Ahmadu Bello University, Zaria-Nigeria

Abstract: A computational approach was employed to study the reaction mechanism for the copper(II) complex from 2-hydrazinyl-4,5-dihydro-1H-imidazole and anthracene-9-carbaldehyde at DFT (B3LYP) theory level. The reaction mechanism was proposed and found to have five elementary steps which involve intermediate elementary step and three transition states. The reaction mechanisms are observed to have bimolecular and unimolecular steps which give rise to two-step reaction pathway. The bimolecular step appeared to be rate determining step with highest energy barrier (2925.75 kJ/mol) at the third transition state (TS3). The geometrical variations in bond length of the intermediate and the transition states during the course of the reaction were also studied which signified that transformation has occurred from the initial state to a final state of product formation. The rate equation and general rate law for the reaction pathways were also established. The kinetics study shows that the reaction mechanism for the formation of copper(II) complex follows the pseudo-first order and second order reaction with high correlation, while the thermodynamic study indicates that the overall reaction is non-spontaneous and endothermic.

Keywords: Bimolecular, Copper(II) complex, kinetics, Transition state, Rate law.

Submitted: February 15, 2019. **Accepted:** October 11, 2019.

Cite this: Adeniji SE. Density functional theory (DFT) approach for kinetic and thermodynamic study of reaction mechanism of copper(II) complex from 2-hydrazinyl-4,5-dihydro-1h-imidazole and anthracene-9-carbaldehyde. JOTCSA. 2020; 7(1): 77-86.

DOI: <https://doi.org/10.18596/jotcsa.527827>.

Corresponding Author. E-mail: shola4343@gmail.com.

INTRODUCTION

Compounds containing nitrogen are very widely distributed in nature, play significant roles in the metabolic activities of all living organisms. At present, imine functionality is found in 60-80 % of the chemical compounds which accounts for the biological activities due to the nitrogen units. The synthesis of peptide antibiotics and other bio-active compounds are as a result of stereoselectivity of imines.

Schiff base which is a derivatives of imine with N-containing ligands have been reported to have significant biological activities (1,2). Recently, the pharmacological and biological activities of copper(II) complexes with N-containing ligands have been studied extensively and linked with the DNA cleavage and intercalation. The mitochondrial activation pathway for cell apoptosis via the redox activity of the copper(II) center has also been reported (3,4). (5) reported the synthesis and antitumor mechanisms of a copper(II) complex of anthracene-9-imidazoline hydrazone (9-AIH). However, the reaction

mechanisms, the thermodynamic and kinetic parameters of the synthesized complex are not explained. To the best of our knowledge, literature on theoretical and computational evaluation of kinetic and thermodynamic parameters on the reaction mechanisms of this complex is not yet carried out.

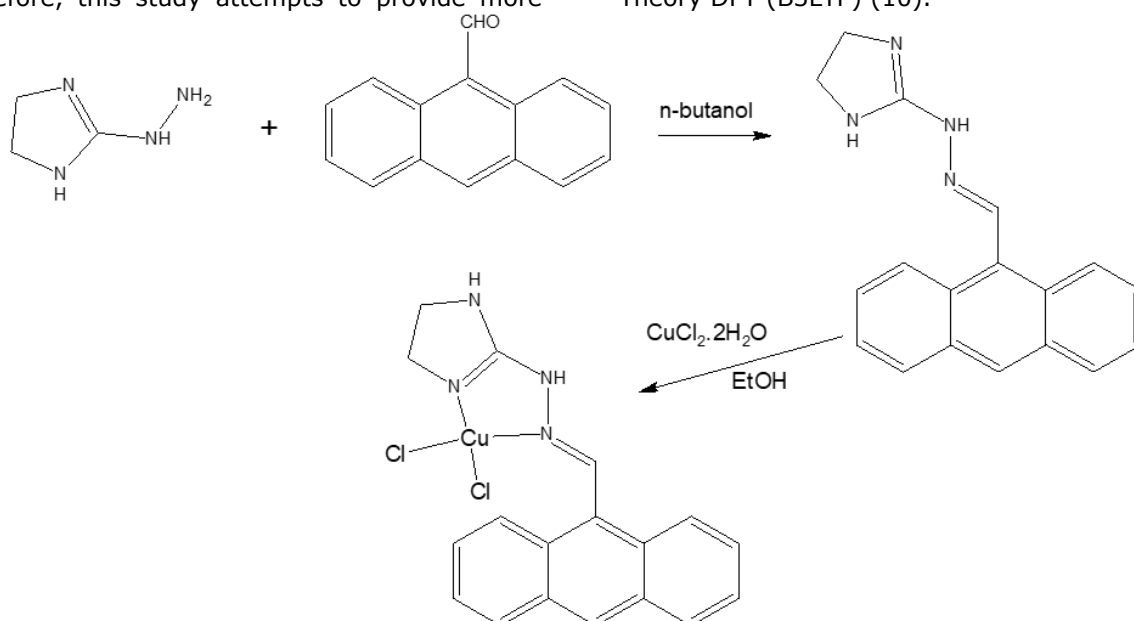
The advents of computational techniques help to predict the mechanism of new systems and explore the chemical relativities of different systems. Semi-empirical models such as PM3, AM1, DFT and MNDO are computational approaches employed to study and examine system(s) that have complicated reaction mechanism within short period of time. Meanwhile, computational study with Density Functional Theory (DFT) approach give more accurate results than Semi-empirical method. The use of computational technique to monitor reaction and proposed reaction mechanisms have been reported by some of the researchers (6–9). Therefore, this study attempts to provide more

information in this area by using theoretical and computational methods to elucidate the reaction mechanism, rate equations and derive the rate law for the formation of copper(II) complex from 2-hydrazinyl-4,5-dihydro-1H-imidazole and anthracene-9-carbaldehyde.

COMPUTATIONAL METHODOLOGY

Structure optimization

The 2D molecular structure presented in Scheme 1 and 2 were drawn by the Chemdraw software. The compounds were exported from 2D structure to 3D format using the Spartan 14 V1.1.4 Wave Function programming software. The entire three dimensions (3D structures) were geometrically optimized by minimizing energy. Molecular mechanics force field (MMFF) approach was employed to minimize the compounds in order to remove strain energy. Thereafter, the total geometric optimization of the molecular structures was achieved using Density Functional Theory DFT (B3LYP) (10).



Scheme 1. The synthetic route of synthesis copper(II) complex from 2-hydrazinyl-4,5-dihydro-1H-imidazole and anthracene-9-carbaldehyde. (5)

Structure optimization

Fundamental reaction coordinate calculation and molecular properties were achieved with the aid of Spartan 14 V1.1.4 Wave Function programming software at DFT level. Activating energy (E_a), rates (k) reaction, the enthalpy of the reaction and equilibrium constants (K_{eq}) were all computed using the expressions (1) – (5) given below:

$$E_a = \Delta H + RT \quad (1)$$

$$k_{(298.15K)} = \frac{K_B T}{hc^0} e^{-\Delta G^\# / RT} \quad (2)$$

$$k_{(298.15K)} = \frac{K_B T}{hc^0} e^{-\Delta G^0 / RT} \quad (3)$$

$$k_{eq(298.15K)} = e^{-\Delta G^\# / RT} \quad (4)$$

$$A = \Delta K_{(298.15K)} e^{-E_a / RT} \quad (5)$$

where k (298.15 K) is the reaction rate at temperature (298.15 K); K_B is the Boltzmann constant (1.380662×10^{-23} J/K); T is temperature (298.15 K); h is Planck's constant

(6.626176×10^{-34} Js); c^0 is concentration (taken as unity); R is the molar gas constant (8.31441 J/mol/K).

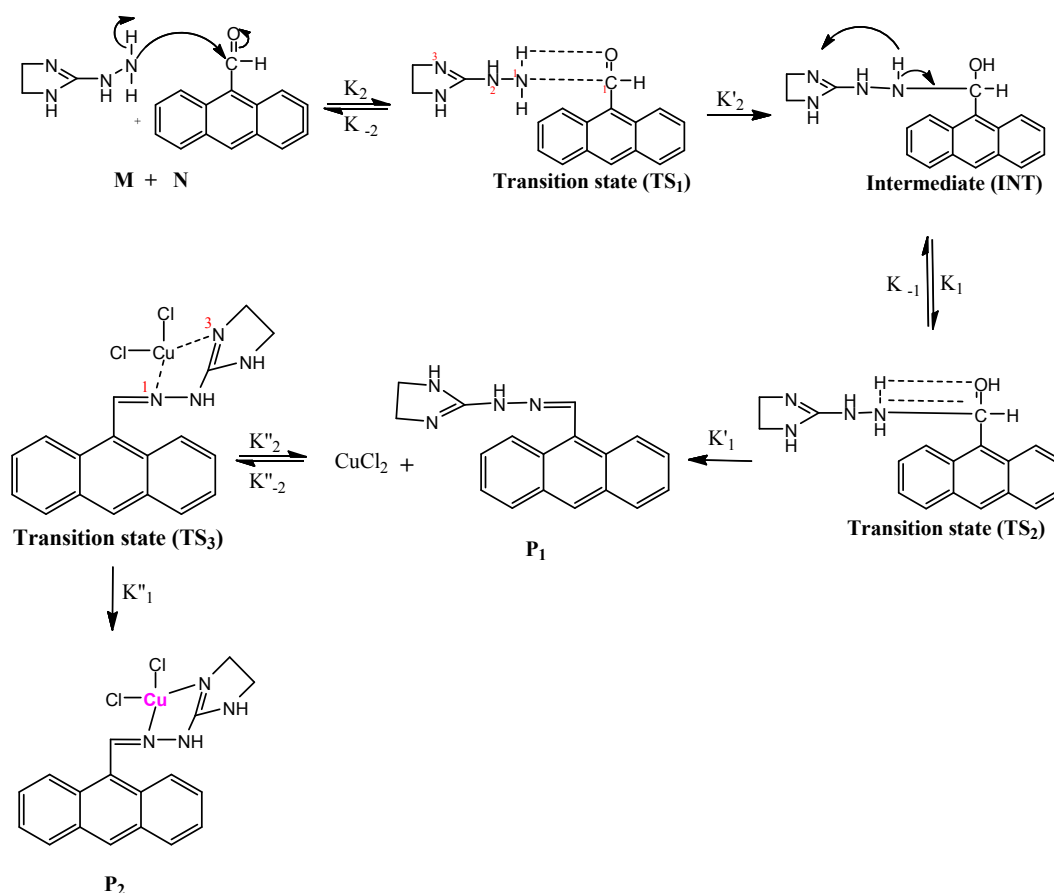
RESULTS AND DISCUSSION

A computational approach was employed to study the reaction mechanism for the copper(II) complex from 2-hydrazinyl-4,5-dihydro-1H-imidazole and anthracene-9-carbaldehyde at DFT theory level. The Scheme 2 and 3 show the proposed 2D and 3D reaction mechanism and schematic diagram for the formation of copper(II) complex. Figure 1 shows the energy profile of the relative electronic energy of reaction while Tables 1, 2, 3 and 4 respectively, present the molecular properties, thermodynamics, kinetic parameters of the computed reaction mechanism and of variation in bond length. The reaction mechanism involves three activation complexes (transition state) and intermediate elementary steps. The mechanism is a two-step reaction pathway with bimolecular and a unimolecular step as shown in Scheme 2 and 3.

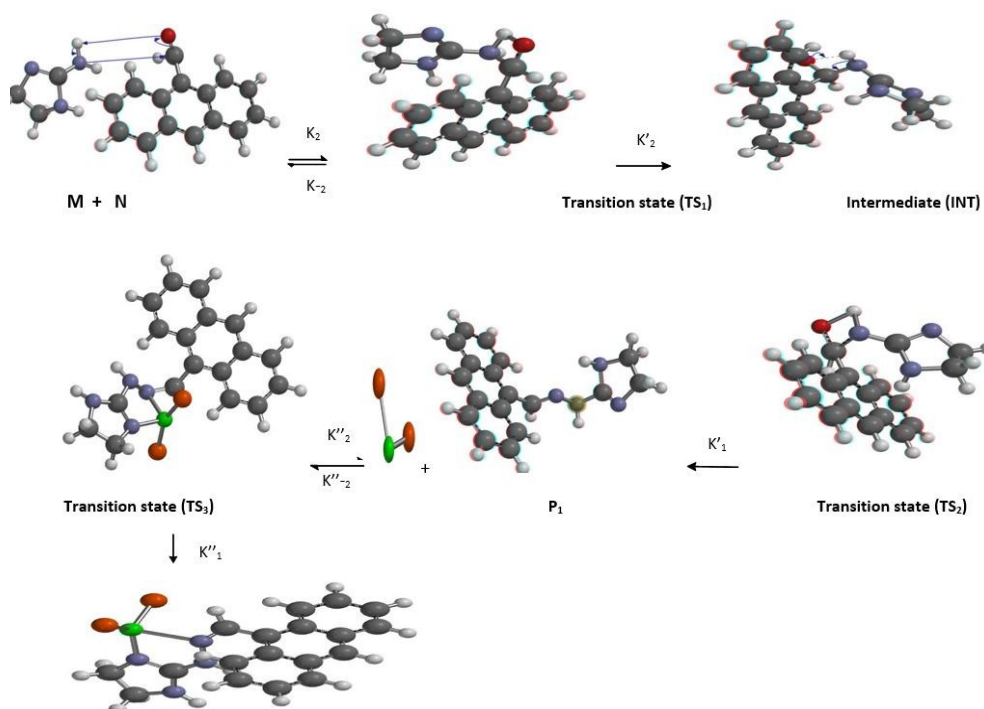
In the scheme, the mechanism began with partial cleavage of the C=O and N-H, C-N and O-H with an observed activation energy of +2664.84 kJ/mol at the first transition state (TS₁). The first (TS₁) formation is endothermic with Gibbs' free energy found to be non-spontaneous. The first transition state (TS₁) proceeds to form the intermediate (INT) through O-H single bond formation, C-N single bond formation, C=O bond cleavage to the single bond formation and N-H single bond cleavage with their corresponding bond length presented in Table 4. The intermediate has a lower stabilization energy of (144.34 kJ/mol) and non-spontaneous step (+54.42 kJ/mol) lower than the activated complex (TS₁) as shown in Figure 1 below. The intermediate state is found to be endothermic and non-spontaneous which is accomplished through C=N, O-H bond formation and N-H bond cleavage with an energy barrier of 2624.95 kJ/mol. The intra-molecular interaction of the intermediate state proceeds to form the second transition state (TS₂) via the C=N double bond formation, O-H single bond formation, N-H single bond cleavage and C-O bond cleavage. The second transition state (TS₂) has the higher activation energy of (2814.95 kJ/mol), enthalpy of (334.34 kJ/mol) and Gibbs' free energy of (+88.13 kJ/mol). The transition state (TS₂)

formed the first product (2-(2-(anthracen-9-ylmethylene)hydrazinyl)-4,5-dihydro-1H-imidazole) via cleavage bond of C-O bond and successful removal of the molecule. The first product formed reacted with the copper(II) chloride to form the third transition state (TS₃) which is accomplished through Cu-N₁ and Cu-N₃ partial bond formation with an energy barrier of (2925.75 kJ/mol). The interaction is found to be endothermic and non-spontaneous with (445.12 kJ/mol) and (+90.14 kJ/mol) respectively. Finally, through Cu-N₁ and Cu-N₃ partial bond formation, the third transition state (TS₃) form the second product copper(II) complex of anthracene-9-imidazoline hydrazine). Unimolecular and bimolecular were the two consecutive steps competing for the reaction rate determination, but as a result of the highest energy barrier (2925.75 kJ/mol) at the third transition state (TS₃) as shown in Figure 1, the bimolecular step is considered to be the rate-determining step. The two-step reaction mechanism presented by the potential and free energy profiles shows that the overall transformation is endothermic while Gibbs' free energy for each elementary step reported in Table 3 indicate that the reaction is non-spontaneous. The kinetics parameters reported in Table 3 shows that the reaction mechanism follows the pseudo-first order and second order reaction.

Variations in bond length as the reaction progress from transition state to intermediate were reported Table 4. A Decrease of about 0.05 Å in N₁-C₁ bond length as the reaction proceeds from TS₁ to INT was observed while an increase of 0.03 Å was observed as the reaction proceeds from INT to TS₂. The bond length also decreases with 0.02 Å in C₁-O as the reaction proceed from TS₁ to INT while an increase of 0.06 was observed as the reaction proceed to TS₂. A similar trend was observed in Cu-N₁ with variation in bond length of 0.168 Å and 0.134 Å as the reaction progresses from the third transition state (TS₃) to the final product. Also, the same trend was also noticed in Cu-N₃ with variation in bond length of 0.154 Å and 0.136 Å as the reaction progresses from the third transition state to the final product. All these variations that arise from the aforementioned states signified that transformation has occurred from the initial state to a final state of product formation.



Scheme 2. 2D structure of reaction mechanism for the formation of copper(II) complex.



Scheme 3. 3D structure of reaction mechanism for the formation of copper(II) complex. **Key:** **M** = 2-hydrazinyl-4,5-dihydro-1H-imidazole, **N** = anthracene-9-carbaldehyde, **P₁** = 2-(2-(anthracen-9-ylmethylene)hydrazinyl)-4,5-dihydro-1H-imidazole, **Q** = copper(II)chloride, **P₂** = copper(II) complex of anthracene-9-imidazoline.

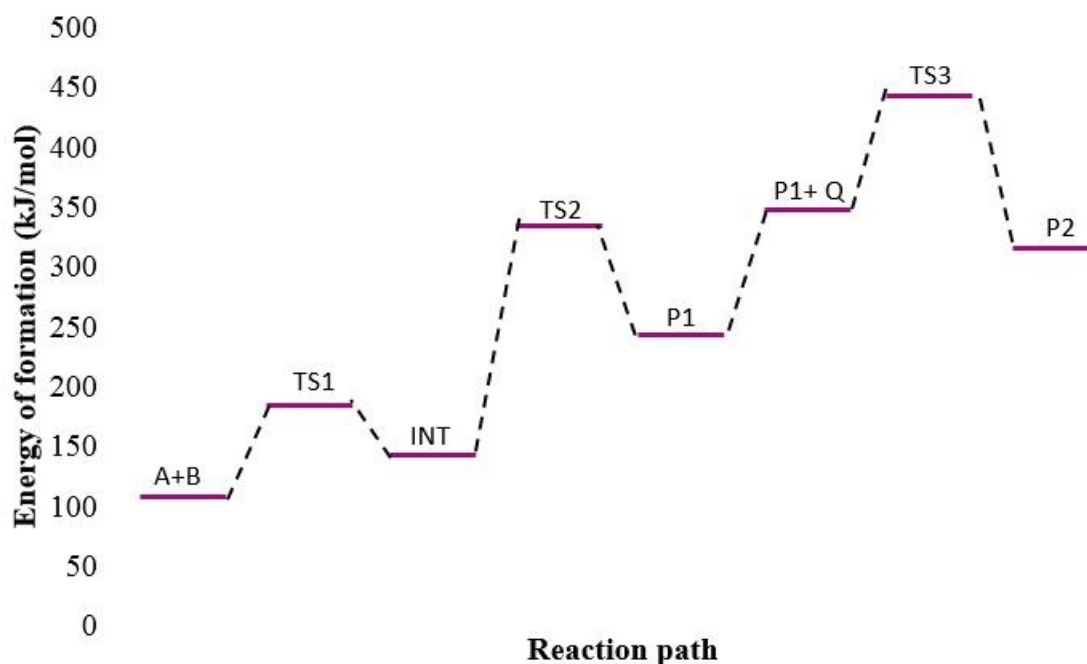
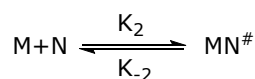


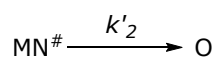
Figure 1: Profiles of the potential energy surface for copper(II) complex from 2-hydrazinyl-4,5-dihydro-1H-imidazole and anthracene-9-carbaldehyde.

Mechanism and derived rate law of the Reaction

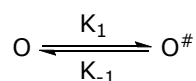
From reaction scheme given above, the reaction mechanism, rate equations and derived rate law for copper(II) complex form 2-hydrazinyl-4,5-dihydro-1H-imidazole and anthracene-9-carbaldehyde are expressed below:



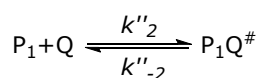
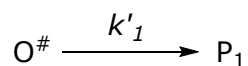
where "MN#" represent the first Transition state (TS₁)



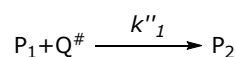
where "O" represent the Intermediate state (INT)



where "O#" represent the second Transition state (TS₂)



where "P₁Q#" represent the third Transition state (TS₃)



The rate law for the first product (P₁) is derived below;

$$\frac{d[P_1]}{dt} = k'_1[O^\#] \quad (6)$$

$$\frac{d[O^\#]}{dt} = -k'_1[O^\#] - k_{-1}[O^\#] + k_1[O] \quad (7)$$

$$\frac{d[O]}{dt} = -k[O] + k_{-1}[O^\#] + k'_2[MN^\#] \quad (8)$$

$$\frac{d[MN^\#]}{dt} = -k'_2[MN^\#] - k_{-2}[MN^\#] + k_2[M][N] \quad (9)$$

Applying steady state approximation, Equation (7) becomes;

$$[O^\#] = \frac{k_1}{k'_1 + k_{-1}} [O] \quad (10)$$

Substitute Equation (8) in (10)

$$[O] = \frac{k'_2(k'_1 + k_{-1})[MN^\#]}{k_1 k'_1} \quad (11)$$

Similarly, from Equation (9) we have

$$[MN^\#] = \frac{k_2}{k'_2 + k_{-2}} [M][N] \quad (12)$$

Equation (11) and (12) yield

$$[O] = \frac{k_2' k_2 (k_1' + k_{-1}) [MN^{\#}]}{k_1 k_1' (k_2' + k_{-2})} \quad (13)$$

From Equation (13) and (10), we have

$$[O^{\#}] = \left(\frac{k_2' k_2}{k_2' + k_{-2}} \right) [M][N] \quad (14)$$

Substituting Equation (14) in (6), the overall rate law for the first product will be written as;

$$\frac{d[P_1]}{dt} = k_1' \left(\frac{k_2' k_2}{k_2' + k_{-2}} \right) [M][N] \quad (15)$$

The rate law for the second product (P_2) is derived below;

$$\frac{d[P_2]}{dt} = k_1'' [P_1 Q^{\#}] \quad (16)$$

$$\frac{d[P_1 Q^{\#}]}{dt} = -k_1'' [P_1 Q^{\#}] - k_{-2}'' [P_1 Q^{\#}] + k_2'' [P_1][Q] \quad (17)$$

Applying steady state approximation Equation (17) becomes;

$$[P_1 Q^{\#}] = \left(\frac{k_2''}{k_1'' + k_{-2}''} \right) [P_1][Q] \quad (18)$$

Substituting Equation (18) in (16), the overall rate law for the second product will be written as;

$$\frac{d[P_2]}{dt} = k_1'' \left(\frac{k_2''}{k_1'' + k_{-2}''} \right) [P_1][Q] \quad (19)$$

CONCLUSION

A reaction mechanism for the copper(II) complex from 2-hydrazinyl-4,5-dihydro-1H-imidazole and anthracene-9-carbaldehyde have been investigated at the DFT theory level. The mechanism of the reaction was found to consist of three transition states with the bimolecular and unimolecular step. The bimolecular step was found to be the rate-determining step with the highest energy barrier of 2925.75 kJ/mol at the third transition state (TS_3) while the fastest reaction is observed with the unimolecular step. The rate laws have been derived for the reaction mechanism. The kinetics study shows that the reaction mechanism follows the pseudo-first order and second order reaction with high correlation while the thermodynamic study shows that the overall reaction is endothermic and non-spontaneous.

REFERENCES

1. Kostova I, Saso L. Advances in research of Schiff-base metal complexes as potent antioxidants. *Curr Med Chem.* 2013; 20(36): 4609–32.
2. Sztanke K, Maziarka A, Osinka A, Sztanke M. An insight into synthetic Schiff bases revealing antiproliferative activities in vitro. *Bioorg Med Chem.* 2013; 21(13): 3648–66.
3. Maheswari PU, Roy S, den Dulk H, Barends S, van Wezel G, Kozlevcar B, et al. The square-planar cytotoxic [CuII (pyrimol) Cl] complex acts as an efficient DNA cleaver without reductant. *J Am Chem Soc.* 2006; 128(3): 710–11.
4. Qiao X, Ma Z-Y, Xie C-Z, Xue F, Zhang Y-W, Xu J-Y, et al. Study on potential antitumor mechanism of a novel Schiff Base copper(II) complex: synthesis, crystal structure, DNA binding, cytotoxicity and apoptosis induction activity. *J Inorg Biochem.* 2011; 105(5): 728–37.
5. Qin Q-P, Liu Y-C, Wang H-L, Qin J-L, Cheng F-J, Tang S-F, et al. Synthesis and antitumor mechanisms of a copper(II) complex of anthracene-9-imidazole hydrazone (9-AIH). *Metallomics.* 2015; 7(7): 1124–36.
6. Ambundo EA, Deydier M-V, Ochrymowycz L, Rorabacher D. Kinetics and mechanism of copper(II) complex formation with tripodal aminopolythiaether and aminopolypyridyl ligands in aqueous solution. *Inorg Chem.* 2000; 39(6): 1171–79.
7. Jasiński R, Jasińska E, Dresler E. A DFT computational study of the molecular mechanism of [3+ 2] cycloaddition reactions between nitroethene and benzonitrile N-oxides. *J Mol Model.* 2017; 23(1): 13.
8. Siaka A, Adamu U, Sulaiman I, Hamza A, others. Density functional theory (B3LYP/6-311+G**) study of some semicarbazones formation mechanism. *Orient J Chem.* 2015; 31(4): 1985–97.
9. Siakaa A, Uzairub A, Idrisb S, Abbaa H. DFT (B3LYP) computational study on the mechanisms of formation of some semicarbazones. *Chem J Mold Gen.* 2016; 11(1): 74–85.
10. Adeniji SE, Uba S, Uzairu A. A Novel QSAR Model for the Evaluation and Prediction of (E)-N'-Benzylideneisonicotinohydrazide Derivatives as the Potent Anti-mycobacterium Tuberculosis Antibodies Using Genetic Function Approach. *Phys Chem Res.* 2018; 6(3): 479–92.

Table 1. Calculated molecular properties for copper(II) complex from 2-hydrazinyl-4,5-dihydro-1H-imidazole and anthracene-9-carbaldehyde using DFT at 298.15 K.

Reacting species	Formular	Energy (Vacuum) (kJ/mol)	Energy (aq) (kJ/mol)	Solvation Energy (kJ/mol)	Weight (amu)	Point group	Dipole Moment (debye)	E HOMO (ev)	E LUMO (ev)
A	C ₃ H ₈ N ₄	41.43	77.54	-63.90	100.125	C ₁	2.94	-9.34	0.90
B	C ₁₅ H ₁₀ O	51.71	54.73	-2.26.96	206.244	C _s	2.56	-8.45	-1.22
TS₁	C ₁₈ H ₁₇ N ₃ O	129.68	131.74	-53.91	291.354	C ₁	1.77	-8.25	-1.05
INT	C ₁₈ H ₁₇ N ₃ O	107.96	110.07	-62.93	291.354	C ₁	2.63	-8.32	-1.12
TS₂	C ₁₈ H ₁₆ N ₃ O	308.89	321.67	-187.09	290.346	C ₁	4.43	-12.07	-6.35
P₁	C ₁₈ H ₁₆ N ₄	83.06	94.23	-60.75	288.354	C ₁	2.03	-8.34	-1.14
C	CuCl ₂	77.74	89.43	-126	134.45	C _{2v}	3.65	-16.58	-8.89
TS₃	C ₁₈ H ₁₆ CuCl ₂ N ₄	357.7	376.34	-176	422.806	C ₁	9.91	-10.67	-6.31
P₂	C ₁₈ H ₁₆ CuCl ₂ N ₄	143.98	157.54	-143	422.81	C ₁	8.40	-11.13	-5.85

Table 2. Calculated thermodynamic parameters for copper(II) complex from 2-hydrazinyl-4,5-dihydro-1H-imidazole and anthracene-9-carbaldehyde using DFT at 298.15 K.

Reacting Species	C _v (J/mol)	Zero Point Energy (kJ/mol)	ΔH^0 (kJ/mol)	ΔS^0 (kJ/mol)	ΔG^0 (kJ/mol)	E _a (kJ/mol)	ΔH^\ddagger (kJ/mol)	ΔS^\ddagger (kJ/mol)	ΔG^\ddagger (kJ/mol)
A	30.63	44.11	48.87	+0.23748	24.66	2529.48			
B	48.42	44.54	56.85	+0.3308	35.41	2537.46			
TS₁	168.85	161.41				2664.84	184.23	+0.515	73.68
INT	138.04	137.76	144.34	+0.4149	54.42	2624.95			
TS₂	164.48	310.34				2814.95	334.34	+0.4093	88.13
P₁	164.14	224	243.88	+0.4146	76.45	2724.49			
C	-22.59	94.18	104.32	+0.196	63.13	2584.93			
TS₃	192.63	423.70				2925.75	445.12	+0.4766	90.54
P₂	163.65	345.5	317.75	+0.4624	82.04	2798.36			

Table 3. Calculated rate constant (k 's), equilibrium constant (Keq) and frequency factor (A) for copper(II) complex from 2-hydrazinyl-4,5-dihydro-1h-imidazole and anthracene-9-carbaldehyde using DFT at 298.15 K.

Kinetics parameters								
Step	k_2 ($dm^3mol^{-1}S^{-1}$)	k_2' ($dm^3mol^{-1}S^{-1}$)	k_1 (S^{-1})	k_1' (S^{-1})	k_2'' ($dm^3mol^{-1}S^{-1}$) 1)	k_1'' (S^{-1})	Keq	A
$M+N \rightleftharpoons TS_1$	6.04×10^{12}						0.971	2.06×10^{12}
$TS_1 \longrightarrow INT$		6.08×10^{12}						2.11×10^{12}
$INT \rightleftharpoons TS_2$			6.00×10^{12}				0.965	1.93×10^{12}
$INT \longrightarrow P_1$				6.03×10^{12}				2.01×10^{12}
$P_1+Q \rightleftharpoons TS_3$					5.99×10^{12}		0.964	1.84×10^{12}
$TS_3 \rightleftharpoons P_2$						6.02×10^{12}		1.18×10^{12}

Table 4. Variations in bond length during transformation through TS₁, INT, TS₂ TS₃ and P₂

TS₁	INT		TS₂		TS₃		P₂		
Bond	Bond length (Å)	Bond	Bond Length (Å)	Bond	Bond length (Å)	Bond	Bond Length (Å)	Bond	Bond Length (Å)
N₁-C₁	1.499	N₁-C₁	1.494	N₁-C₁	1.497	Cu-N₁	1.886	Cu-N₁	1.732
C₁-O	1.412	C₁-O	1.409	C₁-O	1.415	Cu-N₃	1.930	Cu-N₃	1.794



Comparison of Antioxidant Activities of Mono-, Di- and Tri-substituted Coumarins

Hülya Çelik Onar^{1*}  , Hasniye Yaşa¹   and Oktay Sin²  

¹ Istanbul University-Cerrahpaşa Engineering Faculty Chemistry Department Organic Chemistry Division, Avcılar/İstanbul/Turkey.

² Istanbul University-Cerrahpaşa Institute of Graduate Studies Avcılar/İstanbul/Turkey.

Abstract: In this study, numerous coumarin compounds were synthesized by Pechmann and Knoevenagel methods, and the substitution of the formyl group was provided by the Duff reaction. The FTIR spectra and melting points of the synthesized compounds were compared with the literature values. The structures were also confirmed by GC/MS analysis. Besides, the synthesized coumarin derivatives were compared in terms of antioxidant activity according to DPPH and CUPRAC methods. The main aim of the study is to determine the effects of substituents on antioxidant activity.

Keywords: Coumarin, Pechmann reaction, Knoevenagel reaction, Duff reaction, DDPH method, CUPRAC method.

Submitted: September 25, 2019. **Accepted:** October 30, 2019.

Cite this: Çelik Onar H, Yaşa H, Sin O. Comparison of antioxidant activities of mono-, di- and tri-substituted coumarins. JOTCSA. 2020; 7(1): 87–96.

DOI: <https://doi.org/10.18596/jotcsa.624265>.

Corresponding Author. E-mail: hcelik@istanbul.edu.tr.

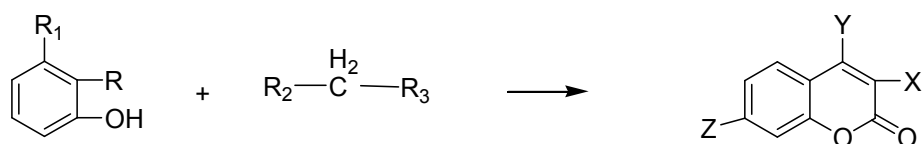
INTRODUCTION

Studies on heterocyclic compounds have intensified over the past decade because they have important medicinal properties, especially small-ring heterocyclic compounds. Coumarin derivatives are also one of these and some properties such as antibacterial, antifungal, and anticoagulant agents in pharmaceutical industry were studied (1). As well as being an optical whitening reagent, it is present in the structure of fluorescent and laser dyes (2), perfumes, soaps, cleansing products and food, because of their pleasant smell and sweetening effect (3).

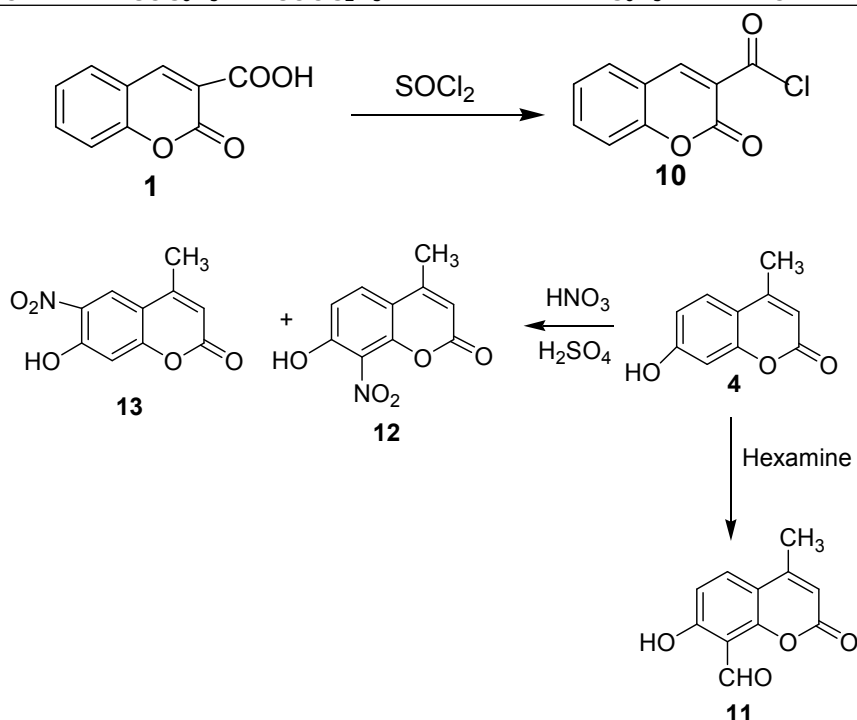
Coumarin is an oxygen-containing heterocyclic compound that is isolated from plants, especially

from green plants. Synthesis of coumarin is usually performed with one of the reactions known as Pechmann, Perkin, Knoevenagel, Reformatsky, and Wittig. Various catalysts such as H₂SO₄, H₃PO₄, CF₃COOH, p-toluenesulfonic acid, POCl₃, Bi(NO₃)₃·5H₂O, AlCl₃, TiCl₄, ZnI₂ and ionic liquids were used in these reactions.

Coumarin is a compound suitable for substitution at six points in the structure. The attachment of different substituents at different points adds different properties to the coumarins. Therefore, various mono-, di-, and tri-substituted coumarins have been synthesized (Scheme 1) and compared with standards for antioxidant activity according to DPPH and CUPRAC methods.



R	R ₁	R ₂	R ₃	X	Y	Z	Compound
CHO	H	COOH	COOH	COOH	H	H	1
CHO	H	COCH ₃	COOC ₂ H ₅	COCH ₃	H	H	2
CHO	H	COC ₆ H ₅	COOC ₂ H ₅	COC ₆ H ₅	H	H	3
H	OH	COCH ₃	COOC ₂ H ₅	H	CH ₃	OH	4
H	NH ₂	COCH ₃	COOC ₂ H ₅	H	CH ₃	NH ₂	5
H	OCH ₃	COCH ₃	COOC ₂ H ₅	H	CH ₃	OCH ₃	6
H	NH ₂	COC ₆ H ₅	COOC ₂ H ₅	H	C ₆ H ₅	NH ₂	7
H	OH	COC ₃ H ₇	COOC ₂ H ₅	H	C ₃ H ₇	OH	8
H	OH	COC ₆ H ₅	COOC ₂ H ₅	H	C ₆ H ₅	OH	9



Scheme 1. Synthesized compounds.

EXPERIMENTAL SECTION

Instruments

Recovery of the solvents during the recovery of the products and during the crystallization processes was carried out in a BÜCHI Rotavapor R-200 rotary evaporator. In thin layer chromatography (TLC), a Silicagel 60F₂₅₄ layer (Merck) was used. The plates were illuminated with a UV lamp to make the stains on the film sheets visible. Melting points of the coumarin compounds were examined in a Buchi Melting Point B-540 melting point apparatus. Fourier Transform Infrared (FT-IR) spectra of the synthesized coumarin compounds were taken on a Mattson 1000 Series FT-IR spectrometer. Mass spectra were checked with a Shimadzu GC-MS

2010 device.

Coumarin-3-carboxylic acid synthesis (1)

The synthesis was carried out by Knoevenagel reaction. 1.05 mL (10 mmol) of salicylaldehyde and 1.56 g (15 mmol) of malonic acid were refluxed with 1 mL of KSF catalyst with 3.3 mL of H₂O at 110-120 °C for 24 hours. The reaction was checked by TLC and when a new product was formed, the reaction was terminated with TLC control about the termination of the starting material. It was cooled down to room temperature. The remaining solid was triturated with 60 mL of methanol or ethyl acetate (4).

Yield(%): 95 m.p. 192 °C. Analysis of the GC / MS revealed MS peaks at m/z 190, 173, 146,

118, 89, 77, 63. $M=(190)$, $M-OH = M^{+1}(173)$, $M^{+1}-CO = M^{+2}(145)$, $M^{+2}-CO = M^{+3}(117)$. FTIR spectrum shows a 3174 cm^{-1} (-OH) stretching, 3057 cm^{-1} (Ar, C-H) aryl stretching, 1737 cm^{-1} (C=O) lactone carbonyl stretching, 1672 cm^{-1} (C=O) acid carbonyl stretching, 1607 cm^{-1} , 1566 cm^{-1} (C=C) double band stretching, and 1226 cm^{-1} (C-O) stretching (4,5).

Synthesis of 3-acetylcoumarin (2)

It was synthesized by Knoevenagel reaction with triethylamine as catalyst. 2.65 mL (0.025 mol) of salicylaldehyde and 3.175 mL (0.025 mol) of ethyl acetoacetate were refluxed in 15 mL of ethanol and 5 mL of triethylamine as catalyst at $80\text{ }^{\circ}\text{C}$ for 12 hours. The reaction was continued until TLC showed that a new product was formed. When the starting material completely finished, the reaction was terminated and cooled to room temperature, then filtered through a Büchner funnel, then the remaining solid was crystallized from ethanol (6).

Yield(%): 60 m.p. $120\text{ }^{\circ}\text{C}$. Analysis of the GC / MS revealed MS peaks at 188, 173, 145, 118, 101, 89, 63. $M=(188)$, $M-CH_3 = M^{+1}(173)$, $M^{+1}-CO = M^{+2}(145)$, $M^{+2}-CO = M^{+3}(117)$. FTIR spectrum shows a 3031 cm^{-1} (Ar, C-H) aryl stretching, 2983 cm^{-1} (C-H) aliphatic carbon - hydrogen stretching, 1740 cm^{-1} (C=O) lactone carbonyl stretching, 1675 cm^{-1} (C=O) ketone carbonyl stretching, 1612 cm^{-1} (C=C) double band stretching, 1265 cm^{-1} (C-O) stretching (6,7).

Synthesis of 3-benzoylcoumarin (3)

It was synthesized by Knoevenagel reaction with pyridine as catalyst. 1.05 mL (0.01 mol) of salicylaldehyde and 3.47 mL (0.020 mol) of ethylbenzoylacetate were refluxed with 10 mL of ethanol with 0.08 mL of pyridine as catalyst at $80\text{ }^{\circ}\text{C}$ for 12 hours. The reaction was checked by TLC and when a new product was formed and the starting material completely finished, the reaction was terminated. It was cooled to room temperature and filtered through a Büchner funnel. The remaining solid was crystallized from ethanol (8).

Yield(%): 60 m.p. $138\text{ }^{\circ}\text{C}$. Analysis of the GC / MS revealed MS peaks at 250, 222, 194, 173, 105, 77, 51. $M=(250)$, $M-CO = M^{+1}(222)$, $M^{+1}-CO = M^{+2}(194)$. IR spectrum shows a 3046 cm^{-1} (Ar, C-H) aryl stretching, 1716 cm^{-1} (C=O) lactone carbonyl stretching, 1658 cm^{-1} (C=O) ketone carbonyl stretching, 1608 cm^{-1} (C=C) double band stretching, 1264 cm^{-1} (C-O) stretching (8).

Synthesis of 4-methyl-7-hydroxycoumarin (4)

It was synthesized by Pechmann reaction in the presence of a catalytic amount of oxalic acid. 1.1 g (10 mmol) of resorcinol (1,3-

dihydroxybenzene) and 2.54 mL (20 mmol) ethylacetoacetate were reacted at 0.09 g (1 mmol) of oxalic acid catalyst and at $80\text{ }^{\circ}\text{C}$ for 12 hours with some molecular sieve. The reaction was checked by TLC and when a new product was formed and the starting materials completely finished, the reaction was stopped and allowed to cool. As the reaction cooled, ice was added and then filtered on a Büchner funnel. The remaining solid was crystallized from ethanol (9).

Yield(%): 60. m.p. $118\text{ }^{\circ}\text{C}$. Analysis of the GC / MS revealed MS peaks at 176, 148, 133, 116, 105, 91, 74, 65. $M=(176)$, $M-CO = M^{+1}(148)$, $M^{+1}-CH_3 = M^{+2}(133)$, $M^{+2}-OH = M^{+3}(116)$. FTIR spectrum shows a 3225 cm^{-1} (-OH) stretching, 3077 cm^{-1} (Ar, C-H) aryl stretching, 1673 cm^{-1} (C=O) lactone carbonyl stretching, 1586 cm^{-1} (C=C) double band stretching, 1272 cm^{-1} (C-O) stretching (9,10).

Synthesis of 4-methyl-7-amino-, 4-methyl-7-methoxy-, 4-phenyl-7-aminocoumarin

They were synthesized by Pechmann reaction with oxalic acid as catalyst. (10 mmol) of 3-substituted phenol and (12 mmol) of ethyl acetoacetate or ethylbenzoyl acetate were reacted at 0.09 g (1 mmol) of oxalic acid catalyst and a quantity of molecular sieve at $80\text{ }^{\circ}\text{C}$ for 12 hours. The reaction was checked by TLC and when a new product was formed and the starting materials completely finished, the reaction was turned off and allowed to cool. As the reaction cooled, ice was added and then filtered through a spinner funnel. The remaining solid was crystallized from a mixture of ethanol-water (9:1) (11-13).

4-Methyl-7-aminocoumarin (5): Yield(%): 80 m.p. $223,8\text{ }^{\circ}\text{C}$. Analysis of the GC/MS revealed MS peaks at 175, 147, 132, 116, 91, 73, 65, 44. $M=(175)$, $M-CO = M^{+1}(147)$, $M^{+1}-CH_3 = M^{+2}(132)$, $M^{+2}-NH_2 = M^{+3}(116)$. FTIR spectrum shows a 3249 cm^{-1} (-NH₂) stretching, 1661 cm^{-1} (C=O) lactone carbonyl stretching, 1603 cm^{-1} (C=C) double band stretching, and 1294 cm^{-1} (C-O) stretching (9,14).

4-Methyl-7-methoxycoumarin (6): Yield(%): 80 m.p. $159,2\text{ }^{\circ}\text{C}$. Analysis of the GC / MS revealed MS peaks at 190, 162, 147, 116, 91, 77, 65. $M=(190)$, $M-CO = M^{+1}(162)$, $M^{+1}-CH_3 = M^{+2}(147)$, $M^{+2}-OCH_3 = M^{+3}(116)$. FTIR spectrum shows a 3028 cm^{-1} (Ar, C-H) aryl stretching, 1711 cm^{-1} (C=O) lactone carbonyl stretching, 1605 cm^{-1} (C=C) double band stretching, 1264 cm^{-1} (C-O) stretching (12,15).

4-Phenyl-7-aminocoumarin (7): Yield(%): 75 m.p. $222,6\text{ }^{\circ}\text{C}$. Analysis of the GC / MS revealed MS peaks at 237, 209, 193, 116. $M=(237)$, $M-CO = M^{+1}(209)$, $M^{+1}-NH_2 = M^{+2}(193)$, $M^{+2}-C_6H_5 =$

M⁺³ (116). FTIR spectrum shows a 3245 cm⁻¹(N-H) stretching, 1661 cm⁻¹ (C=O) lactone carbonyl stretching, 1598 cm⁻¹ (C=C) double band stretching, 1293 cm⁻¹(C-O) stretching (13).

Synthesis of 4-propyl-7-hydroxycoumarin (8)

It was synthesized by Pechmann reaction in the presence of oxalic acid as catalyst. 1.1 g (10 mmol) of resorcinol (1,3-dihydroxybenzene) and 1.6 mL (10 mmol) of ethylbutyryl acetoacetate were added to the reaction mixture at 0.08 g (1 mmol) of oxalic acid and a quantity of molecular sieve were introduced. The reaction was checked by TLC and when a new product was formed and the starting materials completely finished, the reaction was turned off and allowed to cool. As the reaction cooled, ice was added and then filtered on a Büchner funnel. The remaining solid was crystallized in ethanol. Column chromatography was performed for purifying using chloroform: methanol (5: 1) as the eluent phase (16).

Yield(%): 65 m.p.133 °C. Analysis of the GC/MS revealed MS peaks at 204, 189, 176, 161, 148, 133, 105, 91, 77, 44. M=(204), M-CH₃ = M⁺¹ (189) M-CO = M⁺¹(176), M⁺¹- C₃H₇ = M⁺² (133). FTIR spectrum shows a 3253 cm⁻¹ (O-H) stretching, 1691 cm⁻¹ (C=O) lactone carbonyl stretching, 1614 cm⁻¹ (C=C) double band stretching, and 1310 cm⁻¹(C-O) stretching (16,17).

Synthesis of 4-phenyl-7-hydroxycoumarin (9)

It was synthesized by Pechmann reaction with oxalic acid as catalyst. 2.0 g (12 mmol) of ethylbenzoyl acetate were reacted with 1.1 g (10 mmol) of resorcinol (1,3-dihydroxybenzene) and 0.314 g (1 mmol) of amberlyte 15 catalyst and a quantity of molecular sieve at 80 °C for 12 hours. The reaction was checked by TLC and in case a new product was formed, the starting materials were waited to finish completely, the reaction was turned off and allowed to cool. As the reaction cooled, ice was added and then filtered on a Büchner funnel. The remaining solid was crystallized from ethanol (18).

Yield(%): 65 m.p. 249 °C. Analysis of the GC / MS revealed MS peaks at 238, 210, 181, 152, 139, 127, 76, 63, 51. M=(238), M-CO = M⁺¹(210), C₃H₇⁺ = (76). FTIR spectrum shows a 3115 cm⁻¹(O-H) stretching, 1684 cm⁻¹ (C=O) lactone carbonyl stretching, 1592 cm⁻¹ (C=C) double band stretching, 1268 cm⁻¹(C-O) stretching (18).

Synthesis of coumarin-3-carboxylic acid chloride (10)

To 1.9 g (0.1 mol) of coumarin-3-carboxylic acid,

10 mL of thionyl chloride (SOCl₂) was added to a round bottom flask, a few drops of pyridine was introduced, and the reboiler was fitted with a 5% NaOH solution in a hose over the cooler. It was refluxed at 80°C for three hours and cooled to room temperature. The white precipitate was washed several times with dry n-hexane (19).

Yield(%): 95 m.p. 145 °C. Analysis of the GC / MS revealed MS peaks at 208, 173, 145, 101, 89, 63. M=(208), M-Cl = M⁺¹(173), M⁺¹-CO = M⁺² (145). FTIR spectrum shows a 3038 cm⁻¹(Ar, C-H) aryl stretching, 1747cm⁻¹ (C=O) lactone carbonyl stretching, 1693 cm⁻¹ (C=O) acyl carbonyl stretching, 1605 cm⁻¹ (C=C) double band stretching, 1179 cm⁻¹(C-O) stretching and 759 cm⁻¹ (C-Cl) stretching (19,20).

Synthesis of 4-methyl-7-hydroxy-8-formylcoumarin (11)

This compound was synthesized by Duff reaction. 6.5 g of 4-methyl-7-hydroxycoumarin, 12 g of hexamethylene tetramine (hexamine), 61.5 mL of glacial acetic acid were added and the mixture was refluxed at 85-90 °C for 12 hours. 92.18 mL of 20% HCl solution (49.83 mL of HCl, 42.33 mL of distilled water) was added and refluxed for a further 4 hours. The reaction was checked by TLC and when a new product was formed, it was cooled to room temperature and extracted with diethyl ether. The resulting extract was dried in sodium sulfate (Na₂SO₄) for 15 min. The solvent was removed on the evaporator to give a pale yellow solid. The residue was purified by crystallization from a solvent mixture of ethanol-1,4-dioxane (9:1) (21).

Yield(%): 65 m.p. 176 °C. Analysis of the GC/MS revealed MS peaks at 204, 176, 148, 119, 91, 77, 65, 44 M=(204), M-CO = M⁺¹(176), M⁺¹ -CO = M⁺²(148). FTIR spectrum shows a 3125 cm⁻¹(O-H) stretching, 1742 cm⁻¹ (C=O) lactone carbonyl stretching, 1644 cm⁻¹ (C=O) aldehyde carbonyl stretching, 1518 cm⁻¹ (C=C) double band stretching, 1268 cm⁻¹(C-O) stretching (21-23).

Syntheses of 4-methyl-7-hydroxy-8-nitrocoumarin and 4-methyl-7-hydroxy-6-nitrocoumarin

1.2 g of 4-methyl-7-hydroxycoumarin was dissolved in 10 mL of H₂SO₄ at 0-5 °C. 1.5 mL of H₂SO₄ and 0.5 mL of HNO₃ were added dropwise to the reaction flask. It was stirred at 0-5 °C for four hours and then filtered on a Büchner funnel. When crystallized from ethanol, the solid residue on the filter paper was separated as 4-methyl-7-hydroxy-6-nitrocoumarin. The 4-methyl-7-hydroxy-8-nitrocoumarin which remains in the filtrate is cooled in the refrigerator and crystallized, then filtered through Büchner funnel (24).

4-Methyl-7-hydroxy-8-nitrocoumarin (12):

Yield(%): 40 m.p. 254,6 °C. Analysis of the GC/MS revealed MS peaks at 221, 193, 176, 147, 135, 119, 91, 77, 65, 51, 44. M=(221), M-CO = M⁺¹(193), M⁺¹- OH = M⁺²(176). FTIR spectrum shows a 3265 cm⁻¹(O-H) stretching, 1703 cm⁻¹ (C=O) lactone carbonyl stretching, 1569 cm⁻¹ (C=C) double band stretching, and 1314 cm⁻¹(C-O) stretching (24,25).

4-Methyl-7-hydroxy-6-nitrocoumarin (13):

Yield(%): 40 m.p. 261 °C. Analysis of the GC/MS revealed MS peaks at 221, 193, 147, 135, 119, 91, 77, 65, 51, 44. M=(221), M-CO = M⁺¹(193), M⁺¹ - NO₂ = M⁺²(147). FTIR spectrum shows a 3244 cm⁻¹(O-H) stretching, 1727 cm⁻¹ (C=O) lactone carbonyl stretching, 1615 cm⁻¹ (C=C) double band stretching, 1290 cm⁻¹(C-O) stretching (24,25).

DPPH assay

Concentrations of standards and coumarin compounds were studied at 250, 500, and 1000 µg/mL. In the experiment, 1 mL of sample solution was mixed with 1 mL of DPPH solution in 0.002% concentration prepared in methanol. After standing for 30 minutes in the dark, absorbance was measured at 517 nm. The spectrophotometer was made zero with methanolic solution. The mixture prepared from 1 mL of methanol with 1 mL of DPPH solution was measured as control sample (26).

The DPPH solution was prepared daily, fresh and kept in the dark and at 4 °C, and covered with aluminum foil around the flask during use. DPPH inhibition is calculated by the following formula:

$$IC(\%) = \left[\frac{(A_0 - A_t)}{A_0} \right] \times 100$$

A₀: Absorbance of the control sample

A_t: The absorbance value of the sample being tested

CUPRAC assay

1 mL of a solution of 0.01.10⁻² M copper(II) chloride, 1 mL of a solution of 7.5.10⁻³ M neocuproine, 1 mL of a 0.1 M ammonium acetate buffer (pH= 7.0) and 1 mL of a sample solution (250, 500, 1000 µg/mL) were placed in the tube and mixed. The mixture was allowed to stand at room temperature for 30 minutes, in the dark and absorbance was read at 450 nm. The reading was performed by zeroing against the blank, which was prepared by placing 1 mL of methanol instead of 1 mL of sample (27).

RESULTS AND DISCUSSION

The physical and spectroscopic values of the synthesized coumarin derivatives are in accordance with the literature values. The DPPH activity results of the coumarin derivatives are shown in Table 1, and the CUPRAC activity results are shown in Table 2.

In DPPH antioxidant capacity determination, as shown in Table 1, DPPH activity was observed to increase more as the concentration of only coumarin-3-carboxylic acid was decreased. DPPH activities decreased as concentration decreased in other substances. Especially some of the coumarin compounds which are coumarin-3-carboxylic acid chloride, 4-methyl-7-aminocoumarin and 4-phenyl-7-aminocoumarin, showed values close to DPPH activity at concentrations of 1000 µg /mL of α- tocopherol, NDGA, BHT, BHA and ascorbic acid as standard antioxidants.

In the determination of CUPRAC antioxidant capacity, as shown in Table 2, as the concentration decreased, CUPRAC reduction activities decreased as well. The compounds 4-Methyl-7-hydroxy-8-formylcoumarin and 4-methyl-7-hydroxy-8-nitrocoumarin showed values close to the CUPRAC reduction activity exhibited by BHA and ascorbic acid. CUPRAC reduction activity of only four of the synthesized compounds was observed. In other compounds, values are too small to be considered, so they are not added to the table.

In particular, 3-carboxylic acid chloride, 4-methyl-7-amino coumarin, 4-phenyl-7-aminocoumarin, 4-methyl-7-hydroxy-8-formyl, 4-methyl-7-hydroxy-8-nitro coumarin compounds have been found to be more effective in terms of antioxidant activity. These coumarin compounds can be evaluated with antioxidant activity properties.

ACKNOWLEDGMENTS

Part of this work is from the master's thesis of Oktay Sin. It was supported by the Research Fund of the İstanbul University-Cerrahpaşa. Project number: FYL-2017-23395.

REFERENCES

1. Khan KM, Saify ZS, Hayat S, Khan MZ, Noor F, Makhmoor T, Choudhary MI, Ziaullah MI, Perveen S. Synthesis, Antioxidant and Insecticidal Activities of Some Coumarin Derivatives. J. Chem. Soc. Pak. 2002; 24 (3): 226-30.

2. Yao C, Zeng H. Synthesis and Spectroscopic Study of Coumarin Derivatives, UV-Vis Absorption Spectroscopy and Fluorescence Spectroscopy, 2011; 27 (4): 599-03.
3. O'Kennedy R, Thornes RD, Coumarins: Biology, Applications and Mode of Action, John Wiley and Sons, Chichester, ISBN: 978-0-471-96997-6, p. 348-60 (1997).
4. Bigi F, Chesini L, Maggi R, Sartori G, Montmorillonite KSF as an Inorganic Water Stable, and Reusable Catalyst for the Knoevenagel Synthesis of Coumarin-3-carboxylic Acids, J. Org. Chem. 1999; 64 (3): 1033-5.
5. Moussaoui Y, Ben Salem R, Catalyzed Knoevenagel reactions on inorganic solid supports: Application to the synthesis of coumarin compounds. C.R. Chim. 2007; 10 (12): 1162-9.
6. Bolakatti GS, Maddi VS, Mamledesai SN, Ronad PM, Palkar MB, Swamy S. Synthesis and evaluation of antiinflammatory and analgesic activities of a novel series of coumarin Mannich bases. *Arzneim. Forsch.* 2008; 58 (10): 515-20.
7. Tanaka T, Yamashita K, Hayashi M. Titanium Tetraisopropoxide Promoted Reactions for the Synthesis of Substituted Coumarins. *Heterocycles.* 2010; 80 (1): 631-6.
8. Yuan HY, Wang M, Liu YJ, Liu Q. Copper(II)-Catalyzed C-C Bond-Forming Reactions of α -Electron-Withdrawing Group-Substituted Ketene S,S-Acetals with Carbonyl Compounds and a Facile Synthesis of Coumarins. *Adv. Synth. Catal.* 2009; 351 (1-2): 112-6.
9. Kokare ND, Sangshetti JN, Shinde DB. Oxalic acid catalyzed solvent-free one pot synthesis of coumarins. *Chinese Chem. Lett.* 2007; 18 (11): 1309-12.
10. Montazeri N, Khaksar S, Nazari A, Alavi SS, Vahdat SM, Tajbakhsh M. Pentafluorophenylammonium triflate (PFPAT): An efficient, metal-free and Reusable catalyst for the von Pechmann reaction. *J. Fluor. Chem.* 2011; 132 (7): 450-2.
11. Pozdnev VF. Improved method for synthesis of 7-amino-4-methylcoumarin, *Chem. Heterocycl. Compd.* 1990; 26 (3): 264-5.
12. Murty KS, Rao PS, Seshadri TR. Geometrical Inversion in the Acids derived from The Coumarins Part 6 The Behaviour of the Acids derive from 4-Methyl-Coumarin, *Proceedings-Indian Academy of Sciences.* 1937; 6A: 316-27.
13. Reszka P, Schulz R, Methling K, Lalk M, Bednarski PJ. Synthesis, Enzymatic Evaluation, and Docking Studies of Fluorogenic Caspase and Tetrapeptide Substrates. *Chem. Med. Chem.* 2010; 5 (1): 103-17.
14. Anand B, Roy N, Sai SSS, Philip R. Spectral dispersion of ultrafast optical limiting in Coumarin-120 by white-light continuum Z-scan. *Appl. Phys. Lett.* 2013; 102 (20): 23302.
15. Jung ME, Allen DA. Use of 4-Cyanocoumarins as Dienophiles in a Facile Synthesis of Highly Substituted Dibenzopyranones. *Org. Lett.* 2009; 11 (3): 757-60.
- Mentzer C, Gley P, Molho D, Billet D. Estrogenic substances of the coumarin series II. *Bull. Soc. Chim. Fr.* 1946; 271-6.
17. Timonen J, Aulaskari P, Hirva P, Vainiotalo P. Coumarin M. *Spectrometry. Eur. J. Mass Spectrom.* 2009; 15 (5): 595-603.
18. Timonen JM, Nieminen RM, Sareila O, Goulas A, Moilanen LJ, Haukka M. Synthesis and anti-inflammatory effects of a series of novel 7-hydroxycoumarin Derivatives. *Eur. J. Med. Chem.* 2011; 46 (9): 3845-50.
19. Adreani LL, Lapi E. One some new esters of coumarin-3-carboxylic acid with balsamic and bronchodilator action. *Boll. Chim. Farm.* 1960; 99: 583-6.
20. Polyansky DE, Necker DC. Photodecomposition of Organic Peroxides Containing Coumarin Chromophore: Spectroscopic Studies. *J. Phys. Chem.* 2005; 109/12: 2793-800.
21. Dong Y, Mao X, Jiang X, Hau J, Cheng Y, Zhu C. Electronic Supplementary Information. *Roy. Soc. Chem. China.* 2011; 1-10.
22. Kulkarni A, Patil SA, Badami PS. DNA cleavage and in vitro antimicrobial studies of Co(II), Ni(II), and Cu(II) complexes with ONNO donor Schiff bases: Synthesis, spectral characterization and electrochemical studies. *J. Enzym. Inhib. Med. Chem.* 2010; 25 (1): 87-96.
23. Huang X, Dong Y, Huang Q, Cheng Y. Hydrogen bond induced fluorescence recovery of coumarin-based sensor system. *Tetrahedron Lett.* 2013; 54 (29): 3822-5.

24. Hussien FAH, Keshe M, Alzobar K, Merza J, Karam A. Synthesis and Nitration of 7-Hydroxy-4-Methyl Coumarin via Pechmann Condensation Using Eco-Friendly Medias. *Int. Lett. Chem. Phys. Astron.* 2016; 69: 66-73.

25. Kanodia S, Thapliyal PC. Regioselective mononitration of coumarins using claycop reagent. *J.Indian Chem. Soc.* 2011; 88 (2): 241-4.

26. Al-Majedy YK, Al-Duhaidahawi DL, Al-Azawi KF, Kadhum AAH, Mohamad AB. Coumarins as

Potential Antioxidant Agents Complemented with suggested Mechanisms and Approved by Molecular Modeling Studies. *Molecules.* 2016; 21 (2): 135-9.

27. Apak R, Güçlü K, Özyürek M, Karademir SE. A novel total antioxidant capacity index for dietary polyphenols, vitamin C and E, using their cupric ion reducing capability in the presence of neocuproine, CUPRAC method. *J. Agric. Food Chem.* 2004; 52: 7970-81.

Table 1. The DPPH activity results of the coumarin derivatives

Entry	Sample	%DPPH (1000 µg/mL)	%DPPH (500 µg/mL)	%DPPH (250 µg/mL)
1	3-Benzoylcoumarin	5.6	0.4	0
2	Coumarin-3-carboxylic acid	3.2	4.4	5.2
3	3-Acetylcoumarin	6	2.8	0
4	Coumarin-3-carboxylic acid chloride	84	64.4	42.8
5	4-Methyl-7-hydroxycoumarin	18.4	11.2	10.4
6	4-Propyl-7-hydroxycoumarin	13.6	6.4	5.2
7	4-Phenyl-7-hydroxycoumarin	22	11.6	6.4
8	4-Methyl-7-methoxycoumarin	4.4	2	1.6
9	4-Methyl-7-hydroxy-8-formylcoumarin	14.4	11.6	7.6
10	4-Methyl-7-hydroxy-8-nitrocoumarin	28	13.6	3.6
11	4-Methyl-7-aminocoumarin	82	78	70.8
12	4-Phenyl-7-aminocoumarin	82.8	75.2	69.6
13	α-Tocopherol	96.4	93.6	93.2
14	NDGA*	95.6	93.2	92
15	BHT*	95.6	95.2	94.8
16	BHA*	96.8	94	93.6
17	Ascorbic acid	97.2	97.2	96.8

*BHA (Butylated Hydroxy Anisole) BHT (Butylated Hydroxy Toluene) NDGA (Nordihydroguaiaretic Acid)

Table 2. The CUPRAC activity results of the coumarin derivatives

Entry	Sample	%Absorbance (1000 µg/mL)	%Absorbance (500 µg/mL)	%Absorbance (250 µg/mL)
9	4-Methyl-7-hydroxy-8-formylcoumarin	0.664 ± 0.0202	0.199 ± 0.0263	0.022 ± 0.0021
10	4-Methyl-7-hydroxy-8-nitrocoumarin	0.457 ± 0.0025	0.226 ± 0.0036	0.116 ± 0.001
11	4-Methyl-7-aminocoumarin	0.209 ± 0.0035	0.136 ± 0.0062	0.095 ± 0.0043
12	4-Phenyl-7-aminocoumarin	0.196 ± 0.0020	0.142 ± 0.0037	0.098 ± 0.0049
16	BHA*	0.734 ± 0.0117	0.489 ± 0.001	0.456 ± 0.0035
17	Ascorbic acid	0.476 ± 0.0041	0.443 ± 0.001	0.432 ± 0.0007

*BHA (Butylated Hydroxy Anisole) Values are means ± SD.



Investigation of Photochromic Fluorescence Features and Synthesis of Diarylethene Type Naphthalimide Compounds

Ersin Orhan^{1*}   and Mustafa Narin¹  

¹Department of Chemistry, Faculty of Arts and Science, Düzce University, 81620 Düzce, Turkey.

Abstract: The aim of the study was to synthesise novel photo-exchangeable photochromic fluorescent compounds. 3,4-Bis(3,5-dimethyl-4-pyrazolyl)-N-butyl-1,8-naphthalimide **6** and 3,4-bis (1,3,5-trimethyl-4-pyrazolyl)-N-butyl-1,8-naphthalimide **7** naphthalimide derivative new compounds were prepared via two-step Suzuki coupling reaction of pyrazolylboronic acid esters from N-butyl-4-bromo-3-iodo-1,8-naphthalimide and characterized by ¹H-NMR, ¹³C-NMR, MS and FTIR. Their photochromic fluorescence properties were investigated. Additionally, a solvent effect on the fluorescent properties of **6** and **7** was investigated. Increase of organic solvent polarity results in a red shift (to longer wavelengths) of the fluorescence emissions.

Keywords: Solvent effect, Naphthalimide, Diarylethene, Fluorescent switch, Photochromism.

Submitted: September 19, 2019. **Accepted:** November 01, 2019.

Cite this: Orhan E, Narin M. Investigation of photochromic fluorescence features and synthesis of diarylethene type naphthalimide compounds. JOTCSA. 2019; 7(1): 97-106.

DOI: <https://doi.org/10.18596/jotcsa.622256>.

Corresponding Author. E-mail: ersinorhan@duzce.edu.tr

INTRODUCTION

Photochromic compounds can be divided into several groups according to their type of photoreaction. The most studied photochromic series are fulgides, spiropyranes and diarylethenes. Among these, diarylethenes are the most promising compounds for many industrial applications due to their fatigue resistance and superior thermal stability.

There are many studies on the synthesis and photochromic properties of non-fluorescence photochromic diarylenes in different environments. Photochromic fluorescent diarylethenes have attracted attention in the development and use of possible optical-electronic devices in recent years as molecular switches and optical memory systems (1-6).

Photochromic fluorescent diarylethenes must have many important features for industrial application such as fatigue resistance, thermal stability, high quantum yields (for both photochromic and fluorescence behaviour), and so on.

It is difficult to synthesise excellent photochromic fluorescent compounds with all the necessary properties for industrial applications. It is almost impossible to predict the detailed photochromic and also fluorescent properties of the compounds before synthesising. It is important to synthesise new photochromic compounds that may exhibit this fluorescence.

On the other hand, research on photochromic fluorescent diarylethenes is limited. Photochromic fluorescent diarylethenes must meet many important criteria in order to find an application. These criteria can be listed as

follows: Criteria for photochromic properties: quantum data on ring opening and closing reactions, the repeatability of ring opening and ring closing reactions of the molecular structure over time without degradation, this is called resistance to fatigue. Thermal stability of the open and closed forms should not be degraded at normal temperatures and so on. In addition, there are criteria for the fluorescent properties of the molecules of interest (7-13).

In the criteria related to fluorescent properties, undoubtedly one of the most important features is high fluorescent quantum yields. In photochromic fluorescent molecules, the fluorescent properties of both the open form and closed forms are measured, and in some cases it is known that the open form exhibits more fluorescence and in some cases the closed form exhibits stronger fluorescence. What is important here is that there is a significant difference in fluorescent property between the ring-open or closed form of the photochromic molecule.

One of the important points of both the photochromic and fluorescent properties mentioned above is the absorption bands of the open form and the closed form. Open forms are more sensitive to UV light in photochromic compounds, while closed forms (usually coloured) are sensitive to light in the visible region. It is also important that the maximum wavelength difference between open forms and closed forms is large. Similarly, in terms of fluorescent properties, the absorption wavelength and emission wavelength values of the molecule are important for many applications. In short, it is difficult to synthesise photochromic fluorescent diarylethenes with ideal properties and it is often not possible to predict all of the aforementioned properties. In this respect, it is important to synthesise different photochromic compounds that may exhibit fluorescence (14-23).

For this reason, in this study we aimed to synthesise a diethylether-like photochromic fluorescent molecule which has a novel pyrazole structure based on bisaryl naphthalimide.

EXPERIMENTAL

Material and Methods

Materials

4-Bromo-1,8-naphthalic anhydride, 3,5-dimethyl-4-pyrazole-4-boronic acid pinacol ester, 1,3,5-trimethyl-4-pyrazole-4-boronic acid pinacol ester and other starting chemical compounds were purchased from the company Merck, Sigma-Aldrich, Acros Organics and ABCR. 4-bromo-N-butyl-3-iodo-1,8-naphthalimide 1

was prepared according to the procedures in the literature (24).

Methods

Some parts of solvent were of analytical grade and purified by distillation before use. Other reagents were used as received without further purification. Some part of studies of naphthalimide derivatives were performed under argon using standard schlenk techniques and dry solvents. All chemicals were purchased from Merck, Acros Organics, ABCR and Aldich Chemical Company. ^1H and ^{13}C NMR spectra were recorded on Bruker 400 MHz spectrometers for samples in CDCl_3 . The signals are expressed as parts per million down fields from tetramethylsilane, used as an internal standard (δ value). Splitting patterns are indicated as s, singlet; d, doublet; t, triplet; q, quartet; m, multiplet. Mass spectra were taken with an AB Sciex 4000 QTRAP LC-MS/MS. FT-IR spectra were measured using a SHIMADZU FT-IR spectrometer. Luminescence spectra were measured on a SHIMADZU RF-5301PC fluorescent spectrophotometer. UV-Vis spectra were recorded on a T80+ UV-Vis spectrophotometer. Photochemical reactions in organic solvents were carried out in a 10 mm path length quartz cell using an 8W Three-Way UV lamp (Cole-Parmer) (for 365 nm) and an Obelux CR9 Forensic Lights Green (for 530 nm). During the photoreaction, solutions in the cell were stirred. Melting points were measured in open capillary tubes with Thermo Scientific 9200 melting point apparatus and are not corrected. Solvents were dried over anhydrous sodium sulphate. Flash column chromatographic separation was carried out on Merck Kieselgel 60 (230-400 mesh) using ethyl acetate and n-hexane as the eluent. Analytical thin-layer chromatography was performed on Merck pre-coated silica gel 60 F-254, 0.25-mm thick TLC plates.

Synthesis

3-(3,5-Dimethyl-4-pyrazolyl)-4-bromo-N-butyl-1,8-naphthalimide (4)

Naphthalimide derivative (**1**) (0.2 g, 0.43 mmol), 3,5-dimethyl-4-pyrazoleboronic acid pinacol ester (0.59 g, 4.3 mmol), tetrakis(triphenylphosphine)palladium(0) (0.25 g, 1.29 mmol), potassium carbonate (0.049 g, 0.043 mmol), catalyst ratio of tris(dibenzylideneacetone)dipalladium(0), THF (30 mL), aqueous (10 mL) stirred for 5 hours at room temperature. No photochromicity was observed when TLC was checked. Boiling at 65 °C for 3 hours, the reaction was found to complete by TLC control. 10% sodium bicarbonate solution was added. The organic fraction was dried with sodium sulphate. The organic fraction was then evaporated. The

residual raw product was purified via column chromatography over ethyl acetate-n-hexane (5-20%). ¹H NMR analysis showed that 1 mole was attached. **4** Light coloured brown solid 0.09 g, 50%, m.p.: 141-144 °C. ¹H NMR (400 MHz, CDCl₃, ppm): δ 0.83 (t, 3H, -CH₂CH₃), 1.30-1.40 (m, 2H, -CH₂CH₃), 1.57-1.63 (m, 2H, -NCH₂CH₂-), 1.98 (s, 3H, -CH₃, pyrazole), 2.10 (s, 3H, -CH₃, pyrazole), 4.10 (t, 2H, -NCH₂-), 7.02-8.80 (m, 4H, Ar-napht-H), 12.81 (s, 1H, NH). ¹³C NMR (100 MHz, CDCl₃, ppm): δ= 13.86, 20.02, 22.18, 29.34, 30.63, 39.99, 125.09, 128.16, 128.35, 129.17, 129.52, 130.25, 130.89, 131.58, 132.43, 134.91, 141.65, 143.34, 143.76, 188.96, 189.04. ESI-MS(+) [M⁺]: m/z= C₂₁H₂₀BrN₃O₂ Found : 426,3064; Calc. : 426,8538. IR (ATR) ν_{\max} (cm⁻¹) 2920, 2854, 1695 (C=O), 1653 (C=O), 1608, 1575, 1435, 1384, 1352, 1303, 1269, 1226, 1182, 1093, 1033, 995, 958, 918, 823, 779, 744, 691.

3-(1,3,5-Trimethyl-4-pyrazolyl)-4-bromo-N-butyl-1,8-naphthalimide (5)

Naphthalimide derivative compound (**1**) (0.2 g, 0.43 mmol), **1,3,5-dimethyl-4-pyrazoleboronic acid pinacol ester** (0.9 g, 1.3 mmol), tetrakis(triphenylphosphine)palladium(0) (0.049 g, 0.043 mmol), potassium carbonate (0.59 g, 4.3 mmol), catalyst ratio of tris(dibenzylideneacetone)dipalladium(0), THF (30 mL), aqueous (10 mL) stirred for 5 hours at room temperature. When TLC control was performed, it was observed that the product was not photochromic. After heating for 3 hours at 65 °C, TLC was checked. 10% sodium bicarbonate solution was added. The organic fraction was dried with sodium sulphate. The organic fraction was then evaporated. The residual raw product was purified via column chromatography eluting over ethyl acetate-n-hexane (5-20%). ¹H NMR was taken and it was found to bind 1 mol. **5** Pale coloured yellow solid 0.12 g, 63%, m.p.: 157-160 °C. ¹H NMR (400 MHz, CDCl₃, ppm): δ 0.83 (t, 3H, -CH₂CH₃), 1.29-1.37 (m, 2H, -CH₂CH₃), 1.51-1.64 (m, 2H, -NCH₂CH₂-), 2.02 (s, 3H, -CH₃, pyrazole), 2.34 (s, 3H, -CH₃, pyrazole), 3.50 (s, 3H, -NCH₃, pyrazole), 4.01 (t, 2H, -NCH₂-), 7.00-8.50 (m, 4H, Ar-napht-H). ¹³C NMR (100 MHz, CDCl₃, ppm): δ= 13.67, 14.32, 20.07, 23.13, 29.46, 30.25, 40.18, 125.10, 125.33, 128.24, 128.61, 129.30, 129.73, 130.15, 130.47, 131.51, 131.83, 134.16, 134.38, 143.55, 189.03, 189.13. ESI-MS(+) [M⁺]: m/z= C₂₂H₂₂BrN₃O₂ Found : 440,3330; Calc. : 440,0051. IR (ATR) ν_{\max} (cm⁻¹) 2925, 2884, 1701 (C=O), 1667 (C=O), 1613, 1556, 1438, 1377, 1355, 1315, 1267, 1226, 1145, 1078, 1041, 996, 947, 854, 785, 746, 698, 634.

3,4-Bis(3,5-dimethyl-4-pyrazolyl)-N-butyl-1,8-naphthalimide (6)

3,5-dimethyl-4-pyrazolyl naphthalimide derivative (**4**) (0.09 g, 0.21 mmol), 3,5-dimethyl-4-pyrazoleboronic acid pinacol ester (0.094 g), 0.42 mmol), tetrakis(triphenylphosphine)-palladium(0) (0.024 g, 0.021 mmol), potassium carbonate (0.29 g, 2.1 mmol), catalyst ratio of tris(dibenzylideneacetone)dipalladium(0), THF (30 mL), water (10 mL) stirred for 5 hours at room temperature. TLC control showed that the product was formed. After heating at 65 °C for 3 hours, the reaction mixture product was terminated by checking with TLC. 10% sodium bicarbonate solution was added. Extraction was performed over ethyl acetate-n-hexane. The organic fraction was dried with sodium sulphate. The organic fraction was then evaporated in vacuo. The residual raw product was purified via column chromatography, with an ethyl acetate-n-hexane (5-20%) mixture. ¹H NMR of the product was taken. **6** Yellow-orange solid 0.03 g, 33%, m.p.: 160-162 °C. ¹H NMR (400 MHz, CDCl₃, ppm): δ 0.81 (t, 3H, -CH₂CH₃), 1.30-1.38 (m, 2H, -CH₂CH₃), 1.55-1.60 (m, 2H, -NCH₂CH₂-), 1.99 (s, 6H, -CH₃, pyrazole), 2.12 (s, 6H, -CH₃, pyrazole), 4.06 (t, 2H, -NCH₂-), 7.01-8.80 (m, 4H, Ar-napht-H), 12.89 (s, 1H, NH). ¹³C NMR (100 MHz, CDCl₃, ppm): δ= 13.84, 14.05, 20.03, 20.32, 29.06, 29.41, 30.08, 40.49, 121.40, 125.14, 125.62, 128.10, 128.46, 129.21, 129.53, 130.18, 130.65, 131.73, 132.28, 132.84, 134.07, 134.35, 141.19, 143.57, 189.04, 189.24. ESI-MS (+) positive ion mode [M⁺]: m/z= C₂₆H₂₇N₅O₂ Found : 441,5249; Calculated : 441,5629. IR (ATR) ν_{\max} (cm⁻¹) 3051, 2954, 2924, 2856, 1697 (C=O), 1649 (C=O), 1622, 1583, 1492, 1444, 1390, 1336, 1309, 1261, 1224, 1188, 1101, 1074, 1039, 981, 921, 883, 850, 825, 756, 688, 624.

3,4-Bis(1,3,5-Trimethyl-4-pyrazolyl)-N-butyl-1,8-Naphthalimide (7)

3-(1,3,5-Trimethyl-4-pyrazolyl)-4-bromo-1,8-naphthalimide (**5**) (0.12 g, 0.27 mmol), **1,3,5-dimethyl-4-pyrazoleboronic acid pinacol ester** (0.12 g, 0.54 mmol), tetrakis(triphenylphosphine)palladium(0) (0.031 g, 0.027 mmol), potassium carbonate (0.37 g, 2.7 mmol), catalyst ratio of tris(dibenzylideneacetone)dipalladium(0), THF (30 mL), water (10 mL) was stirred for 5 hours at room temperature. When TLC control was performed, it was observed that the product was not photochromic. After heating at 65 °C for 3 hours, the reaction mixture product was terminated by checking with TLC. 10% sodium bicarbonate solution was added. Extraction was performed over ethyl acetate-n-hexane. The

organic fraction was dried with sodium sulfate. The organic fraction was then evaporated in vacuo. The residual raw product was purified via column chromatography, with an ethyl acetate-n-hexane (5-20%) mixture. **7** Light brown coloured solid 0.05 g, 42%, m.p.: 169-171 °C.

¹H NMR (400 MHz, CDCl₃, ppm): δ 0.82 (t, 3H, -CH₂CH₃), 1.28-1.36 (m, 2H, -CH₂CH₃), 1.50-1.62 (m, 2H, -NCH₂CH₂-), 2.06 (s, 6H, -CH₃, pyrazole), 2.33 (s, 6H, -CH₃, pyrazole), 3.57 (s, 6H, -NCH₃, pyrazole), 4.09 (t, 2H, -NCH₂-), 7.20-8.60 (m, 4H, Ar-napht-H).

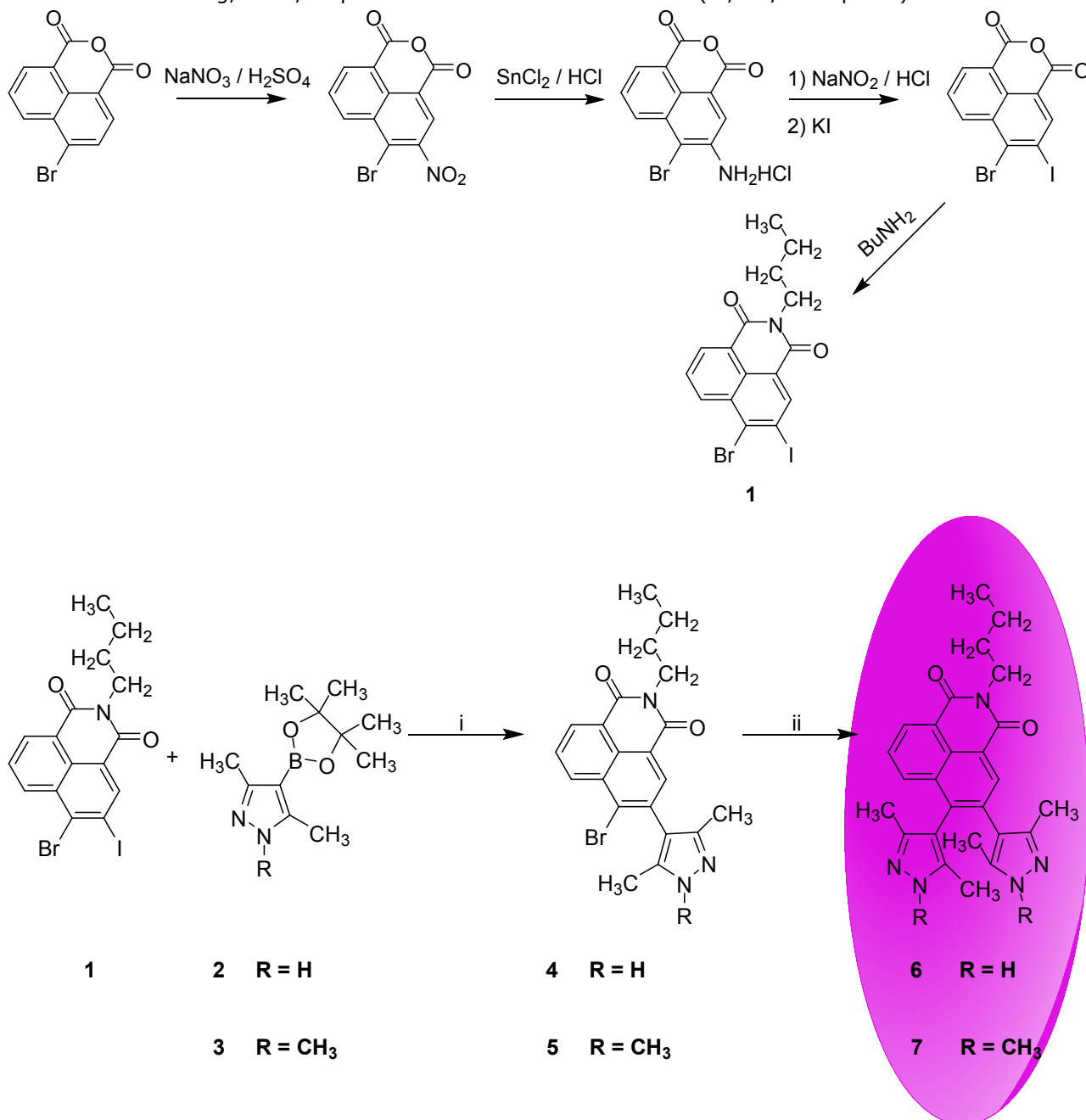


Figure 1. Syntheses of **6** and **7**.

Conditions: i) K₂CO₃/Pd(PPh₃)₄, THF, H₂O, 4 hours at room temperature and 3 hours heating at 65 °C; ii) Excess of **2** or **3** / K₂CO₃/Pd(PPh₃)₄, THF, H₂O, 4 hours at room temperature and 3 hours of heating at 65 °C.

¹³C NMR (100 MHz, CDCl₃, ppm): δ= 13.75, 14.21, 20.46, 23.06, 29.17, 29.74, 30.38, 32.10, 40.24, 40.69, 118.81, 119.09, 121.77, 122.15, 126.36, 127.67, 128.54, 128.73, 129.39, 129.71, 130.22, 130.48, 131.32,

131.55, 135.28, 141.34, 164.37, 166.82. ESI-MS (+) positive ion mode [M⁺]: m/z= C₂₈H₃₁N₅O₂ Found : 469,2478; Calculated : 469,0253. IR (ATR) ν_{\max} (cm⁻¹) 3053, 3026, 2954, 2922, 2854, 1697 (C=O), 1649 (C=O),

1620, 1585, 1490, 1440, 1390, 1336, 1286, 1261, 1222, 1188, 1097, 1076, 1029, 983, 921, 883, 848, 754, 679, 623.

RESULTS AND DISCUSSION

Previously, a study involving naphthalimide derivative compound 1 and pyrazole group with arylboronic acid ester was prepared in the literature by a multi-step reaction method (24).

The Suzuki cross-linking reaction forms a new C-C bond using a palladium catalyst and base. These new C-C bond formation reactions may find application in the development of organic, polymeric and inorganic materials in many industrial fields, particularly in the fields of electrical-electronics, optical properties.

Naphthalimide compound containing 3,5-dimethyl-4-pyrazolyl group 6, naphthalimide compound containing 1,3,5-trimethyl-4-pyrazolyl group 7 were synthesised by a two-step Suzuki coupling reaction of naphthalimide derivative compound 1 and 3,5-dimethyl-4-(4,4,5,5-tetramethyl-1,3,2-dioxaborolan-2-yl)-1H-pyrazole and 1,3,5-dimethyl-4-pyrazoleboronic acid pinacol ester in medium yield (Figure 1).

In the reaction of naphthalimide derivative compound 1 between both 3,5-dimethyl-4-(4,4,5,5-tetramethyl-1,3,2-dioxaborolan-2-yl)-1H-pyrazole and 1,3,5-dimethyl-4-pyrazoleboronic acid pinacol ester (pinacol ester of arylboronic acid) failed to give new compound 6 and compound 7 when taken as two moles. Instead of, the new intermediate product 4 and 5 were obtained light brown coloured solid and pale yellow coloured solid, respectively. Although the one-step reaction is repeated with excessive amounts of 3,5-dimethyl-4-(4,4,5,5-tetramethyl-1,3,2-dioxaborolan-2-yl)-1H-pyrazole 2 and 1,3,5-dimethyl-4-pyrazoleboronic acid pinacol ester 3 in addition to more effective reaction conditions, the desired product 6 and product 7 were not isolated and some by-products which could not be isolated by TLC were observed. However, when the pure intermediate new product 3-(3,5-dimethyl-4-pyrazolyl)-4-bromo-N-butyl-1,8-naphthalimide 4 and 3-(1,3,5-trimethyl-4-pyrazolyl)-4-bromo-N-butyl-1,8-naphthalimide 5 were treated with an extreme quantity of 3,5-dimethyl-4-(4,4,5,5-tetramethyl-1,3,2-dioxaborolan-2-yl)-1H-pyrazole 2 and 1,3,5-dimethyl-4-pyrazoleboronic acid pinacol ester 3, the expected product 6 and product 7 were achieved in 33% yield and 42% yield as a yellow orange coloured solid and light brown coloured solid, respectively.

Irradiation of pyrazole groups bearing N-butyl-1,8-naphthalimide, naphthalimide compound containing 3,5-dimethyl-4-pyrazolyl group 6, naphthalimide compound containing 1,3,5-dimethyl-4-pyrazolyl group 7 in ethyl acetate via 365 nm light did not cause colour change, due to the formation close form. The possible coloured form (in photostationary state, pss) was expected to return to the first colourless or pale yellow coloured naphthalimide compound containing 3,5-dimethyl-4-pyrazolyl group 6, naphthalimide compound containing 1,3,5-dimethyl-4-pyrazolyl group 7 solution when exposed to visible light (530 nm).

When examined for fluorescence, these compounds, namely naphthalimide compound containing 3,5-dimethyl-4-pyrazolyl group 6, naphthalimide compound containing 1,3,5-dimethyl-4-pyrazolyl group 7 exhibited good fluorescence.

Synthesized naphthalimide compound containing 3,5-dimethyl-4-pyrazolyl group 6 and naphthalimide compound containing 1,3,5-dimethyl-4-pyrazolyl group 7 were not photochromic. Otherwise, these prepared naphthalimide compound containing 3,5-dimethyl-4-pyrazolyl group 6 and naphthalimide compound containing 1,3,5-dimethyl-4-pyrazolyl group 7 exhibited a good level of fluorescent properties.

Irradiation via 365 nm light showed no colour change and no spectral change. The reason why naphthalimide compound containing 3,5-dimethyl-4-pyrazolyl group 6 and naphthalimide compound containing 1,3,5-dimethyl-4-pyrazolyl group 7 does not exhibit any photochromism is unclear at this stage. However, it can be said that the methyl groups in these carbon groups form a steric hindrance on the pyrazoles at the 3-position and the naphthalimide group at the 3-position with hydrogen atoms. In the cyclisation step during photoreaction, it is believed that the methyl groups coincide with the hydrogen of the naphthalimide ring as in Figure 2.

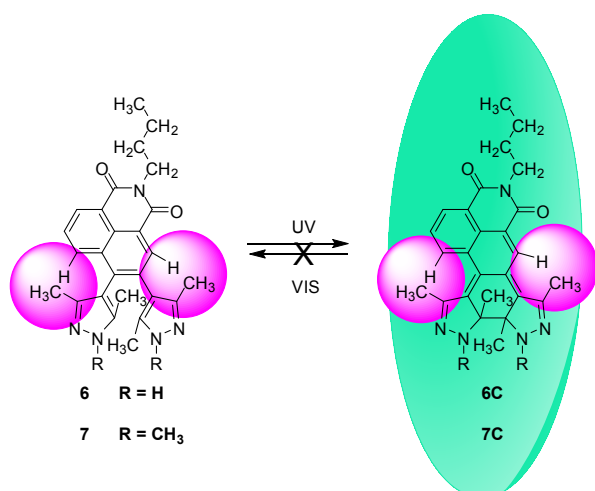


Figure 2. Possible photoreaction of non-photochromic **6C** and **7C**.

Therefore, it causes deviation from the planarity required for cyclization. Although compounds naphthalimide compound containing 3,5-dimethyl-4-pyrazolyl group **6** and naphthalimide compound containing 1,3,5-dimethyl-4-pyrazolyl group **7** are not photochromic compounds, **6** and **7** exhibited fluorescence properties (Figures 3 and 4).

Photochromic and Fluorescent Properties

Naphthalimide compound containing 3,5-dimethyl-4-pyrazolyl group **6**, naphthalimide compound containing 1,3,5-dimethyl-4-pyrazolyl group **7** solutions had no observed absorption band in the visible range and were pale yellow or colourless. After irradiation with 365 nm ultraviolet light, compound **6** and compound **7** solutions were expected to return to the coloured form with an increase in new peaks in the visible region. This would show an expanded π system on the photochromic reaction.

The reversible photoreaction of naphthalimide compound containing 3,5-dimethyl-4-pyrazolyl group **6**, naphthalimide compound containing 1,3,5-dimethyl-4-pyrazolyl group **7** in the solutions were carried out at 365 nm and 530 nm various light wavelengths. It was thought that when irradiated in solutions compound **6** and compound **7** with 365 nm ultraviolet light, from colourless or pale yellow state to coloured state, when they returned (visible light 530 nm), it would be transformed into coloured form due to the formation of closed form C-forms.

In general, for naphthalimide compound containing 3,5-dimethyl-4-pyrazolyl group **6** and naphthalimide compound containing 1,3,5-dimethyl-4-pyrazolyl group **7** compounds are not in the same plane due to steric hindrances between the methyl groups of the two pyrazolyl groups and the naphthalimide hydrogens.

However, they always maintain their parallel and antiparallel shape. Thus, the observed characteristic absorption peaks of the naphthalimide moieties result in poor conjugation between the pyrazolyl ring groups and the naphthalimide moiety. Such a situation prevents the photochromicity from being observed.

The solvent effects on the open forms of compounds naphthalimide compound containing 3,5-dimethyl-4-pyrazolyl group **6** and naphthalimide compound containing 1,3,5-dimethyl-4-pyrazolyl group **7** have been investigated in various solvents. The polarity of the solvent showed a shift to long wavelength in uncoloured forms. Quantum yields could not be calculated because the new compounds **6** and **7** synthesized were not photochromic.

Electrochemical behavior of both the ring-open and ring-closed forms of photochromic fluorescence compounds can be performed such as absorbance and emission properties, recording-deletion, and hologram acquisition. The difference in fluorescence emission between these reversible transformations is remarkable because it is easy to see. Here, the naphthalimide structure serves as a very important core for fluorescence emission.

It can be mentioned that pyrazole groups containing naphthalimide ring show fluorescent photo-transfer property. Naphthalimide compound containing 3,5-dimethyl-4-pyrazolyl group **6** and naphthalimide compound containing 1,3,5-dimethyl-4-pyrazolyl group **7** showed maximum fluorescence emission at 505 nm and 500 nm, respectively, when light stimulation was performed at a wavelength of 400 nm.

In addition, emission intensity-wavelength graph was obtained by taking emission measurements against wavelength in compound naphthalimide compound containing 3,5-dimethyl-4-pyrazolyl group **6** and naphthalimide compound containing 1,3,5-dimethyl-4-pyrazolyl group **7** in non-polar n-hexane and polar acetone solvents. While the maximum wavelengths in non-polar n-hexane solvent were around 460 nm, the maximum wavelength in polar acetone solution gave emission around 520 nm and 510 nm. As solvent polarity increases, the maximum emission intensity shifts to a longer wavelength. In the more polar acetone solvent 50 nm and 60 nm give longer wavelength emission intensity (Figures 3 and 4).

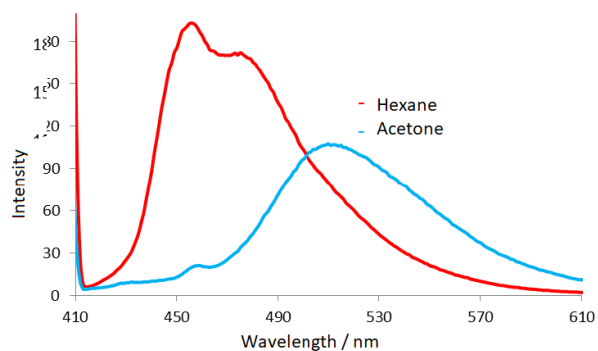


Figure 3. Emission spectra of compound **6** in n-hexane and acetone (1×10^{-5}), (λ_{ex} 400 nm).

It can be seen from the graphs that the solvent polarity for compounds **6** and **7** are an important factor in shifting the luminescent wavelength to the long wavelength between the non-polar solvent and the polar solvent. When the polarity of the solvent increases, the emission intensity gives a peak at a longer wavelength. The fluorescence colour of compounds **6** and **7** can be directly modulated by the naked eye by adjusting the polarity of the solvent.

Naphthalimide compound containing 3,5-dimethyl-4-pyrazolyl group **6** and naphthalimide compound containing 1,3,5-dimethyl-4-pyrazolyl group **7** the emission spectrum of the compounds by the excitation intensity and wavelength at 400

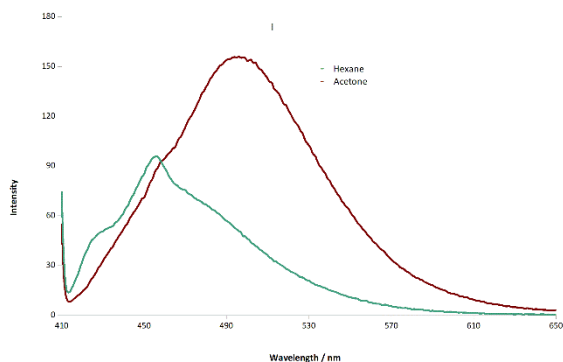


Figure 4. Emission spectra of compound **7** in n-hexane and acetone (1×10^{-5}), (λ_{ex} 400 nm).

nm in the ethyl acetate solvent at a concentration of 1×10^{-5} M is given in Figure 5. At the same concentration maximum naphthalimide compound containing 1,3,5-dimethyl-4-pyrazolyl group **7** at higher wavelengths gives higher emission intensity while naphthalimide compound containing 3,5-dimethyl-4-pyrazolyl group **6** gave a lower emission intensity.

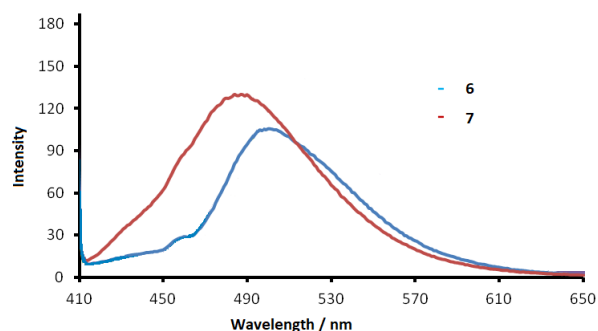


Figure 5. Emission spectrum generated by excitation of different compounds **6** and **7** at 400 nm wavelength in ethyl acetate (1×10^{-5} M).

Compound **7** gives an emission intensity at 480 nm, while compound **6** gives an emission intensity at 510 nm at the same concentration. It is observed that the emission spectrum of compound **6** shifts to a wavelength longer than 30 nm. In addition, compounds **6** emit at longer wavelengths and lower intensity, while compound **7** emit at shorter wavelengths and higher intensity.

CONCLUSIONS

Synthesis of naphthalimide derivative compound **1** from 4-bromo-1,8-naphthalic anhydride starting material was prepared according to literature in several steps. Naphthalimide compound containing 3,5-dimethyl-4-pyrazolyl group **6** and naphthalimide compound containing 1,3,5-dimethyl-4-pyrazolyl group **7** derivatives, naphthalimide derivative compound **1** and 3,5-dimethyl-4-pyrazoleboronic acid pinacol ester **2**, 1,3,5-dimethyl-4-pyrazoleboronic acid pinacol ester **3** were synthesized from the Suzuki coupling reaction of boronic acid pinacol ester.

The photochromic and fluorescent properties of compounds **6** and **7** were examined. None of the N-butyl-1,8-naphthalimides containing both pyrazole and N-methyl pyrazole groups exhibited photochromic properties.

The polar and non-polar solvent factor on the fluorescence properties of compounds **6** and **7** were examined. Increasing solvent polarity was observed to shift fluorescence emissions to longer wavelengths.

ACKNOWLEDGEMENTS

The authors would like to thank Duzce University Research Fund (Project No.: BAP 2012.05.HD.053 and BAP 2012.05.03.097) and Scientific and Technical Research Council of Turkey (TUBITAK) (Project No.: 111T490) for their financial support.

REFERENCES

- Cipolloni M, Ortica F, Bougdid L, Moustrou C, Mazzucato U and Favaro G. New Thermally Irreversible and Fluorescent Photochromic Diarylethenes. *J. Phys. Chem. A.* 2008; 112:4765–71.
- Yamaguchi H, Matsuda K and Irie M. Excited-State Behavior of a Fluorescent and Photochromic Diarylethene on Silver Nano particles. *J. Phys. Chem. C.* 2007; 111: 3853-62.
- Liu HH and Chen Y. The Photochromism and Fluorescence of Diarylethenes with a Imidazole Bridge Unit: A Strategy for the Design of Turn-on Fluorescent Diarylethene System. *J. Phys. Chem. A.* 2009; 113:5550–53.
- Gundogdu L, Kose M, Takeuchi S, Yokoyama Y, Orhan E. Synthesis, photochromic and fluorescence properties of new bithiazole-containing diarylethenes as cation sensors. *Journal of Luminescence.* 2018; 203:568-75.
- Orhan E, Köse M, Yazan T. The synthesis of new 3,4-(bisaryl)-1,8-naphthalimide and 2,3-(bisaryl)-7HH-benzimidazo[2,1-a]benzo[d]isoquinolin-7-one compounds and an investigation of their photochromic properties. *Turk J Chem.* 2018; 42:1086–94.
- Orhan E, Gundogdu L, Kose M, Yokoyama Y. Synthesis and photochromic properties of 4,5-bisaryl-3(2H)-pyridazinones. *Journal of Photochemistry and Photobiology A: Chemistry.* 2016; 314:164–70.
- Yagi K, Soong CF and Irie M. Synthesis of Fluorescent Diarylethenes Having a 2,4,5-Triphenylimidazole Chromophore. *J. Org. Chem.* 2001; 66:5419-23.
- Fukaminato T, Sasaki T, Kawai T, Tamai N and Irie M. Digital Photoswitching of Fluorescence Based on the Photochromism of Diarylethene Derivatives at a Single- Molecule Level. *J. Am. Chem. Soc.* 2004; 126(45):14843-49.
- Uchida K, Nakamura S, Irie M. Photochromism of dinaphthylethene derivatives. Stability of the closed-ring forms. *Res. Chem. Intermed.* 1995; 21(8-9):861-76.
- Milder MTW, Herek JL, Areephong J, Feringa BL and Browne WR. Tunable Aggregation and Luminescence of Bis(diarylethene)sexithiophenes. *J. Phys. Chem. A.* 2009; 113:7717–24.
- Nakagawa T, Hasegawa Y and Kawai T. Photoresponsive Europium(III) Complex Based on Photochromic Reaction. *J. Phys. Chem. A.* 2008; 112(23):5096–103.
- Kose M, Orhan E, Suzuki K, Tutar A, Ünlü CS, Yokoyama Y. Preparation and photochromic properties of 2,3-bisarylbenz[f]indenones. *Journal of Photochemistry and Photobiology A: Chemistry.* 2013; 257:50–53.
- Kose M, Orhan E. Comparison of photochromic properties and thermal stabilities of fulgide, fulgimide, and benzimidazole[1,2-a]pyrrolidine-2-one derivatives. *Turk J Chem.* 2009; 33:579–88.
- Orhan E. Synthesis of Novel Diarylethenes Bearing Naphthalimide Moiety and Photochromic Fluorescence Behaviors. *Journal of the Turkish Chemical Society, Section A: Chemistry.* 2017; 4(2):501-16.
- Tsujioka T, Irie M. Electrical functions of photochromic molecules. *Journal of Photochemistry and Photobiology C: Photochemistry Reviews.* 2010; 11:1-14.
- Irie M. Diarylethenes for Memories and Switches. *Chem. Rev.* 2000; 100:1685-716.
- Kose M, Orhan E, Buyukgungor O. Synthesis of novel photochromic methyl cyanoacetate-condensed fulgide derivatives. *Journal of Photochemistry and Photobiology A: Chemistry.* 2007; 188:358–63.
- Kose M, Orhan E. Studies on photochromic benzimidazol[1,2a]pyrrolidin-2-ones from the condensation of 2-methyl-3-benzothienylethylidene-(isopropylidene)succinic anhydride with 1,2-diaminobenzenes. *Journal of Photochemistry and Photobiology A: Chemistry.* 2006; 177:170–76.
- Lin Q, Xiao S, Li R, Tan R, Wang S, Zhang R. Intermolecular hydrogen bonding- assisted high contrast fluorescent switch in the solid state. *Dyes and Pigments.* 2015; 114:33-39.
- Kanazawa R, Nakashima T and Kawai T. Photophysical Properties of a Terarylene Photoswitch with a Donor–Acceptor Conjugated Bridging Unit. *J. Phys. Chem. A.* 2017; 121(8):1638-46.
- Shirinian ZV, Lonshakov DV, Kachala VV, Zavarzin IV, Shimkin AA, Lvov AG, Krayushkin MM. Regio- and chemoselective bromination of 2,3- diarylcyclopent-2-en-1-ones. *J. Org. Chem.* 2012; 77:8112–23.

Orhan E, Narin M. JOTCSA. 2020; 7(1): 97-106.

22. Jiang GY, Wang S, Yuan WF, Zhao Z, Duan AJ, Xu CM, et al. Photo- and protondual-responsive fluorescence switch based on a bithienylethene-bridged naphthalimide dimer and its application in security data storage. *Eur J Org Chem.* 2007; 2064-67.

23. Pu S, Li H, Liu G, Liu W, Cui S, Fan C. Synthesis and the effects of substitution upon photochromic diarylethenes bearing an isoxazole moiety. *Tetrahedron.* 2011; 67: 1438-47.

24. Meng X, Zhu W, Zhang Q, Feng Y, Tan W and Tian H. Novel Bithienylethenes Containing Naphthalimide as the Center Ethene Bridge: Photochromism and Solvatochromism for Combined NOR and INHIBIT Logic Gates. *J. Phys. Chem. B.* 2008; 112:15636-45.



Synthesis and Photophysical Properties of A₃B-type Unsymmetrically Substituted Anthracene-based Zinc(II)phthalocyanine

Sinem Temizel , Altuğ Mert Sevim* 

Technical University of Istanbul, Chemistry Department, TR 34469, İstanbul, Turkey.

Abstract: A novel unsymmetrical zinc(II) phthalocyanine (ZnPc) (**3**) with an alkynyl functional group was prepared by an efficient mixed statistical condensation of 4-((4-ethynylbenzyl)oxy)phthalonitrile (**1**) and 4-(4-tertbutylphenoxy)phthalonitrile (**2**). FTIR, ¹H NMR, UV-Vis, elemental analysis, and MALDI-TOF were used to characterize this new compound. Working with different concentrations, the compound's aggregation properties were investigated and concluded that no aggregation tendency has been observed in the studied concentration range (1.0 × 10⁻⁶ M to 1.2 × 10⁻⁵ M). Fluorescent quantum yields and lifetimes of the compound were studied and found to be 0.09 and 0.57 ns, respectively. As a fluorescent quencher, 1,4-benzoquinone was used in the experiments at differing concentrations in tetrahydrofuran. The k_q values showed a close follow-up to the diffusion control limits, around 10¹¹ s⁻¹ and they seem to agree with Einstein-Smoluchowski's approximation for bimolecular, diffusion-control-including, interactions. For the new compound, the K_{SV} value was calculated as 27.55, which is lower than that of unsubstituted ZnPc. The fluorescence of the studied compound **3** was effectively quenched by 1,4-benzoquinone.

Keywords: Zinc, anthracene, phthalocyanine, fluorescence, characterization.

Submitted: October 16, 2019. **Accepted:** November 11, 2019.

Cite this: Temizel S, Sevim A. Synthesis and Photophysical Properties of A₃B-type Unsymmetrically Substituted Anthracene-based Zinc(II)phthalocyanine. JOTCSA. 2020;7(1):107–16.

DOI: <https://doi.org/10.18596/jotcsa.633901>.

*Corresponding author. E-mail: sevim@itu.edu.tr.

INTRODUCTION

Phthalocyanines, also referred to as Pcs, are tetrabenzo-containing tetraazaporphyrin macrocycles, famous for their high stability, flexibility, coordination, and fine spectroscopic behavior (1). Photodynamic therapy, optical data storage, reversed saturable absorbers, and solar screens are phthalocyanines' chief important high technological applications (2). Thanks to their π-electron conjugation, Pcs can readily undergo electron transfer reactions (3). There are two main substitution patterns for Pcs: Peripheral (2, 9(10), 16(17), 23(24)) and non-peripheral (1, 8(11), 15(18), 22(25)) and these patterns allow for greater solubility in organic solvents, thereby

increasing the spectral behaviors and applications (4-8). To synthesize substituted Pcs, a reaction called cyclotetramerization must be exercised, and substituted phthalonitriles will give way to substituted phthalocyanines. The substitution of phthalonitriles with hydroxyl, amine, azide or alkynyl functional groups is preferable (9-12).

Second-order nonlinear optics (13), photodynamic therapy of cancer (14), liquid crystals (15), Langmuir-Blodgett (LB) film formation (16), and solar cells (17,18) are popular uses of unsymmetrical phthalocyanines. When there are two different types of substituents on the Pc molecule, multiple properties like enhanced solubility and reactivity on one or two points of the

macrocycle are possible, thereby a better control over the molecule is gained (19). Although there are numerous methods to prepare symmetrically substituted Pcs, the number of methods for unsymmetrically Pcs are fairly limited (20). The simplest technique to prepare an unsymmetrically substituted Pc is to conduct a statistically mixed condensation of two different phthalonitriles. The main drawback of this method is the hardship to isolate the targeted Pc in a mixture of differently substituted Pcs; all of them have similar physical and chemical properties. An alternative to the method above was proposed by Leznoff and Hall (21). This method comprises of an insoluble polymer with a diiminoisoindoline or phthalonitrile attached to it. A differently substituted phthalonitrile is introduced to the medium and the two are reacted, and the symmetrical phthalocyanine is isolated from the medium, then, as the last step, the non-substituted phthalocyanine is released from the polymeric backbone. A yet another method to prepare unsymmetrical Pcs has been described by Kobayashi and his coworkers (22, 23). In this method, a sub-phthalocyanine undergoes ring expansion in the presence of a different phthalonitrile and a unsymmetrical Pc is obtained.

Photovoltaics, molecular transistors, light-emitting devices, and other molecular electronic applications (24, 25) use organic materials, which are capable of absorbing various wavelengths of visible light and fluorescence highly efficiently. Since Pcs highly absorb in the Soret band of ultraviolet spectrum (about 300-400 nm), they are considered as efficient energy acceptors and they provide the required overlap between the emission spectrum of the donor and the absorption spectrum of the acceptor. As a donor group in this study, we have chosen anthracene unit because it is very stable thermally and can act as an antenna to harvest and transfer energy in an efficient manner to longer wavelength emission in blends or composites (26).

The poor solubility of Pcs in common organic solvents (like chlorinated solvents, ethers, and water) hamper the uses of them. If the Pc molecule is decorated with alkyl, alkoxy, alkylsulfanyl, or bulky groups at the peripheral, non-peripheral or axial positions, the solubility increases drastically (27, 28). Aggregation, in general, is the bringing together of molecules in dimers or higher oligomers in solution and aggregates present their hydrophobic part (at the center) as a group. The extended π system (29, 30) is responsible for aggregation. It hampers solubility in many solvents, reduces nonlinear optical properties drastically, and detrimental for photosensitization in photodynamic therapy (31). In Pcs, aggregation is frequently encountered at a concentration as low as 1×10^{-5} M, but if bulky

groups are introduced into the molecule, aggregation rate diminishes considerably.

In this work, we have reacted two different phthalonitriles to obtain a novel, A_3B type, unsymmetrical zinc phthalocyanine with peripheral substitution of three anthracene-9-methoxy and one ethynylbenzyloxy groups. Not only have the anthracene groups the ability to harvest light but also they provide better solubility in organic solvents due to their bulky nature. With the aid of mono alkynyl group, this novel zinc(II)phthalocyanine can be modified further by using well known techniques such as Cu(I)-catalyzed Huisgen 1,3-dipolar cycloaddition (better known as the "click chemistry") or Sonogashira carbon-carbon cross-coupling reactions that leads to expand the application field of this novel complex. The new compound was dissolved in volumetric flasks at different concentrations to see if it undergoes aggregation, by recording the UV-Vis spectrum. The fluorescent quantum yields and lifetimes were tabulated for the new compound by conducting the experiment in tetrahydrofuran. We have found out that 1,4-benzoquinone is an efficient fluorescent quencher in tetrahydrofuran for the Pc molecule we have prepared.

EXPERIMENTAL SECTION

Materials and methods

Fourier transform infrared spectra were collected with a Perkin-Elmer Spectrum One spectrometer by using a universal attenuated total reflectance (ATR) module in the $600\text{-}4000\text{ cm}^{-1}$ range. A Scinco SD 1000 single-beam UV-Vis spectrophotometer was utilized to record the UV-Vis spectra of the compounds in 1 cm path length cuvettes at room temperature. A Perkin-Elmer LS55 fluorescence spectrophotometer was used to obtain fluorescence spectra. Proton NMR spectra were obtained with an Agilent VNMRS 500 MHz spectrometer, employing tetramethylsilane (TMS) as the internal reference. Elemental analyses were obtained in the Instrumental Analysis Laboratory of TUBITAK Marmara Research Center. A Bruker Microflex MALDI-TOF/MS mass spectrometer was used to record the mass spectra of the required compounds. Reagent grade chemicals and solvents were used and procured from commercial suppliers. At each reaction step, we have tested the reaction's status and the purity of the compounds by running thin layer chromatography (TLC) on silica. All reactions were run in nitrogen atmosphere and the solvents we used were dried over molecular sieves. The two phthalonitriles we have used, namely 4-hex-5-ynylloxy-phthalonitrile (**1**) and 4-anthracen-9-ylmethoxy)phthalonitrile (**2**), were synthesized by referring to the reported procedures (32, 33).

Synthesis

Synthesis of 9(10), 16(17), 23(24)-tris-(4-anthracen-9-ylmethoxy)-2(3)-(4-hex-5-ynyloxy)phthalocyaninatozinc (II) (3):

0.045 g (0.20 mmol) of **1**, 0.201 g (0.60 mmol) of **2**, and 0.050 g (0.27 mmol) zinc acetate were charged into a screw-capped tube and immersed into an oil bath, 3 mL of 2-dimethylaminoethanol was added and the temperature of the reaction was raised to 145 °C and sustained for 24 h. After this step, the obtained greenish product was cooled to room temperature, and precipitated by pouring into 3:1 (v/v) water/methanol mixture, then filtered. Hot methanol, n-hexane, and acetone were used to wash the crude product until there were no yellowish-brown impurities observed, then dried in an oven at 110 °C. The dried greenish compound was chromatographed on a silica-loaded glass column with ethyl acetate – n-hexane (3:1, v/v) as eluent.

Solubility: Soluble in tetrahydrofuran, chloroform, dichloromethane, dimethylsulfoxide, and dimethylformamide. Yield: 0.059 g, (23 %). FT-IR ($\nu_{\max}/\text{cm}^{-1}$): 3289 (H-C≡), 3052 (Ar-C-H), 2927-2861 (Aliph. -C-H), 2210 (C≡C), 1601, 1446, 1387, 1315, 1226 1088, 993, 881, 826, 730. UV-Vis λ_{\max} (nm) THF: 339, 351, 367, 387, 678. ¹H-NMR (500 MHz, CDCl₃): δ , ppm: 8.34-7.18 (39H, m, Ar-H), 4.28 (6H, s, Ar-CH₂-O-), 4.11 (2H, t, -CH₂-O-), 2.28 (1H, t, -C≡CH), 1.74 (2H, m, -CH₂-C≡CH), 1.44 (2H, m, -CH₂), 1.27 (2H, m, -CH₂). Anal. Calc. for C₈₃H₅₄N₈O₄Zn (1292,78 g/mol) %: C, 77.11; H, 4.21; N, 8.67 Found: C, 77.42; H, 4.01; N, 8.96. MALDI-TOF MS: m/z 1292.57 [M]⁺.

Photophysical parameters

Fluorescence quantum yields and lifetimes:

To determine the fluorescent quantum yields (Φ_F) comparatively, Equation 1 below was employed, with ZnPc in DMF as the standard compound ($\Phi_F = 0.17$) (34,35):

$$\Phi_F = \Phi_{F(\text{Std})} \frac{F_{\text{Std}} A \eta^2}{F_{\text{Std}} A \eta_{\text{Std}}^2} \quad (\text{Eq. 1})$$

F and F_{std} are the areas calculated under the fluorescence curves of the phthalocyanine (**3**) and the unsubstituted phthalocyanine, respectively. A and A_{std} are absorbances of substituted and unsubstituted phthalocyanines, respectively. Normally they are about 0.04 and 0.05 for all solvents. η and η_{std} are the refractive indices of the solvents used. The standard and sample were excited at the same wavelength.

Fluorescent lifetime (τ_F) is the average time of the molecule residing at the excited state before fluorescing. These data were calculated with the Strickler-Berg equation, which was readily available in the PhotoChemCad software. Fluorescent quantum yield and fluorescent lifetime (τ_F) are directly proportional values. For the calculation of natural radiative lifetime (τ_0), Equation 2 was employed (36):

$$\Phi_F = \frac{\tau F}{\tau_0} \quad (\text{Eq. 2})$$

1,4-benzoquinone-mediated fluorescent quenching:

When increasing amounts of 1,4-benzoquinone (BQ) were added into the solutions of zinc phthalocyanine at a fixed concentration, we observed fluorescent quenching; the concentrations of BQ at each step were 0.008, 0.016, 0.024, 0.032, 0.040, and 0.048 M. A transfer of energy occurs between BQ which is the quencher and ZnPc which is the fluorophore. The fluorescence spectra at each increment of BQ were recorded and by utilizing the Stern-Volmer (SV)

equation given below (see Equation 3), the changes in fluorescent intensity concerning the BQ concentration (37).

Stern-Volmer (SV) equation, which is given below, was used to find the Stern-Volmer constant (K_{SV}) from a graph and this is the product of bimolecular quenching constant (k_q) and τ_F (see Equation 4) (35). In Equation 3, I_0 and I are the fluorescent intensities of the fluorophore in the absence and presence of quencher, respectively. [BQ] is the concentration of the quencher.

$$\frac{I_0}{I} = 1 + K_{SV} [\text{BQ}] \quad (\text{Eq. 3})$$

$$K_{SV} = k_q \times \tau_F \quad (\text{Eq. 4})$$

The ratios of I_0 / I against $[BQ]$ were plotted and K_{SV} was determined from the slope of the line.

RESULTS AND DISCUSSION

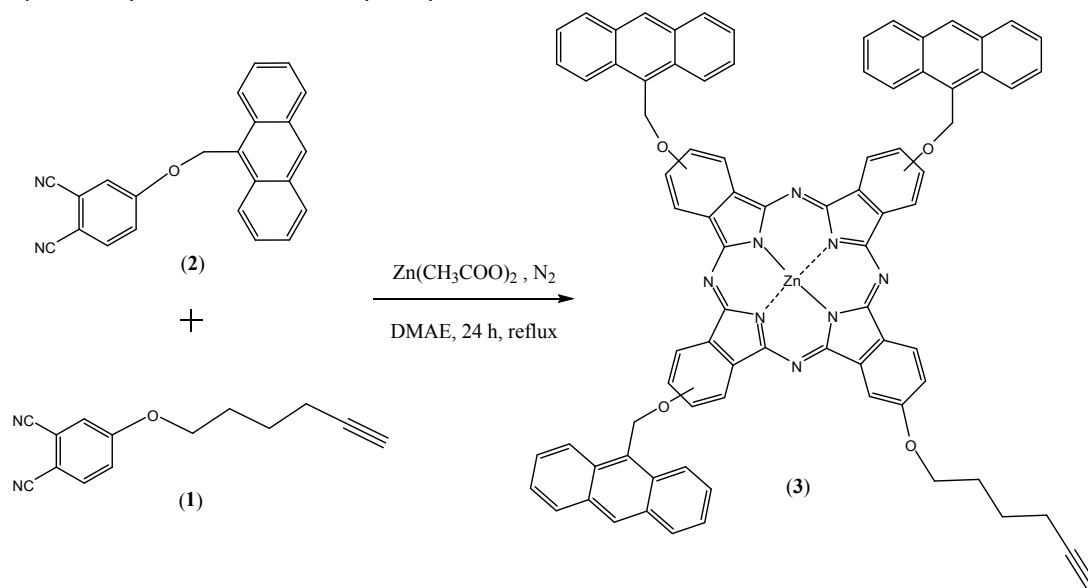
Synthesis and spectroscopic characterization

Scheme 1 indicates the synthetic work of the targeted unsymmetrical ZnPc (**3**). The two phthalocyanine precursors leading to the unsymmetrical phthalocyanine were 4-hex-5-ynylphthalonitrile (**1**) and 4-(anthracene-9-ylmethoxy)phthalonitrile (**2**). The two precursors were synthesized with a base-catalyzed nucleophilic aromatic nitro displacement (at the ipso position) of 4-nitrophthalonitrile with 5-hexyn-1-ol and anthracene-9-ylmethanol (32,33). As a nitro-displacement base, potassium carbonate was used and the synthesis was completed in a single step at 40 °C for (**1**) and room temperature for (**2**). The solvent of choice was dimethylformamide and the reaction flask's atmosphere was maintained with nitrogen.

When a mixture of two phthalocyanine precursors, A and B, considered to have equal reactivity, are reacted in a 3:1 ratio will yield an isomeric mixture of phthalocyanines of A_4 (33%), A_3B (44%) and other cross-condensation products (27%) (20,38). If the solubilities of the phthalocyanine precursors are very different, the final purification of the targeted phthalocyanine will be a very easy one.

The targeted phthalocyaninatozinc(II) compound was synthesized with the cyclotetramerization of three equivalents of dinitrile (**2**) and one equivalent of dinitrile derivative (**1**), in the presence of 2-dimethylaminoethanol as the solvent and zinc acetate as the metal source, at 145 °C under nitrogen. Several other molar ratios were tried to see if the reaction yield increases, but 3:1 ratio of (**1**):(**2**) was found to be the best one (see Scheme 1). In the work-up, the crude product was subjected to column chromatography over silica, the eluent being the 3:1 v/v mixture of ethyl acetate / n-hexane. The first fraction was symmetrical A_4 as compared with authentic samples shown by TLC. The second fraction was the targeted A_3B one (**3**), a bright green solid obtained with a 23% yield.

The new compound (**3**) was characterized by a series of spectral analysis methods, including FT-IR, 1H NMR, MALDI-TOF MS and UV-Vis, along with elemental analysis. The results showed that they are in accordance with proposed structures.



Scheme 1. Synthesis of the unsymmetrical zinc(II)phthalocyanine.

The FT-IR spectrum of (**3**) showed that anthracene and alkyl moieties appeared at expected positions, but $C\equiv N$ stretching disappeared after cyclotetramerization, which is also an expected outcome. The alkynyl proton $H-C\equiv$, aromatic $C-H$, aliphatic $C-H$, $C\equiv C$, aromatic $C=C$ and $C-O-C$ vibrations were observed at 3289, 3052, 2927-2861, 2210, 1601-1446 and 1226 cm^{-1} ,

respectively. The 1H NMR spectrum of (**3**) showed a multiplicity between δ 8.34 – 7.18 ppm in deuterated chloroform as the solvent. The methylene protons situated between the etheric oxygen bonded Pc core and anthracenyl group had a chemical shift of δ 4.28 ppm as a singlet. The other methylene group between the etheric oxygen and the hexynyl group showed a chemical shift of

δ 4.11 ppm as a triplet. Also, the alkynyl proton $\text{H}-\text{C}\equiv$ and the aliphatic CH_2 protons belonging to the hexynyl chain were spotted at δ 2.28 ppm (triplet) and δ 1.74-1.27 ppm (multiplet), respectively. Also, the assignment of the product to a 3:1 combination of the reactants was made based on

elemental analysis and mass spectral data results confirming the proposed structures. Elemental analysis confirmed the 3:1 molar ratio and MALDI-TOF showed the molecular peak of the expected compound (**3**) at m/z 1292.57 (see Figure 1).

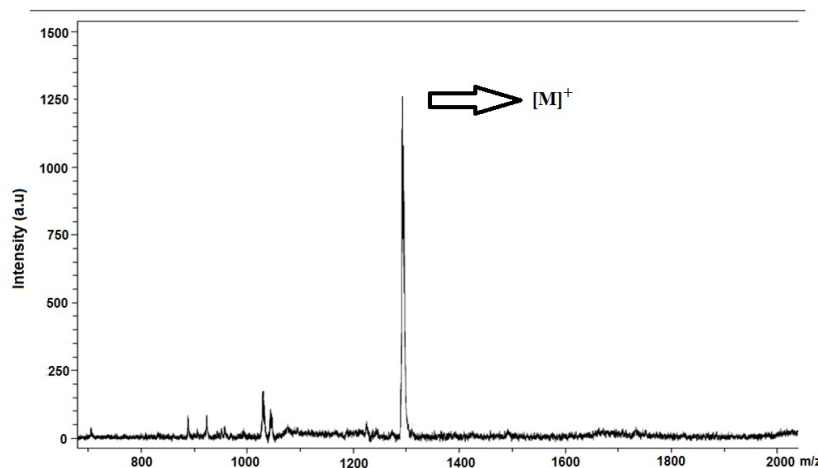


Figure 1. MALDI-TOF Mass spectrum of targeted zinc(II) phthalocyanine.

All phthalocyanines' electronic spectra feature two intense $n - n^*$ transitions. The first one is Soret (or B) band, located around 300 and 400 nm, and the second one is the Q band, located around 600-700 nm. The tetrahydrofuran solution, compound (**3**) showed B and Q bands at 339 and 678 nm, respectively (see Figure 2). Since anthracene is also a UV-active entity, its peaks were also spotted at 351, 367, and 387 nm (see Figure 2). Owing to the presence of anthracenyl group, the B band's intensity is as much as that of the Q band. There are reports in the literature, mentioning of an overlap between phthalocyanine's B band and anthracene moiety's absorption at 350 nm (27).

Phthalocyanine aggregation has been the subject of numerous studies. The extended flat aromatic structure of phthalocyanines leads to attractive $n - n^*$ stacking, thereby forming aggregates starting from monomers to higher order complex structures. Generally, there is a hypsochromic shift of the aggregate owing to the cooperative interaction among the transition dipole moments of the molecules. This leads to a broadening of the Q band and reducing its intensity. In general, concentration, temperature, substituents, the nature of solvents and the metal ion residing at the

inner core are chief factors affecting the phenomenon of aggregation. Since aggregated species are photo-inactive, aggregation is not a desired outcome in phthalocyanines. In polar media like water, the problem is very significant; water tends to self-associate and repels the hydrophobic n system, forming aggregates. In our work, aggregation behaviors of the metallophthalocyanines were investigated in tetrahydrofuran, by recording the absorption at different concentrations; the reason for selection of THF as the solvent is the high solubility of the complexes in this solvent. At the higher energy side of the strong Q band, we have observed weak peaks at 610-630 nm in the electronic spectra. Studying the absorption values for a series of concentrations is a method to see if the system shows aggregation. We have studied a wide range of concentrations (1.0×10^{-6} M to 1.2×10^{-5} M) and absorbance values in Q band maxima showed a linear change (obedience to Lambert-Beer's law) with respect to the increasing concentration for the monomeric species. We can conclude that no aggregation tendency has been observed for our target compound (**3**) in studied concentration range (Figure 2).

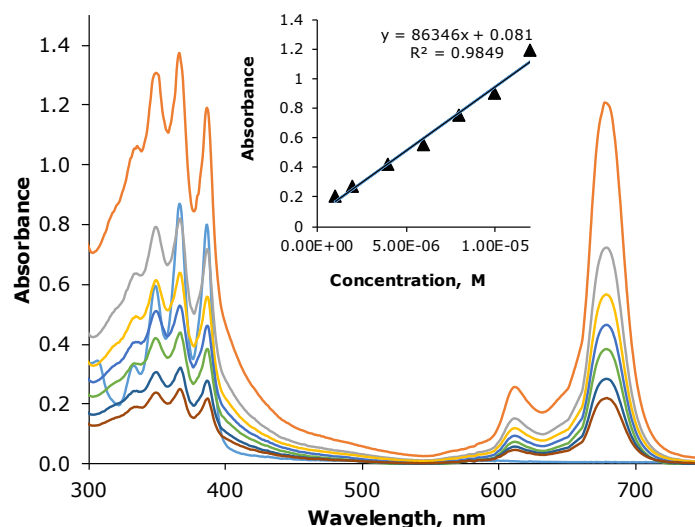


Figure 2. Electronic absorption spectra observed on the increase in the concentration of the compound (**3**) in THF. Inset: Beer-Lambert's plot for (**3**) in THF. The range of concentrations: 1.0×10^{-6} M to 1.2×10^{-5} M).

Measurements of fluorescence and fluorescent quenching studies of compound (**3**) were carried out in tetrahydrofuran, with an excitation of the Q band at 611 nm. Figure 3 shows the fluorescent emission, excitation, and absorption spectra of (**3**) in THF. 697 nm was the peak fluorescent emission value of compound (**3**) and the Stokes' shift was 19 nm, which was within the expected range of 15-

20 nm (11). The excitation spectrum and the absorption spectrum are similar to each other and they are mirror images of the fluorescent spectra for compound (**3**) in tetrahydrofuran. This indicates that the nuclear configurations of the ground and excited states have a similarity and excitation does not affect this (39).

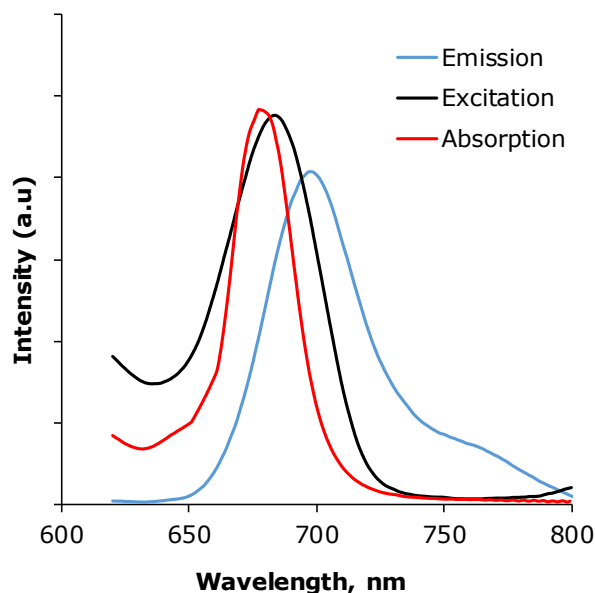


Figure 3. Absorption and fluorescence (excitation and emission) spectra of (**3**) in tetrahydrofuran, excitation wavelength = 611 nm.

Solutions prepared with THF were employed to find the fluorescent quantum yield (Φ_F) of (**3**). As Equation 1 states, the comparative method is used to calculate the fluorescent quantum yield (Φ_F). Unsubstituted zinc phthalocyanine was used as a standard compound, and its solution in dimethylformamide had Φ_F of 0.17 (35), and the

wavelength to excite the sample and standard compounds was the same. The fluorescent quantum yield for (**3**) was found 0.09. In THF solution, the Φ_F value for compound (**3**) was lower than that of the unsubstituted ZnPc ($\Phi_F = 0.25$) (40) and this value is recognized as a typical one for Pc compounds (see Table 1).

τ_F , also known as the fluorescent lifetime, is the average time of a fluorophore which stays at the excited state before fluorescing and fluorescent quantum yield is very close to this value. This means that if the fluorescent lifetime is long, the quantum yield is also high. Intersystem crossing, internal conversions, and such others will cause a reduction of the fluorophore's fluorescent lifetime, thereby causing a reduction in the quantum yield. The fluorescent lifetime is thereby determined by the nature and the surroundings of a compound.

To calculate the fluorescent lifetime, Strickler-Berg equation (see Equation 2) is used. Compound **3**'s τ_F value was calculated was 0.57 ns, which is lower than that of unsubstituted ZnPc in tetrahydrofuran (40), and this has a meaning that there is more quenching after substitution around the periphery.

Natural radiative lifetimes (τ_0) and fluorescent rate constant (k_F) values are shown in Table 1. In THF solution, k_F value of compound (**3**) is higher than the unsubstituted ZnPc solution.

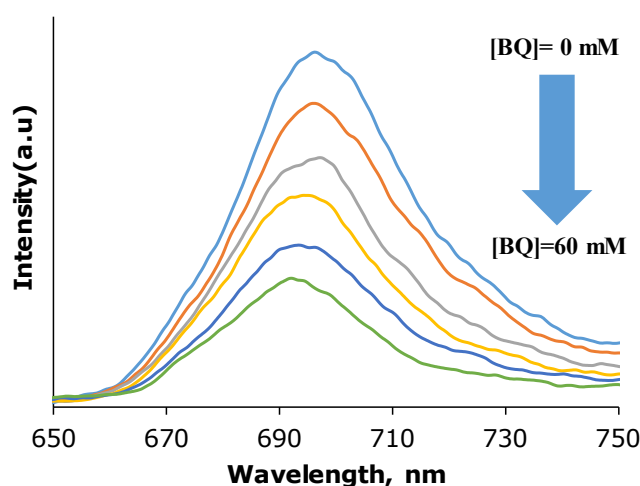


Figure 4. Spectral changes of fluorescent emission for (**3**) (1.50×10^{-6} M) on the addition of increasing amounts of 1,4-benzoquinone in THF. The concentrations of BQ: 0 mM, 12 mM, 24 mM, 36 mM, 48 mM, 60 mM.

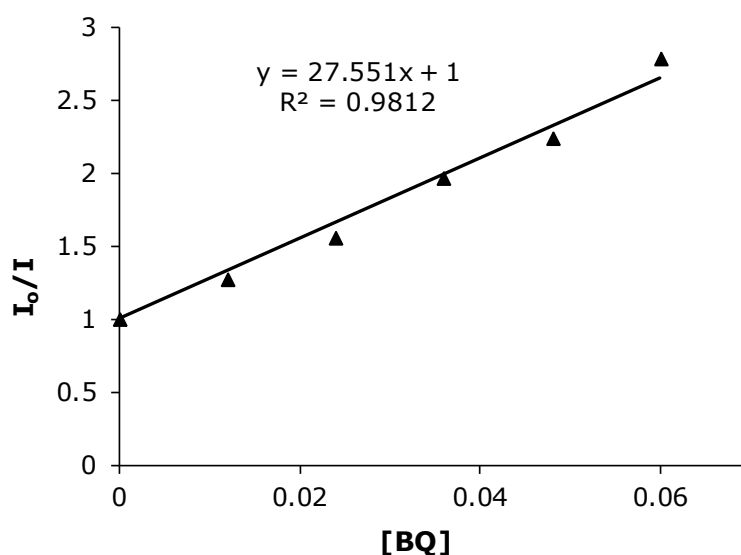


Figure 5. Stern-Volmer plots for benzoquinone (BQ) quenching of compound (**3**) (1.50×10^{-6} M) in THF. The concentrations of BQ: 0 mM, 12 mM, 24 mM, 36 mM, 48 mM, 60 mM.)

Compound (**3**) is quenched by 1,4-benzoquinone in tetrahydrofuran, obeying Stern-Volmer kinetics; it is also in parallel with the diffusion-controlled

bimolecular reactions. Figure 4 shows that compound (**3**) has fluorescent emission spectral changes with increasing BQ concentration in THF.

Using an increased concentration of BQ, fluorescent intensity of compound (**3**) shows a decline. The Stern-Volmer plot of compound (**3**) shows a linear behavior, indicating a quenching mechanism with diffusion control (Figure 5). From Figure 5, the K_{SV} value is found from the slope of the plot and shown in Table 1, which also shows the bimolecular quenching constant (k_q) for 1,4-benzoquinone-induced quenching of compound (**3**) in THF. The k_q values showed a close follow-up to the diffusion control limits, around 10^{11} s^{-1} (see Table 1) and they seem to be in agreement with Einstein-Smoluchowski's approximation for bimolecular, diffusion-control-including, interactions (41). For compound (**3**), the K_{SV} value is 27.55, which is lower than that of unsubstituted ZnPc in THF (40).

CONCLUSION

In this work, we have co-cyclotetramerized anthracene-9-methoxy- and ethynylbenzyloxy-containing phthalonitriles in 3:1 ratio to yield the A_3B -type unsymmetrical zinc phthalocyanine in a statistical condensation route. After the full characterization of compound (**3**), aggregation behavior, photophysics, and photochemistry of it were studied and the data were compiled in Table 1, along with ZnPc (unsubstituted) as a standard compound. Photophysical fluorescence of compound (**3**) was investigated in THF solution. It shows that compound (**3**) has a lower fluorescent quantum yield and shorter lifetime than the unsubstituted counterpart. In tetrahydrofuran solution, compound (**3**) was effectively quenched by 1,4-benzoquinone and Stern-Volmer kinetics were shown.

ACKNOWLEDGMENTS

This work was supported by the Research Fund of the Istanbul Technical University.

REFERENCES

- McKeown NB. Phthalocyanine materials: synthesis, structure, and function. Cambridge, U.K.; New York: Cambridge University Press; 1998. 193 p. (Chemistry of solid state materials).
- Gregory P. Industrial applications of phthalocyanines. *Journal of Porphyrins and Phthalocyanines*. 2000;4(4):432-7.
- Bekaroğlu Ö. Structure and Bonding. In: *Functional Phthalocyanine Molecular Materials*. Berlin, Heidelberg: Springer-Verlag; 2010. p. 105.
- Sevim AM, Arkan S, Koca A, Gül A. Synthesis and spectroelectrochemistry of new phthalocyanines with ester functionalities. *Dyes and Pigments*. 2012 Mar;92(3):1114-21.
- Sevim AM, Ilgün C, Gül A. Preparation of heterogeneous phthalocyanine catalysts by cotton fabric dyeing. *Dyes and Pigments*. 2011 May;89(2):162-8.
- Arslanoglu Y, Mertsevim A, Hamuryudan E, Gul A. Near-IR absorbing phthalocyanines. *Dyes and Pigments*. 2006;68(2-3):129-32.
- Sevim AM. Synthesis and characterization of Zn and Co monocarboxy-phthalocyanines and investigation of their photocatalytic efficiency as TiO₂ composites. *Journal of Organometallic Chemistry*. 2017 Mar;832:18-26.
- Akkurt B, Hamuryudan E. Enhancement of solubility via esterification: Synthesis and characterization of octakis (ester)-substituted phthalocyanines. *Dyes and Pigments*. 2008 Nov;79(2):153-8.
- Quinton D, Antunes E, Griveau S, Nyokong T, Bedioui F. Cyclic voltammetry and spectroelectrochemistry of a novel manganese phthalocyanine substituted with hexynyl groups. *Inorganic Chemistry Communications*. 2011 Jan;14(1):330-2.
- Chen X, Thomas J, Gangopadhyay P, Norwood RA, Peyghambarian N, McGrath DV. Modification of Symmetrically Substituted Phthalocyanines Using Click Chemistry: Phthalocyanine Nanostructures by Nanoimprint Lithography. *J Am Chem Soc*. 2009 Sep 30;131(38):13840-3.
- Sevim AM, Özçeşmeci İ, Gül A. Synthesis and photophysical properties of a novel ethynyl zinc(II) phthalocyanine and its functionalized derivative with click chemistry. *J Porphyrins Phthalocyanines*. 2013 Jun;17(06n07):540-7.
- Akkurt B, Koca A, Hamuryudan E. Synthesis, in situ spectroelectrochemistry and in situ electrocolorimetry of electrochromic octakis(chloroethylsulfanyl) phthalocyaninatomanganese(iii) chloride. *New J Chem*. 2009;33(11):2248.
- O'Flaherty SM, Hold SV, Cook MJ, Torres T, Chen Y, Hanack M, et al. Molecular Engineering of Peripherally And Axially Modified Phthalocyanines for Optical Limiting and Nonlinear Optics. *Adv Mater*. 2003 Jan 3;15(1):19-32.
- Allen CM, Sharman WM, Van Lier JE. Current status of phthalocyanines in the photodynamic therapy of cancer. *J Porphyrins Phthalocyanines*. 2001 Feb;05(02):161-9.
- Iino H, Hanna J, Bushby RJ, Movaghar B, Whitaker BJ, Cook MJ. Very high time-of-flight mobility in the columnar phases of a discotic liquid crystal. *Appl Phys Lett*. 2005 Sep 26;87(13):132102.
- Cook MJ, McKeown NB, Simmons JM, Thomson AJ, Daniel MF, Harrison KJ, et al. Spectroscopic and X-ray diffraction study of Langmuir-Blodgett films of some 1,4,8,11,15,18-hexaalkyl-22,25-bis(carboxypropyl)phthalocyanines. *J Mater Chem*. 1991;1(1):121-7.
- O'Regan BC, López-Duarte I, Martínez-Díaz MV, Forneli A, Albero J, Morandeira A, et al. Catalysis of Recombination and Its Limitation on Open Circuit Voltage

- for Dye Sensitized Photovoltaic Cells Using Phthalocyanine Dyes. *J Am Chem Soc.* 2008 Mar;130(10):2906-7.
18. Bartelmess J, Ballesteros B, de la Torre G, Kiessling D, Campidelli S, Prato M, et al. Phthalocyanine-Pyrene Conjugates: A Powerful Approach toward Carbon Nanotube Solar Cells. *J Am Chem Soc.* 2010 Nov 17;132(45):16202-11.
19. Kobayashi N, Miwa H, Nemykin VN. Adjacent versus Opposite Type Di-Aromatic Ring-Fused Phthalocyanine Derivatives: Synthesis, Spectroscopy, Electrochemistry, and Molecular Orbital Calculations. *J Am Chem Soc.* 2002 Jul;124(27):8007-20.
20. de la Torre G, Claessens C, Torres T. Phthalocyanines: The Need for Selective Synthetic Approaches. *European Journal of Organic Chemistry.* 2000;2000(16):2821-30.
21. Leznoff CC, Hall TW. The synthesis of a soluble, unsymmetrical phthalocyanine on a polymer support. *Tetrahedron Letters.* 1982 Jan;23(30):3023-6.
22. Kobayashi N, Kondo R, Nakajima S, Osa T. New route to unsymmetrical phthalocyanine analogs by the use of structurally distorted subphthalocyanines. *J Am Chem Soc.* 1990 Dec;112(26):9640-1.
23. Dabak S, Gül A, Bekaroğlu Ö. Hexakis(alkylthio)-Substituted Unsymmetrical Phthalocyanines. *Chem Ber.* 1994 Oct;127(10):2009-12.
24. Zhou J, Mi J, Zhu R, Li B, Qian S. Ultrafast excitation relaxation in titanylphthalocyanine thin film. *Optical Materials.* 2004 Dec;27(3):377-82.
25. de la Torre G, Claessens CG, Torres T. Phthalocyanines: old dyes, new materials. Putting color in nanotechnology. *Chem Commun.* 2007;(20):2000-15.
26. Zhang G, Zhang D, Guo X, Zhu D. A New Redox-Fluorescence Switch Based on a Triad with Tetrathiafulvalene and Anthracene Units. *Org Lett.* 2004 Apr;6(8):1209-12.
27. Sevim AM, Arıkan S, Özçeşmeci İ, Gül A. Photophysical properties of anthracenylmethyloxycarbonylmethylsulfanyl-phthalocyanines. *Synthetic Metals.* 2013 Nov;183:1-7.
28. Coşkun NY, Ödevci Ö, Yalçın SM, Gül A. Synthesis, Absorption and Fluorescence Spectral Investigation of Porphyrazines with Eight 9-Anthracenecarboxy Esters. *Main Group Metal Chemistry [Internet].* 2007 Jan [cited 2019 Oct 11];30(2-3). Available from: <https://www.degruyter.com/view/j/mgmc.2007.30.2-3/mgmc.2007.30.2-3.83/mgmc.2007.30.2-3.83.xml>
29. Snow A. Phthalocyanine Aggregation. In: *The Porphyrin Handbook [Internet].* Amsterdam: Elsevier; 2003. p. 129-76. Available from: <https://www.sciencedirect.com/book/9780080923918/the-porphyrin-handbook>
30. Wiggins M, Flom S, Shirk J, Pong R, Lepkowitz R, Ranade A. *Abstract Papers American Chemical Society.* Vol. 228. Washington: American Chemical Society (ACS); 2004.
31. Zoller P, Walsh DJ. *Standard pressure-volume-temperature data for polymers.* Lancaster, PA: Technomic Pub. Co; 1995. 412 p.
32. Bankole O, Britton J, Nyokong T. Photophysical and non-linear optical behavior of novel tetra alkynyl terminated indium phthalocyanines: Effects of the carbon chain length. *Polyhedron.* 2015;88:73-80.
33. Kahouecha M, Hrizb K, Touaitia S, Bassem J. New anthracene-based-phthalocyanine semi-conducting materials: Synthesis and optoelectronic properties. *Materials Research Bulletin.* 2016;75:144-54.
34. Masilela N, Nyokong T. The synthesis and fluorescence behaviour of new unsymmetrically mono-functionalized carboxy Ge, Ti and Sn phthalocyanines. *Dyes and Pigments.* 2011;91(2):164-9.
35. Durmuş M, Nyokong T. Photophysicochemical and fluorescence quenching studies of benzyloxyphenoxy-substituted zinc phthalocyanines. *Spectrochimica Acta Part A: Molecular and Biomolecular Spectroscopy.* 2008 Apr;69(4):1170-7.
36. Du H, Fuh R, Li J, Corkan L, Lindsey J. PhotochemCAD: A Computer-Aided Design and Research Tool in Photochemistry. *Photochemistry and Photobiology.* 1998;68:141-8.
37. Rose J. *Advanced Physico-Chemical Experiments.* London: Sir Isaac Pitman & Sons Ltd; 1964. 257 p.
38. Bakboord J, Cook M, Hamuryudan E. Non-uniformly substituted phthalocyanines and related compounds: alkylated tribenzo-imidazo [4, 5]-porphyrazines. *Journal of Porphyrins and Phthalocyanines.* 2000 Aug;4(5):510-7.
39. Zorlu Y, Dumoulin F, Durmuş M, Ahsen V. Comparative studies of photophysical and photochemical properties of solketal substituted platinum (II) and zinc (II) phthalocyanine sets. *Tetrahedron.* 2010;66(17):3248-58.
40. Saka E, Durmuş M, Kantekin H. Solvent and central metal effects on the photophysical and photochemical properties of 4-benzyloxybenzoxy substituted phthalocyanines. *J Organomet Chem.* 2011;696:913-24.
41. Gümrükcü G, Karaoglan G, Erdoğan A, Gül A, Avciata U. A novel phthalocyanine conjugated with four salicylideneimino complexes: Photophysics and fluorescence quenching studies. *Dyes Pigm.* 2012;95:280-9.

Table 1. Photophysical and photochemical parameters along with fluorescent quenching data of (**3**) and unsubstituted ZnPc complexes in THF.

Complex	$\lambda_{\max}(\text{nm})$	Excitation $\lambda_{\max}(\text{nm})$	Emission $\lambda_{\max}(\text{nm})$	Stokes' shift $\Delta_{\text{stokes}}(\text{nm})$	Φ_F	τ_{F_r} , ns	τ_o , ns	k_{F_r} , s^{-1} ($\times 10^8$)	K_{SV} , M^{-1}	k_{q_r} , s^{-1} ($\times 10^{11}$)
3	678	611	697	19	0.09	0.57	6.33	1.58	27.55	0.48
ZnPc ^a	667	667	672	5	0.25	2.72	10.9	0.92	48.48	1.78

a= Reference 40.



Finding Exact Number Of Peaks in Broadband UV-Vis Spectra Using Curve Fitting Method Based On Evolutionary Computing

Fatih Mehmet AVCU^{1,*}  and Mustafa KARAKAPLAN² 

¹University of İnönü, Department of Informatics, 44280, Malatya, Turkey.

²University of İnönü, Faculty of Arts and Sciences, Department of Chemistry, 44280, Malatya, Turkey.

Abstract: High performance calculations are needed in order to resolve analytic signals of the day. However, it requires very long periods of time to perform these calculations with single processor systems. In order to reduce these calculation times, there is a need to turn to parallel programming algorithms that share more than one processor. Recently, solving complex problems with genetic algorithms has been widely used in computational sciences. In this work, we show a new method of curve fitting via genetic algorithm based on Gaussian functions, for deconvolution of the overlapping peaks and find the exact number of peaks in UV-VIS absorption spectroscopy. UV-VIS spectra are different than other instrumental analysis data. The resolution of UV-VIS spectra are complicated since the absorption bands are strongly overlapped. Useful information about molecular structure and environment can often be obtained by resolving these peaks properly. The algorithm was parallelized with the island model in which each processor computes a different population. This method has been used for resolving of the UV-VIS overlapping spectrum. The method particular algorithm is robust against bad resolution or noise. The results clearly show the effectiveness of the proposed method.

Keywords: UV-Vis spectroscopy, Data fitting, Genetic algorithm, Parallel computing, Peak Numbers.

Submitted: June 28, 2019. **Accepted:** November 15, 2019.

Cite this: Avcu F, Karakaplan M. Finding Exact Number Of Peaks in Broadband UV-Vis Spectra Using Curve Fitting Method Based On Evolutionary Computing. JOTCSA. 2020;7(1):117-24.

DOI: <https://doi.org/10.18596/jotcsa.583632>.

***Corresponding author.** E-mail: fatih.avcu@inonu.edu.tr.

INTRODUCTION

UV-VIS spectroscopy is a common qualitative and quantitative evaluation of samples applied to instrumental analysis. The analysis of the UV-VIS spectroscopy which contains the overlapped peaks reveals information about the molecule's structure and its environment. Each individual band in the UV-VIS spectra is complicated because the UV-VIS absorption spectra are generally strongly overlapped. The resolution of individual bands has different half-height width, and peaks numbers in the overlapped spectra are difficult to estimate. This method is used for analytical signal measurement because of its speed and simplicity, and it has been increasing in importance due to

decreasing cost. Because of these developments there is a need for more intelligent design of software in order to decrease computation time.

A genetic algorithm is a part of the evolutionary computation influenced by the evolutionary theory of Darwin. It is a stochastic method and optimization algorithm. If we simply explain the aim, at the end of the process it gives the best results and this problem using the evolutionary process. The result is that individuals who survive have developed capabilities that will lead to finding the best individuals. The best result is the convergence that managed to stay alive. Method for optimizing is developed by L. A. Rastrigin in 1963 (1). First, evolutionary computation is

defined in the work of I. Rechenberg's "Strategy of Evolution". After that J. Holland developed genetic algorithms to imitate the process of evolution in the computer (2). Holland uses a bit sequence to code complex structures. David E. Goldberg, who was a student of Holland, has published books that genetic algorithm, can be used on various topics (3).

GA gained popularity in almost every branch in science and engineering disciplines (4-7). GA has more solutions for many problems. The GA is widely used in complex, parameter optimization and multi-extrema problems. The fields where the genetic algorithm is most commonly used are applications of the GA to molecular energy optimizations (8-13), signal processing (14,15), curve fitting (5,16), and linear and non-linear function optimization (17,18). The genetic algorithm is robust and highly efficient at the same time (19).

We propose the theory of curve-fitting based on the Gaussian model and both the minimum separable peak-peak interval and the curve-fitting error to resolve overlapping spectra with GA. Finally, we used synthetic spectral and real UV-VIS spectra to verify the performance of our method.

THEORETICAL

Approach to Curve Fitting with Genetic Algorithm

The aim of curve fitting is finding the mathematical model coefficients which minimize the total error over the set of data points being considered. If a function form has been selected from the data, curve fitting becomes an optimization problem. GAs have been used as global optimization techniques problems. They are suitable for curve fitting problems when it is structured as a parameter selection problem. Generally, the point values are data obtained from experimental results. There is no continuous definition between data and functions.

Typically, sum of complex functions must be used; otherwise, a lot of functions must be defined point-by-point. This is the curve fitting process. Since the genetic algorithms for continuous functions global optimization technique as being successful so this technique is suitable for parameter selection problems to curve fitting.

Parallel Genetic Algorithm

Parallel genetic algorithms (PGA)(20-22) are programs which parallelize, distribute, and break into pieces the basic program. Multiple processors then solve simultaneously.

Hardware and Software

Our GA implementation used C++ class libraries and Linux systems. Coarse-grained parallelism, utilizing AMD Opteron 2435 processors with six cores to perform sets of 100 runs, and the OpenMPI (23) parallel programming library was also used.

UV-VIS Peak Shape

UV-VIS spectroscopy is an inexpensive technique applicable to mixtures of organic and inorganic compounds for qualitative and quantitative analysis. Depending on the type and number of components, spectra could become complicated. Location, height and width of overlapping peaks gives knowledge about spectral bands. The spectral bandwidth of UV-VIS is larger than other spectroscopic techniques' spectra. This is because rotation and vibration transitions are overlaid on and overlap the electronic transition energy levels. UV-VIS produces spectra that are simpler, and containing a smaller number of narrower, more than other spectra e.g. NMR, IR, etc. overlapped peaks. Also, these absorption bands may have different functions from each other. In the analysis of spectral bands Lorentzian, Pearson VII and Gaussian functions are preferred to the use of Gaussian functions because UV-VIS spectra contain sum of broad peaks.

In order to simulate overlapping UV-VIS spectra, three type of functions were used as follows;

$$\text{Lorentzian: } A(v) = \sum_{i=1}^n \frac{A_{i,0} H_i^2}{H_i^2 + 4(v - v_{i,0})^2} \quad (1)$$

$$\text{Pearson VII: } A(v) = \sum_{i=1}^n \frac{A_{i,0}}{[1 + 4 Z_i^2 (2^{1/m_i} - 1)]} \quad (2)$$

$$\text{Gaussian: } A(v) = \sum_{i=1}^n A_{i,0} e^{-(v - v_{i,0})^2 / H_i} \quad (3)$$

where parameter of Eq. (1), (2) and (3) are that $A_{i,0}$ is the absorbance in the center of peak i , $Z_i = (v - v_{i,0}) / H_i$ and H_i are the half width of peak i , $v_{i,0}$ is the peak position of peak i , m_i is the tailing factor of peak i , and n is the number of the peak.

EXPERIMENTAL

After synthesized nanoparticles of ZrO_2 disperse in solvent and surface was coated with 2-AAEM. After drying and cooling modified nano particles are prepared, analyzed by a Varian Cary 5000 UV-VIS-NIR to measure absorbance at the solid surface. Powdered sample (1 mm) was set in the sample

container. After inserting the relevant part of the DRA device absorbance between 200-800 nm was measured (see Figure 1).

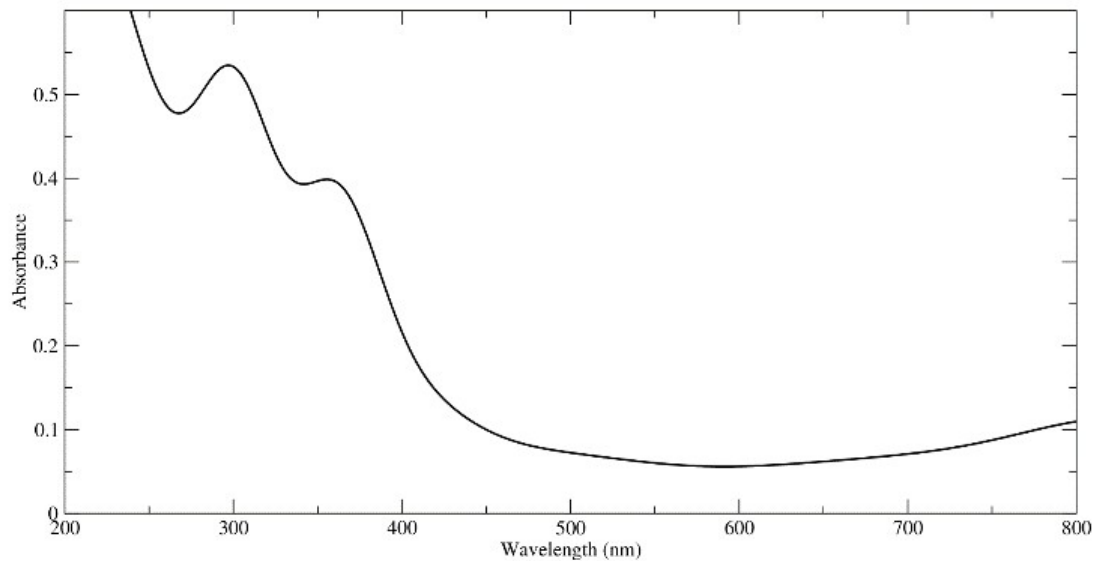


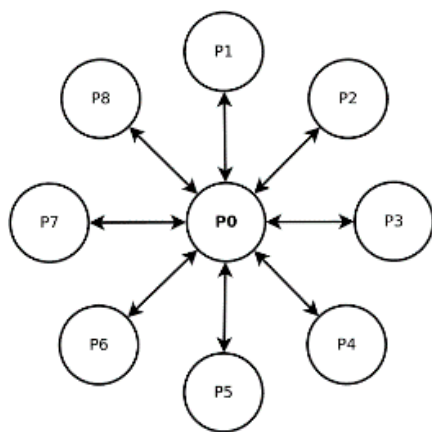
Figure 1: Full UV-Vis Spectrum of ZrO₂ Compound.

RESULTS AND DISCUSSION

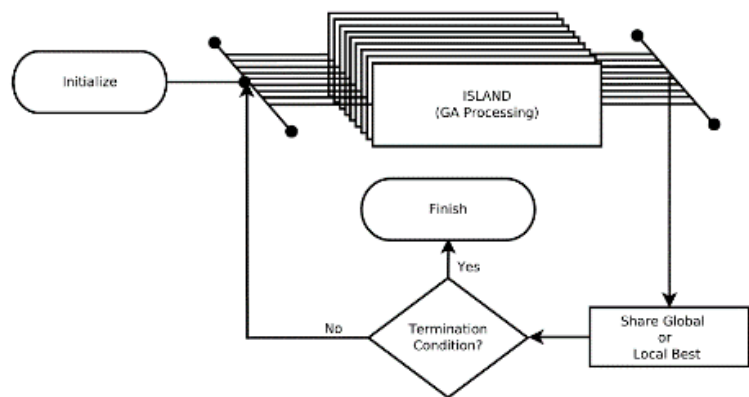
Optimization of PGA-Parameters

Our previous studies show that a centralized type of island model is the most effective one among

other types of island models (24). In this study, the shape of the island model is shown in Figure 2(a) and the flowchart for the algorithm is shown in Figure 2(b).



(a) Centralized



(b) Flowchart of Island Model

Figure 2: Selected Island Model(a) and Flowchart of Island Model(b).

Search space shrinking ratio that is narrowing the search space with this factor is important factor in GA and PGA. If this value is too low, the best solution can be missed or the algorithm called show a local minimum as the best solution. In the

case of wide search space, the algorithm will be inefficient. In the present work a search space factor of 1.9 was adequate to good convergence as shown as in Figure 3.

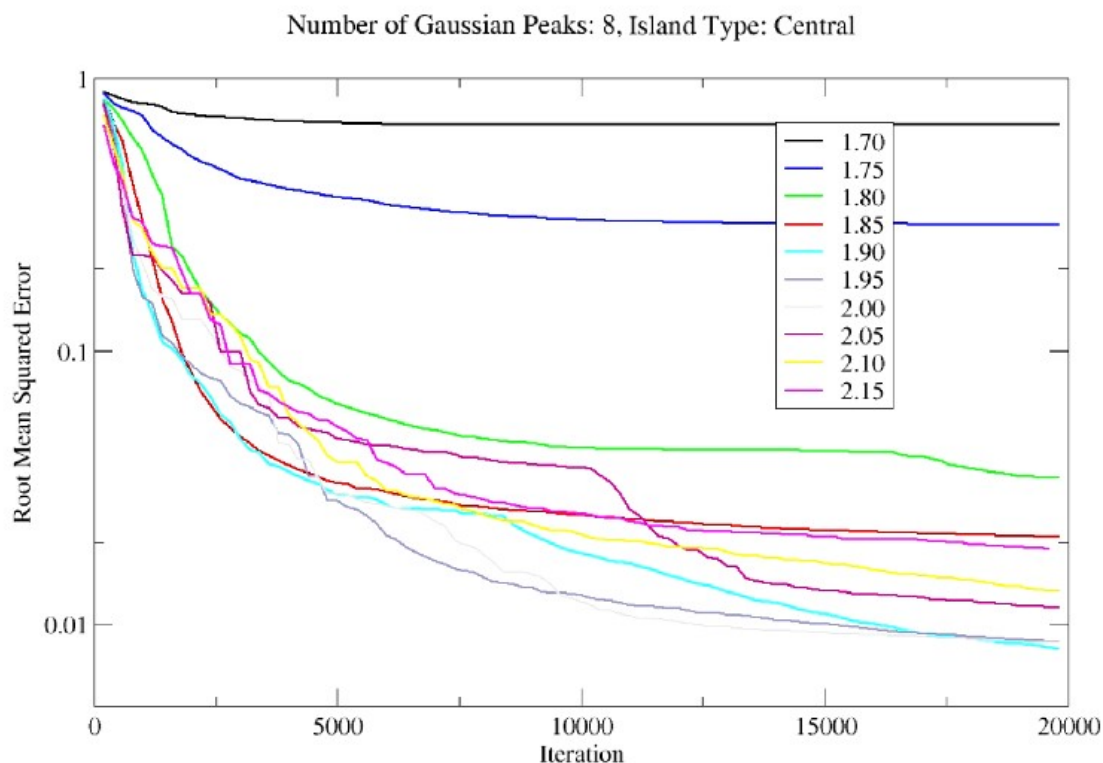


Figure 3: Effect of Search Space Factor on The Convergence of Parallel Genetic Algorithm.

The main problem is the choice of the analytical function describing the contour of the individual spectral band. Although there are many shape functions, the procedure for analysis of the overlapping bands is based on the alternative use of a Gaussian function, a Lorentzian function, or Pearson VII function. Figure 4 showed that Gaussian function most effective in UV-Vis spectra studied.

The algorithm was tested on theoretical data set. This theoretical set showed Figure 5. The spectra in Figure 5 have been calculated with 8 Gaussian functions which include wide and narrow absorption bands. Calculated data and experimental data fully coincide. Automatic detection of peaks enough success in here.

The method is based on minimizing the deviation between calculated data and real model of data. The quality of result was tested by Eq. (4).

$$RMSE = \sqrt{\frac{\sum_{j=1}^{N_p} \sum_{v} [A_j(v) - \bar{A}_j(v)]^2}{N_d}} \quad (4)$$

Where this formula's parameters are that RMSE (Root Mean Squared Error) is the square root of mean sum of squared residuals, N_p is the number of the peak, N_d is the number of the data point is data points number, A_j is the observed absorbance is observed absorbance, and \bar{A}_j is the calculated absorbance.

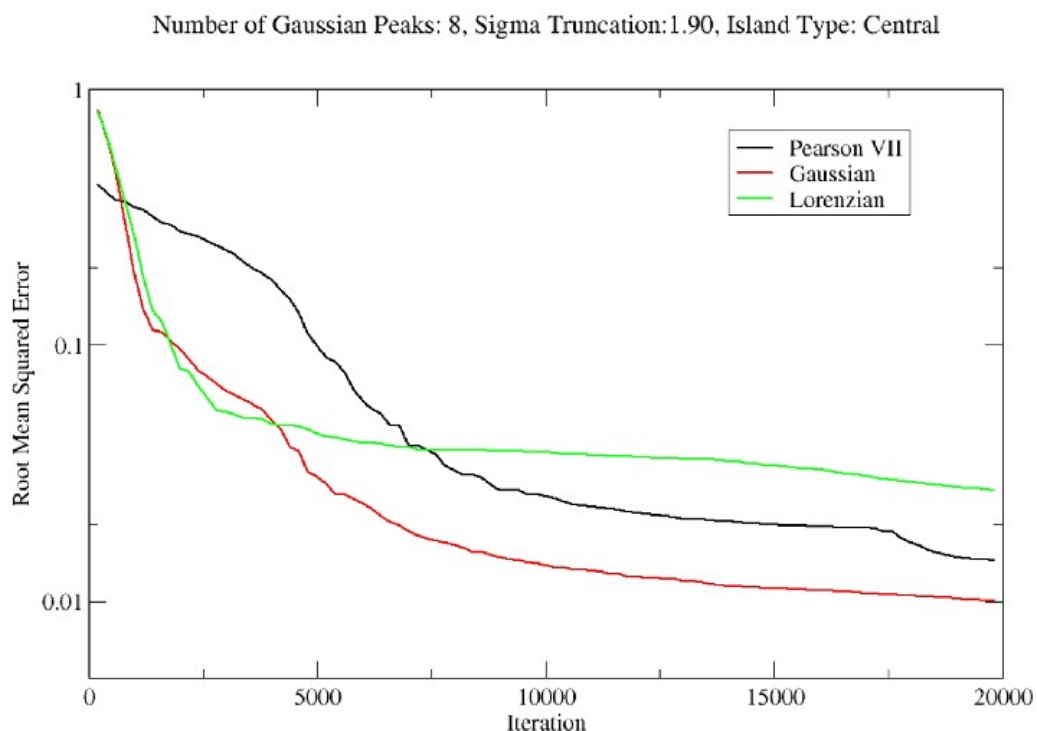


Figure 4: Comparison of Convergence of Three Peak Shapes on Parallel Genetic Algorithm.

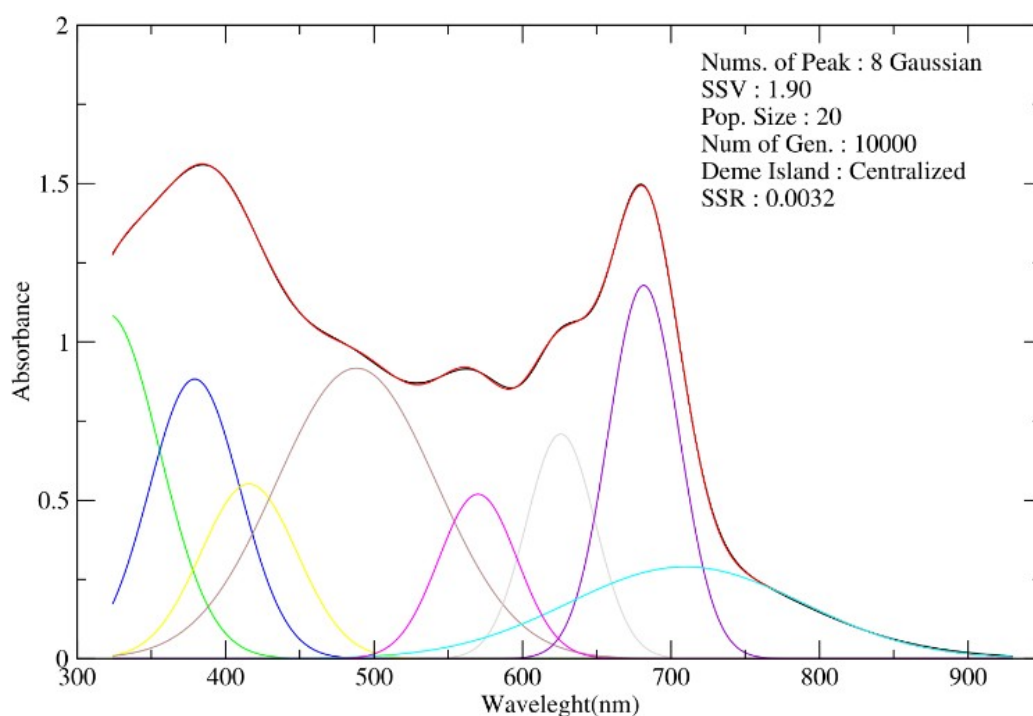


Figure 5: Deconvolution of UV-Vis spectrum of $C_{36}H_{44}FeN_4O_2$ compound.

A spectrum can be expressed with sum of peaks, which is more than the necessary number of peaks, but it cannot be represented by fewer peaks. The synthetic experimental spectrum that

includes 8 peaks was recalculated with different peak numbers and the results in Figure 6 were obtained. When it was calculated again with 8 peaks, a sudden decrease in SSR value was

observed. The minimum number of peaks that must be present in a spectrum can be easily found by using this comparison. In calculations with more peaks than necessary, you can reach the lower

SSR values, but it requires more time for computation. In addition, the positions of the peaks can be changed in every calculation.

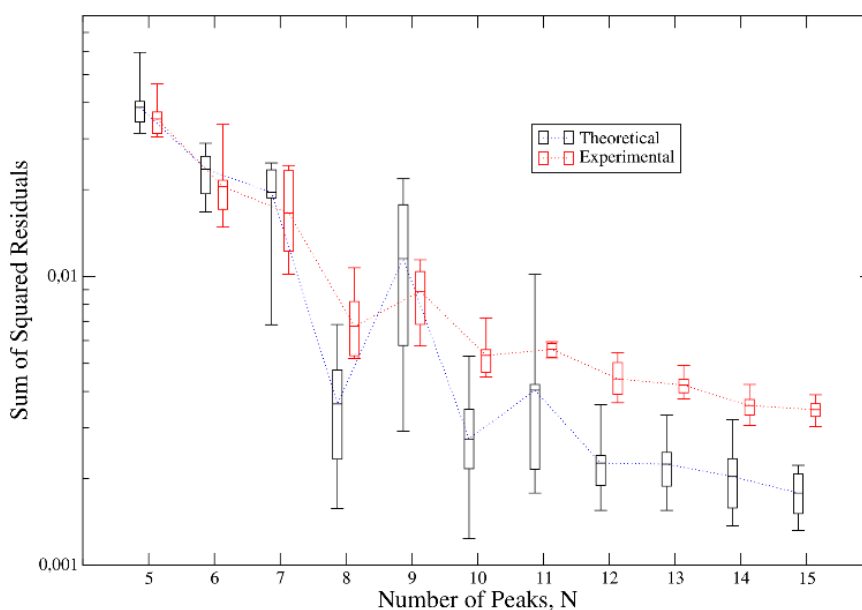


Figure 6: Number of peaks and SSR values in $C_{36}H_{44}FeN_4O_2$ compound.

Experimental Data

The experimental spectrum in Figure 12, with high levels of overlap and noise, was investigated by the proposed method.

Although the spectrum consists of 4 peaks, it is difficult to resolve these with 4 Gaussian peaks. It was resolved with 8 Gaussian peaks. If the number

of iterations is increased, value of SSR will decrease. However, the value of 0.0008 sum of squared residuals was observed to be significant enough. This result shows that a reasonable resolution can be obtained for the experimental data. In addition, this method seems to be a good tool for the resolution of the components with very similar UV-Vis spectra.

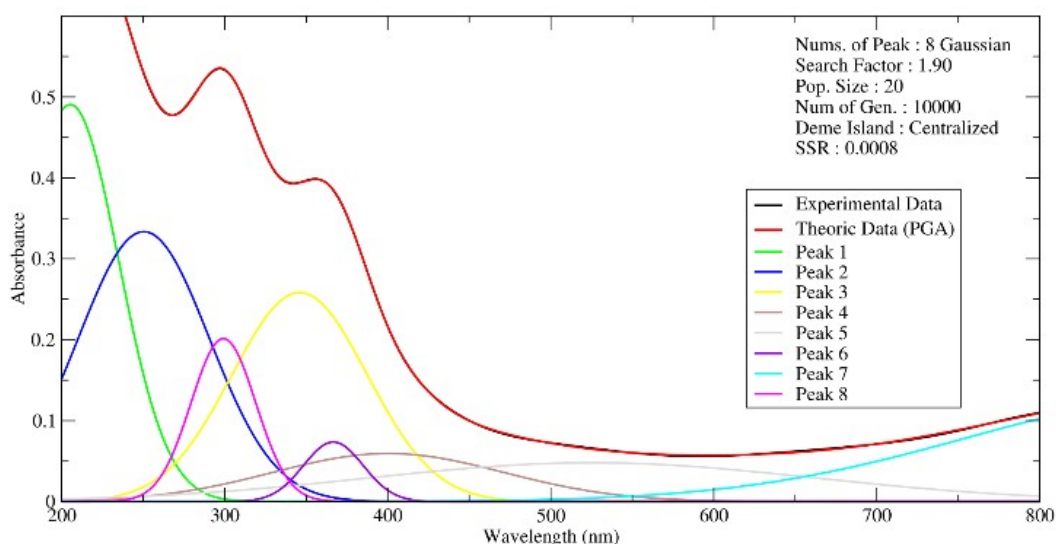


Figure 7: Deconvolution of UV-VIS Spectrum of ZrO_2 Compound.

The individual bands in UV-Vis absorption spectroscopy of ZrO₂ compound are best described with Gaussian functions using PGA. The parameters of individual peaks of ZrO₂ compound are shown in Table 1.

Table 1: Individual Peaks Parameters of UV-VIS Spectrum of ZrO₂ Compound.

Peak Number	X	Y	Half-Height Width
1	0.648942	209.548289	43.992142
2	0.249610	261.542086	38.881243
3	0.359505	300.469008	30.534187
4	0.376847	358.057764	45.094099
5	0.082054	430.533495	48.046265
6	0.039971	504.090613	57.958996
7	0.051891	623.967310	132.833099
8	0.113161	844.744351	130.713092

CONCLUSIONS

In this study, we implemented a PGA to perform curve fitting. The PGA was developed to resolve overlapping spectra with Gaussian peak shapes. The method can be used to represent all peaks of an overlapping spectrum, respectively, by optimizing the parameters of each peak. The performance of PGA was validated by the resolution of the simulated and experimental overlapping spectrum. The results showed that number of individual bands in overlap spectra in UV-VIS spectra that they are best described with Gaussian function estimated easily and the individual peaks can be correctly resolved in very highly overlapped areas. The algorithm shown is unresponsive to poor resolution or noise. In order to perform genetic algorithm accounting more quickly and effectively, we apply parallel computing models to the calculation. This application was shown to improve spectra fit and speed.

ACKNOWLEDGEMENTS

Our article was funded by Inonu University Scientific Research Project Department [Project Number: FBA-2019- 1726].

REFERENCES

- L. A. Rastrigin, The convergence of the random search method in the extremal control of a many-parameter system, *Automat. Remote Control* 24 (11), 1963, pp. 1337-1342
- J. H. Holland, *Adaptation in natural and artificial systems: an introductory analysis with applications to biology, control, and artificial intelligence*, University of Michigan Press, 1975.
- D. E. Goldberg, *Genetic Algorithms in Search, Optimization, and Machine Learning*, Addison-Wesley, 1989.
- C. B. Lucasius, G. Kateman, Application of genetic algorithms in chemometrics, in: *Proceedings of the 3rd International Conference on Genetic Algorithms*, Morgan Kaufmann Publishers Inc., San Francisco, CA, USA, 1989, pp. 170-176
- M. Karakaplan, Fitting lorentzian peaks with evolutionary genetic algorithm based on stochastic search procedure, *Analytica Chimica Acta* 587 (2), 2007 pp. 235-239
- W. D. Whitley, S. B. Rana, R. B. Heckendorn, Island model genetic algorithms and linearly separable problems, in: *Selected Papers from AISB Workshop on Evolutionary Computing*, Springer-Verlag, London, UK, UK, , 1997, pp. 109-125
- R. Wehrens, L. M. Buydens, Evolutionary optimisation: a tutorial, *TrAC Trends in Analytical Chemistry* 17 (4), 1998, pp. 193 - 203
- D. M. Deaven, K. M. Ho, Molecular geometry optimization with a genetic algorithm, *Physical Review Letters* 75 (2), 1995, pp. 288-291
- J. Zhao, R.-H. Xie, Genetic algorithms for the geometry optimization of atomic and molecular clusters, *Journal of Computational and Theoretical Nanoscience* 1 (2), 2004, pp. 117-131
- M. A. Addicoat, A. J. Page, Z. E. Brain, L. Flack, K. Morokuma, S. Irle, Optimization of a genetic algorithm for the functionalization of fullerenes, *Journal of Chemical Theory and Computation* 8 (5), 2012, pp. 1841-1851
- R. P. F. Kanters, K. J. Donald, cluster: Searching for unique low energy minima of structures using a novel implementation of a genetic algorithm, *Journal of Chemical Theory and Computation* 10 (12), 2014, pp. 5729-5737
- N. Alexandrova, A. I. Boldyrev, Search for the lin₀/+1/-1 (n = 57) lowest-energy structures using the ab initio gradient embedded genetic algorithm (gega). elucidation of the chemical bonding in the lithium clusters, *Journal of Chemical Theory and Computation* 1 (4), 2005, pp. 566-580
- M. Chen, D. A. Dixon, Tree growth hybrid genetic algorithm for predicting the structure of small (tio₂)_n, n = 213, nanoclusters, *Journal of Chemical Theory and Computation* 9 (7), 2013, pp. 3189-3200
- K. Tang, K. Man, S. Kwong, Q. He, Genetic algorithms and their applications, *IEEE Signal Processing Magazine* 13 (6), 1996 , pp. 22-37
- E. Jones, P. Runkle, N. Dasgupta, L. Couchman, L. Carin, Genetic algorithm wavelet design for signal classification, *IEEE Trans. Pattern Anal. Mach. Intell.* 23 (8), 2001, pp. 890-895
- M. Gulsen, A. E. Smith, D. M. Tate, A genetic algorithm approach to curve fitting, *International Journal of Production Research* 33 (7), 1995, pp. 1911-1923

17. P. Vankeerberghen, J. Smeyers-Verbeke, R. Leardi, C. L. Karr, D. L. Massart, Robust regression and outlier detection for non-linear models using genetic algorithms, *Chemometrics and Intelligent Laboratory Systems* 28 (1), 1995, pp. 73–87
18. H. Ahonen, P. A. de Souza Jnior, V. K. Garg, A genetic algorithm for fitting lorentzian line shapes in mssbauer spectra, *Nuclear Instruments and Methods in Physics Research Section B: Beam Interactions with Materials and Atoms* 124 (4), 1997, pp. 633–638
19. C. Lucasius, G. Kateman, Genetic algorithms for large-scale optimization in chemometrics: An application, *TrAC Trends in Analytical Chemistry* 10 (8), 1991, pp. 254 – 261
20. H. Muhlenbein, Evolution in time and space - the parallel genetic algorithm, in: *Foundations of Genetic Algorithms*, Morgan Kaufmann, 1991, pp. 316–337
21. H. Muhlenbein, M. Schomisch, J. Born, The parallel genetic algorithm as function optimizer, *Parallel Computing* 17 (67), 1991, pp. 619–632
22. C. B. Louise, M. C. Tran, T. G. Obrig, Sensitization of human umbilical vein endothelial cells to shiga toxin: involvement of protein kinase c and NF-kappaB., *Infection and Immunity* 65 (8), 1997, pp. 3337–3344
23. MPICH | high-performance portable MPI. URL <http://www.mpich.org/> (2019).
24. M. Karakaplan, F. M. Avcu, A parallel and non-parallel genetic algorithm for deconvolution of NMR spectra peaks, *Chemometrics and Intelligent Laboratory Systems* 125 (0), 2013, pp. 147 – 152



Preparation of Anti-bacterial Biocomposite Nanofibers Fabricated by Electrospinning Method

Ömer KESMEZ*  

Department of Chemistry, Faculty of Science, Akdeniz University, 07058 Antalya, Turkey.

Abstract: Developing technology and increasing the number of living creatures on Earth increase the demand for biomaterials each passing day. Recently, biocomposites and biodegradable biomaterials have begun to attract attention in many areas of use. Electrospinning technique is preferred as a quite consolidated technique in the production of outstanding polymer and/or nanofiber matrixes. However, obtained biocomposite nanofibers can cause microbiological infections during or after their usage. Therefore, it is very important that such materials have controlled antibacterial properties. In this study, Hydroxyapatite (HAp), known as biocompatible and bioactive, was firstly synthesized by wet precipitation method. Molecular structure of obtained HAp particles was researched by Fourier Transform Infrared Spectroscopy (FT-IR), its crystal structure was analyzed by X-ray Diffraction analysis (XRD) and its morphology was investigated by Scanning Electron Microscopy (SEM). HAp particles were combined with a mixture of biodegradable polylactic acid (or polylactide, PLA) and polycaprolactone (PCL) and biocomposite nanofibers were prepared by electrospinning method by loading chitosan and /or silver-based inorganic antimicrobial agent in different proportions to this composite structure. Molecular structure of PLA-PCL polymer matrix was investigated by FT-IR analysis. The obtained biocomposites are characterized morphology (SEM analysis), thermal behavior (TGA analysis) and mechanical properties. In vitro degradation test is performed to evaluate anti-bacterial biocomposite nanofibers biodegradability. The anti-bacterial efficiency of biocomposite nano-fibers containing chitosan and/or Ag⁺ in different proportions was investigated against *Escherichia coli* (Gram-negative) and *Staphylococcus aureus* (Gram-positive) bacteria. The results showed increasing mechanical properties and thermal stability. Biocomposite nano-fibers containing 1% chitosan and 0.25% Ag⁺ were found to have ≥ 4.78 log reduction and $\geq 99.99\%$ reduction in the bacterial population against the tested bacterial species and showed strong antibacterial properties. It was also observed that the combination of Ag⁺ and chitosan may show synergistic effects. The results of the study confirm the great potential of biodegradable, biocompatible and bioactive fibers for antibacterial application.

Keywords: Biopolymer, Biocomposite nano-fiber, Hydroxyapatite, Antibacterial efficacy, Electrospinning.

Submitted: July 11, 2019. **Accepted:** November 11, 2019.

Cite this: Kesmez Ö. Preparation of Anti-bacterial Biocomposite Nanofibers Fabricated by Electrospinning Method. JOTCSA. 2020;7(1):125-42.

DOI: <https://doi.org/10.18596/jotcsa.590621>.

*Corresponding author. E-mail: omerkesmez@akdeniz.edu.tr.

Tel: +90 (242) 310 2301. Fax: +90 (242) 310 2294.

INTRODUCTION

The increase in the number of people living on Earth and the increase in the proportion of the

elderly population in the society in parallel with this increase stimulates the demand for biomaterials (1). Facial trauma, bone resection due to cancer, periodontal diseases, bone

atrophy after tooth extraction cause defects on bone and other tissues as a result of various accidents and these problems often do not heal spontaneously (2). Therefore, a variety of medical devices and/or biomaterials are needed for these conditions.

Many medical technologies include the usage of synthetic materials in many fields, from materials used in surgical procedures to scaffolds for tissue engineering. Some materials used in the medical field do not show the biodegradable property (3–5). The major disadvantage of these materials is that they require removal from the implanted site by the second surgical operation. This again leads to tissue damage and recovery time (6). However, these disadvantages can be overcome by the use of biodegradable materials. The most common biodegradable materials are synthetic polyesters which are polylactic acid, polyglycolic acid, polycaprolactone or copolymers thereof (7–10). These aliphatic polyester polymers are biocompatible materials and are degraded by hydrolytic or enzymatic pathways, and this makes them suitable for medical use. Furthermore, the biodegradation rate and mechanical properties can be varied depending on the polymer composition and concentration of the components (11,12).

Polylactic acid (or polylactide, PLA) and polyglycolide (or poly(glycolic acid), PGA) have glass transition temperatures (T_g) above room temperature and this makes them hard and brittle. However, polycaprolactone (PCL) is a crystal and has a low glass transition temperature, so is tough but has a modulus an order of magnitude smaller than PLA (13). However, these independent features cannot provide ideal conditions for all applications. In order to eliminate the disadvantages of properties of the material, the properties of the obtained materials must be adjustable. The mechanical properties of the polymers are characterized as a competition between elastic and plastic deformation and the preparation of different polymer mixtures is among the alternative methods for adjusting the material properties obtained. The new polymer mixture obtained by combining polymer structures with different properties provides the possibility of obtaining new polymers with different properties depending on the mechanical properties of the components and the microstructure of the mixture and the interface between the phases. In addition to the interface and mixture microstructure between these polymer mixtures and the phases, different properties can be obtained which depend

precisely on the mechanical properties of the components (14–17).

Most natural materials are composites of inorganic and organic components arranged in complex structures. The bone is composed of collagen matrix (organic) strengthened with hydroxyapatite (HAp) (inorganic). Bone cells, in other words, osteoblasts, osteocytes, osteoclasts, and osteoprogenitor cells are present in and around the matrix. While bioactive materials bind physically and chemically to the bone, a bioabsorbable material is slowly absorbed, ideally substituted by new bone formation. In addition, osteoconductive materials (such as calcium orthophosphate) are suitable for adherence, growth, proliferation and spread of bone cells, while osteoinductive materials (such as hydroxyapatite) are effective in the growth and maturation of primitive stem cells or immature bone cells. Also, the inorganic part in the organic matrix not only improves the mechanical properties of the obtained materials but also supports the physical environment (18–20).

Many methods have been developed to synthesize HAp particles. Some of these are precipitation method (21–23), sol-gel method (24,25), hydrothermal technique (26), emulsion technique (27), biomimetic precipitation (28,29) and electrophoretic precipitation (30). Among these methods, the sol-gel allows controlling the purity, composition, and size of the particles to be produced at the molecular level. The crystallization of the amorphous particles produced in this method may require a high temperature. The thermal treatment required for the production of particles having a crystal structure is not required in the hydrothermal method which is operated at high pressure (31).

In recent years, electrospinning method is one of the production methods that are frequently used in the production of tissue scaffolds (32). The length, width, orientation and total porosity of the nanofibers having submicron fineness can be adjusted to the extent expected by this method. Thus, it is provided to form three-dimensional structures very similar to the extracellular matrix form by arranging these fibers dispersedly side by side and on top of each other. Situations such as the fact that as the surface properties become more functional as the diameter of polymer fibers become smaller, increasing in mechanical performance, providing high porosity and high surface area, which are important in terms of tissue engineering emerge (33). In addition, the fact

that it requires a small amount of raw material in the studies carried out by the electrospinning method provides superiority in terms of production. It is also possible to accelerate tissue formation by biological factors that can be added during or after the electrospinning process (34,35).

Most of the biocompatible and biodegradable polymers can be obtained by electrospinning (36). However, many devices can often cause bacterial infections (37). Also, infection of the treatment site should be prevented so that the trauma in the areas of usage of the biomaterials can be eliminated as soon as possible and the wound closes quickly. For this purpose, antibiotic treatment is applied before and after the operation. However, there are also cases where infection develops. The presence of infections can be a serious challenge in the tissue engineering process. The materials obtained in order to minimize these and similar conditions can be gained anti-bacterial (AB) properties. In particular, the use of drug release composites for implant coating is effective in the prevention and treatment of these infections and diseases (38,39).

Antibacterial agents can be classified as inorganic and organic, and the anti-bacterial materials described in the literature include direct impregnation with antibiotics and the use of silver or antibiotic-coated polymer layers. Silver-based anti-microbials have attracted attention due to their non-toxicity for mammalian cells and the anti-microbial effect of silver ions. The addition of Ag^+ ions into polymeric materials has been used extensively for several years. Ag^+ layer decreased infections especially in urinary and venous catheters (40–42). In addition, the antibacterial property can be obtained from natural materials. Chitosan is obtained by deacetylation of chitin which is obtained from shrimp shells (43). Chitosan is widely used in wound treatment. Also, it can be sorted as medical artificial skin, surgical sutures, anti-fungal, anti-bacterial effects, etc. and in-vivo tests have shown that chitosan does not have any adverse effects to the human body (44).

In this study, bioactive Hap particle prepared by wet precipitation method was added to the biodegradable organic PLA / PCL blend to form a composite structure and fiber was obtained by electrospinning method by adding different ratios of various antibacterial agents. The chemical structure of HAp particle obtained by precipitation method was investigated by Fourier Transform Infrared Spectroscopy (FT-IR), its crystal structure was examined by X-ray

Diffraction and its morphology was analyzed by Scanning Electron Microscopy (SEM). The molecular structure of the obtained polymer was analyzed by FT-IR analysis. Morphology of biocomposite nanofibers was examined by SEM. Antibacterial efficiencies were investigated against *Staphylococcus aureus* (Gram-positive) and *Escherichia coli* (Gram-negative) by ASTM: E2149-01. In addition, the obtained biocomposites were characterized thermal behavior, mechanical properties, and in vitro degradation test. In particular this study involves setting up anti-bacterial agent parameters in order to achieve an anti-bacterial biocomposite nano-fiber materials to be used various area. Electrospinning process has been investigated by authors in the literature demonstrate that electrospinning process is very important for polymer and their properties. In consequence, according to the author it is important to add their contribution to the literature on the topic, and a novel anti-bacterial biocomposite nano-fiber is suitable for further studies as an alternative material for tissue engineering.

EXPERIMENTAL SECTION

Materials

The poly(lactic acid) (PLA, 6252D, $M_w = 150.000$ (45)) was obtained from Nature-works Co., Ltd. (USA) and the Polycaprolactone (PCL, average M_w 80.000) was obtained from Aldrich. Both polymers were used as received. Chloroform (analytical grade) was supplied by Merck and used without further purification. Diammonium hydrogen phosphate ($(NH_4)_2HPO_4$, Merck), calcium nitrate tetrahydrate ($Ca(NO_3)_2 \cdot 4H_2O$, Merck), ammonium hydroxide (NH_4OH , Merck) were used for the HAp powder synthesis. All reagents were of analytical reagent grade and used without further purification. Deionized water was used in all synthetic steps. Chitosan (Sigma-Aldrich), silver-based inorganic antimicrobial agent (2.5 wt% Ag^+ , AJ10N, Sinanen Zeomic Co. Ltd.) were used as anti-bacterial agents.

Preparation of HAp powder and biocomposite solution, electrospinning process

Hydroxyapatite nanoparticles were synthesized by the wet chemical method (46). 200 mL 3 M diammonium hydrogen phosphate was stirred in a beaker at room temperature and 200 mL 5 M calcium nitrate tetrahydrate was added drop wise over 2 h. The pH of the system was maintained at 10.8 throughout the stirring process, by using 25% NH_4OH solution. The mixture was allowed to remain stirred overnight. A white precipitate was formed. A

milky and somewhat gelatinous precipitate was held at 100 °C for 12 h in the oven followed by calcination at 750 °C for 8 h. The prepared powder was used for further characterization. The schematic presentation of the procedure is

given in Figure 1. This precipitation reaction for the synthesis of hydroxyapatite nanoparticles was first proposed by Yagai and Aoki, as indicated by Bouyer et al. (2000).

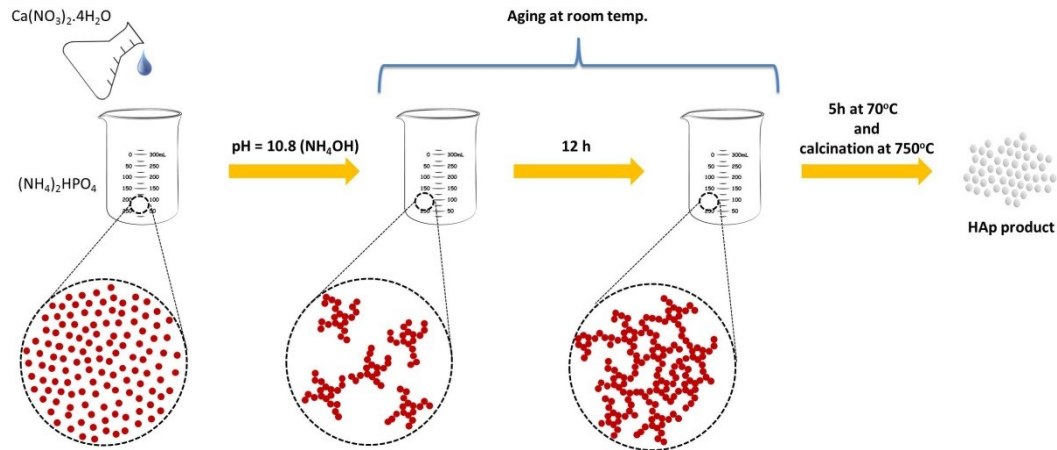


Figure 1: Flowchart of hydroxyapatite powder preparation by wet chemical method.

The required amounts of PLA and PCL were dissolved in chloroform. The PLA solution was then transferred into the PCL solution drop wise with continuous stirring. After all the PLA solution was transferred into the PCL solution, the resultant mixture was then stirred for 1 h. PLA and PCL blends were prepared with a total polymer mass fraction of 10%. The required prepared HAP was then added into the dissolved PLA/PCL blend in the small portion. The mixture was then ultrasonically stirred for 15 min to make sure that the HAP particles fully dispersed in the organic solution. In the next step, chitosan and/or Ag^+ (as AJ10N) were added and stirred for 1 hour. Each final nanofiber solutions were designed as shown in Table 1. Then, the nanocomposite nanofibers were produced by an electrospinning method.

Electrospinning was performed using an Inovenso, NE300 model Electrospinning Machine. A high voltage supply was used to generate an electric field, in the range 20–25 kV between needle and collector. The biocomposite solution was placed in a 10 mL syringe and a pump system was used to feed the solution through the needle at 5 mL/h flow rates. The needle was set up vertically in the spinneret. The collector was a rectangular copper plate covered with aluminum foil and located 15 cm from the needle tip and electrospinning time of 30 min were used. The electrospinning process was performed at room temperature (25 °C) and controlled humidity value (~50% R.H.).

Table 1. Composition of organic-inorganic biocomposite materials.

Sample	w/w content in the biocomposite nanofiber mixture					
	Organic matrix			Inorganic matrix	AB Agent, % in solid	
	PLA	PCL	Chloroform	HAp	Chitosan	Ag ⁺
PLA-PCL				-	-	-
CF-0					-	-
CF-1C					1.00	-
CF-2.5C					2.50	-
CF-5C					5.00	-
CF-0.25A					-	0.25
CF-0.5A	4	6	90	1	-	0.50
CF-1A					-	1.00
CF-2.5A					-	2.50
CF-5A					-	5.00
CF-1C-0.25A					1.00	0.25
CF-2.5C-0.25A					2.50	0.25
CF-1.5C-0.25A					1.00	0.50

Characterization

Structural characterization and functional groups identification of the obtained HAp particle was done using Fourier Transform Infrared Spectroscopy (FT-IR) analyses with a Tensor 27 model spectrophotometer. X-ray Diffraction (XRD) patterns were collected using Bruker Axs d8 advance model XRD. The morphological pattern of granules was observed using a Scanning Electron Microscope (ZEISS-LEO 1430 SEM equipment).

The FTIR spectra of the organic matrix were recorded on Tensor 27 model spectrophotometer at ambient temperature. The sample was scanned at 16 scans at wavenumber range of 400-4000 cm^{-1} . The morphological aspect of the biocomposite nanofibers was measured by a scanning electron microscope (ZEISS-LEO 1430 SEM equipment). Thermogravimetric analysis (TGA) of the obtained samples was performed by using a Seiko SII TG/DTA 7200 thermogravimetric analyzer. The tests were run from 30 to 800 $^{\circ}\text{C}$ with a heating rate of 10 $^{\circ}\text{C}/\text{min}$ under a nitrogen atmosphere. Tensile test was carried out on Shimadzu Autograph AGS-X series at ambient environment. The specimens were cut into approximate dimensions of 65 mm \times 10 mm. The cross head speed was 10 mm/min and load applied was 10 N/ mm^2 . In vitro degradation studies were carried out in a simulated bodily fluid (SBF) at 37 $^{\circ}\text{C}$. SBF solution was prepared with the reagents NaCl, NaHCO_3 , KCl, $\text{K}_2\text{HPO}_4 \cdot 3\text{H}_2\text{O}$, $\text{MgCl}_2 \cdot 6\text{H}_2\text{O}$, $\text{CaCl}_2 \cdot 2\text{H}_2\text{O}$ and Na_2SO_4 into distilled water (47). Samples were immersed in SBF solution for time periods of 144, 288, 432, 576 and 720

hours. Before the weight losses were determined, the samples were extracted from the SBF solution, and left to dry at room temperature to a stable mass. Three samples were measured for the obtained weight loss value. The modified American standard ASTM: E2149-01 was used to investigate the antibacterial activity by using facultative gram-negative *Escherichia coli* (*E. Coli*, ATCC 11775) and gram-positive *Staphylococcus aureus* (*S. aureus*, ATCC 25923).

RESULTS AND DISCUSSION

Hydroxyapatite powder

The wavenumber of the peaks observed in the FT-IR spectrum of the wet chemically precipitated HAp powder in Table 2 are reported as details about which types of vibration they are and to which organic groups they belong.

The FT-IR spectrum showed a characteristic peak of hydroxyapatite in Figure 2; the stretching and bending vibrations of water (corresponded to adsorbed water) were observed at 3448 cm^{-1} and 1644 cm^{-1} wavenumbers, respectively. The peaks appeared at 3572 cm^{-1} and 636 cm^{-1} wavenumbers, respectively, was corresponded to the stretching and bending vibrations of the (OH⁻) ions in the molecular structure of HAp. Characteristic bands that belong to the (PO₄³⁻) ions were detected at 1096 cm^{-1} , 1036 cm^{-1} , 962 cm^{-1} , 604 cm^{-1} , 596 cm^{-1} wavenumber values (22,48). These results confirm the synthesis of HAp structure.

The peaks in the XRD spectra (Figure 3)

demonstrated that hexagonal hydroxyapatite (HAp, syn., $\text{Ca}_5(\text{PO}_4)_3\text{OH}$) phase with COD 9011092 card number exist in the sample. The obtained results with narrow and sharp peaks are the signs of well-developed crystals.

Table 2. FTIR wavenumbers and observed assignments of HAp powder.

Assignments	Observed peak (cm^{-1})	Definition
ν^s -OH	3572	OH ⁻ structural
ν_{as} H ₂ O	3448	Stretching vibrations of H ₂ O
δ H ₂ O	1644	bending vibrations of H ₂ O
ν_{as} P-O	1096	PO ₄ bending
ν_{as} P-O	1036	PO ₄ bending
ν^s P-O	962	PO ₄ tension
ν^s -OH	636	OH structural
δ O-P-O	604, 596	PO ₄ of bending

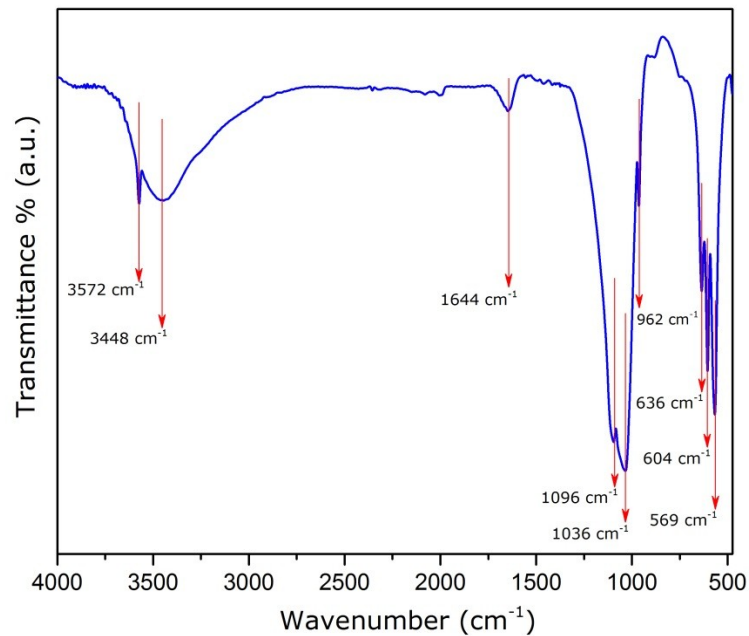


Figure 2: FT-IR spectrum of the hydroxyapatite powder sample.

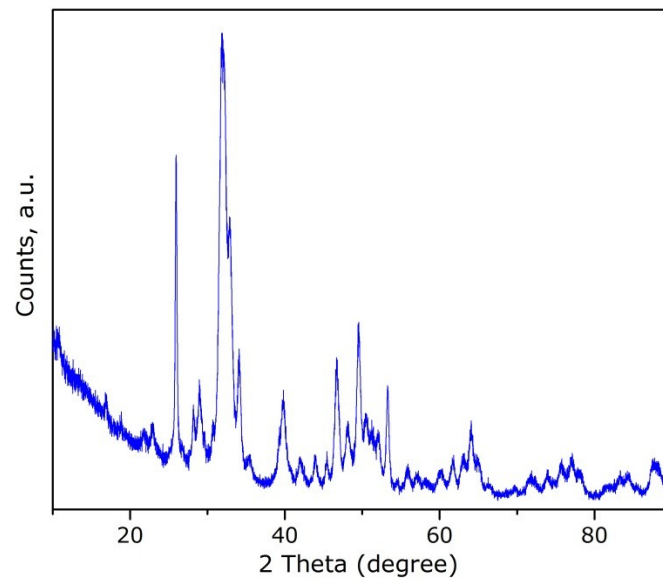


Figure 3: XRD results of the hydroxyapatite powder sample.

Scanning Electron Micrograph (SEM) of the obtained HAp is shown in Figure 4. As can be seen from the morphologies of particles, there is a distribution of small particles and large

agglomerates. The particle size ranged between 1 and 15 μm (120 particles were measured). These agglomerates consist of fine particles.

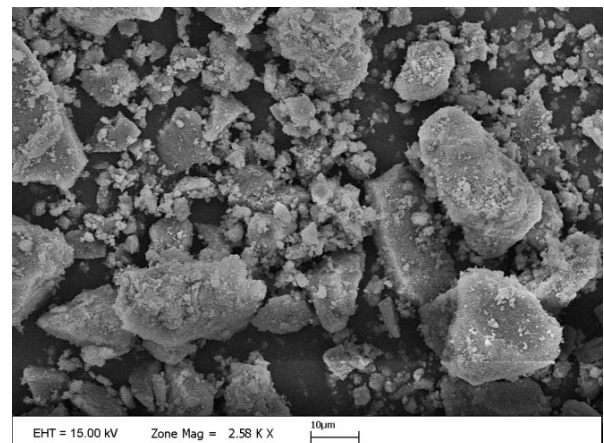
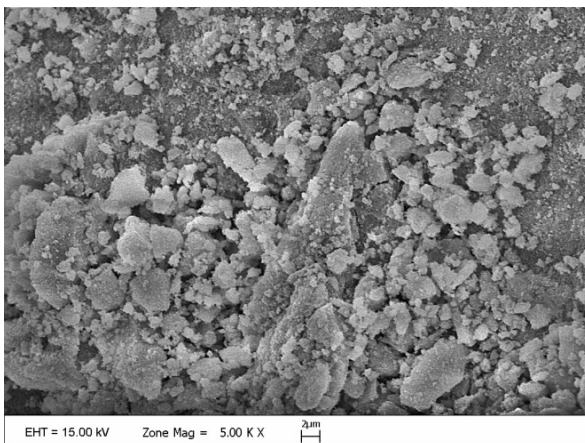


Figure 4: SEM images of the hydroxyapatite powder sample.

Organic matrix and biocomposite materials FT-IR analysis gives information on the molecular structure of the PLA, PCL and PLA/PCL blends.

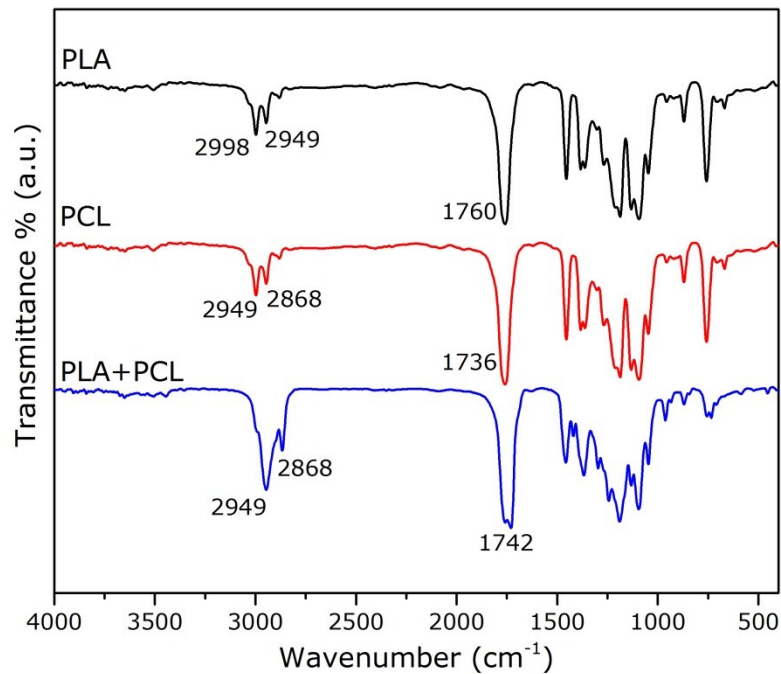


Figure 5: FTIR spectra of PLA, PCL, PLA/PCL blend.

The FT-IR spectrum of the polymer (Figure 5) shows peaks in the 3000–2900 cm^{-1} and 1760 cm^{-1} of PLA and 2949, 2869 and 1736 cm^{-1} of PCL range due to CH (CH_2 and CH_3) stretching and due to ester $-\text{C}=\text{O}$ group stretching, respectively. In the PLA/PCL blend, these peaks were found in the neutralized regions of 2949, 2868 and 1742 cm^{-1} .

Figure 6 shows SEM images of electrospun ultrafine biocomposite nanofibers. The diameter of the obtained electrospun nanofibers was around 172 ± 90 nm. It was observed that HAp was homogeneously formed on the nanofiber material. The SEM results suggest that HAp particles can be homogeneously incorporated with PLA+PCL matrix.

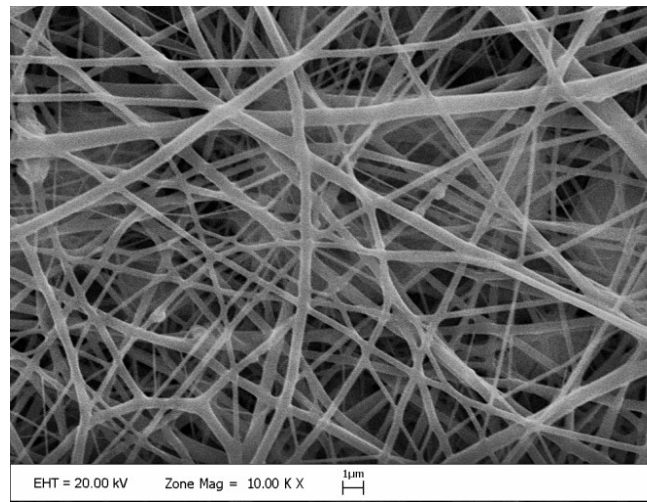
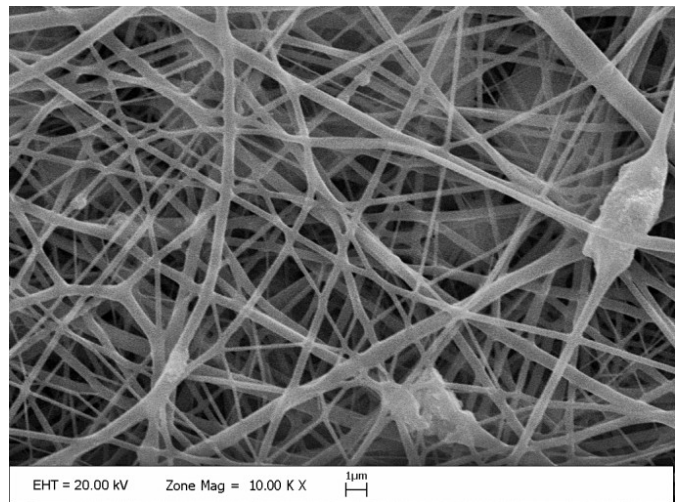
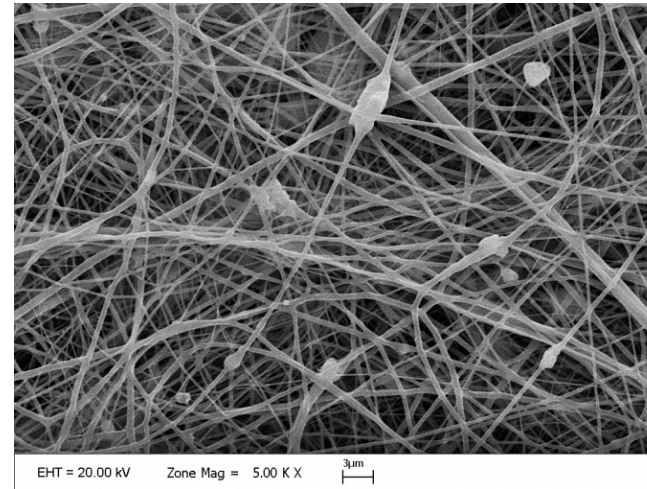
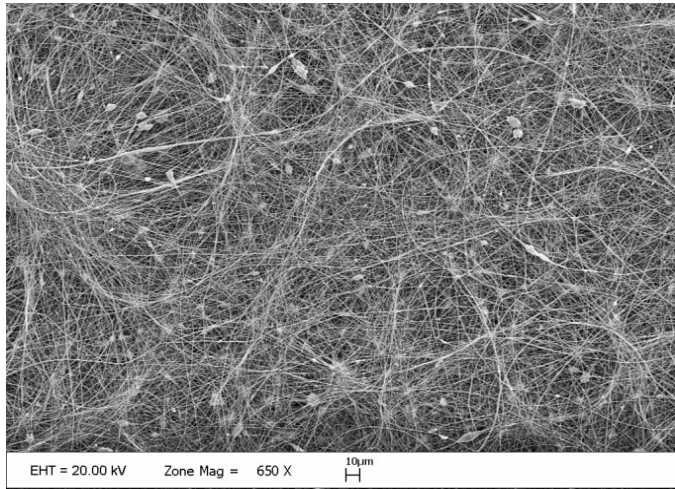


Figure 6. SEM images of the biocomposite nanofibers containing Hap.

The thermal properties of the samples were evaluated with the TGA analysis. When we examine the TGA and differential thermogravimetric (DTG) thermograms for the sample PLA/PCL, CF-0 and CF-1C-0.25A given in Figure 7, the main weight loss for PLA/PCL organic matrix was observed in the temperature range 265 °C – 456 °C due to the decomposition of polymer structure. The residual mass might due to PCL, which may not completely decompose over 700 °C. The DTG curve of PLA/PCL organic matrix follows a two-stage at 367°C and 411°C respectively, consistent with the result shown in the literature (49,50). The degradation temperature of the composite sample for the sample CF-0 increase with the adding of HAP to the PLA/PCL

organic matrix, the decomposition of the sample CF-0 starts at around 279 °C and completes at 462 °C the DTG curve of the sample CF-0 shows a two-stage thermal decomposition at 372 °C and 415 °C. The degradation temperature of the AB composite sample for the sample CF-1C-0.25A increase with the adding of HAP and AB agents to the PLA/PCL organic matrix, the decomposition of the sample starts at around 301 °C and completes at 463 °C the DTG curve of the sample shows a two-stage peak at 376 °C and 416 °C. The temperature of the main degradation is shifted towards a higher value when HAP and HAP/AB agents are used compare to the PLA/PCL organic matrix (51).

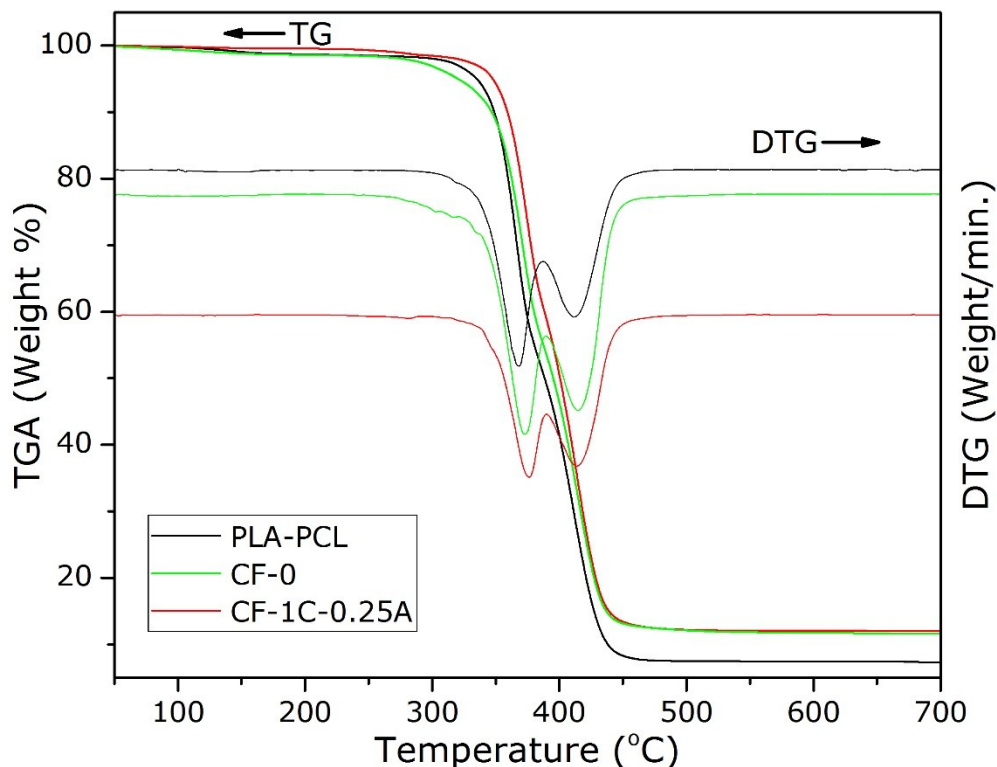


Figure 7: Thermo-gravimetric analysis (TGA) thermograms for the samples.

According to the literature Hap particle which is thermally stable up to 1300 °C (52). Therefore, the residual mass remaining in these samples were assigned to the Hap particle and AB agents. 10 wt.% HAP particle and 10 wt.% HAP particle, 1 wt.% chitosan, and 0.25 wt.% Ag were added to PLA/PCL organic matrix during the preparation of sample CF-0 and CF-1C-

0.25A, respectively. According to the obtained results of the TGA measurement, it was detected that the percentage of residual in sample CF-0 and CF-1C-0.25A were 11.25 and 12.06 wt. %, respectively (Table 3), which is in accordance with their initial addition. In this case, the content of HAp particle and AB agents in the final composite samples can be precisely

manipulated with predetermined HAp particle solution to fabricate fibers through and AB agents concentrations in the mixed electrospinning.

Table 3. Thermal analysis results for the samples.

Sample	Weight Loss Temperature (°C)			Residual (%)
	T _{10%}	T _{30%}	T _{50%}	
PLA-PCL	342	366	387	5.25
CF-0	347	371	395	11.75
CF-1C-0.25A	359	378	401	12.06

In Table 3 the results obtained from the TGA curves of Figure 7 are summarized. The temperature corresponding to the degradation of 10 – 30 and 50 wt. % of the samples (T_{10%}, T_{30%}, T_{50%}) is higher than for the sample PLA-PCL, indicating that the HAP particle and AB agents addition improve the thermal stability of PLA-PCL organic matrix. In order to determine the mechanical properties of the obtained samples, tensile strength and

elongation at break tests were performed. Tensile strength value of the sample PLA-PCL and CF-0 were 21.20 and 24.54 MPa respectively. As it can be observed in Figure 8, the addition of HAP particle leads to a clear change in the fracture behavior of PLA-PCL. In addition, there was not a noticeable difference in tensile strength and elongation at break between the sample CF-0 and CF-1C-0.25A containing AB agents.

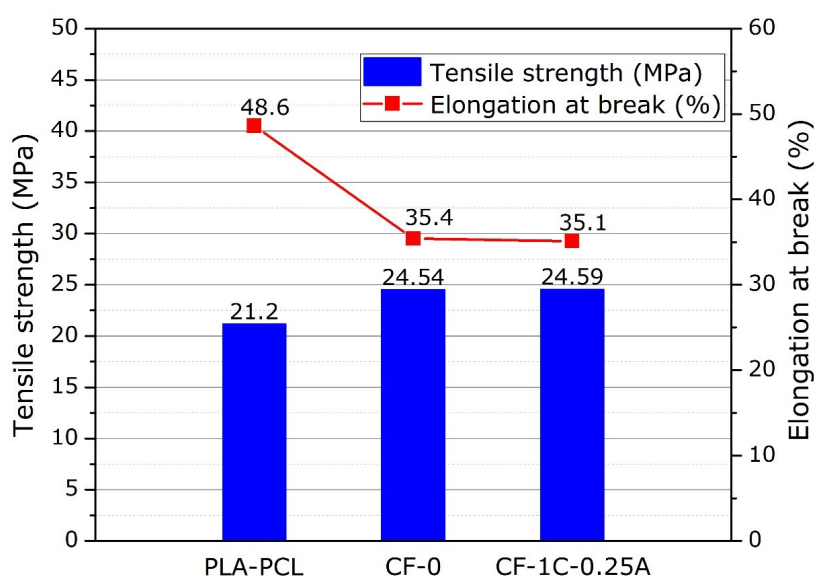


Figure 8: Results of the tensile strength and elongation-at-break of the samples.

It is known from the literature that PCL degradation time can be 12 or 24 months, according to its molecular weight, while PLA degradation time can be from 15 days up to 6 months, according to its molecular weight (53). The changes in weight loss of the samples as a function of degradation time in SBF are shown in Figure 9. After 144-hour of immersion in SBF, the mass loss was less than 2% for the sample PLA-PCL, less than 3% for the samples CF-0

and CF-1C-0.25A. After 720-hour of immersion in SBF, a linear mass loss was observed for all the samples. The highest weight loss was determined for CF-0 and CF-1C-0.25A whereas the lowest for the sample PLA-PCL. According to the obtained results, degradation rate of the biocomposite samples increased with HAP particle and AB agents added to PLA-PCL organic matrix.

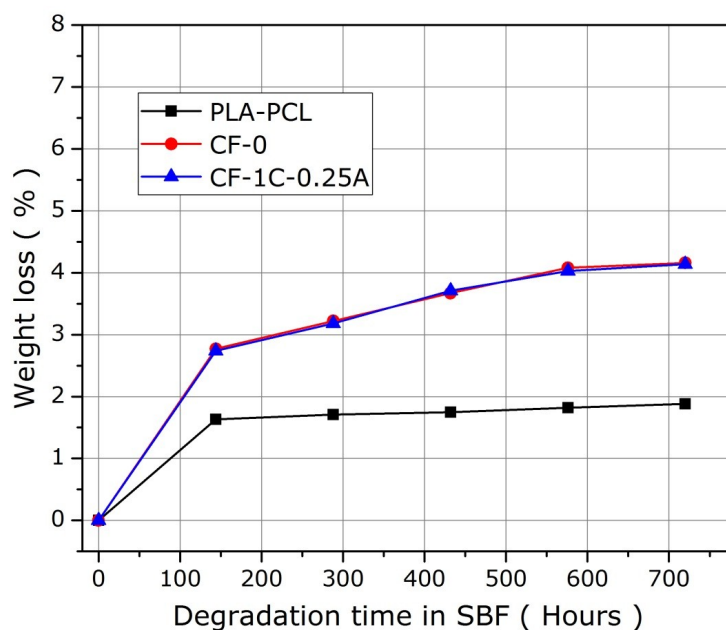


Figure 9: Weight loss of the samples as a function of degradation time in SBF solution.

According to the modified E2149-10 standard, anti-microbial tests were performed at 12 and 24 hour contact times. An obtained average reduction of colony formation unit (CFU) and Log reduction for *E.coli* and *S.aureus* bacteria samples were shown in Tables 4 and 5, and change of % reduction in bacteria population compared to anti-bacterial agent were shown in Figure 10 and visual results were presented in Figure 11. Anti-bacterial efficiency was investigated by adding different amounts of chitosan and/or Ag^+ to the biocomposite structure prepared as anti-bacterial agent. Increased rates of both AB agents increased the antibacterial effect.

The sample containing 5% chitosan provided a reduction in the bacterial population of up to 60% at the end of 24 hours against both bacterial species, while similar results could be achieved in the sample containing 0.25% Ag^+ under the same conditions. In the biocomposite

sample containing 1% Ag^+ , an effective AB property is achieved and a decrease in the 99.99% bacterial population is observed.

The biocomposite nanofibers containing chitosan inhibit the growth of bacterial populations considering AB efficiency and show that chitosan has a bacteriostatic effect compared to Ag^+ .

It was found that samples containing 1% chitosan and 0.25% Ag^+ separately reduced bacterial populations at the end of 12 hours by 2.5% and 40%, respectively. However, it was determined that composite nanofibers prepared by using these amounts of AB agents together, decreased at the end of the same period in approximately 80% bacterial population. It was concluded that both AB agents were in compliance with each other and had effects on test bacteria with a synergistic interaction.

Table 4: Anti-Bacterial activity against *E. coli* of biocomposite nanofibers.

Sample	Initially (CFU/ mL)	<i>Escherichia coli</i>					
		After 12h			After 24h		
		(CFU/ mL)	Average Reduction, Log ₁₀	Average CFU Reduction, %	(CFU/ mL)	Average Reduction, Log ₁₀	Average CFU Reduction, %
Control, Blank		8.85x10 ⁷	-	-	2.17x10 ⁸	-	-
CF-0		8.52x10 ⁷	-	-	2.11x10 ⁸	-	-
CF-1C		1.19x10 ⁶	0.01	2.46	8.50 x10 ⁵	0.16	30.32
CF-2.5C		1.09x10 ⁶	0.05	10.83	6.10x10 ⁵	0.30	50.00
CF-5C		0.77x10 ⁶	0.20	36.89	4.68x10 ⁵	0.42	61.64
CF-0.25A		0.72x10 ⁶	0.23	40.98	4.24x10 ⁵	0.46	65.25
CF-0.5A	1.22x10 ⁶	0.49x10 ⁶	0.40	59.84	3.48x10 ⁵	0.54	71.48
CF-1A		0.59x10 ⁵	1.32	95.16	< 20	4.78	>99.99
CF-2.5A		< 20	4.78	>99.99	< 20	4.78	>99.99
CF-5A		< 20	4.78	>99.99	< 20	4.78	>99.99
CF-1C-0.25A		2.93x10 ⁵	0.62	75.98	< 20	4.78	>99.99
CF-2.5C-0.25A		2.43x10 ⁵	0.70	80.08	< 20	4.78	>99.99
CF-1C-0.5A		9.65x10 ⁴	1.10	92.09	< 20	4.78	>99.99

Table 5: Anti-bacterial activity against *S. aureus* of biocomposite nanofibers.

Sample	Initially (CFU/ mL)	<i>Staphylococcus Aureus</i>					
		After 12h			After 24h		
		(CFU/ mL)	Average Reduction, Log ₁₀	Average CFU Reduction, %	(CFU/ mL)	Average Reduction, Log ₁₀	Average CFU Reduction, %
Control, Blank		7,25x10 ⁷	-	-	1.98x10 ⁸	-	-
CF-0		6,92x10 ⁷	-	-	2,03x10 ⁸	-	-
CF-1C		1.35x10 ⁶	< 0.01	2.17	1.02x10 ⁶	0.13	26.09
CF-2.5C		1.26x10 ⁶	0.04	8.70	0.70x10 ⁶	0.29	49.28
CF-5C		0.90x10 ⁶	0.19	34.78	0.54x10 ⁶	0.41	60.87
CF-0.25A		0.83x10 ⁶	0.22	39.86	0.52x10 ⁶	0.42	62,32
CF-0.5A	1.38x10 ⁶	0.61x10 ⁶	0.35	55.80	0.37x10 ⁶	0.57	73.19
CF-1A		0.15x10 ⁶	0.96	89.13	< 20	4.84	>99.99
CF-2.5A		< 20	4.84	>99.99	< 20	4.84	>99.99
CF-5A		< 20	4.84	>99.99	< 20	4.84	>99.99
CF-1C-0.25A		0.40x10 ⁶	0.54	71.01	< 20	4.84	>99.99
CF-2.5C-0.25A		0.27x10 ⁶	0.71	80.43	< 20	4.84	>99.99
CF-1C-0.5A		0.12x10 ⁶	1.06	91.30	< 20	4.84	>99.99

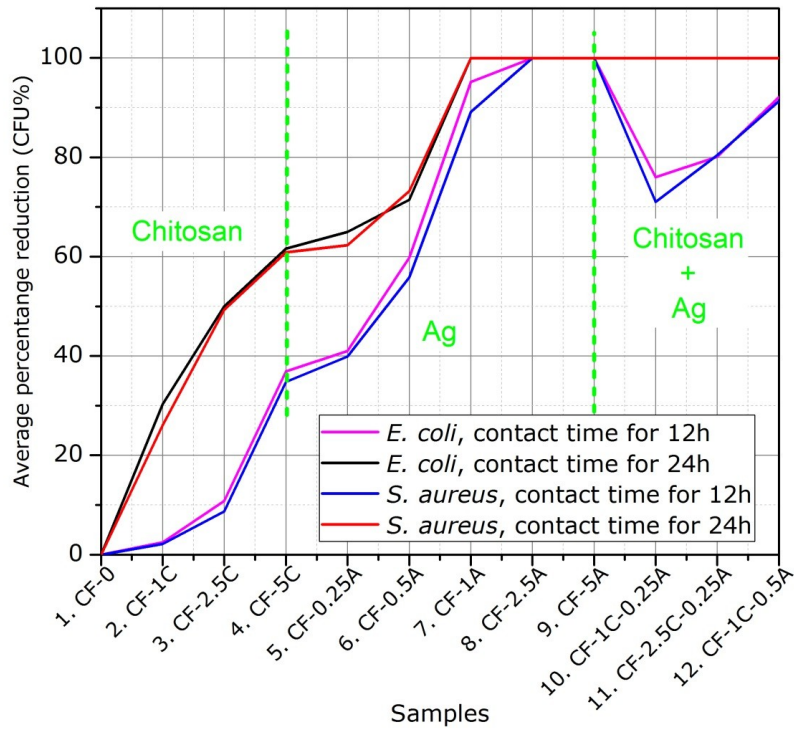


Figure 10: According to the contact time, the percentage of CFU reduction graph for biocomposite nanofibers against *E. coli* and *S. aureus*.

Figure 11 shows the respective 90 mm plates of the CF-0 and CF-1C-0.25A samples antimicrobial activity after 24 h of incubation for *S. aureus* and *E. coli* (from the diluted test solution). Each white round dot in the

photographs shows a CFU. Biocomposite samples containing anti-bacterial agent suppressed the growth of the bacterial population compared to the control group and eliminated live bacteria.

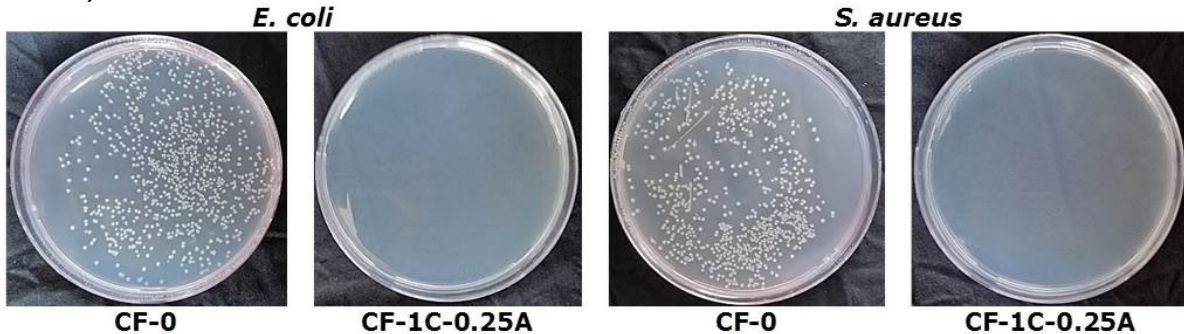


Figure 11: Antibacterial activity for *E. coli* and *S. aureus* (from the diluted test solution) in the Petri dishes.

CONCLUSION

In this study, HAp particles synthesized by wet precipitation method were added to biodegradable PLA/PCL matrix and biocomposite nano-fibers were prepared by providing anti-bacterial properties with chitosan and/or Ag⁺. The efficiencies of *E. coli* and *S. aureus* bacteria at different contact times depending on the type and amount of AB agent were investigated in detail and efficient AB agent amounts were determined. AB efficiency has been carried out from antic times to the present and it has been found that there is a synergistic effect in the use of Ag⁺, chitosan, in which a broad spectrum of AB features and bacterial species do not gain immunity. Thus, the decrease in the 99.99% bacterial population, which can be obtained with min 1% Ag⁺, was provided by using 1% chitosan and 0.25% Ag⁺, and similar results were obtained for both bacterial species. In several studies, it is suggested that the amounts of Ag⁺ used should be reassessed to minimize in a controlled manner. There is sufficient evidence that long-term adverse effects may occur from exposure to silver in an uncontrolled and unconscious manner (54). When taking this situation into account, the most striking result of this study is the quantitative determination of antibacterial efficiency by combining chitosan which is a natural polymer, biodegradable, safe and non-toxic biocompatible chitosan with Ag⁺. It was determined that thermally stable properties increased with HAP particle in the biocomposite fibers. Furthermore in vitro degradation studies have demonstrated, degradation rate of the biocomposite samples increased with HAP particle, but AB agents in the biocomposite were not affected these results. According to the mechanical test HAP particle and AB agents were added to the sample PLA-PCL, it was resulted that the biocomposite samples become more rigid and the elongation at break is slightly reduced. Finally, the experimental results clearly show that the obtained biocomposite nano-fibers allow for the development of new composite materials with anti-bacterial properties, good mechanical strength, thermally stable. The results also confirm the great potential of biodegradable, biocompatible and bioactive fibers for antibacterial application.

COMPLIANCE WITH ETHICAL STANDARDS**Conflict of interest**

The author declares that they have no conflict of interest.

REFERENCES

1. Leó B, Jansen JA. Thin calcium phosphate coatings for medical implants. Thin Calcium Phosphate Coatings for Medical Implants. 2009.
2. Bottino MC, Thomas V, Schmidt G, Vohra YK, Chu TMG, Kowolik MJ, et al. Recent advances in the development of GTR/GBR membranes for periodontal regeneration - A materials perspective. Dent Mater [Internet]. 2012;28(7):703–21. Available from: <http://dx.doi.org/10.1016/j.dental.2012.04.022>
3. Dahlin C, Linde A, Gottlow J, Nyman S. Healing of bone defects by guided tissue regeneration. Plast Reconstr Surg. 1988;
4. Hitti RA. Guided Bone Regeneration in the Oral Cavity: A Review. Open Pathol J. 2011;5(1):33–45.
5. Retzepe M, Donos N. Guided Bone Regeneration: Biological principle and therapeutic applications. Clin Oral Implants Res. 2010;21(6):567–76.
6. Hämmerle, C.H. & Jung RE. Bone augmentation by means of barrier membranes. Periodontology. 2000;33:36–53.
7. Sculean A, Nikolidakis D, Schwarz F. Regeneration of periodontal tissues: Combinations of barrier membranes and grafting materials - Biological foundation and preclinical evidence: A systematic review. J Clin Periodontol. 2008;35(SUPPL. 8):106–16.
8. Gentile P, Chiono V, Tonda-Turo C, Ferreira AM, Ciardelli G. Polymeric membranes for guided bone regeneration. Biotechnol J. 2011;6(10):1187–97.
9. Geurs NC, Korostoff JM, Vassilopoulos PJ, Kang T-H, Jeffcoat M, Kellar R, et al. Clinical and Histologic Assessment of Lateral Alveolar Ridge Augmentation Using a Synthetic Long-Term Bioabsorbable Membrane and an Allograft. J Periodontol. 2008;79(7):1133–40.
10. Milella E, Barra G, Ramires PA, Leo G, Aversa P, Romito A. Poly(L-lactide)acid/alginate composite membranes for guided tissue regeneration. J Biomed Mater Res. 2001;57(2):248–57.
11. Hirenkumar M, Steven S. Poly Lactic-co-Glycolic Acid (PLGA) as Biodegradable Controlled Drug Delivery Carrier. Polymers (Basel). 2012;3(3):1–19.
12. Vert M. Aliphatic polyesters: Great degradable polymers that cannot do everything. Biomacromolecules. 2005;6(2):538–46.

13. Nofar M, Sacligil D, Carreau PJ, Kamal MR, Heuzey MC. Poly (lactic acid) blends: Processing, properties and applications. *Int J Biol Macromol* [Internet]. 2019;125:307–60. Available from: <https://doi.org/10.1016/j.ijbiomac.2018.12.002>
14. Patrício T, Domingos M, Gloria A, D'Amora U, Coelho JF, Bártolo PJ. Fabrication and characterisation of PCL and PCL/PLA scaffolds for tissue engineering. *Rapid Prototyp J*. 2014;20(2):145–56.
15. Latthe SS, Imai H, Ganesan V, Rao AV. Superhydrophobic silica films by sol-gel co-precursor method. *Appl Surf Sci*. 2009;256(1):217–22.
16. Patrício T, Bártolo P. Thermal stability of PCL/PLA blends produced by physical blending process. *Procedia Eng* [Internet]. 2013;59:292–7. Available from: <http://dx.doi.org/10.1016/j.proeng.2013.05.124>
17. Broz ME, VanderHart DL, Washburn NR. Structure and mechanical properties of poly(D,L-lactic acid)/poly(ϵ -caprolactone) blends. *Biomaterials*. 2003;24(23):4181–90.
18. Furukawa T, Matsusue Y, Yasunaga T, Nakagawa Y, Okada Y, Shikinami Y, et al. Histomorphometric study on high-strength hydroxyapatite/poly(L-lactide) composite rods for internal fixation of bone fractures. *J Biomed Mater Res*. 2000;50(3):410–9.
19. Rezwan K, Chen QZ, Blaker JJ, Boccaccini AR. Biodegradable and bioactive porous polymer/inorganic composite scaffolds for bone tissue engineering. *Biomaterials*. 2006;27(18):3413–31.
20. Soundrapandian C, Sa B, Datta S. Organic–Inorganic Composites for Bone Drug Delivery. *AAPS PharmSciTech*. 2009;10(4):1158–71.
21. Santos MH, Oliveira M de, Souza LP de F, Mansur HS, Vasconcelos WL. Synthesis control and characterization of hydroxyapatite prepared by wet precipitation process. *Mater Res*. 2006;7(4):625–30.
22. Yelten-Yilmaz A, Yilmaz S. Wet chemical precipitation synthesis of hydroxyapatite (HA) powders. *Ceram Int* [Internet]. 2018;44(8):9703–10. Available from: <https://doi.org/10.1016/j.ceramint.2018.02.201>
23. Monmaturapoj N. Nano-size Hydroxyapatite Powders Preparation by Wet-Chemical Precipitation Route Particle sizes and density were analyzed by. *J Met aterials Miner*. 2008;18(1):15–20.
24. Chai CS, Ben-Nissan B. Bioactive nanocrystalline sol-gel hydroxyapatite coatings. *J Mater Sci Mater Med*. 1999;10(8):465–9.
25. Liu DM, Troczynski T, Hakimi D. Effect of hydrolysis on the phase evolution of water-based sol-gel hydroxyapatite and its application to bioactive coatings. *J Mater Sci Mater Med*. 2002;13(7):657–65.
26. Manafi SA, Joughehdoust S. Synthesis of Hydroxyapatite Nanostructure by Hydrothermal Condition for Biomedical Application. *J Pharm Sci*. 2009;5(2):89–94.
27. Kimura I. Synthesis of Hydroxyapatite by Interfacial Reaction in a Multiple Emulsion. *Res Lett Mater Sci*. 2007;2007:1–4.
28. Tas AC. Synthesis of biomimetic Ca-hydroxyapatite powders at 37 degrees C in synthetic body fluids. *Biomaterials*. 2000;21:1429–38.
29. Thamaraiselvi T V., Prabakaran K, Rajeswari S. Synthesis of hydroxyapatite that mimic bone mineralogy. *Trends Biomater Artif Organs*. 2006;19(2):81–3.
30. Shirkhazadeh m. Direct formation of nanophase HAP on cathodically polarized electrodes.pdf. *J Mater Sci Mater Med*. 1998;9:67–72.
31. Nayak AK. Hydroxyapatite synthesis methodologies: An overview. *Int J ChemTech Res*. 2010;2(2):903–7.
32. Pham QP, Sharma U, Mikos AG. Review---Electrospinning of Polymeric Nanofibers.pdf. 2006;12(5).
33. Huang ZM, Zhang YZ, Kotaki M, Ramakrishna S. A review on polymer nanofibers by electrospinning and their applications in nanocomposites. *Compos Sci Technol*. 2003;63(15):2223–53.
34. Bhardwaj N, Kundu SC. Electrospinning: A fascinating fiber fabrication technique. *Biotechnol Adv*. 2010;28(3):325–47.
35. Tanaka K, Shiga T, Katayama T. Fabrication of hydroxyapatite/PLA composite nanofiber by electrospinning. *High Perform Optim Des Struct Mater II*. 2016;1(Hpsm):371–9.
36. Gupta B, Revagade N, Anjum N, Atthoff B, Hilborn J. Preparation of poly(lactic acid) fiber by dry-jet-wet-spinning. I. Influence of draw ratio on fiber properties. *J Appl Polym Sci*. 2006;100(2):1239–46.
37. Kurtycz P, Karwowska E, Ciach T, Olszyna A, Kunicki A. Biodegradable polylactide (PLA) fiber mats containing Al₂O₃-Ag nanopowder prepared by electrospinning technique - Antibacterial properties. *Fibers Polym*. 2013;14(8):1248–53.
38. Chou J, Ben-Nissan B, Green DW, Valenzuela SM, Kohan L. Targeting and dissolution characteristics of bone forming and antibacterial drugs by harnessing the structure of microspherical shells from coral beach sand. *Adv Eng Mater*. 2011;13(1–2):93–9.
39. Karacan I, Macha IJ, Choi G, Cazalbou S, Ben-Nissan B. Antibiotic Containing Poly Lactic Acid/Hydroxyapatite Biocomposite Coatings for Dental Implant Applications. *Key Eng Mater*. 2017;758(September):120–5.
40. Björling G, Johansson D, Bergström L, Strekalovsky A, Sanchez J, Frostell C, et al. Evaluation of central venous catheters coated with a

- noble metal alloy—A randomized clinical pilot study of coating durability, performance and tolerability. *J Biomed Mater Res - Part B Appl Biomater*. 2018;106(6):2337–44.
41. Wu K, Yang Y, Zhang Y, Deng J, Lin C. Antimicrobial activity and cytocompatibility of silver nanoparticles coated catheters via a biomimetic surface functionalization strategy. *Int J Nanomedicine*. 2015;10:7241–52.
42. Knetsch MLW, Koole LH. New strategies in the development of antimicrobial coatings: The example of increasing usage of silver and silver nanoparticles. *Polymers (Basel)*. 2011;3(1):340–66.
43. Goy RC, Morais STB, Assis OBG. Evaluation of the antimicrobial activity of chitosan and its quaternized derivative on *E. Coli* and *S. aureus* growth. *Brazilian J Pharmacogn*. 2016;26(1):122–7.
44. Montazer M, Afjeh MG. Simultaneous X-linking and antimicrobial finishing of cotton fabric. *J Appl Polym Sci*. 2007;103(1):178–85.
45. Hablot E, Dharmalingam S, Hayes DG, Wadsworth LC, Blazy C, Narayan R. Effect of Simulated Weathering on Physicochemical Properties and Inherent Biodegradation of PLA/PHA Nonwoven Mulches. *J Polym Environ*. 2014;22(4):417–29.
46. Chandrasekar A, Sagadevan S, Dakshnamoorthy A. Synthesis and characterization of nano-hydroxyapatite (n-HAP) using the wet chemical technique. *Int J Phys Sci*. 2013;8(32):1639–45.
47. Kokubo T, Takadama H. How useful is SBF in predicting in vivo bone bioactivity? *Biomaterials* [Internet]. 2006;27(15):2907–15. Available from: <http://www.ncbi.nlm.nih.gov/pubmed/16448693>
48. Grigorjeva L, Millers D, Smits K, Jankovica D, Pukina L. Characterization of hydroxyapatite by time-resolved luminescence and FTIR spectroscopy. *IOP Conf Ser Mater Sci Eng*. 2013;49(1).
49. Qi H, Ye Z, Ren H, Chen N, Zeng Q, Wu X, et al. Bioactivity assessment of PLLA/PCL/HAP electrospun nanofibrous scaffolds for bone tissue engineering. *Life Sci* [Internet]. 2016;148:139–44. Available from: <http://dx.doi.org/10.1016/j.lfs.2016.02.040>
50. Marei NH, El-Sherbiny IM, Lotfy A, El-Badawy A, El-Badri N. Mesenchymal stem cells growth and proliferation enhancement using PLA vs PCL based nanofibrous scaffolds. *Int J Biol Macromol*. 2016;93:9–19.
51. H. Hoidy W, B. Ahmad M, Jaffar Al- EA, Bt Ibrahim NA. Preparation and Characterization of Polylactic Acid/Polycaprolactone Clay Nanocomposites. Vol. 10, *Journal of Applied Sciences*. 2010. p. 97–106.
52. Locardi B, Pazzaglia UE, Gabbi C, Profilo B. Thermal behaviour of hydroxyapatite intended for medical applications. *Biomaterials*. 1993;
53. Pisani S, Dorati R, Conti B, Modena T, Bruni G, Genta I. Design of copolymer PLA-PCL electrospun matrix for biomedical applications. *React Funct Polym* [Internet]. 2018;124(July 2017):77–89. Available from: <https://doi.org/10.1016/j.reactfunctpolym.2018.01.011>
54. Sim W, Barnard R, Blaskovich MAT, Ziora Z. Antimicrobial Silver in Medicinal and Consumer Applications: A Patent Review of the Past Decade (2007–2017). *Antibiotics*. 2018;7(4):93.



Synthesis of *trans*-diamide derivatives from fumaryl chloride and determine DPPH scavenging activity of synthesized molecules

Özgür YILMAZ*  

Department of Chemistry, Faculty of Arts and Sciences, Mersin University, 33343 Mersin, Turkey.

Abstract: In this work, new *trans*-diamide derivatives were synthesized with the reaction between fumaryl chloride and substituted anilines. After successful synthesis of *trans*-amides, antioxidant activity of all synthesized molecules was investigated via DPPH method and calculated IC₅₀ values. All *trans*-amides were characterized by ¹H-NMR, ¹³C-NMR, ¹⁹F-NMR, GC-MS and FTIR spectroscopic techniques.

Keywords: Amides, DPPH method, antioxidant activity, fluorinated arenes.

Submitted: October 01, 2019. **Accepted:** November 19, 2019.

Cite this: Yılmaz Ö. Synthesis of *trans*-diamide derivatives from fumaryl chloride and determine DPPH scavenging activity of synthesized molecules. JOTCSA. 2020;7(1):143–50.

DOI: <https://doi.org/10.18596/jotcsa.627805>.

***Corresponding author.** E-mail: yilmazozgur@mersin.edu.tr.

INTRODUCTION

Amides are significant groups in organic chemistry because they possess extensive biological activities such as antifungal, antioxidant etc (1–7). Also, they can be used as a precursor for synthesis of plastics, agrochemicals or known drugs in the market such as Valsartan (a), Lidocaine (b) and Bupivacaine (c) (Figure 1) (8). Thus, the synthesis of amides are one of the most important topic in academia. Beside the reaction between carboxylic acids and primary amines (8), there are many methods in the literature about amide synthesis such as Ugi reaction (9), Staudinger reaction (10) and Schmidt reaction (11). Since there are many limiting factors in the methods known scope of literature, researchers are still working to develop new methods based on amide synthesis.

In addition, fluorinated arenes are the crucial and attractive compounds for researchers due to possessing wide application such as agrochemicals, medicine and materials science (12,13). When comparing properties of fluorine-containing compounds with their non-substituted analogues, the compounds which has fluorine groups generally show excellent chemical and biological properties (14). Thus, derivatization of arenes with the fluorine groups provide good properties to the synthesized molecules.

In this paper, new substituted *trans*-diamides which is especially containing fluorine arenes was synthesized and their antioxidant properties were investigated by using DPPH method.

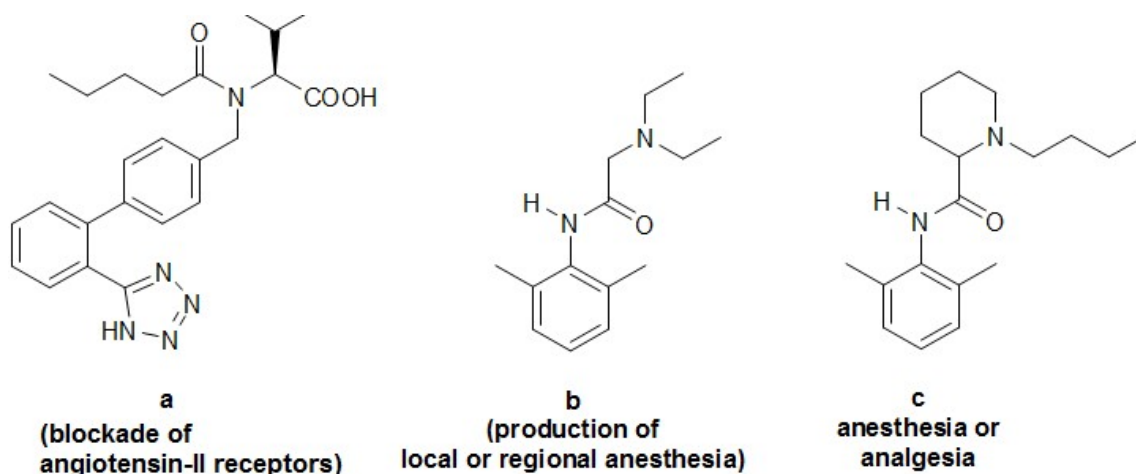


Figure 1. Some significant amide molecules having biological activity.

EXPERIMENTAL SECTION

Materials and Methods

Materials

Commercial chemicals were taken from Sigma-Aldrich or Merck and used directly. NMR, FT-IR and UV analyses were determined using Bruker Ultrashield Plus Biospin Avance III 400 MHz NaNoBay FT-NMR, Perkin Elmer Spectrum-100, and Chebios Optimum-One UV-Vis spectrophotometer, respectively.

General method for the synthesis

Primary amines (10.0 mmol) were dissolved in 10 mL of CH_2Cl_2 and then fumaryl chloride (5.0 mmol) was added dropwise in to the reaction mixture. After the starting materials completely consumed according to TLC analysis, the precipitated product was filtered and crystallized in methanol.

DPPH method for the investigation of antioxidant activity;

2,2-Diphenyl-1-picrylhydrazyl (DPPH) radical scavenging test was investigated for all synthesized molecules according to positive controls that butylated hydroxytoluene (BHT) and butylated hydroxyanisole (BHA). Different concentrations (6,75–800 $\mu\text{g}/\text{mL}$) of all synthesized *trans*-diamides and positive controls were prepared in EtOH. Then, 1 mL of 1×10^{-4} mM DPPH solution were added into tube for each compound, and 1 mL of each sample was added on the DPPH solution. Each tube was incubated in dark for an hour and then absorbance for each sample was measured at 517 nm. The antioxidant activity was calculated with formula given below (15,16). (Equation 1)

$$\% \text{Scavenging} = \frac{A_0 - A_s}{A_0} \times 100 \quad (\text{Eq. 1})$$

(A_0 = absorbance of the control; A_s = absorbance of the sample at 517 nm)

*N*¹,*N*⁴-bis(3-fluorophenyl)fumaramide (**3a**, $\text{C}_{16}\text{H}_{12}\text{F}_2\text{N}_2\text{O}_2$)

3-Fluoroaniline (1.11 g, 10.0 mmol) were dissolved in 10 mL of CH_2Cl_2 and then fumaryl chloride (0.76 g, 5.0 mmol) was added dropwise. After the starting materials come to an end according to TLC analysis, the precipitate was filtered from filter paper and crystallized in methanol. The product **3a** was obtained (1.45 g, 96%).

M.p.: 305-306 °C; **¹H NMR** (400 MHz, $\text{DMSO}-d_6$): δ = 10.41 (s, 2H, -NH), 7.49 (dt, J = 7.8, 1.9 Hz, 2H, ArH), 7.43 (s, 2H, -C=CH), 7.39 – 7.18 (m, 6H, ArH) ppm; **¹³C NMR** (101 MHz, $\text{DMSO}-d_6$): δ = 162.54 (s), 155.19 (d, J = 48.0 Hz), 152.75 (d, J = 48.7 Hz), 134.03 (s), 125.79 (s), 125.68 (s), 123.09 (s), 116.09 (d, J = 18.2 Hz), 115.57 (d, J = 19.3 Hz) ppm; **¹⁹F NMR (376 MHz, $\text{DMSO}-d_6$):** δ = 124.0 (ArC-F) ppm; **FTIR (KBr):** $\bar{\nu}$ = 3260, 3044, 2906, 1646, 1599, 1543, 1457, 1198, 750, 697 cm^{-1} ; **ESI-MS** (70 eV): m/z = 304 (M^+).

*N*¹,*N*⁴-bis(4-fluorophenyl)fumaramide (**3b**, $\text{C}_{16}\text{H}_{12}\text{F}_2\text{N}_2\text{O}_2$)

M.p.: 353-354 °C; **¹H NMR** (400 MHz, $\text{DMSO}-d_6$): δ = 10.76 (s, 2H, -NH), 7.80 – 7.74 (m, 2H, ArH), 7.50 – 7.43 (m, 2H, ArH), 7.35 (t, J = 8.8 Hz, 2H, ArH), 7.24 (s, 2H, -C=CH), 7.21 (t, J = 8.9 Hz, 2H, ArH) ppm; **¹³C NMR** (101 MHz, $\text{DMSO}-d_6$): δ = 161.99 (s), 157.14 (s), 133.95 (s), 124.95 (d, J = 8.7 Hz), 121.20 (d, J = 7.9 Hz), 116.47 (d, J = 23.1 Hz), 115.42 (d, J = 22.3 Hz) ppm; **¹⁹F NMR (376 MHz, $\text{DMSO}-d_6$):** δ = 118.4 (ArC-F) ppm; **FTIR (KBr):** $\bar{\nu}$ = 3252, 3046, 2924, 1650, 1619,

1502, 1408, 1237, 829, 792 cm^{-1} ; **ESI-MS** (70 eV): $m/z = 304$ (M^+).

***N*¹,*N*⁴-bis(3-(trifluoromethyl)phenyl) fumaramide (3c, C₁₈H₁₂F₆N₂O₂)**

M.p.: 302-303 °C; **¹H NMR** (400 MHz, DMSO-*d*₆): $\delta = 11.07$ (s, 2H, -NH), 8.25 (s, 2H, ArH), 7.92 (d, $J = 8.3$ Hz, 2H, ArH), 7.63 (t, $J = 8.0$ Hz, 2H), 7.49 (s, $J = 7.8$ Hz, 2H, -C=CH), 7.47 (dd, $J = 15.5, 7.8$ Hz, 2H, ArH) ppm; **¹³C NMR** (101 MHz, DMSO-*d*₆): $\delta = 162.46$ (s), 139.52 (s), 134.14 (s), 130.44 (s), 130.11 (s), 123.05 (s), 122.69 (s), 115.51 (dd, $J = 7.7, 3.6$ Hz), 114.94 (dd, $J = 4.4, 2.2$ Hz) ppm; **¹⁹F NMR (376 MHz, DMSO-*d*₆):** $\delta = 61.4$ (-CF₃) ppm; **FTIR (KBr):** $\bar{\nu} = 3272, 3014, 2848, 1653, 1601, 1445, 1328, 1116, 799, 695$ cm^{-1} ; **ESI-MS (70 eV):** $m/z = 401$ (M^+).

***N*¹,*N*⁴-bis(4-(trifluoromethyl)phenyl) fumaramide (3d, C₁₈H₁₂F₆N₂O₂)**

M.p.: 379-380 °C; **¹H NMR** (400 MHz, DMSO-*d*₆): $\delta = 11.12$ (s, 2H, -NH), 7.97 (d, $J = 8.5$ Hz, 4H, ArH), 7.74 (d, $J = 8.7$ Hz, 4H, ArH), 7.32 (s, 2H, -C=CH) ppm; **¹³C NMR** (101 MHz, DMSO-*d*₆): $\delta = 162.53$ (s), 142.33 (s), 134.28 (s), 126.47 (q, $J = 3.8$ Hz), 126.11 (d, $J = 3.8$ Hz), 123.51 (dd, $J = 73.6, 35.6$ Hz), 119.44 (s) ppm; **¹⁹F NMR (376 MHz, DMSO-*d*₆):** $\delta = 60.4$ (-CF₃) ppm; **FTIR (KBr):** $\bar{\nu} = 3292, 2843, 1643, 1537, 1317, 1124, 1064, 826, 692$ cm^{-1} ; **ESI-MS (70 eV):** $m/z = 401$ (M^+).

***N*¹,*N*⁴-bis(2-fluoro-3-(trifluoromethyl)phenyl) fumaramide (3e, C₁₈H₁₀F₈N₂O₂)**

M.p.: 261-262 °C; **¹H NMR** (400 MHz, DMSO-*d*₆): $\delta = 10.74$ (s, 2H, -NH), 8.35 (t, $J = 7.4$ Hz, 2H, ArH), 7.59 (t, $J = 6.7$ Hz, 2H, ArH), 7.45 (t, $J = 8.0$ Hz, 2H, ArH), 7.46 (s, 2H, -C=CH) ppm; **¹³C NMR** (101 MHz, DMSO-*d*₆): $\delta = 162.66$ (s), 148.81 (d, $J = 1.6$ Hz), 146.33 (d, $J = 1.2$ Hz), 135.84 (d, $J = 11.4$ Hz), 134.05 (s), 128.79 (s), 127.10 (d, $J = 10.5$ Hz), 124.88 (d, $J = 4.5$ Hz), 113.75 (q, $J = 4.7$ Hz) ppm; **¹⁹F NMR (376 MHz, DMSO-*d*₆):** $\delta = 126.7$ (ArC-F), 59.9 (-CF₃) ppm; **FTIR (KBr):** $\bar{\nu} = 3251, 2811, 1643, 1537, 1484, 1322, 1132, 796, 733$ cm^{-1} ; **ESI-MS (70 eV):** $m/z = 437$ (M^+).

***N*¹,*N*⁴-bis(2-fluoro-4-(trifluoromethyl)phenyl) fumaramide (3f, C₁₈H₁₀F₈N₂O₂)**

M.p.: 336-337 °C; **¹H NMR** (400 MHz, DMSO-*d*₆): $\delta = 10.74$ (s, 2H, -NH), 8.42 (t, $J = 8.1$ Hz, 2H, ArH), 7.80 (dd, $J = 11.0, 1.7$ Hz, 2H, ArH), 7.64 (d, $J = 8.5$ Hz, 2H, ArH), 7.52 (s, 2H, -C=CH) ppm; **¹³C NMR** (101 MHz, DMSO-*d*₆): $\delta = 162.82$ (s), 150.55 (s), 148.18 (s), 140.19 (d, $J = 13.1$ Hz), 134.35 (s), 123.71 (d, $J = 1.4$ Hz), 122.05 (p, $J = 3.0$ Hz), 115.63 (d, $J = 5.3$ Hz), 112.29 (q, $J = 3.7$ Hz) ppm; **¹⁹F NMR (376 MHz, DMSO-*d*₆):** $\delta = 122.2$ (ArC-F), 60.6 (-CF₃) ppm; **FTIR (KBr):** $\bar{\nu} = 3298, 3021, 1659, 1623, 1540, 1430, 1325, 1121, 887, 651$ cm^{-1} ; **ESI-MS (70 eV):** $m/z = 437$ (M^+).

***N*¹,*N*⁴-bis(2-cyanophenyl) fumaramide (3g, C₁₈H₁₂N₄O₂)**

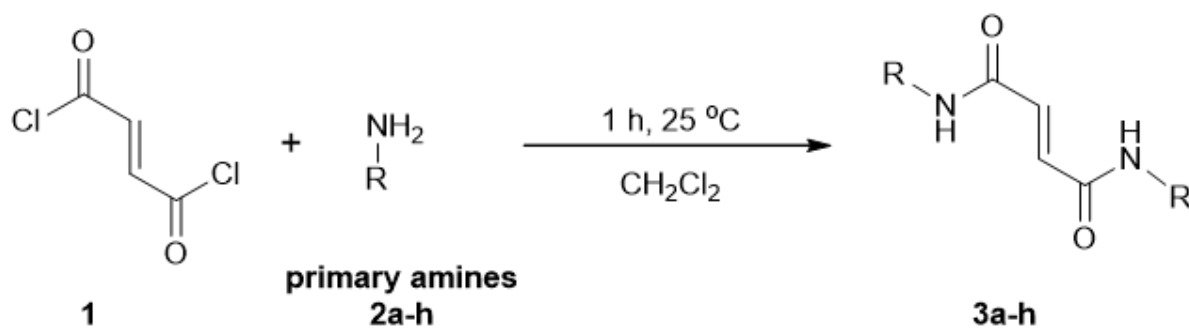
M.p.: 338-339 °C; **¹H NMR** (400 MHz, DMSO-*d*₆): $\delta = 10.94$ (s, 2H, -NH), 7.89 (dd, $J = 7.8, 1.1$ Hz, 2H, ArH), 7.75 (dtd, $J = 9.3, 8.3, 1.3$ Hz, 4H, ArH), 7.45 (td, $J = 7.7, 1.4$ Hz, 2H, ArH), 7.37 (s, 2H, -C=CH) ppm; **¹³C NMR** (101 MHz, DMSO-*d*₆): $\delta = 162.54$ (s, C=O), 139.55 (s, ArC), 133.35 (s, ArC), 126.26 (s, ArC), 125.56 (s, ArC), 118.04 (s, ArC), 116.66 (s), 107.42 (s), 93.64 (s) ppm; **FTIR (KBr):** $\bar{\nu} = 3267, 3036, 2906, 2233, 1648, 1542, 1451, 1335, 995, 773, 675$ cm^{-1} ; **ESI-MS (70 eV):** $m/z = 315$ (M^+).

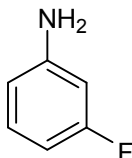
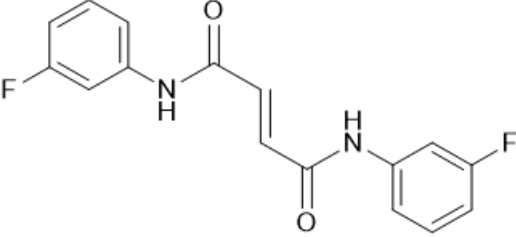
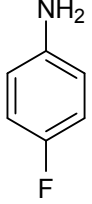
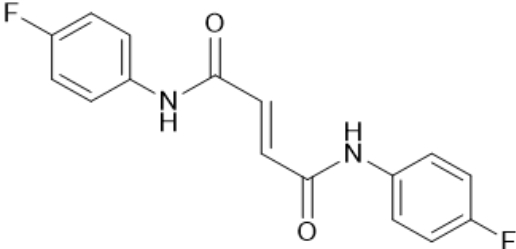
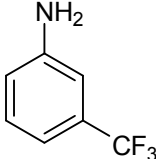
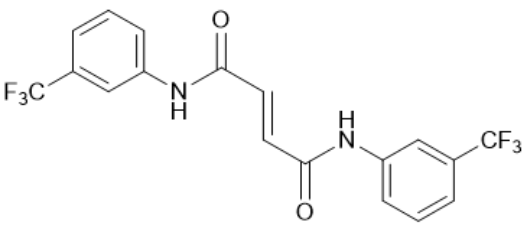
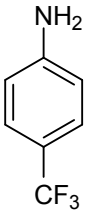
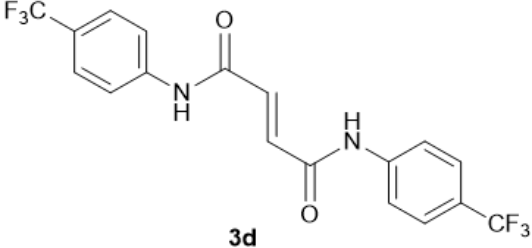
***N*¹,*N*⁴-bis(4-methoxyphenyl) fumaramide (3h, C₁₈H₁₈N₂O₄)**

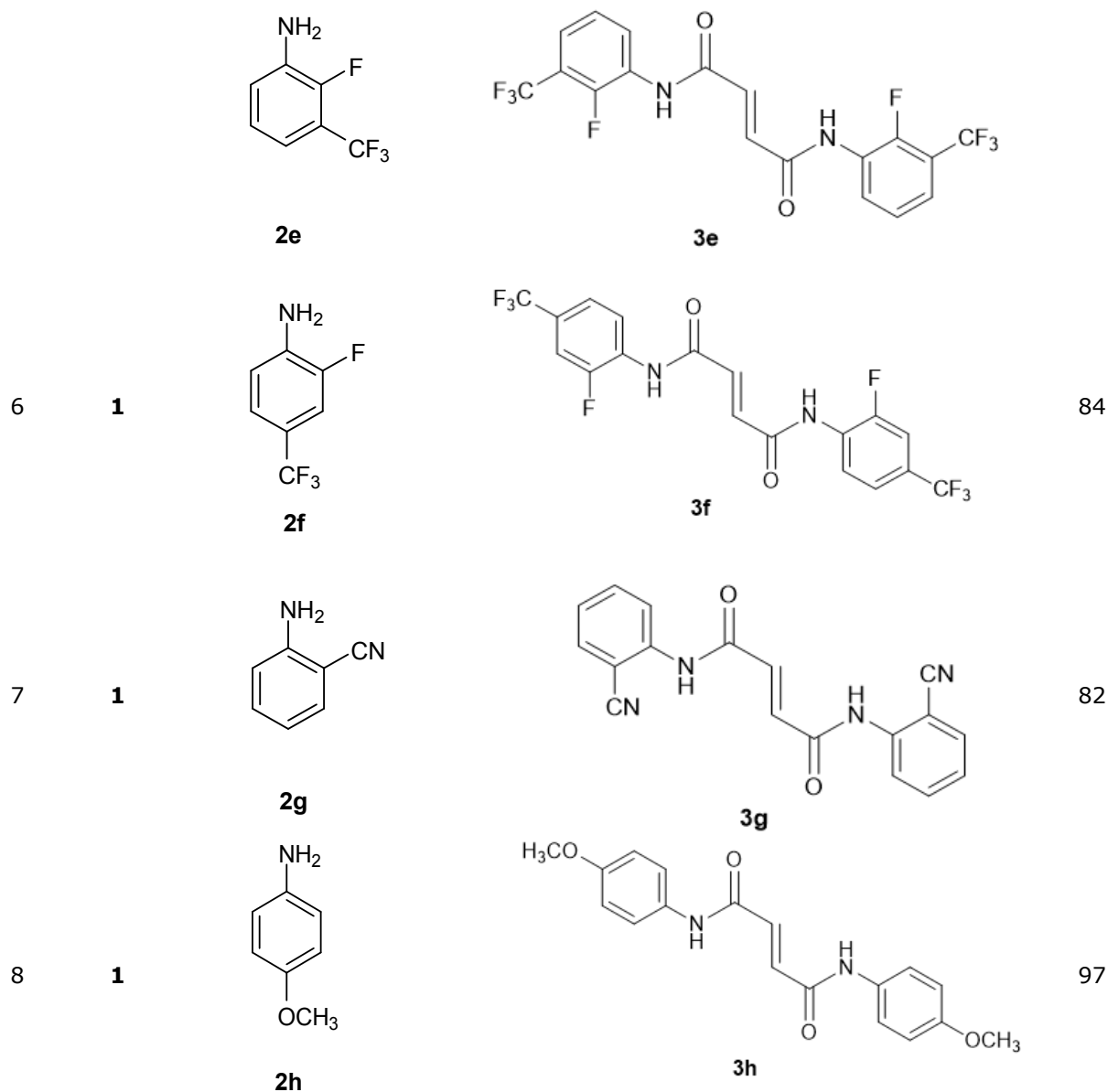
M.p.: 270-271 °C; **¹H NMR** (400 MHz, DMSO-*d*₆): $\delta = 10.49$ (s, 2H, -NH), 7.66 (d, $J = 9.1$ Hz, 4H, ArH), 7.35 (d, $J = 9.0$ Hz, 4H, ArH), 7.18 (s, 2H, -C=CH), 3.76 (s, 6H, -OCH₃); **¹³C NMR** (101 MHz, DMSO-*d*₆): $\delta = 161.72$ (s), 155.66 (s), 133.75 (s), 124.29 (s), 120.90 (s), 114.84 (s), 55.21 (s) ppm; **FTIR (KBr):** $\bar{\nu} = 3274, 3049, 2837, 1634, 1531, 1508, 1245, 1164, 1023, 830, 663$ cm^{-1} ; **ESI-MS (70 eV):** $m/z = 325$ (M^+).

RESULTS AND DISCUSSION

Reactions between 1 equivalent fumaryl chloride **1** and 2 equivalent different primary amines **2a-h** was investigated and obtained substituted *trans*-diamides with high yield (Figure 2). Reaction with the *ortho*-substituted primary amines gave lower yield than *meta*- or *para*-substituted primary amines due to the sterical effect on the amine group (Table 1).

**Figure 2.** General reaction for the synthesis of *trans*-diamides.**Table 1.** Synthesis of *trans*-diamides **3a-h**.

Entry	Acyl chloride	Amines	Product	Yield %
1	1	 2a	 3a	96
2	1	 2b	 3b	95
3	1	 2c	 3c	92
4	1	 2d	 3d	96
5	1			77



All *trans*-diamide structures were characterized with spectroscopic analyses ($^1\text{H-NMR}$, $^{13}\text{C-NMR}$, $^{19}\text{F-NMR}$, LC-MS, FT-IR). In the $^1\text{H-NMR}$ spectra of **3a-h**, it is clearly shown that, -NH protons gave singlets in the area between δ 10.41-11.12 ppm, which approved with known similar compounds in the literature (17,18). Protons of double bond (**3a-h**) were observed as singlets in the region between δ 7.18-7.53 ppm. While the signal of aromatic protons was observed between δ 7.21-8.42 ppm (17,18), methoxy protons of the compound **3h** were observed at 3.76 ppm as a singlet (19). In addition, in the ^{13}C NMR spectra of compounds **3a-h**, the signal of carbonyl carbon appeared between δ 163-161 ppm and the peaks of aromatic/olefinic carbons appeared the area between δ 107.42-155.66 ppm. Also, the signal of nitrile carbon of compound **3g** and the methoxy carbon of compound **3h** appeared at δ 93.64 ppm and δ 55.21 ppm respectively. When ^{19}F NMR of

compound **3a-f** was examined, it was seen that characteristic signals of -F (between δ 118.38 – 126.64 ppm) and -CF₃ (between δ 59.88 – 61.40 ppm) groups were in expected regions (see Supporting Information) (20). Also, NMR results were supported with LC-MS and FT-IR analysis. When the FTIR spectra was examined, the -N-H stretching bands of **3a-h** observed between 3272–3251 cm⁻¹. The Ar-H stretching bands and -C=O stretching bands of **3a-h** was observed between 3049–3014 cm⁻¹ and 1659–1634 cm⁻¹, respectively. In addition, the -CN band of compound **3g** was observed at 2233 cm⁻¹.

After the successful synthesis of *trans*-diamide derivatives, we focused on to investigate DPPH scavenging activity of all the synthesized molecules. Free radicals that are generated permanently in the body included unpaired electrons and, these electrons can easily interact

with biomolecules (15). Common diseases like cardiovascular diseases and cancer, have been occurred due to free radical damage. Thus, synthesis of antioxidant molecules that can convert the radicals to stable compound are so important. Because of these properties, antioxidant molecules have affirmative effects on health (15). DPPH method has been commonly used for investigating the antioxidant activity. This technique easily gives an antiradical potential of molecule with UV measurement at 515 nm (21).

For this purpose, different concentrations of each synthesized molecule and positive controls were prepared (12.5, 25, 50, 100, 200, 400, 800 µg/mL) and added to DPPH solution which was prepared freshly. After 30 minutes of incubation in the dark, $_{515}$ UV measurements was taken for each concentration and the IC₅₀ value was calculated as 302.52 µg, 304.17 µg, 266.74 µg, 251.46 µg, 315.51 µg, 402.44 µg, 325.75 µg, 595.27 µg, 68.65 µg and 39.46 µg for compound **3a**, **3b**, **3c**, **3d**, **3f**, **3g**, **3h**, BHT, and BHA, respectively. According to these results, all synthesized molecules showed lower DPPH scavenging activity when compared with positive controls BHT and BHA. Also, these results showed that the antioxidant activity of synthesized molecules increased in order of 3h<3f<3g<3e<3b<3a<3d<3c<BHT<BHA.

Substituted anilines with electron withdrawing/deactivating group (-CF₃) showed better DPPH scavenging activity than substituted anilines with weakly deactivating (-F) or electron donating/activating (-OCH₃) group. Also, when DPPH scavenging activity of compounds which substituted with the same group was examined, the *meta*-substituted anilines showed better activity than *para*-substituted ones. (3b<3a or 3d<3c)

Table 2. The IC₅₀ values of *trans*-diamides and positive controls.

Compound	IC ₅₀ (µg)
3a	302.52
3b	304.17
3c	251.46
3d	266.74
3e	315.51
3f	402.44
3g	325.75
3h	595.27
BHT	68.65
BHA	39.46

CONCLUSION

In summary, new *trans*-diamides were synthesized with the reaction between primary amines and fumaryl chloride. In addition, the DPPH scavenging activity for each synthesized molecule was

investigated and obtained moderate results compared to positive controls BHT and BHA.

ACKNOWLEDGEMENTS

This research was supported by a grant from Mersin University (BAP 2017-1-AP1-2188). The author would like to thanks to Prof. Dr. Nermin SIMSEK KUS (Mersin University) for offering the laboratory facilities, and to Dr. Pinar KUÇE CEVIK (Mersin University) for assistance with antioxidant measurement.

REFERENCES

- Sathe PA, Karpe AS, Parab AA, Parade BS, Vadagaonkar KS, Chaskar AC. Tandem synthesis of aromatic amides from styrenes in water. *Tetrahedron Lett.* 2018 Jul;59(29):2820–3. Available from: <https://linkinghub.elsevier.com/retrieve/pii/S0040403918307639>
- Srivastava V, Singh PK, Singh PP. Visible light photoredox catalysed amidation of carboxylic acids with amines. *Tetrahedron Lett.* 2019 Jan;60(1):40–3. Available from: <https://linkinghub.elsevier.com/retrieve/pii/S0040403918313972>
- Han Q, Xiong X, Li S. An efficient, green and scale-up synthesis of amides from esters and amines catalyzed by Ru-MACHO catalyst under mild conditions. *Catal Commun.* 2015 Jan;58:85–8. Available from: <https://linkinghub.elsevier.com/retrieve/pii/S1566736714003483>
- Hong G, Wu S, Zhu X, Mao D, Wang L. Peroxide-mediated direct synthesis of amides from aroyl surrogates. *Tetrahedron* 2016 Jan;72(3):436–41. Available from: <https://linkinghub.elsevier.com/retrieve/pii/S0040402015302477>
- Lanigan RM, Starkov P, Sheppard TD. Direct Synthesis of Amides from Carboxylic Acids and Amines Using B(OCH₂CF₃)₃. *J Org Chem.* 2013 May 3;78(9):4512–23. Available from: <https://pubs.acs.org/doi/10.1021/jo400509n>
- Ghorpade SA, Sawant DN, Sekar N. Triphenyl borate catalyzed synthesis of amides from carboxylic acids and amines. *Tetrahedron* 2018 Nov;74(48):6954–8. Available from: <https://linkinghub.elsevier.com/retrieve/pii/S0040402018312365>
- Cadoni R, Porcheddu A, Giacomelli G, De Luca L. One-pot synthesis of amides from aldehydes and amines via C-H bond activation. *Org Lett.* 2012;
- Valeur E, Bradley M. Amide bond formation: beyond the myth of coupling reagents. *Chem Soc Rev.* 2009;38(2):606–31. Available from: <http://xlink.rsc.org/?DOI=B701677H>
- Ugi I. The γ -Addition of Immonium Ions and Anions to Isonitriles Accompanied by Secondary Reactions. *Angew Chemie Int Ed English* 1962 Jan 27;1(1):8–21. Available from: <http://doi.wiley.com/10.1002/anie.196200081>

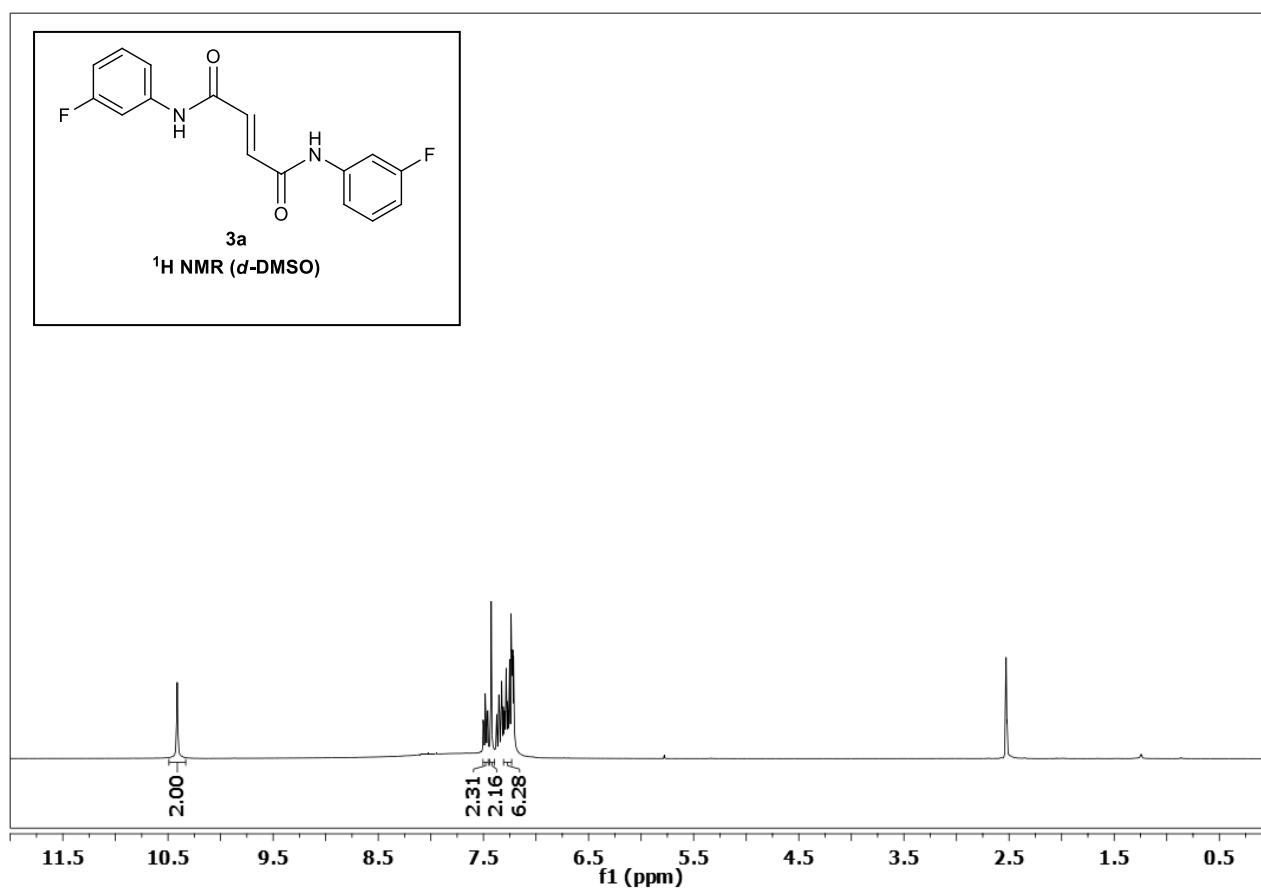
10. Damkaci F, DeShong P. Stereoselective Synthesis of α - and β -Glycosylamide Derivatives from Glycopyranosyl Azides via Isoxazoline Intermediates. *J Am Chem Soc.* 2003 Apr;125(15):4408–9. Available from: <https://pubs.acs.org/doi/10.1021/ja028694u>
11. Ribelin T, Katz CE, English DG, Smith S, Manukyan AK, Day VW, et al. Highly Stereoselective Ring Expansion Reactions Mediated by Attractive Cation- π Interactions. *Angew Chemie Int Ed.* 2008 Aug 4;47(33):6233–5. Available from: <http://doi.wiley.com/10.1002/anie.200801591>
12. Fang X, Huang Y, Chen X, Lin X, Bai Z, Huang K-W, et al. Preparation of fluorinated biaryls through direct palladium-catalyzed coupling of polyfluoroarenes with aryltrifluoroborates. *J Fluor Chem.* 2013 Jul;151:50–7. Available from: <https://linkinghub.elsevier.com/retrieve/pii/S0022113913001413>
13. Politsanskaya L, Petyuk M, Tretyakov E. Transformation of fluorinated 2-alkynylanilines by various catalytic systems. *J Fluor Chem.* 2019 Oct;109394. Available from: <https://linkinghub.elsevier.com/retrieve/pii/S0022113919303185>
14. Li X, Liu J, Li X, Liu H, Liu H, Li Y, et al. Recent advance in the synthesis of (1,1-difluoroethyl)arenes. *J Fluor Chem.* 2018 Dec;216:102–6. Available from: <https://linkinghub.elsevier.com/retrieve/pii/S0022113918303932>
15. Bursal E, Aras A, Kılıç Ö, Taslimi P, Gören AC, Gülçin İ. Phytochemical content, antioxidant activity, and enzyme inhibition effect of *Salvia eriophora* Boiss. & Kotschy against acetylcholinesterase, α -amylase, butyrylcholinesterase, and α -glycosidase enzymes. *J Food Biochem.* 2019 Mar;43(3):e12776. Available from: <http://doi.wiley.com/10.1111/jfbc.12776>
16. Güzel S, Özay Y, Kumaş M, Uzun C, Özkorkmaz EG, Yıldırım Z, et al. Wound healing properties, antimicrobial and antioxidant activities of *Salvia kronenburgii* Rech. f. and *Salvia euphratica* Montbret, Aucher & Rech. f. var. *euphratica* on excision and incision wound models in diabetic rats. *Biomed Pharmacother.* 2019 Mar;111:1260–76. Available from: <https://linkinghub.elsevier.com/retrieve/pii/S0753332218362073>
17. Ding Y, Zhang X, Zhang D, Chen Y, Wu Z, Wang P, et al. Copper-catalyzed oxidative amidation between aldehydes and arylamines under mild conditions. *Tetrahedron Lett.* 2015 Feb;56(6):831–3. Available from: <https://linkinghub.elsevier.com/retrieve/pii/S0040403914021911>
18. Rzhnevskiy SA, Ageshina AA, Chesnokov GA, Gribanov PS, Topchiy MA, Nechaev MS, et al. Solvent- and transition metal-free amide synthesis from phenyl esters and aryl amines. *RSC Adv.* 2019;9(3):1536–40. Available from: <http://xlink.rsc.org/?DOI=C8RA10040C>
19. Agirbas H, Kemal B, Budak F. Synthesis and structure–antibacterial activity relationship studies of 4-substituted phenyl-4,5-dihydrobenzo[f][1,4]oxazepin-3(2H)-thiones. *Med Chem Res.* 2011 Nov 10;20(8):1170–80. Available from: <http://link.springer.com/10.1007/s00044-010-9457-4>
20. Yılmaz MK, Güzel B. Iminophosphine palladium(II) complexes: synthesis, characterization, and application in Heck cross-coupling reaction of aryl bromides. *Appl Organomet Chem.* 2014 Jul;28(7):529–36. Available from: <http://doi.wiley.com/10.1002/aoc.3158>
21. Parhiz H, Roohbakhsh A, Soltani F, Rezaee R, Iranshahi M. Antioxidant and Anti-Inflammatory Properties of the Citrus Flavonoids Hesperidin and Hesperetin: An Updated Review of their Molecular Mechanisms and Experimental Models. *Phyther Res.* 2015 Mar;29(3):323–31. Available from: <http://doi.wiley.com/10.1002/ptr.5256>

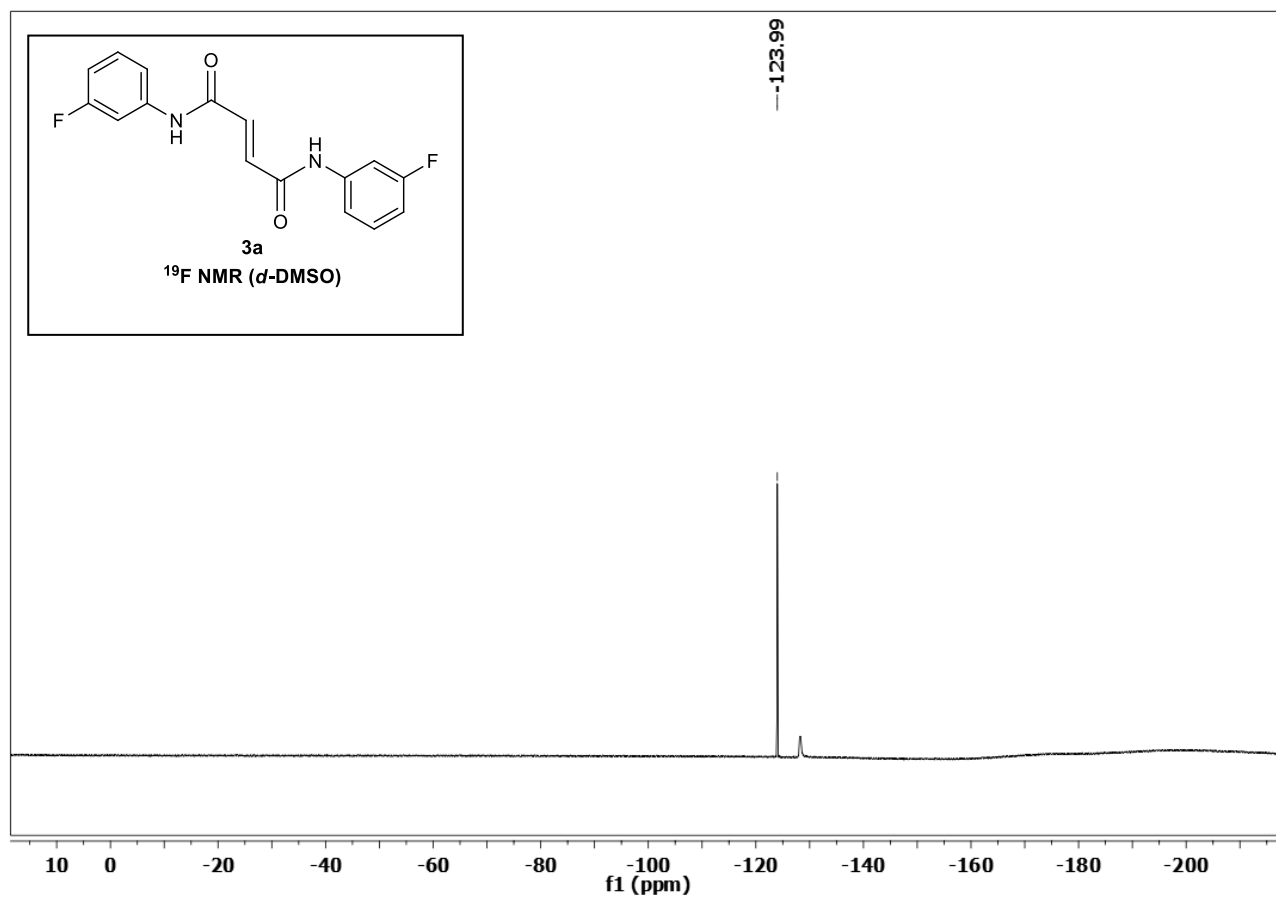
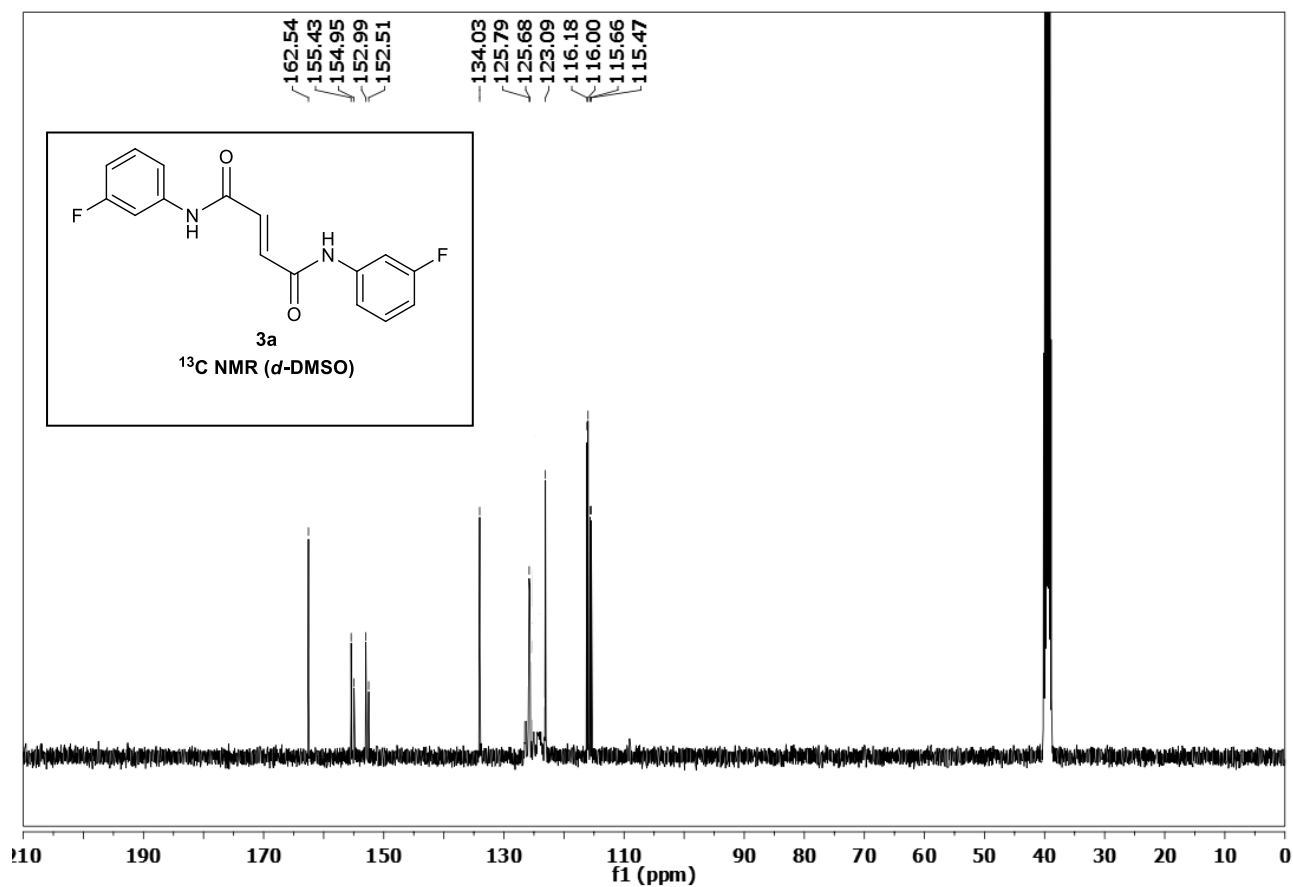
Synthesis of *trans*-diamide derivatives from fumaryl chloride and determine DPPH scavenging activity of synthesized molecules

Özgür YILMAZ*

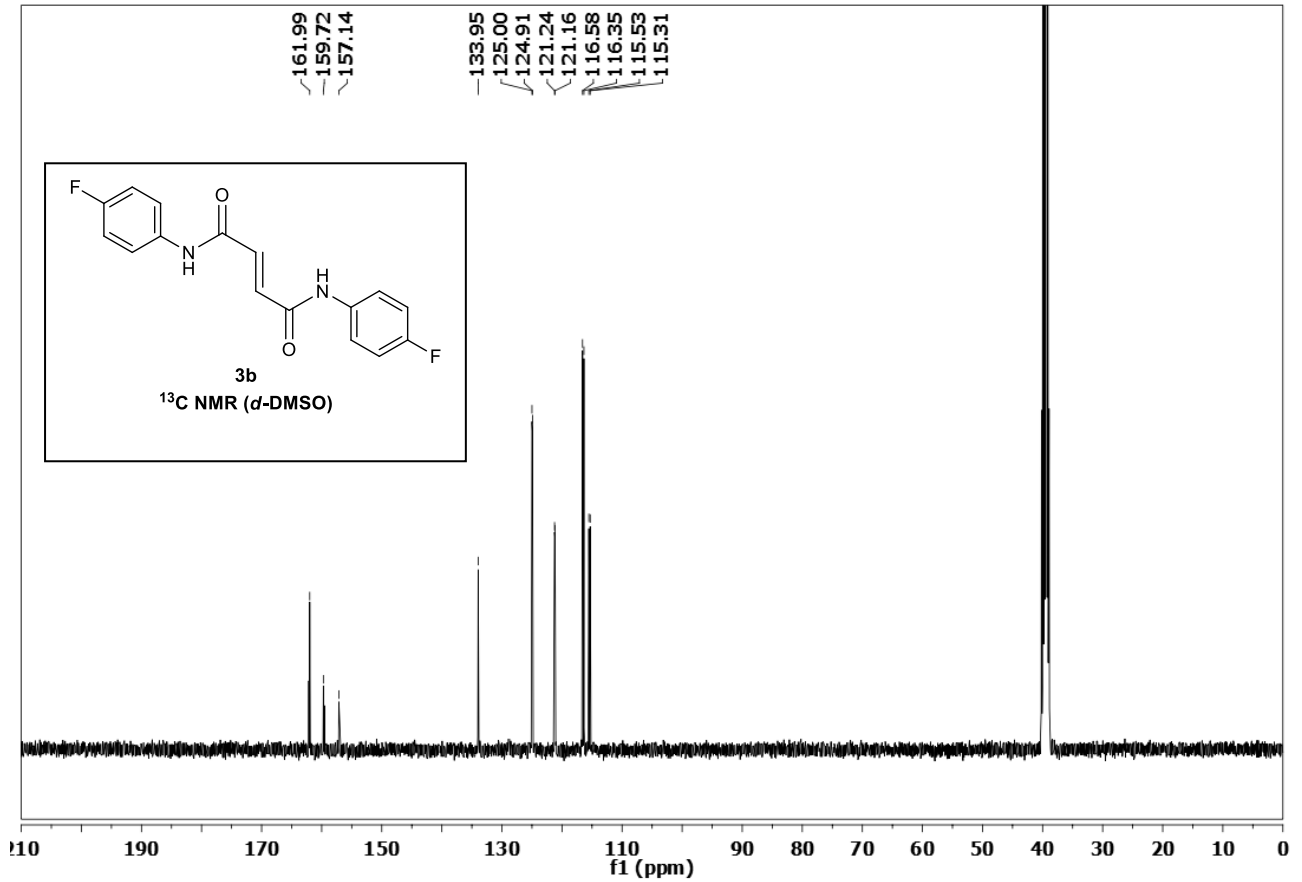
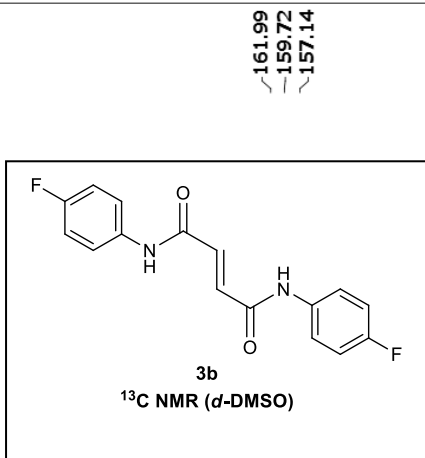
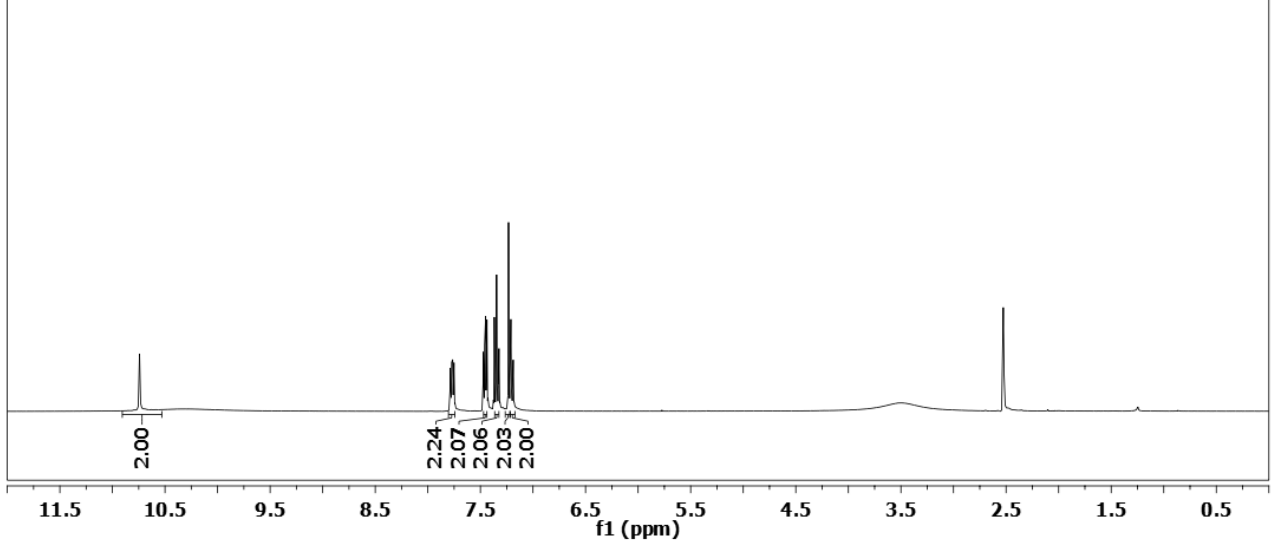
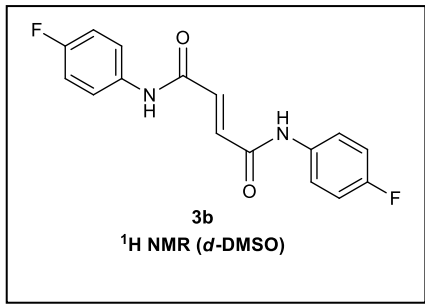
Department of Chemistry, Faculty of Arts and Sciences, Mersin University, 33343 Mersin, Turkey

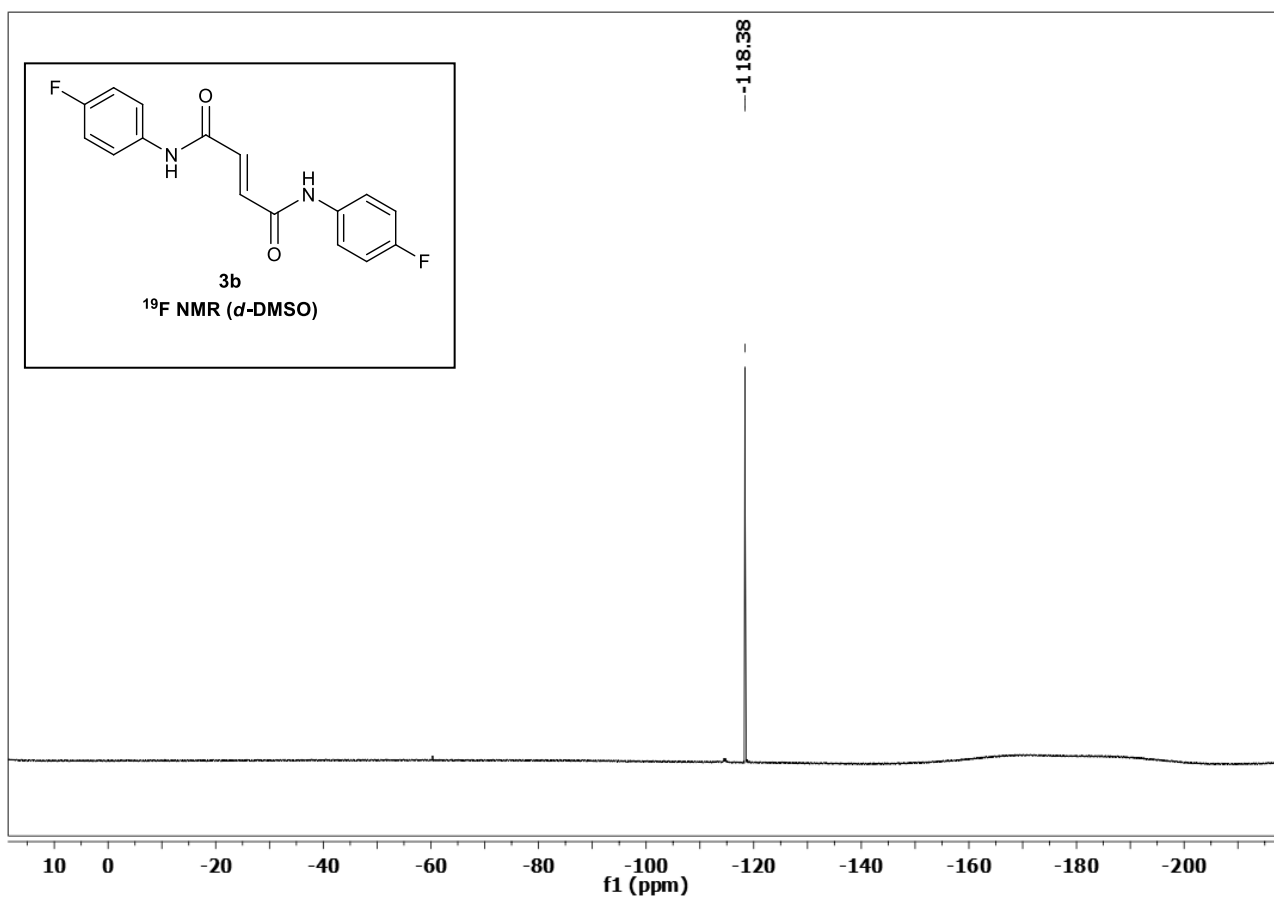
N¹,N⁴-bis(3-fluorophenyl)fumaramide (3a, C₁₆H₁₂F₂N₂O₂)



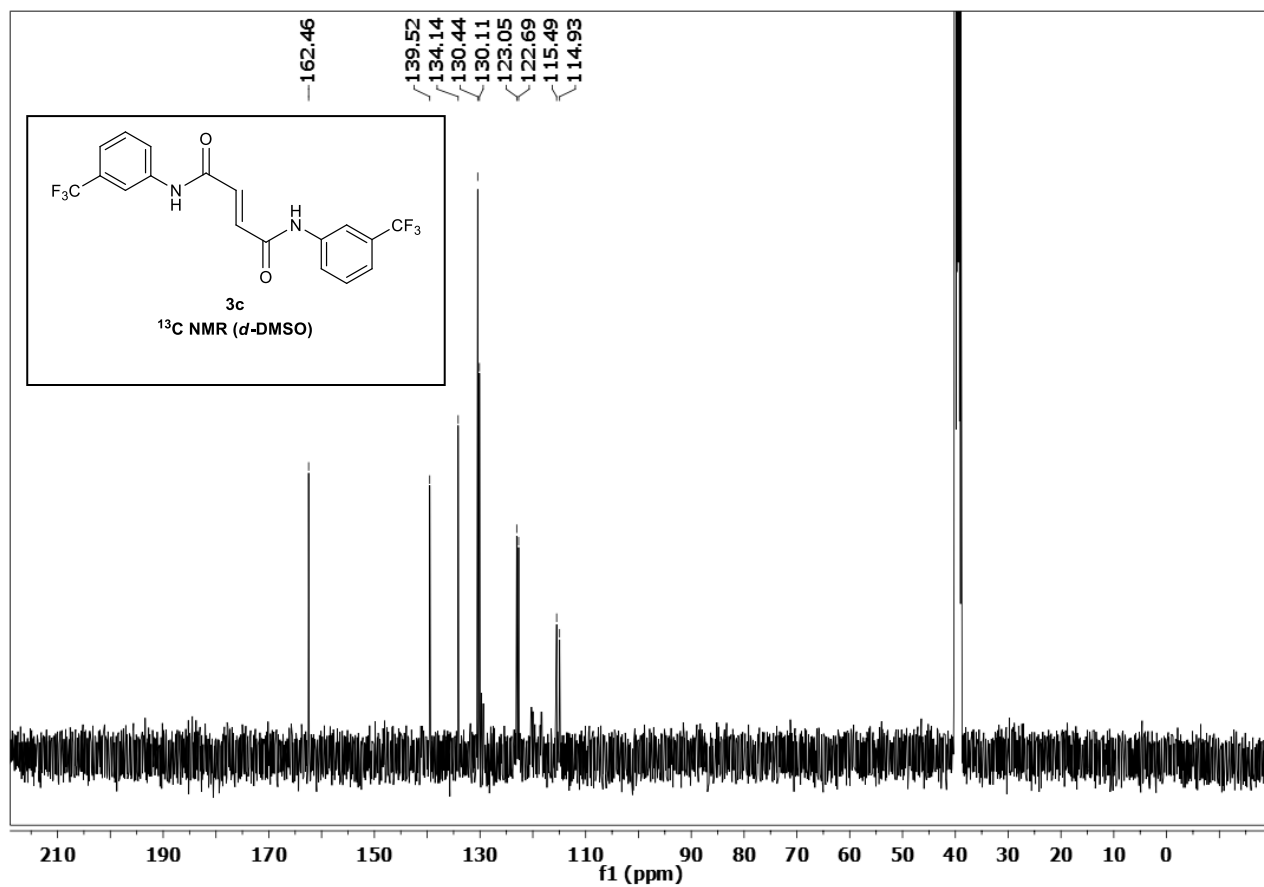
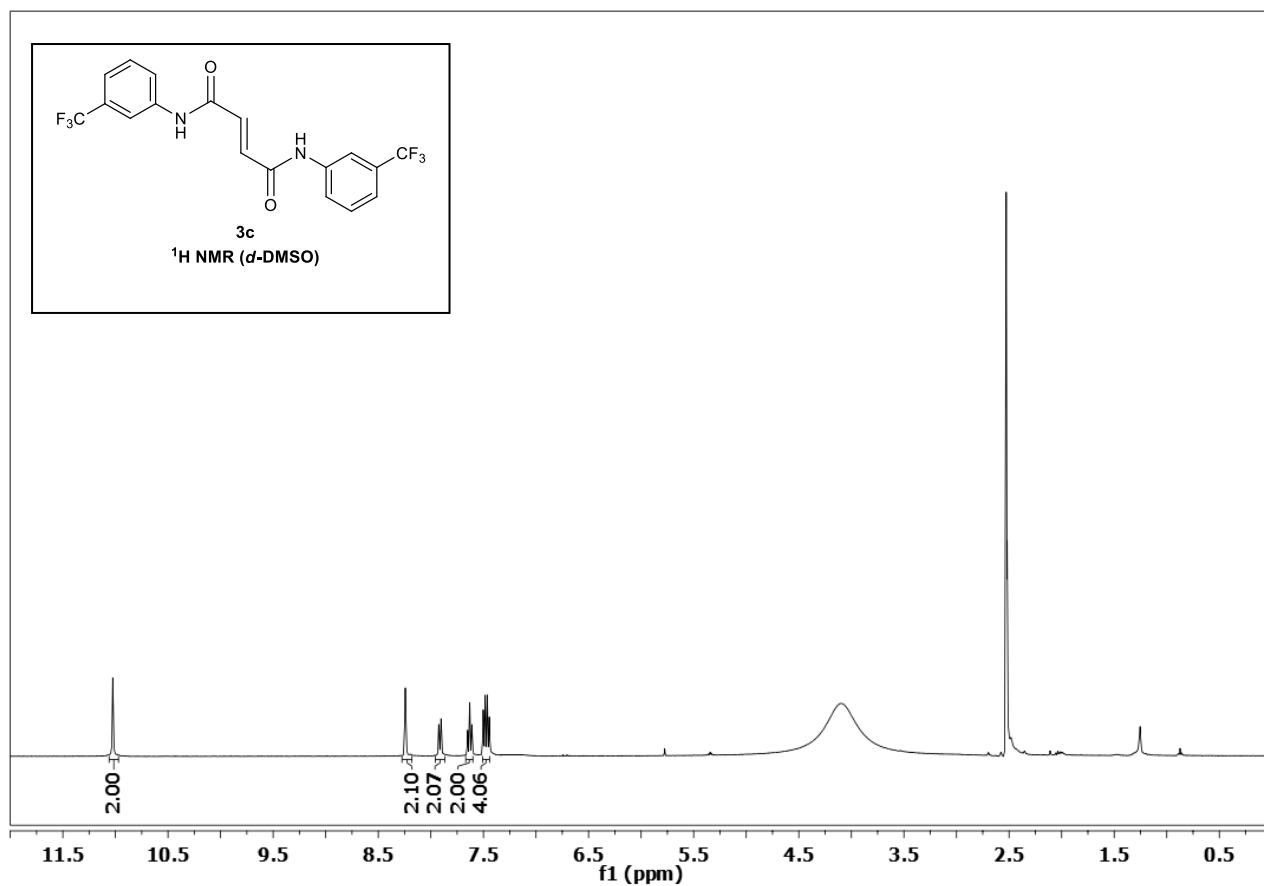


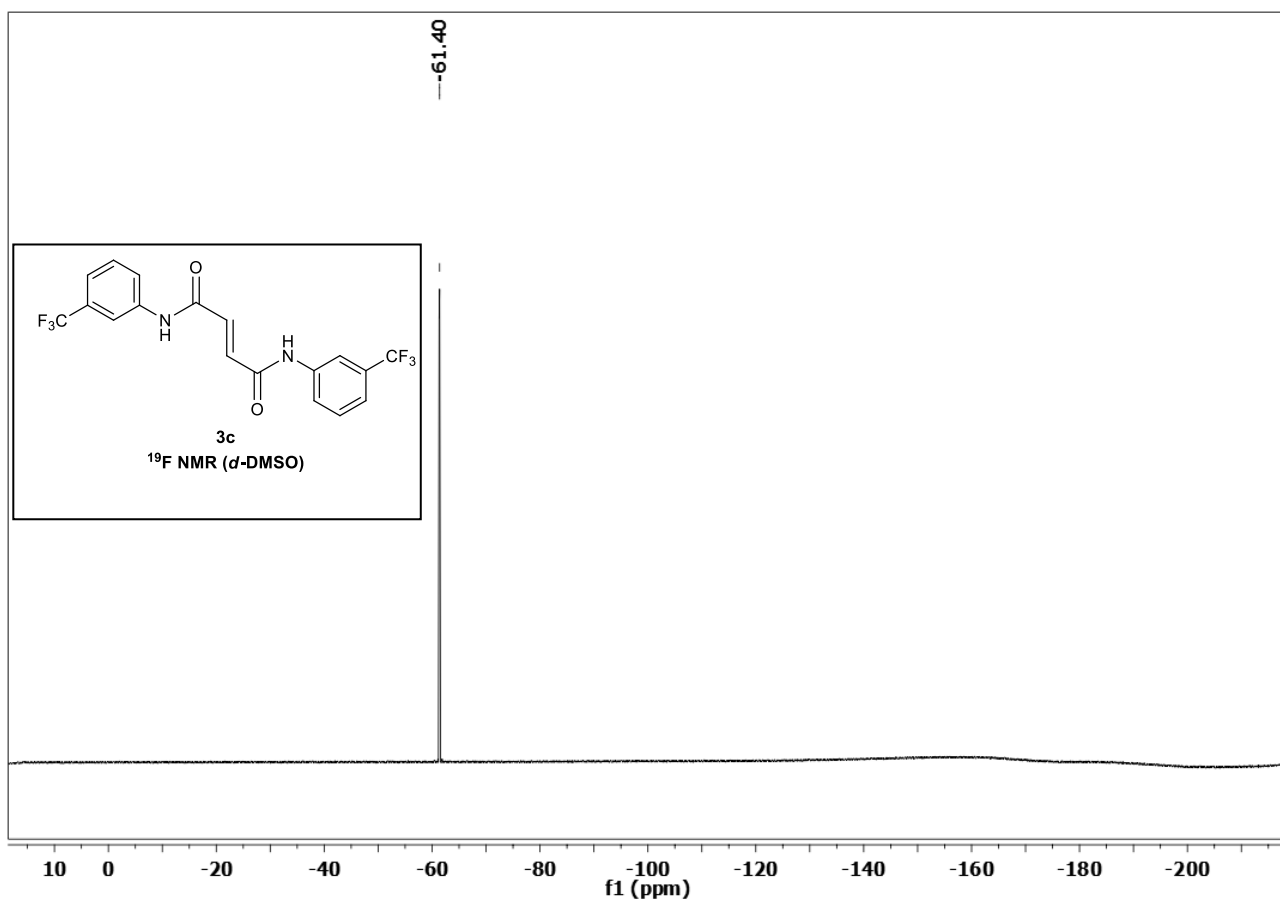
N¹,N⁴-bis(4-fluorophenyl)fumaramide (3b, C₁₆H₁₂F₂N₂O₂)



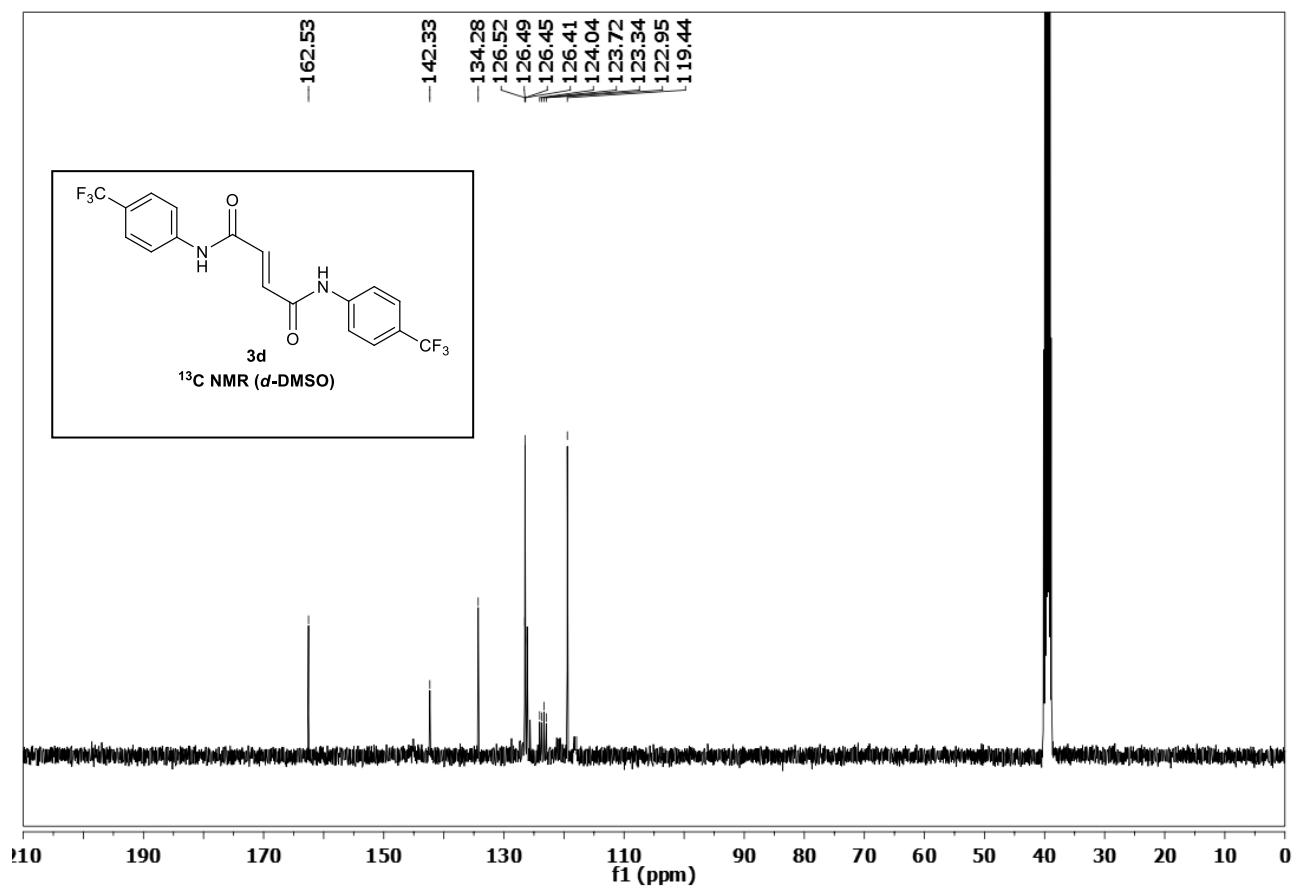
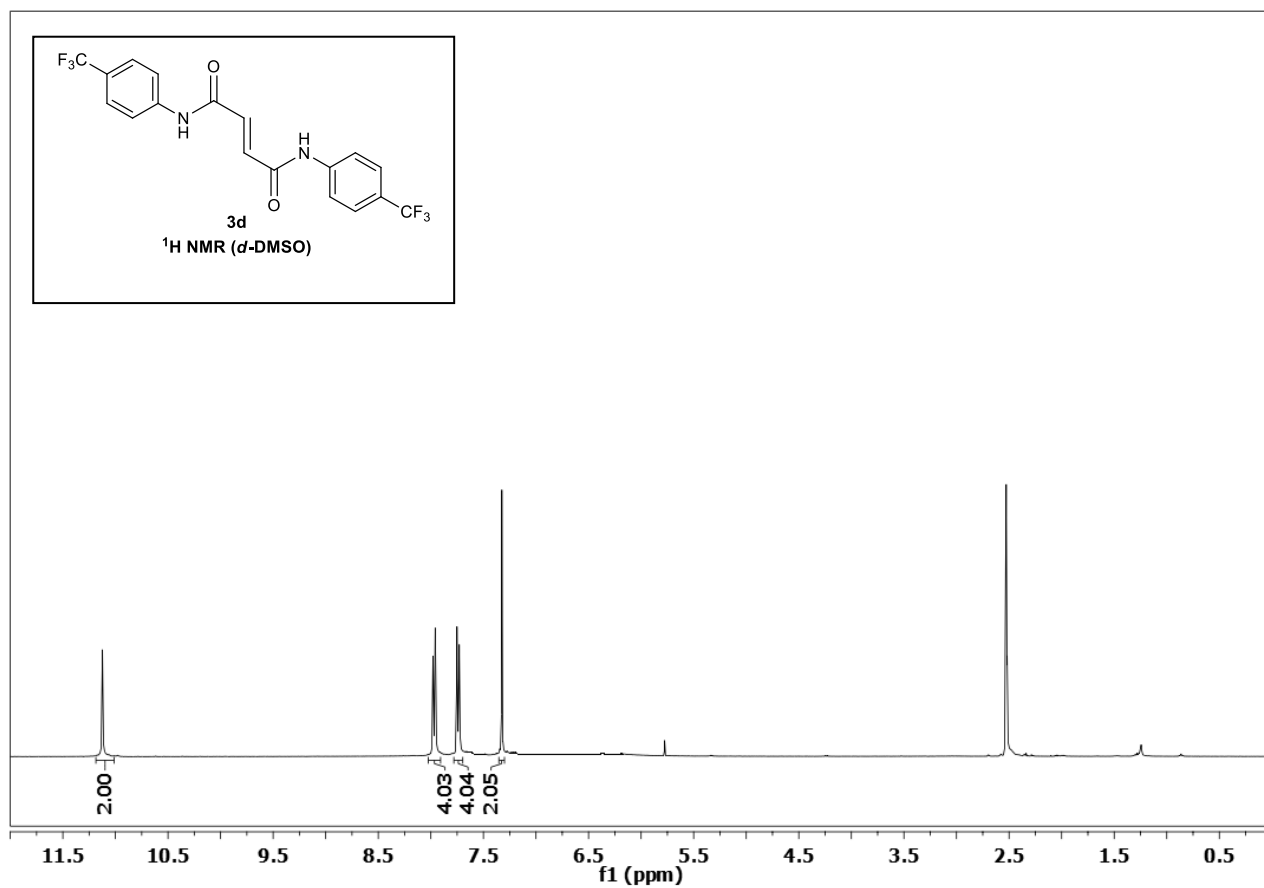


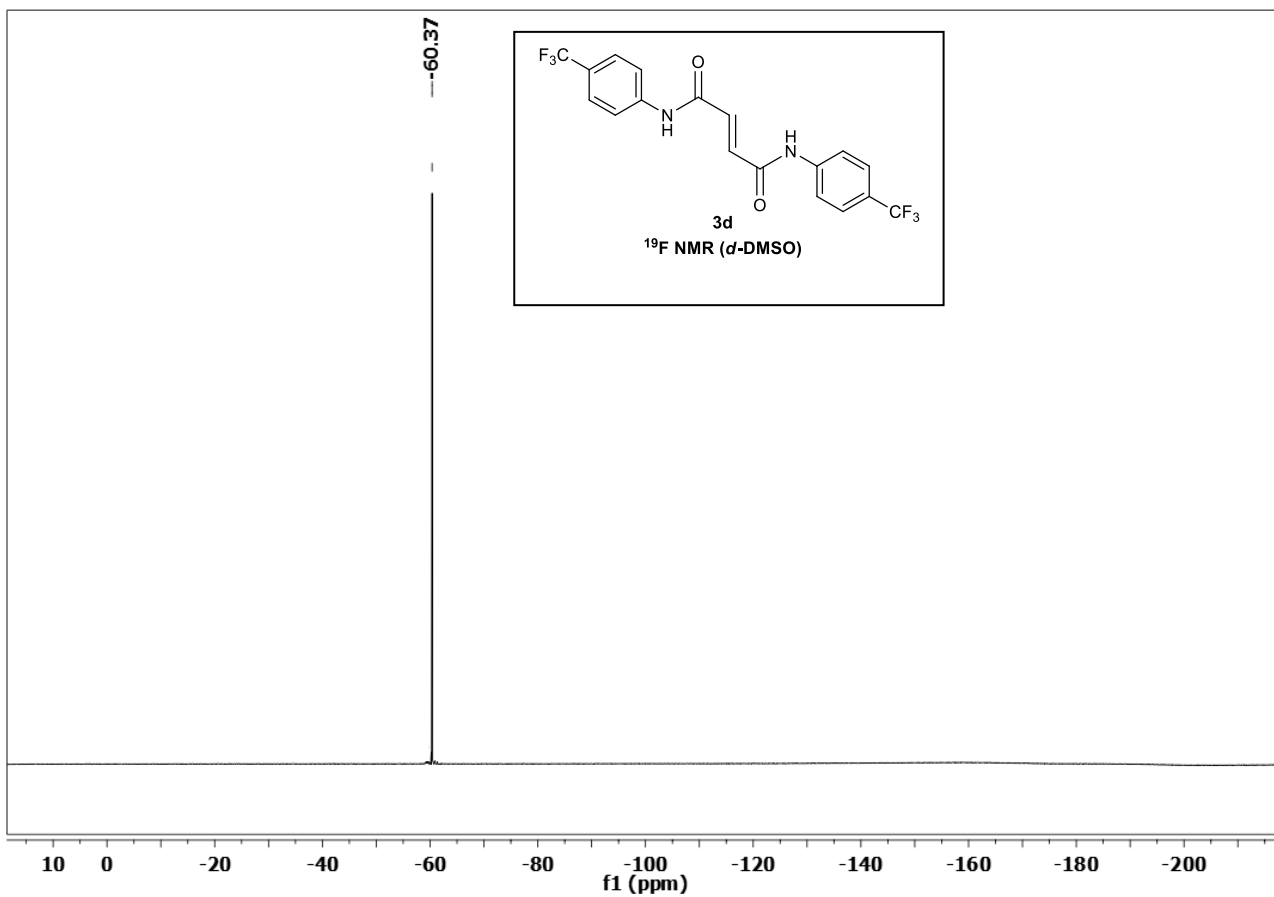
N¹,N⁴-bis(3-(trifluoromethyl)phenyl)fumaramide (3c, C₁₈H₁₂F₆N₂O₂)



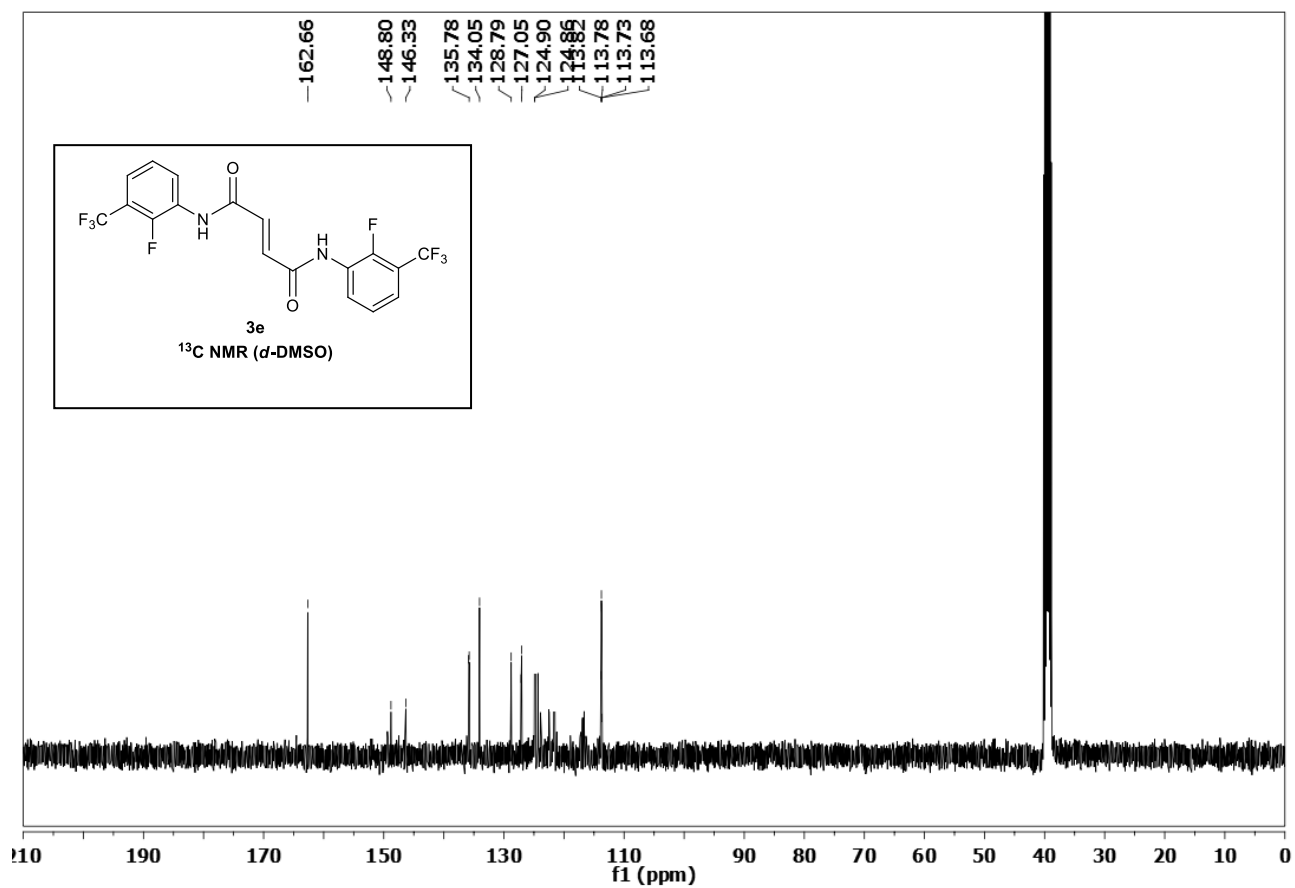
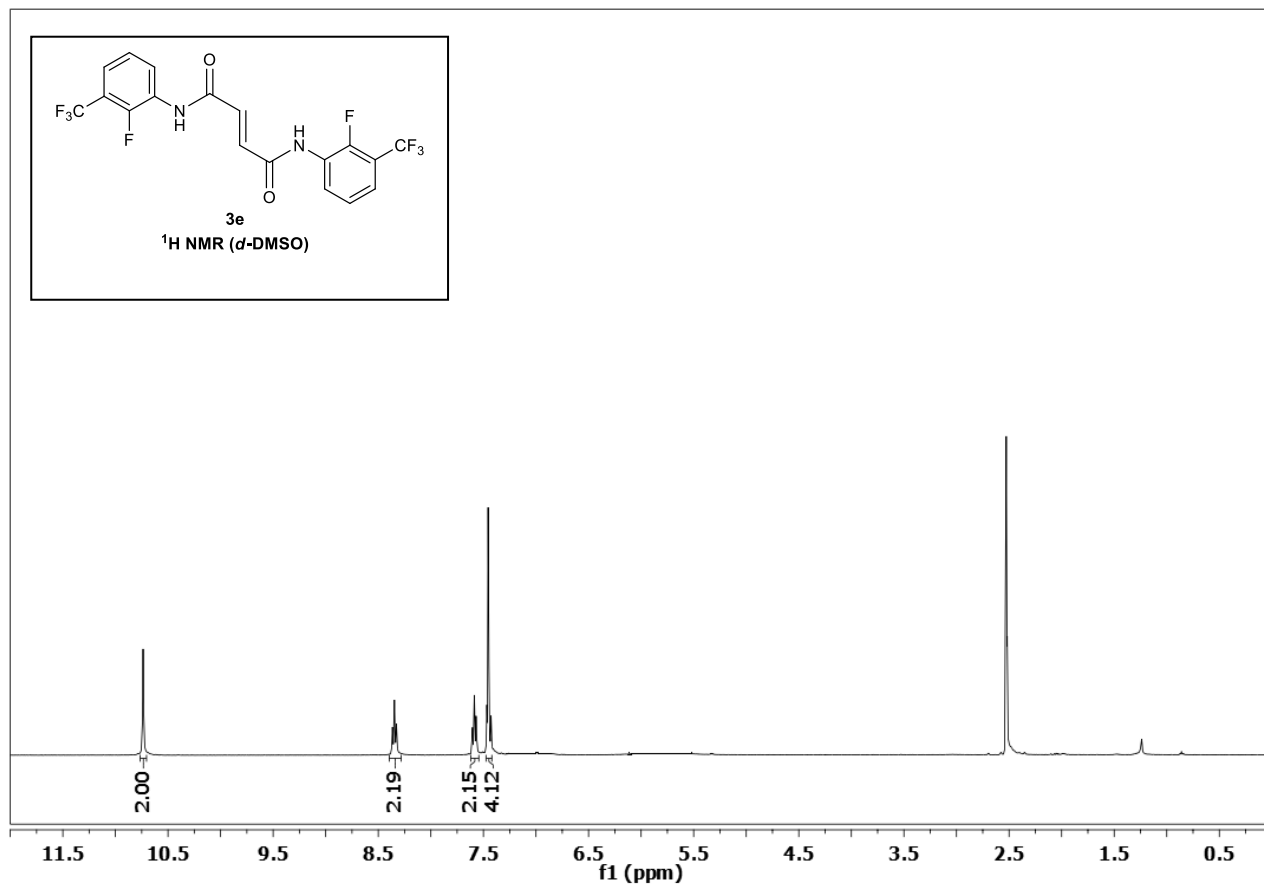


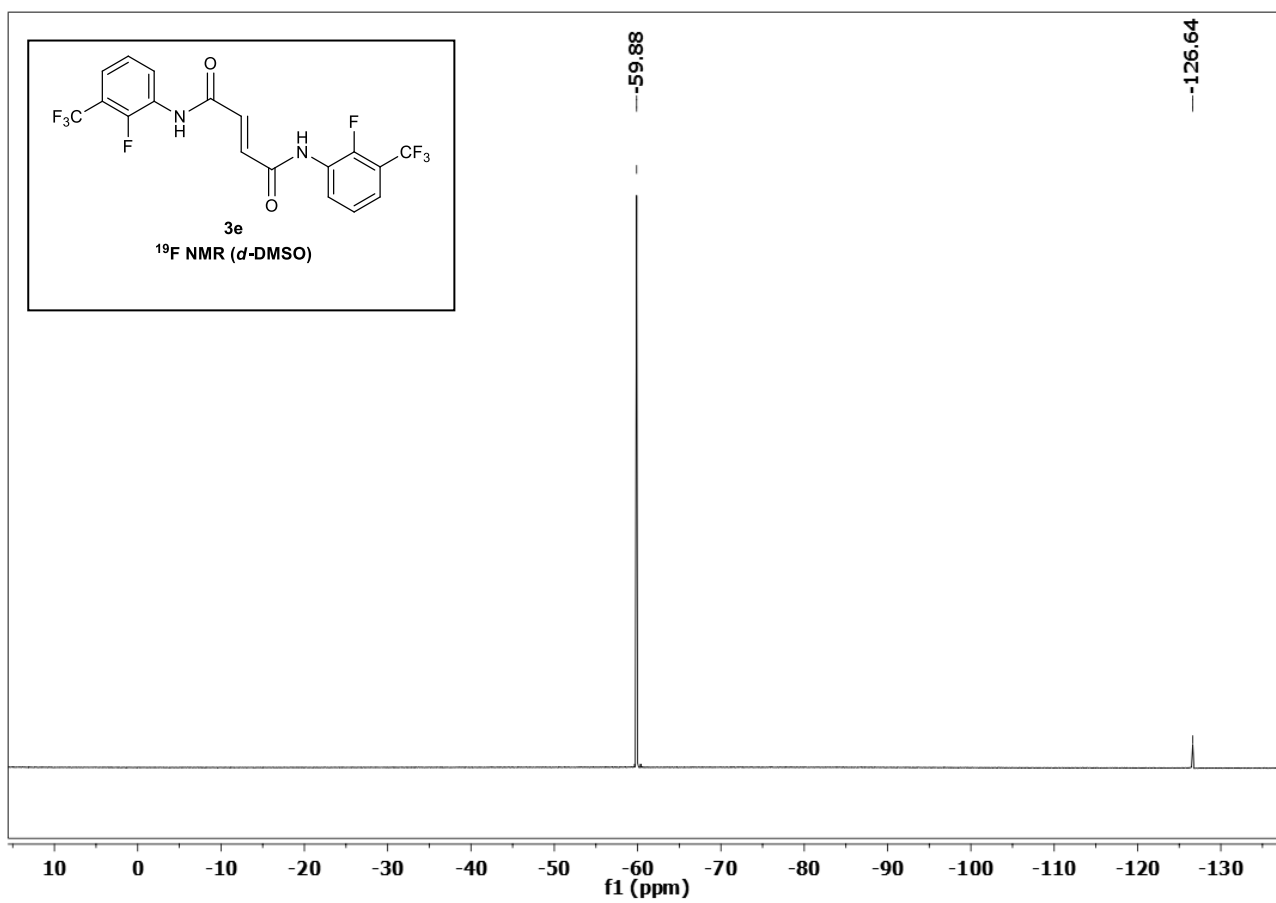
N¹,N⁴-bis(4-(trifluoromethyl)phenyl)fumaramide (3d, C₁₈H₁₂F₆N₂O₂)



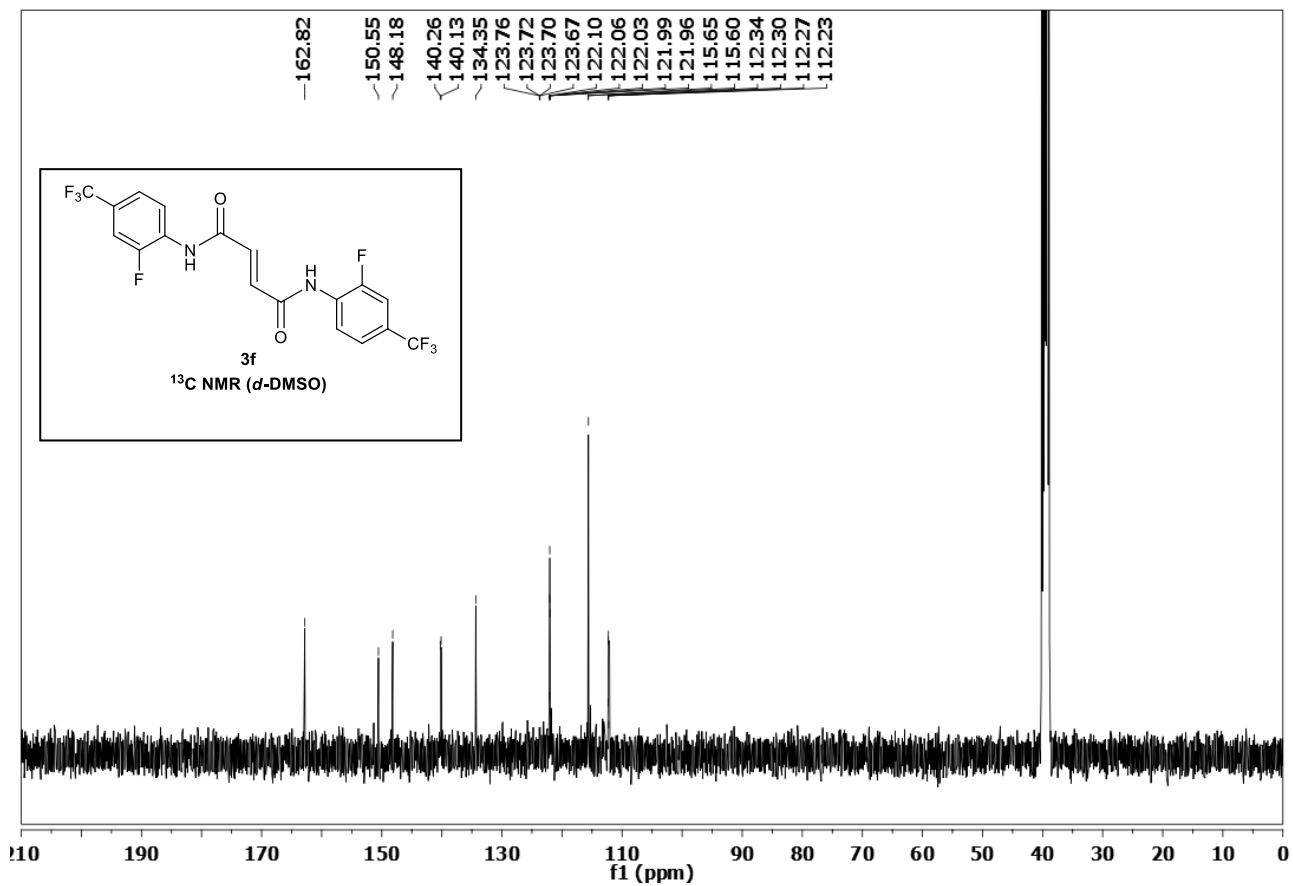
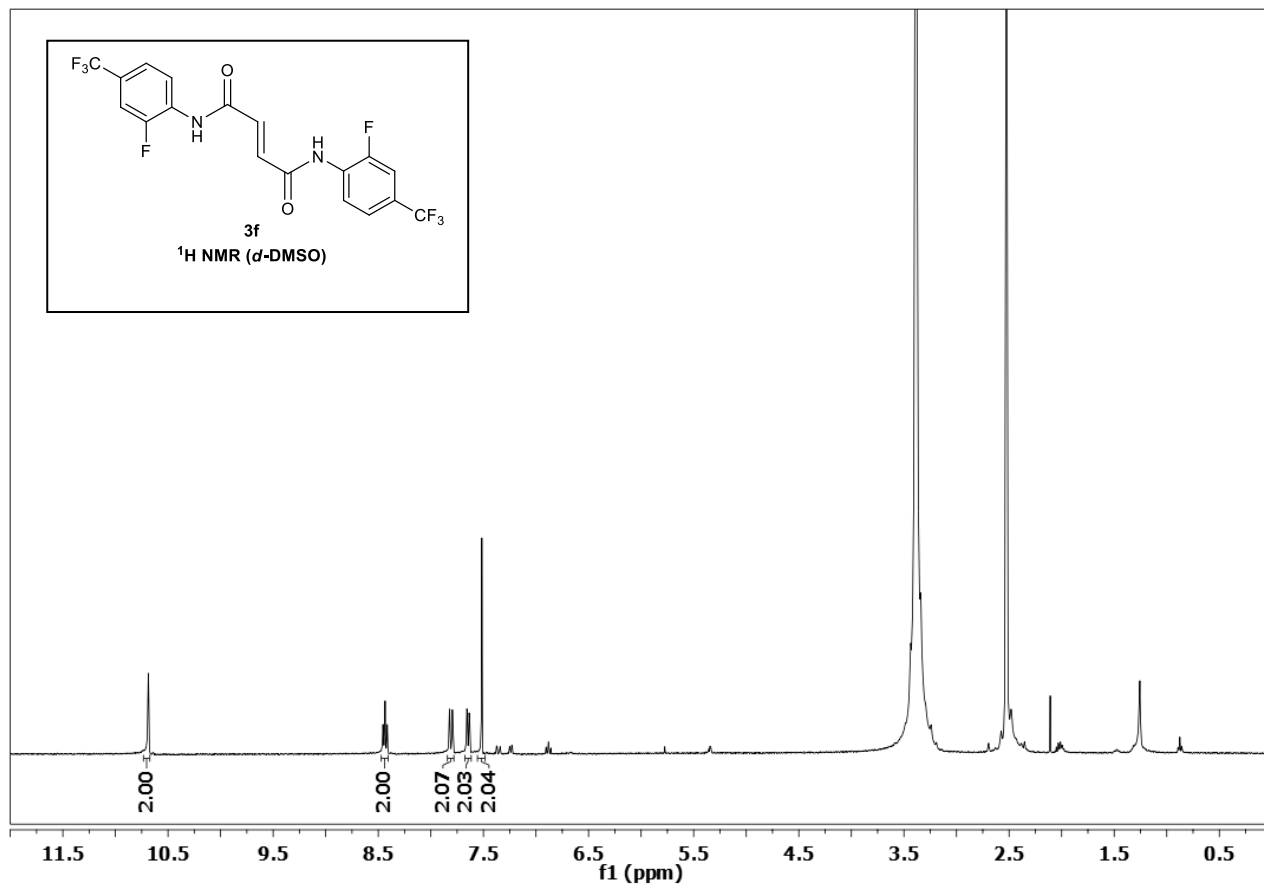


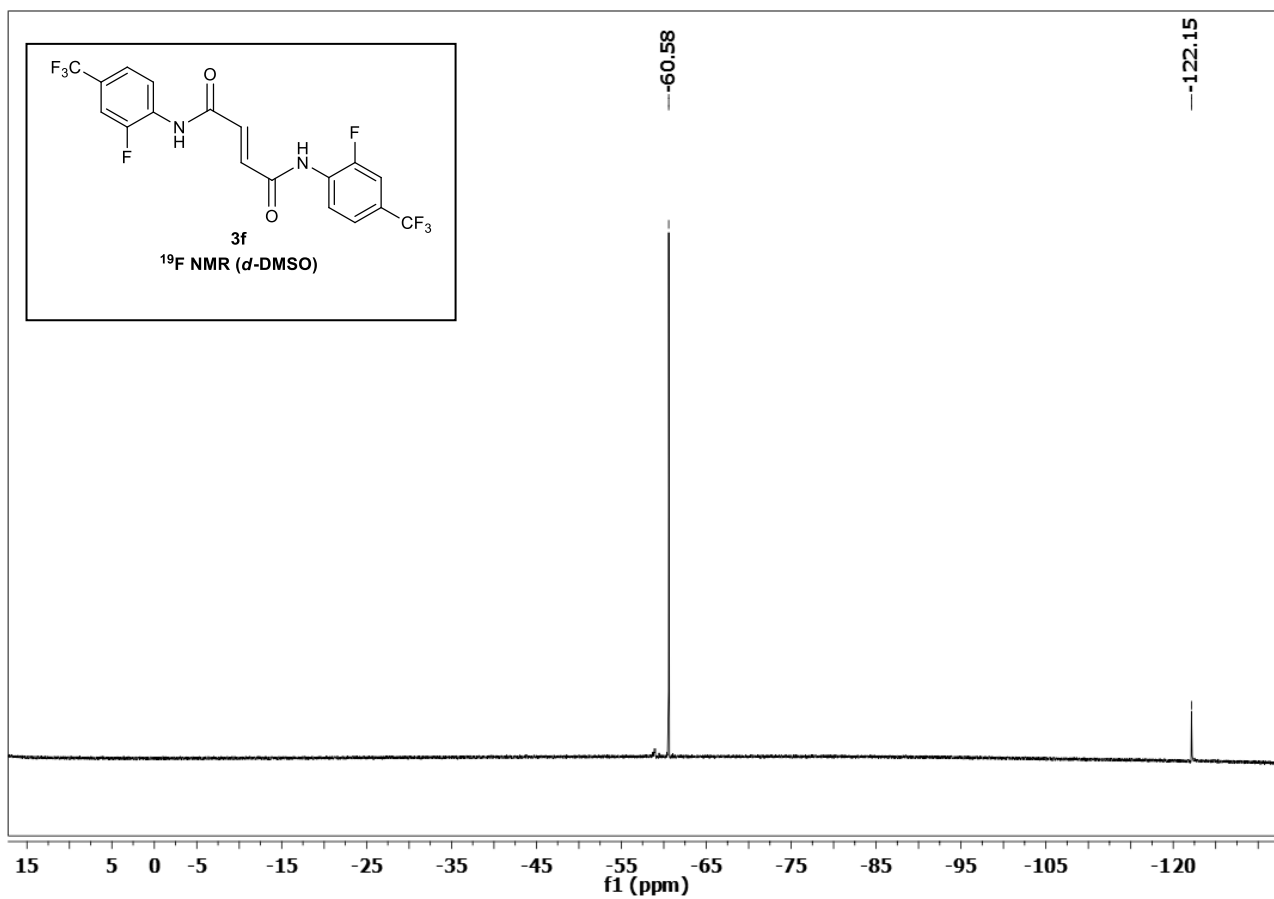
N¹,N⁴-bis(2-fluoro-3-(trifluoromethyl)phenyl)fumaramide (3e, C₁₈H₁₀F₈N₂O₂)



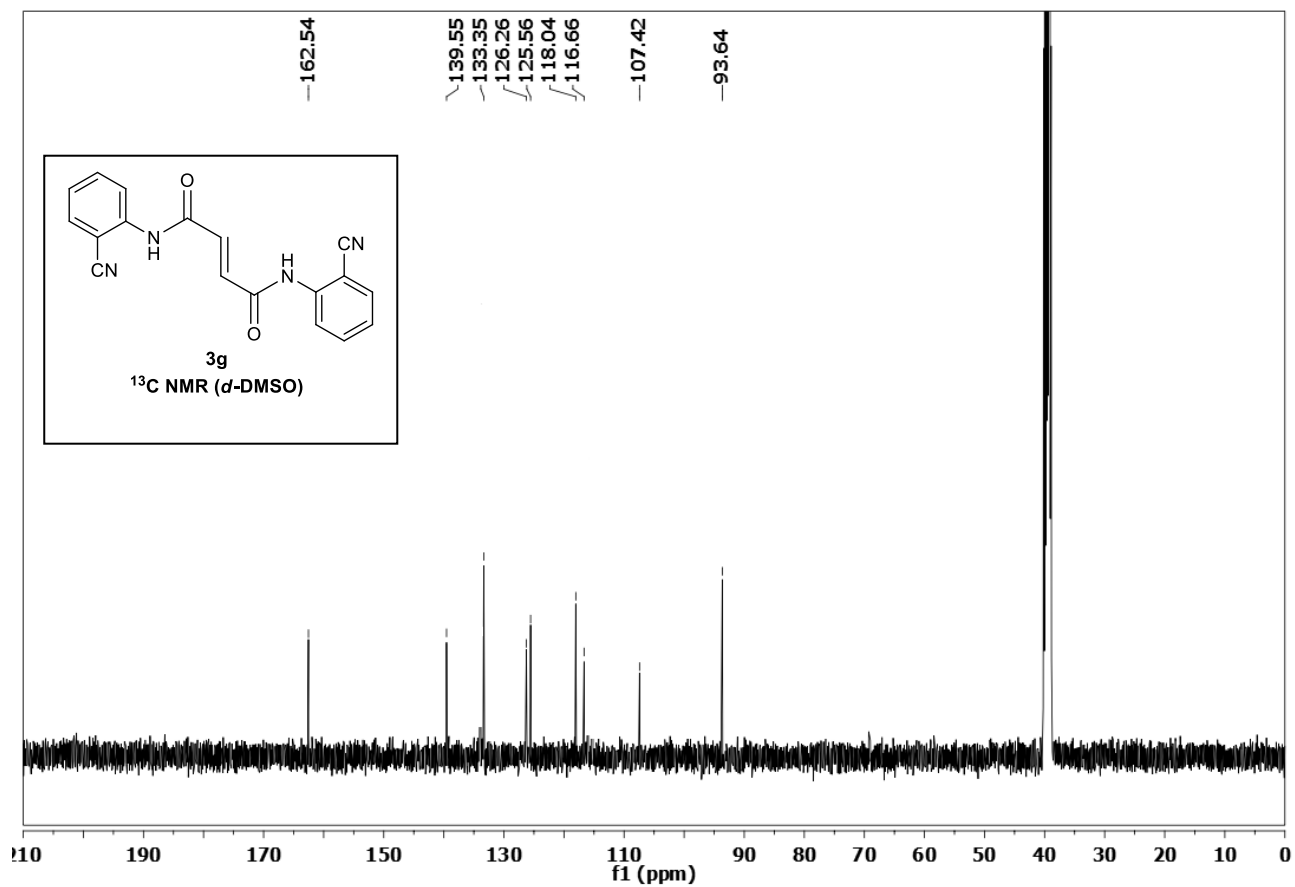
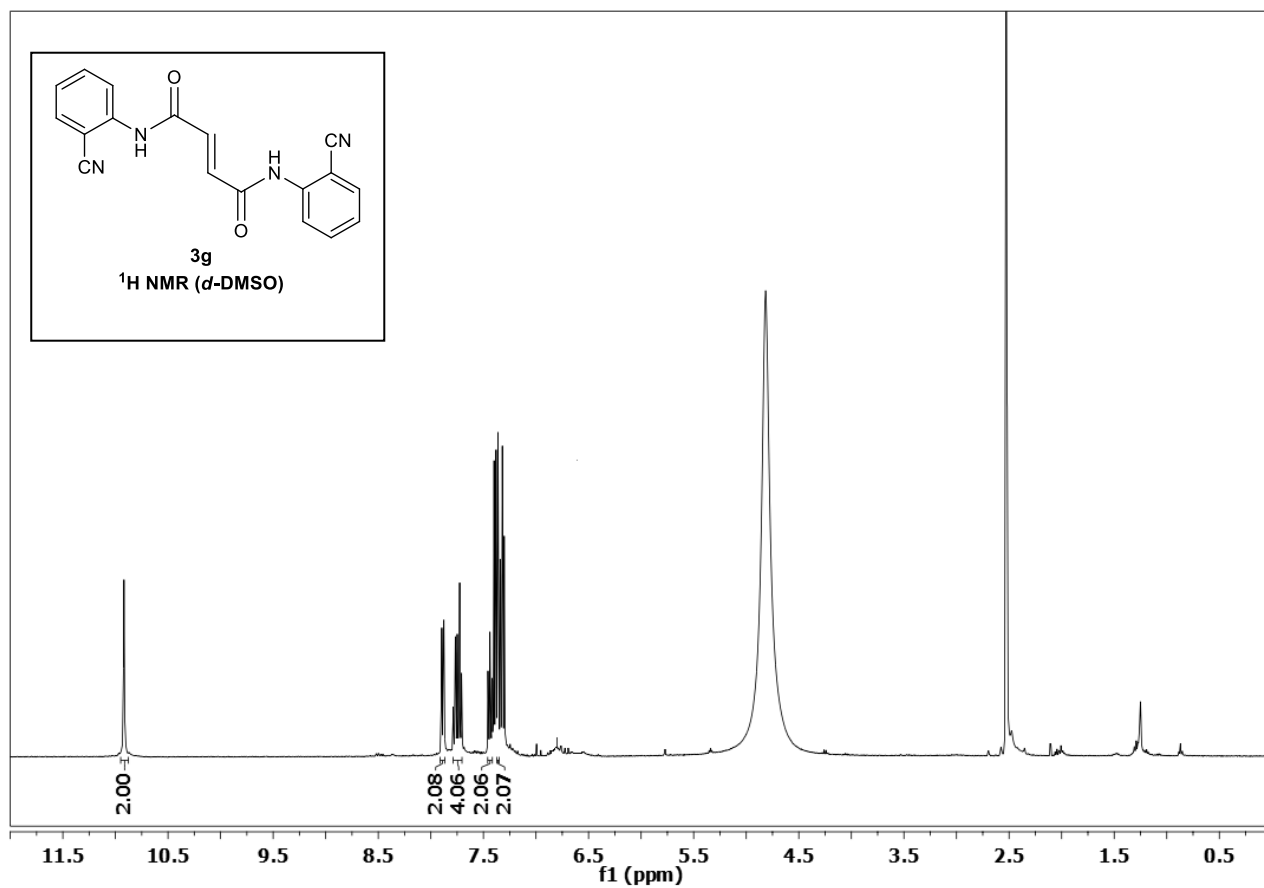


N¹,N⁴-bis(2-fluoro-4-(trifluoromethyl)phenyl)fumaramide (3f, C₁₈H₁₀F₈N₂O₂)

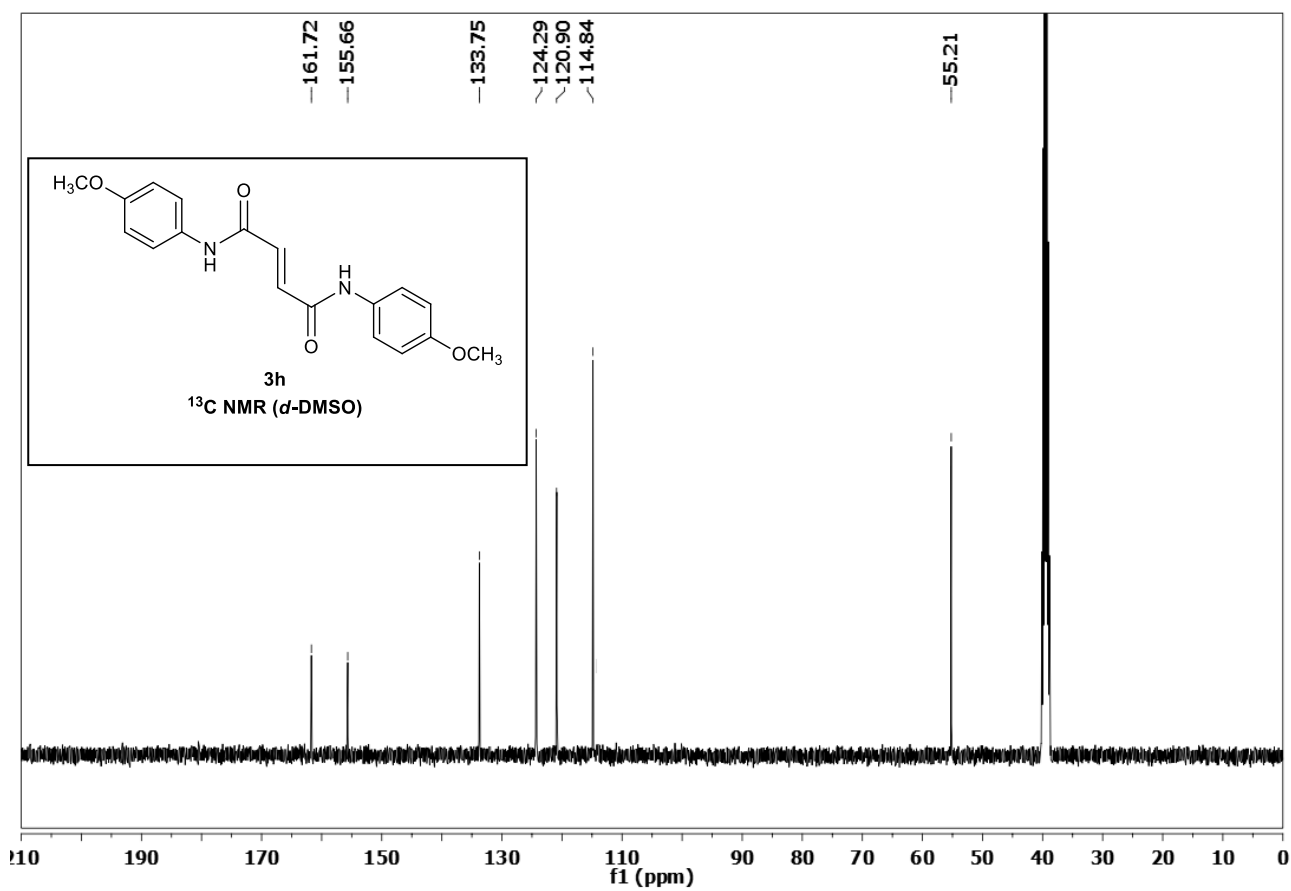
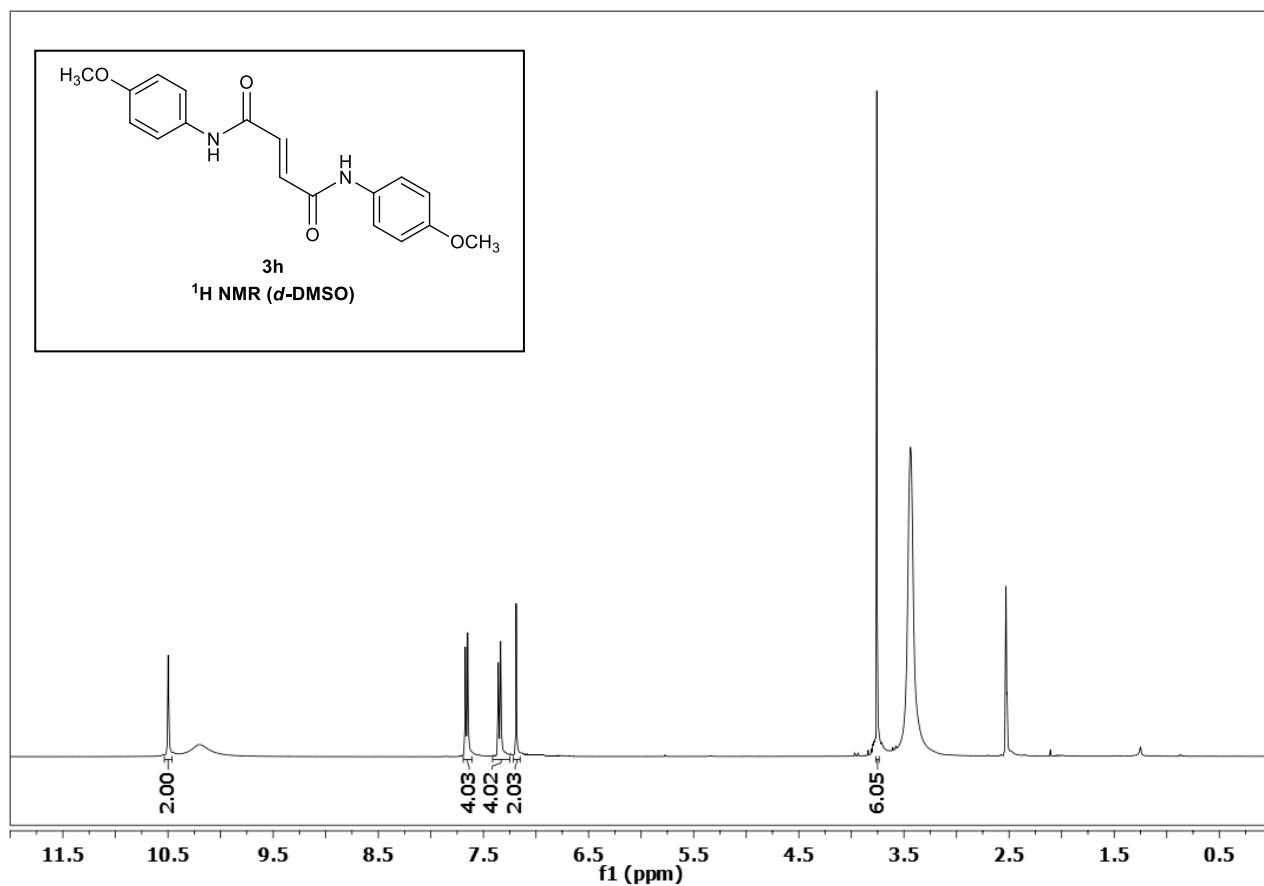




N¹,N⁴-bis(2-cyanophenyl)fumaramide (3g, C₁₈H₁₂N₄O₂)



N¹,N⁴-bis(4-methoxyphenyl)fumaramide (3h, C₁₈H₁₈N₂O₄)





Corrosion Protection of AISI 1010 Using Doped MoS₂ Conductive Polymers

Gülden Asan¹  and Abdurrahman Asan^{2,*} 

¹Hitit University, Vocational School of Technical Sciences, 19030, Corum, Turkey.

²Hitit University, Faculty of Engineering, 19030, Corum, Turkey.

Abstract: In this study, corrosion resistance of the coatings obtained by electrochemical oxidation of pyrrole and aniline on mild steel has been investigated in 0.1 M hydrochloric acid medium. It was aimed to increase the resistance of the coatings to corrosion by adding MoS₂ to the coating solutions while covering the polypyrrole (PPy) and polyaniline (PANI). PPy, PANI, MoS₂ doped PPy and MoS₂ doped PANI coatings on the electrodes produced from mild steel were obtained by cyclic voltammetry in 0.1 M H₂C₂O₄ environment. The voltammogram were carried out at a scan rate 100 mV/s from 0.0 V to 1.0 V with 10 scans. The corrosion resistance of the coatings in 0.1 M HCl medium was determined by Tafel polarization method. Best results were determined in MoS₂ doped PPy coatings. Later, PPy coatings, MoS₂ added PAN coatings and PANI coatings were determined respectively. The addition of MoS₂ to the coating solution increased the corrosion resistance in both coatings. Similar results were obtained in different media in our previous studies. It is understood that MoS₂ additive makes the coating surface impermeable and prevents deformation in the coating.

Keywords: Corrosion, MoS₂, Polypyrrole, Polyaniline, Mild Steel, Tafel Polarization Method.

Submitted: December 15, 2018. **Accepted:** November 19, 2019.

Cite this: Asan G, Asan A. Corrosion Protection of AISI 1010 Using Doped MoS₂ Conductive Polymers. JOTCSA. 2020;7(1):151-4.

DOI: <https://doi.org/10.18596/jotcsa.497889>.

***Corresponding author. E-mail:** asanabdurrahman@hotmail.com. **Tel:** +905053192438

INTRODUCTION

Metals are the most preferred materials due to their superior properties. One of the most restrictive parameters in the use of metals is corrosion. Corrosion is known to cause great losses from national wealth (1). One of the most common ways to protect metals from corrosion is to coat metal surfaces with paint or an organic coating (2). Organic coatings provide extremely good protection when the metal surface is free of defects. However, the scratching or degradation at the micro level during or after the coating accelerates the corrosion of the metal in this area. Conductive polymer coatings also referred to as smart coatings, can protect the exposed metal from corrosion due to the redox property and the repair of these imperfections (3-9). The conductive

polymers can be present in different states (oxidation-conductive state / non-conductive state) and can easily vary depending on the situation (7-12). These important properties of conductive polymer coatings and their electrochemically easy synthesis on the metal surface are widely used in corrosion protection. 2-dimensional MoS₂, which is one of the graphene derivatives, is used in many different areas with its remarkable features in recent years. In this study, corrosion resistance was measured by four different coating to protect the mild steel from corrosion. For conductive polymer coating, pyrrole, aniline and MoS₂, which were separated into two-dimensional layers, were used and positive results were obtained.

Tafel extrapolation is one of the polarization methods widely utilized to measure corrosion

rates, a faster experimental technique compared with the classical weight-loss estimation. The most fundamental procedure for experimentally evaluating I_{corr} is by Tafel extrapolation. This method requires the presence of a linear or Tafel section in the E versus $\log I_{ex}$ curve. A potential scan of approximately ± 300 mV about E_{corr} is generally required to determine if a linear section of at least one decade of current is present, such that a reasonably accurate extrapolation can be made to the E_{corr} potential (13).

In this work, conductive polymer films with 2-D MoS_2 coatings were electrochemically synthesized on AISI 1010 steel electrode in oxalic acid aqueous solution by cyclic voltammetry and then the protective performance of these coatings was evaluated by using Tafel Polarization method in 0.1 M HCl solution.

EXPERIMENTAL METHOD

The experiments were carried out in a 3-necked 250 mL flask. A platinum plate as a counter electrode, a saturated calomel electrode (SCE) as a reference electrode and AISI 1010 steel as the working electrode were used. The chemical composition of AISI 1010 steel is given in Table 1. The chemicals used are of analytical purity of oxalic acid, hydrochloric acid, pyrrole and aniline. Before each test, the surface of the working electrode was polished under water with 2000 grit sandpaper; the surface was cleaned with pure water and acetone. Coatings obtained by cyclic voltammetry were obtained with 100 mV / s scan rate. Tafel polarization curves have obtained with a scan rate 2 mV / s for the determination of the corrosion rate. The coatings were made in 0.1 M conductive polymer monomer and 0.1 M $H_2C_2O_4$ solution containing MoS_2 converted into a 0.1 M two-dimensional form. The corrosion resistance of the coatings were determined by Tafel Polarization method in 0.1 M HCl medium. Cyclic voltammogram and Tafel Polarization Curves were performed with Ivium Technologies De Regent 178 5611 HW Eindhoven model device.

C	Mn	P	Si	S	Fe
0.09	0.35	0.02	0.06	0.04	Balan
%	%	%	%	%	ce

Table 1. Chemical composition of mild steel AISI 1010)

The percentage coating protective efficiency was calculated according to the following equation (14).

$$\text{Protective Efficiency \%} = \frac{CR_{\text{uncoated}} - CR_{\text{coated}}}{CR_{\text{uncoated}}} \times 100$$

Figure 2 shows that the mild steel is passive at -0.2 V in 0.1 M oxalic acid solution and maintains this state up to 1.0 V. This potential indicates that the polymerization will easily occur on the steel surface since it is lower than the potential for polymerization. This passivity can be explained with iron(II) oxalate compound forming on the steel surface. The small peak formed in the reverse current between 0.0V and 0.1V indicates that the iron(III) oxalate is transformed into iron(II) oxalate (15).

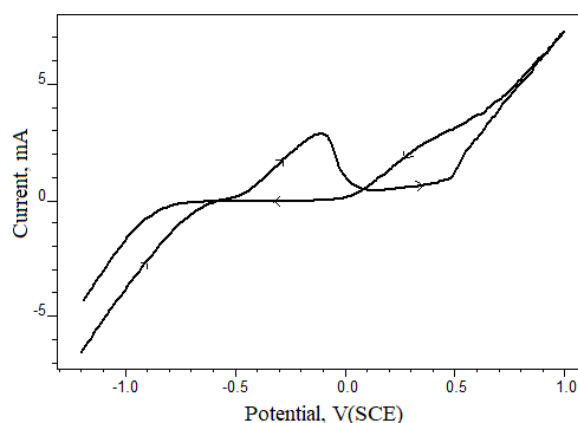


Figure 1. Cyclic voltammogram of Mild Steel in 0.1 M HCl.

Electropolymerization of pyrrole on the steel surface is given in Figure 3. In the first screening, high current passes, but the passivation property of the steel becomes passive and the current decreases rapidly. In subsequent scans, the oxidation current of pyrrole begins approximately at 0.6V.

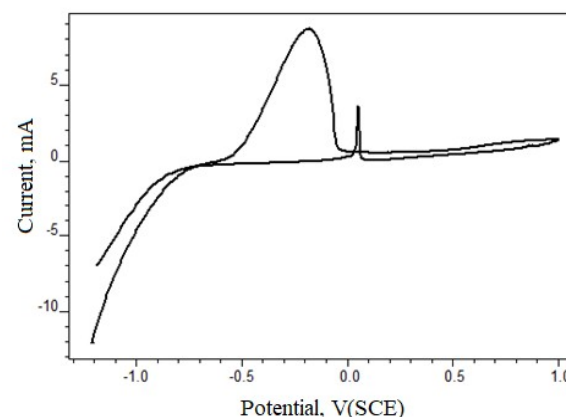


Figure 2. Cyclic voltammogram of mild steel in 0.1 M $H_2C_2O_4$.

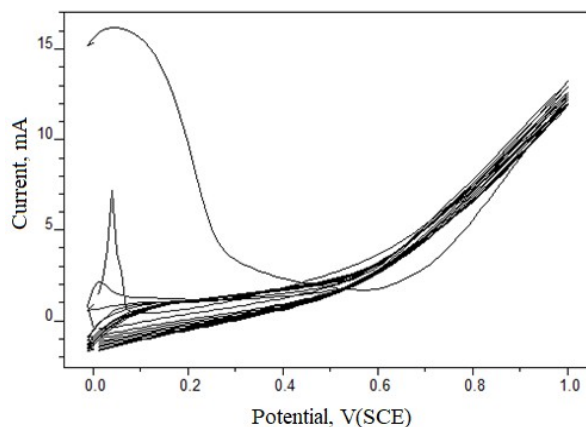


Figure 3. Electropolymerization curves of pyrrole on steel in 0.1 M oxalic acid solution.

Table 2. Corrosion parameters of coated and uncoated mild steel.

	Ecor (mV)	Rp (ohm)	Corrosion rate (mm/year)	Protective Efficiency %
Mild Steel	-645	52	5.52	-
MS+PANI	-652	985	1.25	77.4
MS+PANI+MoS ₂	-441	1050	1.14	79.3
MS+PPy	-821	1253	0.82	85.1
MS+PPy+MoS ₂	-705	1432	0.75	86.4

Figure 4 shows the Tafel polarization curves of the mild steel, PANI and PANI doped with MoS₂ the PANI coating did not have a significant effect on the corrosion potential of the steel, but caused a significant reduction in the corrosion current.

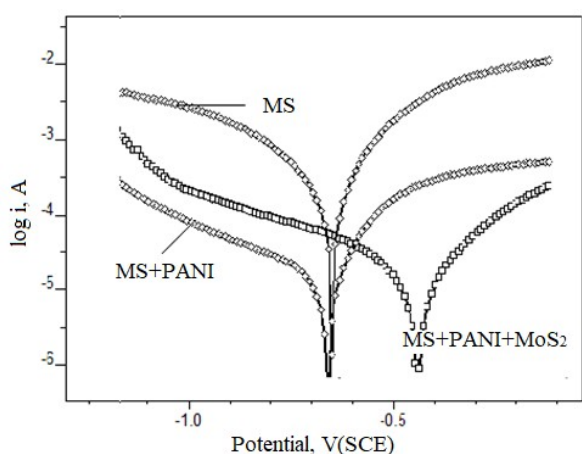


Figure 4. Tafel polarization curves of mild steel, polyaniline and MoS₂ doped polyaniline coatings.

The MoS₂ additive improved the PANI coating and increased the corrosion potential to more positive values. Whereas PANI coating showed corrosion protection efficiency of 77.4%, PANI + MoS₂ coating showed at 79.3%.

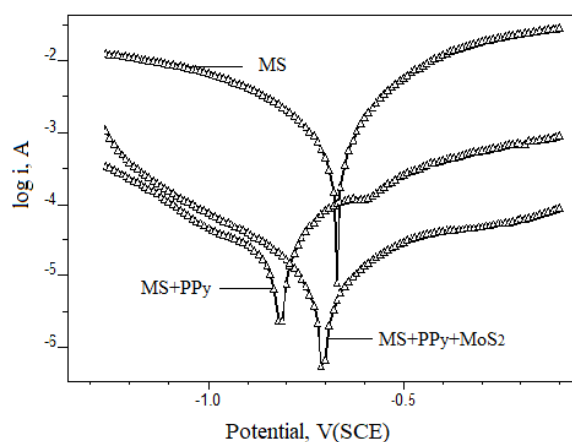


Figure 5. Tafel polarization curves of steel, polypyrrole and MoS₂ doped polypyrrole coatings.

The corrosion potential of the steel coated with polypyrrole was determined to be at -820 mV with more negative potentials, but the corrosion rate was significantly reduced (Figure 5). While corrosion potential is almost unchanged in polypyrrole + MoS₂ coated steel, corrosion current has decreased significantly and provides 86.4% protection.

Corrosion parameters measured by Tafel polarization method are given in Table 2.

Polypyrrole and MoS₂ doped polypyrrole coatings are more successful than polyaniline coatings. It is understood that MoS₂ additive increases the coating efficiency in both conductive polymer coatings and reduces the corrosion rate. In previous studies, studies on 0.1 M H₂SO₄, 0.1 M NaOH and 0.1 M NaCl solutions indicated that MoS₂ additive showed similar effects [14].

CONCLUSIONS

The results confirmed that the corrosion protective effect of PPy, PANI and MoS₂ coatings on mild steel in hydrochloride solution. Furthermore, MoS₂ demonstrated extra protective effect on AISI 1010 steel by shift corrosion potential to positive direction and decrease the oxidation current value. The greatest shift of the corrosion potential values to the positive direction is observed for the PPy+MoS₂ coatings on mild steel. The polarization curves show that doped MoS₂ conductive polymers promise to be a good candidate for corrosion protection of reactive metals.

ACKNOWLEDGMENTS

This article was presented orally in the 30th Chemical Congress.

REFERENCES

1. Fontana MG. Corrosion engineering: Tata McGraw-Hill Education; 2005.
2. Grundmeier G, Schmidt W, Stratmann M. Corrosion protection by organic coatings: electrochemical mechanism and novel methods of investigation. *Electrochim Acta*. 2000;45(15-16):2515-33.
3. Kang E, Neoh K, Tan K. Polyaniline: a polymer with many interesting intrinsic redox states. *Progress in polymer science*. 1998;23(2):277-324.
4. Sazou D, Georgolios C. Formation of conducting polyaniline coatings on iron surfaces by electropolymerization of aniline in aqueous solutions. *J Electroanal Chem*. 1997;429(1-2):81-93.
5. Tallman DE, Spinks G, Dominis A, Wallace GG. Electroactive conducting polymers for corrosion control. *J Solid State Electr*. 2002;6(2):73-84.
6. Sitaram SP, Stoffer JO, O'Keefe TJ. Application of conducting polymers in corrosion protection. *Journal of Coatings Technology*. 1997;69(866):65-9.
7. Spinks GM, Dominis AJ, Wallace GG, Tallman DE. Electroactive conducting polymers for corrosion control. *J Solid State Electr*. 2002;6(2):85-100.
8. Gašparac R, Martin CR. Investigations of the mechanism of corrosion inhibition by polyaniline. Polyaniline-coated stainless steel in sulfuric acid solution. *J Electrochem Soc*. 2001;148(4):B138-B45.
9. Ohtsuka T, Iida M, Ueda M. Polypyrrole coating doped by molybdo-phosphate anions for corrosion prevention of carbon steels. *J Solid State Electr*. 2006;10(9):714-20.
10. Ohtsuka T. Corrosion protection of steels by conducting polymer coating. *Int J Corros*. 2012;2012.
11. Bereket G, Hur E. The corrosion protection of mild steel by single layered polypyrrole and multilayered polypyrrole/poly(5-amino-1-naphthol) coatings. *Prog Org Coat*. 2009;65(1):116-24.
12. Lei YH, Ohtsuka T, Sheng N. Corrosion protection of copper by polypyrrole film studied by electrochemical impedance spectroscopy and the electrochemical quartz microbalance. *Appl Surf Sci*. 2015;357:1122-32.
13. R.A. Buchanan EES. Handbook of Environmental Degradation of Materials. Second Edition ed2012.
14. Yu Y, Kim J, Cho S, Boo J. Plasma-polymerized toluene films for corrosion inhibition in microelectronic devices. *Surface and Coatings Technology*. 2003;162(2-3):161-6.
15. Asan A, Kabasakaloglu M. Electrochemical and corrosion behaviors of mild steel coated with polypyrrole. *Mater Sci+*. 2003;39(5):643-51.



Study of Electronic Transition of Complex Fe(III), Ni(II) and Zn(II)-1,10-Phenanthroline: Modelling and UV-Vis Spectral Analysis

Khusna Arif Rakhman* , Zulkifli Zam Zam , Sudir Umar 
and Muhammad Ikhlas Abdjan 

Department of Chemistry Education, Khairun University, Ternate, 97728, Indonesia

Abstract: Geometric modeling and geometric optimization of Fe(III)-1,10-phenanthroline (Fe-Phen), Ni(II)-1,10-phenanthroline (Ni-Phen) and Zn(II)-1,10-phenanthroline (Zn-Phen) compounds have been carried out computing using the semi-empirical method of PM3. The spectral measurements and the study of complex electronic compositions using the UV-Vis spectrophotometer and simulation of ZINDO/s (Zerner's Neglect of Differential Overlap) calculations. The optimum result of the geometry of complex molecule found there is a change of charge in each complex with stable energy. The UV-Vis spectra measurements showed λ_{max} in the Fe-Phen complex: 315.50 nm, Ni-Phen complex: 325.00 nm and Zn-Phen complex: 315.00 nm. The electronic transition occurring at these three complexes shows the transition characteristics of electrons at the level of the molecular orbitals n to n^* and the degree of the molecular orbitals n to n^* . Electron transition energy in complex orbital molecules can be observed in the energy changes of each molecular orbitals.

Keywords: 1,10-phenanthroline, complex ion, semi-empirical method, zindo/s.

Submitted: July 10, 2019. **Accepted:** November 02, 2019.

Cite this: Rakhman KA, Zam Zam Z, Umar S, Abdjan MI. Study of Electronic Transition of Complex Fe(III), Ni(II) and Zn(II)-1,10-Phenanthroline: Modelling and UV-Vis Spectral Analysis. JOTCSA. 2020;7(1):155-68.

DOI: <https://doi.org/10.18596/jotcsa.5889848>.

***Corresponding author. E-mail:** khusna.arif.rakhman@gmail.com.

INTRODUCTION

The complex compounds have molecular structures composed of ligands/complexes binding in coordination with metal ions as the center of the molecular geometry of complex compounds (1). Generally, metal ions of complex

compounds/ions are derived from transition metals having neutral or positive oxidation numbers (2). For example, Fe(III), Cu(II), Co(II), Mn(II), Zn(II), and Ni(II) are employed as other metals. Metals are often reacted with complexes/ligands having neutral or negative

oxidation numbers to obtain complex compounds/ions (3). Examples of ligands/complexes binding to heavy metals in the form of ions, ie, 1,10-phenanthroline, EDTA, pyrazinamide, pyridine, and ligand/other complexes. Generally, complex compounds have many benefits in the world of health and materials science (4). In addition has been investigated the influence the use of 1,10-phenanthroline ligand with Co(II) metal ions on DNA binding, cleavage, and anticancer properties showed good results (5). The ligand 1,10-phenanthroline often used in complex compounds because it's exhibit good ability to coordinate bonds with metal ions (6). Ion of Fe(III), Ni(II) and Zn(III) are ions of transition metals that can form complexes with ligand 1,10-phenanthroline (7, 8). Interaction between metal ions with two lone pairs electrons in ligand 1,10-phenanthroline forms complexes bound to coordinate with different molecular geometries (9, 10).

Electron transitions that occur in ligands and complex compounds can be calculated using a UV-Vis spectrophotometric analysis (11). The transition of electrons to complex compounds occurs at the level of their molecular orbital with the most urgent electron excitation being σ to δ^* and the electron excitation requiring the least energy is n to n^* . The occurrence of electron transfer from the lowest ground state energy (HOMO) to the excited energy level (LUMO) can be known by its wavelength uptake. Ligands 1,10-phenanthroline and ligand to ligand charge transfer (LLCT) undergo electron transition in orbital molecules (OM) level n to n^* (12). In the meantime, ligands and complex compounds containing nitrogen atoms (RC = N) have an electron transition at OM level n to n^* (13).

Modeling of complex ion has been done using the method of semi-empirical ZINDO/s to analyze the electronic and energy transitions of HOMO and LUMO (14). HOMO and LUMO energy analysis is required as information/reference to know the transfer of charge in a molecule (15). The study of complex molecular modeling aims to facilitate visualization and conducting studies on electronic transition spectra (16, 17, 18). ZINDO / s is one of many semi-empirical calculation methods in computation that is intended for calculation on UV spectra (19). In addition, it has been known that the method of semi-empirical ZINDO/s was very good at performing electronic transition

calculations (20). Thus using the method of semi-empirical ZINDO/s can study geometry and electronic transitions of complexes of Fe (III), Ni (II) and Zn (II) with the 1,10-phenanthroline complex.

EXPERIMENTAL

Measurement of Complex Solutions

In 0.5 mL standard solution, 100 ppm each of FeCl_3 (aq), $\text{Ni}(\text{NO}_3)_2$ (aq) and ZnCl_2 (aq) were added 1.5 mL of 1,10-phenanthroline solution at 1000 ppm, 1.5 mL of acetate buffer solution at pH 3.5 and 5 mL of acetone and diluted to a volume of 10 mL with DM water. The Fe-Phen, Ni-Phen and Zn-Phen complexes formed were measured their absorbance using a UV-Vis spectrophotometer.

Optimization of Complex Molecular Compounds

Ligand and complex geometries can be optimized through computational methods (21). Optimization of molecular geometries for Fe-Phen, Ni-Phen and Zn-Phen metal complexes using PM3 (Parameterized Model 3) with a gradient change limit of 0.01 kcal/Å.mol, with gradient boundaries comrade based on the Polak-Ribiere method in the Windows 8 based version of Hyperchem version 8.0.10. The results of the optimization of molecular geometry using the semi-empirical method of PM3 obtain molecular geometry with smaller and stable energy (22).

Complex ion modeling

The modeling of the structure of the geometric optimization results from the semi-empirical method of PM3, followed by single point calculation using the method of semi-empirical ZINDO/s to produce electronic transition spectra data. The calculations are done with the limit of configuration interaction (CI) and with single excitation (*singly excited-CI*). Spectral calculation data is presented as a discontinuous spectra diagram to analyze the electronic transition.

RESULTS AND DISCUSSION

Complex Ion Modeling

The molecular structure modeling for Fe-Phen, Ni-Phen and Zn-Phen complexes was computed by optimizing its molecular geometry using the semi-empirical PM3 method. Optimization of the

molecular geometry of Fe-Phen, Ni-Phen, Zn-Phen and 1,10-phenanthroline ligands using the semi-empirical PM3 method (Figure 1). The geometric optimization results in molecular geometry with the total energy and the smallest or near-zero heat generation energy (Table 1).

The total energy value shown in each complex through the simulation of the PM3 method determines how much energy it takes for the interconnected atoms to form a complex molecule (23).

Table 1: Optimization of Complex Molecular Geometry Using the Semi-Empirical Method of PM3

Complex	Total Energy (kcal/mol)	Heat Formation (kcal/mol)
Fe-Phen	-141168.5256	389.0235
Ni-Phen	-109936.3877	275.3654
Zn-Phen	-86813.2124	160.8909

The results of the complexes of Fe(III), Ni(II), and Zn(II) ions with the 1,10-phenanthroline complex produce three complexes with molecular geometry, molecular orbital energy levels, charge and different magnetic properties. The three properties of these molecule complex properties

can be reviewed through simulation of geometric optimization of PM3 methods and theoretical approaches (Theory of Molecular Orbital and Hybridization Theory) for the three complex compounds (24).

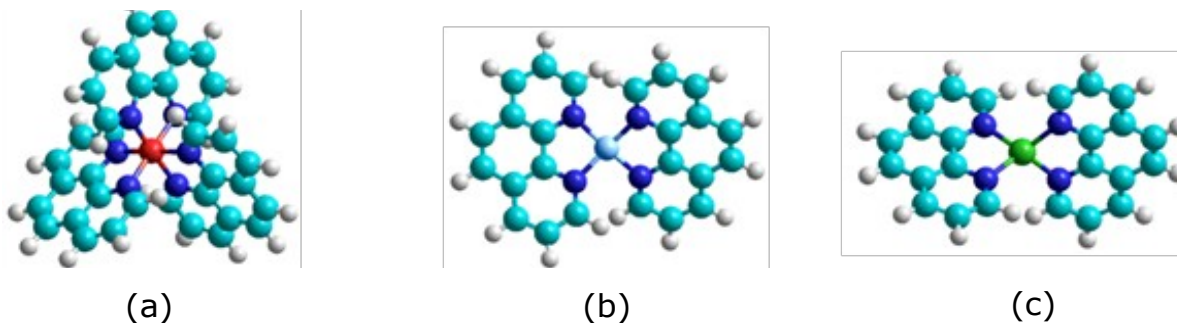


Figure 1. Optimization Geometry of 3D Molecular (a) Fe-Phen, (b) Ni-Phen and (c) Zn-Phen Using PM3.

The calculation of charge and coordinates has been done using the PM3 method to explain how the atoms bind to form the third molecular geometry of the complex. The Fe-Phen complex exhibits a change in values at the coordinates (x, y, and z) of atoms both before and after binding to form a complex (Table 2). The geometry for the Fe-Phen complex forms an octahedron with each ligand (ligand 1: N5' and N11', ligands 2: N19' and N25', 3: N33' and N39' ligands) contributes 2 lone pair electrons to the metal ion (Fe43'). The change in the coordinate value of

each bonded atom (Zn') forms the angle of octahedral geometry in the Fe-Phen complex of 90°. The complex Fe-Phen has analyzed with XRD and processed with Rietica program to find the crystallography of the compound. Diffractogram data shows that geometric prediction Fe-Phen was octahedral with monoclinic crystal system, space group C2/c with parameter a = 10.781 Å, b = 24.53 Å, c = 13.286 Å, $\beta = 103.15^\circ$ and the volume = 3422 Å³, Rp = 5.37 and Rwp = 11.05 (25).

Table 2: List of Charge (eV) and Coordinates of x, y, z (Å) Fe-Phen PM3

Atom	Charge	x	y	z
N ₅	-0.020226	-0.17650	-2.00652	0.00000
N _{5'}	0.458976	-3.11734	0.60509	-0.43874
N ₁₁	-0.020226	-2.65070	-0.60355	0.00000
N _{11'}	0.403515	-1.02197	1.80464	0.57257
N ₁₉	-0.020226	-0.17650	-2.00652	0.00000
N _{19'}	0.368995	0.35957	-0.61562	0.46959
N ₂₅	-0.020226	-2.65070	-0.60355	0.00000
N _{25'}	0.368761	-1.91295	-0.41832	1.77719
N ₃₃	-0.020226	-0.17650	-2.00652	0.00000
N _{33'}	0.459333	-0.83260	0.35945	-1.77590
N ₃₉	-0.020226	-2.65070	-0.60355	0.00000
N _{39'}	0.401748	-1.76790	-1.80346	-0.63729
Fe ₄₃	3.000000	-1.37339	0.11588	0.00000
Fe _{43'}	-0.616334	-1.40230	0.00614	0.00614

Description: (N) is an atom of a metal-ligand/ion prior to bonding and (N ') is an atom of a metal-ligand/ion after binding.

The change in the coordinate of the Ni-Phen complex forms the planar quadrangle molecular geometry of a central atom attached to a bond angle of 90°. The change of charge value at Ni10 (2.0000) to Ni10' (-1.102833) indicates the occurrence of atoms before and after binding of delocalized electrons and forming a more stable charge to form molecules with a charge value

close to the Ni-Phen complex charge value (Table 3). Molecular geometry is formed in the Zn-Phen complex in a tetrahedral geometry. The calculated coordinate using the PM3 method on bonded atoms (N5', N10', N12 ', N21' and Zn11') are coordinated x, y, and z forming a bonding angle of 109.5° (Table 4).

Table 3: List of Charge (eV) and Coordinates of x, y, z (Å) Ni-Phen PM3

Atom	Charge	x	y	z
N ₅	-0.020226	-0.17650	-2.00652	0.00000
N _{5'}	0.709769	-2.55195	0.56285	-0.67382
N ₉	-0.020226	-2.65070	-0.60355	0.00000
N _{9'}	0.709631	-0.58458	1.77623	0.63756
N ₁₁	-0.020226	-0.17650	-2.00652	0.00000
N _{11'}	0.709559	0.33598	-0.71135	1.17883
N ₂₀	-0.020226	-2.65070	-0.60355	0.00000
N _{20'}	0.709639	-0.76838	-1.42299	-1.13126
Ni ₁₀	2.000000	-1.63504	0.74277	0.00000
Ni _{10'}	-1.102833	-0.89210	0.05123	0.00240

Description: (N) is an atom of a metal-ligand/ion prior to bonding and (N ') is an atom of a metal-ligand/ion after binding.

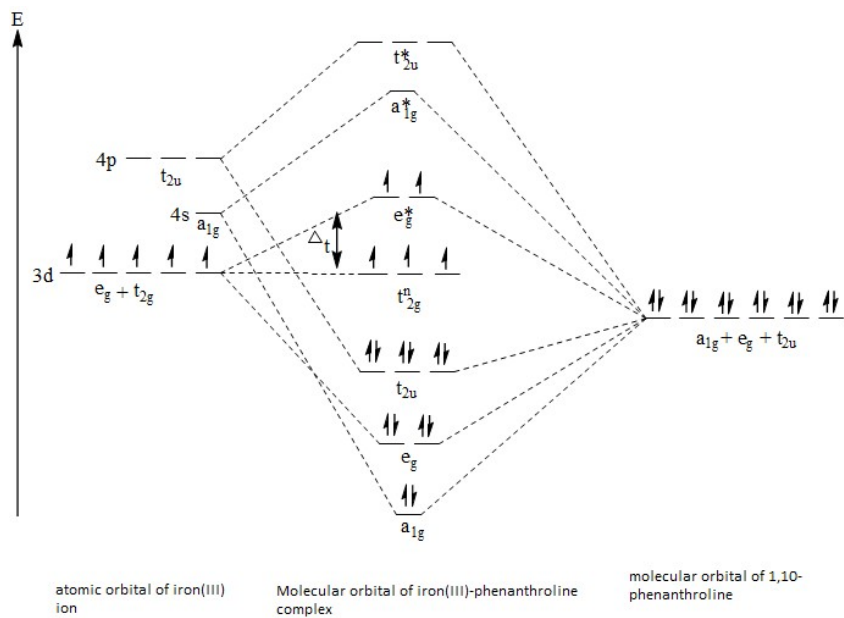
Table 4: List of Charge (eV) and Coordinates of x, y, z (Å) Zn-Phen PM3

Atom	Charge	x	y	z
N ₅	-0.020226	-0.17650	-2.00652	0.00000
N _{5'}	0.262773	-2.82160	0.58788	-0.17861
N ₁₀	-0.020226	-2.65070	-0.60355	0.00000
N _{10'}	0.262542	-0.47977	2.00170	0.18141
N ₁₂	-0.020226	-0.17650	-2.00652	0.00000
N _{12'}	0.264556	0.00334	-1.11636	1.37016
N ₂₁	-0.020226	-2.65070	-0.60355	0.00000
N _{21'}	0.264380	-0.28653	-1.29103	-1.36826
Zn ₁₁	2.000000	-1.32618	0.27897	0.00000
Zn _{11'}	-0.365938	-0.89694	0.04629	0.00118

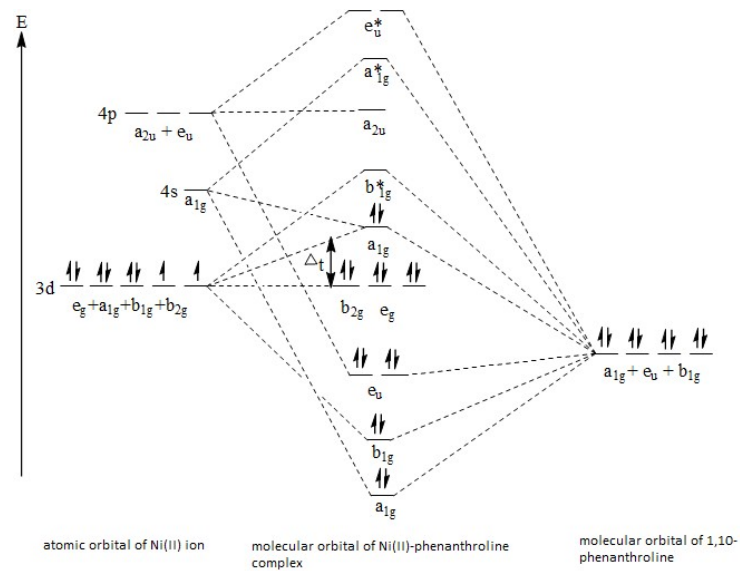
Description: (N) is an atom of a metal-ligand/ion prior to bonding and (N ') is an atom of a metal-ligand/ion after binding.

The bonds that occur in the Fe-Phen, Ni-Phen and Zn-Phen complexes can be explained in the theory of hybridization at the level of their molecular orbital. The simulation of the process of complex molecular orbital fusion explains how the new orbitals (hybrids) formed with Fe(III), Ni(II) and Zn(II) metal ions with 1,10-phenanthroline ligands. Hybrid orbitals formed from the three complexes are able to explain the molecular geometry and complex magnetic properties. The Fe-Phen complex forms a d^2sp^3 hybrid orbital, Ni-Phen: dsp^2 and Zn-Phen forming sp^3 . The hybridization of these complex molecular orbitals is composed of adjustment of

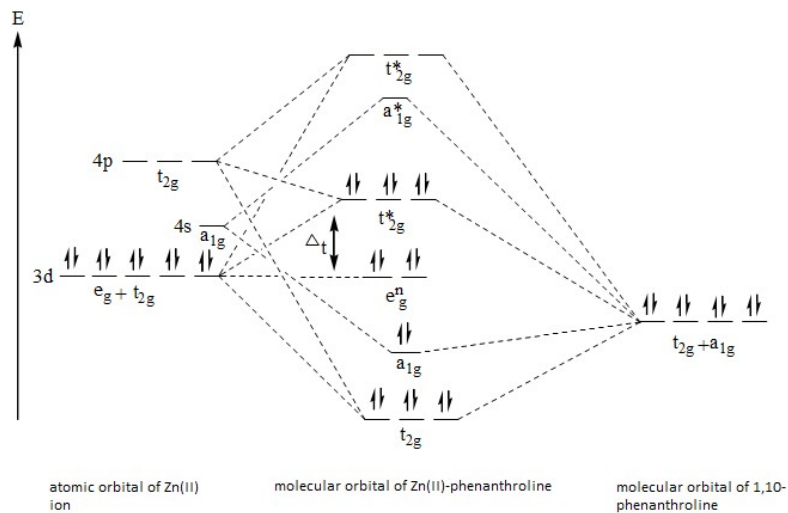
orbital energy to form bonds and produce hybrid orbitals. Based on the filling and position of electrons in complex orbital, it can know the magnetic properties. The Fe-Phen complex is diamagnetic, Ni-Phen is paramagnetic and Zn-Phen is paramagnetic. The orbital interactions are due to the rearrangement of electrons in the orbitals of metal ions with ligands 1,10-phenanthroline. Each ligand of 1,10-phenanthroline binds in coordination with 2 lone pairs electron on Fe(III) forming $[Fe(C_{12}H_8N_2)_3]^{+3}$, Ni(II): $[Ni(C_{12}H_8N_2)_2]^{+2}$ and Zn(II): $[Zn(C_{12}H_8N_2)_2]^{+2}$.



(a)



(b)



(c)

Figure 2. The energy level of the molecular orbital for complexes (a) Fe-Phen, (b) Ni-Phen, and (c) Zn-Phen.

The absorption spectrum of a metal ion produces a change of electron congruity and the maximum wavelength value presented in the measurement value Δ_{oct} (26). Based on the Figure 2 of 5 electrons filling starts from the lowest-energy orbital recall to the highest energy orbitals, ie σ (bond orbital) to n (orbitals not bonded) to σ^* (antibonding orbital). The electron configuration of the metal ion lies in the d^n orbital, with the energy level being split into 2 parts, ie eg and t_{2g} . Configuration of electrons for Fe-Phen: $t_{2g}^3 eg^2$ ($\Delta_{\text{oct}} = 0$), Ni-Phen: $t_{2g}^6 eg^2$ ($\Delta_{\text{oct}}: -1.2$) and Zn-Phen: $t_{2g}^6 eg^4$ ($\Delta_{\text{oct}}: 0$). The division of the d orbital in each complex aims for the adjustment of energy during the electron filling process at the level of the molecular orbital.

Hybridization of molecular orbitals of complex compounds (Figure 2) was the adjustment process in orbital energy to bind and produce hybrid orbital. Based on electron charging and position in an orbital complex, magnetic characteristics can be known. Fe(III)-phenanthroline complex is paramagnetically observed from unpairing orbital electron charging energy so that it has a strong magnetic power, while Ni(II)-phenanthroline and Zn(II)-phenanthroline has a weak magnetic power as it has pairing orbital electron (26, 24). Furthermore, Ni(II) and Zn(II) complexes have a planar and tetrahedral molecule which shows diamagnetic characteristic in complex (11).

Electron charging theoretically based on the theoretical molecular orbital approach in the complex molecules were presented in Figure 2. Electron filling at the orbital level aims to illustrate how the energy adjustments of the orbitals formed from each complex. Meanwhile, to study the electronic transition of each complex is carried out using the ZINDO/s semi-empirical method in the excited state. The computational results, the electronic transition that appear in the ZINDO/s simulation for the Fe-Phen complex

of 18 transition peaks indicate the transition types n to n^* and n to n^* . However, only 3 peaks in the Fe-Phen complex had a large oscillator strength value, which showed transient strength electron n to n^* (Table 7) due to chromophore and auxochrome in the ligand (22).

The spectra results on ZINDO/s show the wavelength at Ni-Phen and Zn-Phen complex to change the transition from n to n^* and n to n^* . The results of this electronic transition calculation see how to translate electrons from HOMO to LUMO with different energy levels. Complex molecules that experience excitation with greater energy absorb light at shorter wavelengths. Conversely, molecules that experience excitation with less energy will absorb light at longer wavelengths. Modeling results, the electron transition for the Ni-Phen and Zn-Phen complex requires more energy to experience the electron transition from HOMO-2 to LUMO+2 which is characterized by peak absorption at short wavelengths in the transition type n to n^* . In contrast, the electron transition from the Ni-Phen and Zn-Phen complex requires less energy to experience the electron transition from HOMO to LUMO which is characterized by absorption of peaks at long wavelengths in transition types n to n^* (Tables 8 and tables 9).

Analysis of Spectra and Electronic Transitions

The determination of complex spectra was done by UV-Vis spectrophotometry and computation were done using method of semi-empirical ZINDO/s. The calculation result using ZINDO/s method is presented in the form of discontinuous spectrum modeling simulation. The result of calculation of electronic transition spectrum is obtained from electron transition process at the level of molecular orbitals, ie HOMO and LUMO complex ion Fe(III), Ni(II), and Zn(II) with complexing 1,10-phenanthroline.

Table 5: Results of Spectral Measurements of Spectra by UV-Vis Spectrophotometry

Complex	λ (nm)	Abs.
Fe-Phen	484.00	0.016
	364.00	0.185
	315.50	1.227
	469.00	0.016
	325.50	0.084
Ni-Phen	366.00	0.021
	343.50	0.069
	325.00	0.219
	355.00	0.017
Zn-Phen	336.50	0.027
Zn-Phen	315.00	1.704

The load values for the Fe-Phen, Ni-Phen, and Zn-Phen complexes have been calculated using the PM3 and ZINDO/s methods. The charge price shows the tendency of the distribution of electrons in the bonds that occur between metal

ions (Fe(III), Ni(II), and Zn(II)) with 1,10-phenanthroline. These electron distributions help indicate how much the coordination covalent bond strengths in the three complexes (27).

Table 6: Comparison of Fe-Phen Complex Charge (eV) Using PM3 and ZINDO/s Methods.

Atom	PM3	ZINDO/s
N _{5'}	0.458976	-0.187097
N _{11'}	0.403515	-0.219591
N _{19'}	0.368995	-0.214342
N _{25'}	0.368761	-0.214750
N _{33'}	0.459333	-0.187022
N _{39'}	0.401748	-0.219964
Fe _{43'}	-0.616334	0.118759

Generally, the total value of charge on each atom shows the identity of the charge on a complex molecule. The charge ratio for the Fe-Phen complex using the PM3 and ZINDO/s methods shows the different results in the atoms involved in the coordination covalent bonds (Table 6). In addition, experimental spectral measurements have been made using UV-Vis spectrophotometers and electronic transition

simulations using ZINDO/s. The measured wavelength in the Fe-Phen complex, ie 315.50 nm with an absorbance value of 1.227 (Table 5). Meanwhile, for ZINDO/s method results obtained wavelength with the number of 18 transitions. The wavelength with the highest peak measured lies at 437.36 nm (f: 0.249), 317.47 nm (f: 0.265) and 305.48 nm (f: 0.521) indicating the electron n transfer to π^* (Table 7).

Table 7: Computational Results of Fe-Phen Complex Using Semi-Empirical Method ZINDO/s

λ (nm)	Osc. (f)	Transition
437.36	0.249	$n \rightarrow \pi^*$
317.47	0.265	$n \rightarrow \pi^*$
305.48	0.521	$n \rightarrow \pi^*$

The calculation of the electron transition simulation in the Fe-Phen complex involves 67 atoms and 201 orbitals from HOMO to LUMO can not be selected using the ZINDO/s method. The reason was optimization of geometry (PM3) with a 0.01 kcal/Å.mol gradient was not capable of simulating geometry calculations that have

minimum energy based on half electron orbital filling approach, consequently calculations using ZINDO/s especially on electron transition energy from orbital (HOMO- LUMO) Fe-Phen complex is not readable on its calculated output. The peak with a large oscillator strength taken in the ZINDO/s simulation was expected to be

measured at that wavelength by UV-Vis spectrophotometer experiments. Some small oscillator strength may not appear or be measured experimentally at these wavelengths (22, 28).

Table 8: Computational Results of Ni-Phen Complex Using Semi-Empirical Method ZINDO/s.

$\lambda(\text{nm})$	Osc. (f)	MO level	DE (eV)	Transition
325.73	0.239	70→71 69→72	6.71 7.31	$n \rightarrow \pi^*$
283.26	0.133	68→71	7.31	$n \rightarrow \pi^*$
272.85	0.054	68→72	7.55	$n \rightarrow \pi^*$
258.46	0.102	69→73	7.57	$n \rightarrow \pi^*$
254.51	0.085	70→71 69→72	6.71 7.31	$n \rightarrow \pi^*$
253.35	1.208	70→73	7.48	$n \rightarrow \pi^*$
244.44	0.855	68→73	7.80	$n \rightarrow \pi^*$

The measured spectra of the UV-Vis spectrophotometer showed the greatest absorbance, ie 0.219 at the 325 nm wavelength for the Ni-Phen complex (Table 5). The spectral results in ZINDO/s show the wavelength with 7 peaks. One of the measured peaks in the absorbance near the experimental value is at the wavelength 325.73 (f: 0.239) which shows the electronic transition n to π^* (Table 8). This is due to the presence of benzene ring chromophores and amide groups in ligands 1,10-phenanthroline so that the measured wavelength range is in the UV region.

Semi-empirical ZINDO/s modeling method on the Ni-Phen complex involves 45 atoms and 137 orbitals. Energy changes in each molecular

orbitals of Ni-Phen complex shift from HOMO to LUMO. The levels of molecular orbital 68 (HOMO-2 / π_3), 69 (HOMO-1 / π_2) and 70 (HOMO / π_1), the molecular orbital level 71 (LUMO / $\pi-1$), 72 (LUMO +1 / $\pi-2$) and 73 (LUMO +2 / $\pi-3$) (29, 30). The energy differences of the gap (DE) influenced the electron for excitation from HOMO to LUMO. The lower energy differences of a molecule, the easier it will be to excel from HOMO to LUMO, as in Ni-Phen complex, there's a shift from the 70 to 71 orbital which is the largest electron transition and the 68 to 73 orbital which is the smallest electron transition. The energy level of HOMO-LUMO of complex Fe-Phen, Ni-Phen, and Zn-Phen was shown in Figure 3.

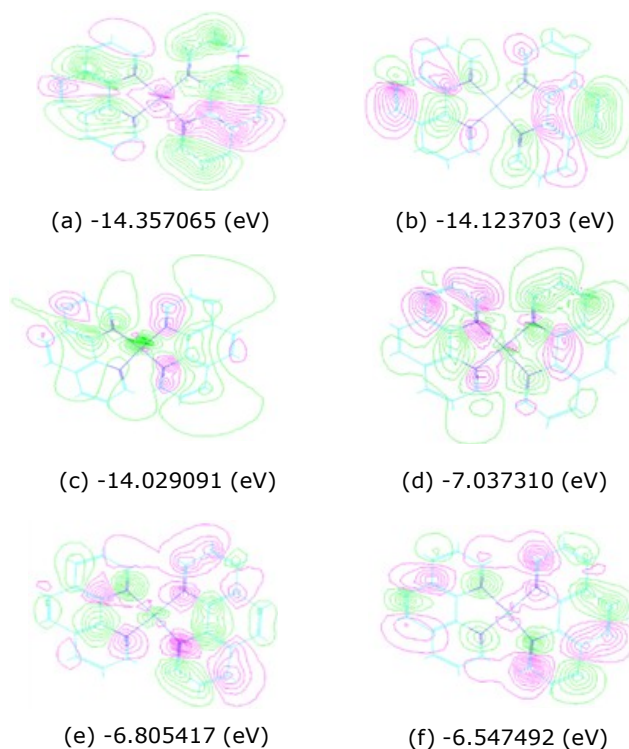


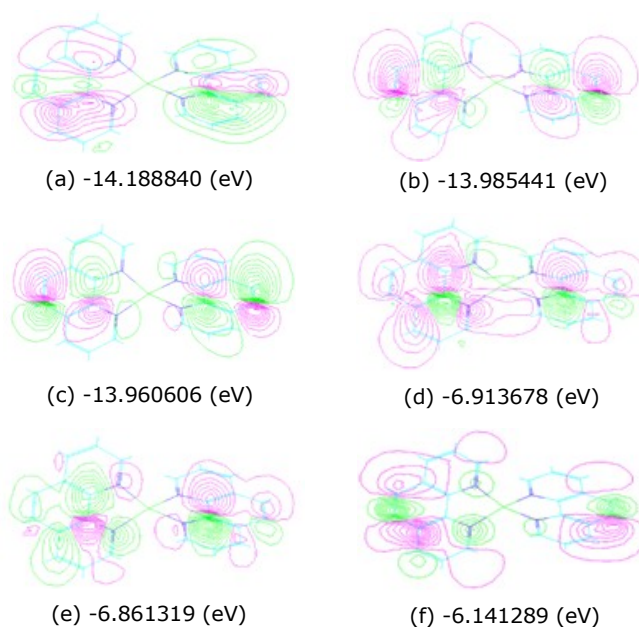
Figure 3. Levels of Complex OM Ni-Phen (a), (b), (c) HOMO 68, 69, 70 and (d), (e), (f) LUMO 71, 72, 73.

The measured Zn-Phen spectra on the UV-Vis spectrophotometer were at a wavelength of 315 nm with an absorbance of 1.704 (Table 5). Computational determination of the spectra has also been performed using the ZINDO/s method by showing 6 different transitions of intensity (Osc). The transition of electrons to the Zn-Phen complex involves 55 atoms and 132 orbitals,

shifting the degree of complex molecular orbitals leading to changes in energy. Where some of the peaks that arise may not be like the data obtained experimentally. One of the peaks approaching the experimental result is 325.91 nm (f: 0.334) with n electron transition to n* (Table 9).

Table 9. Computational Results of Zn-Phen Complex Using Semi-Empirical Method ZINDO/s.

λ (nm)	Osc (f)	MO Level	DE (eV)	Transition
325.91	0.334	64→67	7.27	n→π*
		64→68	7.32	
289.79	0.568	64→67	7.27	n→π*
		64→68	7.32	
261.97	0.050	64→67	7.27	n→π*
		64→68	7.32	
246.24	0.682	66→69	7.81	n→π*
		65→69	7.84	
230.15	0.380	66→69	7.81	n→π*
		65→69	7.84	
226.20	0.714	64→69	8.04	n→π*

**Figure 4.** Levels of Complex OM Zn-Phen (a), (b), (c) HOMO 64, 65, 66 and (d), (e), (f) LUMO 67, 68, 69.

The electron transition energy in the Zn-Phen orbital molecule of the complex can be observed in the energy changes of each molecular orbital (Figure 4). The occurrence of electronic transition from the HOMO orbital level to the LUMO was due to the free electron pair in the ligand 1,10-phenanthroline, consequently the optimum wavelength shift in the larger complex compound.

CONCLUSION

Optimization of complex molecular geometry using PM3 shows the results of total energy and different forms of geometry. The total energy for the Fe-Phen complex is -185756 (kcal / mol) (octahedral), the Ni-Phen complex was -135552 (kcal/mol) (planar quadrilateral) and Zn-Phen complex of -113570 (kcal/mol) (tetrahedral). Spectrophotometric UV-Vis spectrometric spectra measurements were measured at the highest absorbance with wavelength for Fe-Phen complex of 315.50 nm (1.227), Ni-Phen complex of 325.00 nm (0.017), and Zn-Phen complex of 315.00 nm (1.704). The electronic transition of complex molecules is carried out using the ZINDO/s semi-empirical method by reviewing some of the peaks that appear on the discontinuous spectrum and energy in the HOMO-LUMO molecular orbital. The transition type for the three complexes was in the transition range $n \rightarrow n^*$ and $n \rightarrow n^*$.

REFERENCES

1. Cimen E, Gumus I, Arslan H. The Role of Intermolecular Interactions in the Assembly of Zinc(II) and Lead(II) Complexes Containing Carboxylate Ligand and Their Conversion to Metal Oxides. *J. Mol. Struct.* 2018; 1166, 397-406.
2. Chang R, Overby J. *General Chemistry: The Essential Concepts*. The McGraw-Hill Companies, New York; 2011.
3. El-Shafiy HF. Synthesis, Spectral, Photoluminescence, DFT Studies and Bioassay of New Fe(III), Co(II), Ni(II), Cu(II) and Zn(II) Complexes of 1-ethyl-4-hydroxy-3-(nitroacetyl) quinolin-2(1H)-one. *J. Mol. Struct.* 2018; 1166, 348-61.
4. Lin JQ, Xiong C, Xin JH, Li M, Guo WH, Liu F, Tong XL, Ge YC. Structural Variation and Luminescence Properties of d10 Metal Ions Complexes from 5-aminotetrazolate Ligand. *J. Mol. Struct.* 2018; 1166, 1-6.
5. Tosonian, S., Ruiz, C. J., Rios, A., Frias, E., and Eichler, J. F., Synthesis, characterization, and stability of iron (III) complex ions possessing phenanthroline-based ligands *J. Inorg. Chem.*, 2013, 3, 7-13.
6. Anbu S, Killivalavan A, Alegria ECBA, Mathan G, Kandaswamy M, Effect of 1,10-Phenanthroline on DNA Binding, DNA Cleavage, Cytotoxic and Lactate Dehydrogenase Inhibition Properties of Robson Type Macrocyclic Dicopper(II) Complex. *J. Coord. Chem.* 2013; 66(22), 3989-4003.
7. Syiemlieh I, Kumar A, Kurbah SD, Lal RA, Synthesis, Characterization and Structure Assessment of Mononuclear and Binuclear Low-Spin Manganese(II) Complexes Derived from Oxaloyldihydrazones, 1,10-Phenanthroline and 2,2'-Bipyridine. *J. Mol. Struct.* 2018; 1166, 252-61.
8. Aljahdali MS, El-Sherif AA, Hilal RH, Karim ATA. Mixed Bivalent Transition Metal Complexes of 1,10-Phenanthroline and 2-aminomethylthiophenyl-4-Bromosalicylaldehyde Schiff Base: Spectroscopic, Molecular Modeling and Biological Activities. *Eur. J. Chem.* 2014; 4(4), 370-8.
9. Miessler GL, Fischer PJ, Tarr DA, *Inorganic chemistry* 5th edn. Pearson Education, USA; 2014.
10. Prior TJ, Rujiwatra A, Chimupala Y. [Ni (1,10-phenanthroline)₂ (H₂O)₂](NO₃)₂: A Simple Coordination Complex with a Remarkably Complicated Structure that Simplifies on Heating. *J. Crystals*; 2011, 1, 178-94.
11. Shah RS, Shah RR, Pawar RB, Gayakar PP. UV-Visible Spectroscopy-A Review. *J. Pharm. Sci.* 2015; 5(5), 491-505.
12. Zheng SL, Chen XM, Recent Advances in Luminescent Monomeric, Multinuclear, and Polymeric Zn (II) and Cd (II) Coordination Complexes. *Aus. J. Chem.* 2004; 57, 703-21.
13. Pavia DL, Lampman GM, Kriz GS, Vyvyan ZR. *Introduction of Spectroscopy*. Cengage Learning, USA; 2013.
14. Toma HE, Kuwabara IH, de Faria DLA. ZINDO/s Calculations and Resonance Raman Spectra of the bis (2,6-diacetyl-methyl-imine-pyridine)iron(II) Complex. *J. Braz. Chem. Soc.* 1996; 7(6), 391-4.
15. Gayathri R. An Experimental and Theoretical Investigation of The Electronic Structure and Photoelectrical Properties of 1, 4-diacetoxy-2-

methylnaphthalene for DSSC Application. *J. Mol. Struct.* 2018; 1166, 63-74.

16. Hadi AA. Quantum-Chemical Study for Some Coumarin Compounds by Using Semi-Empirical Methods. *J. ChemTech Research*, 2016; 9(10), 139-48.

17. Gonta S, Utinans M, Kirilov G, Belyakov S, Ivanova I, Fleisher M, Savenkov V, Kirilova E. Fluorescent Substituted Amidines of Benzanthrone: Synthesis, Spectroscopy and Quantum Chemical Calculations. *J. Spectrochim Acta Part A : Mol. Biomol. Spectrosc.* 2013; 101, 325-34.

18. Mirzaei M, Hassanpoor A, Alizadeh H, Gohari M, Blake AJ. An Eight-Coordinate Zinc Complex Containing the Highly Pre-Organized Ligand 1,10-Phenanthroline-2,9-Dicarboxylic Acid: Solvothermal Synthesis, Supramolecular Structure and CSD Studies. *J. Mol. Struct.* 2018; 1171, 626-30.

19. Lewars E. Computational chemistry: introduction to the theory and applications of molecular and quantum mechanics. Kluwer Academic Publishers, USA; 2014.

20. Marković Z, Manojlović N, Zlatanović S. Electronic Absorption Spectra of Substituted Anthraquinones and Their Simulation Using ZINDO/s Method. *Int. J. Serb.Soc.Comput. Mechan.* 2008; 2(2), 73-9.

21. Uddin MN, Khandaker S, Moniruzman, Amin S, Sumi W, Rahman MA, Rahman SM. Synthesis, Characterization, Molecular Modeling, Antioxidant and Microbial Properties of Some Titanium(IV) Complexes of Schiff Bases. *J. Mol. Struct.* 2018; 1166, 79-90.

22. Saraha AR, Rakhman KH, Sugrah N. Anti UV-Activity and Elektronic Transition Study of 1,3-diphenyl-2-propenone Using Semi-Empirical Method

ZINDO/s. *Asian Journal of Chemistry.* 2018; 30(5), 1057-60.

23. Jensen F. Introduction to computational chemistry. John Wiley & Sons Ltd, England; 2007.

24. Brown TL, LeMay HE, Bursten BE, Murphy CJ, Woodward PM, Stoltzfus MW. Chemistry the Central Science. Pearson Education, USA; 2015.

25. Kusyanto, A., and Sugiyarto, K. H., Synthesis and characterization of iron(III) complex with 1,10-phenanthroline ligand and trifluoromethanesulfonate anion, *Jurnal Kimia Dasar*, 2017; 6, 51-8.

26. Housecroft CE, Sharpe AG. Inorganic chemistry. Pearson Education Limited, England; 2005.

27. Gao, H. Z., Su, Z. M., Qin, C. S., Mo, R. G., and Kan, Y. H., Electronic structure and molecular orbital study of the first excited state of the high-efficiency blue OLED material bis(2-methyl-8-quinolinolato)aluminum(III) hydroxide complex from Ab initio and TD-B3LYP, *Int. J. Quantum chem.*, 2004, 97, 992-1001.

28. Rakhman K, Khadijah, Abdjan M, Kumendong N, Puspitasari S. Modeling of Anthocyanin Derivatives as Anti-UV Agents. *JOTCSA.* 2019; 5: 1287-94.

29. Nepras, M., Almonasy, N., Michl, M., Dvorák M., and Fidler, V., Electronic structure, spectra and photophysical properties of N-triazinylderivatives of 1-aminopyrene. Semi-empirical theoretical study, *J. Dyes and pigments*, 2012, 92, 1331-6.

30. Suendo, V., and Viridi, S., Ab initio calculation of UV-Vis absorption spectra of a single chlorophyll a molecule: comparison study between RHF/CIS, TDDFT, and semi-empirical methods, *ITB J. Sci.*, 2012, 44, 93-112.



Determination of Gluconate Binding Properties on Magnetite Surface and Investigation of Carboxymethylation and Hydrazination Mechanisms of the Gluconated Magnetite Surface: A Computational Study

Işıl ÖZTÜRK^{a*}, Şenay ŞANLIER^b, Armağan KINAL^a

^aEge University, Faculty of Science, Department of Chemistry 35100 Bornova IZMIR, TURKEY

^bEge University, Faculty of Science, Department of Biochemistry 35100 Bornova IZMIR, TURKEY

Abstract: In the present study, the probable binding structure of a gluconate molecule with magnetite, (Fe₃O₄) nanoparticles, as well as, carboxymethylation and hydrazination mechanisms of the gluconate bound to the iron oxide surface have been computationally investigated by the DFT-B3LYP method. The B3LYP/LanL2DZ calculations together with experimental IR data available revealed that the probable binding structure of gluconate is bidentate bridged binding to the magnetite surface. The carboxymethylation and hydrazination mechanisms of gluconate were calculated at B3LYP/6-31+G(d,p) level of theory. The results indicate that the reaction between gluconate and chloroacetate in aqueous medium has one step mechanism passing through a low activation barrier (12.3 kcal/mol) with a reaction enthalpy of -42.8 kcal/mol. In addition, hydrazone bond formation reaction of the gluconate bound to the iron oxide surface has a highly-exothermic two-step-mechanism with barriers of 7.1 and 2.4 kcal/mol, respectively, in water. The activation barrier of the overall reaction is accepted as the barrier of the first step since the barrier of this step is greater than that of the second one. Consequently, it can be predicted that both carboxymethylation and hydrazination reactions should be spontaneous under moderate conditions.

Keywords: Magnetite nanoparticles, Gluconate, Binding properties, Carboxymethylation, Hydrazination, Density functional theory (DFT).

Submitted: September 05, 2019. **Accepted:** October 29, 2019.

Cite this: Öztürk I, Şanlıer Ş, Kinal A. Determination of Gluconate Binding Properties on Magnetite Surface and Investigation of Carboxymethylation and Hydrazination Mechanisms of the Gluconated Magnetite Surface: A Computational Study. JOTCSA. 2020;7(1):169-78.

DOI: <https://doi.org/10.18596/jotcsa.615671>.

***Corresponding author.** E-mail: isilayozturk@gmail.com. Telephone: +90 232 311 23 95. Fax: : +90 232 388 82 64.

INTRODUCTION

Cancer is one of the major dangers to human health. Scientists have been trying to find different strategies employing synergistic effects to kill cancer cells. In recent years, a number of therapeutic and diagnostic agents in nanobiotechnology such as nanocarrier systems for

drug delivery (e.g. liposomes, micelles, nanogels, dendrimers, polymeric nanoparticles, and magnetic nanoparticles) have been developed for the treatment of cancer (1-8). One of the biggest challenges for targeted drug delivery practices is to develop nanomolecules that can be loaded with special drugs and can be transported in a simple way (9-11). In this context, magnetite (Fe₃O₄) is

the most studied material due to its biocompatibility and sufficient magnetic properties (12-14). When the size of magnetite is on the nanoscale, its magnetic property switches over ferromagnetic to superparamagnetic. This feature enhances the application of magnetite to the biomedical field (6, 15, 16) since they are responsive to an external magnetic field so that they can be directed to specific locations. Fe_3O_4 nanoparticles can both agglomerate due to their high magnetic interaction and large surface area, and they can easily be oxidized in a biological environment. These drawbacks can be overcome by coating the magnetite surface with another biocompatible material. The coating of magnetite will also allow drug binding via trapping on the particles, adsorption, or covalent binding (15, 17, 18). Sun et al (19) efficiently synthesized glucose and gluconic acid coated magnetite nanoparticles via a simple and facile hydrothermal reduction route of Fe(III) precursor with sucrose decomposition products. In our laboratories (20), we have also synthesized gluconic acid coated magnetite nanoparticles with the hydrothermal reduction route of Fe(III) proposed by Sun et al (19). In addition, these gluconic acid-coated magnetite nanoparticles were made suitable for carrying doxorubicin drug via carboxymethylation and hydrazination processes. (Experimental details of this study is discussed elsewhere (20).)

In this study, we present computational findings related to the interaction of gluconate molecules with Fe_3O_4 nanoparticles as well as carboxymethylation and hydrazination mechanisms of gluconate bound to iron oxide surface. In particular, we investigated the interaction of a gluconate molecule with a model Fe_6O_8 surface employing the DFT-B3LYP method and we try to determine binding characteristics of gluconate on the magnetite surface. In addition, we computationally determine the carboxymethylation and hydrazination mechanisms, which makes the nanoparticles ready for drug binding, of the gluconate molecule bound to a modeled magnetite surface.

COMPUTATIONAL METHODOLOGY

This study consists of two main parts: a) the interaction sites of (binding type) gluconate with modeled magnetite surface; b) the carboxymethylation and hydrazination reaction mechanisms of modeled gluconate molecule bound to magnetite surface. Therefore, different computational methodologies were employed for these parts. In the gluconate-magnetite interaction part, it is needed to create a magnetite surface to model the interaction of gluconate molecules with the magnetite surface. The Cartesian coordinates of the magnetite unit cell with the reverse spinel

crystal structure, which will be the basis for this magnetic surface, were obtained from the American Mineralogist Crystal Structure Database, where crystallographic data obtained from X-ray spectroscopy are included (21). Then, we prepared a Fe_6O_8 model-magnetite-surface from the Cartesian coordinates of the magnetite unit cell. The reason for the selection of this small size surface is to make its calculation affordable with rather accurate but computationally demanding DFT-B3LYP method that enables us to obtain more plausible binding characteristics. LanL2DZ basis set is employed for both gluconate molecule and the Fe_6O_8 surface. Since magnetite nanoparticles are in solid phase, the model Fe_6O_8 surface was frozen throughout the optimization.

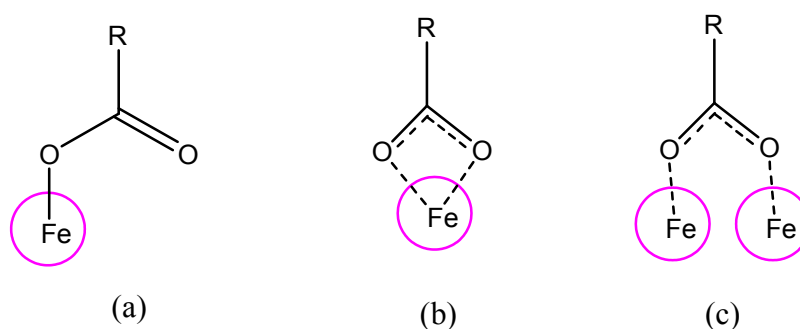
The B3LYP method was also employed in the second part of the study containing the carboxymethylation and hydrazination reaction mechanisms of the modeled gluconate molecule bound to magnetite surface. Since the gluconate coated iron oxide nanoparticle systems is enormously large for a quantum chemical calculation like DFT methods, the carboxylate anion moiety of gluconate molecule, which binds to positively charged iron atoms of the magnetite surface, were frozen during the DFT calculations. Such modeling does not involve the secondary effects of the iron surface, but it allows the DFT method to be used on the system. All DFT-B3LYP calculations, in all of which the 6-31+G(d,p) basis set was utilized, were performed using the Gaussian 09 program suite. All stationary points on electronic potential energy surfaces of the mechanisms found by optimizations were characterized by the harmonic vibrational frequency calculations. In addition, the transition state (TS) structures were verified by the internal reaction coordinate (IRC) analysis that identifies the correctness of TS structure by following the paths down to both desired reactant and product in the forward and backward directions of the imaginary TS mode. The activation energies of both mechanisms were determined after verification of the TSs by IRC profiles.

RESULTS AND DISCUSSION

The Interaction of Gluconate with The Modeled Magnetite Surface

In this section, we aimed to reveal the binding characteristics of gluconate molecules to magnetite surface. There are discussions about binding characteristics of organic acids, especially amino acids, onto magnetite surface in a large number of studies (18, 22-28). The common binding site of organic acid onto magnetite surface referred in all these studies is from the either $-\text{COOH}$ or $-\text{COO}^-$ moiety depending on the pH of the medium. There are three most probable binding structures of -

COO⁻ in basic medium onto magnetite surface: a) (BC) binding c) bidentate bridging (BB) binding monodentate (MB) binding b) bidentate chelating (Scheme 1)(27).



Scheme 1. Three most probable binding structure of -COO- onto magnetite surface.

Although there are other methods for binding structure determination such as zeta potential measurements, Raman spectroscopy etc. (26), the most important and widely used binding structure determination method is the vibrational spectroscopy (IR). Free (unbound) carboxylate groups show a symmetric stretch vibration at around 1400 cm^{-1} and an asymmetric stretch vibration at around 1600 cm^{-1} (24). There is 200 cm^{-1} difference between symmetric and asymmetric vibrations, $\Delta\nu$, in the unbound state. For -COO- bound to magnetite surface, if $\Delta\nu$ is in

between $300\text{-}400\text{ cm}^{-1}$ then the binding is monodentate (MB), if it is approximately equal to 200 cm^{-1} ($150\text{-}250\text{ cm}^{-1}$) then the binding is bridged (BB) and finally if it this difference is considerably less than 200 cm^{-1} then it is bidentate chelating (BC) binding (24, 26). Although there are some discrepancies in binding structures of -COO- containing molecules such as carboxylic acids, amino acids, etc., the proposed binding type is either bidentate bridged (BB) or bidentate chelating (BC) type.

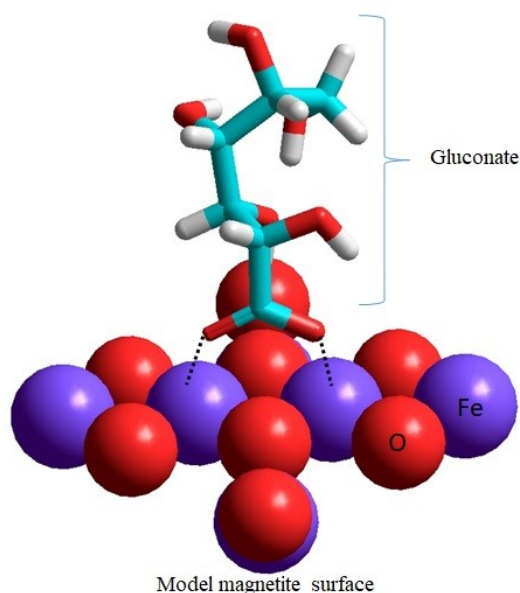


Figure 1. The optimized structure of gluconate bonded to model magnetite surface (Fe_6O_8) calculated at DFT-B3LYP/LanL2DZ level.

Figure 1 shows the optimized structure of gluconate bonded to model magnetite surface (Fe_6O_8) calculated at DFT-B3LYP/LanL2DZ level. The IR spectrum of glucose/gluconate coated magnetite nanoparticles (a) and the computed IR spectrum of the gluconate bonded to model

magnetite surface (Fe_6O_8) (b) are given in Figure 2. The gluconate coated magnetite nanoparticles synthesized by our group demonstrate IR peaks at 1350 cm^{-1} and 1600 cm^{-1} for symmetric and asymmetric stretch vibrations, respectively, implying that the binding type should be bridged

one (BB) since the difference is slightly higher than 200 cm^{-1} . In addition to that, the DFT-B3LYP calculations on bridged bonded gluconate on modeled magnetite surface revealed IR peaks at 1350 cm^{-1} and 1521 cm^{-1} for symmetric and asymmetric stretch vibrations, respectively,

confirming the experimental findings. Consequently, the gluconate is most probably bonded to the magnetite surface through bidentate bridged binding as indicated both experimental and theoretical findings.

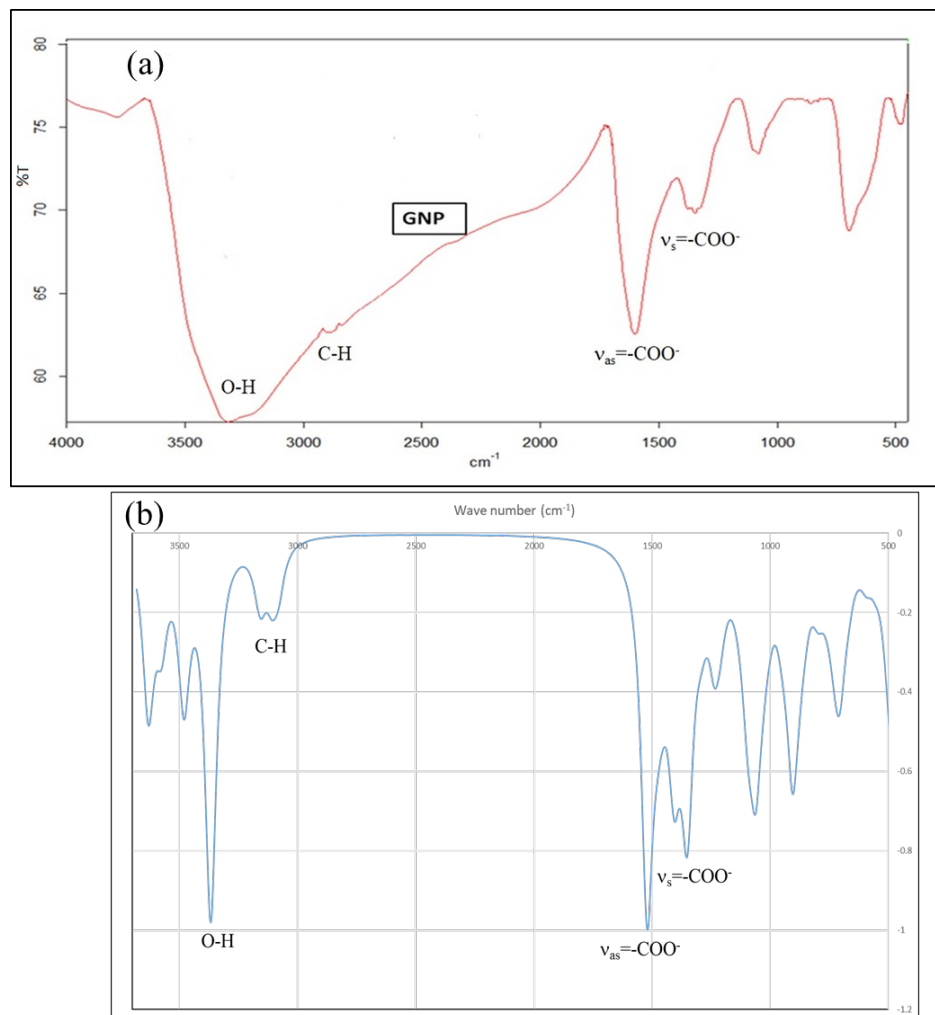


Figure 2. (a) the IR spectrum of glucose/gluconate coated magnetite nanoparticles and (b) the computed IR spectrum of the gluconate bonded to model magnetite surface (Fe₃O₄).

The Carboxymethylation Mechanism of The Gluconate Bound To Modeled Magnetite Surface

The experimental carboxymethylation procedure of gluconate coated magnetite nanoparticles occurs in a highly basic medium at elevated temperature (about 70 °C) (20). Therefore, the base form of

chloroacetic acid were used in the calculations. The mechanism proposed for the carboxymethylation reaction of gluconate coated iron oxide nanoparticle model and its energetics aqueous medium calculated at B3LYP/6-31+G(d,p) level are given in Figures 3 and 4, respectively.

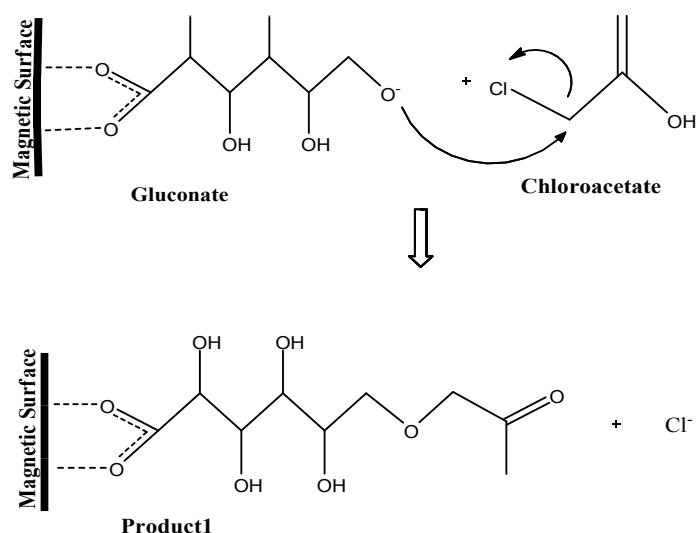


Figure 3. Mechanism of carbonyl group attached on gluconate bonded to magnetite surface.

The reaction between gluconate and chloroacetate occurring in the aqueous medium is well-known single-step nucleophilic substitution reaction (S_N2). As seen from Figure 4, the nucleophilic O1 atom, which has a Mulliken charge of $-0.927e$, the gluconate of molecule attacks the primer C1 atom ($-0.377e$, aliphatic sp^3 carbon center) of the chloroacetic acid. In the TS structure formed, while these atoms come close to each other (the distance between O1 and C1 is 2.319 \AA), chlorine atom leaves the molecule as a chloride ion (the distance between C1 and Cl1 is 2.156 \AA). Hence,

the carboxymethylated gluconate (product1) is obtained. Experimentally, this reaction takes place relatively quickly (2-6 hours) under moderate conditions (at $70 \text{ }^\circ\text{C}$ and atmospheric pressure). The DFT method predicts the activation energy of the reaction to be 12.3 kcal/mol and the reaction enthalpy to be -42.8 kcal/mol . The low activation barrier and the exothermic nature of the reaction can be attributed to the fact that the carboxymethylation reaction is relatively easy under moderate conditions.

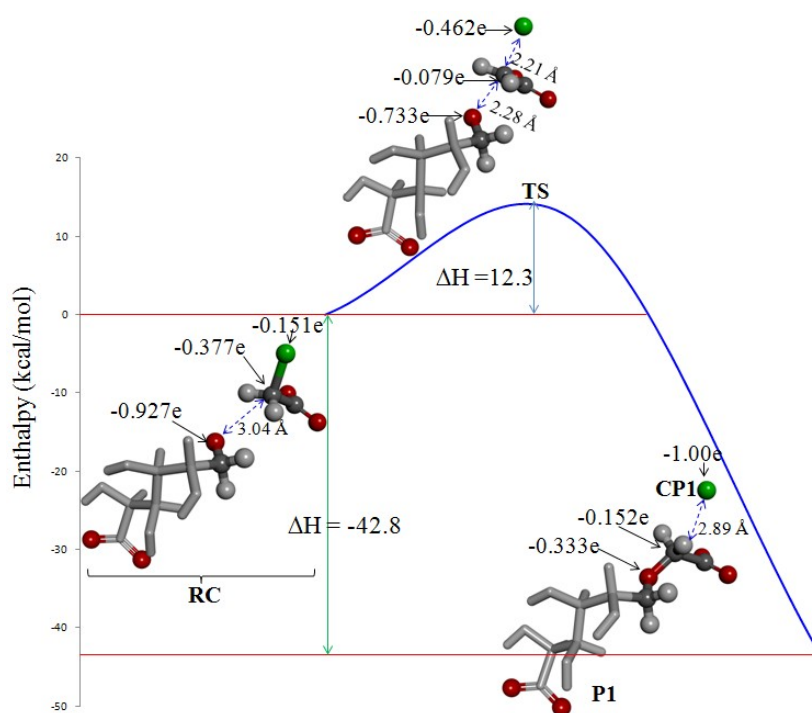


Figure 4. Energy profile (in kcal/mol) of carboxymethylation mechanism in water. Some important Mulliken partial charges on atoms are also given (RC: reactants; P1: product2; CP1: Cleaved part from TS).

The Hydrazination Mechanism of The Modeled Carboxymethylated Gluconate Bound To Magnetite Surface

The hydrazination reaction starts when P1 (the carboxymethylated gluconate) is reacted with EDC [1-ethyl-3-(3-dimethylaminopropyl) carbodiimide] and hydrazine, consecutively. According to the literature (29), this reaction occurs in two steps.

Figure 5 shows the reagents, intermediates, and products involving in this reaction. In the first step of the mechanism, P1 was interacted with EDC to form the intermediate (o-acyl isourea). In the second step where a Wolff-Kishner's reduction actually takes place (30), this intermediate reacts with hydrazine molecule to form the product2.

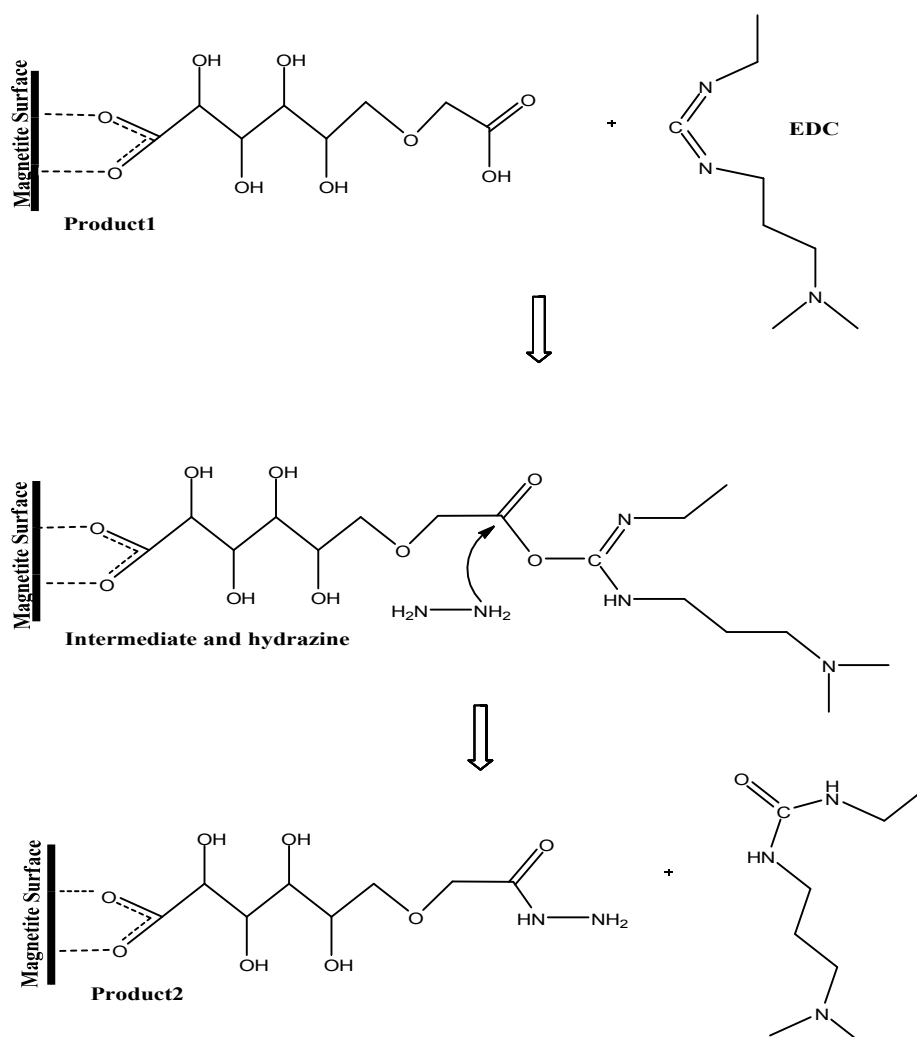


Figure 5. Hydrazine mechanisms in two-stage of product1.

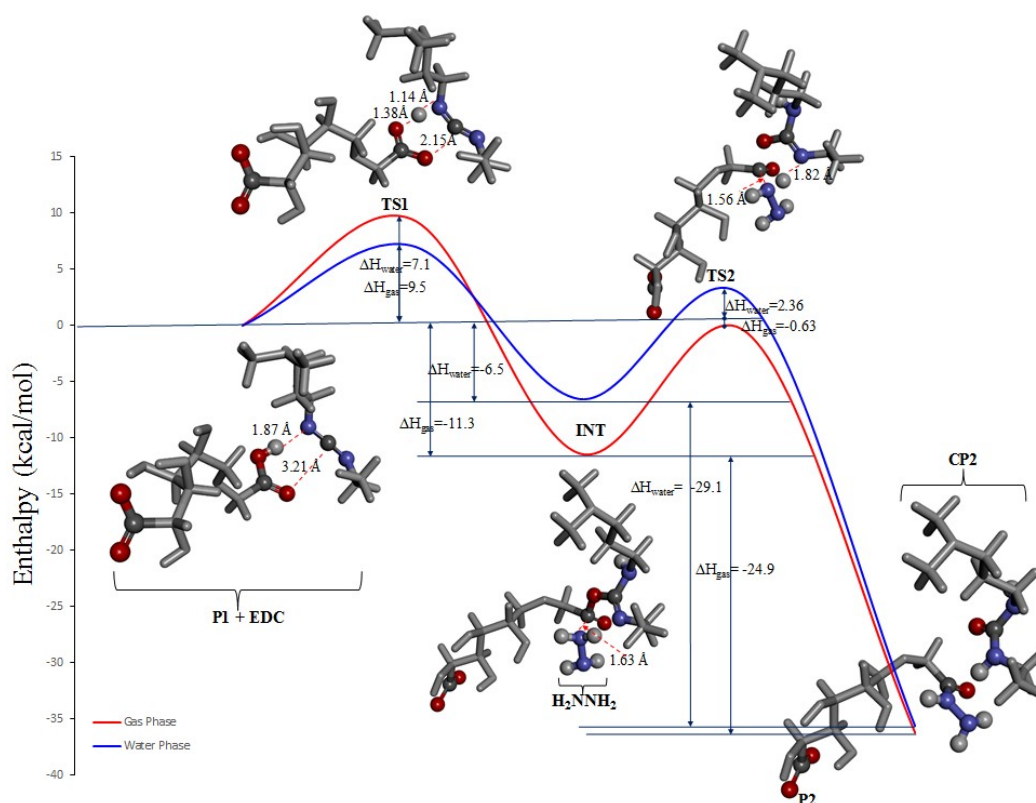
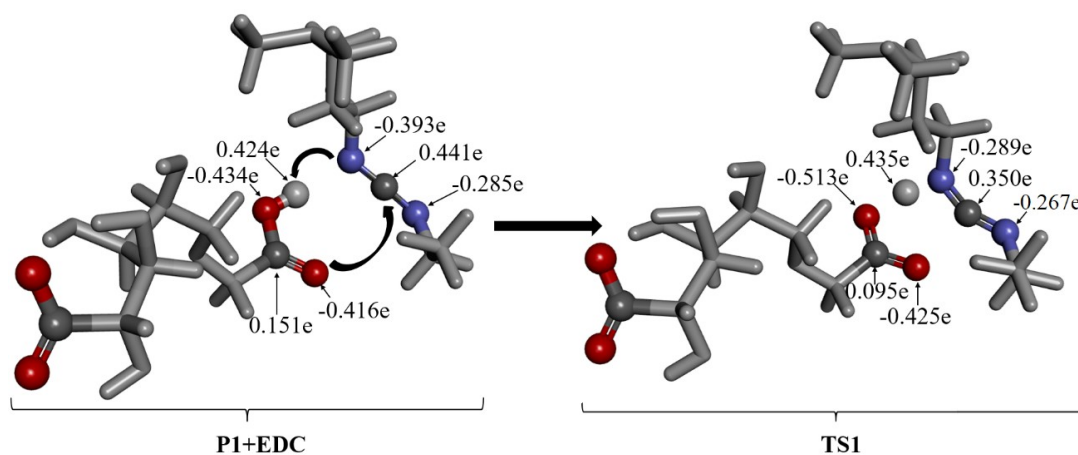


Figure 6. Hydrazination mechanism occurring in two steps (RC: reactants; INT: intermediate; P2: product2; CP2: Cleaved part from TS2).

The reactant, TS, intermediate and product geometries involved in the hydrazination reaction mechanism, activation barriers and reaction enthalpies calculated at B3LYP/6-31+G(d,p) level are given in Figure 6. Activation barriers of first and second steps of the hydrazination reaction with respect to the reactant molecules are found to be 7.1 kcal/mol and 2.4 kcal/mol in water (9.5 kcal and -0.63 kcal in the gas phase), respectively. In a multistep mechanism, the step with the highest energy TS is called the rate-determining step. Accordingly, the activation energy of the first step is greater than that of the second step, so the

overall reaction activation barrier predicted by the DFT method is the barrier of the first step (7.1 kcal/mol). In addition, the DFT method predicted that both the first step and the second step of the reaction is highly exothermic. Low barrier and high exothermicity indicate that this reaction can occur rather easily without the need for heat. Experimentally, this reaction takes place relatively quickly (4 hours) under ordinary conditions (at 25 °C and atmospheric pressure). Consequently, the results of the calculations completely agree with the experimental findings.



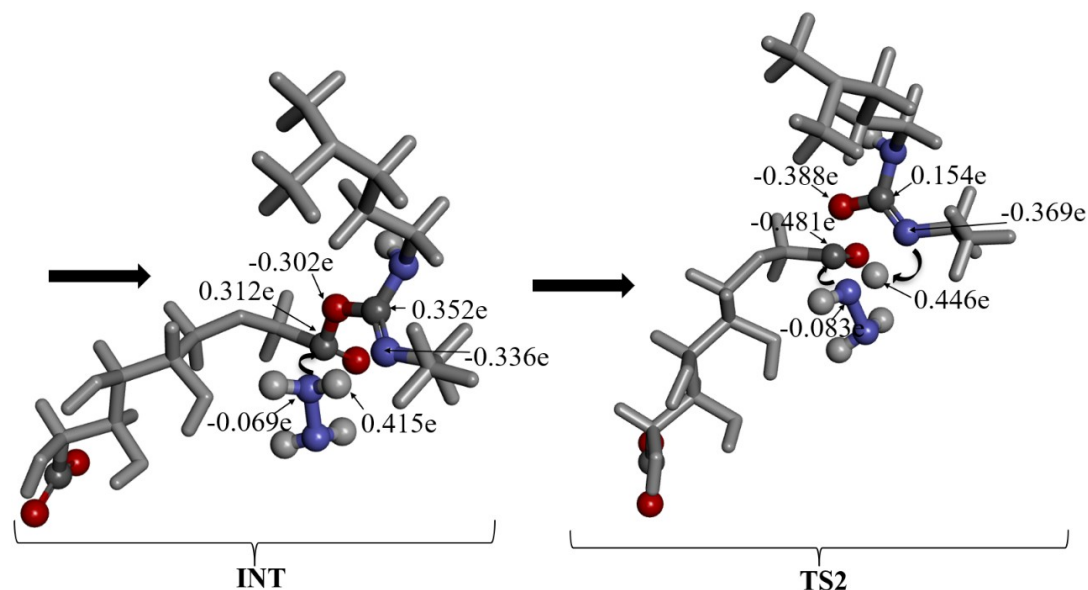


Figure 7. Optimized geometries and important Mulliken partial charges of the species involved in the first and second steps of hydrazination mechanism.

In the first step, the H atom (0.424e) of carboxylic acid moiety of P1 transfers onto the N (-0.393e) atom of carbodiimide part of the EDC molecule while the C atom (0.441e) of carbodiimide part of the EDC molecule interacts with the O atom (-0.416e) of carboxylic acid moiety of P1 to form the o-acyl iso urea intermediate (Figure 7). This step is an exothermic one with a reaction enthalpy of -6.5 kcal/mol in water (-11.3 kcal/mol in the gas phase).

In the second step, the N atom (-0.069e) of hydrazine molecule attacks the C atom of the carbonyl group of the o-acyl iso urea intermediate (INT), then an instant zwitterionic intermediate formation occurs and this attack ends with the removal of the iso-urea derivative. Meanwhile, one proton (0.446e) coming from hydrazine is transferred to the N atom (-0.369e) of the iso-urea derivative. This reaction is known as the Wolff-Kishner reduction (30). The second step is also an exothermic step with a reaction enthalpy of -29.1 kcal/mol in water and -24.9 kcal/mol in the gas phase. As a result of these two exothermic steps, the P1 is converted into P2 via carboxylic acid to an amide (hydrazine addition). Since the DFT calculations predict the overall reaction enthalpy of hydrazination reaction as -35.6 kcal/mol in water and -36.2 kcal/mol in the gas phase, it can be concluded that this reaction occurs spontaneously at room temperature.

CONCLUSION

In this article, we first determined the binding properties of a gluconate molecule to the model magnetite surface. We then investigated the carboxymethylation and hydrazination mechanisms

of gluconate bound to the magnetite surface employing the DFT-B3LYP method. When the computationally determined IR spectra of the gluconate molecule interacting with the model Fe₆O₈ surface are investigated, the bonding type is found to be the bidentate bridging binding. This is also confirmed with the experimental IR spectra obtained from the gluconated iron oxide nanoparticles. For the carboxymethylation reaction, the calculation results are revealed that the reaction between gluconate and chloroacetate has one step mechanism passing through a low activation barrier and that the reaction is exothermic. Therefore, the carboxymethylation reaction can be said to be relatively easy to perform under moderate conditions. On the other hand, the hydrazination reaction is found to be a two-step reaction. The DFT calculations show the activation energy barrier of the former step being higher than that of the latter step, leading to the fact that the rate determining step is the first step. They also reveal that the hydrazination reaction can be carried out spontaneously at room temperature due to both steps being considerably exothermic. This finding is also confirmed by the experimental data.

ACKNOWLEDGMENT

The authors thank the Scientific and Technological Research Council of Turkey (TUBITAK) (Project ID: 113Z165) and Ege University Scientific Research Project Office (Project ID: 2014 BIL 006 and 2015 FEN 055) for their financial support. All calculations reported in this paper were performed at High Performance and Grid Computing Center (TRUBA resources), ULAKBIM. IO acknowledges the contributions of Guliz Ak and Habibe Yilmaz.

REFERENCES

1. Manchun S, Dass CR, Sriamornsak P. Targeted therapy for cancer using pH-responsive nanocarrier systems. *Life Sci.* 2012;90(11-12):381-7.
2. Wei H, Zhuo RX, Zhang XZ. Design and development of polymeric micelles with cleavable links for intracellular drug delivery. *Prog Polym Sci.* 2013;38(3-4):503-35.
3. Etrych T, Kovář L, Strohalm J, Chytil P, Říhová B, Ulbrich K. Biodegradable star HEMA polymer-drug conjugates: Biodegradability, distribution and anti-tumor efficacy. *J Control Release.* 2011;154(3):241-8.
4. Chang Y, Meng X, Zhao Y, Li K, Zhao B, Zhu M, vd. Novel water-soluble and pH-responsive anticancer drug nanocarriers: Doxorubicin-PAMAM dendrimer conjugates attached to superparamagnetic iron oxide nanoparticles (IONPs). *J Colloid Interface Sci.* 2011;363(1):403-9.
5. Deng C, Jiang Y, Cheng R, Meng F, Zhong Z. Biodegradable polymeric micelles for targeted and controlled anticancer drug delivery: Promises, progress and prospects. *Nano Today.* 2012;7:467-80.
6. Jun YW, Huh YM, Choi JS, Lee JH, Song HT, Kim S, vd. Nanoscale Size Effect of Magnetic Nanocrystals and Their Utilization for Cancer Diagnosis via Magnetic Resonance Imaging. *J Am Chem Soc.* 2005;127(16):5732-3.
7. Uribe Madrid SI, Pal U, Kang YS, Kim J, Kwon H, Kim J. Fabrication of Fe₃O₄@mSiO₂ Core-Shell Composite Nanoparticles for Drug Delivery Applications. 2011;
8. Ray Chowdhuri A, Bhattacharya D, Sahu SK. Magnetic nanoscale metal organic frameworks for potential targeted anticancer drug delivery, imaging and as an MRI contrast agent. *Dalt Trans. Royal Society of Chemistry;* 2016;45(7):2963-73.
9. Singh R, Lillard JW. Nanoparticle-based targeted drug delivery. *Exp Mol Pathol.* 2009;86(3):215-23.
10. Paper R, Manish G, Vimukta S. Targeted drug delivery system: A Review. *Res J Chem Sci ResJChemSci.* 2011;1(2):1-24.
11. Zhang L, Li Y, Yu JC. Chemical modification of inorganic nanostructures for targeted and controlled drug delivery in cancer treatment. *J Mater Chem B.* 2014;2(5):452-70.
12. Arruebo M, Fernández-Pacheco R, Ibarra MR, Santamaría J. Magnetic nanoparticles for drug delivery. *June.* 2007;2(3).
13. Sun C, Lee JSH, Zhang M. Magnetic nanoparticles in MR imaging and drug delivery. *Adv Drug Deliv Rev.* 2008;60(11):1252-65.
14. McCarthy JR, Weissleder R. Multifunctional magnetic nanoparticles for targeted imaging and therapy. *Adv Drug Deliv Rev.* 2008;60(11):1241-51.
15. Uribe Madrid SI, Pal U, Kang YS, Kim J, Kwon H, Kim J. Fabrication of Fe₃O₄@mSiO₂ Core-Shell Composite Nanoparticles for Drug Delivery Applications. *Nanoscale Res Lett.* Aralık 2015;10(1):217.
16. Akbarzadeh A, Samiei M, Davaran S. Magnetic nanoparticles: Preparation, physical properties, and applications in biomedicine. *Nanoscale Res Lett.* 2012;7(1):144.
17. Harris LA, Goff JD, Carmichael AY, Riffle JS, Harburn JJ, St. Pierre TG, vd. Magnetite nanoparticle dispersions stabilized with triblock copolymers. *Chem Mater.* 2003;15(6):1367-77.
18. Chen C, Jiang X, Kaneti YV, Yu A. Design and construction of polymerized-glucose coated Fe₃O₄magnetic nanoparticles for delivery of aspirin. *Powder Technol. Elsevier B.V.;* 2013;236:157-63.
19. Sun X, Zheng C, Zhang F, Yang Y, Wu G, Yu A, vd. Size-controlled synthesis of magnetite (Fe₃O₄) nanoparticles coated with glucose and gluconic acid from a single Fe(III) precursor by a sucrose bifunctional hydrothermal method. *J Phys Chem C.* 2009;113(36):16002-8.
20. Ak G, Yilmaz H, Güneş A, Hamarat Sanlier S. In vitro and in vivo evaluation of folate receptor-targeted a novel magnetic drug delivery system for ovarian cancer therapy. *Artif Cells, Nanomedicine, Biotechnol. Informa UK Limited, trading as Taylor & Francis Group; Şubat 2018;0(0):1-12.*
21. Haavik C, Stølen S, Fjellvåg H, Hanfland M, Häusermann D. Equation of state of magnetite and its high-pressure modification: Thermodynamics of the Fe-O system at high pressure. *Am Mineral.* 2000;85(3-4):514-23.
22. Salafranca J, Gazquez J, Pérez N, Labarta A, Pantelides ST, Pennycook SJ, vd. Surfactant organic molecules restore magnetism in metal-

oxide nanoparticle surfaces. *Nano Lett.* 2012;12(5):2499–503.

23. Demir A, Topkaya R, Baykal A. Green synthesis of superparamagnetic Fe₃O₄ nanoparticles with maltose: Its magnetic investigation. *Polyhedron.* Elsevier Ltd; 2013;65:282–7.

24. Schwaminger SP, García PF, Merck GK, Bodensteiner FA, Heissler S, Günther S, vd. Nature of Interactions of Amino Acids with Bare Magnetite Nanoparticles. *J Phys Chem C.* 2015;119(40):23032–41.

25. Nosrati H, Salehiabar M, Davaran S, Ramazani A, Manjili HK, Danafar H. New advances strategies for surface functionalization of iron oxide magnetic nano particles (IONPs). *Res Chem Intermed.* Springer Netherlands; 2017;43(12):7423–42.

26. Schwaminger SP, Blank-Shim SA, Scheifele I, Fraga-García P, Berensmeier S. Peptide binding to metal oxide nanoparticles. *Faraday Discuss.* 2017;

27. Śmiłowicz M, Pogorzelec-Glaser K, Łapiński A, Motała R, Grobela M, Andrzejewski B. Spectroscopic and quantum chemical studies of interaction between the alginic acid and Fe₃O₄ nanoparticles. *Spectrochim Acta - Part A Mol Biomol Spectrosc.* 2017;182:1–7.

28. Sanchez LM, Martin DA, Alvarez VA, Gonzalez JS. Polyacrylic acid-coated iron oxide magnetic nanoparticles: The polymer molecular weight influence. *Colloids Surfaces A Physicochem Eng Asp.* Elsevier; 2018;543(December 2017):28–37.

29. Custer TG, Kato S, Bierbaum VM, Howard CJ, Morrison GC. Gas-Phase Kinetics and Mechanism of the Reactions of Protonated Hydrazine with Carbonyl Compounds. *Gas-Phase Hydrazone Formation: Kinetics and Mechanism.* 2004;1(2):2744–54.

30. Taber DF, Stachel SJ. On the mechanism of the Wolff-Kishner reduction. *Tetrahedron Lett.* Pergamon; Şubat 1992;33(7):903–6.



Quantitative Structure-Activity Relationship (QSAR) Studies and Molecular docking Simulation of Norepinephrine Transporter (NET) Inhibitors as Anti-psychotic Therapeutic Agents

Sabitu Babatunde Olasupo^{1*}  , Adamu Uzairu²  , Gideon Shallangwa²  
and Sani Uba²  

¹National Agency for Food and Drug Administration and Control (NAFDAC), Nigeria.

²Department of chemistry, Ahmadu Bello University Zaria, Nigeria .

Abstract: The Norepinephrine transporter (NET) is a Na⁺/Cl⁻ coupled neurotransmitter transporter responsible for reuptake of released norepinephrine (NE) into neural terminals in the brain, an important therapeutic agent used in the treatment of psychiatric disorders. A quantitative structural activity relationship (QSAR) investigation was carried out on 50 Molecules of NET Inhibitors to investigate their inhibitory potencies against norepinephrine transporter as novel agents for anti-psychotic disorders. The molecules were optimized by employing Density functional theory (DFT) with basis set of B₃LYP/6-31G*. The genetic function Algorithm (GFA) approach was used to generate a highly predictive and statistically significant model with good correlation coefficient $R^2_{\text{Train}} = 0.952$, Cross validated coefficient $Q^2_{\text{cv}} = 0.870$ and adjusted squared correlation coefficient $R^2_{\text{adj}} = 0.898$. The predictability and accuracy of the developed model was evaluated through external validation using test set molecules, Y-randomization and applicability domain techniques. The results of Molecular docking simulation by using two neurotransmitter transporters PDB ID 2A65 (resolution = 1.65 Å) and PDB ID 4M48 (resolution = 2.955 Å) showed that two of the ligands (compound numbers 12 and 44) having higher binding affinity were observed to inhibit the targets by forming hydrogen bonds and hydrophobic interactions with amino acids of the two receptors respectively. The results of this study are envisaged to provide very important new insights into the molecular basis and structural requirements that would help in designing more potent and more specific therapeutic anti-psychotic agents.

Keywords: Norepinephrine transporter Inhibitors, antipsychotic, QSAR, Disorder, DFT, Drug.

Submitted: June 13, 2019. **Accepted:** November 26, 2019.

Cite this: Olasupo SB, Uzairu A, Shallangwa G, Uba S. Quantitative Structure-Activity Relationship (QSAR) Studies and Molecular docking Simulation of Norepinephrine Transporter (NET) Inhibitors as Anti-psychotic Therapeutic Agents. JOTCSA. 2020;7(1):179-96.

DOI: <https://doi.org/10.18596/jotcsa.577259>.

***Corresponding author. E-mail:** olasabit@yahoo.com.

INTRODUCTION

Mental disorder or psychotic disorder is a clinical syndrome in which some loss of contact with reality has occurred and it is generally applied to persons whose mental functioning is sufficiently impaired to interfere with their capacity to meet the ordinary demand of life (1). Psychotic disorders are common to all countries and cause immense human suffering, social exclusion, disability, poor quality of life, staggering economic and social costs. It is estimated that one in every four people have a mental disorder(1). The combined costs of mental disorder, including loss of productivity, loss of earning due to illness and social costs, are estimated to total at least USD 113 billion annually (2). The major depressive disorders (MDDs) had been estimated as the second largest global burden among all diseases by 2030 which makes the discovery of novel and efficacious anti-psychotic drugs very urgent (3). Persons with psychotic disorder are at risk for complications and derivatives' effects of psychosis such as suicide attempts, substance abuse, homelessness, victimization by others and committing act of violence (4).

Norepinephrine (NE) is a neurotransmitter, a crucial neurochemical messenger employed in central noradrenergic and peripheral sympathetic synapses (5) responsible for reuptake of released norepinephrine (NE) into nerve terminals in the brain. Dysregulation of this neurotransmitter is associated with many debilitating psychotic disorders and mental illnesses (6). Inhibition of the norepinephrine transporter by NET inhibitors has emerged as important drug targets with a multitude of therapeutic potentials for the treatment of psychiatric disorders and mental diseases (7).

Quantitative structure-activity relationship (QSAR) analysis is a useful technique to find correlations between biological activities and molecular descriptors of different classes of compound (8). QSAR plays a significant role in novel drug discovery, and it finds application in predicting the activity of novel compounds by mathematical expression which figure out the relationships between a chemical structure to their biological activity and a QSAR models give information that is very useful for drug design and medicinal chemistry.

In recent time, computer assisted drug design base on QSAR has been of great important to develop novel medications for the treatment of different ailments (9).

The aim of this study is to build up a QSAR model to explore the inhibitory potency of some NET inhibitors and likewise to elucidate the interactions between the inhibitor compounds, and the receptor sites.

MATERIALS AND METHODS

Dataset collection and Geometry optimization

A dataset of fifty (50) compounds of norepinephrine transporter (NET) inhibitors were sourced from ChEMBL Database.

Optimization is the process of finding the equilibrium or concept energy geometry of molecules. Chemdraw software Ultra-version 12.0 was used to draw the chemical structures of the compounds and subsequently imported into Spartan 14 software (10) to optimize the molecular geometry at the Density Functional Theory (DFT) using the B₃LYP at 6-31G⁺ basis set (11) to generate quantum chemical and molecular descriptors.

Division of Dataset

The dataset of the studied compounds was partitioned into a training set and a test set by using Kennard stone algorithm (12) "Dataset Division GUI 1.2" software. The training set was used to develop the QSAR model, while the test set was employed to validate the developed model.

Model Building

A statistical analysis by genetic function approximation (GFA) techniques in the Material studio software 8.0 version was used to build the QSAR models. GFA has a distinctive attribute to generate a population of model equations rather than a singular model as most other statistical methods do. It also selects the basic function genetically, generate better models than those made using stepwise regression techniques. The range of variations in this population gives added information on the quality of fit and importance of the descriptors (13). The Friedman's Lack of Fit (LOF) was employed to evaluate the quality of the model as a method that measures fitness of a model. LOF is estimated by this mathematical expression;

$$LOF = \frac{SEE}{(1 - (C + d \times p) / M)^2} \quad (1)$$

Where c is the number of basic functions, d is the smoothing parameter, M is the number of samples in the training set, SEE is the sum of square error and p is the sum number of descriptors contained in the model.

Molecular descriptors calculation

Molecular descriptors are arithmetical values that describe properties of molecules obtained from a well-defined algorithm or experimental procedure. The OD, ID, 2D and 3D molecular descriptors were calculated using paDel-Descriptor software 2.20 version (14) in addition to quantum chemical descriptors generated by the Spartan 14 software.

Data pre-treatment

Data pre-treatment for the generated molecular descriptors after normalization was done by using "Data pretreatment GUI 1.2" software that uses V-WSP algorithm (15) to remove noise and redundant data. This helps to overcome productivity and generalization failure of the model due to constant value and highly correlated descriptors in forming QSAR models.

Data normalization and Descriptors Transformation

Molecular descriptors values were normalized by employing "normalized data 1.0 version software" to give each variable the same opportunity and make the relationship between descriptors considerably less demanding. The molecular descriptors of the training set were transformed through normalization (16) using the mathematical equation below:

$$X^n = \frac{X - X_{max}}{X_{max} - X_{min}} \quad (2)$$

Where X^n is the normalized descriptor, X_{max} is the maximum value in a descriptor column and X_{min} is the minimum value in the column of the training dataset.

Assessing Quality Assurance of the Model

Statistical parameters of the model were reviewed and evaluated to ascertain its fitting ability, reliability, predictive ability, stability and robustness of the model generated. The quality assurance of a developed model is guaranteed if

the following parameters are satisfied; $R^2_{pred} > 0.5$, $Q^2 > 0.6$, P (95%) < 0.05 , high value of F-test, low values of R^2_{random} and Q^2_{random} .

Validation of the Model

Leave-one-out cross validation technique was employed to determine the predictive power of the model. This was evaluated by using this mathematical expression:

$$Q^2_{cv} = 1 - \left[\frac{\sum (Y_{pred} - Y_{exp})^2}{\sum (Y_{exp} - \bar{Y}_{training})^2} \right] \quad (3)$$

Where Y_{pred} , Y_{exp} and $\bar{Y}_{training}$ symbolized the experimental, the predicted and mean values of experimental activity of training set compounds.

Also, the square of the correlation coefficient for the test set (R^2_{test}) was evaluated for the predictive capacity of the developed model as part of the external validation technique. The closer the value of R^2_{test} value to 1.0 the better the model. The R^2_{test} is evaluated by using this mathematical equation:

$$R^2_{test} = 1 - \frac{\sum (Y_{pred} - Y_{test})^2}{\sum (Y_{pred} - \bar{Y}_{training})^2} \quad (4)$$

Where Y_{pred} and Y_{test} are the predicted and experimental activity values of the test set compounds. $\bar{Y}_{training}$ is the mean (average) activity value of the training set.

Y - Randomization test

Y - randomization is an important external validation technique to ascertain that a developed QSAR model is strong and reliable and is not inferred by luck. Y-randomization test is performed on the training dataset. The low values of R^2 and Q^2 is an indication that the model is very robust and highly reliable, and the cR^2_p value of the model must be greater than 0.5 to pass the Y-randomization test. The cR^2_p value is calculated by using this mathematical formula:

$$cR^2_p = R \times [R^2 - (R_r)^2] \quad (5)$$

Where cR^2_p = coefficient of determination for Y-Randomization

R = Coefficient of correlation for Y-Randomization
 R_r = Average "R" of random models.

Degree of contribution of selected descriptors

The level of contribution of each descriptor in the model is determined by calculating its standardized regression coefficients b_j using this mathematical equation:

$$b_j = \frac{S_j b_j}{SY} = J = 1, \dots, d \quad (6)$$

Where b_j is the regression coefficient of descriptor j . S_j and S_y are the standard deviations for each descriptor and activity respectively.

The descriptor of higher absolute standardized coefficient implies a greater importance to the rest of molecular descriptors.

Multi-co-linearity evaluation

Multi-co-linearity estimation among descriptors selected by GFA analysis is evaluated using variance inflation factor (VIF) by the mathematical expression below:

$$VIF_i = \frac{1}{1 - R_{ij}^2} \quad (7)$$

Where R_{ij}^2 is the correlation coefficient of the multiple regression between the descriptor i and the rest j descriptors in the developed model (17).

Assessment of the applicability domain of the model

Evaluation of the applicability domain of a model is a significant step to confirm that the developed model is capable to make a reliable prediction within the chemical space for which it was developed (16). To describe the applicability domain of the QSAR model, the leverage approach was employed.

Leverage of a given dataset h_i , is defined by this mathematical expression:

$$H_i = x_i (X^T X)^{-1} X_i^T \quad (8)$$

Where x_i the descriptor row is vector of the considered compound i , h_i is the $n \times k$ descriptor

matrix of the training set compound used to generate the model.

The warning leverage (h^*) is the limit of normal values of x outliers and is expressed mathematically as:

$$h^* = \frac{3(p+1)}{n} \quad (9)$$

Where n = number of training compounds and P is the number of predictor variables (descriptors) in the model.

If the leverages $h_i < h^*$ for the test compounds, it considered to be reliably predicted by the developed model.

The relevance area of the model in terms of chemical space is visualized by the plot of standardized residuals against leverage values (Williams plot).

MOLECULAR DOCKING SIMULATION

The molecular interactions studies were carried out on a Dell computer system, with processor properties of Intel® Core i5-6100U CPU Dual@2.30GHz, 12 GB (RAM) between the ligands and two neurotransmitter transporters (targets); the Crystal structure of LEUTAA, a bacterial homolog of Na⁺/Cl⁻-dependent neurotransmitter transporters and X-ray structure of dopamine transporter elucidates antidepressant mechanism as to elucidate which of the NET inhibitors will have the best binding affinity against any of these two receptors, because the current structural findings of human monoamine neurotransmitters transporters (MATs) is based on X-ray crystal structures of bacterial and invertebrate homologs (18).

Making of Ligand and Target

All the compounds were optimized using Spartan software initially saved as SDF files and were appropriately later saved as Protein Data Bank (PDB) files. Subsequently, crystal structure of LEUTAA, a bacterial homolog of Na⁺/Cl⁻-dependent neurotransmitter transporters and X-ray structure of dopamine transporter elucidates antidepressant mechanism (targets) were downloaded from Protein Data Bank website with PDB codes 2A65 and 4M48 respectively. Fig.1 below displays the prepared structure of the receptors.

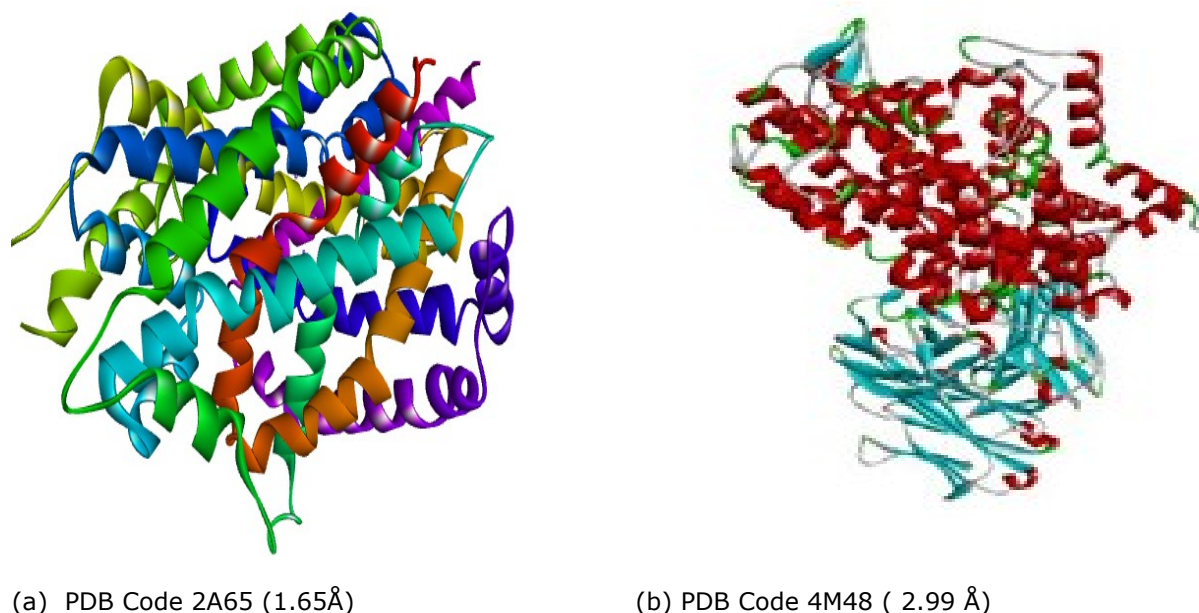


Figure 1: Prepared structures of the targets.

Docking process

The docking of the prepared ligands with the receptors 2A65 and 4M48 were conducted using the AutoDock Vina version 4.0 of Pyrex software. Hence, Discovery Studio software was used in visualizing the molecular interactions of the stable complex.

RESULTS AND DISCUSSIONS

QSAR study was explored to investigate the structure–activity relationship of 50 compounds with distinguishing organic fragments acting as norepinephrine transporter (NET) inhibitors. The nature of models in a QSAR study is expressed by its fitting the data points through regression and making predictions of isolated dataset.

QSAR on pKi of norepinephrine transporter (NET) inhibitors

A data set of 50 compounds was divided into a training set of 36 compounds used in developing the model and a test set of 14 compounds was used to evaluate the predictive ability of the QSAR model for the inhibition of norepinephrine transporter. The predicted and experimental activities alongside with their residual values were presented in Supplementary Table S1. The

low residual values resulted from the experimental and predicted activities is a good indication that the developed model has good predictability.

The descriptive statistics parameters for the training set and test set activities value were reported in Table 2. Comparison the descriptive statistics parameters between training and test set in Table 2, the values for the training set were approximately equal to that of test set. This shows that the test set is interpolative within the training set, and the similarity in the activity distribution of training set and test set. This is a good quality assurance that Kennard Stone's algorithm used in this research generates a test set that is a true reflection of the training set.

The genetic algorithm-multiple linear regression (GA-MLR) examination prompted the choice of 6 descriptors, which were eventually used to amassed a linear regression model for calculating pKi of norepinephrine transporter inhibitors within the chemical space of the model. The model with statistical significance was selected and represented by equation (10) below:

$$pKI = 2.788 (A\text{Log}P) + 3.382 (A\text{ATS7i}) + 3.782 (A\text{TSC3p}) + 2.234 (IC2) - 5.147 (GGI10) + 3.728 (RDF75u) + 0.989$$

..... (10)

$$N_{\text{train}} = 36, R^2_{\text{train}} = 0.9156, R^2_{\text{adjusted}} = 0.8982, Q^2_{\text{Loo}} = 0.8755, \text{Outliers} > 3.0 = 0, N_{\text{test}} = 14, R^2_{\text{test}} = 0.5832$$

N is the total number of the datasets, R^2 is the squared correlation coefficient, Q^2_{Loo} is the squared cross-validation coefficients for leave one out. In the model, the number of ratio of training set data to the ratio number of descriptors present in the model was 6 and in agreement with Topliss ratio (19). This implies that the developed model obeyed the QSAR semi-empirical rule of thumb (20). The name and the symbol of the descriptors, the standardized regression coefficients (degree of contribution) and percentage contribution of the descriptors were reported in Table 5. The combined presence of 2D and 3D descriptors in the developed model is an evidence that these types of descriptors are able to characterize good antipsychotic activity of the compounds. The sign, magnitude and

percentage contribution of each descriptor is not only to give critical information on the direction of influence of the descriptor but also pinpoint the strength of contribution to the activity of the compound.

The model generated was subjected to internal and external validations. The outcome of internal and external validations of the model is in conformity to Occam's razor rule. The generally acceptable QSAR Model Validation Tools and the validated parameters of the model were presented in Table 1. The values of validation parameters of the model were in agreement with generally acceptable QSAR Model Validation Tools reported in Table 1. This confirmed the reliability, stability and robustness of the developed model.

Table 1: Accepted QSAR Model Validation Tools (21).

Validation Tools	Interpretation	Acceptable Value	Developed model Value	Remarks
R^2	Co-efficient of determination	≥ 0.6	0.911	pass
P(95%)	Confidence interval at 95% confidence level	< 0.05	2.446	pass
Q^2_{cv}	Cross-Validation Co-efficient	> 0.5	0.870	pass
$R^2 - Q^2_{cv}$	Difference between R^2 and Q	≤ 0.3	0.04	pass
$N_{\text{Ext testset}}$	Minimum number of external and test sets	≥ 5	14	pass
R^2_{Testset}	Co-efficient of determination of external and test set	≥ 0.5	0.5850	pass
cR^2_p	Coefficient of determination for Y-randomization	> 0.5	0.840	pass
R^2_{adj}	Adjusted R-squared	> 0.6	0.893	Pass
VIF	Variance Inflation Factor	< 10	1.4-4.4	Pass
t-test	t-Statistic value	> 2	5-9	Pass

The Pearson's correlation matrix and other statistical tools employed for validation of the model were reported in Table 3. The low value in correlation coefficients between each pair of descriptors (< 7.0) is a clear indication that there was no significant multi-collinearity among the descriptors in the developed model. The Variance

Inflation Factor (VIF) values reported in Table 3 were less than 10 and the t-statistics values were greater than 2 for all the descriptors. This is a quality assurance that the developed model was statistically significant, and the descriptors contributed appreciably to the model at 95% level (21) and they were orthogonal.

Table 2: Descriptive statistical analysis of NET inhibitor compounds

Descriptive values	Training dataset	Test dataset
Dataset Number	36	14
Standard Error	0.185	0.296
Median	7.054	7.497
Standard Deviation	1.108	106
Sample Variance	1.227	1.223
Kurtosis	-0.632	2.677
Skewness	0.229	-1.264
Range	4.439	4.436
Minimum	5.084	4.500
Maximum	9.523	8.936
Mean	6.940	7.394

Table 3: Pearson's correlation matrix and model quality assurance

	<i>A</i> Log <i>P</i>	<i>A</i> AT <i>S</i> 7 <i>i</i>	<i>A</i> T <i>S</i> C3 <i>p</i>	<i>I</i> C2	<i>G</i> G <i>I</i> 10	<i>R</i> D <i>F</i> 75 <i>u</i>	VIF	t-statistics	p value
<i>A</i> Log <i>P</i>	1						1.5021	7.5604	2.47E08
<i>A</i> AT <i>S</i> 7 <i>i</i>	-0.3321	1					1.4789	7.4649	3.16E-08
<i>A</i> T <i>S</i> C3 <i>p</i>	-0.2592	-0.2991	1				1.4376	9.4970	2.1E-10
<i>I</i> C2	-0.2742	0.0487	0.0765	1			1.4177	5.8502	2.4E-06
<i>G</i> G <i>I</i> 10	-0.2382	0.0921	-0.1711	0.5005	1		4.5022	-9.5663	1.79E-10
<i>R</i> D <i>F</i> 75 <i>u</i>	-0.2940	0.2215	-0.1337	0.4759	0.6377	1	4.3800	6.7912	1.87E-07

Table 4: Y-randomization table for QSAR Analysis

Model	R	R ²	Q ²
Original	0.9545	0.9111	0.8702
Random 1	0.4197	0.1762	-0.2759
Random 2	0.3402	0.1157	-0.4558
Random 3	0.3943	0.1555	-0.3333
Random 4	0.4690	0.2199	-0.2220
Random 5	0.4408	0.1943	-0.1861
Random 6	0.1560	0.0243	-0.6456
Random 7	0.3589	0.1288	-0.3166
Random 8	0.3237	0.1048	-0.3536
Random 9	0.3323	0.1104	-0.4357
Random 10	0.3646	0.1329	-0.3307

Random Models Parameters

Average r :	0.3599
Average r ² :	0.1363
Average Q ² :	-0.3555
cRp ² :	0.8439

Table 5: Names of the model descriptors and their respective degree of contribution

Descriptor	Descriptor Name	Type	Degree of contribution	of percentage of contribution
AlogP	Ghose-Crippen LogKow	2D	0.513	13.3
AATS7i	Average Broto-Moreau autocorrelation - lag 7 / weighted by first ionization potential	2D	0.500	13.0
ATSC3p	Centered Broto-Moreau autocorrelation - lag 3 / weighted by polarizabilities	2D	0.631	16.4
IC2	Information content index (neighborhood symmetry of 2-order)	2D	0.383	10.0
GGI10	Topological charge index of order 10	2D	-1.061	27.6
RDF75u	Radial distribution function - 075 / unweighted	3D	0.756	19.7

The model generated was used to predict the test set data, and the results were reported in Supplementary Table S1. The predicted pK_i values for the training and test sets were plotted against the experimental pK_i values as shown in Figure 3. Similarly, the plot of the standardized residuals values for both the training and test

sets against the leverage values of the descriptors in the model were shown in Fig. 4. As can be seen from Supplementary Table S1, Figure 3 and Figure 4, the calculated values for the pK_i were in excellent agreement with those of the test set, as a result of this, no any form of error was displayed by the model.

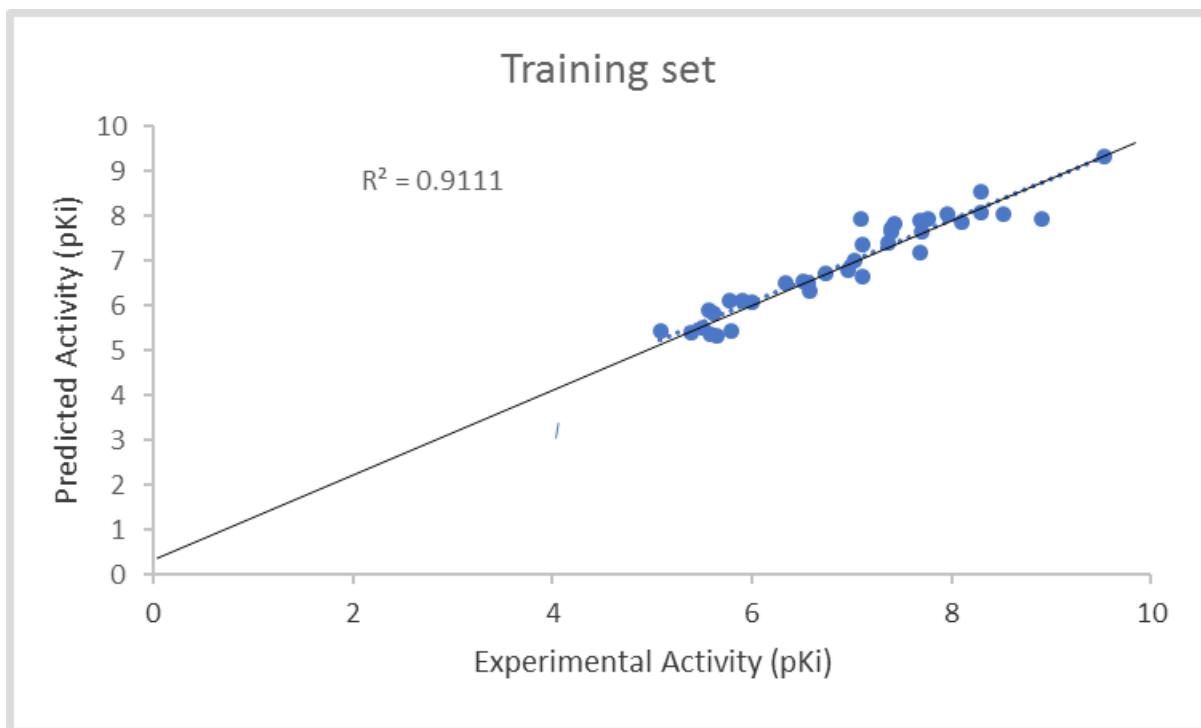


Figure 2: Plot of predicted pKi values against Experimental pKi values for Training.

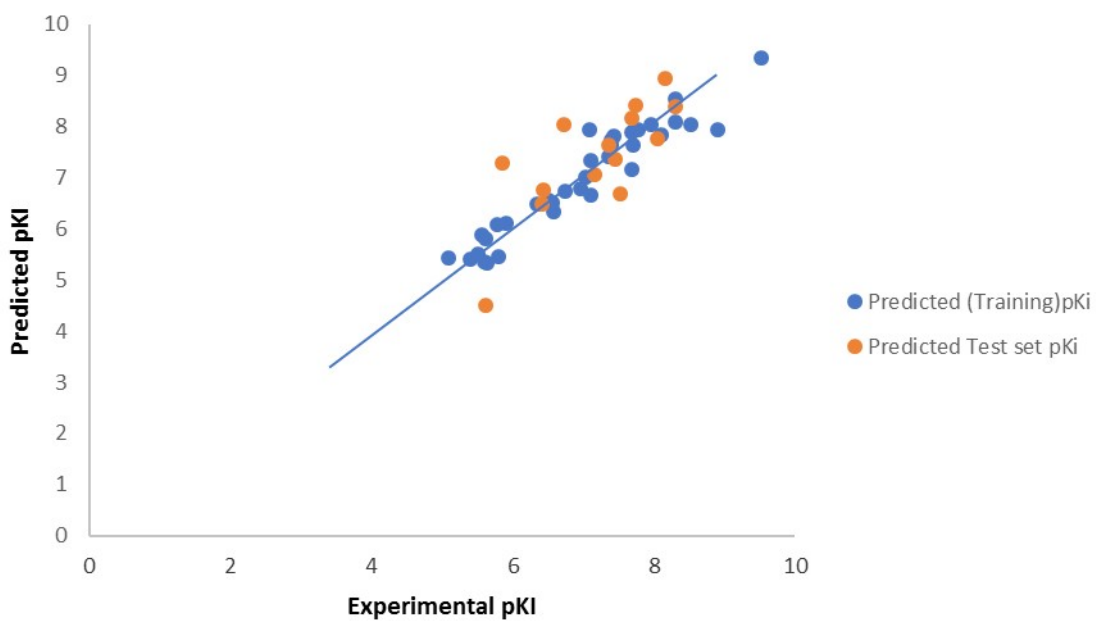


Figure 3: Plot of predicted pKi values against Experimental pKi values for Training and Test sets.

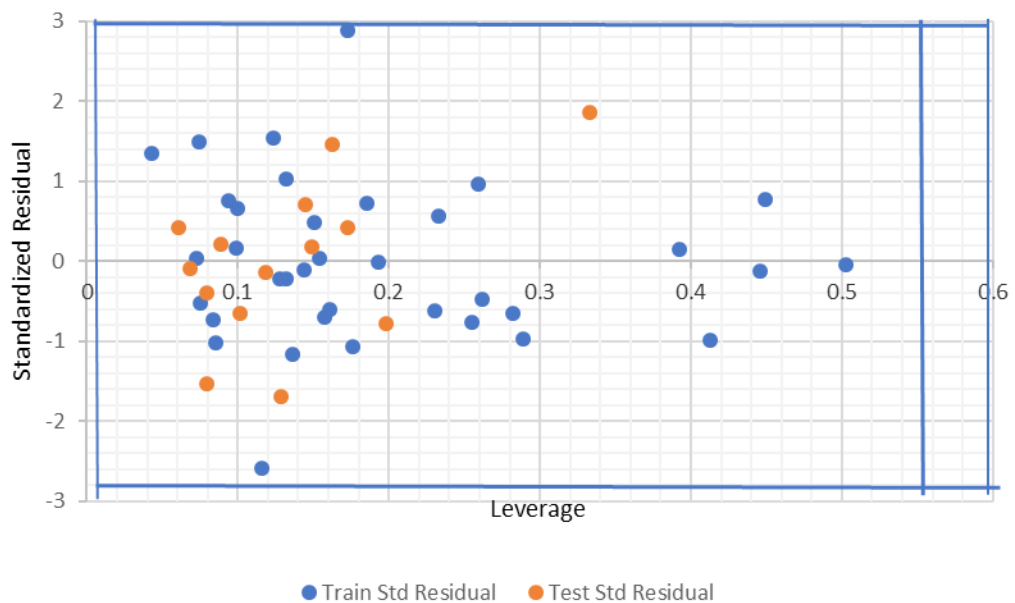
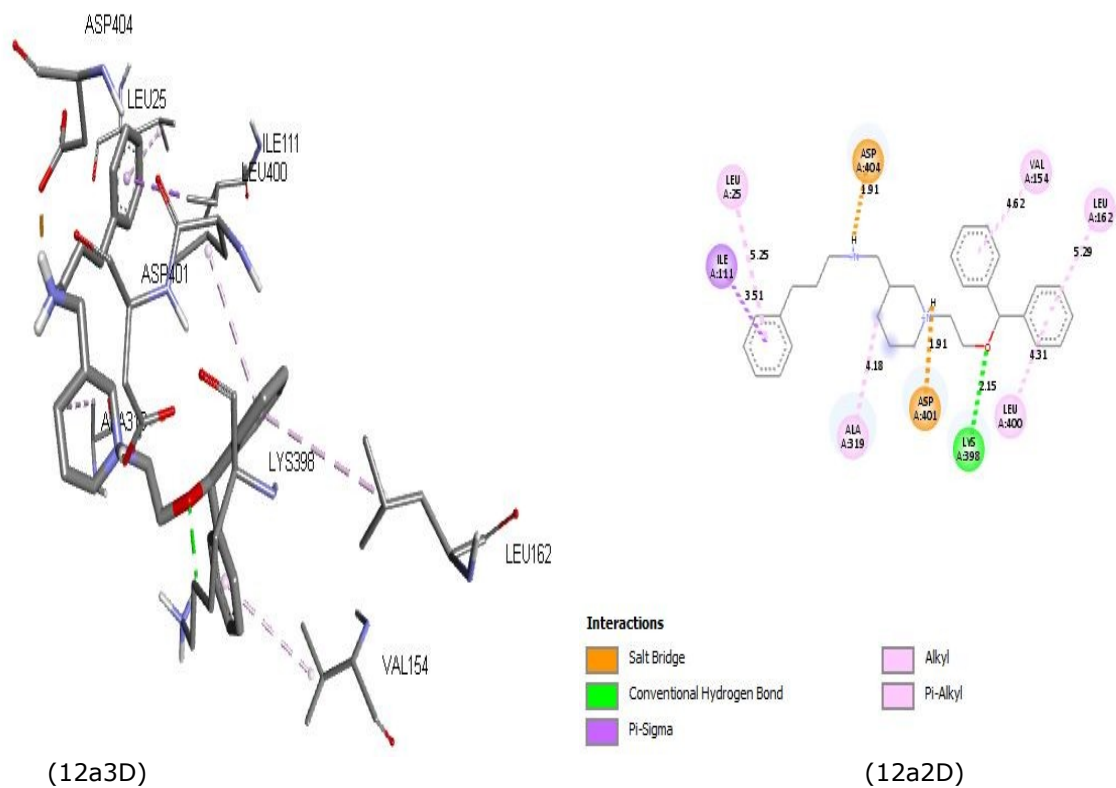
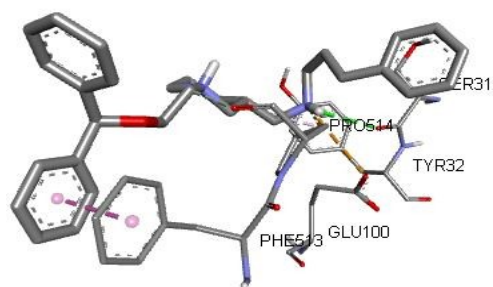
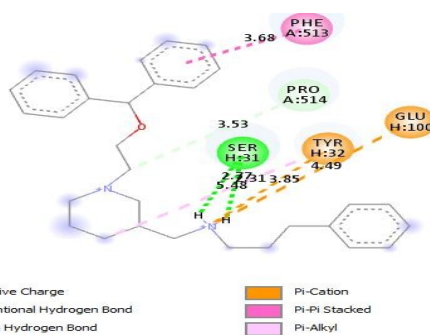


Figure 4: A Williams plot for the data set of pKi standardized residual against its descriptor space.

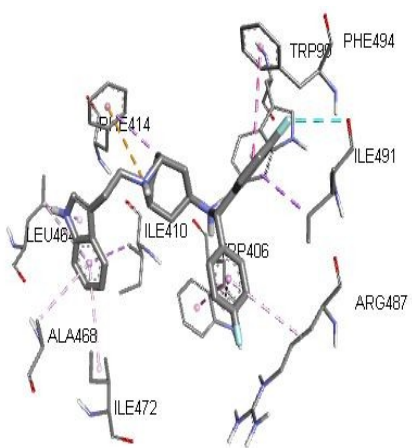




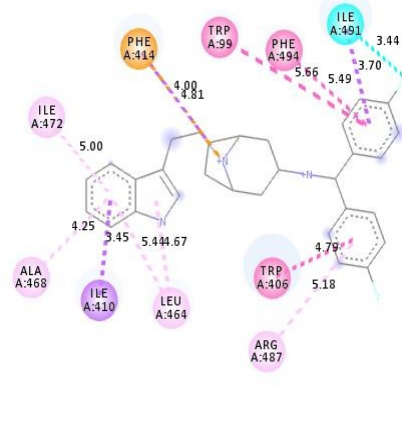
(12m3D)



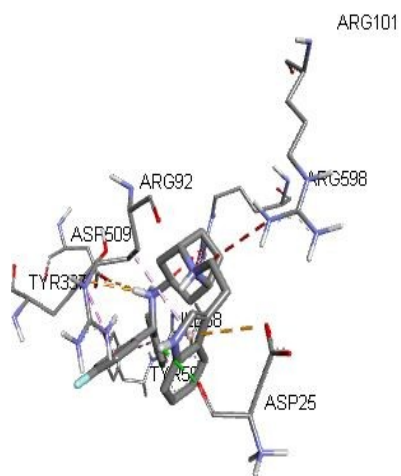
12m2D



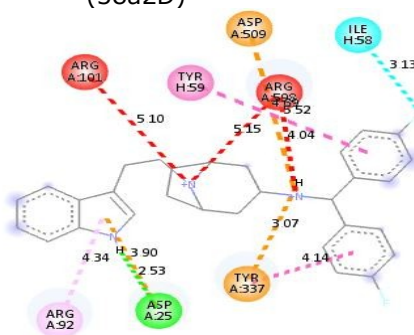
(38a3D)



(38a2D)



(38m3D)



(38m2D)

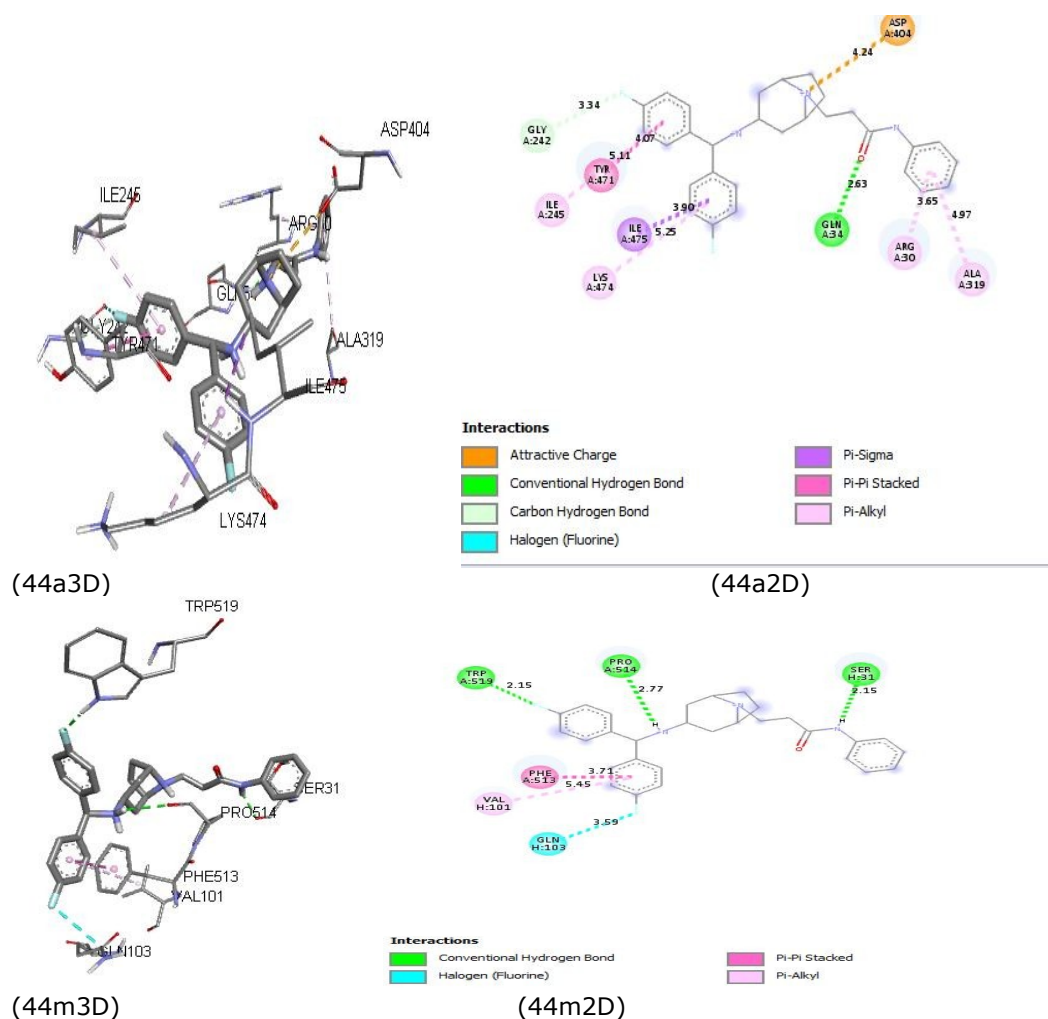


Figure 5. (12a 2D&3D), (38a 2D&3D) and (44a 2D&3D) depict 2D and 3D interactions at the binding site between receptor PDB code 2A65 with ligand 12, 38 and 44 while (12m 2D&3D), (38m 2D&3D) and (44m 2D&3D) show 2D and 3D interactions at the binding site between receptor PDB code 4M48 with ligand 12, 38 and 44 respectively.

QSAR model validation

The internal coherence of the training set was established by using leave-one-out cross-validation technique to ascertain the strength and reliability of the developed model, because the candid significance of a QSAR model is not merely their ability to mimic known activities of chemicals, set by their fitting power (R^2), but above all is their prospective for guessing biological activity accurately. The great value of Q^2_{Loo} for pKi of NET inhibitors used (0.8755) speak well of a fully clad internal validation of the model.

The plot of experimental pKi values against predicted pKi values for training set was presented in Figure 2. The displayed of linear

relationship was observed in the plot between the experimental and predicted activities of the training set ($R^2 = 0.911$). The fact that all these results were in agreement with QSAR validation tools presented in Table 1 is a confirmation of the reliability, robustness and stability of the developed model (21).

The Fig. 4, depicts the Williams plot of the NET dataset, in which the standardized residuals for each compound in the dataset were plotted against their leverage values, coming about to acknowledgment of likely outliers and outstanding chemicals in the models.

The applicability domain is set up inside a defined domain where all the data point were within the

boundary ± 3 for residuals and a leverage threshold $h^*(h^* = 3p^0 / n)$ where p^0 is the number of model parameters and n is the number of compounds (15). Based on our findings, it is clear that every one of the compounds of the training set and test set for the dataset were inside the domain (square area) and no statistical value far from others compounds (outlier) with standardized residuals $> 3d$ for the dataset exist.

The percentage of contribution was calculated to determine the relative importance and the contribution of every descriptor in the model. The degree of contribution of each descriptor and variance inflation factor (VIF) of the descriptor were estimated to evaluate the percentage and the significance of contribution of the descriptors as reported in Table 3 and Table 5 respectively. The descriptor GGI10 showed highest contribution value (27.6%) in the model with VIF value of 4.502 as reported in the two tables, but the contribution negatively affects the model as it is observed in the equation (10) with negative regression coefficient.

The robustness and reliability of the model was evaluated through Y-randomization test to ascertain whether the developed model is by chance correlation or not. After few repeated trials to compare the stemmed scores with the scores of the original model with non-randomized data, the new QSAR model generated was observed to have low R^2 and Q^2_{LOO} values as reported in Table 4. The results of this test were clearly in agreement with QSAR validation tools presented in Table 1. This is an indication that the developed model is robust, good and dynamic. The fact that cR^2_p value > 0.5 , confirms that the model possesses good quality assurance and that the model is not only inferred by chance but also very powerful.

Elucidation of Descriptors in NET pKi model

By interpreting the molecular descriptors presented in the model (Table 5), it is possible to increase supportive chemical functional groups, fingerprints and pharmacophores into the activities of the NET inhibitors. Therefore, a sufficient interpretation of the QSAR results is given below.

AlogP is a 2D type molecular descriptor, and the first in our QSAR model. It defined as Ghose-Crippen LogKow or Ghose-Crippen-Viswanathan octanol-water partition coefficient. (AlogP) is

calculated from the AlogP model consisting of a regression equation based on the hydrophobicity contribution of 115 atom types(22)(23). AlogP estimates are provided only for compounds having atoms of types C, H, O, N, S, Se, P, B, Si, and halogens.

Each atom in every structure is classified into one of the 115 atom types. Then, estimated logP for any compound is given by:

$$AlogP = \sum_i n_i a_i$$

where n is the number of atom of type i and a_i is the corresponding hydrophobicity constant. The list of the atom types with the corresponding hydrophobicity contributions is given under the list of atom-centered fragments. This descriptor tells us the higher the number of hetero atoms in a molecule, the higher the tendency for this molecule to be less hydrophobic. Since the percentage contribution of the descriptor in this model is 13%, it indicates that more than 10% of the bioactivity of a lead compound will improve should the number of heteroatoms present be increased.

AATS7i and ATSC3p are defined as Average Broto-Moreau autocorrelation - lag 7 / weighted by first ionization potential and Centered Broto-Moreau autocorrelation - lag 3 / weighted by polarizabilities respectively. They are both 2D autocorrelation descriptors and their respective percentage contribution to the models are given as 13 and 16.4% respectively in Table 2. The ATS descriptor describes how a property is distributed along the topological structure. It is a spatial autocorrelation on a molecular graph, which can be used to improve the activity of the compounds by altering the ionization potential and polarizability of the compounds. Since these molecular descriptors contributed positively to the model the pKi values of the compounds can be improved by adding fragments to the compounds that can increase the polarity of the compounds thereby creating the charge stability of the ligands' interaction with the binding sites. GGI10 is a topological charge descriptor defined as Topological charge index of order 10. GGI10 gave the highest contribution in the model, but since its contribution negatively affect the model, then the steady reduction in this descriptor value can improve the Ki values of the dataset. The ability of topological charge indices to describe molecular charge distribution has been

established by correlating them with the dipole moment of a heterogeneous set of hydrocarbons, and so reducing the number of heterogeneous hydrocarbons presently correlated with the dipole moment of the molecule will lead to an increase in the bioactivity of the compounds.

IC2 is defined in Table 2 as Information content index (neighborhood symmetry of 2-order), it is a 2D type information content descriptor. It gave the least contribution to the model, but 10% contribution can be significant depending on the nature of the molecule. The IC2 molecular descriptor suggests that by introducing other bonds at that carbon, the structural complexity of the molecules will be increased and the Shannon entropy will also be increased thereby easily activating the interactions of the molecule with the binding site.

RDF75u is an RDF descriptor (Radial Distribution Function descriptors), this descriptor is based on the distance distribution in the geometrical representation of a molecule and constitute a radial distribution function code (RDF code) that shows certain characteristics in common with the 3D-MORSE code. The radial distribution function in this form meets all the requirements for a 3D descriptor, it also provides further valuable information such as bond distances, ring types, planar and non-planar systems. This fact is a most valuable consideration for a computer-assisted code elucidation(24). The positive regression coefficient of this descriptor in the model as contained equation (7) with the highest value of degree of contribution as reported in Table 5 is a good indication of its influential contribution to the antipsychotic activity with variation in the bond distance and ring types of the studied compounds.

Docking results

The docking result of this study is presented in terms of binding affinity (kcal/mol) as reported in Supplementary Table S1. All the ligands were docked into the active site of the receptors, the Crystal structure of LEUTAA, a bacterial homolog of Na⁺/Cl⁻-dependent neurotransmitter transporters and X-ray structure of dopamine transporter elucidates antidepressant mechanism in order to evaluate their abilities to inhibit these neurotransmitters. The current available findings of human neurotransmitters transporters are based on X-ray crystal structures of bacterial and invertebrate homologs which includes the bacterial amino acid transporters LeuT (PDB:

2A65) and the *Drosophila melanogaster* (PDB: 4M48) (18) as employed in this study.

The binding affinity values of the two receptors (PDB: 4M48 and PDB: 2A65) for all the studied compounds ranged from 4.4 kcal/mol to 10.3 kcal/mol and were reported in Supplementary Table S1. Ligands 8, 12,26, and 38 had higher binding affinity with the receptor PDB 4M48 and Ligands 9, 10,12,38 and 44 had higher binding affinity with the receptor PDB 2A65 respectively. The Discovery Studio Visualizer was used to visualize and analyze the three ligands of higher binding affinity that were found to display higher binding affinity and common to the two receptors as shown in Fig. 5.

The binding affinity, hydrogen bond, hydrophobic and electrostatic interactions of the three ligands having higher binding affinity with the two receptors were reported in Table 6. The number 12a,38a & 44a represent the interactions of the Ligands (compound 12, 38 and 44) between the receptor (PDB ID 2A65) while 12m, 38m & 44m depict the interaction of the ligands (compound 12, 38 and 44) between the receptor (PDB ID 4M48) respectively.

All the three ligands (compound 12, 38 and 44) with the higher binding affinity were observed to inhibit the targets by forming hydrogen bonds and hydrophobic interactions with amino acids of the two receptors (PDB ID 2A65) and (PDB ID 4M48) respectively except compound 38 that could not form hydrogen bond with the receptor (PDB ID 2A65) as reported in Table 6. This may inform the higher resolution (2.99 Å) of the receptor (PDB ID 4M48) compare to the lower resolution (1.65 Å) of the other receptor (PDB ID 2A65) (<https://www.rcsb.org>). The three ligands were found to be firmly bonded with hydrogen bonds of the receptor (PDB ID 4M48) pocket amino acids (SER31, ASP25, PRO514 and TRP519). The higher number of hydrogen bonds were observed in the two ligands (compound 12 and 44) with the target pockets of the receptor (PDB ID 4M48) which might be connected to their higher activity (compound 12, pKi = 7.383 and compound 44, pKi = 5.607) contrast with to the other ligand (compound 38, pKi =5.084) with the lowest activity which formed just a single hydrogen bond with the receptor. This infers a direct relationship between the binding affinity and inhibitory activity of the studied compounds proved from the number of hydrogen bonds formed between the ligands and the receptor.

However, high binding affinity is evident in the ligand 38 and this might be because of its large number of hydrophobic interactions and electrostatic effect due to the presence of fluorine atom, Pi- Cation, Pi- Sigma, Pi-Pi- stacked, Pi-Pi-T-shaped, Pi-Alkyl with amino acid residues (ILE491, ILE410, TRP406, TRP99, PHE494, ARG487, LEU464, ALA464, ILE472).

CONCLUSIONS

The QSAR investigation was successfully performed on dataset of 50 norepinephrine transporter (NET) inhibitors, mined from ChEMBL database. The result of the QSAR modelling was reliable because it satisfied the OECD criteria set for a model development. The combination of 2D and 3D descriptors generate a good model to predict the inhibitory activity of the studied compounds. The internal validation reported in the work as Q_2cv was estimated to 0.870, while the external validation reported as R^2_{Pred} was given to be 0.583. This is an excellent indication of a good predictive ability of the model.

The result of Applicability Domain (AD) shows that all the studied compounds were within the defined domain. Molecular docking study were carried out on all the compounds using two neurotransmitter transporters (receptors) PDB IDs 2A65 and 4M48 respectively. Three ligands (compound number 12, 38 and 44) showed higher binding affinity were found to best inhibit the two receptors by forming strong hydrogen bonds and hydrophobic interactions with amino acids of the targets. However, higher number of hydrogen bonds were observed between the receptor (PDB ID 4M48) and two ligands (compound 12 and 44) out of the three ligands with higher activity, compound 12 ($pK_i = 7.387$) and compound 44

($pK_i = 5.607$) compare to compound 38 with the lowest activity ($pK_i = 5.084$). This suggests a good correlation between the binding affinity and inhibitory activity of the ligands and that the mechanisms or mode of action of the ligands could be a direct interaction with the receptor (PDB ID 4M48) of higher resolution value (2.99 Å). Therefore, the two ligands, compound 12, [1-(2-(benzhydryloxy)ethyl)-3-(((3-phenylpropyl)ammonio)methyl)piperidin-1-ium] and compound 44 [3-((bis(4-fluorophenyl)methyl)ammonio)-8-(3-oxo-3-(phenylamino)propyl)-8-azabicyclo[3.2.1]octan-8-ium)] proved to be the most promising hit compounds and the receptor PDB ID 4M48 (2.99 Å) shows to be a better receptor for this investigation which could be linked to its higher resolution value.

The information derived from the QSAR investigation and molecular docking analysis of this study could find a robust application in pharmaceutical industries to design novel NET inhibitors with more potent and more specific therapeutic anti-psychotic agents.

FUNDING

The Authors received no direct funding for this study.

ACKNOWLEDGEMENTS

We wish to acknowledge members of theoretical and physical chemistry group, chemistry department, Ahmadu Bello University Zaria. We sincerely appreciate David Arthur and Abdulfatai Usman for their technical support and advice in the course of this study.

Table 6. Molecular interactions between the three ligands of higher binding affinity and the two receptors.

Ligand ID	CHEMBL	Ligand Number	Binding Affinity (kcal/mol)	Hydrogen bond	Hydrophobic interactions	Electrostatics Interactions	
				Amino acid	Bond length (Å)	Amino Acid	Amino Acid
CHEMBL67078		12a	-9.3	LYS398	2.15279	ILE111, ALA319, VAL154, LEU162, LEU400, LEU25	
		12m	-7.35	SER31	2.76717	PHE513, TYR32	TYR32
				SER31	2.31044		
CHEMBL197384		38a	-10.3			ILE491, ILE410, TRP406, TRP99, PHE494, ARG487, LEU464, ALA464, ILE472	PHE414
		38m	-7.5	ASP25	2.53334	TYR337, TYR59, ARG92	ASP25
CHEMBL200310		44a	-9.9	GLN34	2.62533	ILE475, TYR471, ILE245, LYS474, ARG30, ALA319	ASP404
		44m	-8.45	PRO514	2.15327	PHE513, VAL101	
				SER31	2.76554		
TRP519	2.1523						

REFERENCES

1. Zhou J. NIH Public Access. 2006;29(12):1235-44.
2. Rice DP, Miller LS. Health economics and cost implications of anxiety and other mental disorders in the United States. *Br J Psychiatry*. 1998;173(S34):4-9.
3. Xue W, Yang F, Wang P, Zheng G, Chen Y, Yao X, et al. What Contributes to Serotonin-Norepinephrine Reuptake Inhibitors' Dual-Targeting Mechanism? The Key Role of Transmembrane Domain 6 in Human Serotonin and Norepinephrine Transporters Revealed by Molecular Dynamics Simulation. *ACS Chem Neurosci*. 2018;9(5):1128-40.
4. Blakely RD, Bauman AL. Biogenic amine transporters: regulation in flux. *Curr Opin Neurobiol*. 2000;10(3):328-36.
5. Deorah S, Lynch CF, Sibenaller ZA, Ryken TC. Trends in brain cancer incidence and survival in the United States: Surveillance, Epidemiology, and End Results Program, 1973 to 2001. *Neurosurg Focus*. 2006;20(4):E1.
6. Penmatsa A, Wang KH, Gouaux E. X-ray structure of dopamine transporter elucidates antidepressant mechanism. *Nature* [Internet]. 2013;503(7474):85-90. Available from: <http://dx.doi.org/10.1038/nature12533>
7. Dessalew N. QSAR study on dual SET and NET reuptake inhibitors: an insight into the structural requirement for antidepressant activity. *J Enzyme Inhib Med Chem*. 2009;24(1):262-71.
8. Om A-S, Ryu J-C, Kim J-H. Quantitative structure-activity relationships for radical scavenging activities of flavonoid compounds by GA-MLR technique. *Mol Cell Toxicol*. 2008;4(2):170-6.
9. Davis GDJ, Vasanthi AHR. QSAR based docking studies of marine algal anticancer compounds as inhibitors of protein kinase B (PKB β). *Eur J Pharm Sci*. 2015;76:110-8.
10. Hehre WJ, Huang WW. Chemistry with computation: an introduction to SPARTAN. Wavefunction, Inc.; 1995.
11. Bauernschmitt R, Ahlrichs R. Treatment of electronic excitations within the adiabatic approximation of time dependent density functional theory. *Chem Phys Lett*. 1996;256(4-5):454-64.
12. Kennard RW, Stone LA. Computer aided design of experiments. *Technometrics*. 1969;11(1):137-48.
13. Zeng H, Zheng R, Guo Y, Zhang S, Zou X, Wang N, et al. Cancer survival in China, 2003-2005: A population-based study. *Int J cancer*. 2015;136(8):1921-30.
14. Yap CW. PaDEL-descriptor: An open source software to calculate molecular descriptors and fingerprints. *J Comput Chem*. 2011;32(7):1466-74.
15. Roy K, Kar S, Ambure P. On a simple approach for determining applicability domain of QSAR models. *Chemom Intell Lab Syst*. 2015;145:22-9.
16. Tropsha A, Gramatica P, Gombar VK. The importance of being earnest: validation is the absolute essential for successful application and interpretation of QSPR models. *QSAR Comb Sci*. 2003;22(1):69-77.
17. Arthur DE, Uzairu A, Mamza P, Abechi SE, Shallangwa G. Qsar Modelling of Some Anticancer Pgi 50 Activity on HI - 60 Cell Lines. 2016;3(1).
18. Andersen J, Ringsted KB, Bang-Andersen B, Strømgaard K, Kristensen AS. Binding site residues control inhibitor selectivity in the human norepinephrine transporter but not in the human dopamine transporter. *Sci Rep*. 2015;5:15650.
19. Topliss JG, Edwards RP. Chance factors in studies of quantitative structure-activity relationships. *J Med Chem*. 1979;22(10):1238-44.
20. Damme S Van, Bultinck P. A new computer program for QSAR-analysis: ARTE-QSAR. *J Comput Chem*. 2007;28(11):1924-8.
21. Tropsha A. Best practices for QSAR model development, validation, and exploitation. *Mol Inform*. 2010;29(6-7):476-88.
22. Viswanadhan VN, Ghose AK, Revankar GR, Robins RK. Atomic physicochemical

parameters for three dimensional structure directed quantitative structure-activity relationships. 4. Additional parameters for hydrophobic and dispersive interactions and their application for an automated superposition of certain . J Chem Inf Comput Sci. 1989;29(3):163-72.

23. Ghose AK, Crippen GM. Atomic physicochemical parameters for three-

dimensional structure-directed quantitative structure-activity relationships I. Partition coefficients as a measure of hydrophobicity. J Comput Chem. 1986;7(4):565-77.

24. Caballero J, Fernández M. Artificial neural networks from MATLAB® in medicinal chemistry. Bayesian-regularized genetic neural networks (BRGNN): Application to the prediction of the antagonistic activity against human platelet thrombin receptor (PAR-1). Curr Top Med Chem. 2008;8(18):1580-605.

Quantitative Structure-Activity Relationship (QSAR) Studies and Molecular docking Simulation of Norepinephrine Transporter (NET) Inhibitors as Anti-psychotic Therapeutic Agents

Sabitu Babatunde Olasupo^{1*}, Adamu Uzairu², Gideon Shallangwa²
and Sani Uba²

¹National Agency for Food and Drug Administration and Control (NAFDAC),

²Department of chemistry, Ahmadu Bello University Zaria, Nigeria

Supplementary Table S1: Molecule ID, Chemical Names, RMSD values (PDB: 4M48 and PDB: 2A65) with Predicted pKi, Experimental pKi and Binding Affinity values of the studied molecules

S/N	CHEM ID	NAME	Experimental pKi	Predicted pKi	Residual	Binding Affinity (kcal/mol) PDB: 4M48	RMSD (PDB: 4M48)	Binding Affinity (kcal/mol) PDB: 2A65	RMSD (PDB: 2A65)
1.	CHEMB L32540	(Z)-5-((Z)-2-(7a-methyl-1-(6-methylheptan-2-yl)hexahydro-1H-inden-4(2H)-ylidene)ethylidene)-	6.000	6.072	-0.073	-7.2	±1.889	-8.6	±1.853

		4-methylenecyclohexane-1,3-diol							
2.	CHEMB L781	5-(4-chlorophenyl)-3,5-dihydro-2H-imidazo[2,1-a]isoindol-5-ol	8.899	7.945	0.954	-6.9	±1.789	-7.2	±1.966
3.	CHEMB L808	1-(2-((4-chlorobenzyl)oxy)-2-(2,4-dichlorophenyl)ethyl)-1H-imidazole	5.617	5.817	-0.200	-6.15	±1.204	-7.5	±1.617
4.	CHEMB L822	(E)-N,6,6-trimethyl-N-(naphthalen-1-ylmethyl)hept-2-en-4-yn-1-amine	5.388	5.404	-0.016	-6.7	±1.237	-8.0	±0.146
5.	CHEMB L828	10H-phenothiazine	6.340	6.496	-0.156	-5.7	±1.943	-7.1	±0.504
6.	CHEMB L42553	methyl 3-(3,4-dichlorophenyl)-8-methyl-8-azabicyclo[3.2.1]octane-2-carboxylate	8.301	8.531	-0.230	-6.15	±0.349	-6.9	±1.851
7.	CHEMB L926	N-(3,4-dihydroxyphenethyl)-4-(4-	6.420	6.482	-0.062	-6.8	±0.535	-6.5	±0.575

		hydroxyphenyl)buta n-2-aminium							
8.	CHEMB L48290 3	2-(3-(5-fluoro-1H- indol-3-yl)propyl)- 6-methoxy-1,2,3,4- tetrahydroisoquinoli n-2-ium	5.775	6.095	0.010	-7.4	±0.743	-8.0	±0.835
9.	CHEMB L63703	4-((2- (benzhydryloxy)eth yl)ammonio)-1- benzylpiperidin-1- ium	6.745	6.735	0.447	-7.1	±1.207	-9.2	±1.072
10.	CHEMB L67024	1-(2- (benzhydryloxy)eth yl)-4-((4- fluorophenethyl)am monio)piperidin-1- ium	7.102	6.655	0.316	-7.0	±1.527	-8.9	±1.112
11.	CHEMB L165	(E)-5-(4- hydroxystyryl)benz ene-1,3-diol	5.639	5.323	-0.252	-6.25	±0.655	-7.1	±0.963
12.	CHEMB L67078	1-(2- (benzhydryloxy)eth yl)-3-(((3- phenylpropyl)ammo nio)methyl)piperidi n-1-ium	7.387	7.639	-0.214	-7.35	±1.365	-9.3	±1.379

13.	CHEMB L99653	1-(1-hydroxycyclohexyl)-N,N-dimethyl-1-(3-(trifluoromethyl)phenyl)methanaminium	7.678	7.891	0.047	-6.5	±1.723	-6.7	±1.707
14.	CHEMB L81	1-(2-(4-(6-hydroxy-2-(4-hydroxyphenyl)benzo[b]thiophene-3-carbonyl)phenoxy)ethyl)piperidin-1-ium	6.553	6.506	0.159	-8.0	±0.140	-8.5	±1.453
15.	CHEMB L10957 1	N,N-dimethyl-1-(3-(naphthalen-2-yl)bicyclo[2.2.1]heptan-2-yl)methanaminium	6.955	6.796	-0.854	-7.0	±0.111	-8.3	±1.623
16.	CHEMB L12102 7	N1-(2-(benzhydryloxy)ethyl)-N2-(4-fluorophenethyl)-N1,N2-dimethylethane-1,2-diaminium	6.432	6.751	-0.319	-6.0	±0.672	-7.9	±1.795
17.	CHEMB L12161	N1-(2-(bis(4-fluorophenyl)metho	7.086	7.939	0.239	-6.5	±1.232	-8.9	±1.589

	1	xy)ethyl)-N3-phenethylpropane-1,3-diaminium							
18.	CHEMB L12325 2	N1-(2-(benzhydroxy)ethyl)-N1,N3-dimethyl-N3-(3-phenylpropyl)propane-1,3-diaminium	7.523	6.696	0.826	-5.9	±1.444	-8.2	±0.395
19.	CHEMB L12146 0	N1,N2-bis(2-(bis(4-fluorophenyl)methoxy)ethyl)-N1,N2-dimethylethane-1,2-diaminium	6.583	6.328	-0.336	-5.85	±0.121	-6.5	±0.186
20.	CHEMB L1231	3-(2-cyclohexyl-2-hydroxy-2-phenylacetoxy)-N-isopropylprop-2-yn-1-aminium	5.589	5.350	0.510	-6.4	±1.329	-7.2	±1.50
21.	CHEMB L13924 5	3-(4-chlorophenyl)-N-methyl-3-(naphthalen-1-yloxy) propan-1-aminium	7.108	7.349	0.053	-7.25	±1.043	-7.6	±1.307
22.	CHEMB L13927 7	N-methyl-3-(naphthalen-1-yloxy)-3-(m-	7.398	7.734	-0.326	-6.8	±1.803	-8.3	±1.823

		tolyl)propan-1-aminium							
23.	CHEMB L14111 4	N-methyl-3-(naphthalen-1-yloxy)-3-(p-tolyl)propan-1-aminium	7.444	7.357	0.086	-6.7	±0.884	-6.7	±0.873
24.	CHEMB L14202 8	N-methyl-3-(naphthalen-1-yloxy)-3-(thiophen-3-yl)propan-1-aminium	7.678	7.168	0.186	-6.25	±1.432	-7.4	±1.271
25.	CHEMB L14168 1	N-methyl-3-(naphthalen-1-yloxy)-3-phenylpropan-1-aminium	7.699	7.645	-0.383	-6.55	±1.754	-6.5	±1.087
26.	CHEMB L14197 4	N-methyl-3-(naphthalen-1-yloxy)-3-(3-(trifluoromethyl)phenyl)propan-1-aminium	7.155	7.074	0.081	-7.35	±1.076	-8.0	±0.870
27.	CHEMB L1289	1,2,4-trichloro-5-((3-iodoprop-2-yn-1-yl)oxy)benzene	5.561	5.887	-0.174	-4.4	±0.555	-5.0	±0.510
28.	CHEMB	4-nonylphenol	5.905	6.110	0.250	-5.45	±1.111	-5.9	±1.813

	L15306 2								
29.	CHEMB L17924 9	2-(phenyl(o- tolylthio)methyl)mo rpholin-4-ium	9.523	9.337	-0.355	-6.75	±1.332	-7.1	±2.640
30.	CHEMB L18824 8	1-(2-((2- aminophenyl)thio)p henyl)-N- methylmethanami um	7.426	7.809	0.492	-5.4	±1.266	-6.5	±1.209
31.	CHEMB L18937 4	1-(2-((2-amino-4- methylphenyl)thio) phenyl)-N- methylmethanami um	6.719	8.035	-1.316	-5.85	±1.543	-7.1	±1.733
32.	CHEMB L19070 0	1-(2-((2- aminophenyl)thio)p henyl)-N,N- dimethylmethanami nium	8.305	8.399	-0.094	-5.25	±1.355	-6.5	±1.066
33.	CHEMB L19420 5	N-methyl-3-(3- methyl-2-oxo-1- phenyl-1,2,3,4- tetrahydroquinolin- 3-yl)propan-1- aminium	7.357	7.636	-0.279	-5.9	±0.923	-7.4	±0.315

34.	CHEMB L19478 1	3-(6-fluoro-2-oxo-1-(p-tolyl)-1,2,3,4-tetrahydroquinolin-3-yl)-N-methylpropan-1-aminium	8.301	8.082	-0.039	6.6	±1.541	-7.9	±1.901
35.	CHEMB L19675 1	3-(3-ethyl-2-oxo-1-(p-tolyl)-1,2,3,4-tetrahydroquinolin-3-yl)-N-methylpropan-1-aminium	7.769	7.942	-0.072	-6.3	±1.894	-6.7	±1.897
36.	CHEMB L19611 0	3-(3-butyl-2-oxo-1-(p-tolyl)-1,2,3,4-tetrahydroquinolin-3-yl)-N-methylpropan-1-aminium	8.097	7.846	0.010	-5.75	±0.123	-6.9	±0.428
37.	CHEMB L19636 8	3-(1-(3-fluorophenyl)-2-oxo-1,2,3,4-tetrahydroquinolin-3-yl)-N-methylpropan-1-aminium	7.745	8.429	-0.684	-6.95	±1.325	-7.4	±1.021
38.	CHEMB L19738	8-(2-(1H-indol-3-yl)ethyl)-3-((bis(4-	5.084	5.438	-0.319	-7.5	±1.721	-10.3	±1.817

	4	fluorophenyl)methyl)ammonio)-8- azabicyclo[3.2.1]oc tan-8-ium							
39.	CHEMB L19803 3	N-methyl-3-(2-oxo- 1-(p-tolyl)-1,2,3,4- tetrahydroquinolin- 3-yl)propan-1- aminium	8.523	8.031	0.826	-6.6	±1.974	-7.5	±1.481
40.	CHEMB L19821 5	3-(6-chloro-3- methyl-2-oxo-1-(p- tolyl)-1,2,3,4- tetrahydroquinolin- 3-yl)-N- methylpropan-1- aminium	7.367	7.403	0.086	-6.4	±1.024	-6.8	±1.140
41.	CHEMB L19764 3	3-(1-(4- chlorophenyl)-2- oxo-1,2,3,4- tetrahydroquinolin- 3-yl)-N- methylpropan-1- aminium	7.678	8.177	-0.499	-6.7	±1.437	-6.8	±1.531
42.	CHEMB L19770 7	3-((bis(4- fluorophenyl)methyl)ammonio)-8-(4- phenylbutyl)-8-	5.788	5.449	-1.316	-7.0	±1.543	-7.9	±1.697

		azabicyclo[3.2.1]oc tan-8-ium							
43.	CHEMB L19880 7	3-(((4- chlorophenyl) (phenyl)methyl)am monio)-8-methyl-8- azabicyclo[3.2.1]oc tan-8-ium	5.499	5.504	-0.094	-7.35	±0.822	-7.2	±0.744
44.	CHEMB L20031 0	3-((bis(4- fluorophenyl)methyl)ammonio)-8-(3- oxo-3- (phenylamino)prop yl)-8- azabicyclo[3.2.1]oc tan-8-ium	5.607	4.500	1.107	-8.45	±1.237	-9.9	±0.281
45.	CHEMB L19896 0	N-methyl-3-(2-oxo- 1-phenyl-4-propyl- 1,2,3,4- tetrahydroquinolin- 4-yl)propan-1- aminium	8.155	8.936	-0.781	-6.25	±1.398	-7.3	±2.716
46.	CHEMB L19884 2	3-(3,4- dichlorophenyl)-8- (2-(4-(9- (dimethyliminio)- 11,11-dimethyl-	6.511	6.550	-0.499	-7.5	±2.124	-8.4	±1.570

		3,4-dihydronaphtho[2,3-g]quinolin-1(2H,9H,11H)-yl)butanamido)ethyl)-2-(methoxycarbonyl)-8-azabicyclo[3.2.1]octan-8-ium							
47.	CHEMB L19911 6	N-methyl-3-(2-oxo-3-propyl-1-(p-tolyl)-1,2,3,4-tetrahydroquinolin-3-yl)propan-1-aminium	7.959	8.031	1.107	-6.15	±2.332	-6.6	±1.422
48.	CHEMB L19817 6	N-methyl-3-(3-methyl-2-oxo-1-(p-tolyl)-1,2,3,4-tetrahydroquinolin-3-yl)propan-1-aminium	8.046	7.760	-0.781	-6.4	±0.978	-7.6	±1.792
49.	CHEMB L20241 0	1-(1-oxo-1-(p-tolyl)pent-4-en-2-yl)pyrrolidin-1-ium	5.854	7.285	0.286	-5.75	±1.521	-6.9	±1.471
50.	CHEMB	1-(1-(4-(furan-2-	7.022	7.012	-1.431	-6.3	±1.379	-7.1	±1.285

	L20197 6	yl)phenyl)-1- oxopentan-2- yl)pyrrolidin-1-ium							
--	-------------	--	--	--	--	--	--	--	--



Determination of Contents of Rutin and Quercetin Isolated from Syrian *Ficus carica* L. Leaf Extracts

Shaza AlShaal^{1*} , Manal Daghestani¹ , Francois Karabet¹ 

¹Department of Chemistry, Faculty of Sciences, Damascus University, Syria.

Abstract: The major flavonoid glycoside in Syrian *Ficus carica* L. leaf extracts (rutin) was identified quantitatively and isolated, then transformed into its aglycone (quercetin) by acidic hydrolysis of ethanolic and aqueous extracts. The influence of the hydrolysis process on isoquercitrin content was investigated, too. The determination of contents of Rutin and Quercetin isolated from Syrian *Ficus carica* L. leaf extracts was carried out by high performance liquid chromatography, and the isolation was done by using thin layer chromatography plates, then identified by mass spectra. Results showed that rutin content in the ethanolic extract (78.79%) was higher than the aqueous one (61.90%) by using ultrasonic extraction procedure. The quercetin content by hydrolysis process was more satisfactory in the ethanolic extract (81.00%) than the aqueous one (72.53%). Acidic hydrolysis process destroyed some of the isoquercitrin in the extracts. The detection of isoquercitrin was done qualitatively by noticing the mass spectrum and the photo diode array spectrum. Rutin and quercetin were successfully isolated, the relative peak areas for isolated rutin and quercetin were 99.80% and 96.46%, respectively. It was concluded that rutin can be easily converted into quercetin by acidic hydrolysis, allowing the use of Syrian ficus leaf extracts as an optimal cheap natural antioxidant source.

Keywords: Syrian *Ficus carica* L. leaf, rutin, quercetin, isoquercitrin.

Submitted: September 20, 2019. **Accepted:** November 21, 2019.

Cite this: AlShaal S, Daghestani M, Karabet F. Determination of Contents of Rutin and Quercetin Isolated from Syrian *Ficus carica* L. Leaf Extracts. JOTCSA. 2020;7(1):199–208.

DOI: <https://doi.org/10.18596/jotcsa.622442>.

***Corresponding author. E-mail:** shazamalshaal@gmail.com.

INTRODUCTION

Ficus carica L. (*Moraceae*) is a native bush of South West Asia cultivated since years ago. There are at least 800 kinds of ficus known worldwide, originally from Persia and Syria, spread later in Europe and America (1). *Ficus carica* is vastly cultivated over Syria, mainly as individual trees in private gardens for family consumption. The total Syrian ficus cultivated area is ca. 9,663 ha, with an estimated sum production of about 53.7×10^3 tones (2). Part of the plants, the bark, root, leaf and fruit are often used to overcome various diseases. Ficus species are known to be wealthy of

polyphenolics and flavonoids which are correlated to the antioxidant power (3). There are enormous reports on the plant's bioactivities, which are potential to overcome many diseases (4) such as Haemostatic, anti-Herpes Simplex Virus (HSV), hypolipidemic, hypoglycemic (5) and anticancer (6). The power of flavonoids to act as antioxidants depends upon their molecular structure (7). The hydroxyl groups play a role in the antioxidant and free radical scavenging activities of flavonoids, by rapid donation of a hydrogen atom to radicals (equations 1 and 2),

$$R \cdot + \text{phOH} \rightarrow \text{RH} + \text{phO} \cdot \quad (\text{Eq. 1})$$



where pHOH stands for phenolic compounds. Quercetin is considered as a reference substance for measuring the antioxidant activity (8). Quercetin accumulates in plants as glycosides such as glucosides, rutosides (9). In nature there are more than 180 glycosides

of quercetin in different structures, the most popular is rutin (10). Rutin (quercetin-3-O-rutinoside) is composed of one molecule of quercetin as aglycone and rutinose. Although there is structural similarity in rutin, isoquercitrin (isoquercetin) and quercetin, as shown in Figure 1 (11) there are some remarkable differences in physical, chemical and biological properties (12).

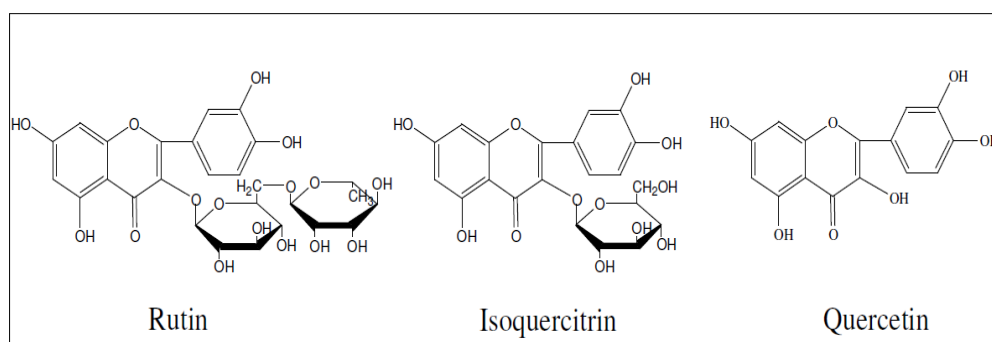


Figure 1. Chemical structures of rutin, isoquercitrin and quercetin (11).

Rutin is the master flavonoid glycoside found in ficus (13). It can be converted to quercetin the aglycone form, via breaking one terminal rhamnose by hydrolysis process; also it can be converted to isoquercitrin which has more advantageous than rutin, because of its better bioavailability and more anti-proliferative effect than rutin and quercetin (14). Rutin is an important food component necessary for human health since it affects the capillary fragility and positively permeability (15). It has a protective effect on the expansion of diabetes and mitigates the effects on the consequences of diabetes (16, 17). Studies indicate that rutin has many functional properties such as antioxidant, anti-inflammatory effect in humans (18). However, its antioxidant activity and its bioavailability were lower than quercetin in rats by oral management (19-21). The disadvantage of quercetin is poorly absorbed in the small intestine, and the bioavailability of it was mentioned to be less than one per cent in the capsule form in human beings (22). Lately, isoquercitrin has attracted attention as a promising compound because of its higher solubility than quercetin in aqueous solutions (11, 23), but its antioxidant activity is a little lower than that of quercetin (24). It is eligible to maximize the production of isoquercitrin together with quercetin during the hydrolysis of rutin (11). The aim of this research was to determine the amount of the major important flavonoid (rutin) in aqueous and ethanolic extracts of Syrian Ficus leaf, hydrolyze it to produce quercetin, then isolate both of rutin and quercetin by Thin Layer Chromatography (TLC) and HPLC-MS techniques. The effect of

hydrolysis process on isoquercitrin content was also studied.

EXPERIMENTAL

Plant material

Ficus leaves were collected on April 2017 from Baniyas (Latakia-Governorate), Syria. The plant was identified by Prof. Jurjet Babojian (Department of Plant Biology, Faculty of science, Damascus University, Syria). The ficus leaves were dried in the shade away from the sunlight for 10 days, ground with an electric mill, then stored in a dark, dry, tightly sealed container at room temperature until use.

Chemicals

Rutin hydrate (95%), quercetin (98.0%) and HPLC grade acetonitrile (99.9%) were purchased from Sigma-Aldrich. Ethanol (99.8%), acetic acid (99.5%), formic acid and HCl (36.5-39.0%) from Panreac, toluene (99.5%) for the analytical grade from Scharlau, ethyl acetate (99%) for general purpose reagent from BDH chemicals Ltd. pool England.

Instruments

Vortex MS1 Mini shaker (KAI) was used to homogenize ficus leaf powder with solvent, ultrasonic water bath Transsonic Model 460/H (Elma) was used for extraction procedure. High Performance Liquid Chromatography (HPLC) (KNAUER, Germany) and HPLC-MS (Shimadzu, Japan) were used for separation and identification of rutin and quercetin. In order to isolate rutin and quercetin silica gel 60 F254 pre-coated plates (5*20 cm/layer thickness

0.25 mm) from MERCK were used.

Preparation of extracts

Ultrasonic extraction method was used for its ability to improve extraction by speeding up the release of bioactive substances from cell walls and facilitating their ease of transference (25). One gram of ficus leaf powder was added to 10 mL of ethanol 70%, was stirred well by piping for homogenization for one minute, then placed in ultrasonic bath at 75 °C, for 30 minutes, filtered from 0.45 µm filters and kept in a refrigerator (4 °C) until use. The aqueous extracts were prepared in the same way with 10 mL distilled water. The experiments were repeated three times.

Hydrolysis of plant extracts

To convert rutin into quercetin, according to the method presented by Chen et al., (26), acid hydrolysis was mainly completed by adding 2.0 mL (2.8 M) HCl to 2.0 mL of ficus leaf extracts, then placed in water bath at 90 °C, for different

periods (5, 7, and 10 min.), placed in cool at room temperature (25 °C) for 30 minutes, passed from the filter (0.45µm) and kept in a refrigerator (4 °C) until analyzed. The experiment was repeated three times.

Determination of rutin and quercetin in leaf extracts by HPLC-PDA

HPLC system (KNAUER 2850) with 4050 pump, column oven, and 2850 PDA (Photo Diode Array) Detector was employed. For determination of rutin from ficus leaf extracts, HPLC method was used with C₁₈ column Eurospher (C₁₈, 250 mm×4.6 mm ID, 5 µm) with mobile phase gradient program, consisting of A:water and B:acetonitrile (containing 0.3% acetic acid) as depicted in Table 1, at a flow rate of 0.9 mL/min. PDA detector at 370 nm was used for rutin and quercetin determination. The injection volume used was 20.0 µL for both standards and sample solutions. The extracts were injected 3 times.

Table 1. Solvents gradient program for separation of ficus leaf extracts by HPLC-PDA

Time/min	A	B
0	90	10
15	50	50
20	40	60
25	20	80
30	20	80
35	90	10
40	90	10

Identification of rutin and quercetin in ficus leaf extracts were based on comparison of retention times of rutin and quercetin with standards. That is concentration of rutin and quercetin in the extracts were calculated using the peak area of the calibration curves obtained from standard solutions. The concentrations were expressed as mg/g.

Thin layer chromatography (TLC)

In this study thin layer chromatography (TLC) was used to separate and identify both quercetin and rutin, from Syrian ficus leaf extracts, which is a simple, cheap and more easily available chromatographic method at research laboratories. It is more time-effective compared to high-performance liquid chromatography. TLC is considered as a public analytical technique, exceedingly used for plant constituents (27). Available standards (rutin and quercetin) and ficus leaf extracts (ethanolic and aqueous) before and after hydrolysis, were run on glass-backed silica gel TLC GF254 pre-

coated plate. The optimal solvent for the identification of compounds were determined by varying the ratios of various solvents for developing the solvent system, the more suitable one was: (toluene/ethyl acetate/formic acid) (9/8/0.2 v/v/v) for 30 minutes. The plates were dried at room temperature for 15 minutes, and visualized by exposure to UV light (366 nm). The bands of the desired compounds in the extracts were collected, dissolved in 0.5 mL 70% ethanol, centrifuged (1000 rpm) at room temperature (25 °C) for 10 minutes, then filtered with 0.45 µm filters for HPLC-MS analysis.

Identification of rutin and quercetin and isoquercitrin by HPLC-MS

HPLC system (Shimadzu) with LC-20ADXR pump, CTO-20A column oven, and SPD-20A UV detector was employed. For determination of rutin, quercetin and isoquercitrin in ficus leaf extracts, HPLC method was used with C₁₈ column (C₁₈, 250 mm × 4.5 mm ID, 5 µm) with

the same mobile phase gradient program mentioned in Table 1. The operating conditions of mass spectrometry were: ESI source was operated in negative mode to generate $(M-H)^-$ ions with the following conditions: interface temperature 350 °C; dry gas (nitrogen) and nebulizing gas flow was 1.5 L/min. Detector and interface voltages were 0.5 KV and 4.5 KV, respectively.

RESULTS AND DISCUSSION

HPLC-PDA results

Figures 2 and 3 show the HPLC-PDA chromatograms for the ethanolic ficus leaf extracts before and after acid hydrolysis, respectively. The major component in the extracts is rutin, the quercetin content in the extract is almost traces, shown in Figure 2. However, after hydrolysis, the extract contained only traces of rutin and all the glycosidic bonds, as well as isoquercitrin, were ruined, resulted in an ultimate increase in quercetin as shown in Figure 3. The PDA spectrums of rutin, isoquercitrin, and quercetin, respectively also included.

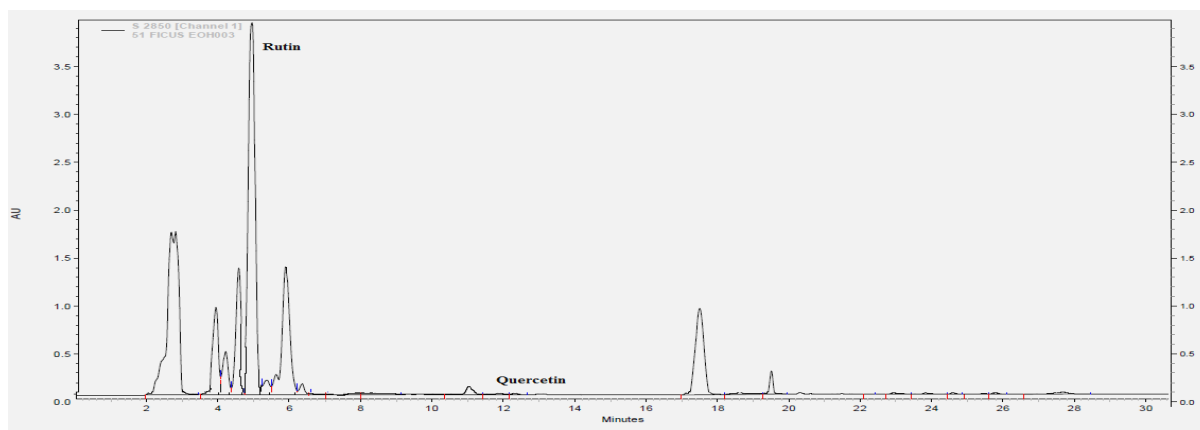


Figure 2. HPLC-PDA chromatogram of ethanolic ficus leaf extract. flow rate 0.9 mL/min, wavelength at 370 nm, C_{18} column (C_{18} , 250 mm×4.5 mm ID, 5 μ m) with gradient mobile phase program.

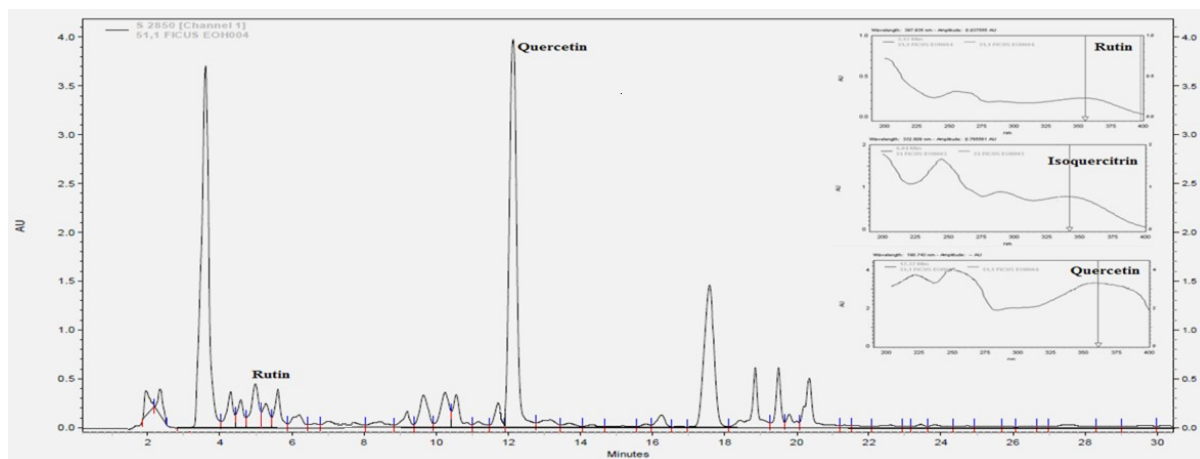


Figure 3. HPLC-PDA chromatogram of hydrolyzed ethanolic ficus leaf extract. The inset figures represent the PDA spectrums of rutin, isoquercitrin and quercetin, respectively.

3-D plots of the UV spectra for ethanolic ficus leaf extracts to illustrate the transformation of rutin into quercetin after the acid hydrolysis

process, are shown in Figure 4, where (a) represents rutin and (b) represents quercetin.

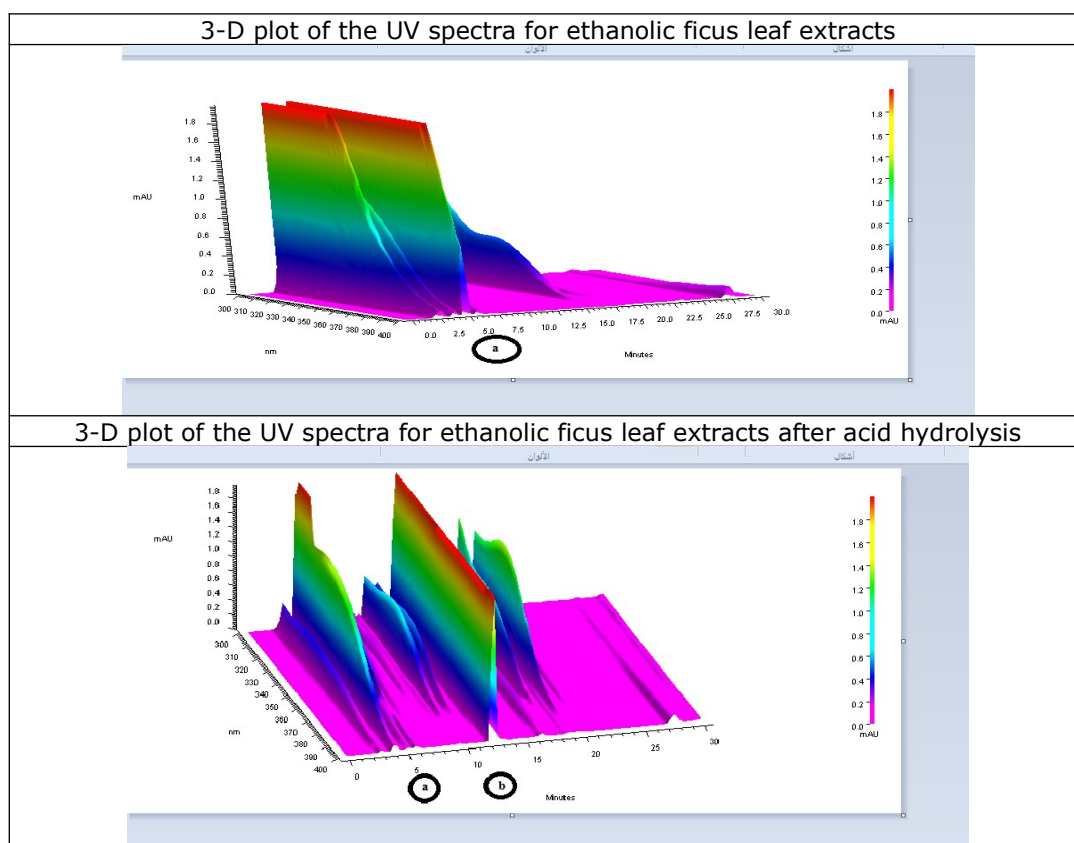


Figure 4. 3-D plots of the UV spectra ethanolic ficus leaf extracts before and after acid hydrolysis (a) rutin, (b) quercetin

Table 2 shows that the ethanolic extract contained a higher concentration of rutin (16.82 ± 0.06 mg/g) compared to the aqueous extract (7.87 ± 0.02 mg/g). This phenomenon might be attributed to the higher viscosity of water than that of the other solvents, which is a matter of mass transfer. Therefore, the

mixture of water and ethanol as solvent agent showed the best performance to extract polyphenols of all the extraction solvents used (28). Figure 5 shows a comparison between the relative peak areas% of the components in the ethanolic and aqueous extracts, before and after the hydrolysis process.

Table 2. Content of rutin and quercetin in Syrian ficus leaf and relative peak area% before and after acidic hydrolysis

		Rutin		Quercetin	
		Concentration (mg/g)	Relative peak Area%	Concentration (mg/g)	Relative peak Area%
Extract	Ethanolic	16.820 ± 0.060	78.79	0.001 ± 0.010	0.02
	Aqueous	7.870 ± 0.020	61.90	0.003 ± 0.010	0.06
Hydrolysis	Ethanolic	1.170 ± 0.020	4.32	6.950 ± 0.100	81.00
	Aqueous	0.290 ± 0.010	2.03	3.300 ± 0.090	72.53

Values represent mean \pm SD, n=3

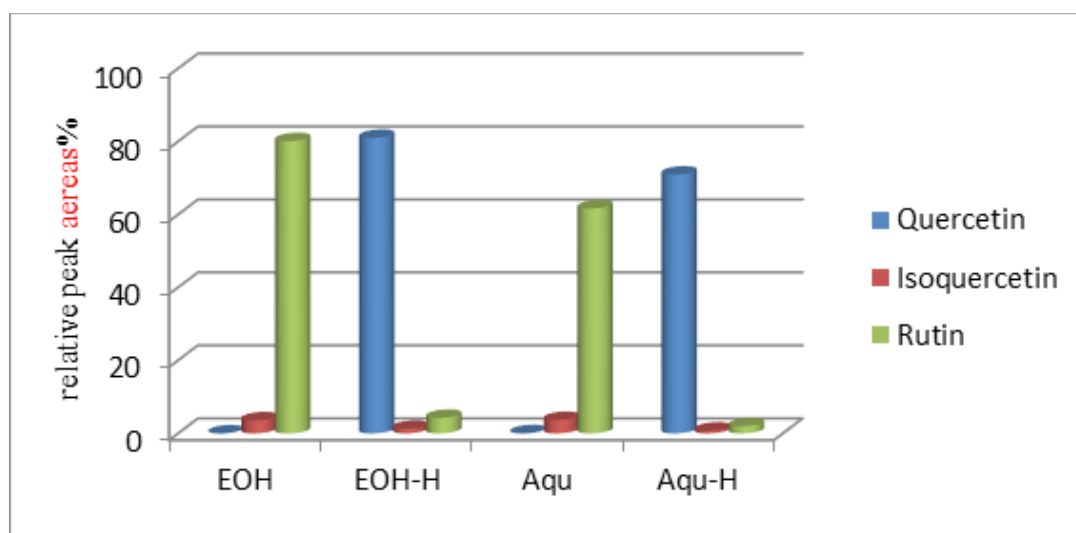


Figure 5. The effect of acid hydrolysis on relative peak areas % of rutin, isoquercitrin and quercetin in ethanolic, aqueous extracts.

The effect of acid hydrolysis time on quercetin formation was investigated, by hydrolyzing the extracts in different periods of time (5, 7, and 10 minutes). The greatest amount of hydrolyzed quercetin was measured at 7

minutes then decreased at 10 minutes (Figure 6). However, since the hydrolysis process broke isoquercitrin, rutin hydrolyzed for only 5 minutes, in order to preserve isoquercitrin in the extracts.

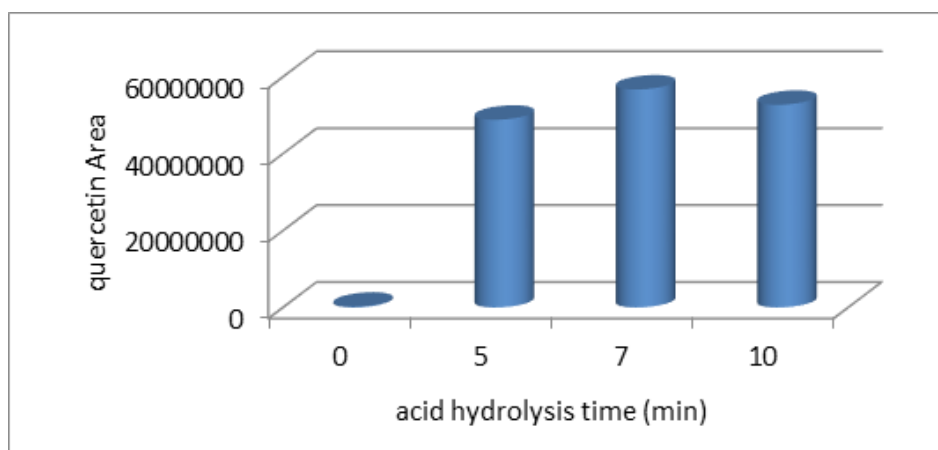


Figure 6. The effect of acid hydrolysis time on the quercetin formation.

Identification and isolation of rutin and quercetin by TLC

Figure 7 shows the TLC plates of ficus leaf extracts before and after acid hydrolysis under UV light (366nm). The bands of the desired

compounds, (rutin is the third one in (a)), (quercetin is the fourth one in (b)) were collected, dissolved in 0.5 mL 70% ethanol, centrifuged, then prepared for HPLC-MS analysis.

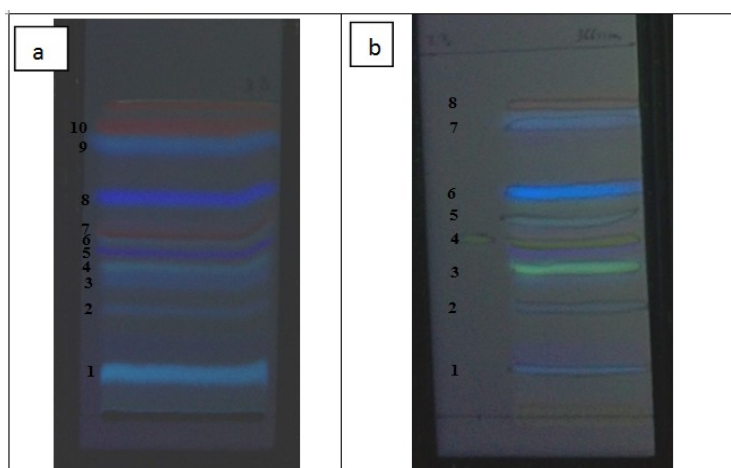


Figure 7. TLC of ficus leaf extracts (third band in a is rutin; fourth band in b is quercetin) after acid hydrolysis, under UV light (366nm). Chromatography conditions: Run on glass-backed silica gel TLC GF254 pre-coated plate. Mobile phase: (toluene/ethyl acetate/formic acid) (9/8/0.2 v/v/v) for 30 minutes.

Identification of rutin, quercetin and isoquercitrin in ficus leaf extracts by HPLC-MS

The detection of isoquercitrin was done

qualitatively by MS and PDA spectrum. MS product ion spectra for $(M-H)^-$ ions of isolated rutin, quercetin and isoquercitrin in ficus leaf extracts are presented in Figure 8.

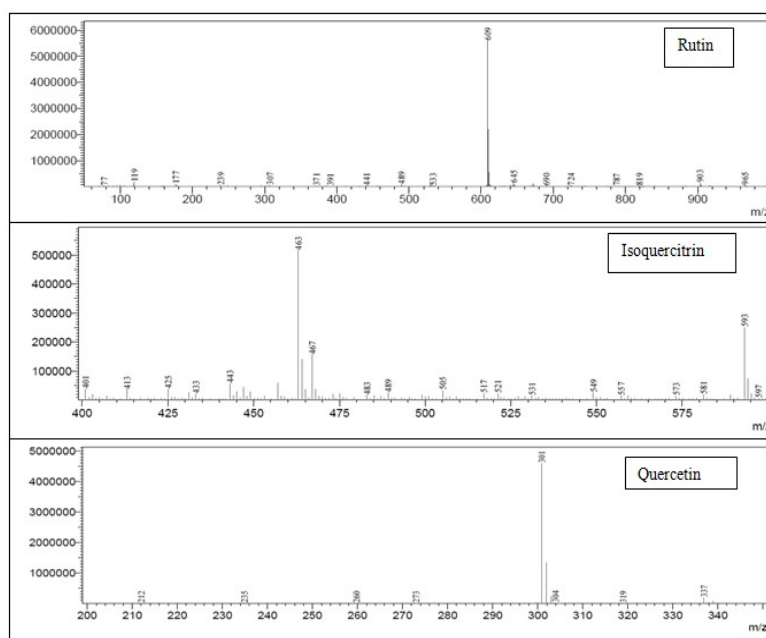


Figure 8. ESI-MS spectra of ficus leaf extracts' compounds in negative mode, interface temperature 350 °C; dry gas (nitrogen) and nebulizing gas flow was 1.5 L/min. Detector and interface voltages were 0.5 kV and 4.5 kV, respectively.

Identification of rutin, isoquercitrin and quercetin in extracts by HPLC-MS is presented in Table 3.

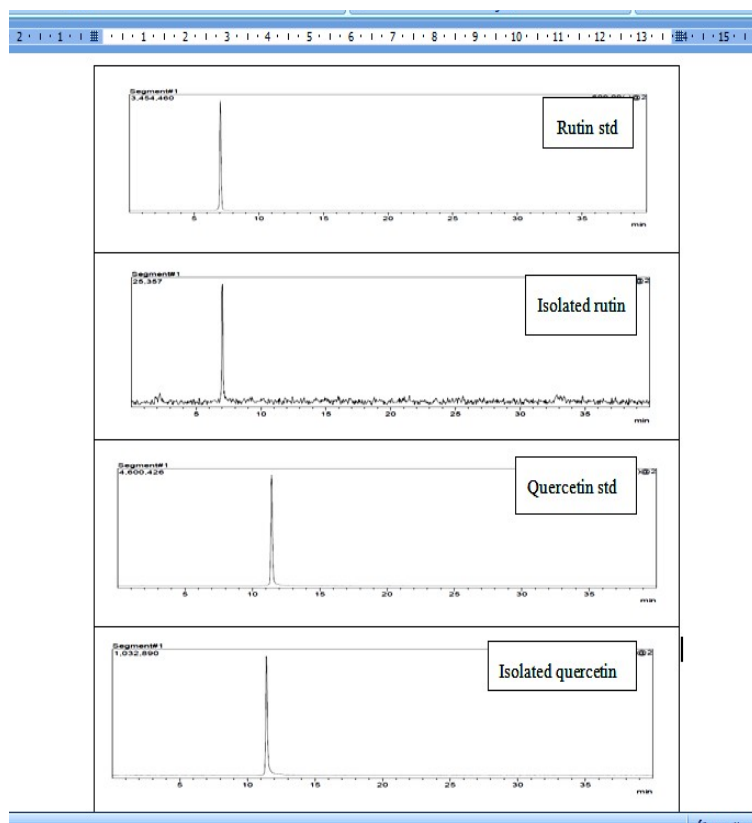
Table 3. Retention time and (M-H)⁻ ions of separated compounds from ficus leaf extracts by HPLC-MS

Compound	R.t (min)	[M-H] ⁻ (m/z)
Rutin	6.93	609
Isoquercitrin	7.41	463
Quercetin	11.39	301

Isolation of rutin and quercetin from ficus extracts

The total ion chromatogram (TIC) of isolated rutin and quercetin in ficus leaf extracts by TLC, with those of standards are presented in Figure

9. It shows the perfect and successful isolation of these compounds. The relative peak areas for rutin and quercetin are 99.80 and 96.46%, respectively.

**Figure 9.** TIC of standards and isolated compounds from the ficus leaf extracts.**CONCLUSION**

In this presented study, the compound plant (rutin) was extracted from Syrian ficus leaves by ultrasonic extraction procedure, then successfully converted into quercetin, which is the most powerful antioxidant compound. It was found that the solvent plays main role in the extraction of plant constituents. Ethanol (70%) is less polar than water which means it is a better solvent for organic compounds. Therefore it extracted higher amount of flavonoids when compared to aqueous solvent. Best hydrolyzing time was chosen as 5 minutes, in order to preserve isoquercitrin in the extracts. Rutin and quercetin were identified by

comparison with standards using chromatography. Both rutin and quercetin were successfully isolated from Syrian ficus leaf which is a cheap, available source, and identified by TLC, and HPLC-MS techniques.

ACKNOWLEDGMENT

The authors thank Mrs Alyamama Alaskar from the central laboratory in the faculty of science-Damascus University for her help in MS data analysis.

REFERENCES

- Trifunsi S I, Munteanu M F F, Ardelean D G, Orodan M, Osser G M, Gligor R I. Flavonoids and polyphenols content and antioxidant activity of *Ficus carica* L. extracts from Romania. *Zbornik Matice srpske za prirodne nauke*. 2015; 128: 57-65.
- Anonymous. The Agricultural Statistics Annual Group, 2008. Directorate of Planning and Statistics, Statistics Division, Ministry of Agriculture and Agrarian Reform, Damascus, Syria. 2009.
- Sirisha N, Sreenivasulu M, Sangeeta K, Chetty C M. Antioxidant Properties of *Ficus* Species – A Review, *Int. J. Pharm. Tech. Res.* 2010; 2: 2174 - 2182.
- Solomon A, Golubowicz S, Yablowicz Z, Grossman S, Bergman M, Gottlieb H, et al. Antioxidant Activities and Anthocyanin Content of Fresh Fruits of Common Fig (*Ficus carica* L.). *J. Agric. Food Chem.* 2006; 54: 7717 - 7723.
- Chawla A, Kaur R, Sharma A K. *Ficus carica* Linn.: A Review on its Pharmacognostic, Phytochemical and Pharmacological Aspects. *Int. J. Pharm. Sci Res.* 2012; 1: 215 - 232.
- Rubnov S, Kashman Y, Rabinowitz R, Schlesinger M, Meehoulam R. Suppressors of Cancer Cell Proliferation from Fig (*Ficus carica* Linn.) Resin: Isolation and Structure Elucidation, *J. Natu. Pro.* 2001; 64: 993-996.
- Kruzlicova D, Danihelova M, Veverka M. Quantitative structure-antioxidant activity relationship of quercetin and its new synthesised derivatives. *Nova Biotechnologica et Chimica.* 2012; 11: 37-44.
- Yashin Ya I, Ryzhnev V Yu, Yashin A Ya, Chernousova N I. Prirodnye antioksidanty. Soderzhanie v pishchevykh produktakh i ikh vliyanie na zdorov'e i starenie cheloveka. 2009.
- Mauludin R, Müller R H, Keck C M. Development of an oral rutin nanocrystal formulation. *Int. J. Pharm Sci Res.* 2009; 370: 202-209.
- Chen H, Zuo Y, Deng Y. Separation and determination of flavonoids and other phenolic compounds in cranberry juice by high-performance liquid chromatography. *J. Chrom A.* 2001; 913: 387- 395.
- Wang J, Zhao L L, Sun G X, Liang Y, Wu F A, Chen Z I, et al. A comparison of acidic and enzymatic hydrolysis of rutin. *African J. Biotech.* 2011; 10: 1460-1466.
- Seyoum A, Asres K, El-Fiky F K. Structure-radical scavenging activity relationships of flavonoids. *Phytochem.* 2006; 67: 2058-2070.
- Vaya J, Mahmood S. Flavonoid content in leaf extracts of the fig (*Ficus carica* L.), carob (*Ceratonia siliqua* L.) and pistachio (*Pistacia lentiscus* L.). *Biofactors.* 2006; 28: 169–175.
- Takahama U, Tanaka M, Hirota, S, Yamauchi R. Formation of an oxathiolone compound from rutin in acidic mixture of saliva and buckwheat dough: Possibility of its occurrence in the stomach. *Food Chem.* 2009; 116: 214-219.
- Kamalakkannan N, Stanely Mainzen P P. Antihyperglycaemic and antioxidant effect of rutin, a polyphenolic flavonoid, in streptozotocin-induced diabetic wistar rats. *Basic & Clinical Pharm & Toxi.* 2006; 98: 97-103.
- Je H D, Shin C Y, Park S Y, Yim SH, Kum C, Huh I H, et al. Combination of vitamin C and rutin on neuropathy and lung damage of diabetes mellitus rats. *Archives. Pharm. Res.* 2002; 25: 184-190.
- Srinivasan K, Kaul C L, Ramarao P. Partial protective effect of rutin on multiple low dose streptozotocin-induced diabetes in mice. *Ind. J. Pharm.* 2005; 37: 327- 328.
- Li X, Park N I, Xu H, Woo SH, Park, CH, Park SU. Differential expression of flavonoid biosynthesis genes and accumulation of phenolic compounds in common buckwheat (*Fagopyrum esculentum*). *J. Agri. Food Chem.* 2010; 58: 12176- 12181.
- Scherer RI, Godoy HT. Effects of extraction methods of phenolic compounds from *Xanthium strumarium* L. and their antioxidant activity. *Revista Brasileira de Plantas Medicinai.* 2014; 16: 41-46.
- Zhang Y, Wang D, Yang L, Zhou D, Zhang J. Purification and characterization of flavonoids from the leaves of *Zanthoxylum bungeanum* and correlation between their structure and antioxidant activity. *PLoS One.* 2014; 9: e105725.
- Makino T, Shimizu R, Kanemaru M, Suzuki Y, Moriwaki M, Mizukami H. Enzymatically modified isoquercitrin, α -oligoglucosyl quercetin 3-O-glucoside, is absorbed more easily than other quercetin glycosides or aglycone after

oral administration in rats. *Bio. Pharm Bull.* 2009; 32: 2034-2040.

22. Erlund I. Review of the flavonoids quercetin, hesperetin, and naringenin. Dietary sources, bioactivities, bioavailability and epidemiology. *Nut Res.* 2004; 24: 851- 874.

23. Valentova K, Vrba J, Banciřova M, Ulrichova J, Křen V. Isoquercitrin: pharmacology, toxicology, and metabolism. *Food. Chem. Toxi.* 2014; 68: 267- 282.

24. Yi J, Wu J G, Wu Y B, Peng W. Antioxidant and anti-proliferative activities of flavonoids from *Bidens pilosa* L var *radiata* Sch Bip. *Tro. J. Pharm. Res.* 2016; 15: 341-348.

25. Achat S, Tomao V, Madani K, Chibane M, Elmaataoui M, Dangles O, et al. Direct

enrichment of olive oil in oleuropein by ultrasound-assisted maceration at laboratory and pilot plant scale. *Ultr. Sonochem.* 2012; 19: 777-786.

26. Chen C, Zhou J, Ji C. Quercetin: A potential drug to reverse multidrug resistance. *Life Sci.* 2010; 87: 333-338.

27. Cimpoiu C. Analysis of some natural antioxidants by thin-layer chromatography and high performance thin-layer chromatography, *J. Liquid Chrom Rel. Tech.* 2006; 29: 1125–1142.

28. Şahin S, Şamlı R. Optimization of olive leaf extract obtained by ultrasound-assisted extraction with response surface methodology. *Ultr. Sonochem.* 2013; 20: 595-602.



GAMMA DOSE VALUES OF STRATIGRAPHIC UNITS OF BEHRAMKALE (ÇANAKKALE) - ZEYTİNLİ (EDREMİT-BALIKESİR) SECTION OF KAZ MOUNTAINS

Zeki Ünal Yümün¹  , Erol Kam²  , Melike Önce¹  

¹Tekirdağ Namık Kemal University, Tekirdağ

²Yıldız Technical University, Istanbul

Abstract: In this study, gamma dose values were measured at 25 locations around a distance of 60 km parallel to the Aegean Sea in Güre, Küçükuyu and Kazdağı regions. These measurements were made by keeping the Eberline Smart Portable (ESP) scintillator detector constant at a height of 1 meter above ground level. A SPA-6 plastic scintillation sensor is connected to the instrument tip to perform the measurement. These devices are direct measurement of external radiation. As the measurements were carried out in the open area, 0.2 occupancy factor was used in the calculations. In the studies, the highest effective dose value was calculated as 0.3 mSv at the location 2 (Asos Kadirga Bay). The lowest effective dose value is 0.054 mSv at the 15th location (Avcılar Village Mountain slope) and the average annual gamma dose is 0.14 mSv. For the study area, when the lifetime risk of cancer was calculated using gamma effective dose values, it was determined at the highest 2. locations (0.0012) and the lowest at the 15th locations (0,21x10⁻³). The average lifetime cancer risk value (2,39x10⁻⁴) of Turkey, were compared with values calculated in this study. In this comparison, the gamma dose values of locations 9 and 15 were lower and the values of other locations were higher.

Keywords: Gamma dose, annual effective dose, Kaz Mountains, Behramkale, Edremit Bay.

Submitted: May 14, 2019. **Accepted:** November 26, 2019.

Cite this: Yümün ZÜ, Kam E, Önce M. GAMMA DOSE VALUES OF STRATIGRAPHIC UNITS OF BEHRAMKALE (ÇANAKKALE) - ZEYTİNLİ (EDREMİT-BALIKESİR) SECTION OF KAZ MOUNTAINS. JOTCSA. 2020;7(1):209-16.

DOI: <https://doi.org/10.18596/jotcsa.565054>.

***Corresponding author. E-mail:** zyumun@nku.edu.tr.

INTRODUCTION

The world is always under the influence of cosmic radiation coming from outer space. An average of 82% of the radiation dose of living organisms per year is due to natural sources (1-5). Environmental ionized background radiation levels are determined by two different sources, natural and artificial. Natural radiation sources consist of ionized particles derived from cosmic rays and radioactive isotopes originating from earth's crust. Cosmic rays produce secondary reaction products by interacting with

the nuclei of atmospheric components. These products start from the upper layers of the atmosphere and form cosmic radiation exposures at decreasing density towards ground level.

Natural radionuclides of terrestrial origin are present in various concentrations in all surrounding environments, including the human body itself (6 and 1). In addition, people receive radiation doses from industrial or medical applications of artificially produced radioactive substances. An important part of the

dose from radiation sources defined as artificial radiation sources is due to X-rays used for diagnostic purposes and radioactive substances used in nuclear medicine (7-10).

Apart from these, nuclear tests and nuclear reactor accidents caused by radioactive substances spread to the atmosphere, dry sprinkling and rainfall, soil, water and vegetation is infected.

Radioactive substances that accumulate in the receiving environment (soil, water, air) significantly alter local and regional radioactivity. Cosmic sources, radioactive elements in rocks and radially generated radionuclides provide environmental gamma radiation. When the geological structure of the world is examined, it is seen that there are rock beds just below the soil layer of certain thickness. It is known that a significant part of

gamma radiation is caused by the surface layer at a depth of 0-25 cm (11).

Gamma radiation from naturally occurring radioisotopes such as ^{238}U , ^{232}Th and ^{40}K is known as terrestrial background radiation and contributes to the total. The calculations show that 50-80% of the total gamma dose is due to ^{238}U , ^{232}Th and ^{40}K natural radionuclides on the ground surface (12).

Natural radioactive nuclei are found in high concentration especially in granite, volcanic, phosphate, and salt rocks. Besides, the lowest radioactivity concentration is found in lime rocks. The metamorphic rocks have a concentration of rocks in which they are formed. Table 1 shows the gamma radiation dose rates of radium, uranium, thorium, and potassium in rocks (13).

Table 1. Gamma radiation dose rates caused by radium, uranium, thorium, and potassium in rocks (14).

Rock type	Dose Intensity (mSv h ⁻¹)			
	^{226}Ra	^{238}U	^{232}Th	^{40}K
Volcanic Rocks	2.4	2.6	3.7	3.5
Sedimentary rocks				
Sandstone	1.3	0.7	1.8	1.5
Stratified	2.0	0.7	3.1	3.6
Limy	0.7	0.8	0.4	0.4

Considering the values in Table 1, the annual effective dose taken from natural radiation sources exposed to living organisms worldwide is 2.4 mSv. The dose from a lung film is 0.02 mSv. Lung examination with computed tomography is 8 mSv. due to Chernobyl Accident, the average dose of Turkish people is 0.5 mSv (15).

Several studies have been conducted in the previous years regarding the determination of gamma dose and effective dose rates (16-22).

In this study, Gamma dose rates were measured at 25 different points around a 60 km area in Güre, Küçükuyu and Kazdağı regions. This study gave important results in terms of determining the gamma dose values for the region.

MATERIAL AND METHODS

The study area lies between the Behramkale district of the Gulf of Edremit and the Zeytinli village in the province of Balıkesir and Çanakkale (Figure 1). There are many fault zones and thermal water resources in the region. The gamma dose rate absorbed in the air, consists of the sum of cosmic and terrestrial radiations. Measurements were taken with a gamma radiation measuring device at a height of 1 meter from the soil surface to determine background levels of the district. The gamma dose velocity values (ADRA) absorbed in the air are composed of terrestrial and cosmic radiation values. The difference between the values of terrestrial radiation due to the concentration of radionuclides in the soil and the total radiation value is equal to the gamma dose rate components of cosmic radiation. The samples were collected at an interval of approximately 2.5 km from an area of 60 kilometer square between Behramkale and Zeytinli Village. Twenty-five measurements were taken from the

study area. The sample coordinates of the study area are given in Table 2. Portable Eberline Smart Portable (ESP) scintillator device is used in measurements. The absorbed gamma doses obtained in nGy / h were converted into the annual effective dose in mSv / y using 0.7 Sv / Gy conversion factor and 0.8 for the closed area and 0.2 for the open area.

As the measurements were made for the open area, the factor of 0.2 was used in the calculations. The annual effective dose was calculated using the following equation (23, 6). The formula used in the calculation is given below.

$$AEDE = ADRA \times DCF \times OF \times T$$

$$E_H \text{ (mSv/y)} = D_H \text{ (nGy/h)} \times 365.25 \times 24 \times 0.7 \text{ Sv/Gyx} 10^{-6} \times 0.2$$

The terrestrial and cosmic radiation risk values (ELCR) of the people living in the area were calculated by the following equation (24).

$$ELCR = AEDE \times DL \times RF$$

Here, the annual exposure value in the AEDE mSv / y unit, DL average life span (70 years), RF refers to the risk factor (0.055 Sv^{-1}) recommended by International Commission on Radiological Protection-103 (ICRP 103) (25).

Geological characteristics of the study area

The main units in the study area begin with unallocated gneisses, metagranites, schists, amphibolites and marbles from the Cambrian or Precambrian age. To the top, Precambrian amphibolites, Paleozoic and Permian marbles and metabasic rocks form the basic units. These basement units represent the Mesozoic rocks of the Upper Cretaceous ophiolitic melange. Mesozoic is unconformably overlain by Miocene granitoids, Middle Miocene unspoiled volcanics, andesite, dacite, rhyolite, rhyodacite type volcanic rocks. The upper Miocene pyroclastic rocks, Upper Miocene terrestrial crumbs and neritic limestones are found on these units. All these old rocks are locally overlain by Quaternary slope and alluviums (Figure 1).

The stratigraphic descriptions and regional distributions of the geocronologically defined units are as follows. In the Küçükuyu section of the study area there are geologically Arıklı ignebrite, Küçükuyu Formation and Hallaçlar Volcanites. In Güre region, there are mainly Pliocene Bayramiç Formation, Hallaçlar Volcanite, Oligocene-Miocene Granitoids and Çetmi Melange (26).

In the Oligo-Miocene period, a thick sedimentary deposit was developed at the southern foothills of Kazdağı. Starting with the red terrestrial sediments, this sequence passes to the upper lacustrine flysch sequence. In the upper levels of the sequence, the white colored tuff is clearly identified on the southern and western skirts of Kazdağı and its continuity is observed. This explosive volcanism, which is also a predictor of the early Miocene active volcanism, has more common older units, a common lava and prioclastic equivalent, and covered the area like a carpet. In the region, the representative products of this volcanic community such as lava, dyke and vein are widely seen. The Behramkale Village flow structures are located on a beautiful lava flow (27).

The youngest unit recognized in the Kazdağları is a sedimentary group of Upper Miocene - Pliocene age and consisting mainly of lacustrine marls and limestones. This unit, which can be easily recognized and distinguished in the field with its white color, was deposited after the development of the anticline formed in Kazdağı. While rising to the present position of the Kaz Mountains, these rocks also were risen on the shoulder of the mountain (27).

RESULTS

Gamma dose values of the study area and calculated annual effective dose values are given in Table 2. The measurement locations are given in Figure 1 and Table 2, and it is clearly seen in Table 2 that the measurement results differ according to the basement rocks. The gamma dose values of undifferentiated massive volcanics and undifferentiated andesitic volcanics were found to be between 117 (nGy / h) and 243 (nGy / h). The gamma dose values of andesitic pyroclastic rocks were found to be between 65.4 (nGy / h) and 79.0 (nGy / h). In the measurements made in the ophiolitic rocks, the gamma dose values are 238 (nGy / h). In the metamorphic rocks, slope debris and alluvium areas, the gamma dose values are between 43.8 (nGy / h) and 85.6 (nGy / h). It was observed that the measured values were high especially in the areas with massive unstabilized volcanic rocks and massive metamorphic rocks.

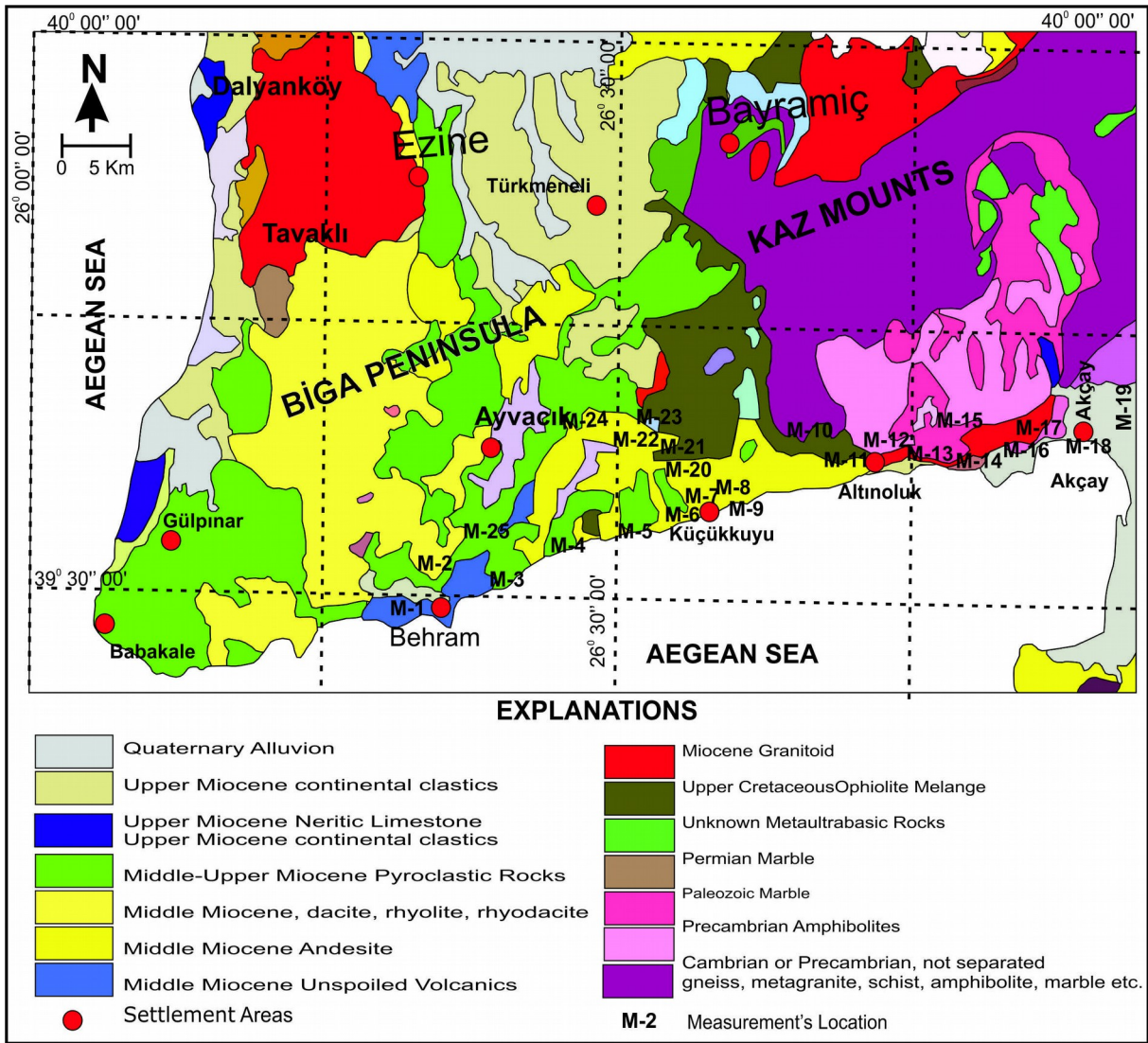


Figure 1. Geological Map of the Biga Peninsula (28)

Table 2. Gamma dose and annual effective dose rates obtained from the study area.

GEOLOGICAL UNIT DEFINITIONS	GEOGRAPHIC COORDINATES		GAMMA DOSE RATE (ADRA) (nGy/y)	ANNUAL EFFECTIVE DOSE EQUIVALENT (AEDE) (mSV)	CANCER RISK VALUES (ELCR) [E-4]
	X	Y			
Unspoiled Volcanic Rocks	0442927	4371703	134	0,16	6,16
Andesitic Volcanites	0445878	4371896	243	0,3	12
	0449392	4373146	143	0,18	6,93
Andesitic Pyroclastic Rocks	0452207	4374415	65,4	0,08	3,08
	0456961	4375580	77,5	0,095	3,7
Andesitic Volcanites	0462376	4376462	148	0,18	6,93
Alluvium of Andesitic Components	0464541	4377369	80,8	0,1	3,85
Andesitic Volcanites	0464852	4377464	236	0,3	12
Alluvium of Andesitic Components	0572859	4556510	45,2	0,06	2,31
	0474996	4379777	75,6	0,09	3,5
	0477218	4379930	82,5	0,1	3,85
Precambrian Amphibolites	0477192	4380513	106	0,13	5
	0481992	4380036	115	0,14	5,4
Separated Metamorphic Rocks, Slope Debris and Alluvium	0483329	4380043	73,8	0,09	3,5
	0483443	4382665	43,8	0,054	2,1
	0488830	4381631	84,9	0,108	4,2
	0489468	4382094	85,6	0,19	7,3
	0493609	4382077	71,1	0,088	3,4
	0495860	4383050	61,8	0,076	2,9
Andesitic Volcanites	0463639	4378276	117	0,14	5,3
Ophiolitic Melange Rocks	0462270	4378696	238	0,29	11
Andesitic Pyroclastic Rocks	0460286	4381191	71,8	0,088	3,4
	0458926	4382298	79,0	0,097	3,7
	0453822	4382974	86,3	0,105	4
Andesitic Volcanites	0447112	4373791	215	0,26	10
AVERAGE VALUE			111,2	0,14	5,4

Annual effective dose values were calculated by using gamma dose values. According to the results, the highest effective dose was calculated as 0.3 mSv (Asos Kadirga Bay) at location 2. The lowest effective dose value was calculated at the 15th location: 0.054 mSv (Küçükuyu Outlet) and the average effective dose value: 0.14 mSv was calculated. For the study area, when the lifetime risk of cancer was calculated by using gamma effective dose values, it was found in the highest number 2 location (0.0012) and the lowest in 15 (0.00021).

CONCLUSION

According to the results of the analysis, the environmental gamma radiation dose velocity varies between locations. This change is directly related to the concentrations of radioisotopes in the soil structure of the region because the main sources of dose values are land and space origin (11).

The geological formation of each location in the study area was determined lithologically and the gamma dose values were measured and evaluated in detail. According to the results, the

highest effective dose was calculated as 0.3 mSv at the location 2 (Asos Kadirga Bay). The lowest effective dose value was calculated as 0.054 mSv at the 15th location (Avclar Village Mountain slope) and 0.14 mSv at the average annual gamma dose. These values are smaller than those of TAEK 2009 (Average Annual Effective Dose: 0.48 mSv). For the study area, when the lifetime risk of cancer was calculated by using gamma effective dose values, it was found in the highest number 2 location (0.0012) and the lowest in 15 (0.00021). If these calculated values compared with Turkey's average lifetime cancer risk value (0.000239) (29), except ninth and fifteenth locations, all locations' values are higher than Turkey average lifetime risk values of cancer.

REFERENCES

1. Kapdan, E, Varinlioglu A ve Karahan G. Outdoor Radioactivity and Health Risks in Balıkesir, Northwestern Turkey. Radiation Protection Dosimetry. 2011a, (3) 148: 301-309p.
2. Aközcan S. Annual effective dose of naturally occurring radionuclides in soil and sediment, Toxicological and Environmental Chemistry. 2014, 96(3): 379-386p.
3. Akkurt İ, Uyanik NA, Günoğlu K. Radiation Dose Estimation: An In Vitro Measurement For Isparta-Turkey. Ijcesen 2015, 1 (1): 1-4p.
4. Çetin B, Öner F and Akkurt I. Determination of Natural Radioactivity and Associated Radiological Hazard in Excavation Field in Turkey (Oluz Höyük), Acta Physica Polonica. 2016, 130 (1): 475-478p.
5. Günay O, Aközcan S And Kulalı F. Determination of Indoor Radon Concentrations. European Journal of Science and Technology. 2018, 13 : 91-97p.
6. UNSCEAR. Report of the United Nations Scientific Committee on the Effects of Atomic Radiation, Sources, Effects, and Risks of Ionizing Radiation. United Nations sales publication, New York. United Nations. 2000. 659p.
7. Kara U, Kaya A, Tekin HO, Akkurt I. Adult Patient Radiation Doses with Multislice Computed Tomography Exam: MSCT Standard Protocols. Acta Physica Polonica. 2017, 3 (132): 1126-1127p.
8. Demir N, Kıvrak A, Üstün M, Cesur A, Boztosun I. Experimental Study for the Energy Levels of Europium by the Clinic LINAC. IJCESEN. 2017, 3(1): 47-49p.
9. Karahan G, Bayulken A. Assessment of gamma dose rates around Istanbul (Turkey). J. Environ. Radioact. 2000, 47: 213-221p.
10. Kapdan E, Varinlioglu A ve Karahan G. Radioactivity Levels and Health Risks due to Radionuclides in the Soil of Yalova, Northwestern Turkey. International Journal of Environmental Research. 2011b, 5(4): 837-846p.
11. Kam E. Environmental Natural Radioactivity Concentrations of Tekirdag. Yildiz Technical University. Graduate School of Natural and Applied Sciences. Department of Physics, Master Thesis. 2004. 124p. İstanbul.
12. Karayığit AI, Akgün F, Gayer RA, Temel A. Quality, Palynology, and Palaeoenvironmental Interpretation of the Ilgın Lignite, Turkey, International Journal of Coal Geology. 1999, (38): 219-236p.
13. NCRP. Report 45, National Council on Radiation Protection and Measurements No.45, Natural Background Radiation in the U.S., Soil Radioactivity. 1975, 270p.
14. NCRP. National Council on Radiation Protection and Measurements. Environmental Radiation Measurement, NCRP Report No.50. 1977, 150p.
15. Keçeci M. Radiation and radioactivity <http://mehmetkececi.com/blog/2012/04/08/radiation-and-radioactivity/>. 2007.
16. Kam E, Yümün ZÜ, Önce M, Açıkgöz G. Gamma Dose Rate Values In The Kulakçayırı Natural Lake And The Vicinity (Arnavutköy, İstanbul). Journal of Engineering Technology and Applied Sciences. 2016, 1(1): 29-33p.
17. Kam E, Bozkurt A. Environmental radioactivity measurements in Kastamonu region of northern Turkey. Applied Radiation and Isotopes. 2007, 4 (65): 440-444p.
18. Bozkurt A, Yorulmaz N, Kam E, Karahan G, Osmanlioğlu AE. Assessment of Environmental Radioactivity for Şanlıurfa Region of Southeastern Turkey. Radiation Measurements. 2007, 8(42): 1387-1391p.
19. Osmanlioğlu AE, Kam E, Bozkurt A. Assessment of Environmental Radioactivity Level for Gaziantep Region of Southeastern Turkey.

Radiation Protection Dosimetry. 2007, 124 (4): 407-410p.

20. Otansev P, Karahan G, Kam E, Barut İ, Taşkın H. Assessment of Enviromental Radioactivity Concentrations and Gamma Dose Rate Levels in Kayseri, Turkey. Radiation Protection Dosimetry. 2012, 148 (2): 227-236p.

21. Yümün ZÜ, Bayrak K, Aksoy H, Ayseli U. A Study of Background Radioactivity Level for Edirne, Turkey. Journal of Engineering Technology and Applied Sciences. 2018, 3(2): 135-139p.

22. Turgay ME. Cancer Risk Determination for IDA villages by using Annual Gamma Doses in Air, around Edremit&Ayvacık District; Balıkesir&Çanakkale, Turkey. European Journal of Science and Technology. 2019, 15: 433-439p.

23. Kurnaz A. and Turfan N. The Effects of Different Storage Conditions on the Radiometric and Element Content of the Taşköprü Garlic (*Allium sativum* L.). Turkish Journal of Agriculture - Food Science and Technology. 2017, 5 (4): 373-379p.

24. UNSCEAR. Report of the United Nations Scientific Committee on the Effects of Atomic

Radiation, Sources, Effects, and Risks of Ionizing Radiation. United Nations sales publication. 2008. New York. United Nations. 683p.

25. ICRP. ICRP Publication 103 Recommendations of the ICRP: Annals of the ICRP Volume 37/2-4, Pergamon Press. International Commission on Radiological Protection. 2007. 35p

26. Bingol E, Akyurek B, Korkmazer B. Geology of Biga Peninsula and some properties of Karakaya Formation. 50th Anniversary of the Republic Congress of Earth Sciences, MTA Ens. Ankara. 1973, 70-77p.

27. Yılmaz Y. Geology and Seismicity of Biga Peninsula. National Workshop of Kazdagları Abstract.23 June 2012.Güre, Edremit, Balıkesir. 19-32p.

28. Şenel M. 1/500000 Scale Geological Map of Turkey (İzmir), the General Directorate of Mineral Research and Exploration. 2002. Ankara.

29. Günay O. Determination of Natural Radioactivity and Radiological Effects in some Soil Samples in Beykoz-İstanbul. European Journal of Science and Technology. 2018. No. 12.



The Synthesis of New Phosphazene-Bearing Ethyl p-Hydroxybenzoate and Ferrocenyl Pendant Groups and their Spectroscopic and Crystallographic Characterizations

Yasemin Tümer^{1*}, Mahmut Çayırbaşı¹, Onur Şahin²,
Tuncer Hökelek³

¹Department of Chemistry, Karabük University, 78050 Karabük, Turkey.

²Scientific and Technological Research Application and Research Center, Sinop University, 57000 Sinop, Turkey.

³Department of Physics, Hacettepe University, 06800 Ankara, Turkey.

Abstract: This is a study of new hexachlorocyclotriphosphazene ($N_3P_3Cl_6$) derivatives bearing ethyl p-hydroxybenzoate and ferrocenyl pendant groups. Characterizations of the products [mono- **2**, di-(geminal **3a**; non-geminal **trans^a-3b**, **trans^b-3c** and **cis-3d**), tri- **4** and tetra- **5** substituted phosphazene derivatives] were performed using elemental analysis and spectral methods. The structures of the two compounds (**2** and **5**) were explained by the use of X-ray diffraction techniques.

Keywords: Ferrocenylphosphazenes, ethyl p-hydroxybenzoate, crystal structure, spectroscopy.

Submitted: March 14, 2019. **Accepted:** December 03, 2019.

Cite this: Tümer Y, Çayırbaşı M, Şahin O, Hökelek T. The Synthesis of New Phosphazene-Bearing Ethyl p-Hydroxybenzoate and Ferrocenyl Pendant Groups and their Spectroscopic and Crystallographic Characterizations. JOTCSA. 2020;7(1):217-26.

DOI: <https://doi.org/10.18596/jotcsa.540169>.

***Corresponding author. E-mail:** yasemintumer@karabuk.edu.tr.

INTRODUCTION

Halogenocyclophosphazenes are remarkable multi-branched phosphorus-nitrogen compounds used in the synthesis of cyclophosphazene derivatives, from organocyclophosphazenes to dendrimeric cyclophosphazenes. Each phosphorus atom is connected to two exocyclic substituents such as chlorine, fluorine or bromine atoms. The sequential replacement of these halogen atoms in halogenocyclophosphazenes with different reagents can produce new phosphazene derivatives (1, 2). The reactions of $N_3P_3Cl_6$ with bidentate reagents produce different geometrical and optical isomers, e.g., spiro-

(mono, di or tri) and bino-structures (3-7). Monospiro products have four reactive P-Cl bonds. The reactions of monospiro cyclophosphazenes with monodentate reagents produce mono-, di- (gem-, nongeminal cis- or nongeminal trans-), tri- and tetra- substituted phosphazene derivatives (8, 9).

Because of their structural features, organocyclophosphazenes are used as polydentate ligands for coordination complexes and multi-branched cores for dendrimers. Recently, organocyclophosphazene-containing coordination complexes have been used as chemosensors for different metals (10-12) and luminescent materials (13). Also, cyclic

phosphazene core-based materials are widely implemented in OLED technology (14–16) and in biomedical applications (17, 18).

In previous studies, geometrical and optical isomers of mono- and dispiroferrocenylphosphazenes were produced, and their chirality was investigated using ^{31}P -NMR spectroscopy and X-ray crystallography (19, 20). Langmuir-Blodgett thin films, DNA interactions, and the cytotoxic and antimicrobial activities of mono- and dispiroferrocenylphosphazenes were also investigated (21–23).

In this study, the reactivity of the P–Cl groups present in chlorocyclophosphazenes was taken advantage of to prepare new phosphazene derivatives. In the first step, monospiroferrocenylphosphazene derivative **1** was obtained by the reaction of hexachlorocyclotriphosphazene with potassium[3-(N-ferrocenylmethylamino)-1-propanoate with a formula $\text{FcCH}_2\text{NH}(\text{CH}_2)_3\text{OK}$ (24). In the second step, the gradual Cl replacement reactions of compound **1** with ethyl p-hydroxybenzoate resulted in partly and fully substituted phosphazene derivatives (25). The structures of the synthesized products were characterized using elemental analysis, FTIR and Nuclear Magnetic Resonance (^{31}P -, ^{13}C - and ^1H -NMR) techniques. The solid-state structures of the two phosphazene derivatives (**2** and **5**) were investigated by X-ray crystallography.

MATERIAL AND METHODS

Reagents used for synthesis

Hexachlorocyclotriphosphazatriene (phosphonitrilic chloride) (Aldrich); ethyl p-hydroxybenzoate, (Aldrich) and ferrocenecarboxaldehyde (Acros organics) were used without further purification. The solvents (THF, ethanol, toluene, n-hexane, acetonitrile, and benzene) were dried by standard methods. Reactions have been monitored with TLC (Merck silica gel 60 B254 sheets). The column chromatography was performed on Merck silica gel 60 (0.040–0.063 mm).

Physical measurements

Melting points were measured with a Gallenkamp apparatus using a capillary tube. The ^1H , ^{13}C and ^{31}P NMR spectra were recorded on a Bruker DPX FT-NMR (300 MHz) spectrometer (SiMe₄ as internal and 85% H₃PO₄ as external standards). The IR spectra were recorded on Perkin Elmer FTIR spectrometer (4000–650 cm⁻¹).

X-ray crystallography

Suitable crystals of **2** and **5** were selected for data collection which was performed on a D8-QUEST diffractometer equipped with a graphite-monochromatic Mo-K α radiation. The structures were solved by direct methods using SHELXS-97 (26) and refined by full-matrix least-squares methods on F² using SHELXL-2013 (27). All non-hydrogen atoms were refined with anisotropic parameters. The following procedures were implemented in our analysis: data collection: Bruker APEX2 (28); program used for molecular graphics were as follows: MERCURY programs (29); software used to prepare material for publication: WinGX (30).

Synthesis of compounds

The spiroferrocenylphosphazene derivative **1** was synthesized from the reactions of hexachlorocyclotriphosphazene with potassium salt of [3-(N-ferrocenylmethylamino)-1-propanoate according to the literature (24).

Synthesis of compound 2; A solution of ethyl p-hydroxybenzoate (0.325 g, 1.95 mmol) in dry THF (100 mL) was added to a solution of **1** (1.00 g, 1.95 mmol) with K₂CO₃ (1.08 g) in dry THF (100 mL). Reaction mixture was refluxing for 12 h with stirring. Reaction mixture was purified by column chromatography with benzene used as eluent. The product eluted was mono-ethyl p-hydroxybenzoate substituted derivative **2** (0.499 g, 1.95 mmol, 37.7%, mp 146–147 °C). Anal. Calcd for **2** C₂₃H₂₆N₄O₄FeP₃Cl₃: C, 40.77; H, 3.87; N, 8.27. Found: C, 40.55; H, 3.93; N, 8.14. FTIR (cm⁻¹): 3098 (C–H arom.), 2906 (C–H aliph.), 1711 (C=O), 1598; 1500 (C=C arom.), 1200 (P=N). **Synthesis of compounds geminal- (3a) and nongeminal- (trans^a-3b, trans^b-3c and cis-3d);** The work-up procedure was similar to that of compound **2**, using **1** (1.00 g, 1.95 mmol), ethyl p-hydroxybenzoate (0.65 g, 3.90 mmol) and K₂CO₃ (1.58 g). Reaction mixture was purified by column chromatography with benzene/THF (80/1). The disubstituted compounds were not separated but they have been identified by ^{31}P -NMR spectrum from different elution. [geminal (**3a**); non-geminal (**trans^a-3b**, **trans^b-3c** and **cis-3d**)] (0.60 g, 40.8%). Anal. Calcd for mixture of **3a**, **trans^a-3b**, **trans^b-3c** and **cis-3d** C₃₂H₃₅N₄O₇FeP₃Cl₂: C, 47.61; H, 4.37; N, 6.94. Found: C, 48.39; H, 4.84; N, 6.66. FTIR (cm⁻¹): 3083 (C–H arom.), 2980; 2981; 2934; 2853 (C–H aliph.), 1714 (C=O), 1601; 1502 (C=C arom.), 1198 (P=N).

Syntheses of compounds 4 and 5; The work-up

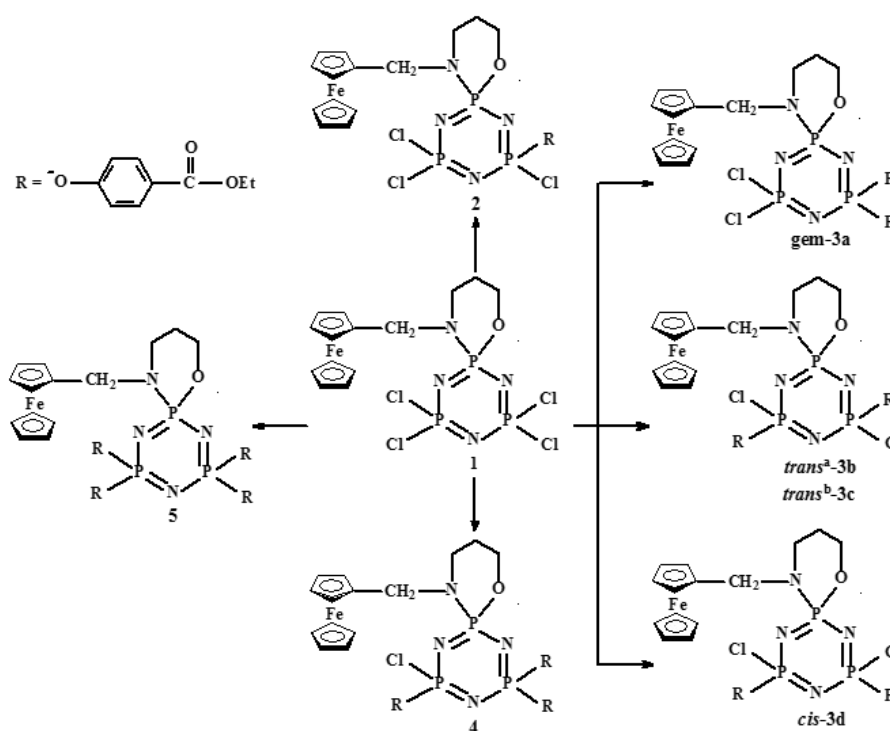
procedure was similar to that of compound **2**, using **1** (0.70 g, 1.36 mmol), ethyl p-hydroxybenzoate (0.70 g, 4.21 mmol) and K_2CO_3 (2.30 g). The tri- **4** (0.41 g, 35.9%, mp 89-90 °C) and tetra- **5** substituted (0.23 g, 17%, mp 110-111 °C) compounds were purified from reaction mixture by column chromatography (benzene/THF (30/1)). Anal. Calcd for **4** $C_{41}H_{44}N_4O_{10}FeP_3Cl$: C, 52.55; H, 4.73; N, 5.98. Found: C, 51.88; H, 4.51; N, 5.85. FTIR (cm^{-1}): 3082 (C-H arom.), 2982; 2903 (C-H aliph.), 1716 (C=O), 1601; 1501 (C=C arom.), 1199 (P=N). Anal. Calcd for **5** $C_{50}H_{53}N_4O_{13}FeP_3$: C, 56.29; H, 5.01; N, 5.25. Found: C, 56.07; H, 5.19; N, 4.86. FTIR (cm^{-1}): 3082 (C-H arom.), 2981; 2936 (C-H aliph.),

1709 (C=O), 1600; 1501 (C=C arom.), 1198 (P=N).

RESULTS AND DISCUSSION

Synthesis

The precursor molecule spirocyclicferrocenylphosphazene **1**, which has four P-Cl bonds, was synthesized according to the procedure (24). The reactivity of the P-Cl groups was then used to produce mono- **2**, di- [geminal (**3a**); non-geminal (**trans^a-3b**, **trans^b-3c** and **cis-3d**)], tri- **4** and tetra- **5** substituted phosphazene derivatives (**Scheme 1**).



Scheme 1. The synthesis route of compounds mono- **2**, di- [geminal (**3a**); non-geminal (**trans^a-3b**, **trans^b-3c** and **cis-3d**)], tri- **4** and tetra- **5**.

The reaction of a 1:1 molar ratio of compound **1** and ethyl p-hydroxybenzoate produced the corresponding monosubstituted phosphazene **2** as a major product and disubstituted phosphazenes as minor products. These minor products, which were observed by TLC, were separated from the major product by chromatographic methods. The reaction of a 1:2 mol ratio of compound **1** and ethyl p-hydroxybenzoate produced the expected disubstituted phosphazenes. Disubstituted phosphazenes were not separated from the

reaction mixture using chromatographic methods. When the ^{31}P -NMR analyses of two different samples taken from the column were examined, geminal- **3a** and nongeminal- (**trans^a-3b**, **trans^b-3c** and **cis-3d**) isomers were observed. When a 1:3.3 mol ratio of compound **1** and ethyl p-hydroxybenzoate was used in the reaction, tri-substitute **4** and tetra-substitute **5** phosphazenes were synthesized. Compound **2** was crystallized from an acetonitrile/THF mixture (5:1); compound **5** was crystallized from an n-hexane/THF mixture

(10:1) at room temperature.

Spectroscopic Analysis

The ^1H -decoupled ^{31}P -NMR spectral data for mono- **2**, di- [geminal (**3a**); non-geminal (**trans^a-3b**, **trans^b-3c** and **cis-3d**)], tri- **4** and tetra- **5** are listed in **Table 1**. The ^{31}P -NMR signals of all compounds were found on the NMR spectrum (**Figure 1-3**). Disubstituted phosphazene isomers [geminal (**3a**); non-geminal (**trans^a-3b**, **trans^b-3c** and **cis-3d**)] could not be purified from the reaction mixtures using column chromatography. When the ^{31}P -NMR spectrum of two different samples obtained by column chromatography were

analyzed, *cis*- and *trans*- isomers were observed in first sample while geminal isomers as well as *cis*- and *trans*- isomers were observed in the second sample. The mono- **2**, geminal- **3a** and tri- **4** substituted phosphazene derivatives showed a 12-line resonance pattern consisting of a doublet of doublets for all the P atoms. **Trans^a-3b** and **trans^b-3c** have three stereogenic P-centers, exhibiting a total of 16 signals, and indicating that **trans^a-3b** and **trans^b-3c** are diastereoisomers (9). The nongeminal-**cis 3d** and tetra-substituted ferrocenylphosphazene **5** gave rise to one triplet and one doublet.

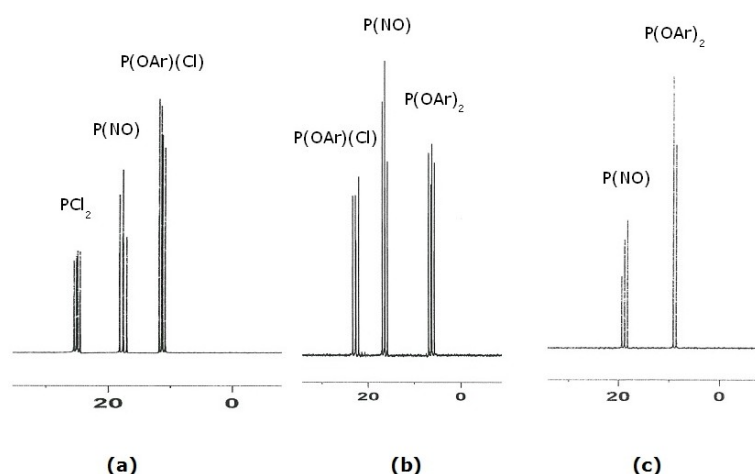


Figure 1. The $^{31}\text{P}\{^1\text{H}\}$ NMR spectra of mono- **2** (a), tri- **4** (b) and tetra- **5** (c) substituted phosphazenes, respectively.

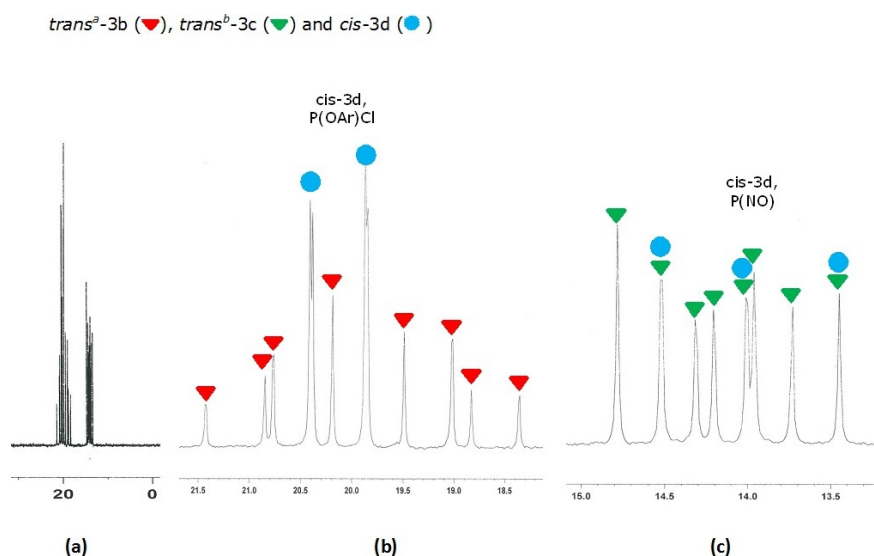


Figure 2. (a) The ^{31}P -NMR spectra of the mixture of **trans^a-3b**, **trans^b-3c** and **cis-3d**; (b) 21.5-18.0 ppm; (c) 15.0-13.0 ppm.

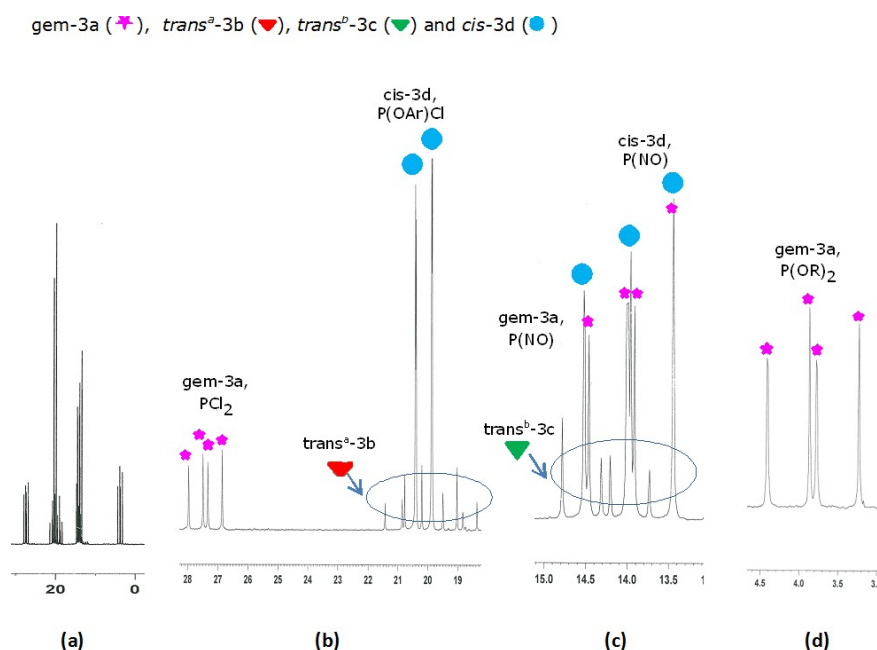
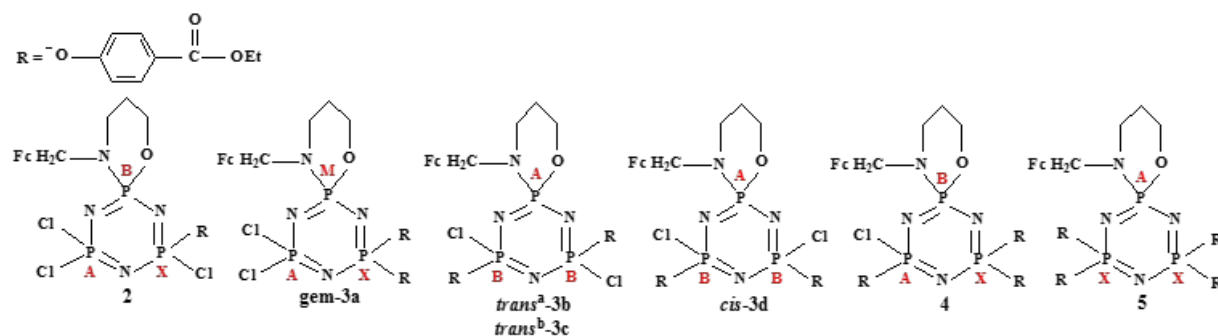


Figure 3. (a) The ^{31}P -NMR spectra of the mixture of **gem-3a**, **trans^a-3b**, **trans^b-3c** and **cis-3d**; (b) 28.0-18.0 ppm; (c) 15.0-13.0 ppm; (d) 4.5-3.5 ppm.

Table 1. The ^{31}P -NMR (decoupled) spectral data of mono- **2**, di- [geminal (**3a**); non-geminal (**trans^a-3b**, **trans^b-3c** and **cis-3d**)], tri- **4** and tetra- **5**. (Chemical shifts are reported in ppm and J values in Hz; ^{31}P -NMR measurements in CDCl_3 solutions at 293 K)



Compound	δ (ppm)				$^2J_{PP}$ (Hz)	Spin System
	PCl_2	$\text{P}(\text{NO})_{(\text{spiro})}$	$\text{P}(\text{OAr})$	$\text{P}(\text{OAr})(\text{Cl})$		
2	25.24 (dd)	17.65 (dd)	-	11.53 (dd)	72.9; 47.4; 66.8	ABX
gem-3a	27.41 (dd)	13.95 (dd)	3.83 (dd)	-	77.8; 65.6; 58.3	AMX
trans^a-3b	-	20.76	-	19.16	76.5	AB ₂
trans^b-3c	-	14.31	-	13.87	43.7	AB ₂
cis-3d	-	13.99 (t)	-	20.13 (d)	65.6	AB ₂
4	-	16.49 (dd)	6.38 (dd)	22.72 (dd)	85.1; 72.9; 65.6	ABX
5	-	18.78 (t)	8.58 (d)	-	69.3	AX ₂

The expected signals from the carbon atoms and hydrogen atoms were present in the ^{13}C and ^1H NMR spectra (**Table S1** and **S2**) of all the new compounds. The carbon peaks for the carbonyl (COCH_2CH_3) and phenyl groups in the ethyl benzoate groups were observed ranging from 165.84 to 165.70 ppm and from 154.51 to 120.75 ppm, respectively. Also, the carbon peaks for the ferrocenyl group were observed in a range from 82.47 to 67.15 ppm as expected. All the synthesized substituted phosphazenes have aliphatic protons that are diastereotopic, so the ^1H -NMR spectra of the new compounds are highly complex. When the ^1H -NMR spectra of the synthesized compounds were examined, three different peaks were observed for the H2, H3 and H4 protons of the ferrocenyl group at 3.92 to 4.31 ppm. The protons of H4 are equivalent and were observed as a single peak. The H6 protons belonging to the substituent were observed as quadrupole peaks at 4.25 to 4.44 ppm, and the H7 protons were observed as triple peaks at 1.35 to 1.44 ppm. The H2 and H3 protons of the aromatic rings were observed

in the range from 7.20 to 8.17 ppm.

The IR spectra of the new phosphazene derivatives displayed characteristic bands between 1200 and 1198 cm^{-1} and between 1174 and 1169 cm^{-1} . These vibration bands were attributed to the stretching frequencies (asymmetric and symmetric) of the P-N bonds in the phosphazene rings. At the same time the substitute ethyl p-hydroxybenzoate groups have characteristic IR absorbance peaks in the range from 1709 to 1716 cm^{-1} due to the stretching of the C=O bonds.

X-ray structures of compounds **2** and **5**

The molecular structures of **2** and **5**, with the atom numbering schemes, are shown in **Figure 4**. The crystallographic data are given in **Table S3**, and the selected bond lengths and angles are listed in **Table S4** for compounds **2** and **5**. The crystallographic analyses reveal that compounds **2** and **5** are very similar. Compound **2** crystallizes in the space group $P2_1/c$, while compound **5** crystallizes in the space group Pn.

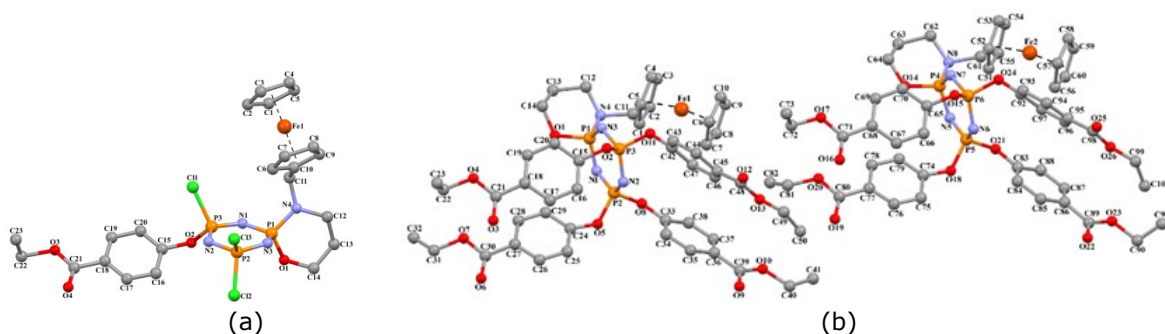


Figure 4. The molecular structures of **2** (a) and **5** (b) showing the atom numbering schemes.

In compound **2**, the phosphazene ring is in a flattened-boat conformation [$\varphi = -62.7(3)^\circ$ and $\theta = 60.2(3)^\circ$] having a total puckering amplitude QT of $0.180(1)\text{ \AA}$. In compound **5**, the values of the ring puckering parameters are $\varphi = 191(2)$ to $196(3)^\circ$, $\theta = 78.3(3)$ to $80.0(3)^\circ$ and QT = $0.121(5)$ to $0.114(5)\text{ \AA}$, indicating that each phosphazene ring has a chair conformation. The P1/O1/C12-C14/N4 ring was

in a chair conformation [$\varphi = 36.5(1)^\circ$ and $\theta = 89.6(1)^\circ$] having a total puckering amplitude QT of $0.659(2)\text{ \AA}$ in **2**, while in **5**, the values of the ring puckering parameters were $\varphi = 191(2)$ to $196(3)^\circ$, $\theta = 78.3(3)$ to $80.0(3)^\circ$ and QT = $0.121(4)$ to $0.114(5)\text{ \AA}$. In the phosphazene rings, the P-N bond lengths were in the range of $1.561(3)$ to $1.612(3)\text{ \AA}$ [average value is $1.582(3)\text{ \AA}$] (**Table S4**).

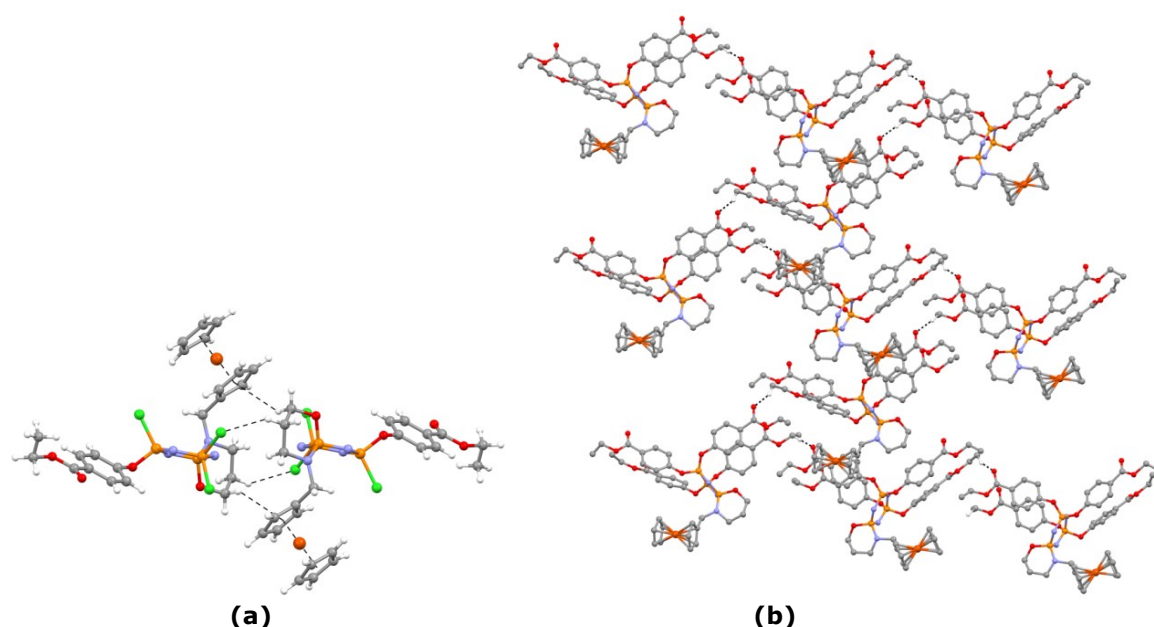


Figure 5. The C-H...Cl hydrogen bonds and C-H... π interactions in the compound **2** (a); **5b.** an infinite 1D supramolecular network in the compound **5** (b).

As shown in **Figure 5**, the C-H...Cl hydrogen bonds produced a centrosymmetric $R_2^2(14)$ ring in **2** (a), while the intermolecular C-H...O hydrogen bonds produced a 1D supramolecular network running parallel to the [101] direction in **5** (b). Compounds **2** and **5** also contain C-

H... π (**Table 2**) and π ... π interactions. Each π ... π contact between the ferrocenyl rings may stabilize the structure, with a center to center distance of 3.287(2) Å in **2** and 3.303(6) and 3.308(6) Å in **5**.

Table 2. The hydrogen bonds and C-H... π interactions parameters for compounds **2** and **5** (Å, °)

D-H...A	D-H	H...A	D...A	D-H...A
Compound 2				
C13-H13A...Cl3 ⁱ	0.99	2.77	3.649 (4)	148
C14-H14A...Cg(2) ⁱ	0.99	2.87	3.624	134
Compound 5				
C29-H29...N1	0.93	2.59	3.228 (11)	126
C50-H50B...O19	0.96	2.52	3.39 (2)	151
C72-H72A...O6 ⁱ	0.97	2.56	3.497 (19)	162
C79-H79...N5	0.93	2.58	3.221 (12)	126
C84-H84...N6	0.93	2.61	3.163 (11)	119
C13-H13A...Cg(1) ⁱ	0.97	2.92	3.661 (13)	134
C62-H62B...Cg(2) ⁱⁱ	0.97	2.93	3.710 (13)	138

Symmetry codes: (i) $-x+1, -y, -z+1$; Cg(2)=C6-C10 for **2**; (i) $x-1/2, -y, z+1/2$; (ii) $x-1/2, 1-y, z+1/2$; Cg(1)=C33-C38; Cg(2)=C83-C88 for **5**.

CONCLUSIONS

The Cl replacement reactions of monoferrocenylphosphazene **1**, which has four P-Cl bonds with ethyl benzoate, resulted in the formation of new cyclotriphosphazene derivatives: [mono- **2**, di- [geminal (**3a**); nongeminal (**trans^a-3b**, **trans^b-3c** and **cis-3d**)], tri- **4** and tetra- **5**]. The structures of these new compounds were characterized using elemental analyses, FTIR and NMR (¹H-, ¹³C-

and ³¹P-) techniques. The peaks observed in the ³¹P-NMR spectrum were evaluated by comparison with the results obtained in previous studies. The presence of geminal (**3a**), non-geminal (**trans^a-3b**, **trans^b-3c** and **cis-3d**) compounds was detected in the reaction mixtures. Furthermore, the molecular geometries of **2** (monosubstituted ferrocenylphosphazene) and **5** (tetrasubstituted ferrocenylphosphazene) were determined from the X-ray crystallography data.

REFERENCES

- Chandrasekhar V, Narayanan RS, Mamidala R, Venkatasubbaiah K. Phosphazenes. In *Organophosphorus Chemistry Volume 47*, Eds. Allen, DW, Loakes, D and Tebby, JC. Royal Society of Chemistry, Cambridge, UK; 2018, 363-424.
- Stewart FF. Phosphazenes. In *Organophosphorus Chemistry Volume 44*, Eds. : Allen DW, Loakes D, Tebby JC. Royal Society of Chemistry, Cambridge, UK; 2015, 397-430.
- Chandrasekhar V, Krishnan V. Advances in the chemistry of chloro-cyclophosphazenes. *Advances in Inorganic Chemistry*. 2002;53:159-211.
- Beşli S, Coles SJ, Coles LS, Davies DB, Kılıç A. Investigation of a spiro to ansa rearrangement with di-functional alcohols in cyclotriphosphazene derivatives. *Polyhedron*. 2012;43:176-84.
- Türe S. Phosphorus-nitrogen compounds: Reinvestigation of the reactions of hexachlorocyclotriphosphazene with 1,4-butane- and 1,6-hexane-diols—NMR studies of the products. *Phosphorus, Sulfur, and Silicon and the Related Elements*. 2016;191(8): 1174-82.
- Muralidharan K, Elias A. Preparation of the First Examples of Ansa-Spiro Substituted Fluorophosphazenes and Their Structural Studies: Analysis of C—H...F—P Weak Interactions in Substituted Fluorophosphazenes. *Inorg. Chem*. 2003;42:7535-43.
- Koran K, Tekin Ç, Biryant F, Tekin S, Sandal S, Görgülü AO. Synthesis, structural and thermal characterizations, dielectric properties and in vitro cytotoxic activities of new 2,2,4,4-tetra(4'-oxy-substituted-chalcone)-6,6-diphenylcyclotriphosphazene derivatives. *Medicinal Chemistry Research*. 2017;26(5):962-74.
- Tümer Y, Şehirli E, Yüksektepe Ataoğ Ç. Syntheses and Structural Characterizations of First Paraben Substituted Ferrocenyl Phosphazene Compounds. *JOTCSA*. 2017;4(1):299-312.
- Tümer Y, Koç LY, Asmafiliz N, Kılıç Z, Hökelek T, Soltanzade H, Açık L, Yola ML, Solak AO. Phosphorus-nitrogen compounds: Part 30. Syntheses and structural investigations, antimicrobial and cytotoxic activities and DNA interactions of vanillinato-substituted NN or NO spirocyclic monoferrocenyl cyclotriphosphazenes. *J. Biol. Inorg. Chem*. 2015;20:165-78.
- Kundu A, Hariharan PS, Prabakaran K, Anthony SP. Synthesis of new colori/ A fluorimetric chemosensor for selective sensing of biologically important Fe³⁺, Cu²⁺ and Zn²⁺ metal ions. *Spectrochimica Acta Part A: Molecular and Biomolecular Spectroscopy*. 2015;151:426-31.
- Yenilmez Çiftçi G, Şenkuytu E, Bulut M, Durmuş M. Novel Coumarin Substituted Water Soluble Cyclophosphazenes as "Turn-Off" Type Fluorescence Chemosensors for Detection of Fe³⁺ ions in Aqueous Media. *Journal of Fluorescence*. 2015;25:1819-30.
- Şenkuytu E. Novel Aminopyrene Substituted Monospiro/Dispiro Cyclotriphosphazenes: Synthesis, Characterization and Chemosensor Properties. *Celal Bayar University Journal of Science*. 2018;14(2):209-16.
- Sudhakar S, Sellinger A. Nanocomposite Dendrimers Based on Cyclic Phosphazene Cores: Amorphous Materials for Electroluminescent Devices. *Macromolecular Rapid Communications*. 2006;27(4):247-54.
- Bolink HJ, Santamaria GS, Sudhakar S, Zhenb C, Sellinger A. Solution processable phosphorescent dendrimers based on cyclic phosphazenes for use in organic light emitting diodes (OLEDs). *Chemical Communications*. 2008;5:618-20.
- Schrögel P, Hoping M, Kowalsky W, Hunze A, Wagenblast G, Lennartz C, Stohriegel P. Phosphazene-Based Host Materials for the Use in Blue Phosphorescent Organic Light-Emitting Diodes. *Chemistry of Materials*. 2011;23(22):4947-53.
- Soh SM, Santamaria SAG, Perez-Morales M, Bolink HJ, Sellinger A. Solution processable high band gap hosts based on carbazole functionalized cyclic phosphazene cores for application in organic light-emitting diodes. *Journal of Polymer Science Part B*. 2011;49(7):531-9.
- Wang L, Yang YX, Shi X, Mignani S, Caminade AM, Majoral JP. Cyclotriphosphazene core-based dendrimers for biomedical

applications: an update on recent advances. *Journal of Materials Chemistry B*. 2018;6:884-95.

18. Caminade AM, Hameauab A and Majoralab JP. The specific functionalization of cyclotriphosphazene for the synthesis of smart dendrimers. *Dalton Transactions*. 2016;5:1810-22.

19. Tümer Y, Asmafiliz N, Zeyrek CT, Kılıç Z, Açık L, Çelik SP, Türk M, Çağdaş Tunalı B, Ünver H, Hökelek T. Syntheses, spectroscopic and crystallographic characterizations of cis- and trans-dispirocyclic ferrocenylphosphazenes: molecular dockings, cytotoxic and antimicrobial activities. *New J. Chem*. 2018;42(3):1740-56.

20. Tümer Y, Asmafiliz N, Kılıç Z, Aydın B, Açık L, Hökelek T. Phosphorus-nitrogen compounds: Part 43. Syntheses, spectroscopic characterizations and antimicrobial activities of cis- and trans-N/O dispirocyclotriphosphazenes containing ferrocenyl pendant arms. *J. Mol. Struct*. 2018;1173:885-93.

21. Elmas G, Okumuş A, Cemaloğlu R, Kılıç Z, Çelik SP, Açık L, Tunalı BÇ, Türk M, Çerçi NA, Güzel R, Hökelek T. Phosphorus-nitrogen compounds. part 38. Syntheses, characterizations, cytotoxic, antituberculosis and antimicrobial activities and DNA interactions of spirocyclotetraphosphazenes with bis-ferrocenyl pendant arms. *Journal of Organometallic Chemistry*. 2017;853:93-106.

22. Asmafiliz N, Civan M, Uzunaliolu N, Özben A, Kılıç Z, Kayalak H, Açık L, Hökelek T. Phosphorus-nitrogen compounds. Part 41.

Ferrocenyl pendant-armed spirocyclopiperidinocyclotriphosphazatrienes; Langmuir-Blodgett thin films and biological activity studies. *J. Chem. Sci*. 2018;130:152.

23. Asmafiliz N, Kılıç Z, Civan M, Avcı O, Gönder LY, Açık L, Aydın B, Türk M and Hökelek T. Phosphorus-nitrogen compounds. Part 36. Syntheses, Langmuir-Blodgett thin films and biological activities of spiro-bino-spiro trimeric phosphazenes. *New J. Chem*. 2016;40:9609-26.

24. Asmafiliz N, Kılıç Z, Öztürk A, Hökelek T, Koç LY, Açık L, Kısa Ö, Albay A, Üstündağ Z, Solak AO. Phosphorus-Nitrogen Compounds : Part 18. Syntheses, Stereogenic Properties, Structural and Electrochemical Investigations, Biological Activities and DNA Interactions of New Mono- and Bis-Ferrocenyl Spirocyclic Phosphazene Derivatives. *Inorg. Chem*. 2009;48:10102-16.

25. Çayırbaşı M. Etil p-hidroksibenzoat süstitüe ferrosenilfosfazen türevlerinin sentezi ve yapılarının aydınlatılması, [Yüksek Lisans Tezi]. [Karabük]: Karabük Üniversitesi; 2013.

26. Sheldrick GM, *Acta Cryst*. 2008; A64: 112.

27. Sheldrick GM, *Acta Cryst*. 2015; C71: 3.

28. APEX2, Bruker AXS Inc. Madison Wisconsin USA. 2013.

29. Mercury, version 3.3; CCDC, available online via cdc.cam.ac.uk/products/mercury.

30. Farrugia LJ, *J. Apply. Cryst*. 1999; 32: 837.



The Synthesis of New Phosphazene-Bearing Ethyl p-Hydroxybenzoate and Ferrocenyl Pendant Groups and their Spectroscopic and Crystallographic Characterizations

Yasemin Tümer^{1*}  , **Mahmut Çayırbaşı¹**  , **Onur Şahin²**  ,
Tuncer Hökelek³  

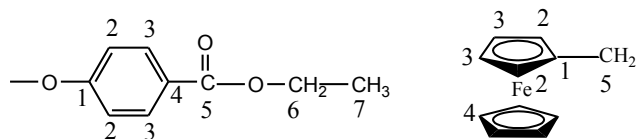
¹Department of Chemistry, Karabük University, 78050 Karabük, Turkey.

²Scientific and Technological Research Application and Research Center, Sinop University, 57000 Sinop, Turkey.

³Department of Physics, Hacettepe University, 06800 Ankara, Turkey.

Supplementary Materials

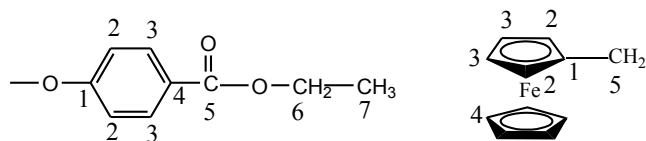
Table S1 ^{13}C NMR (decoupled) spectral data for **2**, *gem*-**3a**, *trans*^a-**3b**, *trans*^b-**3c**, *cis*-**3d**, **4** and **5** [Chemical shifts (δ) reported in ppm and *J* values in Hz].



	N-CH ₂ -CH ₂ -			Fc-CH ₂ carbon atoms					Substituent carbon atoms						
	<u>CH₂</u> -	<u>CH₂</u> - <u>CH₂</u> -	<u>CH₂</u> -	C5	C4	C3	C2	C1	C7	C6	C5	C4	C3	C2	C1
2	25.77(d)	45.10	68.42(d)	47.20(d)	68.66	67.85	69.98(d)	81.90(d)	14.34	61.17	165.72	131.47	128.28(d)	121.32(d)	153.39(d)
	³ J _{PC} =4.5		² J _{PC} =7.5	² J _{PC} =3.0			⁴ J _{PC} =13.5	³ J _{PC} =9.8					⁴ J _{PC} =2.3	³ J _{PC} =5.3	² J _{PC} =9.8
gem-3a	25.79	44.96	68.54	46.88	68.02	67.71	69.60	82.26	14.33	61.19	165.84	131.43	127.93	121.16(d)	153.96(d)
													127.74	³ J _{PC} =4.5	² J _{PC} =7.5
													125.53		153.69
															² J _{PC} =6.0
trans^a-3b.	29.71	45.06	69.66	47.11	68.66	67.65	70.07	82.16	14.33	61.16	165.70	131.38	128.08	121.62	153.59
trans^b-3c															
and cis-3d	25.85				68.57		69.90							121.56	
					68.47									121.41	
					68.37									121.34	
					68.12									121.17	
4	25.90	44.89	67.91	46.73	68.53	67.35	69.93	82.47	14.33	61.16	165.74	131.35	127.85(d)	121.52(d)	153.74(d)
					68.44	67.26	69.61	82.32		61.10		131.28	⁴ J _{PC} =1.5	³ J _{PC} =4.5	² J _{PC} =9.8
										61.08			127.77(d)	121.12(d)	154.07(d)
													⁴ J _{PC} =1.5	³ J _{PC} =5.3	² J _{PC} =7.5

													127.47	120.86(d)	
														³ J _{PC} =5.3	
5	25.99	44.98	68.11	46.77	68.46	67.15	69.48	82.30	14.33	61.14	165.80	131.33	127.35	120.82(dd)	154.51(dd)
										61.04	165.74	131.17	127.33	³ J _{PC} =6.0	² J _{PC} =7.5
														120.75(dd)	154.13(dd)
														³ J _{PC} =5.3	² J _{PC} =7.5

Table S2 ¹H-NMR spectral data for 2, gem-3a, *trans*^a-3b, *trans*^b-3c, *cis*-3d, 4 and 5. [s: singlet, d: doublet, t: triplet, m: multiplet and bp: broad peak].



	N-CH ₂ - CH ₂ -	N-CH ₂ - CH ₂ -	O-CH ₂ - CH ₂ -	Fc-CH ₂ hydrogen atoms				Substituent hydrogen atoms			
				H5	H4	H3	H2	H2	H3	H6	H7
2	1.92	3.08	4.15	3.89 (m)	4.14	4.29	4.31	7.40	8.10	4.40 (d)	1.42 (t)
	2H	2H	2H	2H	5H	2H	2H	2H	2H	2H	3H
										³ J _{HH} =7.2	³ J _{HH} =7.2
<i>trans</i>^a-3b, <i>trans</i>^b-3c and <i>cis</i>-3d	1.88	3.05	4.05	3.92	4.14	4.25	4.30	7.29-7.46	8.05-8.15	4.25-4.44	1.37-1.45
	2H	2H	2H	2H	5H	2H	2H	4H	4H	4H	6H
<i>trans</i>^a-3b, <i>trans</i>^b-3c, gem-3a and <i>cis</i>-3d	1.88	3.04	4.01	3.71	4.13	4.21	4.31	7.28-7.47	8.03-8.17	4.34-4.43	1.35-1.45
	2H	2H	2H	2H	5H	2H	2H	4H	4H	4H	6H
4								7.45	8.14(d)		
	1.84 (bp)	2.99 (bp)	3.75	3.32	4.02	4.07	4.19	2H	2H		
	2H	2H	2H	2H	5H	2H	2H	³ J _{HH} =8.7	³ J _{HH} =9.6	4.33-4.42	1.35-1.44
								7.24	9.00	(m) 6H	(m) 9H
								4H	4H		
								³ J _{HH} =9.3	³ J _{HH} =4.8		
5	1.81(bp)	2.98 (m)	4.18 (m)	3.40 (d)	3.92	4.03	4.03	7.36 (d)	8.07 (d)	4.382 (d)	1.42 (t)
	2H	2H	2H	2H	5H	2H	2H	4H	4H	4H	6H

$^3J_{PH} = 8.8$

$^3J_{HH} = 8.7$

$^3J_{HH} = 8.7$

$^3J_{HH} = 7.2$

$^3J_{HH} = 7.2$

7.14 (d)

7.93 (d)

4.382 (d)

1.38 (t)

4H

4H

4H

6H

$^3J_{HH} = 9.0$

$^3J_{HH} = 8.7$

$^3J_{HH} = 7.2$

$^3J_{HH} = 7.2$

Crystallographic data for the structural analysis have been deposited with the Cambridge Crystallographic Data Centre, CCDC No. 1816268 for **2** and 1816269 for **5**. Copies of this information may be obtained free of charge from the Director, CCDC, 12 Union Road, Cambridge CB2 1EZ, UK (fax: +44-1223-336033; e-mail: deposit@ccdc.cam.ac.uk or [www: http://www.ccdc.cam.ac.uk](http://www.ccdc.cam.ac.uk)).

Table S3 Crystal data and structure refinement parameters for compounds **2** and **5**.

Crystal data	2	5
Empirical formula	C ₂₃ H ₂₆ Cl ₃ FeN ₄ O ₄ P ₃	C ₅₀ H ₅₃ FeN ₄ O ₁₃ P ₃
Formula weight	677.59	1066.72
Crystal system	Monoclinic	Monoclinic
Space group	P2 ₁ /c	Pn
<i>a</i> (Å)	13.8402 (2)	11.9429 (12)
<i>b</i> (Å)	18.8222 (2)	31.543 (3)
<i>c</i> (Å)	10.7335 (3)	13.6725 (13)
β (°)	97.377 (1)	90.535 (4)
<i>V</i> (Å ³)	2772.97 (9)	5150.5 (9)
<i>Z</i>	4	4
<i>D_c</i> (g cm ⁻³)	1.623	1.376
θ range (°)	2.2-28.1	3.0-26.4
μ (mm ⁻¹)	1.05	0.45
Measured refls.	29809	19462
Independent refls.	6882	14820
<i>R</i> _{int}	0.036	0.065
<i>S</i>	1.04	1.16
<i>R</i> ₁ / <i>wR</i> ₂	0.049/0.122	0.071/0.158
$\Delta\rho_{\max}/\Delta\rho_{\min}$ (eÅ ⁻³)	1.60/-1.04	0.55/-0.60

Table S4 Selected bond distances and angles for compounds **2** and **5** (Å, °)

Compound 2			
P1-O1	1.573(2)	P1-N1	1.591(2)
P1-N3	1.612(3)	P1-N4	1.632(2)
P2-N1	1.568(2)	P2-N2	1.586(3)
P3-N3	1.561(3)	P3-N2	1.576(3)
N1-P1-N3	114.99(13)	O1-P1-N4	103.76(12)
N1-P2-N2	120.15(13)	N3-P3-N2	119.33(14)
Compound 5			
N2-P2	1.581(7)	N2-P1	1.580(7)
N3-P3	1.578(7)	N3-P2	1.584(7)
N4-P3	1.573(7)	N4-P1	1.598(7)
N6-P5	1.572(7)	N6-P4	1.594(7)
N7-P5	1.573(7)	N7-P6	1.593(7)
N8-P6	1.580(7)	N8-P4	1.598(8)
N2-P1-N4	116.6(4)	O1-P1-N1	103.7(3)
N2-P2-N3	118.6(4)	N4-P3-N3	118.0(4)
N6-P4-N8	115.7(4)	O14-P4-N5	103.6(3)
N6-P5-N7	118.7(4)	N8-P6-N7	118.7(4)



The Effect of Polymer Capping Group to the Electrocatalytic Water Oxidation Activities of Prussian Blue Analogues

Emine ÜLKER*  

Recep Tayyip Erdogan University, Faculty of Arts & Sciences, Department of Chemistry, 53100, Rize, Turkey.

Abstract: Prussian Blue (PB) nanoparticles can be obtained by reacting the hexacyanometal center with metal ions in the existence of polymers such as polyethyleneglycol (PEG). In this study, a pentacyanometal complex, $[\text{Fe}(\text{CN})_5\text{NO}]^{2-}$, was used in addition to hexacyanometal ion, $[\text{Fe}(\text{CN})_6]^{3-}$, to obtain nanoparticles coated with PEG. PB nanoparticles have been prepared, characterized, and comprehensive electrochemical studies were performed to investigate their performance for water oxidation electrocatalysis. The effect the ratio of PEG to the morphology and the water oxidation electrocatalytic performance have also been interrogated. Overall, the study clearly indicates that Co-FeNO@PEG with 1:10 and 1:25 Co:PEG rate show the best electrocatalytic activity with an overpotential of 472 and 489 mV for current density of 1 mA cm^{-2} , respectively.

Keywords: Prussian blue, Polyethyleneglycol, Cyanide, Water oxidation, Electrocatalysis.

Submitted: April 15, 2019. **Accepted:** December 09, 2019.

Cite this: Ülker E. The Effect of Polymer Capping Group to the Electrocatalytic Water Oxidation Activities of Prussian Blue Analogues. JOTCSA. 2020;7(1):225–32.

DOI: <https://doi.org/10.18596/jotcsa.554229>.

***Corresponding author. E-mail:** emine.kapancik@erdogan.edu.tr . **Tel:** +90 (464) 223 6126.

INTRODUCTION

Due to the increasing energy demand and environmental problems based on using fossil fuels, it has been necessary to find alternative energy resources (1). Water splitting is one of the cheap and promising ways to provide environmentally friendly future energy needs (2). There occurs two half reactions: water oxidation (oxygen evolution reaction (OER)) and water reduction (hydrogen evolution reaction (HER)). The OER ($2\text{H}_2\text{O} \rightarrow 4\text{H}^+ + 4\text{e}^- + \text{O}_2$) is considerably more complex and the rate-limiting step because it requires a 4e^- process. Hence, the robust, efficient and low-cost water oxidation catalysts (WOCs) are necessary to oxidize water with low kinetic overpotential (3).

Although metal oxides such as IrO_2 and RuO_2 have excellent catalytic activity for OER, their scarcity

and high-cost limit the usability for large-scale applications (4). Therefore, various materials including non-noble 3d metal ions such as metal oxides (5–7), Prussian Blue derivatives (8,9), perovskite structures (10,11) and amorphous materials (12,13) have also been investigated for WOCs with competing activities those of noble-metal catalysts. Because of the high catalytic activities, cobalt oxides stand out among them. However, they are inefficient at neutral or unstable at acidic medium. Furthermore, it is difficult to determine correlation of the catalytic activities with structure due to their amorphous nature (8).

In 2008, Kanan et al. reported that cobalt phosphate (Co-Pi) film easily prepared by electrodeposition of Co^{2+} salts in neutral water containing phosphate as a new area of exploration for non-noble catalysts that oxidize water (14). After this research, many studies have been focus

on Co-Pi catalysts (15–17).

Prussian Blue (PB) structure is a mixed valence iron hexacyanoferrate with a face-centered cubic structure (FCC) that is two different iron centers as Fe^{2+} and Fe^{3+} and CN^- groups that bridge them. Prussian Blue and its analogues draw attention because of their porous structure. Cobalt hexacyanoferrate, members of the well-known Prussian Blue analogue (PBA) family, was coated on fluoride-doped tin oxide (FTO) electrode by electrochemical method and investigated as WOCs by Galán-Mascarós et al (9). This study shows that PBA extraordinary candidates for electrocatalytic WOCs due to their high electrocatalytic activities, robustness, and durability at neutral pH and an alternative to cobalt oxide matrices. Galán-Mascarós et al. also prepared thin films of PBAs with a new synthetic method, which involves chemical etching of cobalt oxides with a hexacyanoferrate solution. This new method provided an impressive improvement on the stability of the electrode and the electrocatalytic performance in a wide pH value(18). Karadas et al. have been investigated electrocatalytic activity of a group of cobalt hexacyanometallates, (CoHCMs) including various $\text{M}(\text{CN})_6$ units ($\text{M}=\text{Co}^{3+}$, Cr^{3+} and $\text{Fe}^{2+/3+}$), and impact of the metal and its oxidation state in the $\text{M}(\text{CN})_6$ unit on the catalytic efficiencies of PBAs (8). In addition, Karadas shows the cobalt hexacyanocobaltate, as an ideal composition of metal hexacyanocobaltates, exhibits the highest electrocatalytic activity toward the OER (19).

In this study, it is aimed to obtain PB nanoparticles' presences of polyethylene glycol (PEG) as stabilizing agent. The synthesis and characterization of PB nanoparticles@PEG hybrid compounds are presented. Cyclic voltammetric and chronoamperometric studies were performed with catalyst-coated FTO electrode in phosphate buffer (KPi) solution (pH 7). Also, effect of PEG amount on electrocatalytic water oxidation activity was investigated.

EXPERIMENTAL SECTION

Chemicals

All chemicals, including $\text{Co}(\text{CH}_3\text{COO})_2 \cdot 4\text{H}_2\text{O}$, $\text{K}_4[\text{Fe}(\text{CN})_6] \cdot 3\text{H}_2\text{O}$, $\text{Na}_2[\text{Fe}(\text{CN})_5\text{NO}]$, PEG (used molecular weight of PEG8000), KH_2PO_4 (>99.0%), K_2HPO_4 (>99.0%), orthophosphoric acid (H_3PO_4 , 85%), KOH, fluoride-doped tin oxide, and solvents were supplied from Sigma or Merck and used without purification.

Instrumentation

XRD studies were performed by PanAnalytical X'PertPro multipurpose X-ray diffractometer (MPD) operating $\text{CuK}\alpha$ radiation ($\lambda=1.5418 \text{ \AA}$). FTIR spectra were performed with a Bruker Alpha

Platinum-ATR spectrometer over the wavenumber range $4000\text{--}400 \text{ cm}^{-1}$. Dynamic light scattering (DLS) measurements were performed with a photon correlation spectroscopy using a Malvern Nano ZS ZEN3600 (Malvern Instruments Inc.) at a fixed scattering angle of 173° to specify the particle sizes of samples. A transmission electron microscope (TEM, Tecnai G2-F30, FEI) was performed at 200 kV. All electrochemical measurements were carried out by Gamry Instrument Interface 1000 Potentiostat/Galvanostat with a conventional three-electrode electrochemical cell used with Ag/AgCl electrode (satd. KCl) as the reference electrode, Pt as a counter electrode, and catalyst loaded fluoride-doped tin oxide (FTO) as a working electrode. All potentials were reported versus Ag/AgCl reference electrode.

Instrumentation

FTO electrodes were obtained from Sigma-Aldrich (with $1 \times 2 \text{ cm}$, 2 mm slides with $7 \Omega/\text{sq}^{-1}$ surface resistivity and $\sim 80\%$ transmittance). Electrodes were cleaned by sonication for 10 minutes in basic soapy solution, deionized water and isopropanol, respectively. Then they were annealed at $400 \text{ }^\circ\text{C}$ for 30 minutes. Catalyst-modified electrodes were prepared by drop-casting method. A mixture of 5 mg of PBA catalyst, 500 μL of DMF, 500 μL of water, and 100 μL of Nafion solution were mixed and sonicated for 30 minutes. After making a stable suspension, 50 μL of it was taken and dropped onto the mixture by covering 1 cm^2 of the FTO electrode. Electrodes were then dried at room temperature for 10 min followed by $80 \text{ }^\circ\text{C}$ for 10 min in an oven. They were then left in desiccator until further use for electrochemical experiments and characterization.

Electrochemical Methods

Cyclic voltammograms (CV) were recorded with a scan rate of 50 mV s^{-1} in potassium phosphate buffer (KPi) solution with 1M KNO_3 between 0 V and 1.5 V vs Ag/AgCl reference electrode. Surface concentration of active metal site was determined by CV taken in the region of $\text{Co}^{2+/3+}$ redox couple with different scan rates. Bulk water electrolysis was performed with a two compartment cell with separation of a glass frit. The electrolysis and steady state chronoamperometric experiments were performed in KPi buffer solution containing 1 M KNO_3 as a supporting electrolyte and the potential was increased with 0.02 V increments to obtain a Tafel plot. Tafel data were collected using equilibrium current density after 600 s at applied potentials. All experiments were performed under nitrogen atmosphere.

Potassium phosphate buffers (0.05 M KPi, pH 7.0) including 1 M KNO_3 were prepared using K_2HPO_4 , KH_2PO_4 , KNO_3 , and deionized water and then set by adding H_3PO_4 or KOH to the desired pH. The

solution was prepared with Millipore Milli-Q deionized water with a resistivity of 18.2 MΩ cm.

RESULTS AND DISCUSSION

Synthesis of Prussian Blue Nanoparticles with PEG

$K_4[Fe(CN)_6] \cdot 3H_2O$ and $[Fe(CN)_5NO]$ were used as initiators in the presence of $Co(CH_3COO)_2 \cdot 4H_2O$. The existence of a stabilizing agent prevents the growth of an unlimited number of three-dimensional cyano-bridged coordination polymer networks by providing the formation of metal ions on the surface and stable colloidal (20). Therefore, the particle size was controlled by using PEG as a stabilizing agent of molecular weight of PEG8000. PEG was added to both of two aqueous precursor solutions separately. These two solutions were mixed with each other dropwise until a solid form formation was observed and centrifuged at 9000 rpm for 25 minutes (Figure 1).

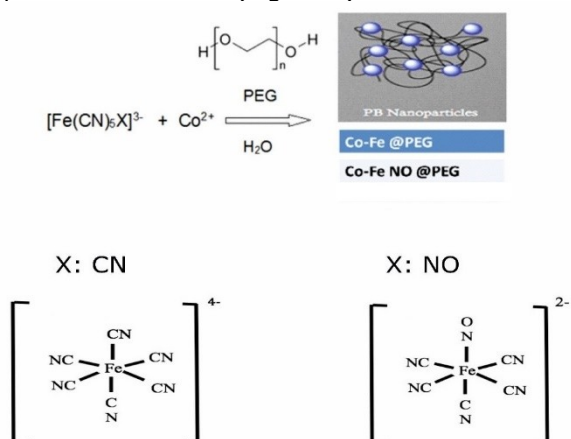


Figure 1. Schematic representation of PBn@PEG formation.

The liquid layer is taken and modest amount of solution pulled away in order to use for DLS measurements. Acetone was added to separate the nano-sized products and stored at 4 °C for a day. Table 1 shows the experimental condition to obtain the structures.

Table 1. Experimental condition to obtain the structures.

Sample	Co/PEG Ratio
Co-Fe@PEG	1/10
Co-Fe@PEG	1/25
Co-FeNO@PEG	1/10
Co-FeNO@PEG	1/25

¹Co/Fe ratio is 1/1. +
²[Co²⁺] / M = 10⁻²

Synthesis of Prussian Blue Nanoparticles with PEG

Powder XRD studies were performed on powder

samples of derivatives to investigate their crystalline nature. XRD patterns displayed in Figure 2 clearly indicate that all samples adopt identical Prussian Blue nanoparticle structure (20–22).

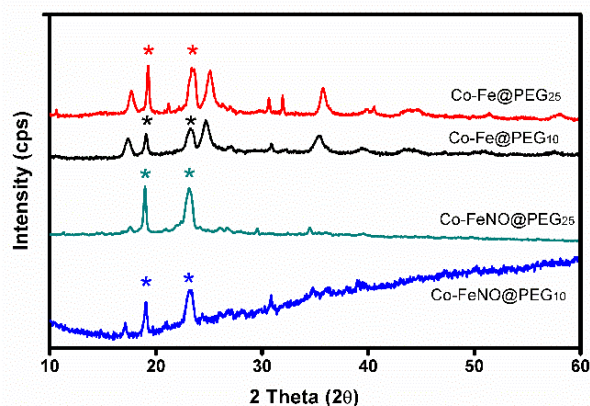


Figure 2. XRD patterns for samples.

PBAs structures exhibit characteristic bands related with PB- structure systems in infrared spectrum: i) HOH bending and OH stretching are observed as a sharp band at around 1610 cm⁻¹ and a broad band at 3200–3500 cm⁻¹ respectively. ii) CN stretching is observed as a sharp band at around 2000-2200 cm⁻¹. Therefore, FTIR is one of the reliable techniques for the characterization of PBAs. FTIR spectra of each sample exhibit sharp peak at around 2080 cm⁻¹ attributed to CN stretching. Also, each compound has a sharp stretch at around 1580 cm⁻¹ and a broad one at 3400 cm⁻¹, which correspond to H-OH bending and O-H stretch, respectively (Figure 3).

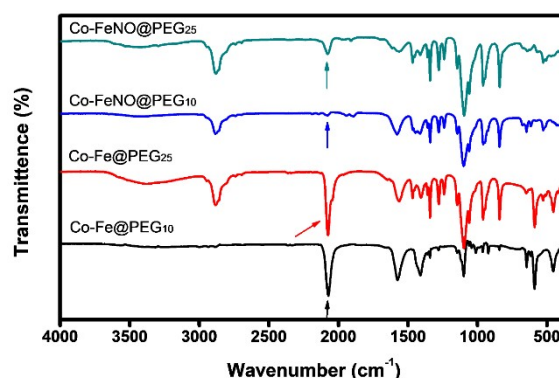


Figure 3. FTIR spectra of the samples.

Dynamic light scattering (DLS) measurements were carried out to specify particle size of Co-Fe@PEG and Co-FeNO@PEG. According to DLS measurements, uniform distribution was observed in the sample and it indicates the formation of particles with diameters of around 15 nm (Figure 4). Transmission Electron Microscopy (TEM) measurements were also performed to determine the size and morphology of the nanoparticles

(Figure 5). The mean particle size for both samples consistent with DLS measurements. was approximately obtained 20 nm. This result is

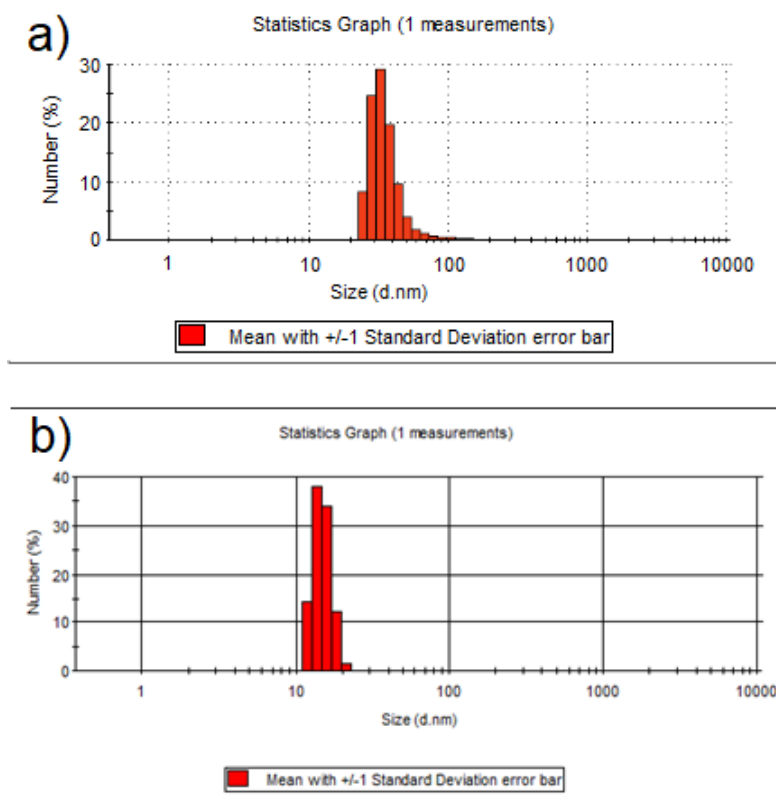


Figure 4. DLS diagrams of a) Co-Fe@PEG b) Co-FeNO@PEG

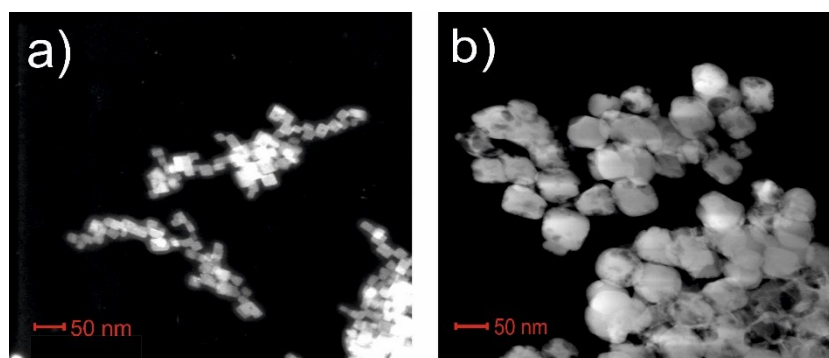


Figure 5. TEM images of a) Co-Fe@PEG and b) Co-FeNO@PEG

Electrochemical Studies

Electrochemical properties of FTO (PBn@FTO) electrodes coated with Prussian Blue nanoparticles are investigated by cyclic voltammetry (CV) performed in KPi solution (pH 7) containing 1 M KNO₃ as an electrolyte in the range of 0–1.5 V vs. Ag/AgCl reference electrode at a scan rate of 50 mV s⁻¹ (Figure 6). All catalysts show the higher irreversible peak attributed to water oxidation process than blank FTO electrode. According to Figure 6a, Co-FeNO@PEG (1:10) exhibits the

lowest overpotential, highest current density and thus the highest catalytic activity, among all.

It is also observed that the overpotential value for water oxidation process shifted to more negative regions with the addition of PEG. Figure 6b shows the effect of PEG amount on Co-FeNO catalyst. Co:PEG rate of 1:25 exhibits the best catalytic activity towards the water oxidation.

Both structures exhibit quasi-reversible peaks at around ~ 0.9 V (vs Ag/AgCl), which is attributed to

the $\text{Co}^{2+}/^{3+}$ redox process. Redox-active metal concentration on electrode surface was detected by CV performed with various scan rates in the region of $\text{Co}^{2+}/^{3+}$ redox couple (19,23). The surface concentrations (Γ) of Co-FeNO@PEG_{10} and Co-FeNO@PEG_{25} were obtained from the slope of current density (j) vs. scan rate plots according to Equation 1:

$$\text{slope} = \frac{n^2 F^2 A \Gamma}{4 R T} \quad (\text{Eq. 1})$$

where n is the number of electrons involved in the redox process, F is the Faraday constant, A is the electrode area, Γ is the electroactive surface concentration, R is the gas constant and T is the temperature. For calculated surface concentration, CVs at different scan rates were recorded at potential ranges of 0.4 V-1.1 V (vs. Ag/AgCl). electroactive surface concentration of Co-FeNO@PEG_{10} and Co-FeNO@PEG_{25} were calculated as 7.8 and 9.3 nmol cm^{-2} (Figure 7). This result suggests that surface concentration of redox-active metal increased with the increase in the amount of PEG.

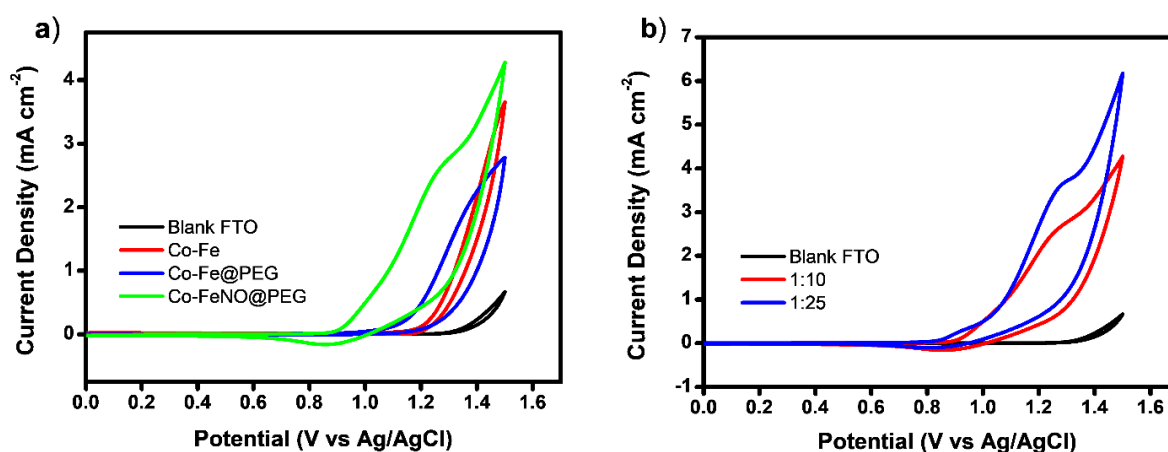


Figure 6. a) CV comparison of PEG modified FTO electrodes at pH 7.0 with a 50 mV s^{-1} scan rate; b) CV of the Co-FeNO@PEG_{10} (red line), Co-FeNO@PEG_{25} (blue line) in the same conditions.

The catalytic activity of the catalysts toward the OER is investigated by corresponding Tafel plots ($\log j-\eta$) obtained chronoamperometric measurements. The experiments were performed in 50 mM KPi solution with 1 M KNO_3 as supporting electrolyte, at pH 7, and the potential was increased with 0.02 V increments to obtain a Tafel slope for each catalysts (Figure 8). A linear trend was obtained in the 280–400 mV region. Tafel slope of Co-FeNO@PEG_{10} and Co-FeNO@PEG_{25}

were found to be 96 and 95 mV dec^{-1} , respectively. The similarity in Tafel slopes indicate that the mechanism of water oxidation with these electrodes are similar, however, it is difficult to determine which pathway occurs for the reaction from this analysis. The slopes are similar with previously reported Prussian Blue catalysts (8,9,19), metal dicyanamides [Mdc_2] (24), cobalt-sulfide catalyst (25), while it is higher than CoPi catalyst film (26).

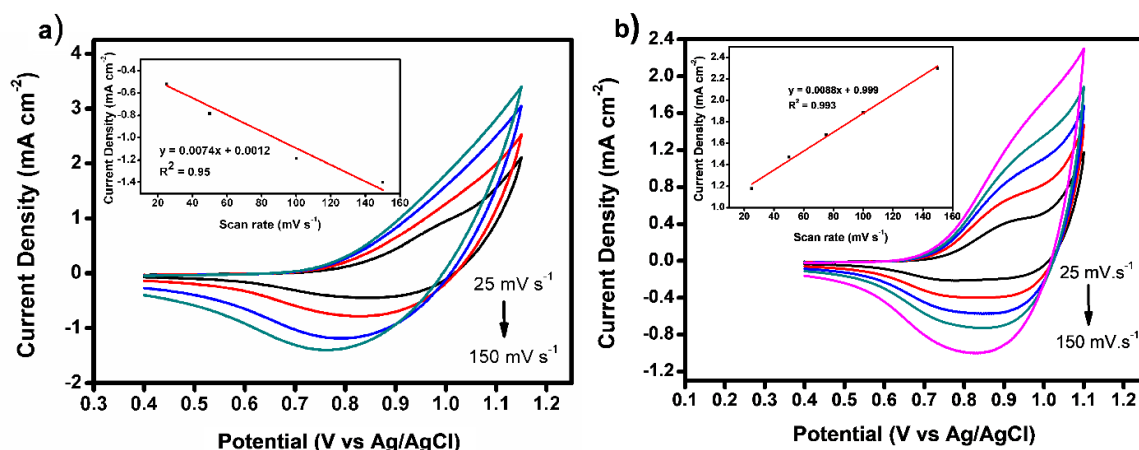


Figure 7. Cyclic voltammograms of a) Co-FeNO@PEG10 and b) Co-FeNO@PEG25 coated FTO electrodes at different scan rates in 50 mM KPi solution containing 1 M KNO₃, pH 7; inset shows the linear trend between the scan rate and the Co²⁺/³⁺ peak current density.

Catalytic current densities of 55 $\mu\text{A cm}^{-2}$ (η_{onset}) and 1 mA cm^{-2} ($\eta_{1\text{mA}}$) for Co-FeNO@PEG₁₀ and Co-FeNO@PEG₂₅ were calculated from Tafel linearity as 351, 369, 472 and 489 mV. Onset overpotentials are similar with [CoFe(CN)₅-PVP@FTO; 360 mV] (27) and other Co-based catalysts (η : 310 mV for Co(PO₃)₂, η : 434 mV for Co₃O₄, and η : 480 mV for CoNCN) (26,28,29). The catalytic onset overpotentials of Co-FeNO@PEG₁₀ and Co-FeNO@PEG₂₅ are also lower than previous reported [Fe-Co]-coated FTO electrode (η : 475 mV)(19). In addition, catalysts require lower overpotential for 1 mA cm^{-2} than previous reported Prussian Blue catalysts of [CoFe(CN)₆@FTO; η > 600 mV] (9), [Co-Co]@ FTO (η : 531 mV), [Co_{0.9}Fe_{0.1}-Co]@ FTO (η : 569 mV), [Co_{0.5}Fe_{0.5}-Co]@ FTO (η : 591 mV), [Fe-Co]@ FTO (η : 730 mV) (19) and [CoFe(CN)₅-PVP@ FTO; η : 510 mV] (27) fundamentally as a result of the change in the number of active metal sites on electrode surface.

chronoamperometric measurement were plotted versus overpotential (Figure 9). TOF of $2 \times 10^{-3} \text{ s}^{-1}$ can be reached at overpotentials of 251 and 287 mV, respectively. These values are lower than reported for CoFe(CN)₆@FTO (η = 300)(9) and Co-Pi catalysts (η = 410)(16), as a result of the surface concentration.

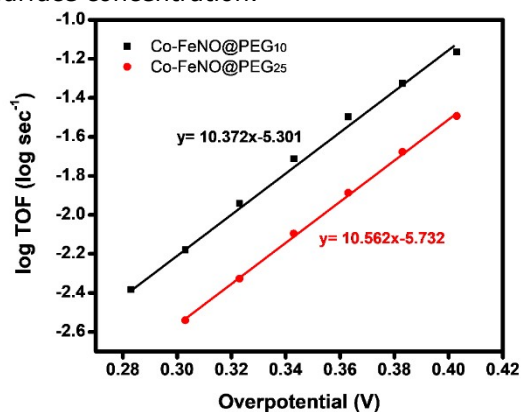


Figure 9. log TOF vs. overpotential plots for Co-FeNO@PEG₁₀ and Co-FeNO@PEG₂₅ extracted from Tafel plots at pH 7.

To determine the long-term stability of Co-FeNO@PEG₁₀ and Co-FeNO@PEG₂₅ coated FTO electrodes, chronoamperometric measurement was carried out at 1.2 V for 16 hours at pH 7 (Figure 10). The current density increased for the first 2 hours over Co-FeNO@PEG₁₀ coated FTO electrode and remained constant at 0.3 mA cm^{-2} during the electrolysis. A beginning increase in the current density can be assigned to morphological changes on the electrode surface like those of previously reported Cu-based catalysts (30,31). Over Co-FeNO@PEG₂₅ coated FTO electrode, the current density decreases gradually with time and it stable at 0.2 mA cm^{-1} during the electrolysis. This observation is similar to previous reported Prussian Blue catalysts (9,19).

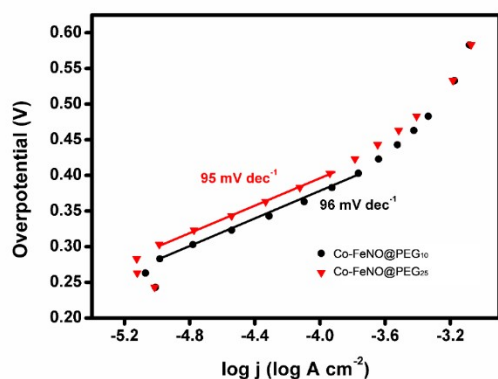


Figure 8. Tafel plots for Co-FeNO@PEG₁₀ and Co-FeNO@PEG₂₅ coated FTO electrode at pH 7.

To further evaluate the catalytic activity of Co-FeNO@PEG₁₀ and Co-FeNO@PEG₂₅, turnover frequency (TOF) values calculated using surface concentration and current density obtained from

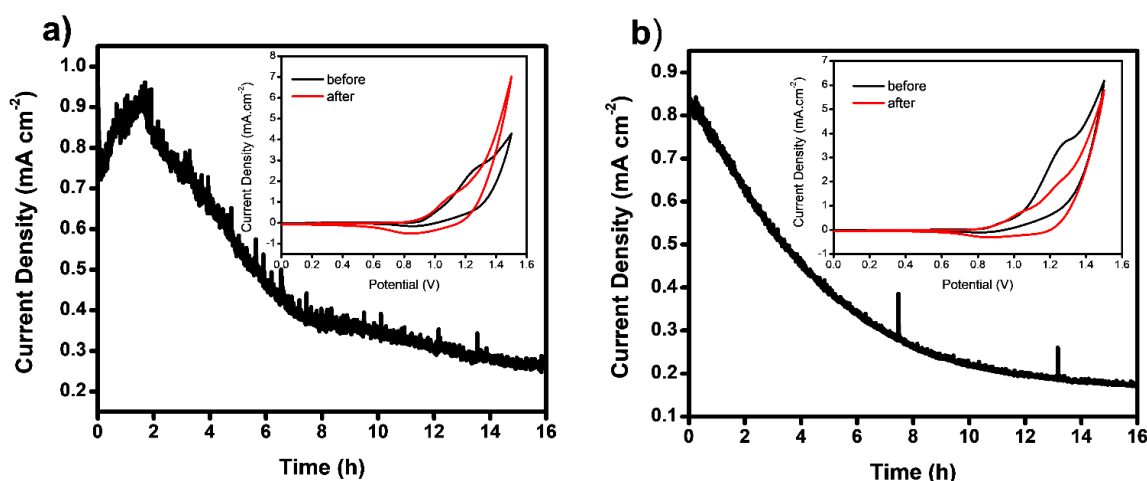


Figure 10. Long-term studies of electrolysis for a) Co-FeNO@PEG10 and b) Co-FeNO@PEG25 coated FTO electrode performed at 1.2 V (vs Ag/AgCl) at pH 7.0. The insets display the CVs obtained pristine and post-catalytic electrode.

In addition, the long-term stability of the catalysts was assessed by comparison of CVs performed before and after 16 hours of electrolysis (Figure 10, inset). An increment in the current density was obtained in the voltammogram of Co-FeNO@PEG₁₀ performed after electrolysis, which is consistent with the chronoamperometric measurement. The similarity in the cyclic voltammetric profiles obtained before and after chronoamperometric experiments also supports the stability of both catalysts.

CONCLUSION

Prussian Blue nanoparticles have been synthesized in the presence of PEG as a stabilizing agent, which were used for electrocatalytic water oxidation studies. The effect of the ratio of PEG and the type of cyanide precursor to the electrocatalytic activity were investigated. It is known that the crystallinity of the PB structure decreases formed penta-cyanometal complexes by removing the one CN group from the PB structure, and thus a significant increase in the surface concentration of Co sites. It is observed that the overpotential value for water oxidation process shifted to more negative regions and current density increased by replacing the CN group with the NO group and also with increase in the ratio of PEG, suggesting that surface concentration of redox-active metal increases as a result of increase in the surface area. The current density of 1 mA cm⁻¹ was reached at an overpotential of 472 and 489 mV for Co-FeNO@PEG₁₀ and Co-FeNO@PEG₂₅, respectively. The catalysts offer a TOF = 2 × 10⁻³ s⁻¹ at an overpotential of 262 and 298 mV. The similarity of CVs obtained for the before and after electrolysis suggest the stability of Prussian blue nanocubes during electrocatalysis.

ACKNOWLEDGEMENTS

The author thanks TUBITAK for the support (Project No. 1929B011500059)

REFERENCES

- Feng Y, Wei J, Ding Y. Efficient Photochemical, Thermal, and Electrochemical Water Oxidation Catalyzed by a Porous Iron-Based Oxide Derived Metal-Organic Framework. *J Phys Chem C*. 2016;120:517–26.
- Zeng M, Wang H, Zhao C, Wei J, Wang W, Bai X. 3D graphene foam-supported cobalt phosphate and borate electrocatalysts for high-efficiency water oxidation. *Sci Bull*. 2015;60(16):1426–33.
- Sala X, Romero I, Rodríguez M, Escriche L, Llobet A. Molecular catalysts that oxidize water to dioxygen. *Angew Chemie - Int Ed*. 2009;48(16):2842–52.
- Zou X, Su J, Silva R, Goswami A, Sathe BR, Asefa T. Efficient oxygen evolution reaction catalyzed by low-density Ni-doped Co₃O₄ nanomaterials derived from metal-embedded graphitic C₃N₄. *Chem Commun*. 2013;49:7522–4.
- Smith RDL, Prevot MS, Fagan RD, Zhang Z, Sedach PA, Siu MKJ, et al. Photochemical Route for Accessing Amorphous Metal Oxide Materials for Water Oxidation Catalysis. *Science*. 2013;340(6128):60–3.
- Surendranath Y, Dinca M, Nocera DG. Electrolyte-dependent electrosynthesis and activity of cobalt-based water oxidation catalysts. *J Am Chem Soc*. 2009;131(7):2615–20.
- Jung S, McCrory CCL, Ferrer IM, Peters JC, Jaramillo TF. Benchmarking nanoparticulate metal oxide electrocatalysts for the alkaline water oxidation reaction. *J Mater Chem A*. 2016;4(8):3068–76.
- Alsac EP, Ülker E, Nune SVK, Dede Y, Karadas F. Tuning the Electronic Properties of Prussian Blue

- Analogues for Efficient Water Oxidation Electrocatalysis: Experimental and Computational Studies. *Chem - A Eur J*. 2018;24(19):4856–63.
9. Pintado S, Goberna-ferro S, Escudero-Adan EC, Galán-Mascarós JR. Fast and Persistent Electrocatalytic Water Oxidation by Co – Fe Prussian Blue Coordination Polymers. *J Am Chem Soc*. 2013;135:13270–3.
10. May KJ, Carlton CE, Stoerzinger K a., Risch M, Suntivich J, Lee YL, et al. Influence of oxygen evolution during water oxidation on the surface of perovskite oxide catalysts. *J Phys Chem Lett*. 2012;3(22):3264–70.
11. Kudo A, Kato H, Nakagawa S. Water Splitting into H₂ and O₂ on New Sr₂M₂O₇ (M = Nb and Ta) Photocatalysts with Layered Perovskite Structures: Factors Affecting the Photocatalytic Activity. *J Phys Chem B*. 2000;104(3):571–5.
12. Xu L, Zhang F-T, Chen J-H, Fu X-Z, Sun R, Wong C-P. Amorphous NiFe Nanotube Arrays Bifunctional Electrocatalysts for Efficient Electrochemical Overall Water Splitting. *ACS Appl Energy Mater*. 2018;1:1210–7.
13. Masa J, Weide P, Peeters D, Sinev I, Xia W, Sun Z, et al. Amorphous Cobalt Boride (Co₂B) as a Highly Efficient Nonprecious Catalyst for Electrochemical Water Splitting: Oxygen and Hydrogen Evolution (*Adv. Energy Mater*, 2016, 6, 1502313, 10.1002/aenm.201502313). *Adv Energy Mater*. 2016;6(12):1502313.
14. Kanan MW, Nocera DG. In situ formation of an oxygen-evolving catalyst in neutral water containing phosphate and Co²⁺. *Science*. 2008;321:1072–5.
15. Xie L, Zhang R, Cui L, Liu D, Hao S, Ma Y, et al. High-Performance Electrolytic Oxygen Evolution in Neutral Media Catalyzed by a Cobalt Phosphate Nanoarray. *Angew Chemie Int Ed*. 2017;56(4):1064–8.
16. Surendranath Y, Kanan MW, Nocera DG. Mechanistic studies of the oxygen evolution reaction by a cobalt-phosphate catalyst at neutral pH. *J Am Chem Soc*. 2010;132(46):16501–9.
17. Gonzalez-Flores D, Sanchez I, Zaharieva I, Klingan K, Heidkamp J, Chernev P, et al. Heterogeneous water oxidation: Surface activity versus amorphization activation in cobalt phosphate catalysts. *Angew Chemie - Int Ed*. 2015;54(8):2472–6.
18. Han L, Tang P, Reyes-Carmona A, Rodriguez-Garcia B, Torrens M, Morante JR, et al. Enhanced activity and acid pH stability of Prussian blue-type oxygen evolution electrocatalysts processed by chemical etching. *J Am Chem Soc*. 2016;138:16037–45.
19. Karadaş F. Investigation of the ideal composition of metal hexacyanocobaltates with high water oxidation catalytic activity. *Turkish J Chem*. 2019;43:511–9.
20. Perrier M, Kenouche S, Long J, Thangavel K, Larionova J, Goze-Bac C, et al. Investigation on NMR relaxivity of nano-sized cyano-bridged coordination polymers. *Inorg Chem*. 2013;52(23):13402–14.
21. Uemura T, Kitagawa S. Prussian blue nanoparticles protected by poly(vinylpyrrolidone). *J Am Chem Soc*. 2003;125(26):7814–5.
22. Uemura T, Ohba M, Kitagawa S. Size and surface effects of prussian blue nanoparticles protected by organic polymers. *Inorg Chem*. 2004;43(23):7339–45.
23. Ma M, Qu F, Ji X, Liu D, Hao S, Du G, et al. Bimetallic Nickel-Substituted Cobalt-Borate Nanowire Array: An Earth-Abundant Water Oxidation Electrocatalyst with Superior Activity and Durability at Near Neutral pH. *Small*. 2017;13(25):1700394.
24. Nune SVK, Basaran AT, Ülker E, Mishra R, Karadas F. Metal Dicyanamides as Efficient and Robust Water-Oxidation Catalysts. *ChemCatChem*. 2017;9(2):300–7.
25. Sun Y, Liu C, Grauer DC, Yano J, Long JR, Yang P, et al. Electrodeposited cobalt-sulfide catalyst for electrochemical and photoelectrochemical hydrogen generation from water. *J Am Chem Soc*. 2013;135(47):17699–702.
26. Ahn HS, Tilley TD. Electrocatalytic water oxidation at neutral pH by a nanostructured Co(PO₃)₂ Anode. *Adv Funct Mater*. 2013;23(2):227–33.
27. Aksoy M, Nune SVK, Karadas F. A Novel Synthetic Route for the Preparation of an Amorphous Co/Fe Prussian Blue Coordination Compound with High Electrocatalytic Water Oxidation Activity. *Inorg Chem*. 2016;55(9):4301–7.
28. Biesinger MC, Payne BP, Grosvenor AP, Lau LWM, Gerson AR, Smart RSC. Resolving surface chemical states in XPS analysis of first row transition metals, oxides and hydroxides: Cr, Mn, Fe, Co and Ni. *Appl Surf Sci*. 2011;257(7):2717–30.
29. Ressnig D, Shalom M, Patscheider J, Moré R, Evangelisti F, Antonietti M, et al. Photochemical and electrocatalytic water oxidation activity of cobalt carbodiimide. *J Mater Chem A*. 2015;3(9):5072–82.
30. Liu X, Zheng H, Sun Z, Han A, Du P. Earth-abundant copper-based bifunctional electrocatalyst for both catalytic hydrogen production and water oxidation. *ACS Catal*. 2015;5:1530–8.
31. Mishra R, Ülker E, Karadas F. One-Dimensional Copper(II) Coordination Polymer as an Electrocatalyst for Water Oxidation. *ChemElectroChem*. 2017;4(1):75–80.



Isolation, Characterisation and In Silico Toxicity Evaluations of Thiocarbamates, Isothiocyanates, Nitrile, Glucosinolate and Lipids from *Moringa oleifera* Lam. Seed

Atolani O^{a,b,*}  , Olorundare O.E.^c  , Banerjee P^d  , Osin O.A.^b  ,
Preissner R^d  , Njan A.A.^c  

^aDepartment of Chemistry, University of Ilorin, P.M.B. 1515, Ilorin, Nigeria.

^bDepartment of Chemical Sciences, Redeemer's University, Ede, Osun State, Nigeria.

^cDepartment of Pharmacology and Therapeutics, University of Ilorin, P.M.B. 1515, Ilorin, Nigeria.

^dStructural Bioinformatics Group, Institute for Physiology, Charité – University Medicine Berlin, Berlin, Germany.

Abstract: The phytochemical composition of medicinal plants is responsible for the ethnopharmacological applications. These phytochemicals vary in plants of same species planted in various geographical locations. The seed of *Moringa oleifera* Lam., a widely consumed multi-medicinal plant was examined for the bioactive phytochemicals. With the aid of Nuclear Magnetic Resonance (¹H-NMR/¹³C-NMR) spectrometer, Electrospray Ionisation Mass Spectrometry (ESI-MS) and Fourier Transform Infrared (FT-IR) spectroscopy, the phytochemical investigation of the seed of *M. oleifera* afforded nine compounds which included niazimicin **1**, niazidin **2**, glucomoringin isothiocyanate **3**, niazinin acetate **4**, niazinin triacetate **5**, niazirin **6**, glucotropaeolin **7**, triolein **8**, trivaccenin **9**. The Gas Chromatography-Mass Spectrometry (GC-MS) analysis of a major oily fraction revealed the presence of additional ten compounds which include oleic acid (major), 13-docosenoic acid, stearic acid, p-hydroxybenzyl cyanide, α-L-rhamnopyranose and other fatty acids/esters. This is the first account of a fully acetylated niazinin (a 4-(2',3',4'-O-triacetyl-α-L-rhamnosyloxy)benzyl isothiocyanate) **5** from *Moringa oleifera* seed. The *in silico* toxicity evaluation indicated that most of the isolated compounds are either immunotoxic, carcinogenic or mutagenic. The result thus obtained could serve a basis for the pharmacological and toxicological evaluation and profiling of the seed. The result further implied the need for dosage regulation of the consumption of the seed.

Keywords: *Moringa oleifera*; Niazimicin; Niazidin; Isothiocyanate; Glucosinolate; Nitrile.

Submitted: May 24, 2019. **Accepted:** December 12, 2019.

Cite this: Atolani O, Olorundare OE, Banerjee P, Osin OA, Preissner R, Njan AA. Isolation, Characterisation and In Silico Toxicity Evaluations of Thiocarbamates, Isothiocyanates, Nitrile, Glucosinolate and Lipids from *Moringa oleifera* Lam. Seed. JOTCSA. 2020;7(1):235–44.

DOI: <https://doi.org/10.18596/jotcsa.569960>.

***Corresponding author. E-mail:** atolani.o@unilorin.edu.ng.

INTRODUCTION

The phytochemicals of plants used in folkloric medicine are apparently responsible for the ethnopharmacological applications. These phytochemicals within plants of same species vary due to differences in their geographical locations. *Moringa oleifera* Lam. of the monogenetic family, Moringaceae is a widely cultivated medicinal plant with many attributes (1-3). All parts of the plant

which include the stem bark, leaves, root, flowers, fruits, pods, and seeds are used in folkloric medicine. Particularly, the seed is used for water purification as flocculants and de-immobiliser of some pathogens (2). Apart from the application of the seed in water purification, the seed is widely consumed by locals in Africa and Asia as a cheap source of anti-hypertension therapy (4). It is also consumed as food or used as food supplement in many part of Africa while its oil is also used for

cosmeceutical purposes (5, 6). Prior to the commencement of this work, there has been paucity of comprehensive detail chemical composition of the seed of *M. oleifera* of Nigerian origin. However, major compounds which include thiocarbamates, isocyanates, glucosinolates, triglyceride, triterpenes and fatty acids have been isolated from the seed majorly of Asian origin (7-10). Various reports have been documented about the chemical and biological applications of the plant (4, 11, 12). Despite the numerous emerging reports on *M. oleifera*, the plant is still considered underexplored and underutilised for its many great potential (2, 4). Due to environmental impact and geological differences, the phytochemicals of plants often vary from place to place (13). In our previous report (14), we indicated that the ethanolic seed extract of *M. oleifera* of Nigerian origin could trigger infertility of the male through decreased semen pH and also induce hepatotoxicity due to persistent increase in AST and ALP despite withdrawal of the administration of the extract. In addition, we have also previously shown that the seed has the potential to cause renal toxicity (15). Our previous studies further indicated that though the *Moringa oleifera* seed extracts had high anti-oxidant potentials, it however showed low proteinase and membrane stabilisation responses (10). In the continuation of our work on the chemical and biological investigations on *Moringa oleifera* seeds of Nigerian origin (10, 14, 16), we here report the isolation and characterisation of nine bioactive compounds and additional ten compounds identified with the aid of GC-MS.

MATERIAL AND METHOD

General Method

Solvents and chemicals used were analytical grade and where applicable, solvents were re-distilled before use. Infrared spectra were recorded on Shimadzu (8400S) Fourier Transform-Infrared, Shimadzu, Japan, using KBr pellets. $^1\text{H-NMR}$ (300 MHz) and $^{13}\text{C-NMR}$ (75 MHz) spectra were recorded in deuterated chloroform (CDCl_3) on Bruker 300 Nuclear Magnetic Resonance Spectrometer. Adopting tetramethylsilane (TMS) as an internal standard, all chemical shifts were expressed in parts per million (ppm) downfield from it. Mass spectral data were taken on JMS spectrometer (ESI+) ion trap LCQ and Thermolectron Corporation. Chromatography was carried out on a silica gel gravity loaded column. Thin layer chromatography (TLC) was performed on pre-coated plates of silica gel 60F-264 (Merck), and spots were visualised using an ultraviolet-light lamp or by exposure to iodine vapour.

GC-FID/GC-MS Analyses

One of the major oil fraction obtained from the column chromatography was subjected to GC-FID/GC-MS using an Agilent Technology 7890A gas chromatograph equipped with a HP-5MS column with size 30 m by 0.32, 0.5 μm and coupled to a mass spectrometer. The injection and interface

were operated at 250 and 380 $^\circ\text{C}$ respectively while the oven temperature was set to operate from 60 to 300 $^\circ\text{C}$ at 5 $^\circ\text{C min}^{-1}$ and held isothermally at that temperature using a splitless mode at the injection volume of 0.2 μL . The scan was operated for a total time of 0.5 h and chemical constituents identified primarily by comparing the fragmentation pattern of each spectrum with reference compounds in the NIST library and literature.

Preparation of Plant Material

The seed of *M. oleifera* was collected from Northern Nigeria and authenticated at the herbarium of the department of Plant Biology, University of Ilorin, Nigeria. The voucher number UILH/002/1008 was assigned.

Extraction, Column Chromatography Fractionation and Isolation

The dried, de-husked seed material (2 kg) was pulverised and extracted exhaustively with ethanol for nine days followed by water extraction for 5 days. The aqueous extract was partitioned with dichloromethane (DCM) and the DCM extract was collected and concentrated *in vacuo* to afford 46.30 g extract while the ethanolic extract was also concentrated *in vacuo* using a rotary evaporator to afford 37.10 g of thick brown syrup-like extract. Both the DCM and ethanol extracts were subjected to silica gel column chromatography separately with elution using n-hexane, DCM, and methanol in an increasing order of polarity. The DCM extract afforded 23 fractions while the ethanolic extract afforded 42 fractions which were further pulled together based on their TLC profile to afford 7 and 11 major fractions for DCM and ethanol extracts respectively. The major fractions were re-chromatographed and some partially purified compounds were further subjected to preparative thin layer chromatography or washing with solvents as appropriate. Thus, compounds **1-9** were obtained and subjected to various spectroscopic studies for the elucidation of the structures. An oily fraction obtained from the fractionation of the ethanolic extract was subjected to GC-MS analysis.

Extraction, Column Chromatography Fractionation and Isolation

In order to further identify if any of the compounds have toxic potentials, computational methods were used to predict their toxic effects using ProTox-II web server (17), which has a total 33 models for the prediction of various toxicity endpoints was used for this study, such as acute toxicity, hepatotoxicity, cytotoxicity, carcinogenicity, mutagenicity, immunotoxicity, adverse outcomes pathways and toxicity targets. Additionally, in house based-cytochrome (1A2, 2C9, 2C19, 2D6 and 3A4) models were used for the prediction. The respective cytochrome models were based on the SuperCyp database (SuperCyp), and were validated both on internal and external datasets.

RESULTS AND DISCUSSION

The silica gel column chromatography of the dichloromethane and methanolic extracts of *M. oleifera* seed afforded nine compounds which were characterised using a combination of Nuclear Magnetic Resonance ($^1\text{H-NMR}/^{13}\text{C-NMR}$) spectrometry, Electrospray Ionisation Mass Spectrometry (ESI-MS) and Fourier Transform Infrared (FT-IR) spectroscopy as well as in conjunction with literature.

Compound 1: Niazimicin or (O-ethyl-4[α -L-rhamnosyloxy]thiocarbamate). ESI-MS (+) 358 [M+H] $^+$ and 453 [M+26] $^+$, fragment at m/z 311 and 253. m/z 357 [M] $^+$ observed for $\text{C}_{16}\text{H}_{23}\text{NO}_6\text{S}$. $^1\text{H-NMR}$ (300 MHz, CDCl_3): δ_{H} (ppm) 6.97 (H-2, H-6, *d*), 7.27 (H-3, H-5, *d*), 4.53 (H₂-7, *d*), 5.32 (H-1', *d*), 3.98 (H-2', *m*), 3.66 (H-3', *m*), 3.23 (H-4', *m*), 3.65 (H-5', *m*), 1.08 (H-6', *d*), 5.01 (OH, *d*), 4.67 - 4.85 (OH, *m*), 4.38 (H, *q*), 1.25 (H, *t*), 9.85 (NH). $^{13}\text{C-NMR}$ [75 MHz, (CDCl_3)]: δ_{C} 155.8 (C-1), 116.7 (C-2, C-6), 128.4 (C-3), 130.6 (C-4), 131.0 (C-5), 48.6 (C-7), 190.7 (C-8), 98.2 (C-1'), 70.4 (C-2'), 70.9 (C-3'), 71.9 (C-4'), 69.4 (C-5'), 17.7 (C-6'), 66.5, 14.2 (OCH_2CH_3).

Compound 2: Niazidin or (O-cyano-4-(R-L-rhamnosyloxy)benzenethiocarbamate). IR; u_{max} (cm^{-1}) 3389 (NH/OH), 3005 (Ar C-H), 2924/2854 (CH), 2077, 1739, 1647 (N-H bend), 1612 (C=C stretch), 1510 (C = C), 1465, 1420 (O-H bend), 1379 (C-H bend), 1232 (C-N stretching), 1093 (C=S stretch). ESI-MS (+) 355 [M+H] $^+$, 311 and 270 fragments. m/z 355 [MH] $^+$ observed for $\text{C}_{15}\text{H}_{18}\text{N}_2\text{O}_6\text{S}$. $^1\text{H NMR}$ (300 MHz, CDCl_3): δ_{H} (ppm) 6.95 (H-2, H-6, *d*, *J* = 8.4 Hz), 7.19 (H-3, H-5, *d*, *J* = 8.4 Hz), 4.58 (H-7, *d*), 5.32 (H-1', *d*), 3.82 (H-2' *d*), 3.66 (H-3', *m*), 3.23 (H-4', *s*), 3.65 (H-5', *m*), 1.00 (H-6', *d*), 4.70 - 5.01 (OH, *m*), 7.80 (NH). $^{13}\text{C-NMR}$ [75 MHz, (CDCl_3)]: δ_{C} 156.5 (C-1), 117.3 (C-2, C-6), 129.2 (C-3), 130.1 (C-4), 129.7 (C-5), 179.1 (C-8), 98.5 (C-1'), 70.2 (C-2'), 70.4 (C-3'), 70.8 (C-4'), 69.3 (C-5'), 17.7 (C-6').

Compound 3: Glucomoringin isothiocyanate or 4-(α -L-rhamnosyloxy)benzyl isothiocyanate. IR; u_{max} (cm^{-1}) 3358 (OH), 2928/2854 (CH), 2210 (CN), 2065, 1743, 1654 (N-H bend), 1612 (C=C stretch), 1510, 1450 (C = C), 1388 (C-H bend), 1230 (C-N stretching), 1093 (C=S stretch). ESI-MS (+) 312 [M+H] $^+$, 311, 270 and 253 fragments. m/z 310.5 [M] $^+$ observed for $\text{C}_{14}\text{H}_{17}\text{O}_5\text{NS}$. $^1\text{H NMR}$ (300 MHz, CDCl_3): δ_{H} (ppm) 7.21 (H-2, H-6, *d*), 7.02 (H-3, H-5, *d*, *J* = 9.3 Hz), 4.62 (H₂-7, *s*), 5.45 (H-1', *d*, *J* = 1.2), 4.10 (H-2' br, *s*), 3.99 (H-3', *dd*, *J* = 6 Hz), 3.56 (H-4', *s*), 3.79 (H-5', *m*), 1.26 (H-6', *d*, *J* = 5.4 Hz), 4.81 (OH, *s*), 2.63 (2OH, br *s*), 7.80 (NH). $^{13}\text{C-NMR}$ [75 MHz, (CDCl_3)]: δ_{C} 156.1 (C-1), 116.7 (C-2), 129.3 (C-3), 129.0 (C-4), 129.1 (C-5), 116.6 (C-6), 48.8 (C-7), 130.9 (C-8), 98.2 (C-1'), 70.7 (C-2'), 70.3 (C-3'), 72.7 (C-4'), 69.1 (C-5'), 17.4 (C-6').

Compound 4: Niazinin acetate or 4-(3'-O-acetyl- α -L-rhamnosyloxy)benzyl isothiocyanate. ESI-MS (+)

432 [MH+Na+Na] $^+$, 310 and 270 fragments. m/z 432.02 [M+NH₄] $^+$ observed for $\text{M}^+ \text{C}_{17}\text{H}_{23}\text{NO}_7\text{S}$. $^1\text{H NMR}$ (300 MHz, CDCl_3): δ_{H} (ppm) 7.03 (H-2, H-6, *d*), 7.18 (H-3, H-5, *d*), 4.63 (H₂-7, *d*), 5.543 (H-1', *d*), 4.10 (H-2' br, *s*), 4.07 (H-3', *d*), 4.87 (H-4', *t*), 3.96 (H-5', *m*), 1.01 (H-6', *d*), 3.77, 3.24 (2'-OH, 4'-OH, *s*), 7.60 (NH, *t*), 2.19 (OAc, br, *s*).

Compound 5: Niazinin triacetate or 4-(2',3',4'-O-triacetyl- α -L-rhamnosyloxy)benzyl isothiocyanate. IR; u_{max} (cm^{-1}) 3381 ($u_{\text{N-H/O-H}}$), 2926/2854 ($u_{\text{C-H}}$), 2171 (u_{CN}), 2088, 1741 ($u_{\text{C=O}}$), 1654 ($u_{\text{C-N bend}}$), 1612 ($u_{\text{C=C stretch}}$), 1510, 1458 ($u_{\text{C=C}}$), 1379 ($u_{\text{C-H bend}}$), 1236 ($u_{\text{C-N stretch}}$), 1093 ($u_{\text{C=S stretch}}$). ESI-MS (+) 487 [M+NH₄] $^+$, 325, 310 and 270 fragments. m/z 487.15 [M+NH₄] $^+$ observed for $\text{C}_{21}\text{H}_{27}\text{NO}_9\text{S}$. $^1\text{H NMR}$ (300 MHz, CDCl_3): δ_{H} (ppm) 7.00 (H-2, H-6, *d*, *J* = 8.4 Hz), 7.12 (H-3, H-5, *d*, *J* = 8.4 Hz), 4.58 (H₂-7, *d*, *J* = 6.9 Hz), 5.56 (H-1', *d*), 5.32 (H-2' br, *dd*, *J* = 5.1 Hz), 5.21 (H-3', *dd*), 4.99 (H-4', *t*), 3.93 (H-5', *m*), 1.01 (H-6', *d*, *J* = 6.9 Hz), 3.45 (OMe, *s*), 4.62 (NH, *t*), 1.99 (OAc, br, *s*). $^{13}\text{C-NMR}$ [75 MHz, (CDCl_3)]: δ_{C} 156.2 (C-1), 116.7 (C-2), 128.4 (C-3), 131.0 (C-4), 128.2.1 (C-5), 116.9 (C-6), 48.3 (C-7), 190.7 (C-8), 97.8 (C-1'), 76.8 (C-2'), 72.5 (C-3'), 71.5 (C-4'), 71.0 (C-5'), 17.7 (C-6'), 174.2, 174.0, 173.7 (3C=O), 22.8, 21.2 and 19.9 (3OAc).

Compound 6: Niazirin. 4-[(4'-O-acetyl- α -L-rhamnosyloxy)benzyl] nitrile. ESI-MS (+) m/z 357.89 [M+NH₄+NH₄] $^+$ was obtained for $\text{C}_{16}\text{H}_{19}\text{NO}_6$. $^1\text{H NMR}$ (300 MHz, CDCl_3): δ_{H} 7.07 (H-2, H-6, *d*, *J* = 9.0 Hz), 7.16 (H-3, H-5, *d*, *J* = 9.0 Hz), 3.68 (H₂-7, *s*), 5.38 (H-1', *d*, *J* = 2.4), 4.15 (H-2' *m*), 4.09 (H-3', *dd*), 4.62 (H-4', *t*), 3.58 (H-5', *m*, *J* = 9.3), 1.19 (H-6', *d*, *J* = 7.2 Hz), 2.00 (2OH, br, *s*), 2.04 (OCOME, *s*), 4.62 (NH, *t*), 1.99 (OAc, br, *s*). $^{13}\text{C-NMR}$ [75 MHz, (CDCl_3)]: δ_{C} 156.1 (C-1), 116.7 (C-2), 129.3 (C-3), 131.2 (C-4), 129.7 (C-5), 116.9 (C-6), 22.9 (C-7), 123.8 (C-8), 98.0 (C-1'), 71.3 (C-2'), 70.8 (C-3'), 72.5 (C-4'), 66.7 (C-5'), 17.6 (C-6'), 173.9, (OCOCH₃), 21.1 (OCOCH₃).

Compound 7: Glucotropaeolin or (glucosinolate). IR; u_{max} (cm^{-1}) 3412 ($u_{\text{O-H}}$), 2931 ($u_{\text{C-H}}$), 1645 ($u_{\text{C=N stretch}}$), 1610 ($u_{\text{C=C stretch}}$), 1510 ($u_{\text{C-H}}$), 1384 ($u_{\text{S=O stretch}}$), 1254 ($u_{\text{C-O-C/C-N stretch}}$), 1234 ($u_{\text{C-N stretch}}$). ESI-MS (+) m/z 425.11 [M+H] $^+$ was obtained for $\text{C}_{14}\text{H}_{18}\text{NO}_{10}\text{S}_2$. $^1\text{H NMR}$ (300 MHz, CDCl_3): δ_{H} (ppm) 3.30-3.66 (*m*, 4H, H-2', H-3', H-4', H-5'), 3.67-3.73 (*m*, 2H, H-6a', H-6b'), 2.00 (3OH', br, *s*), 4.07 (*s*, 2H, CH₂Ph), 4.77 (*d*, 1H, H-1'), 5.33 (*s*, br, ArOH), 7.18 (*dd*, ArH-4, 8, *J* = 8.4 Hz), 7.02 (*dd*, ArH-5, 7, *J* = 8.4 Hz).

Compound 8: Triolein. IR; u_{max} (cm^{-1}) 2926/2854 ($u_{\text{C-H}}$), 1747 ($u_{\text{C=O}}$), 1610 ($u_{\text{C=C stretch}}$), 1456 ($u_{\text{C=N stretch}}$), 1238 ($u_{\text{C-O-C stretch}}$). ESI-MS (+) m/z 903.47 [M+NH₄] $^+$ obtained for $\text{C}_{57}\text{H}_{104}\text{O}_6$. $^1\text{H-NMR}$ (300 MHz, CDCl_3): δ_{H} (ppm) 0.88-0.90 (*t*, -CH₃), 1.25-1.30, 1.60 (*m*, -CH₂-), 1.97 (*m*, -CH₂C=C-), 5.39 (*m*, -CH of olefins), 5.24 (*m*, CH

of glycerol), 4.10-4.32 (ddd, CH₂ of glycerol). ¹³C-NMR [75 MHz, (CDCl₃)]: δ_c (ppm) 173.3 (C=O, C-

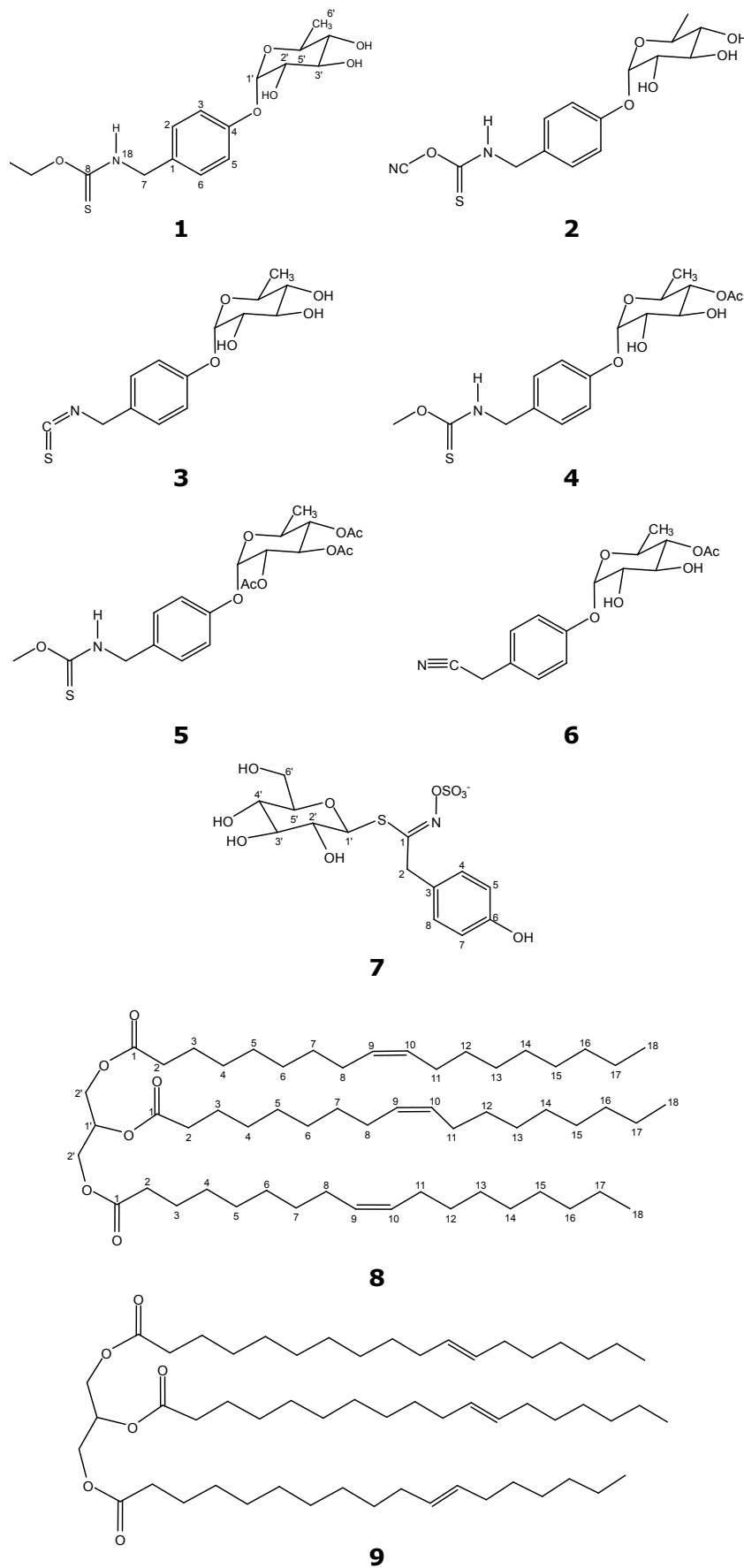


Figure 1: Structures of Niazimicin **1**, Niazidin **2**, Glucomoringin isothiocyanate **3**, Niazinin acetate **4**, Niazinin triacetate **5**, Niazirin **6**, Glucotropaeolin **7**, Triolein **8**, Trivaccenin **9**.

1), 34.3 (C-2), 25.0 (C-3), 29.1 (C-4), 29.9 (C-5), 29.8 (C-6), 32.0 (C-7), 29.6 (C-8), 129.9 (C-9), 129.8 (C-10), 29.5 (C-11), 31.9 (C-12), 29.4 (C-13), 29.3 (C-14), 29.3 (C-15), 32.0 (C-16), 22.8 (C-17), 14.2 (C-18), 69.1 (C-1' of glycerol backbone), 62.2 (O-C-2' of glycerol backbone).

Compound **9**: Trivaccenin. IR; ν_{\max} (cm^{-1}) 2926/2854 ($\nu_{\text{C-H}}$), 1747 ($\nu_{\text{C=O}}$), 1612 ($\nu_{\text{C=C}}$ stretch), 1465 ($\nu_{\text{C=N}}$ stretch), 1238 ($\nu_{\text{C-O-C}}$ stretch). ESI-MS (+) m/z 903.47 [$\text{M}+\text{NH}_4$]⁺ observed for $\text{C}_{57}\text{H}_{104}\text{O}_6$. m/z 824 observed for [$\text{M}^+ - \text{C}_9\text{H}_{18}$]⁺ fragment. ¹H-NMR (300 MHz, CDCl_3): δ_{H} (ppm) 0.88-0.90 (t, - CH_3), 1.25-1.30, 1.61 (m, - CH_2 -), 1.98 (m, - $\text{CH}_2\text{C}=\text{C}$ -), 5.39 (m, -CH of olefins), 5.25 (m, CH of glycerol), 4.10-4.32 (ddd, CH_2 of glycerol). ¹³C-NMR [75 MHz, (CDCl_3): δ_{C} (ppm) 173.3 (C=O), 34.1 (C-2), 25.0 (C-3), 29.1 (C-4), 29.2 (C-5), 29.3 (C-6), 29.4 (C-7), 29.7 (C-8), 29.8 (C-9), 31.9 (C-10), 129.9 (C-11), 129.8 (C-12), 31.9 (C-13), 29.8 (C-14), 29.7 (C-15), 29.4 (C-16), 22.8 (C-17), 14.2 (C-18), 69.0 (C-1' of glycerol backbone), 62.2 (O-C-2' of glycerol backbone).

Composition of the Fraction: The major oily fraction obtained from the silica gel fractionation of the ethanolic extract was subjected to GC-FID/GC-MS and FT-IR analyses. Ten compounds, primarily fatty acids/esters, were identified (**Table 1**). The major compound was oleic acid (45.19%), followed by 13-docosenoic acid (16.15%), stearic acid (10.56%), palmitic acid (9.21%) and methyl trans-vaccenate (6.48%). Other compounds which were obtained in low yield includes methyl palmitate (2.48%), α -monopalmitin (2.12%), methyl stearate (1.32%). Two non-fatty acids/esters, p-

hydroxybenzyl cyanide (4.16%) and α -l-rhamnopyranose (2.33%) were however obtained in minute quantities. The FT-IR spectrum of the fraction indicated major peaks at 3392, 2926, 2854, 2173, 2090, 1741, 1612, 1510, 1386, 1236, 1021, 983 and 669 cm^{-1} .

From the *in silico* studies, compounds which include niazidin, niazinin acetate, and niazinin triacetate were estimated to possess high immunotoxicity (as shown in **Table 2**). Also, most of the compounds were predicted as cytochrome 3A4 substrate and/or inhibitors with good probability. Additionally, triolein and trivaccenin were predicted to be carcinogenic and mildly mutagenic. Triolein and trivaccenin were predicted with good pharmacophore fit values to justify probable binding with amine oxidase.

Sixteen carbon signals were depicted by the C-13 spectrum of the compound **1** with the characteristic C=S signal appearing at 190 ppm. The C-O carbon of the aromatic was observed at 155 ppm while the aromatic C=C bonds were clearly depicted 116, 128, 130 and 131 ppm. The aromatic carbon signals were corroborated by the proton NMR signals between 6.97 and 7.27 ppm. The fragment ion at 311 resulting from the loss of the ethoxy group of from the niazimicin in the ESI-MS spectrum strengthens the claim about the structure of the elucidated compound as O-ethyl-4[α -L-rhamnosyloxy]thiocarbamate with molecular formula $\text{C}_{16}\text{H}_{23}\text{NO}_6\text{S}$. The spectra data of the niazimicin was confirmed by comparing with literatures (7, 18-20). The proton and carbon 13 NMR of niazidin **2** ran in deuterated chloroform was carefully compared to the literature (8).

Table 1: Compounds identified in a major oily fraction of the ethanolic extract.

SN	RT (min)	Compounds	MF	% Composition	Important Fragments
1	6.93	α -l-rhamnopyranose	$\text{C}_6\text{H}_{12}\text{O}_5$	2.33	43, 73, 128
2	12.41	p-Hydroxybenzyl cyanide	$\text{C}_8\text{H}_7\text{NO}$	4.16	51, 78, 133
3	17.24	Methyl palmitate	$\text{C}_{17}\text{H}_{34}\text{O}_2$	2.48	74, 87, 270
4	18.65	Palmitic acid	$\text{C}_{16}\text{H}_{32}\text{O}_2$	9.21	43, 73, 256
5	20.27	Methyl trans-vaccenate	$\text{C}_{19}\text{H}_{36}\text{O}_2$	6.48	55, 69, 296
6	20.59	Methyl stearate	$\text{C}_{19}\text{H}_{38}\text{O}_2$	1.32	74, 87, 298
7	21.41	Oleic acid	$\text{C}_{18}\text{H}_{34}\text{O}_2$	45.19	41, 55, 280
8	21.60	Stearic acid	$\text{C}_{18}\text{H}_{36}\text{O}_2$	10.56	43, 55, 284
9	25.22	α -Monopalmitin	$\text{C}_{19}\text{H}_{38}\text{O}_4$	2.12	43, 57, 313
10	27.10	13-Docosenoic acid	$\text{C}_{22}\text{H}_{42}\text{O}_2$	16.15	41, 55, 325

RT: Retention Time; MF: Molecular Formula

Table 2: Computational toxicity evaluation result from the ProTox-II platform.

Compound name	Pubchem ID	Predicted LD50 value and Tox class	Prediction accuracy (%)	Toxicity targets	Average pharmacophore fits (%)	Toxicity end points	Prediction probability	Cytochrome prediction
Niazimicin	5471459	3750 (mg/kg), Tox class: 5	68.07	-	-	Immunotoxicity	0.62	CYP3A4 substrate (60%)
Niazidin	11792427	3750 (mg/kg), Tox class: 5	68.07	-	-	Immunotoxicity	0.84	CYP3A4 substrate/inhibitor (60%)
Glucomoringin isothiocyanate	153557	3750 (mg/kg), Tox class: 5	69.06	-	-	Immunotoxicity	0.64	CYP3A4 substrate (59%)
Niazinin acetate	-	3750 (mg/kg), Tox class: 5	69.26	Amine Oxidase	31.28	Immunotoxicity	0.98	CYP3A4 substrate (67%)
				Prostaglandin G/H synthase 1	42.44			
Niazinin triacetate	-	3750 (mg/kg), Tox class: 5	69.26	Amine Oxidase	31.28	Immunotoxicity	0.98	CYP3A4 substrate, CYP3A4 inhibitor, CYP2C19 inhibitor (68%)
				Prostaglandin G/H synthase 1	42.44			
Niazirinin	10426197	4000 (mg/kg), Tox class: 5	70.97	-	-	-	-	CYP3A4 substrate (59%)
Glucotropaeolin	656498	2000 (mg/kg), Tox class: 4	23.00	-	-	-	-	CYP3A4 substrate (52%)
Triolein	5497163	3520 (mg/kg), Tox class: 5	72.90	Amine Oxidase	63.88	Carcinogenicity	0.70	-
				Prostaglandin G/H synthase 1	58.45	Mutagenicity	0.57	
Trivaccenin	14029829	3520 (mg/kg), Tox class: 5	72.90	Amine Oxidase	63.88	Carcinogenicity	0.70	-
				Prostaglandin G/H synthase 1	58.45	Mutagenicity	0.57	

NB: Compounds marked in red have higher toxicity potential.

The sugar moiety was confirmed following the appearance of the proton doublet at 5.32, 3.82, 3.66, 3.23, 3.65, 1.00 and broad hydroxyl proton signals at 4.70 – 5.01 ppm. The anomeric (H-1') proton signal indicates that the sugar moiety is linked with the aglycone by a α -glycosidic bond suggesting an α -L-rhamnoside (8, 18). The aglycone moiety had protons which mutually coupled at 7.19 (J = 8.4 Hz) and 6.95 (J = 8.4 Hz) supporting a para-substituted benzene structure. The evidence of the para-disubstituted benzene was also affirmed by the characteristic stretching vibration at 835 cm^{-1} in the infrared spectrum. The N-H bond linked to benzylic methylene was characteristically supported by the peaks at m/z 253, 270 and 311 corresponding to the fragment ions at $[(M^+ + 1) - C_2H_2N_2OS]$, $[(M^+ + 1) - C_2HN_2S]$ and $[(M^+ - HOCN)]$ respectively.

In the infrared spectrum, the overlap of the N-H and O-H stretching vibration was observed at 3389 cm^{-1} while the C-H bond stretching of the methyl group appeared at 2962 cm^{-1} with a corresponding bending vibration at 1379 cm^{-1} . The asymmetric stretching and symmetrical stretching vibrations of the methylene appeared at 2924 and 2854 cm^{-1} .

The O-H bending appeared at 1420 cm^{-1} . The characteristic cyanate (R-O-CN) and C-S vibrations appeared at 2077 and 671 cm^{-1} respectively. Thus, the structure of the compound **2** was unambiguously established as *O*-cyano-4-(*R*-L-rhamnosyloxy)benzenethiocarbamate otherwise known as niazidin (**Fig. 1**).

In order to confirm the structure of the compound **3**, the spectra data were compared with those

reported in the literature (8, 18, 20, 21). The $^1\text{H-NMR}$ spectrum indicated two aromatic protons resonating at δ 7.21 and 7.02 with coupling constant of 9.3 Hz suggesting a para-substituted benzene structure. The absence of the N-H chemical shift in the $^1\text{H-NMR}$ spectrum supports the isothiocyanate nature of the compound. The anomeric proton at δ 5.45 confirms the glycosidic nature which was further strengthened by the carbon signal at δ 98.2. The bands at 3358, 2210 and 1230 cm^{-1} corresponding to the hydroxyl, nitrile (CN) and C-N stretching vibration in the infrared spectrum corroborate this position. The mass spectrum exhibited the molecular ion at m/z 310.5 corresponding to $C_{14}H_{17}O_5NS$. Thus, the combination of the mass spectra data and NMR data with the infrared report unequivocally assisted the identification of the compound as 4-(α -L-rhamnosyloxy)benzyl isothiocyanate otherwise called glucomoringin isothiocyanate. Many isothiocyanates and glucosinolates have been reportedly isolated from various plants (22).

Compound **4** was identified principally using the ESI-MS and $^1\text{H-NMR}$ data and comparing with the literature (8, 23, 24). The molecular weight of the compound was obtained as a disociated species at m/z 432.02. The compound was identified as 4-(3'-*O*-acetyl- α -L-rhamnosyloxy)benzyl isothiocyanate also called niazinin acetate **4**. The compound has been isolated as a minor constituent of the seed of *M. oleifera* previously (24).

Compound **5** has structural similarity with niazinin. However, when the $^1\text{H-NMR}$ data was compared with that of niazinin (18, 23, 25), the broad OH peak appearing between 4.8-5.1 ppm was absent, implying that the hydroxyl groups have been acetylated. In addition, the molecular ion adduct peak at m/z 487.15 in the mass spectrum in

conjunction with the three carbonyl carbon signals (at δ 174.2, 174.0 and 173.7) and three addition signals at 22.8, 21.2 and 19.9 for methyl carbons of the acetyl in the ^{13}C -NMR attested to the triacetate nature of the compound. The δ 190.7 signal confirms the presence of the CS carbon while the isothiocyanate band was confirmed at 2171 cm^{-1} in the infrared data. The N-H stretching vibration was slightly reduced and observed at 3381 cm^{-1} due to intra-molecular hydrogen bonding. The study of the combined spectral data and comparison with literature data facilitated the establishment of the compounds as 4-(2',3',4'-O-triacetyl- α -L-rhamnosyloxy)benzyl isothiocyanate otherwise referred to as niazinin triacetate an analogue of and niazinin and 4-(3'-O-acetyl- α -L-rhamnosyloxy)benzyl isothiocyanate previously isolated from the seed of *M. oleifera* (18, 19). This is the first account of a fully acetylated niazinin (with three acetyl group) from *Moringa oleifera* seed.

The structure of the compound **6** was elucidated using the ^1H -NMR, ^{13}C -NMR and ESI-MS data and further confirmed by comparing the data to that reported for niazirin (7). The molecular ion adduct peak at m/z 357.89 in the ESI mass spectrum in conjunction with the carbonyl carbon signals (at δ 173.9) in the ^{13}C -NMR spectrum which were absent in spectrum of niazirin added credence to the position. Other observations are as rightly indicated for niazidin. Thus, the structure of niazirin, 4-[(4'-O-acetyl- α -L-rhamnosyloxy)benzyl] nitrile was established as the 4'-acetyl derivative of niazirin, a nitrile glycoside.

The structural elucidation of compound **7** was based on the ^1H -NMR and ESI-MS data generated in conjunction with the infrared data which were compared to data reported in the literature (26, 27). The molecular ion $[\text{M}+\text{H}]^+$ peak at m/z 425.11 in the mass spectrum confirms the molecular weight of the compound which corresponding to $\text{C}_{14}\text{H}_{18}\text{NO}_{10}\text{S}_2$. The aglycone moiety with protons resonating at 7.18 and 7.02 with a coupling constant of 8.4 Hz supports a para-substituted benzene structure. The infrared spectrum affirms the presence of the major functional groups at 3412, 1610 and 1384 corresponding to N-H, C=C and S=O stretching vibrations. The C=N of the glucosinolate was observed at 1645 cm^{-1} . With comparison with literature data, the compounds were established as 4-(α -L-rhamnopyranosyloxy)benzyl glucosinolate also called glucotropaeolin. Glucotropaeolin has been isolated from the *Moringa oleifera* and *Bretschneidera sinensis* (28). It is also known to occur in many edible plants that include broccoli and cabbage (22, 29). The glucosinolates are water-soluble glycosides which constitute an interesting class of natural products with its aglycone containing nitrogen and sulphur. A class of the glucosinolates known as benzylglucosinate (glucotropaeolin) is presumed to be the precursor of the benzyl isothiocyanate (30). The toxicity of glucosinolates is not fully

established but evidence of the potential anti-cancer activities exist in literature (31, 32).

Compound **8** obtained as a viscous oil was characterised using the infrared, mass spectrometry, ^1H -NMR and ^{13}C -NMR data and comparison with the literature (33-35). Precisely, the infrared spectrum showed characteristic absorption bands 2926, 1747 and 1610 cm^{-1} corresponding to the C-H, C=O (carbonyl of esters) and C=C (olefin) along with stretchings of the triglycerol. The absence of the O-H stretching at $3200 - 3600\text{ cm}^{-1}$ confirms that the absence of fatty acid but instead, an ester. The presence of the carbonyl chemical shift at 173.3 ppm (typical of esters) in the ^{13}C -NMR spectrum attests to the claim. The molecular weight of the compound was depicted by the $[\text{M}+\text{NH}_4]^+$ observed at m/z 903.47 $[\text{M}+\text{NH}_4]^+$ which corresponds to the molecular formula $\text{C}_{57}\text{H}_{104}\text{O}_6$. In the ^1H -NMR, the equivalent terminal methyl protons were observed between 0.88-0.90 ppm as triplets while methylene protons were clearly depicted at 1.25-1.30, 1.60 ppm. The chemical shift at 5.39 and 5.23 ppm confirms the presence of the vicinal methine protons (olefin) and the methine proton of the glycerol backbone. Furthermore, the ^{13}C -NMR spectrum also indicated the chemical shifts typical of C=C (129 ppm) and triglycerol backbone at 69.1 and 62.2 ppm (33). The compound was thus identified as triolein **8**, a triglyceride. Triolein have been reportedly identified in the plants previously (25).

The structure of compound **9** was established by using the infrared, mass spectrometry, ^1H -NMR and ^{13}C -NMR data and comparison with literature (33, 34). However, the infrared and ^1H -NMR data were quite identical with that of compound **8** with minor differences. The major difference was observed in the ESI-MS spectrum where an additional fragment peak at m/z 824 observed for $[\text{M}^+ - \text{C}_9\text{H}_{18}]^+$ corresponding to $\text{C}_{48}\text{H}_{86}\text{O}_6$ fragment was observed. This fragment which was not observed in the triolein is supposedly as a result of cleavage of the C=C bond at position 7 from the lipidic tail. It was reported that the slight shift in the chemical shift of the carbonyl and olefinic carbon signals in the C-13 NMR are sufficient to distinguish between the triolein and the trivaccenin (34). The hydrolysis of the triolein yields omega-9 fatty acids while the trivaccenin hydrolysis yields omega-7 fatty acids both liberating the glycerol. The omega-7 and omega-9 fatty acids obtained in the *Moringa oleifera* seed are both monounsaturated fatty acids that are found in various other animal fats and plant oils and reported to possess various important pharmacological potentials (36).

The GC-MS analysis of the major fraction of the ethanol extract depicted ten peaks corresponding to ten known natural compounds (**Table 1**). Our previous report indicated that oleic acid is the most abundant fatty acid in the seed oil of *Moringa oleifera* [10]. The fatty acid profile reported is in agreement with other reports (2, 4). The fatty

acids which include the stearic acid, palmitic acid and vaccenic acid (5) have been reported as part of the fatty acid profile of the seed. The presence of monopalmitin is suspected to be from the partial enzymatic hydrolysis of palmitin triglyceride while the methyl trans-vaccenate could also be hydrolysis product of trivaccenin reported as compound **9** in this report. The α -l-rhamnopyranose and p-hydroxybenzyl cyanide are likewise rationalised to be hydrolysis products of niazirin (compound **6**), a 4-[(4'-O-acetyl- α -L-rhamnosyloxy)benzyl] nitrile also reported in this work. The GC-MS result of the fraction was further corroborated by the infrared data obtained. The FT-IR spectrum of the fraction revealed the presence of prominent O-H stretching vibration at 3392 cm^{-1} and C-H of aliphatic hydrocarbon at 2926 and 2854 cm^{-1} . Interestingly, the cyanide stretching vibration apparently from the hydroxybenzyl cyanide was observed at 2173 cm^{-1} . The carbonyl of esters and C=C stretching vibration of olefins were significantly represented at 1716 and 1612 cm^{-1} respectively. The complexity of the infrared spectrum indicated that the fraction is a mixture of compounds with numerous functional groups.

The compounds identified in this work belonged to the thiocarbamate, isothiocyanate, nitrile, glucosinolate and lipid class of naturally occurring compounds and are presumably responsible for the primary biological activities observable in the seed. Additionally, the *in silico* evaluations revealed that compounds which include niazirin triacetate and trivaccenin are probable immunotoxic, carcinogenic, and mutagenic compounds on the computational toxicity models. Most of the compounds were predicted as cytochrome 3A4 substrate and/or inhibitors with good probabilities. The seed of *M. oleifera* has been implicated for some measure of toxicities in various models (37, 38). This result partly validates the previous report of the potential toxicity of the *M. oleifera* seeds (39).

CONCLUSION

In this work, a comprehensive phytochemical investigation of the seed of *M. oleifera* of Nigerian origin has been carried out and nine compounds comprising of niazimicin **1**, niazidin **2**, glucomoringin isothiocyanate **3**, niazirin acetate **4**, niazirin triacetate **5**, niazirin **6**, glucotropaeolin **7**, triolein **8** and trivaccenin **9** have been characterised. Ten other compounds were identified from the GC-MS of a fraction obtained from the column chromatography. Oleic acid, 13-docosenoic acid, and stearic acid were the major compounds in the fraction. All the nineteen compounds identified thus far belong to the thiocarbamate, isothiocyanate, nitrile, glucosinolate, and lipid class of naturally occurring compounds. The *in silico* studies implicated niazirin triacetate and trivaccenin as possible immunotoxic, carcinogenic, and mutagenic compounds indicating the need to take caution in

the consumption of the seed. The report thus obtained serves as a basis for the evaluation of the pharmacological actions and toxicities of the seed.

ACKNOWLEDGEMENTS

Authors are grateful to the Raw Materials Research and Development Council, Abuja, Nigeria for the financial assistance with grant number RMRDC/AF/20/S.102/1.

Conflict of Interest: Authors have no conflict of interest.

REFERENCES

- Sastari BN. The Wealth of India, Council of Scientific and Industrial Research, New Delhi, 1962; p. 425.
- Liu Y, Wang X, Wei X, Gao Z, Han J. Values, properties and utility of different parts of *Moringa oleifera*: an overview. Chinese Herbal Medicines. 2018; 10 (4): 371-378.
- Ravani A, Prasad RV, Gajera RR, Joshi DC. Potentiality of *Moringa oleifera* for food and nutritional security - a review, Agric. Rev. 2017; 38: 228-232.
- Tiloke C, Anand K, Gengan, RM, & Chuturgoon AA. *Moringa oleifera* and their phytonanoparticles: Potential antiproliferative agents against cancer. Biomedicine & Pharmacotherapy. 2018; 108, 457-466.
- Falowo AB, Mukumbo FE, Idamokoro EM, Lorenzo JM, Afolayan AJ, Muchenje V. Multi-functional application of *Moringa oleifera* Lam. in nutrition and animal food products: A review. Food Research International. 2018; 106, 317-334.
- Atolani O, Olabiyi ET, Issa AA, Azeez HT, Onoja EG, Ibrahim SO, Zubair MF, Oguntoye OS, Olatunji GA. Green synthesis and characterization of natural antiseptic soaps from the oils of underutilized tropical seed. Sustainable Chemistry and Pharmacy. 2016; 4: 32-39.
- Faizi S, Siddiqui BS., Saleem R, Siddiqui S, Aftab K, Gilani A. Isolation and Structure Elucidation of New Nitrile and Mustard Oil Glycosides from *Moringa oleifera* and Their Effect on Blood Pressure. J. Nat. Prod., 1994, 57 (9), 1256-126.
- Faizi S, Siddiqui BS, Saleem R, Noor F, Husnain S. Isolation and Structure Elucidation of a Novel Glycoside Niazidin from the Pods of *Moringa oleifera* J. Nat. Prod. 1997, 60, 1317-1321.
- Dayrit FM, Alcantar AD, Villasenor IM. Studies on *Moringa oleifera* seeds, the antibiotic compound and its deactivation in aqueous solution. Philippine Journal of Science. 1990; 119: 23.

10. Ataloni O, Olorundare OE, Anoka AN, Osin AO, Biliaminu SA. Antioxidant, Proteinase Inhibitory and Membrane Stabilization Potentials of Moringa oleifera Seed Oil. *FABAD Journal of Pharmaceutical Sciences*. 2018; 43 (2), 1-13.
11. Fahey JS. Moringa oleifera: A review of the medical evidence for its nutritional, therapeutic, and prophylactic properties. *Trees for Life Journal*. 2005; 1: 5.
12. Kambizi L, MT Bakare-Odunola AT, Oladiji AT, Kola-Mustapha TO, Amusa O, Ataloni NS, Njinga, A.L. Quadri. Proteinease inhibition, membrane stabilization, antioxidant and phytochemical evaluations of leaves, seeds and calyces of four selected edible medicinal plants. *Cogent Chemistry*. 2017; 3: 1314064.
13. Şanlı A, Tahsin KT. Geographical impact on essential oil composition of endemic Kundmannia anatolica Hub.-Mor. (Apiaceae). *African Journal of Traditional, Complementary and Alternative Medicines*. 14; (1): 131-137.
14. Njan AA, Ataloni O, Olorundare OE, Afolabi SO, Ejimkonye BC, Crucifix PG, Salami B, Olajide JO, Oyewopo AO. Oyeleke SA. Chronic toxicological evaluation and reversibility studies of Moringa oleifera ethanolic seed extract in Wistar rats. *Tropical Journal of Health Sciences*. 2018; 25 (1), 59-71.
15. Olorundare OE, Bello MK, Biliaminu SA, Babatunde SA, Ibrahim OK, Njan AA. Acute and Subacute Toxicity of Defatted Ethanolic Extract of Moringa oleifera Seed in Albino Rats. *West. Afr. J. Pharmacol. Drug Res*. 2015; 30:46-51.
16. Njan AA, Ataloni O, Olorundare OE, Afolabi SO, Ejimkonye BC, Crucifix PG, Salami B, Olajide JO, Oyewopo AO. Assessment of developmental toxicity of Moringa oleifera (seed) in pregnant wistar rats. *Centrepoin Journal (Science Edition)*, 2017; 23 (1): 1-18.
17. Banerjee P, Eckert AO, Schrey AK, Preissner R. ProTox-II: a webserver for the prediction of toxicity of chemicals. *Nucleic Acids Research*, 2018; 46, 257–263.
18. Faizi S, Siddiqui BS, Saleem R, Siddiqui S, Aftab K, Gilani A. Isolation and structure elucidation of novel hypotensive agents, Niazinin A, Niazinin B, Niazimicin and Niaziminin A + B from Moringa oleifera: The first naturally occurring thiocarbamate. *Journal of the Chemical Society Perkin Transactions*. 1992; 1: 3237- 3241.
19. Faizi S, Siddiqui BS, Saleem R, Siddiqui S, Aftab K, Gilani AUH. Fully acetylated carbamate and hypotensive thiocarbamate glycosides from Moringa oleifera. *Phytochemistry*. 1995; 38(4), 957–963.
20. Ragasa CY, Levida RM, Don MJ, Shen CC. Cytotoxic isothiocyanates from Moringa oleifera Lam. *Philippine Science Letters*. 2012; 5(1):46-52.
21. de Graaf R.M., Krosse S, Swolfs AEM., Brinke E, Prill N, Leimu R, Galen PM, Wang Y., Aarts MGM. and Dam NM. Isolation and identification of 4-*rhamnosyloxy benzyl glucosinolate* in *Noccaea caerulescens* showing intraspecific variation. *Phytochemistry*. 2014; 110: 166-171.
22. Fahey JW, Zalcmann AT, Talalay P. The chemical diversity and distribution of glucosinolates and isothiocyanates among plants. *Phytochemistry*. 2001: 56(1), 5–51.
23. Kjær A, Malver O, El-Menshaw B, Reisch J,. Isothiocyanates in myrosinase-treated seed extracts of Moringa peregrina. *Phytochemistry*. 1979; 18, 1485–1487.
24. Waterman C, Cheng DM, Rojas-Silva P, Poulev A, Dreifus J, Lila MA, Raskin I. Stable, water extractable isothiocyanates from Moringa oleifera leaves attenuate inflammation in vitro. *Phytochem* 2014; 103:114–122.
25. Ragasa CY, Ng VAS, Shen CC. Chemical Constituents of Moringa oleifera Lam. Seeds. *International Journal of Pharmacognosy and Phytochemical Research*. 2016; 8(3); 495-498.
26. Lamar S. and Rollin P. Synthesis of an Artificial Phosphate Bio-isostere of Glucotropaeolin. *Tetrahedron Letters*, 1994; 35, 14: 2173-2174.
27. Aucagne V, Gueyrard D, Tatibouet A, Cottaz S, Driguez H, Lafosse M and Rollin P. The first synthesis of C-glucotropaeolin. *Tetrahedron Letters* 1999; 40: 7319-7321.
28. Montaut S, Zhang W, Nuzillard, J., De Nicola G.R., Rollin P. Glucosinolate Diversity in *Bretschneidera sinensis* of Chinese Origin. *Journal of Natural Products*. 2015; 78 (8): 2001–2006.
29. Ishida M, Hara M. Fukino, N; Kakizaki, T; Morimitsu, Y. "Glucosinolate metabolism, functionality and breeding for the improvement of Brassicaceae vegetables". *Breeding Science*. 2014; 64 (1): 48–59.
30. Agerbirk N, Olsen CE. "Glucosinolate structures in evolution". *Phytochemistry*. 77: 16–45.
31. Samuni BM, Arad Z, Dearing MD, Gerchman Y, Karasov WH, Izhaki I. "Friend or foe? Disparate plant–animal interactions of two congeneric rodents". *Evolutionary Ecology*. 27 (6): 1069–1080.
32. Fuentes F, Paredes-Gonzalez X, Kong AN. Dietary Glucosinolates Sulforaphane, Phenethyl Isothiocyanate, Indole-3-Carbinol/3,3'-Diindolylmethane: Anti-Oxidative Stress/Inflammation, Nrf2,

Epigenetics/Epigenomics and in Vivo Cancer Chemopreventive Efficacy". *Current Pharmacology Reports*. 1 (3): 179–196.

33. Singh B, Agrawal PK, Thakur RS. (1989). Long chain esters of *Aesculus indica*. *Journal of Natural Products*. 2015; 52 (1): 180-183.

34. Vlahov G, Chepkwony PK, Ndalut PK. 13C NMR Characterization of Triacylglycerols of *Moringa oleifera* Seed Oil: An Oleic-Vaccenic Acid Oil. *J. Agric. Food Chem*. 2002; 50 (5): 970–975.

35. Díaz M, Gavín JA, Andrade JB. Structural characterization by Nuclear Magnetic Resonance of ozonized triolein. *Grasas Aceites*. 2008; 59: 274-281.

36. Vessby B, Uusitupa M, Hermansen K, Riccardi G, Rivellese AA, Tapsell LC, Näslén C, Berglund L, Louheranta A, Rasmussen BM, Calvert GD, Maffetone A, Pedersen E, Gustafsson IB, Storlien LH. "Substituting dietary saturated for monounsaturated fat impairs insulin sensitivity in healthy men and women: The KANWU Study". *Diabetologia*. 2001; 44 (3): 312–319.

37. Kavitha C, Ramesh M, Kumaran S. S., and Lakshmi SA. Toxicity of *Moringa oleifera* seed extract on some hematological and biochemical profiles in a freshwater fish, *Cyprinus carpio*. *Experimental and Toxicologic Pathology*. 2012; 64(7-8), 681–687.

38. Ayotunde EO, Fagbenro OA, Adebayo OT, Amoo AI. Toxicity of aqueous extracts of drumstick *Moringa oleifera* seeds to Nile tilapia *Oreochromis niloticus*, fingerlings and adults. In: *Proceedings of 6th international symposium on tilapia*; 2004.

39. Kim Y, Jaja-Chimedza A, Merrill D, Mendes O, Raskin I. A 14-day repeated-dose oral toxicological evaluation of an isothiocyanate-enriched hydroalcoholic extract from *Moringa oleifera* Lam. seeds in rats. *Toxicology Reports*. 2018; 5, 418–426.



pH Effect on Hydrothermal Synthesis of the Coordination Polymers Containing Pyrazine-2,3-dicarboxylate: Investigation of Thermal Stability, Luminescence, and Electrical Conductivity Properties

Burak AY ^{1,*} , Emel YILDIZ ¹ , Jon ZUBIETA ² 

¹Çukurova University, Arts and Science Faculty, Department of Chemistry, 01330, Adana, Turkey.

²Department of Chemistry, Syracuse University, Syracuse, NY 13244, USA.

Abstract: Hydrothermal reactions of the lanthanide(III) salt with 2,3-pyrazinedicarboxylic (2,3-pzdc) acid yielded the coordination polymers $[\text{La}_2(2,3\text{-pzdc})_3(\text{H}_2\text{O})]_n \cdot 3n\text{H}_2\text{O}$ (**1**) and $[\text{La}_2(2,3\text{-pzdc})_3(\text{H}_2\text{O})]_n \cdot 2n\text{H}_2\text{O}$ (**2**). Compounds were obtained in a three dimensional form with different pH values under subcritical water conditions. The structures had variable coordination numbers. In addition, pH values play an important role in the structural chemistry of these materials. Different characterization techniques (elemental analysis, FT-IR, ICP-OES, TG/DTA, FESEM, PXRD, BET and single crystal X-ray) were carried out to confirm crystallinity, porosity, purity and chemical composition of the coordination polymers. Crystal structures of the polymers were examined in detail. Their thermal stability, luminescence and electrical conductivity properties were investigated in the solid state.

Keywords: pH effect, hydrothermal synthesis, lanthanum coordination polymer, electrical conductivity.

Submitted: May 15, 2019. **Accepted:** December 16, 2019.

Cite this: Ay B, Yildiz E, Zubieta J. pH Effect on Hydrothermal Synthesis of the Coordination Polymers Containing Pyrazine-2,3-dicarboxylate: Investigation of Thermal Stability, Luminescence, and Electrical Conductivity Properties. JOTCSA. 2020;7(1):243–58.

DOI: <https://doi.org/10.18596/jotcsa.565700>.

***Corresponding author. E-mail:** bay@cu.edu.tr.

INTRODUCTION

Coordination polymers (CPs) have structures consisting of metal nodes and organic linkers that are connected together via coordination bonds (1-3). Synthesis of the CPs have attracted ever-increasing interest not only their structural aesthetics but also their potential applications such as heterogeneous catalyst (4-6), luminescence (7-9), gas storage (10-12), molecular separation (13), sensor (14), drug encapsulation (15) and so on. Several methods have been used for the synthesis of CPs. Among them, some important synthetic routes are hydro/solvothermal synthesis, sonochemical, slow evaporation, microwave assisted synthesis, mechanochemical and electrochemical synthesis (16). It is well known

that the crystallization, structure, and morphology of CPs depend on the metal or ligand type, solvent type (17-19), pH value of reaction mixture (20-23), stoichiometric ratio of metal/ligand (24), mineralizing agent (25), temperature (26-28), and time (29). These parameters play a profound effect on the structural chemistry of compounds. In this study, pH effect of the solution on polymer formation under subcritical conditions was investigated. For this purpose, multifunctional 2,3-pzdc was selected as a ligand due to the six potential coordination sites. There are many studies on the coordination modes of the 2,3-pzdc acid ligand in the literature. These modes are available in many different coordination modes, including mono-to-heptadentate and bridging mode ligands (30-42). However, the number of

works with mixed coordination mode is very few (43). In this work, the ligand 2,3-pzdc adopted three different coordination modes in the polymeric

chains through which lanthanum ions are linked together to form a three-dimensional structure.

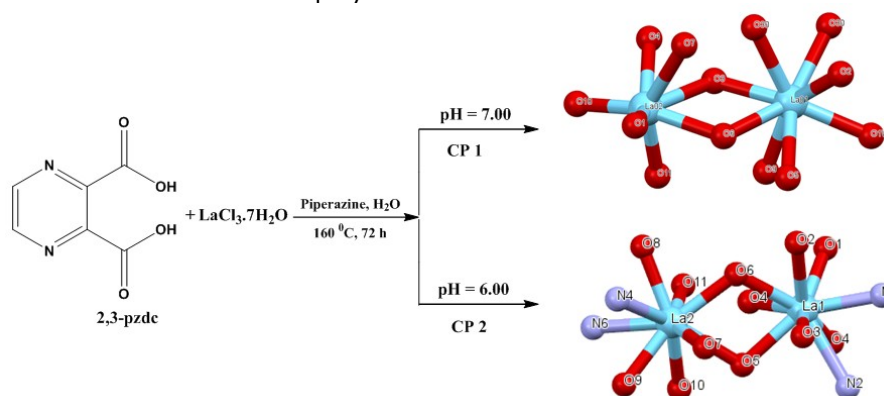


Figure 1: Schematic representation of CPs synthesized at different pH values in hydrothermal conditions.

In this work, our aim is hydrothermal synthesis of CPs to better understand the pH effect under subcritical conditions. In the synthesis of CPs, stoichiometric ratio, reaction temperature, and time were kept constant and pH values were changed from 1.00 to 7.00. pH values were adjusted by a mineralizing agent piperazine. At the pH values of 6.00 and 7.00, three dimensional lanthanum-based coordination polymers, namely $[\text{La}_2(2,3\text{-pzdc})_3(\text{H}_2\text{O})]_n \cdot 3n\text{H}_2\text{O}$ (**1**) and $[\text{La}_2(2,3\text{-pzdc})_3(\text{H}_2\text{O})]_n \cdot 2n\text{H}_2\text{O}$ (**2**), with different coordination numbers and coordination modes were obtained (Figure 1). Electrical conductivity, thermal stability, and luminescence properties of CPs were investigated.

EXPERIMENTAL

Materials and methods

All chemicals were purchased from commercial sources and used without further purification. PTFE-lined stainless steel containers with 23 mL capacity were used for hydrothermal synthesis. Perkin Elmer Pyris Diamond TG/DTA equipment (50-800 °C range) at a heating rate of 10 °C/min was used for TGA analysis. Thermo Flash 2000 CHNS analyzer was used for the elemental analysis. Quantitative lanthanide analyses were performed with Perkin-Elmer Optima 2100DV Inductively Coupled Plasma Optical Emission Spectrometry (ICP-OES) instrument. Perkin-Elmer RX-1 FT-IR with KBr pellets spectrometer in the range of 4000-400 cm^{-1} was used for the IR analysis of the compounds. The Field Emission Scanning Electron Microscope (FESEM) images of the compounds were recorded using Carl Zeiss, SUPRA-55. Rigaku Miniflex system with CuK α radiation ($\lambda = 1.54059 \text{ \AA}$) was used for the Powder X-Ray Diffraction (PXRD) studies. The electrical conductivity properties of the coordination polymers were determined by four-point probe method with an Electrometer Entek Electronic FPP-

470. Asimeto AS-105 digital micrometer was used for thickness measurements. Perkin-Elmer LS 55 Luminescence Spectrometer was used for the solid state fluorescence excitation and emission spectra. LEICA EZ4W stereo microscope was used for the high definition views of the CPs. Autosorb-6B surface area and pore size analyzer was used for the Brunauer, Emmett and Teller (BET) analysis.

Synthesis of $[\text{La}_2(2,3\text{-pzdc})_3(\text{H}_2\text{O})]_n \cdot 3n\text{H}_2\text{O}$ (**1**)

A mixture of $\text{LaCl}_3 \cdot 7\text{H}_2\text{O}$ (0.1114 g, 0.30 mmol), 2,3-pzdc acid (0.0504 g, 0.30 mmol), piperazine (0.0517 g, 0.60 mmol) and H_2O (5.00 mL, 277.80 mmol) with the mole ratio of 1:3:3:927 were added 23 mL volumetric steel Parr Acid reactor. The heterogeneous solution was stirred for 30 minutes at ambient temperature. The white solution with an initial pH of 7.00 was heated at 160 °C for 72 hours. At the end of the reaction, the system was cooled to room temperature. The final pH of the solution was measured by separating the yellow solution and crystals (pH = 6.10). The resulting yellow crystals were washed with pure water and dried (Figure 2). Single crystals suitable for X-ray diffraction analysis were obtained in 78% yield. Anal. Calcd. for $\text{C}_{18}\text{H}_{18}\text{N}_6\text{O}_{15}\text{La}_2$: C, 25.86; H, 2.17; N, 10.05. Found: C, 25.83; H, 2.08; N, 10.34%. The ICP-OES analysis (%) showed that **1** contained La: 33.22; Calcd.: 34.17. IR (KBr pellet, cm^{-1}): 3500, 3362 (m, b), 1618 (s), 1558 (s), 1366 (m), 558 (m), 442 (m).

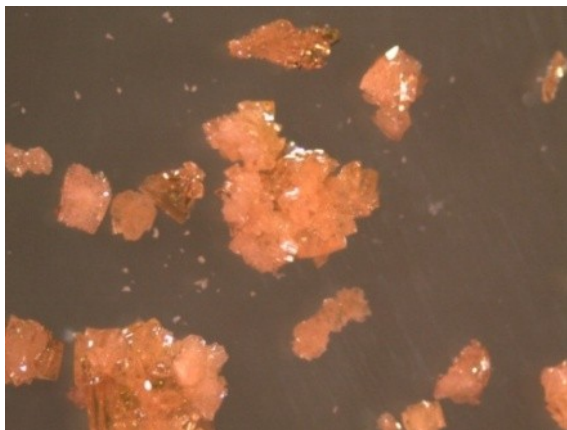


Figure 2: High resolution microscope image of **1** crystals.

Synthesis of $[\text{La}_2(2,3\text{-pzdc})_3(\text{H}_2\text{O})]_n \cdot 2n\text{H}_2\text{O}$ (**2**)

A mixture of $\text{LaCl}_3 \cdot 7\text{H}_2\text{O}$ (0.3714 g, 1.00 mmol), 2,3-pzdc acid (0.1681 g, 1.00 mmol), piperazine (0.1292 g, 1.50 mmol) and H_2O (5.00 mL, 277.80 mmol) with the mole ratio of 1.00: 1.00: 1.50: 277.8 were added 23 mL volumetric steel Parr Acid reactor. The heterogeneous solution was stirred for 30 minutes at ambient temperature. The white solution with an initial pH of 6.00 was heated at 160 °C for 72 hours. At the end of the reaction, the system was cooled to room temperature. The final pH of the solution was measured by separating the yellow solution and crystals (pH = 5.30). The resulting light yellow crystals were washed with pure water, and dried (Figure 3). The single crystals suitable for X-ray diffraction analysis were obtained in 86.8% yield. Anal. Calcd. for $\text{C}_{18}\text{H}_{16}\text{N}_6\text{O}_{14}\text{La}_2$: C, 26.42; H, 1.97; N, 10.27. Found: C, 26.91; H, 2.05; N, 9.87%. The ICP-OES analysis (%) showed that **2** contained La: 32.52; Calcd.: 33.45. IR (KBr pellet, cm^{-1}): 3494, 3335 (m, b), 1606 (s), 1557 (s), 1363 (vs), 556 (s), 434 (s).

X-ray Crystallography

A Bruker SMART system equipped with a CCD diffractometer at low temperature (100 K) using MoK α radiation (MoK α = 0.71073 Å) was used for the X-ray single-crystal analysis (44). The data

were corrected for Lorentz and polarization effects, and absorption corrections were made using SADABS (45, 46). The structure solution and refinement were carried out using the SHELXLTL crystallographic (47) software package. The structure was solved by direct methods and the nonhydrogen atoms refined against F^2 anisotropically. Crystal data are summarized in Table 1, and selected bond distances and bond angles are given in Tables 2 and 3. Full tables bond lengths and angles for CPs are available as Supplementary materials (Tables S1-S4).

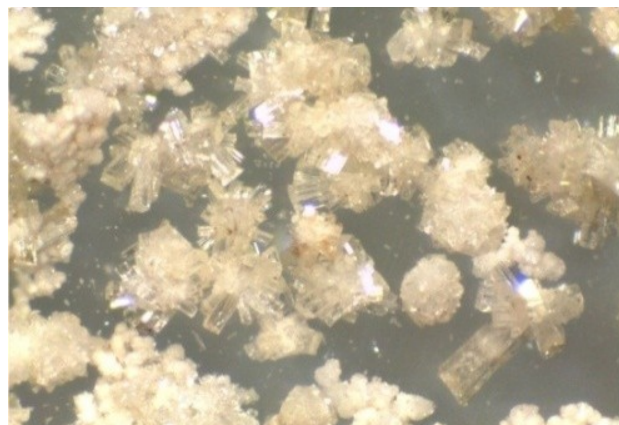


Figure 3: High resolution microscope image of **2** crystals.

RESULTS AND DISCUSSION

Crystal structures of CPs

Three-dimensional **1** and **2** have $[\text{La}_2(2,3\text{-pzdc})_3(\text{H}_2\text{O})]_n \cdot 3n\text{H}_2\text{O}$ and $[\text{La}_2(2,3\text{-pzdc})_3(\text{H}_2\text{O})]_n \cdot 2n\text{H}_2\text{O}$ closed formulas. They have monoclinic $P2_1/c$ crystal systems and these polymers differ from each other in terms of coordination modes and uncoordinated water molecules. Dimeric lanthanum atoms in **1** have trigonal prismatic geometry (seven coordination) and close to a trigonal dodecahedron (eight coordination) geometry, respectively. In **2**, because of the pH effect of under hydrothermal conditions dimeric lanthanum atoms have tricapped trigonal prismatic geometry (nine coordination) (Figure 4).

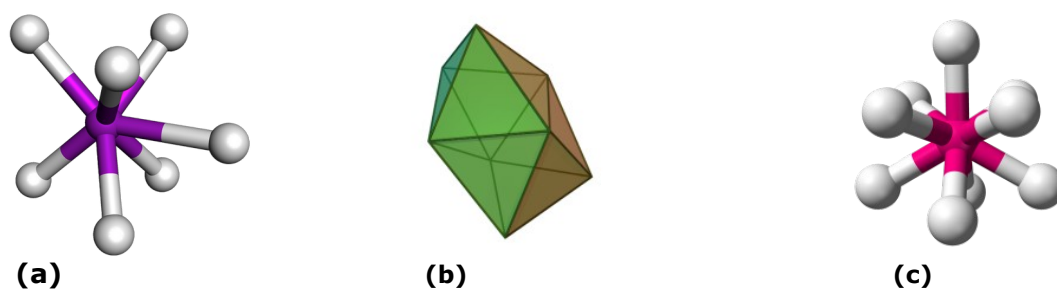


Figure 4: Trigonal prismatic geometry (a), trigonal dodecahedron (b) and tricapped trigonal prismatic geometry (c).

Table 1. Crystal data and structure refinement for the CPs.

Compound	1	2
Empirical Formula	C ₁₈ H ₁₈ N ₆ O ₁₅ La ₂	C ₁₈ H ₁₆ N ₆ O ₁₄ La ₂
Temperature (K)	100(2)	100(2)
Formula weight	836.20	818.16
Crystal system	Monoclinic	Monoclinic
Space group	P2 ₁ /c	P2 ₁ /c
a (Å)	8.9545(13)	8.9637(3)
b (Å)	16.9040(3)	16.9171(6)
c (Å)	15.468(2)	15.4942(5)
α (°)	90	90
β (°)	101.348(2)	101.36
γ (°)	90	90
Volume (Å ³)	2295.57	2303.51
Z	4	4
Density _{calculated} (g/cm ⁻³)	2.354	2.423
Absorp. coeff. (μ, mm ⁻¹)	3.689	4.354
Wavelength (λ, Å)	0.71073	0.71073
R indices (all data) (R1 / wR2)	0.0150 / 0.0489	0.0332 / 0.0545

Single crystal X-ray analysis showed that 2,3-pzdc ligands show multiple chelation at 7.00 and 6.00 pH values. When the pH of the solution was adjusted to 7.00, during synthesis of **1**, 2,3-pzdc

ligand behaved as 3, 5 and 6 dentate ligands in the polymeric chains (Figure 5). Due to the differences in the number of coordination modes in the frameworks, multiple metal bridges occurred.

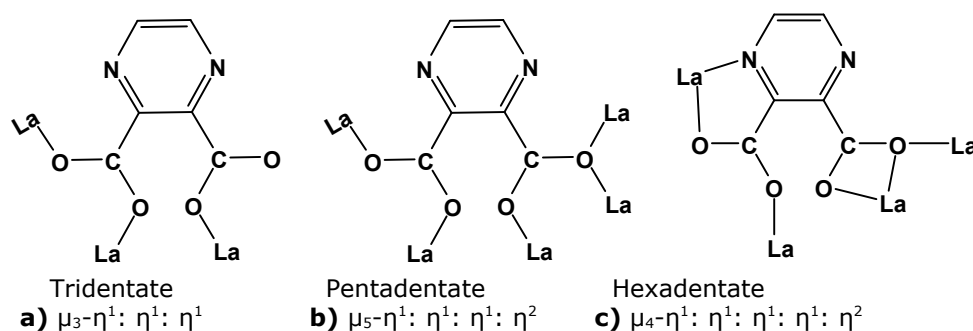


Figure 5: Coordinating modes of the 2,3-pzdc ligand at pH = 7.00 in compound **1**.

Asymmetric units contain two La(III) ions. The La01 atom has eight coordination, while La02 atom of seven and together form a dimeric unit (Figure 6). As seen in the asymmetric unit of **1**, nitrogen atoms of 2,3-pzdc ligand are not coordinated to metals in the case of pH at 7.00. Only oxygen atoms in the carboxyl groups are coordinated to

metals. La01 and La02 atoms are linked to each other by oxygen bridges [(O30)]. Around the La01 atom, five oxygen atoms from carboxyl groups, two oxygen bridges and with an oxygen atom in a coordinated water molecule, has totally eight coordination numbers. Nevertheless, there are a total of seven coordination numbers with the five

oxygen atoms and two oxygen bridges from the carboxyl groups around around the La02 atom.

Asymmetric unit of **1**, there are three water molecules outside the coordination sphere.

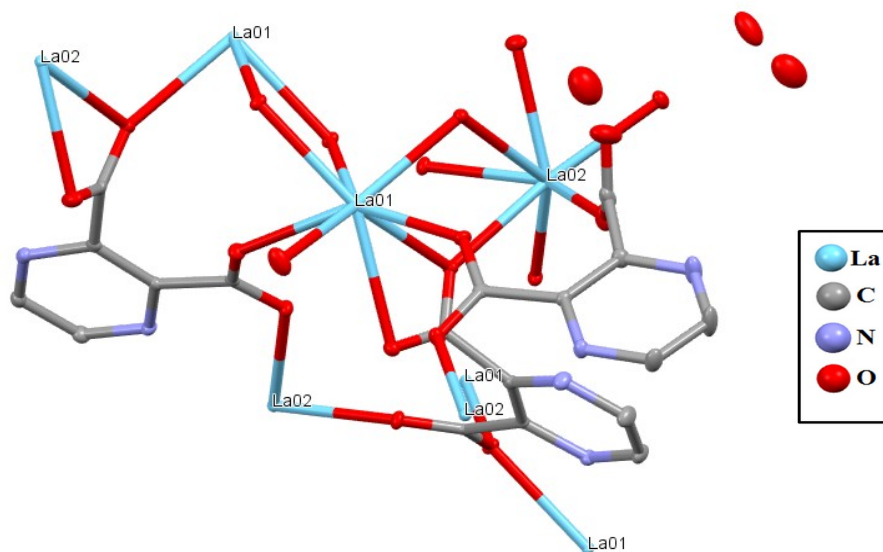
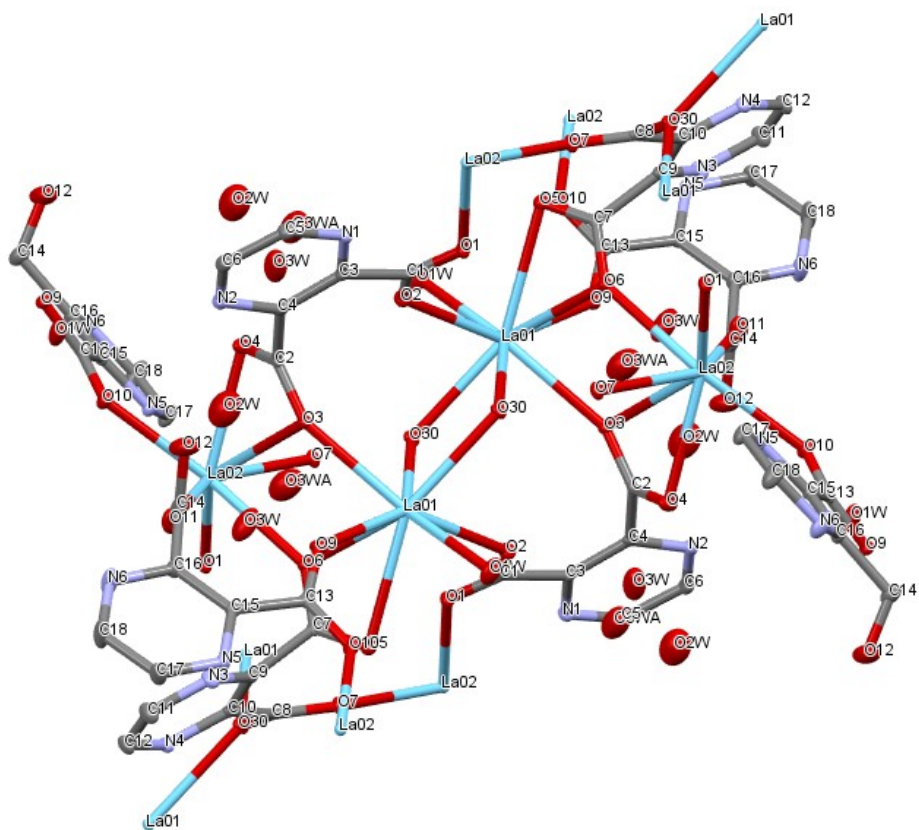


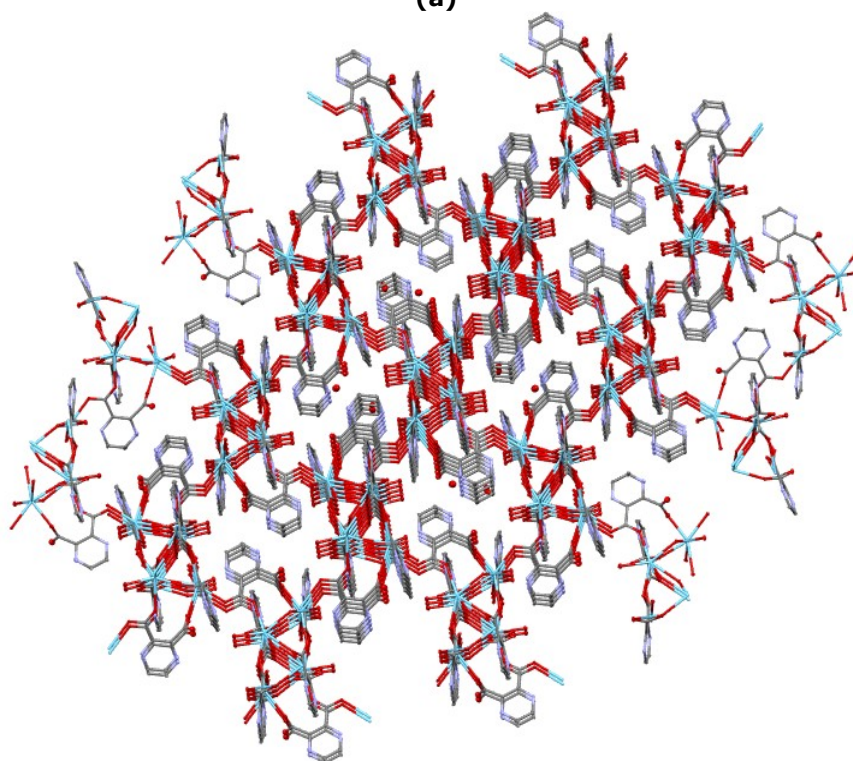
Figure 6: Coordination environment of different coordinated La(III) monomeric structure of **1**. All hydrogen atoms are omitted for clarity.

Figure 7 shows the coordination environment of **1**. La01 atom has eight coordination numbers and only oxygen atoms are coordinated to lanthanum atom. An oxygen atom [(O9)] of the tridentate ligand, oxygen atoms [(O3), (O2)] of the pentadentate ligand, oxygen atoms [(O5), (O6)] of the hexadentate ligand, oxygen atom of a coordinated water molecule [(O1W)] and oxygen atoms in the bridge position are coordinated. However, La02 atom has a coordination number of seven. Oxygen atoms [(O3), (O4)] of the pentadentate ligand, oxygen atoms [(O10), (O11)]

of the tridentate ligands, an oxygen atom [(O6)] of the hexadentate ligand, and two oxygen atoms in the bridge position are coordinated. [(O3), (O6)] oxygen atoms coordinated to La(III) atoms and caused different structural positioning in the polymeric chain. La-O's bond lengths ranged from 2.396 to 2.695 Å, while O-La-O's bond angles are between 69.24 and 145.20°. The selected bond length and bond angle values of the atoms around the coordination sphere are given in Tables 2 and 3.



(a)



(b)

Figure 7: Coordination environment of the **1** (a) and 3D packing diagram linked by tridentate, pentadentate and hexadentate pzdc ligands (b). All hydrogen atoms are omitted for clarity.

The pH of the solution was adjusted to 6.00 in the synthesis of **2**. The 2,3-pzdc ligands behaved as 4-, 6-, and 7-dentate ligands in the polymer chain of **2** and showed differences from **1** (Figure 8).

Asymmetric units have two La(III) ions and both of them have a coordination number of 9. The asymmetric unit consist of three 2,3-pzdc ligands with different coordination modes (Figure 9).

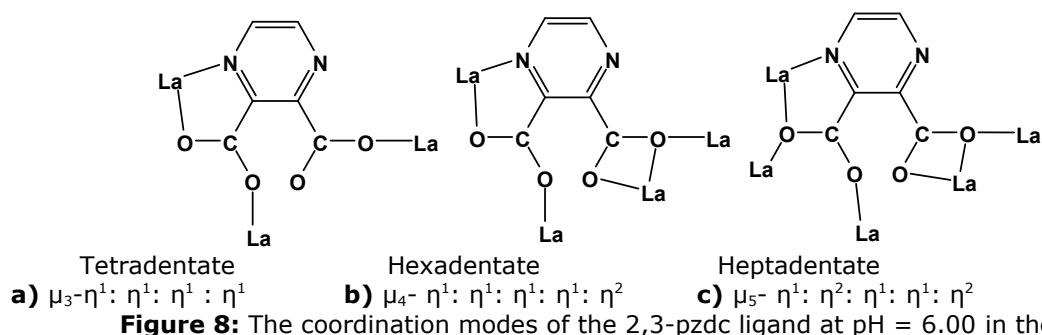


Figure 8: The coordination modes of the 2,3-pzdc ligand at pH = 6.00 in the **2**.

Unlike **1**, the nitrogen and oxygen atoms are also coordinated to metal atoms due to the pH value in the polymeric **2**. Two water molecules in

monomeric structure are in the cage structure with hydrogen bonds outside the coordination sphere.

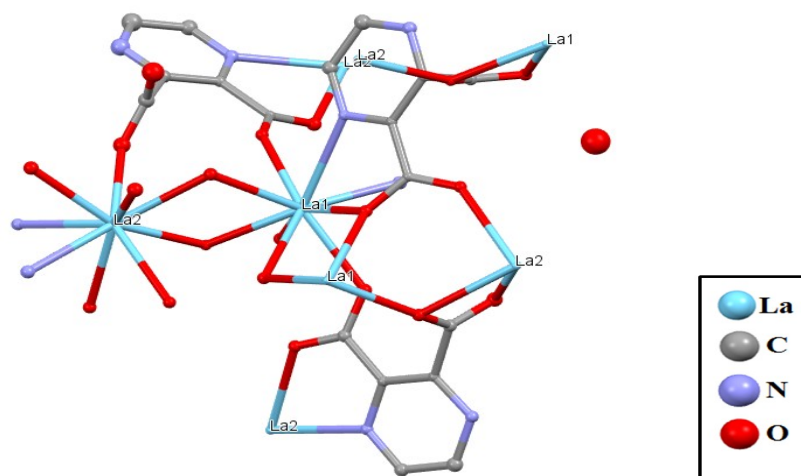


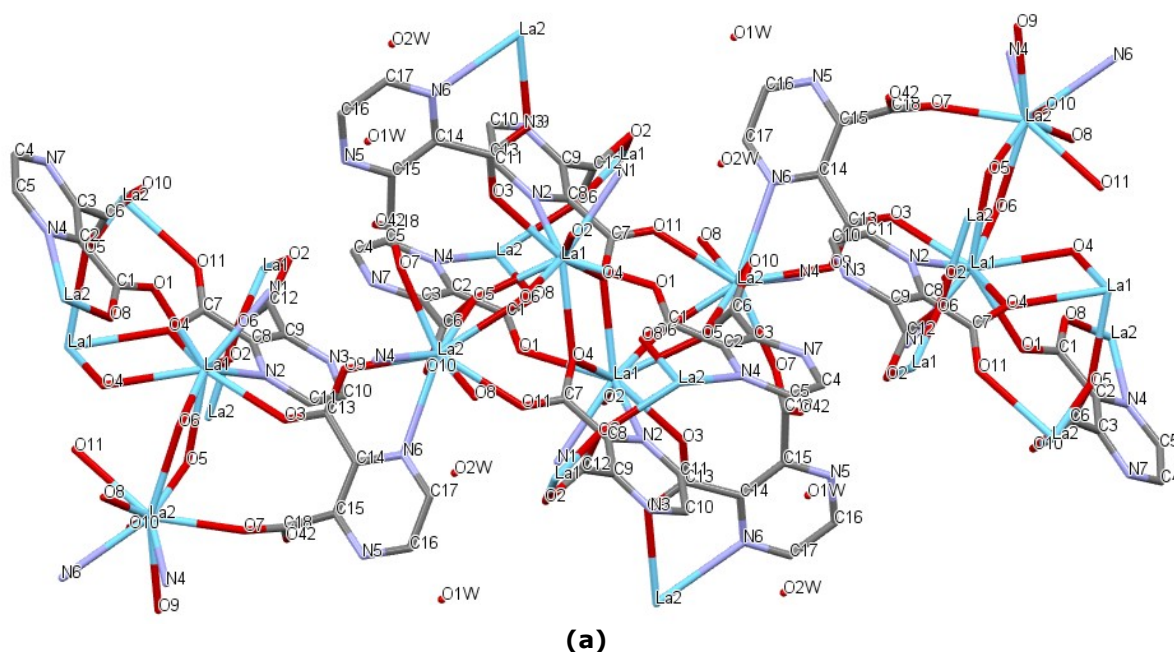
Figure 9: Coordination environment of nine coordinated monomer structures of **2**. All hydrogen atoms are omitted for clarity.

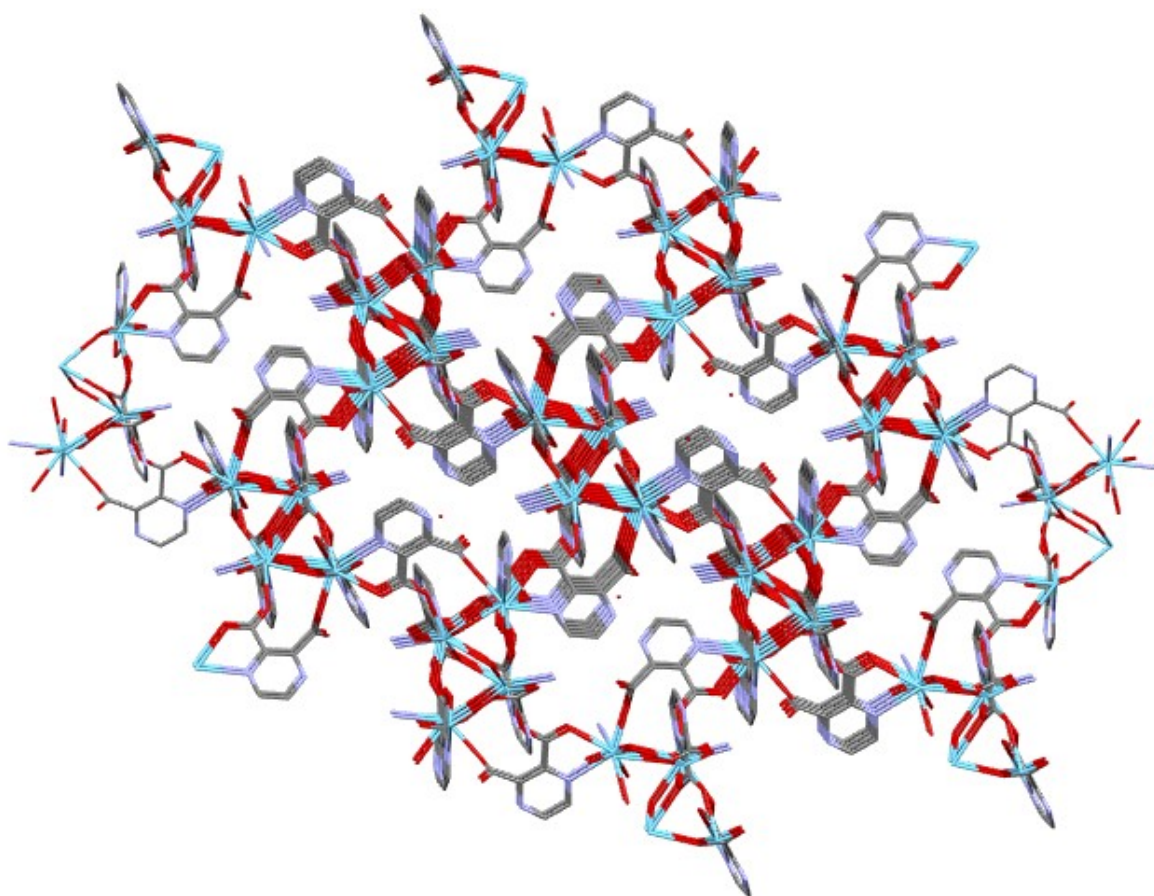
Table 2. Selected bond length [Å] and bond angles [°] for **1**.

La01-O1W	2.515(2)	La02-O1	2.503(1)
La02-O6	2.496(1)	La02-O10	2.491(2)
La01-O2	2.494(2)	La02-O11	2.396(2)
La01-O5	2.713(1)	La01-O9	2.442(1)
La01-O6	2.572(2)	La02-O7	2.565(1)
La02-O4	2.606(1)	La01-O3	2.536(2)
La02-O3	2.695(2)	La01-O30	2.628(1)
O1W-La01-O2	73.28(5)	O1W-La01-O5	79.28(5)
O1W-La01-O6	128.29(5)	O1W-La01-O9	83.35(5)
O1W-La01-O3	145.20(5)	O1W-La01-O30	83.93(5)
O1W-La01-O30	137.69(5)	O2-La01-O5	79.66(5)
O2-La01-O6	98.25(5)	O2-La01-O9	144.04(5)
O2-La01-O3	138.33(5)	O2-La01-O30	73.01(5)
O2-La01-O30	69.45(5)	O5-La01-O6	49.24(5)
O5-La01-O9	69.24(5)	O5-La01-O3	114.88(5)

There are three different coordination modes of the bridge 2,3-pzdc ligands in the polymeric chain (Figure 10), and the pyrazine rings are oriented in different ways in the framework. Although lanthanum ions have nine coordination number, coordination environments are different. The pzdc ligand, acting as hexa- and hepta-dentate, was coordinated to the lanthanum atom by the nitrogen [N(2)] and the oxygen [O(4)] atoms in the carboxyl group. Two oxygen atoms [O(1), O(5)] in the carboxyl group (μ^2, η^3 -carboxyl) of the hexadentate pzdc ligand, an oxygen [O(3)] atom in the carboxyl group of the tetradentate ligand, an oxygen [O(11)] atom in the μ^2, η^2 -carboxyl group of the heptadentate pzdc ligand and an oxygen [O(4)] atom in the μ^2, η^3 -carboxyl group of the other heptadentate pzdc ligand was coordinated to the La1 atom. Compared to La1, there is only one

pzdc ligand that acts just like a heptadentate ligand around the coordination of La2 atom. La2 atom was coordinated through nitrogen and oxygen atom in the carboxyl group. La2 was also coordinated from two oxygen atoms in the carboxyl group of the heptadentate pzdc ligand and four oxygen atoms from the 4-, 6-, and 7-dentate ligands. The oxygen atom from a water molecule coordinated by lanthanum centers and has completed nine coordination numbers. In total, six pzdc ligands are linked to the lanthanum ions. La-O's bond lengths ranged from 2.403 to 2.713 Å, while La-N's bond lengths were 2.531 and 2.767 Å. When the bond angles were examined, it was determined that O-La-O, O-La-N and N-La-N angles were between 69.2 and 144.1°, respectively, which are consistent with those of reported literature (48, 49).





(b)

Figure 10: Coordination environment of the **2** (a) and 3D packing diagram linked by tetradentate, hexadentate, and heptadentate pzdc ligands (b). All hydrogen atoms are omitted for clarity.

Table 3. Selected bond length [\AA] and bond angles [$^\circ$] for **2**.

La1-O3	2.450(3)	La1-O1	2.501(5)
La1-O4	2.561(4)	La1-N1	2.531(5)
La1-N2	2.767(4)	La1-O5	2.544(3)
La1-O6	2.577(4)	La1-O2	2.713(3)
La1-O4	2.625(4)	La2-O7	2.403(5)
La2-O5	2.699(4)	La2-O10	2.610(3)
La2-O9	2.502(4)	La2-O6	2.497(3)
La2-O8	2.509(4)	La1-O6	2.577(4)
O3-La1-O1	144.1(1)	O3-La1-O4	132.0(1)
O3-La1-N1	83.0(1)	O3-La1-N2	71.7(1)
O3-La1-O5	73.7(1)	O3-La1-O6	75.2(1)
O3-La1-O2	69.2(1)	O3-La1-O4	138.9(1)
O1-La1-O4	72.8(1)	O1-La1-N1	73.5(1)
O1-La1-N2	122.3(1)	O1-La1-O5	138.5(1)
O4-La1-O5	92.2(1)	N1-La1-N2	70.2(1)
O4-La1-O2	151.0(1)	N1-La1-O6	128.2(1)

IR spectra

FT-IR spectra of free ligands **1** and **2** are given in Figures S1-S3. The peaks seen in the range of 3300-3500 cm^{-1} are belong to $\nu(\text{O-H})$ stretching vibrations of the coordinated and uncoordinated

water molecules in the structures. In the IR spectrum of the 2,3-pzdc, the band at 1712 cm^{-1} is attributed to $\nu(\text{C=O})$ stretching band (50). After coordination, this peak shifted to 1618 cm^{-1} (for **1**) and 1606 cm^{-1} (for **2**) as strong peaks in the

spectrum of complexes. These shifts support that the oxygen atoms in carbonyl groups are coordinated to lanthanides. The symmetric stretching vibrations of $\nu(\text{C}=\text{O})$ in the polymeric chain are observed at 1366 and 1363 cm^{-1} , respectively. In the IR spectrum of the 2,3-pzdc, the band at 1687 cm^{-1} is attributed to $\nu(\text{C}=\text{N})$ stretching band. This peak shifted to 1557 cm^{-1} for **2** after coordination. New bands at 442 and 434 cm^{-1} in the spectrum of complexes are attributed to $\nu(\text{La}-\text{O})$. The coordination of the oxygen atoms to the metal ions indicates that the CPs are formed. A new and strong band at 556 cm^{-1} in the spectrum of **2** is attributed to $\nu(\text{La}-\text{N})$ stretching vibrations (51).

Thermal properties

TG/DTG curves of **1** and **2** are given in Figures S4 and S5. Three-step mass losses are observed in the TG/DTG curve of **1**. Two mass losses at around 100-300 °C temperatures are thought to belong to coordinated and uncoordinated water molecules in the structure. The final mass loss between temperatures of 357 and 600 °C is related to the degradation of organic ligands in the structure. When the TG/DTG curve of the **2** was examined, two-step mass loss occurred. The coordination polymer exhibited thermal stability up to about 150 °C. The first mass loss between 150-285 °C belongs to the degradation of water molecules in the framework. The second mass loss at around 372-590 °C corresponds to the degradation of organic ligands. As seen in thermal curves, **2** is more thermally stable than **1**. It is due to the fact

that the uncoordinated water molecules in the structure **2** are connected to the main structure by hydrogen bonds from N1-O2W-O10, O1W-O42 atoms (Figures S6 and S7).

PXRD patterns

To determine the phase purities of the CPs, powder XRD analysis was performed at room temperature. For this purpose, simulated and experimental XRD results were compared. The simulated X-ray diffraction patterns were determined by Mercury diffraction-crystal module program with the help of data obtained as a result of single crystal analysis. The experimental and simulated powder XRD patterns of the synthesized compounds are given in Figure S8. These patterns were compared with each other in terms of peak positions. When the experimental and theoretical curves of the samples are examined, they are compatible, and obtained with high purity. These results are supported with high resolution microscope images.

Morphologies of the CPs

BET and FESEM analysis were performed to determine surface morphology, pore volume, and pore size of CPs. When the surface morphology of **1** was examined, it was seen that obviously the crystals have both porous structures and regional cracks in different approximations (Figure 11). The surface area of **1** was determined as 5.82 m^2/g and the pore volume was $18.25 \times 10^{-3} \text{ cm}^3/\text{g}$ as a result of BET analysis. In addition, the average pore size of the crystal having mesoporous structure was calculated as 3.21 nm diameter.

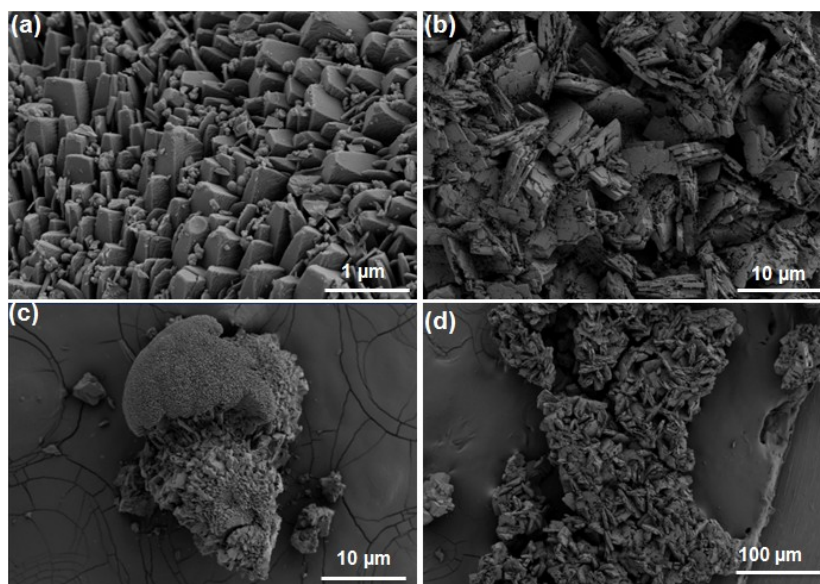


Figure 11: FESEM images of **1**.

When the surface morphology of **2** was examined, there are regional crystallizations in different approximations of the crystals (Figure 12). The surface area of the crystal was 6.43 m^2/g , and the

pore volume was $6.80 \times 10^{-3} \text{ cm}^3/\text{g}$. It is also in mesoporous form due to the average pore diameter of 3.08 nm.

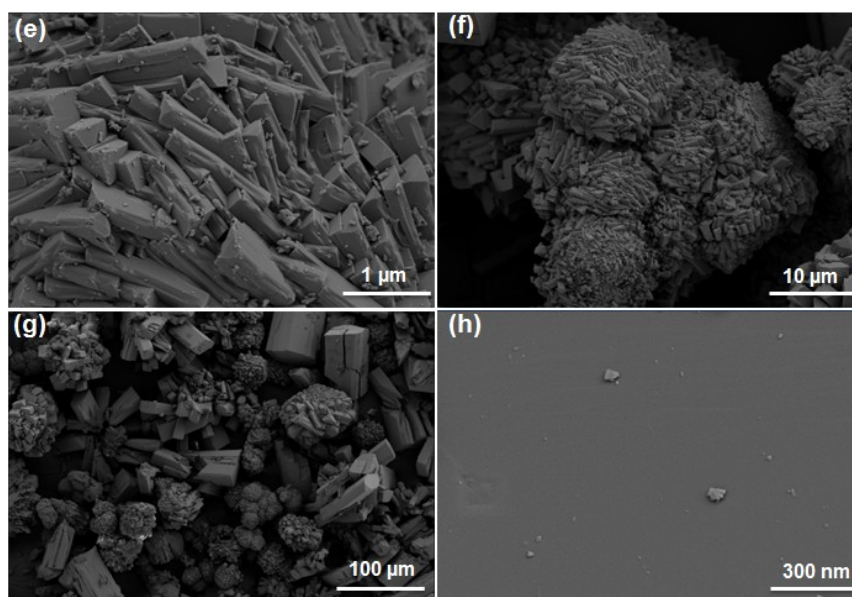


Figure 12: FESEM images of **2**.

Luminescence properties

Lanthanides are of great significance for designing new luminescent materials and cause new areas of application. Narrow-band light-emitting performances of lanthanides are excellent (52). Luminescence properties of free ligand and CPs are investigated in solid state at room temperature, as shown in Figure 13. The free 2,3-pzdc acid ligand displays an emission maximum at 415 nm ($\lambda_{ex} = 300$ nm), which is attributed to the n^*-n transition. Bathochromic (red) shifts are observed in **1** and **2** polymers compared with the 2,3-pzdc. **1** gives a narrow and strong emission band from 505 nm to 520 nm with the maximum at 517 nm upon excitation at 285 nm, and similarly **2** gives a narrow and strong emission band from 565 nm to 602 nm with the maximum at 584 nm upon excitation at 290 nm. These emission values are supported by similar La(III) studies in the

literature (53). According to the above results, the emission of complexes may be assigned to the ligand-to-metal-charge-transfer bands (LMCT) (54, 55), rather than the n^*-n transition of the ligand. Although the polymers have the same ligand and metal, the emission values are different due to the difference in the coordination numbers and modes formed by various pH values. The excitation and emission values, Stokes' shifts and emitted colors of the synthesized coordination polymers are summarized in Table 4. It was observed that there was no overlap in excitation and emission values in all of the compounds and they give bands at distal wavelengths. Very large Stokes' shift values (232 nm for **1**, 294 nm for **2**) are observed. Large Stokes' shifts, thermal stability, brightness, and suitable material size lead to be in many different sensor applications (56, 57).

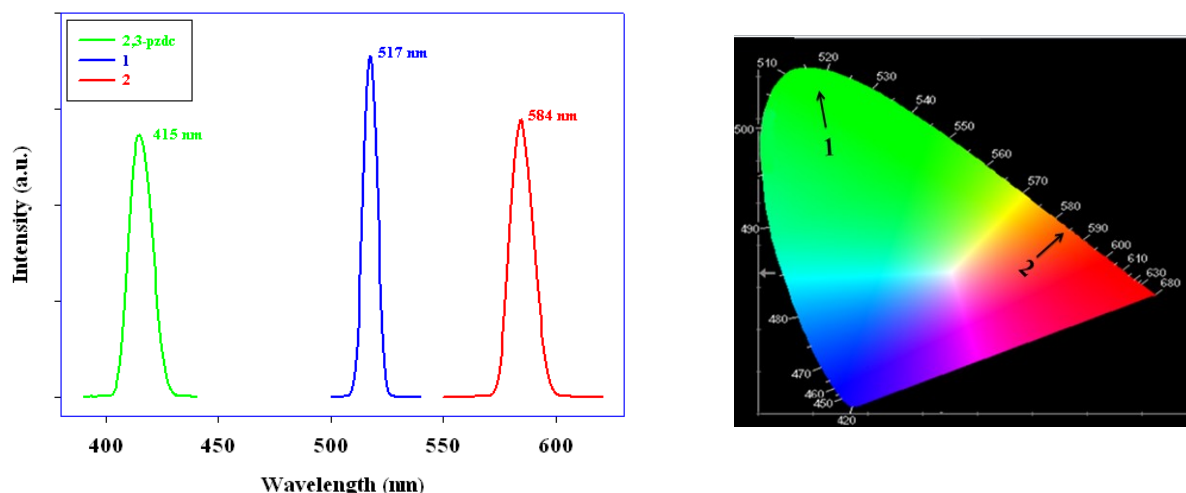


Figure 13: Solid-state emission spectra of 2,3-pzdc, chromaticity diagram of compounds **1** and **2** at room temperature.

Table 4. The luminescence results of free ligand and coordination polymers.

Compounds	Excitation (λ , nm)	Emission (λ , nm)	Stokes' Shift (nm)	Emitted Color
2,3-pzdc	300	415	115	-
1	285	517	232	Green
2	290	584	294	Yellow

Electrical conductivity

Liquid based electrolytes are widely used as batteries and supercapacitors. Moreover, because of their high thermal stability, easier processability, and mechanical properties, inorganic-organic solid polymers attract more attention than others. Therefore, solid polymer conductors (organic or organic-inorganic) have been proposed as an alternative to liquid based electrolytes. Because of the facile synthesis of CPs by hydrothermal method, and having high thermal stability, we aimed to examine their electrical conductivity properties in a solid phase. Crystal samples of CPs were compressed under 12 tons of pressure as a solid phase. Their thickness (0.274 mm for **1**; 0.435 mm for **2**) and diameters (12 mm) were measured by using digital micrometer. Solid electrical conductivity measurements were performed at room temperature. Electrical conductivity values of the CPs were measured by four-point probe technique. In order to obtain the most accurate results, the conductivity values were measured in five parallel measurements. The highest electrical conductivity was exhibited by **1** with 3.45×10^{-6} S/cm at ambient temperature. **2** showed the maximum conductivity of 2.08×10^{-6} S/cm at 25 °C. Both mesoporous samples showed very close electrical conductivity values. Due to having different framework structures, **1** exhibited slightly more conductivity values than that of **2**. The conductivity range of the conducting polymers

is between 10^{-12} and 10^4 S/cm, while the electro active polymeric composite ranges from 10^{-8} to 10^3 S/cm. However, the semiconductor range is between 10^{-8} and 10 S/cm (58). In our study, mesoporous CPs showed conductivity values at 10^{-6} S/cm. According to the literature, the synthesized polymers can be used as semiconducting materials in solid phase. These materials have found a wide range of applications because of their low cost, compactness, power efficiency and reliability.

CONCLUSION

In summary, three dimensional La(III) coordination polymers based on multifunctional 2,3-pzdc acid were synthesized under subcritical conditions in different pH values and were fully characterized. It is noteworthy that 2,3-pzdc acid in the frameworks have different coordination modes. Therefore, it is found that the pH value of the solution plays an important role in their coordination modes and frameworks under hydrothermal conditions. **1** and **2** show good electrical conductivity values of 3.45×10^{-6} and 2.08×10^{-6} S/cm at room temperature, respectively. Moreover, the compounds have thermal stability up to 150 °C. It is foreseen that the obtained semiconductor CPs can be employed in the manufacture of various kinds of electronic devices, including integrated circuits, transistors and diodes. Photoluminescent spectra of **1** and **2**

showed that CPs are the potential luminescent materials at the maximum emission 517 and 584 nm with sharp and narrow bands. Because of their very large Stokes shifts and low cost, the synthesized CPs may find applications in different sensor applications and light-emitting devices.

ACKNOWLEDGEMENT

The authors gratefully acknowledge financial support from the Research Unit of Çukurova University (Grant No. FEF2013D5).

REFERENCES

- Guillerm V, Kim D, Eubank JF, Luebke R, Liu X, Adil K, Lah MS, Eddaoudi M. A supermolecular building approach for the design and construction of metal-organic frameworks. *Chemical Society Reviews* 2014; 43: 6141-6172. DOI: 10.1039/c4cs00135d
- Zhou X, Liu P, Huang W-H, Kang M, Wang Y-Y, Shi Q-Z. Solvents influence on sizes of channels in three fry topological Mn(II)-MOFs based on metal-carboxylate chains: syntheses, structures and magnetic properties. *CrystEngComm* 2013; 15: 8125-8133. DOI: 10.1039/C3CE41120F
- Wang P, Fan R-Q, Liu X-R, Wang L-Y, Yang Y-L, Cao W-W, Yang B, Hasi W, Su Q, Mu Y. Two-/three-dimensional open lanthanide-organic frameworks containing rigid/flexible dicarboxylate ligands: synthesis, crystal structure and photoluminescent properties. *CrystEngComm* 2013; 15: 1931-1949. DOI: 10.1039/c3ce26684b
- Dhakshinamoorthy A, Alvaro M, Garcia H. Commercial metal-organic frameworks as heterogeneous catalysts. *Chemical Communications* 2012; 48: 11275-11289. DOI: 10.1039/c2cc34329k
- Nguyen LTL, Le KKA, Truong HX, Phan NTS. Metal-organic frameworks for catalysis: the Knoevenagel reaction using zeolite imidazolate framework ZIF-9 as an efficient heterogeneous catalyst. *Catalysis Science & Technology* 2012; 2: 521-528. DOI: 10.1039/c1cy00386k
- Tan Y-X, He Y-P, Zhang J. Cluster-Organic Framework Materials as Heterogeneous Catalysts for High Efficient Addition Reaction of Diethylzinc to Aromatic Aldehydes. *Chemistry of Materials* 2012; 24: 4711-4716. DOI:10.1021/cm302953x
- Tian D, Li Y, Chen R-Y, Chang Z, Wang G-Y, Bu X-H. A luminescent metal-organic framework demonstrating ideal detection ability for nitroaromatic explosives. *Journal of Materials Chemistry A* 2014; 2: 1465-1470. DOI: 10.1039/c3ta13983b
- Guo Y, Feng X, Han T, Wang S, Lin Z, Dong Y, Wang B. Tuning the Luminescence of Metal-Organic Frameworks for Detection of Energetic Heterocyclic Compounds. *Journal of the American Chemical Society* 2014; 136: 15485-15488. DOI: 10.1021/ja508962m
- Kim TK, Lee JH, Moon D, Moon HR. Luminescent Li-Based Metal-Organic Framework Tailored for the Selective Detection of Explosive Nitroaromatic Compounds: Direct Observation of Interaction Sites. *Inorganic Chemistry* 2012; 52: 589-595. DOI: 10.1021/ic3011458
- Gándara F, Furukawa H, Lee S, Yaghi OM. High Methane Storage Capacity in Aluminum Metal-Organic Frameworks. *Journal of the American Chemical Society* 2014; 136: 5271-5274. DOI: 10.1021/ja501606h
- Peng Y, Krungleviciute V, Eryazici I, Hupp JT, Farha OK, Yildirim T. Methane Storage in Metal-Organic Frameworks: Current Records, Surprise Findings, and Challenges. *Journal of the American Chemical Society* 2013; 135: 11887-11894. DOI: 10.1021/ja4045289
- Li Y-W, Li J-R, Wang L-F, Zhou B-Y, Chen Q, Bu X-H. Microporous metal-organic frameworks with open metal sites as sorbents for selective gas adsorption and fluorescence sensors for metal ions. *Journal of Materials Chemistry A* 2013; 1: 495-499. DOI: 10.1039/c2ta00635a
- Bloch ED, Hudson MR, Mason JA, Chavan S, Crocellà V, Howe JD, Lee K, Dzubak AL, Queen WL, Zadrozny JM, Geier SJ, Lin L-C, Gagliardi L, Smit B, Neaton JB, Bordiga S, Brown CM, Long JR. Reversible CO Binding Enables Tunable CO/H₂ and CO/N₂ Separations in Metal-Organic Frameworks with Exposed Divalent Metal Cations. *Journal of the American Chemical Society* 2014; 136: 10752-10761. DOI: 10.1021/ja505318p
- Dou Z, Yu J, Cui Y, Yang Y, Wang Z, Yang D, Qian G. Luminescent Metal-Organic Framework Films As Highly Sensitive and Fast-Response Oxygen Sensors. *Journal of the American Chemical Society* 2014; 136: 5527-5530. DOI: 10.1021/ja411224j
- Cunha D, Ben Yahia M, Hall S, Miller SR, Chevreau H, Elkaïm E, Maurin G, Horcajada P, Serre C. Rationale of Drug Encapsulation and Release from Biocompatible Porous Metal-Organic Frameworks. *Chemistry of Materials* 2013; 25: 2767-2776. DOI: 10.1021/cm400798p

16. Seetharaj R, Vandana PV, Arya P, Mathew S. Dependence of solvents, pH, molar ratio and temperature in tuning metal organic framework architecture. *Arabian Journal of Chemistry* 2016; 12: 295-315. DOI: 10.1016/j.arabjc.2016.01.003
17. Li P-Z, Wang X-J, Li Y, Zhang Q, Tan RHD, Lim WQ, Ganguly R, Zhao Y. Co(II)-tricarboxylate metal-organic frameworks constructed from solvent-directed assembly for CO₂ adsorption. *Microporous and Mesoporous Materials* 2013; 176: 194-198. DOI: 10.1016/j.micromeso.2013.03.052
18. Sun F, Zhu G. Solvent-directed synthesis of chiral and non-centrosymmetric metal-organic frameworks based on pyridine-3,5-dicarboxylate. *Inorganic Chemistry Communications* 2013; 38: 115-118. DOI: 10.1016/j.inoche.2013.10.018
19. Liu T, Luo D, Xu D, Zeng H, Lin Z. Solvent induced structural variation in magnesium carboxylate frameworks. *Inorganic Chemistry Communications* 2013; 29: 110-113. DOI: 10.1016/j.inoche.2012.12.017
20. Chen L, Jia H-Y, Hong X-J, Chen D-H, Zheng Z-P, Jin H-G, Gu Z-G, Cai Y-P. Construction of one pH-independent 3-D pillar-layer lead-organic framework containing tetrazole-1-acetic acid. *Inorganic Chemistry Communications* 2013; 27: 22-25. DOI: 10.1016/j.inoche.2012.10.010
21. Li S-L, Tan K, Lan Y-Q, Qin J-S, Li M-N, Du D-Y, Zang H-Y, Su Z-M. pH-Dependent Binary Metal-Organic Compounds Assembled from Different Helical Units: Structural Variation and Supramolecular Isomers. *Crystal Growth & Design* 2010; 10: 1699-1705. DOI: 10.1021/cg9012763
22. Gabriel C, Perikli M, Raptopoulou CP, Terzis A, Psycharis V, Mateescu C, Jakusch T, Kiss T, Bertmer M, Salifoglou A. pH-Specific Hydrothermal Assembly of Binary and Ternary Pb(II)-(O,N-Carboxylic Acid) Metal Organic Framework Compounds: Correlation of Aqueous Solution Speciation with Variable Dimensionality Solid-State Lattice Architecture and Spectroscopic Signatures. *Inorganic Chemistry* 2012; 51: 9282-9296. DOI: 10.1021/ic300850g
23. Ollivier PJ, DeBoard JRD, Zapf PJ, Zubieta J, Meyer LM, Wang C, Mallouk TE, Haushalter RC. Hydrothermal synthesis and crystal structures of two novel vanadium oxides containing interlamellar transition metal complexes. *Journal of Molecular Structure* 1998; 470: 49-60. DOI: 10.1016/S0022-2860(98)00469-4
24. Kim D, Song X, Yoon JH, Lah MS. 3,6-Connected Metal-Organic Frameworks Based on Tricarboxylate as a 3-Connected Organic Node and a Linear Trinuclear Co₃(COO)₆ Secondary Building Unit as a 6-Connected Node. *Crystal Growth & Design* 2012; 12: 4186-4193. DOI: 10.1021/cg300686n
25. Darling K, Ouellette W, Prosvirin A, Walter S, Dunbar KR, Zubieta J. Hydrothermal synthesis and structures of materials of the M(II)/tetrazole/sulfate family (M(II)=Co, Ni; tetrazole=3- and 4-pyridyltetrazole and pyrazinetetrazole). *Polyhedron* 2013; 58: 18-29. DOI: 10.1016/j.poly.2012.07.043
26. Sun Y-X, Sun W-Y. Influence of temperature on metal-organic frameworks. *Chinese Chemical Letters* 2014; 25: 823-828. DOI: 10.1016/j.ccllet.2014.04.032
27. Liu G-X, Xu H, Zhou H, Nishihara S, Ren X-M. Temperature-induced assembly of MOF polymorphs: Syntheses, structures and physical properties. *CrystEngComm* 2012; 14: 1856-1864. DOI: 10.1039/c1ce05369h
28. Calderone PJ, Banerjee D, Plonka AM, Kim SJ, Parise JB. Temperature dependent structure formation and photoluminescence studies of a series of magnesium-based coordination networks. *Inorganica Chimica Acta* 2013; 394: 452-458. DOI: 10.1016/j.ica.2012.08.033
29. Mahata P, Prabu M, Natarajan S. Role of Temperature and Time in the Formation of Infinite -M-O-M Linkages and Isolated Clusters in MOFs: A Few Illustrative Examples. *Inorganic Chemistry* 2008; 47: 8451-8463. DOI: 10.1021/ic800621q
30. Wenkin M, Touillaux R, Devillers M. Bismuth derivatives of 2,3-dicarboxypyrazine and 3,5-dicarboxypyrazole as precursors for bismuth oxide based materials. *New Journal of Chemistry* 1998; 22: 973-976. DOI:10.1039/A801161C
31. Xu H, Ma H, Xu M, Zhao W, Guo B. catena-Poly[[[diaquairon(II)]-μ-pyrazine-2,3-dicarboxylato] dihydrate]. *Acta Crystallographica Section E Structure Reports Online* 2007; 64: m104-m104. Doi:10.1107/S1600536807064501
32. Liu H-Y, Wang H-Y, Shi Y-H. Pyrazine-2,3-dicarboxylate-bridged polymeric and dinuclear complexes involving decameric water clusters. *Journal of Coordination Chemistry* 2011; 64: 2859-2868. DOI: 10.1080/00958972.2011.608161
33. Okubo T, Kondo M, Kitagawa S. Synthesis, Structure, and Magnetic Properties of One-Dimensional Copper(II) Coordination Polymer, {[Cu(pyrazine-2,3-dicarboxylate)(H₂O)₂]₂H₂O}_n.

- Synthetic Metals 1997; 85: 1661-1662. DOI: 10.1016/S0379-6779(97)80386-4
34. Beobide G, Castillo O, Luque A, Garcia-Couceiro U, Garcia-Teran JP, Roma'n P. Supramolecular Architectures and Magnetic Properties of Coordination Polymers Based on Pyrazinedicarboxylate Ligands Showing Embedded Water Clusters. *Inorganic Chemistry* 2006; 45: 5367-5382. DOI: 10.1021/ic060221r
35. Yeşilel OZ, Mutlu A, Büyükgüngör O. Novel dinuclear and polynuclear copper(II)-pyrazine-2,3-dicarboxylate supramolecular complexes with 1,3-propanediamine, N,N,N',N'-tetramethylethylenediamine and 2,2'-bipyridine. *Polyhedron* 2009; 28: 437-444. DOI: 10.1016/j.poly.2008.11.044
36. Yang K, Luo J-H, Liu Z-H. Synthesis, structures and luminescent property of two lanthanon complexes assembled from 2,3-pyrazinedicarboxylic acid and ammonia. *Inorganica Chimica Acta* 2012; 391: 206-209. DOI: 10.1016/j.ica.2012.04.040
37. Zou J, Xu Z, Chen W, Lo KM, You X. Synthesis, structure and magnetic properties of new polymeric compounds containing manganese(II)-Pzdc (PzdcH : 2,3-Pyrazinedicarboxylic acid). *Polyhedron* 1999; 18: 1507-1512. DOI: 10.1016/S0277-5387(99)00019-4
38. Yeşilel OZ, Mutlu A, Büyükgüngör O. A new coordination mode of pyrazine-2,3-dicarboxylic acid and its first monodentate complexes: Syntheses, spectral, thermal and structural characterization of [Cu(pzdc)(H₂O)(en)₂].H₂O and [Cu(pzdc)(H₂O)(dmpen)₂]. *Polyhedron* 2008; 27: 2471-2477. DOI: 10.1016/j.poly.2008.04.046
39. Li X-H, Shi Q, Hu M-L, Xiao H-P. A crossing double chain {[Cu(PZDC2)·3(H₂O)·2(IDZC)]_n (H₂PZDC=2,3-pyrazinedicarboxylic acid, IDZC=imidazole cation). *Inorganic Chemistry Communications* 2004; 7: 912-914. DOI:10.1016/j.inoche.2004.05.017
40. Bayon JC, Net G, Real J, Rasmussen PG. Synthesis and reactivity of rhodium(I) and iridium(I) complexes of the dianions of 2,3-pyrazinedicarboxylic and 2,5-pyrazinedicarboxylic acid. *Journal of Organometallic Chemistry* 1990; 385: 409-415. DOI: 10.1016/0022-328X(90)85012-N
41. Wenkin M, Devillers M, Tinant B, Deleercq J-P. Diammine(pyrazine-2,3-dicarboxylato-N,O)palladium(II): synthesis, crystal structure, spectroscopic and thermal properties. *Inorganica Chimica Acta* 1997; 258: 113-118. DOI: 10.1016/S0020-1693(96)05533-8
42. Yin H, Liu S-X. Syntheses, crystal structures and photoluminescence of three coordination polymers with 2,3-pyrazinedicarboxylic acid and N-donor ligands. *Polyhedron* 2007; 26: 3103-3111. DOI: 10.1016/j.poly.2007.02.011
43. Yang L-R, Song S, Zhang W, Zhang H-M, Bu Z-W, Ren T-G. Synthesis, structure and luminescent properties of neodymium(III) coordination polymers with 2,3-pyrazinedicarboxylic acid. *Synthetic Metals* 2011; 161: 647-654. DOI: 10.1016/j.synthmet.2010.12.005
44. SMART DCS, version 5.630, Bruker-AXS Inc., Madison, WI, 1997-2002.
45. SAINT PLUS DRS, version 6.45A, Bruker-AXS Inc., Madison, WI, 1997-2002.
46. Sheldrick GM, University of Göttingen, Göttingen, Germany, 1996.
47. SHELXTL PC v, Bruker-AXS Inc., Madison, WI, 2002.
48. Yang Q, Xie G, Wei Q, Chen S, Gao S. Structures and standard molar enthalpies of formation of a series of Ln(III)-Cu(II) heteronuclear compounds with pyrazine-2,3-dicarboxylic acid. *Journal of Solid State Chemistry* 2014; 215: 26-33. DOI: 10.1016/j.jssc.2014.03.021
49. Zhuang G, Chen W, Zeng G, Wang J, Chen W. Position of substituent dependent dimensionality in Ln-Cu heterometallic coordination polymers. *CrystEngComm* 2012; 14: 679-683. DOI: 10.1039/c1ce05864a
50. Beaula TJ, Joe IH, Rastogi VK, Jothy VB. Chemical Computations and Vibrational Spectral Studies of 2,3-Pyrazinedicarboxylic Acid. *Materials Today: Proceedings* 2015; 2: 977-981. DOI: 10.1016/j.matpr.2015.06.020
51. Sriramula VSB, Katreddi HR. Rare Earth Nitrate Complexes with an ONO Schiff Base Ligand: Spectral, Thermal, Luminescence and Biological Studies. *Iranian Journal of Chemistry and Chemical Engineering* 2017; 36: 101-109.
52. Chen Y, Li H, Yue B, Liu Y, Chu H, Zhao Y. Synthesis, characterization and luminescent property of metal-ion-doped terbium complexes of 2,3-Pyrazinedicarboxylate. *Journal of Luminescence* 2012; 132: 1414-1419. DOI: 10.1016/j.jlumin.2012.01.030

53. Zhao Q, Liu X-M, Li H-R, Zhang Y-H, Bu X-H. High-performance fluorescence sensing of lanthanum ions (La³⁺) by a polydentate pyridyl-based quinoxaline derivative. Dalton Transactions 2016; 45: 10836-10841. DOI: 10.1039/c6dt01161f

54. Yin H, Liu S. Copper and zinc complexes with 2,3-pyridinedicarboxylic acid or 2,3-pyrazinedicarboxylic acid: Polymer structures and magnetic properties. Journal of Molecular Structure 2009; 918: 165-173. DOI: 10.1016/j.molstruc.2008.07.033

55. Mahata P, Ramya KV, Natarajan S. Synthesis, structure and optical properties of rare-earth benzene carboxylates. Dalton Transactions 2007: 4017-4026. DOI: 10.1039/b706363f

56. Santiago-González B, Vázquez-Vázquez C, Blanco-Varela MC, Gaspar Martinho JM, Ramallo-López JM, Requejo FG, López-Quintela MA. Synthesis of water-soluble gold clusters in nanosomes displaying robust photoluminescence with very large Stokes shift. Journal of Colloid and Interface Science 2015; 455: 154-162. DOI: 10.1016/j.jcis.2015.05.042

57. Raj PJ, Bahulayan D. "MCR-Click" synthesis of coumarin-tagged macrocycles with large Stokes shift values and cytotoxicity against human breast cancer cell line MCF-7. Tetrahedron Letters 2017; 58: 2122-2126. DOI: 10.1016/j.tetlet.2017.04.052

58. Kaur G, Adhikari R, Cass P, Bown M, Gunatillake P. Electrically conductive polymers and composites for biomedical applications. RSC Advances 2015; 5: 37553-37567. DOI: 10.1039/c5ra01851j



Development of docking programs for Lomonosov supercomputer

Vladimir Sulimov^{1,2}  , Ivan Ilin^{1,2}  , Danil Kutov^{1,2}  ,
Alexey Sulimov^{1,2}  

¹Dimonta, Ltd, 15 Nagornaya Street, Building 8, 117186, Moscow, Russia.

²Research Computing Center, Lomonosov Moscow State University, 1 Leninskie Gory, Building 4, 119992, Moscow, Russia.

Abstract: The initial step of the rational drug design pipeline extremely needs an increase in effectiveness. This can be done using molecular modeling: docking and molecular dynamics. Docking programs are popular now due to their simple idea, quickness and ease of use. Nevertheless accuracy of these programs still leaves much to be desired and discovery by chance and experimental screening still play an important role. Docking performs ligand positioning in the target protein and estimates the protein-ligand binding free energy. While in many cases positioning accuracy of docking is satisfactory, the accuracy of binding energy calculations is insufficient to perform the hit-to-lead optimization. The accuracy depends on many approximations which are built into the respective model. We show that all simplifications restricting docking accuracy can be withdrawn and this can be done on the basis of modern supercomputer facilities allowing to perform docking of one ligand using many thousand computing cores. We describe in short the SOL docking program which is used during years for virtual screening of large ligand databases using supercomputer resources of Lomonosov Moscow State University. SOL to some extent is organized similarly to popular docking programs and reflects their limitations and advantages. We present our supercomputer docking programs, FLM and SOL-P, developed over the past 5 years for Lomonosov supercomputer of Moscow State University. These programs are free of most important simplifications and their performance shows the road map of the docking accuracy improvement. Some results of their performance for very flexible ligand docking into the rigid protein and docking of flexible ligands into the protein with some moveable protein atoms are presented. The so-called quasi-docking approach combining a force field and quantum chemical methods is described and it is shown that best docking accuracy is reached with the PM7 method and the COSMO solvent model.

Keywords: Docking, drug design, global optimization, force field, binding energy.

Submitted: October 17, 2019. **Accepted:** December 04, 2019.

Cite this: Sulimov V, Ilin I, Kutov D, Sulimov A. Development of docking programs for Lomonosov supercomputer. JOTCSA. 2020;7(1):259-76.

DOI: <https://doi.org/10.18596/jotcsa.634130>.

***Corresponding author.** E-mail: vladimir.sulimov@gmail.com, Tel: (+7 916 512 34 18).

INTRODUCTION

Nowadays docking plays (1) an important role at the initial stage of the rational drug design (2,3). Docking programs perform positioning of a ligand (a molecule) in the active site of the target protein responsible for the disease progression and estimate the protein-ligand binding energy. The latter is directly connected with the binding (or dissociating) constant defining the activity of the ligand and the respective inhibition constant. The ligand upon binding with the protein blocks (inhibits) its functioning and changes or stops the progression of a disease. The larger is the protein-ligand binding free energy the low concentration of the inhibitor is needed to reach the desired effect. Several dozens of docking programs exist as well as a dozen of sites presenting docking facilities are available (4–6). Nevertheless, docking accuracy is still unsatisfactory for the reliable separation of strong inhibitors from medium ones and the latter from weak inhibitors on the base of the docking score – the measure of the estimated protein-ligand binding energy, e.g. see Table 6 in (6). The performance of most of docking programs is based on the docking paradigm which assumes that the best position of the ligand in the active site of the target protein corresponds to the global minimum of the energy of the protein-ligand complex. As far as the experimentally determined position of the bound ligand in the protein is defined only by the structure of the crystallized protein-ligand complex the docking paradigm can be paraphrased as follows: the global energy minimum of the protein-ligand complex corresponds to the ligand pose near the crystallized native ligand position. The latter is usually taken from the Protein Data Bank (7). So, the docking problem is boiled down to solving the global optimization problem. And the dimensionality of the energy surface where the global minimum should be found is large: even if the ligand and the protein are rigid there are 6 degrees of freedom, 3 translations of the ligand as a rigid body, and 3 rotations of the ligand as a rigid body. Usually drug-like molecules have 5-15 internal rotations around ordinary valence bonds, named torsions, and the number of degrees of freedom of the global optimization problem is usually 10–20. The global optimization problem with such a large number of dimensions is a heavy task and its solution demands powerful heuristic algorithms as well as a lot of computation resources. Another docking problem arises when one asks the question: what is the energy calculation method for which the docking paradigm is true? On the one hand, the answer is simple: the energy calculation method should be adequate for the given protein-ligand system. But, on the other hand, there are many force fields, i.e. classic potentials describing interatomic interactions in the molecular system, or different quantum-chemical

methods, and the energy calculation method for which the docking paradigm should be satisfied is *a priori* unknown. The difficulty of the docking problem is aggravated by the hands-on need to screen large databases of on-shelf or virtual compounds. Such databases or libraries can contain thousands and millions of compounds which can be treated as candidates to become inhibitors for these or those bio-targets.

Initial versions of some docking programs were developed more than 35 years ago, e.g. the DOCK program (8,9), and available restricted computing resources were the main limiting factor resulting in a lot of simplifications and crude approximations used in docking programs. In addition, force fields at that time were only in their infancy, and quantum-chemical methods could not be used for the calculation of the energy of such large molecular systems as protein-ligand complexes containing thousands of atoms. Nevertheless, the necessity of screening large libraries of ligands and limited computer resources bring to somewhat a competing between docking programs for the lowest time of docking of one ligand using 1 CPU. Certainly, the development of docking programs under the mantra “faster and even faster” could not result in high accuracy of docking.

About ten years ago, the supercomputer era began, and hundreds and thousands of computing cores became available for solving of one task (job). For the docking problem, availability of supercomputers resulted in a possibility of screening of databases of ligands containing millions of compounds, and special efforts have been made to use supercomputers for this task with maximal efficiency. For example, one solution of this problem is presented in (10) where a specially designed software ‘wrapper’ called HSP-DOCK on the base of the DOCK6 program has been used for screening a library of 1.4 million lead-like molecules from ZINC database against each of four targets. Another direction of the use of supercomputer resources for docking aims for the increase of docking accuracy (11).

We present here a short descriptions of our docking programs SOL (1,12,13), FLM (14–17) and SOL-P (15,18,19) developed in Lomonosov Moscow State University for the computing resources available in this university during the recent 15 years including the Lomonosov-2 supercomputer. Some applications of these docking programs are presented also in short.

DOCKING PROGRAMS

Actually, docking technique began to be developed in Lomonosov Moscow State University from autumn of 2005 under the government contract #

02.435.11.1008 of August 1, 2005. First version of the SOL docking program was applied to the development of new direct thrombin inhibitors from beginning of 2006 and the program has been implemented in the Web-oriented system Keenbase allowing to perform virtual screening of ligand libraries using the X-Com grid technology (20). In the following years the improvement of SOL and its application to new inhibitors design advanced abreast each other. A parallel version of SOL appeared in 2011, and supercomputer programs of a new generation have been developed from 2013 up till now. SOL is used now for a preliminary probing of new target proteins and for a massive virtual screening of large ligand databases on the Lomonosov supercomputer. The supercomputer docking programs of the new generation are used at the lead optimization stage and for the investigations of ways of improving the docking accuracy.

SOL classic docking program

We designate SOL as a classic docking program because it has many features common for many popular docking programs. However, during the development of this program, the goal was set to make as few model simplifications as possible and to take into account the most important effects that determine the accuracy of docking as much as possible. We foresaw the extraordinary growth of available computer resources in close future and did not take part in the race for the shortest docking time but tried to make calculations maximal accurate in the frame of existing facilities.

Algorithm and implementation

The energy of the molecular system is calculated in the frame of the Merck Molecular Force Field (MMFF94) (21) which was specially created for the description of protein-ligand molecular systems and drug design needs. This force field is based on a large amount of *ab initio* quantum-chemical calculations of different molecules and molecular complexes. As all other force fields it has its own deficiencies in some features but comparisons with different force fields revealed the best performance of MMFF94 (22,23). In addition, MMFF94 combines sufficiently good parameterization covering a broad spectrum of organic molecules and the well-defined procedure of atom typification applicable to an arbitrary organic compound.

As many other docking programs such as AutoDock, ICM, DOCK, and others, SOL uses a preliminary calculated grid of potentials describing interactions (electrostatic, van der Waals interactions) of all protein atoms with all possible types of a ligand probe atom in the frame of the MMFF94 force field practically without serious simplifications. The desolvation effect in the simplified form of the Generalized Born

approximation and respective potentials are also stored in the nodes of the grid. The grid is used to move heavy calculations of all pairwise interactions of a probe ligand atom with all protein atoms from the global optimization docking step to the preliminary step. The grid is generated by the SOLGRID module and during the global optimization it is stored as a binary file in the RAM memory and it is easily accessed from the SOL module performing the global optimization. The size of the grid by default is a cube with the edge 22 Å covering the active site of the target protein. For the native docking the center of the cube is usually chosen in the geometrical center of the native ligand crystallized with the target protein. Such size of the docking cube is sufficient in most cases for the free ligand movement inside it during the global optimization process: the ligand can be at any position inside this docking cube but no one ligand atom cannot be outside the cube. The grid is formed by equidistant nodes along each of three orthogonal directions of cube edges, 101 nodes along one direction. Ligand energy in the field of the protein is calculated as a sum of grid potentials for all ligand atoms. A potential in the position of a given ligand atom is obtained by the interpolation of potentials in eight neighbouring grid nodes. Usually for a given target protein the grid is created for one to several hours on one computing core depending on the number of atoms in the protein and characteristics of the processor. The grid is generated once for the given position of the docking cube for the given target protein and the respective binary file with the grid is used in the following virtual screening of a ligand library.

The global optimization of the energy of a ligand in the field of the protein is performed by the SOL module. The optimized energy function is the sum of the grid energy of the ligand and the ligand internal energy calculated in the frame of the MMFF94 force field. So, the relative ligand stress energy is taken into account in the energy global optimization process: ligand poses with high stress energy have low chances to correspond to the global energy minimum of the protein-ligand system. The genetic algorithm is used for the global optimization. This is one of the most popular docking algorithms: for example it is implemented in the most commonly used docking programs Autodock (24) and Gold (25). The main idea of this mathematical method is a selection of most strong individuals in the evolution of a population of individuals developed through many generations. In our case the individual is a position a ligand inside the docking cube, and the measure of its strength in the competition with other individuals is the target energy function, i.e. the energy of the protein-ligand system. The population of the initial generation is randomly generated by variations of a ligand position in the docking cube. A ligand

position is formed by translation and rotation of a ligand as a whole rigid body and by the change of each ligand torsion. The population size is 30000 by default but it can be set equal to any integer, e.g. in heavy docking cases for too complicated structure of the energy surface or for a too flexible ligand with a large number of torsions, the population size can be increased up to millions. The evolution is driven by the selection of the strongest individuals into the mating pool (by default its size is 70) and creation from them the next generation by their random crossover and direct translation of them into the next generation and random mutations. Several elite individuals (four by default) corresponding to the ligand positions with lowest energy are transformed to the next generation without any changes. The population size is kept fixed through all generations. When selecting individuals into the mating pool the niching is used. Niching prevents a selection into the mating pool close ligand poses and ensures diversity of individuals in the next generation of the population. Niching is realized by providing a positive energy penalty to the next in turn individual, which is a candidate to be selected into the mating pool, if RMSD (the root-mean-square deviation) between coordinates of ligand atoms corresponding to this individual and individuals, which have been already selected into the mating pool, is small. Actually, the value of the penalty is in inverse proportion to the RMSD value. The individual with a large penalty is moved out from the row of strongest individuals which are candidates to be selected into the mating pool. The number of generations is an input parameter of the SOL module and it is equal to 1000 by default. The strongest individual in the final generation, i.e. the ligand pose with the lowest energy, is the solution of the global optimization problem. How can one believe that this solution corresponds to the lowest value of the target energy function? Several independent runs (50 runs by default) of the genetic algorithm are performed to reveal the reliability of the found solution. Then, all 50 solutions (ligand poses) are clustered in respect with their positions: two ligand poses are included in one cluster if RMSD between coordinates of all their atoms is less than a given value (1 Å by default). The clusters are ranked in respect with energies of respective ligand poses and the solution of the global optimization problem corresponds to the ligand pose with the lowest energy from the first cluster. The cluster analysis helps to estimate reliability of the solution: the high population of the first cluster and a low number of separate clusters indicate the high reliability of the found solution of the global optimization problem. It means that in several absolutely independent runs of the genetic algorithm practically one and the same ligand pose corresponding to the lowest energy of the protein-

ligand complex is found. In other words, the high population of the first cluster indicates convergence of independent runs of the genetic algorithm to the unique global minimum. In another utmost case when for 50 runs 50 different clusters are found docking should be considered as failed. With the default parameters SOL docks a ligand on one computing core for one to several hours.

Parallel versions of SOLGRID and SOL modules (26) are created on the base of MPI (message passing interface) allowing to perform calculations, generation of the grid of potentials and the global energy optimization, on many hundreds of cores: the time of the grid generation and fifty runs of the genetic algorithm with the default parameters can be reduced to less than 1 minute. The multi-processor performance of the SOLGRID module is useful for the optimization of the position of the docking cube in the active site of the target protein when a fast generation of the grid is needed. The multi-processor performance of SOL is usually used when docking with standard parameters is failed. In virtual screening of large ligand databases (dozens and hundreds of thousands of molecules) it is more effective to run SOL on the Lomonosov supercomputer (27) distributing ligands over hundreds and thousands computing cores and docking one ligand per one core. Certainly some auxiliary scripts and programs are created to queue up respective jobs and to analyze the docking results.

Applications

The SOL program was used for CSAR2011-2012 benchmark (12,28) together with other docking programs Gold, AutoDock, AutoDock Vina, ICM-VLS, Glide and others which were used by different research groups. The area under the ROC curve (AUC) was used as a measure of the reliability of the predicted inhibitor affinity. For the highest reliability of predictions, the AUC value is equal to 1, and for the worst reliability AUC is equal to 0.5. The AUC value shows the docking ability to find inhibitors among a large number of inactive compounds. AUC values were obtained for three target proteins: Chk1, LpxC, Urokinase. SOL was the best in AUC calculations for LpxC and Urokinase both, but it did not demonstrate a good result for Chk1 (28).

SOL has been successfully used at the initial stage of new low molecular weight direct inhibitors of different target proteins including experimentally confirmed inhibitors of thrombin (29,30), urokinase (uPA) (31,32), and the blood coagulation factor Xa (33,34). It should be noted here that a bad solvation of many newly synthesized compounds is one of most important obstacles for

experimental testing of docking predicted inhibition activity of ligands.

FLM supercomputer docking program

The name of this program (14–17) is the abbreviation of “finding local minima” and reflects its goal which is to find all low energy minima, including the global minimum, of a protein-ligand complex. This is a gridless docking program which is not used the preliminary calculated grid of protein-ligand interaction potentials. In the course of docking the energy of any protein-ligand configuration is calculated directly in the frame of a given force field. FLM uses the MMFF94 force field (21) without simplifications.

Algorithm and implementation

Protein-ligand complexes have a very complicated multi-dimensional energy surfaces and the search and the search for the low energy minima is performed by the process of random throws of a flexible ligand into the docking area covering the active site of the rigid target protein followed by the optimization of the energy of the protein-ligand system from these random ligand poses using the L-BFGS gradient algorithm (35,36) by varying Cartesian coordinates of all ligand atoms. The initial ligand poses are obtained by random continuous translations and rotations of the ligand as a rigid body and by random continuous variations of ligand torsions. The only restriction is that the ligand geometrical center should be inside a sphere of a given radius (8 Å by default). If the ligand center moves out of the sphere in the optimization process the obtained minimum will not be included in the low energy minima set. Special attention is paid to the uniqueness of the ligand poses corresponding to the minima selected into the low energy minima set. The measure of the minima uniqueness is RMSD between the respective ligand poses calculated in the course of docking over heavy ligand atoms without chemical symmetry. Two minima will be considered different if RMSD and the difference of their energies are less than given values. The size of the low energy minima set is restricted by an input integer parameter and can be a sufficiently large number, e.g. several thousand – by default it is $8192 = 2^{13}$. This set consists of the global energy minimum and every successive energy minimum above it. After finishing docking the set of found low energy minima is inspected on uniqueness again but taking into account chemical symmetry and by calculating RMSD over all ligand atoms.

FLM performs a massive parallel search of low energy minima using Message Passing Interface (MPI) and this search continues a given period of time. Basically, there is no the program termination criterion except the performance time and FLM can work as long as possible using as

many as computing cores as available. The latter is defined by FLM good scalability with the number of cores growth. There are two versions, FLM-0.05 and FLM-0.10, working in the frame of MMFF94 either in vacuum or using the PCM continuum model (37) to take into account water solvent. Certainly, FLM-0.10 is much slower than FLM-0.05 and the latter needs about 20000 CPU x hours to dock one ligand and to find almost all low energy minima by performing several hundred thousand local optimization.

Applications

FLM can be useful during the hit-to-lead optimization when several ligands should be compared accurately on their ability to bind with a given target protein. However, the most interesting application of this program is to use it for the validation of new docking algorithms. For example, FLM was used for the verification of the TT-docking algorithm in (15). Another application of FLM is a comparison of different energy functions for docking. It was shown in (14) that the use of the MMFF94 force field with the PCM solvent model resulted in much better docking positioning accuracy than in the case when no solvent was taken into account. Later, the docking accuracy was compared for the CHARMM and MMFF94 force fields, for PM6-D3H4X (38) and PM7 (39) semiempirical quantum chemical methods. It was shown (40,41) that CHARMM is much better than MMFF94 but PM7 with the COSMO solvent model (42) is much better than CHARMM and it is slightly better comparing with PM6-D3H4X with COSMO. So, the best energy function for docking is the semiempirical quantum-chemical PM7 method together with the COSMO solvent model. This model as well as the PM7 method are realized in the MOPAC package (43) where the use of MOZYME module allows to calculate the whole protein-ligand complexes. Unfortunately, to use this quantum chemical energy function in the docking procedure is still impossible due too large computer resources needed. But, these findings bring to the idea of quasi-docking which is a two-step procedure. Firstly, a sufficiently broad spectrum of low energy minima is found in the frame of the given force field. Secondly, all these low energy minima are recalculated using a quantum-chemical method with an implicit solvent model. Results of quasi-docking when MMFF94 is used at the first step and PM7 with COSMO are used at the second step are presented in (17,44). The number of low energy minima which should be found at the first step is a specific number for each protein-ligand but for most of test complexes this number is equal to 4096. The energy (MMFF94 in vacuum) band occupied by these minima can reach several dozen kcal/mol for some complexes (17).

SOL-P supercomputer docking program

This supercomputer program (15,18,19) is also the gridless generalized docking program of the new generation. As the FLM program does SOL-P performs the search for low energy minima spectra of molecular systems, in particular, the protein-ligand complexes. However in opposite to the FLM program SOL-P uses for the search a more keen algorithm of the global optimization and also SOL-P is able to perform docking of flexible ligands into the target protein with moveable atoms. The energy of protein-ligand system depends on variables describing translations and rotations of the ligand as a whole rigid body, internal rotations of ligand molecular groups around ordinary chemical bonds (torsions) and Cartesian coordinates of selected target protein atoms and all these variables are treated simultaneously and equally in the global optimization process at that. For example, if the ligand has 10 torsions and 10 protein atoms must be treated as moveable the number of the independent variables describing the protein-ligand energy surface will be equal to $d = 6 + 10 + 3 \times 10 = 46$ where 6 is the number of ligand translations and rotations as a rigid body. The energy of molecular systems is calculated in the frame of the MMFF94 force field as SOL and FLM programs do.

Algorithm and implementation

SOL-P uses the TT-docking algorithm the idea of which is as follows. The continuous energy function depending on d ligand and target protein variables

$$A(i_1, \dots, i_d) \approx \sum_{(\alpha_1=1, \dots, \alpha_{d-1}=1)}^{(r_1, \dots, r_d)} G_1(i_1, \alpha_1) G_2(\alpha_1, i_2, \alpha_2) \dots G_{(d-1)}(\alpha_{(d-2)}, i_{(d-1)}, \alpha_{(d-1)}) G_d(\alpha_{(d-1)}, i_d) \quad (2)$$

where numbers r_1, \dots, r_{d-1} are called TT-ranks of the tensor; for convenience, dummy ranks $r_0 \equiv r_d \equiv 1$ are also introduced. The 3-dimensional tensors $G_i \in \mathbb{R}^{r_{i-1} \times n_i \times r_i}$ are called cores or carriages of the tensor train.

If TT-ranks are reasonably small, the TT-format will possess very useful properties (45,46): only

$$\sum_{i=1}^d n_i r_{i-1} r_i \quad O(dnr^2)$$

computer memory cells are required ($n = \max(n_i)$, $r = \max(r_i)$, $i = 1, 2, \dots, d$) to store the tensor, operations on tensors are reduced to standard matrix operations, and most of operations on tensors are performed in $O(dnr^3)$ arithmetic operations or even faster. The TT-approximation of a tensor can be constructed in a robust way using TT-SVD (Singular Value Decomposition) method (45). However, the TT-SVD method needs all the elements of the tensor, but for a large tensor to calculate all tensor elements is practically impossible. But, there is a fast method, named TT-Cross, of the large tensor approximation utilizing only a small number of

is converted into a d -dimensional array (a tensor) using a discretization grid in the space of the variables, and modern methods of tensor analysis are applied to find the largest in magnitude element of the tensor. If the grid is fine enough the solutions of the continuous and discrete global optimization problems will be close to one another. The docking problem which is the global minimization problem can be easily transformed to the global maximization problem and we find that it is convenient to apply the magnitude maximization to the following functional (18):

$$f(x, E_*) = \exp\{100 \operatorname{arccot}[E(x) - E_*]\} \quad (1)$$

where $E(x)$ is the dimensionless MMFF94 energy for the given conformation x of the protein-ligand complex, E_* is the global minimum found on the previous iteration.

The number of entries of a d -dimensional tensor grows exponentially in d , and if d is large it will be impossible to use the list of entries for practical needs. For example, the number of tensor entries will be huge, $100^{15} = 10^{30}$, for only 100 points at each dimension and $d = 15$. As a means to fight with this "so-called" *curse of dimensionality* the Tensor Trains (TT) decomposition for d -dimensional tensors was introduced ten years ago (45). TT-format is such a decomposition in which the initial real-valued d -dimensional tensor

$A \in \mathbb{R}^{n_1 \times n_2 \times \dots \times n_d}$ of the size n_i along the i -th dimension is reduced to d tensors of the dimension 3:

tensor elements (47). It finds the TT-decomposition of a tensor evaluating only $O(dnr^2)$ elements and performing just $O(dnr^2)$ arithmetic operations. TT-Cross exploits the well-known matrix cross interpolation method (48) applied to selected submatrices of the unfolding matrices of the given tensor. Unfolding matrices

$A_k(i_1 \dots i_k, i_{k+1} \dots i_d) \in \mathbb{R}^{n^k \times n^{d-k}}$ of the given tensor

$A(i_1, \dots, i_d) \in \mathbb{R}^{n_1 \times \dots \times n_d}$ contain the same elements

of the initial tensor $A(i_1 \dots i_d)$ but reordered, and TT-rank r_k is just the rank of the matrix A_k . The matrix cross interpolation method approximates a

matrix $B(i, j) \in \mathbb{R}^{m \times n}$ using only $O((m+n)r)$ of its elements and performing just $O((m+n)r^2)$ operations, where r is the approximation rank. The matrix cross interpolation method performs the search of the largest in magnitude matrix element,

uses the found element to perform the Gauss elimination and repeats operations with the obtained matrix until the stopping criteria is met. So, the matrix cross interpolation method could be used as a simple global optimization method as it finds the largest in magnitude element among all

evaluated elements of the matrix. Great advantage of the method is that it does not evaluate all matrix elements but only a small portion of them. Similarly, the TT-Cross method iteratively improves the sets of interpolation points searching for submatrices of unfolding matrices of larger volume (determinant in modulus) and consequently containing the elements of larger magnitude. Therefore TT-Cross can be used as a base for the TT global optimization method which uses the same search strategy as TT-Cross, but in more parallel way, and does not explicitly construct the TT-approximation of the whole tensor. To reduce the number of evaluations, the maximal rank is bounded by r_{\max} . After the rank limitation iterations could possibly never converge and the maximal iterations number parameter is introduced.

At each iteration the following operations of the TT global optimization are performed: (i) the generation of submatrices of unfolding matrices using a set of tensor elements, (ii) the interpolation of submatrices using the TT-Cross method with rank $\leq r_{\max}$ and as a result a set of interpolation points obtained for each submatrix contains elements with large values in modulus, (iii) these sets of interpolation points (protein-ligand conformations) are extended by the local optimization and projections of optimized interpolation points to the tensor are added to interpolation point sets, (iv) updating of each set of interpolation points of the unfolding matrix is made by merging the interpolation points of the previous unfolding matrix and ones of the subsequent unfolding matrix, (v) transition to step (i) using the obtained interpolation point (protein-ligand conformations) as the tensor elements for the next iteration step.

The basic optimal parameters of TT-docking are (18): the discretization grid in the domain of each variable $n = 2^{16}$, the maximal rank is bounded by $r_{\max} = 4$, and the number of iterations in the process of optimization equals to 15. More details of the TT global optimization method can be found elsewhere (15,18,19).

The SOL-P program contains a set of modules performing the TT search for low energy minima, selecting only unique minima, performing additional local optimization of the protein-ligand conformations corresponding to selected unique low energy minima by the accurate L-BFGS gradient method and, finally, selecting again only unique minima and ranking them on their energy. In the process of TT-docking the ligand geometrical center (the ligand center of mass for equal ligand atoms' masses) can move inside the docking cube of a given size, by default the cube edge is equal to 10 Å, the center of the cube is

situated either at the geometrical center of the native ligand crystallized with the target or can be selected based on other considerations. The selected protein atoms can move inside their small cubes with the edges 1.0 Å by default and centered at the initial protein atom positions, e.g. which are taken from Protein Data Bank. The docking cube size as well as small cubes sizes are input parameters of the program. More detailed description of SOL-P can be found in (18,19).

The TT docking algorithm is 10 times faster than the genetic algorithm (49) with approximately the same reliability of finding the ligand pose corresponding to the lowest energy of the protein-ligand complex. The comparison was made between TTDock and SOL programs for the same test set of protein-ligand complexes, for the same preliminary calculated grid of potentials in the frame of the same MMFF94 force field but it finds the same ligand poses with the lowest energy. For the rigid protein SOL-P is two orders of magnitude faster than the FLM program, these programs find the same global energy minima for a test set of protein-ligand complexes but some low energy minima are missed from the spectrum of low energy minima found by the SOL-P program comparing with the minima spectrum found by FLM (15). SOL-P can cope with docking of flexible ligands having a large number of torsions into a rigid protein as well as with docking of flexible ligands into protein having some moveable atoms. The latter is demonstrated in (18,19) where a successful docking is demonstrated with up to 157 degrees freedom: unsuccessful docking into a rigid target protein becomes successful when several dozen of protein atoms become moveable. Below we present some results of docking very flexible ligands and docking into proteins with moveable atoms.

Applications

Docking ligands with a larger number of torsions.

Docking highly flexible ligands is still a challenging task in the field of modern molecular modeling. In the same time, some flexible molecules, for example, oligopeptides are of high interest as potential therapeutics. Ability to handle them computationally determines a success rate of projects involved in developing peptide-like bioactive compounds. Most popular docking programs are able to dock ligands having no more than 10 torsions because of high dimensionality of the energy surface on which the search for a ligand bound configuration is performed. The TT-docking algorithm intrinsically aims to work with systems of high dimensionality, and to test its ability to dock very flexible ligands SOL-P is applied for docking oligopeptides and other kinds of flexible and branching non-peptide ligands in the same manner. All crystal complexes selected for docking

have good resolution (better than 2 Å), do not contain any cofactor molecules (including metal ions) and have no gaps near the binding site. Protein structures and oligopeptide molecules are protonated at pH 7.4 using the Aplite program. Special attention was paid to the 1B9J complex. We found that the native ligand of this complex carried one positively charged group which was not involved in the interaction with any residues in the ligand crystal conformation. The global energy minimum found by SOL-P in this complex corresponds to the ligand pose where this ligand charged group is closely situated near the negatively charged carboxylic moiety of Glu32 and this ligand pose is quite different from the crystallized one: $\text{RMSD} \approx 6.7 \text{ \AA}$. This is a simple consequence of positive and negative charges attraction in the absence of screening water solvent effect damping Coulomb interactions: SOL-P works without taking into account a water solvent. To avoid this side effect we neutralized the carboxylic moiety of Glu32 and re-docked the 1B9J native ligand. The difference between the ligand pose corresponding to the global energy minimum and the ligand crystallized pose become small: $\text{RMSD} \approx 1.2 \text{ \AA}$. Non-peptide ligands are protonated at pH 7.4 with the Avogadro program (50). We also perform docking of these flexible ligands by the SOL program to compare efficiency of SOL-P

with a program which has common features with popular docking programs (the grid approximation and the genetic algorithm of the global energy optimization) and uses the same force field as SOL-P does. The root-mean-square deviation (RMSD) between all atoms of the crystallized native ligand pose and the docking pose corresponding to the least energy of the protein-ligand complex is selected as an accuracy metric. Results of docking ligands with a large number of torsions are shown in Table 1.

As can be seen from Table 1, if RMSD cutoff is set to 2.3 Å that justified for such large ligands, SOL-P copes quite well with docking highly flexible ligands except one complex (2FLE), whereas SOL is able to dock correctly only one ligand which has the least number of torsions. Analyzing results for 2FLE complex we find that in the prepared protein structure two hydrogen atoms connected to backbone nitrogen atoms are placed incorrectly disturbing the planar configuration of peptide bonds in which they are involved and interfering with ligand hydrogen atoms when the ligand is in the crystallized position. In Figure 1 these two incorrectly added protein hydrogen atoms are designated by red letters and for the sake of clarity only a central part of the ligand in its crystallized position is shown.

Table 1. Results of docking ligands with a large number of torsions by SOL and SOL-P. N_{tor} stands for a number of torsions. The indicated charge corresponds to the total charge of a ligand at pH 7.4. Note: all oligopeptides carried, at least, two charged groups – the positively charged N-terminus and the negatively charged C-terminus.

#	PDB ID	Sequence of an oligopeptide	Charge	N_{tor}	RMSD after SOL, Å	RMSD after SOL-P, Å
1	6DQQ	AAAA	0	10	1.08	1.24
2	1B9J	KLK	+2	15	8.55	1.22
3	1OLA	VKPG	+1	18	9.94	1.28
4	6DTH	RPPGF	+1	18	10.13	2.12
5	3LIN	Non-peptide	0	20	6.36	0.97
6	6DTG	YLGANG	0	22	10.01	1.04
7	2OLB	KKK	+3	23	9.56	1.37
8	6DQU	GIINTL	0	25	8.49	2.28
9	2FLE	Non-peptide	0	25	8.99	13.78 (1.74)
10	1EC3	Non-peptide	0	25	12.29	2.19

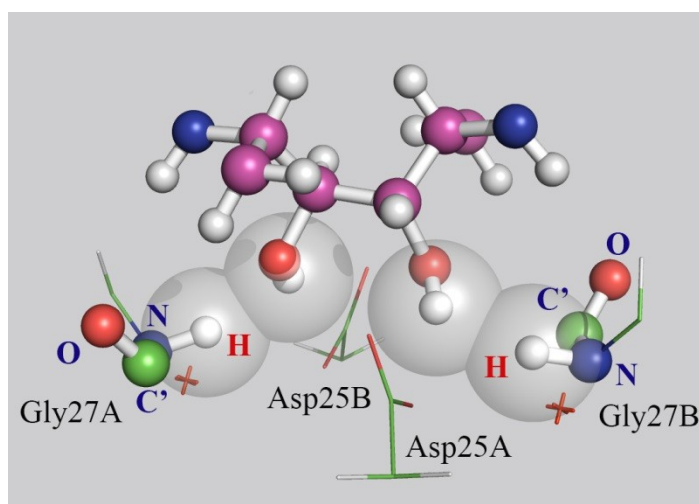


Figure 1. The intersection of Van der Waals radii of two hydrogen atoms of the protein (shown as red letters 'H's) and two hydrogen atoms of the ligand in its crystal state (shown in "balls and sticks" representation: carbon atoms shown in magenta colour, nitrogen atoms – in blue, oxygen atoms – in red, hydrogen atoms – in white).

The mentioned two protein hydrogen atoms are out of the planes (defined by protein atoms designated by blue letters in Figure 1) of the respective peptide bonds and this occurs possibly due to interactions of these hydrogen atoms with neighboring protein atoms of two residues, Asp25A and Asp25B, which are also shown in Figure 1. If a docked ligand pose is close to the ligand crystallized position the energy of the protein-ligand system will be high due to the intersection of Van der Waals radii of the protein and ligand hydrogen atoms. This is the reason of unsuccessful docking for the 2FLE complex in the rigid protein model. We tried two approaches to fix the problem. Firstly, a manual correction of hydrogen

positions in the protein is done which does not lead to successful docking. Secondly, we use docking with SOL-P and add mobility to these two hydrogen atoms (other protein atoms are fixed) during docking. This has resulted in success and the final RMSD value for 2FLE complex is equal to 1.74 Å.

In the protein-ligand configuration corresponding to the global energy minimum found by docking with the two moveable protein hydrogen atoms these atoms are observed to be in the planes of respective peptide bonds and the above mentioned Van der Waals radii do not intersect (see Figure 2).

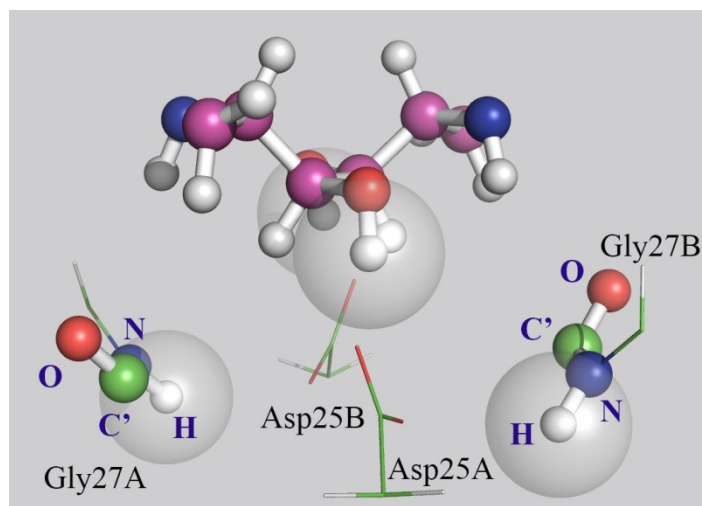


Figure 2. Positions of selected protein and ligand atoms of the 2FLE complex in the conformation corresponding to the global energy minimum found by docking with the two moveable protein hydrogen atoms (see text). The protein hydrogen atoms returned back in the planes of peptide bonds are marked by blue letters. As in Figure 1, the ligand is truncated for clarity.

Summing up, it can be noted that the SOL-P program can perform well in docking flexible ligands having up to 25 torsions. One of the main limitations of applying SOL-P as well as other docking programs can be insufficient quality of the full atomic (including hydrogen atoms) model of the target protein resulting in the presence of untypical distorted conformations to be reproduced. This effect should be taken into account when creating the full-atomic target model. The use of SOL-P with moveable protein atoms which are close to the ligand position, e.g. to the crystallized native ligand position, could be one possible solution of this problem.

Docking flexible ligands into proteins with moveable atoms.

Besides docking oligopeptides and branching ligands, mobility of separate protein atoms during docking is also a daunting task in modern computational chemistry. Each moveable protein atom increases a number of degrees of freedom and dimensionality of the energy space on which the search for a ligand bound configuration is performed. Accounting for mobility of protein

atoms is of great importance for some protein targets and virtual screening projects.

The SOL-P program is able to perform docking with moveable protein atoms and this ability was studied recently (18) where SOL-P was tested by using 30 high quality protein-ligand complexes. As in the case of docking ligands with a large number of torsions, all complexes were split into a ligand and a protein and the estimation of docking accuracy relied upon reproducibility of native ligand crystallized poses after their docking into the corresponding protein structures. Both ligands and proteins were protonated at pH 7.4

For almost one third of complexes SOL-P coped with docking without considering mobility of protein atoms. To cope with the rest ones, we apply SOL-P using mobility of some protein atoms. The selection of moveable protein atoms is based on their proximity to the native ligand crystallized pose and it is made by the Mark-PMA program. For 4 complexes docking succeeds when protein flexibility is added. Features of these complexes and results of docking are presented in Table 2.

Table 2. Complexes from the test set for which docking results are dramatically improved after considering mobility of some protein atoms. N_{tor} stands for the number of ligand torsions, N_{lig} is the number of ligand atoms (including hydrogen atoms), $RMSD_{standart}$ is the root-mean-square deviation for all ligand atoms between the crystallized native ligand pose and the docked ligand pose in the global energy minimum after docking without moveable protein atoms, $RMSD_{moveable}$ is the root-mean-square deviation for all atoms between the crystallized ligand pose and the docked ligand pose in the global energy minimum after docking with moveable protein atoms. The number of these atoms is indicated as $N_{mov prot}$.

PDB ID	N_{tor}	N_{lig}	$RMSD_{standart}$	$RMSD_{moveable}$	$N_{mov prot}$
1J01	6	35	2.35	0.000017	15
1LQD	8	61	5.25	0.00668	17
1O3P	6	46	10.99	1.83	28
3CEN	7	50	7.59	1.59	13

To reveal reasons underlying improvement of docking results, we have visually analyzed docking poses and displaced positions of proteins' atoms. The main factor of the docking improvement is the improved structure of H-bonding: all displaced protein atoms are related to the hydrogen bond donors/acceptors. Ligand poses close to the ligand crystallized pose seem to have more favorable H-bonds in the protein conformation obtained after docking with moveable protein atoms. These H-bonds are less favorable when ligand poses close to the ligand crystallized pose are placed into the rigid protein without any adjustment of protein atoms. For instance, improved geometry of H-bonds between the benzamidine moiety of the ligand and the carboxylic group of Asp189 is observed for 1LQD complex – see Fig.3 in (51). The distance between the hydrogen atom in the amidine and the charged oxygen atom is reduced: from 1.9 Å observed for a complex with accounting the initial positions of the oxygen atoms of the

carboxylic group to 1.6 Å observed for a complex after docking with moveable protein atoms. Actually, this change is quite small but, as can be seen from Table 2, it can lead to dramatic improvement in docking results.

We also apply semiempirical calculations to confirm that the configuration of the complex with displaced protein atoms after docking in SOL-P (denote it as M-complex) is better energetically than a configuration with the initial state of the protein (denote it as R-complex). For both M-complex and R-complex, heat of formation is estimated by a single SCF calculation with the PM7 method. Moreover, calculations were performed both in vacuum conditions and in water environment (solvent effects were modelled in the frame of the COSMO model). All calculations were done in MOPAC2016. The results of the calculations are listed in Table 3.

Table 3. Results of semiempirical calculations for the 1LQD complex aimed to confirm that the M-complex configuration is energetically more favourable than the R-complex configuration. Explanations what M/R-complex stands for can be found in the text above. Δ equals to the heat (M-complex) minus heat (R-complex), where heat (M/R-complex) is the heat of formation of the complex in the output file of MOPAC.

Type of calculation	Heat of formation in MOPAC for R-complex, kcal/mol	Heat of formation in MOPAC for M-complex, kcal/mol	Δ , kcal/mol
1SCF in vacuo	-19787.31	-19791.49	-4.18
1SCF + COSMO	-23030.61	-23032.65	-2.04

The consideration of results presented in Table 3 allows confirming that even the very slight change in positions of protein atoms belonging to the hydrogen bond donors/acceptors makes ligand poses near the ligand crystallized conformation to possess lower energy that is crucial for proper ranking of found ligand poses which are found in the docking procedure. Thus, the model of accounting for protein flexibility which is implemented in SOL-P can improve the energy estimation during docking by adjusting positions of protein atoms involved in H-bonding. The TT global optimization method is capable of successful handling of high dimensionality emerged from considering additional degrees of freedom related to moveable protein atoms.

Cross-docking with moveable protein atoms.

Cross-docking is a type of docking when the crystallized ligand from one complex is docked into the same protein which is taken from another complex containing the same protein but another crystallized native ligand. In other words, the ligand is docked into different protein conformations obtained from other crystal structures. The main purpose of the cross-docking approach is the study of the effects of induced fit upon binding and estimation of ability of model

relied upon the certain protein structure to reproduce experimentally determined poses of chemically diverse ligands. The latter task is immensely important for quality control of the protein model intended to use in the structure-based virtual screening campaign. Cross-docking implies the superimposition of protein structures to the reference protein structure. The native ligands undergo the same transformation. After that, docking of "rotated" ligands can be assessed standardly in the terms of RMSD value calculated between the docking pose which corresponds to the global minimum and the ligand quasi-crystal ("rotated") pose.

We apply SOL-P to cross-docking using two pairs of complexes containing oligopeptides and also three pairs of protein-ligand complexes with ligands of non-peptide nature. The first pair includes 1B9J and 1OLA complexes which both contain oligopeptide-binding protein (OppA) of *S.typhimurium*. For the study we take the protein structure from the 1B9J complex in which Glu32 is neutralized (see Section "Docking ligands with a larger number of torsions"). Complexes of the second pair, 6DQQ and 6DTG, contain the same protein – OppA but of *H.influenzae*. Additional details about selected complexes can be found

above in Table 1. Characteristics of three other pairs of complexes with non-peptide ligands selected for cross-docking are presented in Table 4. It is worthy to note that for all these complexes successful native docking is achieved by the SOL program which utilizes the grid approximation and the genetic algorithm as well as by the gridless supercomputer FLM docking program. In Table 4,

column 6 the RMSD values between the native ligand crystallized pose and the docking pose with the best energy are shown. The values in parentheses corresponds to results of the repeated docking by SOL with heightened parameters of the genetic algorithm (population size = 3×10^6 , number of generations = 1500).

Table 4. Characteristics of complexes with non-peptide ligands for the cross-docking test. N_{lig} – the number of ligand atoms (including hydrogen atoms), N_{tor} stands for the number of ligand torsions, Q_{lig} is the ligand charge.

PDB ID	Protein	N_{lig}	N_{tor}	Q_{lig}	RMSD after SOL, Å	RMSD after FLM, Å
1MRX	HIV-1 Protease group M subtype B (isolate BRU/LAI)	74	11	0	1.51	0.62
1MSM		78	12	0	11.13 (0.71)	0.95
3NU3		70	13	0	1.47	1.34
4LL3		75	13	0	11.16 (0.76)	1.04
2ZDM	Trypsin, Bos Taurus	59	9	1	1.16	0.96
2ZDN		58	9	1	1.98	0.59

The FLM program copes with native docking for all complexes: all calculated global minima are close to the corresponding native poses optimized in the frame of the MMFF94 force field in vacuum. SOL also copes with docking of all native ligands into the proteins they crystallized with either with standard docking parameters or with heightened ones.

The total procedure of preparation includes the following steps. At the beginning, the protein from one complex in each pair is superimposed to another protein and vice versa. Superimposing is conducted with our Super-impose-proteins program. To confirm integrity of aligned proteins, RMSD value for all atoms between the reference protein and the superimposed protein is calculated. For pairs under the consideration this value does not exceed 2 Å that confirms fitness of crystal structures to each other. The corresponding ligands are then superimposed too by the same

transformation which is found at the previous step of proteins' superimposing. For example, the ligand from 1B9J is superimposed to the protein from 1OLA and vice versa; the ligand from 6DQQ is superimposed to the protein from 6DTG and vice versa. Transformed ligand conformations are denoted as quasi-native poses for the sake of brevity. Prior to docking in SOL-P, the quasi-native pose of every ligand is locally optimized in the MMFF94 force field with being placed in the active site of the corresponding protein. We check that this optimization do not cause quasi-native ligands to move more than 2 Å from initial coordinates in order to guarantee that optimization in SOL-P will not add bias into results. Moreover, we visually check that when being placed in the corresponding proteins quasi-native ligands have no clashes with protein atoms. After confirming that all quasi-native ligands satisfy these checks, they are used for cross-docking by SOL-P. Results of this docking are listed in Table 5.

Table 5. Results of cross-docking by SOL-P for pairs of complexes. RMSD value is calculated between the locally optimized quasi-native pose in the MMFF94 force field in vacuum and the docking pose corresponding to the global energy minimum. The INON index is found as the lowest number in sorted by the energy list of minima founded by SOL-P so that the RMSD of such a minimum is less than 2 Å relatively to the optimized quasi-native pose.

Ligand from	Protein from	Protein name, organism	RMSD, Å	INON
1B9J	1OLA	OppA, <i>Salmonella typhimurium</i>	6.709125	12
1OLA	1B9J		0.974301	1
1MRX	1MSM	HIV-1 protease	10.785163	2
1MSM	1MRX		2.416591	6
2ZDM	2ZDN	Trypsin, <i>Bos taurus</i>	7.128926	inf
2ZDN	2ZDM		2.510446	inf
3NU3	4LL3	HIV-1 protease	8.248767	6
4LL3	3NU3		4.517536	81
6DQQ	6DTG	OppA, <i>Haemophilus influenzae</i>	1.560041	1
6DTG	6DQQ		2.884729	6

As can be seen from Table 5, cross-docking for most cases is unsuccessful. The worst-cases correspond to INON=inf for complexes 2ZDN and 2ZDM. In these cases there are no minima with a corresponding ligand pose near (with small RMSD from) the optimized quasi-native ligand pose among all low energy minima found by SOL-P. To improve results, we use docking with moveable protein atoms. Two approaches for the selection of moveable protein atoms are used. The first one is applying the Mark-PMA program (18) which marks protein atoms to be moveable relying upon their proximity to the native crystallized ligand

conformation. It was shown previously (18) that in many cases successful docking is reached when from 25 to 35 protein atoms became moveable using marking by this program. However, in this approach mobility of some protein atoms does not result in docking improvement but docking time can increase noticeably. Therefore the second approach is also tested. In the frame of this approach the selection of protein moveable atoms is made by hands taking into account their role in protein-ligand binding. Results of cross-docking with moveable protein atoms are listed in Table 6.

Table 6. Results of cross-docking with moveable protein atoms for different pairs of complexes. RMSD value was calculated between the locally optimized quasi-native pose in the MMFF94 force fields in vacuum and the docking pose corresponding to the global minimum. N_{mov} stands for the total number of moveable protein atoms.

Ligand from	Protein from	N_{mov} selected by Mark-PMA	RMSD, moveability by Mark-PMA	INON, moveability by Mark-PMA	N_{mov} selected by hand	RMSD, moveability by hand	INON, moveability by hands
1B9J	1OLA	32	6.669763	30	17	6.649110	11
1OLA	1B9J	30	2.430996	7	16	2.624906	7
1MRX	1MSM	28	0.245360	1	19	3.589922	2
1MSM	1MRX	29	1.289056	1	23	1.897655	1
2ZDM	2ZDN	28	0.921806	1	18	0.919140	1
2ZDN	2ZDM	26	2.271176	3	18	1.899394	1
3NU3	4LL3	28	1.607883	1	19	8.382071	7
4LL3	3NU3	25	0.921040	1	21	4.278851	2
6DQQ	6DTG	30	1.236382	1	11	1.167734	1
6DTG	6DQQ	34	0.761266	1	25	1.304007	1

It is clearly seen when comparing Table 5 and Table 6 that for most complexes cross-docking is improved and becomes successful after taking into account mobility of neighboring protein atoms and this improvement is higher when automatic marking moveable atoms is applied. These findings are mainly justified by changes in positions of atoms involved in H-bonding during docking with moveable protein atoms because there are no

dramatic differences in protein structures within each pair and no steric clashes observed for quasi-native poses of rotated ligands when placing into the corresponding protein structures. Consider results of cross-docking with automatic selection of protein atoms to be moveable. They show that for three pairs unsuccessful docking is obtained even after adding mobility to some protein atoms. In the case of 1OLA/1B9J pair (a ligand from 1OLA is

docked into a protein from 1B9J) accuracy of positioning becomes worse after cross-docking with moveable protein atoms. The failure is probably related to facts that the native protein from 1B9J is modified (neutralization of Glu32) and the ligand from 1OLA is not able to bind properly because of the modification. On the contrary, the protein from 1OLA does not contain neutralized Glu32 and thereby allows the ligand from 1B9J to stick to the active site in the wrong way which we have observed earlier performing docking of oligopeptides (see Section "Docking ligands with a larger number of torsions"). Addressing these issues might possibly lead to more adequate results.

In the case of unsuccessful docking of the ligand from 2ZDN into the protein from 2ZDM we find that the docking pose of the ligand both after docking without moveable protein atoms and with moveable protein atoms quite correctly reproduces the ligand crystallized conformation excluding the tail ligand moiety containing a cyclopentyl group (see Figure 3). It is also manifested in the fact that the RMSD values only slightly differ from 2 Å (2.51 Å – in the case of docking without protein flexibility, 2.27 Å – after docking with moveable protein atoms). And besides, the RMSD estimation is actually carried out with considering not only ligand atoms but protein atoms as well. If calculate RMSD using only ligand atoms, one obtain difference being 2.016 Å between the quasi-native pose of 2ZDN ligand and its docking pose found after docking with moveable protein atoms. This

RMSD value is very close to "ideal" boundary – 2.0 Å.

Study (52) which describes obtaining crystal structures of 2ZDM and 2ZDN confirms conformational flexibility of the tail moiety of the ligand from 2ZDN in MD simulations. With regard to successful docking for this pair when applying hand marking moveable protein atoms, it was found that "successful" pose of 2ZDN ligand after this docking is immensely similar to the docking pose after positioning with an automatically selected set of moveable protein atoms (see Figure 3). In that context, the weakness of the RMSD concept for estimating docking results is illustrative. Given all these facts, we can conclude that, despite RMSD being slightly larger than 2 Å SOL-P manages to dock the ligand from 2ZDN in the meaningful way during our cross-docking simulations.

Summing up, one can note that adding protein flexibility in the cross-docking procedure helps to improve accuracy of positioning of quasi-native ligands: for six initially failed complexes the RMSD value is reduced to less than 2 Å after including protein flexibility in the docking process. Considering approaches for selecting protein atoms to be moveable and obtained results, it can be concluded that the first (automatic) approach to choose moveable protein atoms results in more accurate positioning in docking but at the expense of some increase (approximately from 0.5 to 2 hours) of docking time comparing with the second approach.

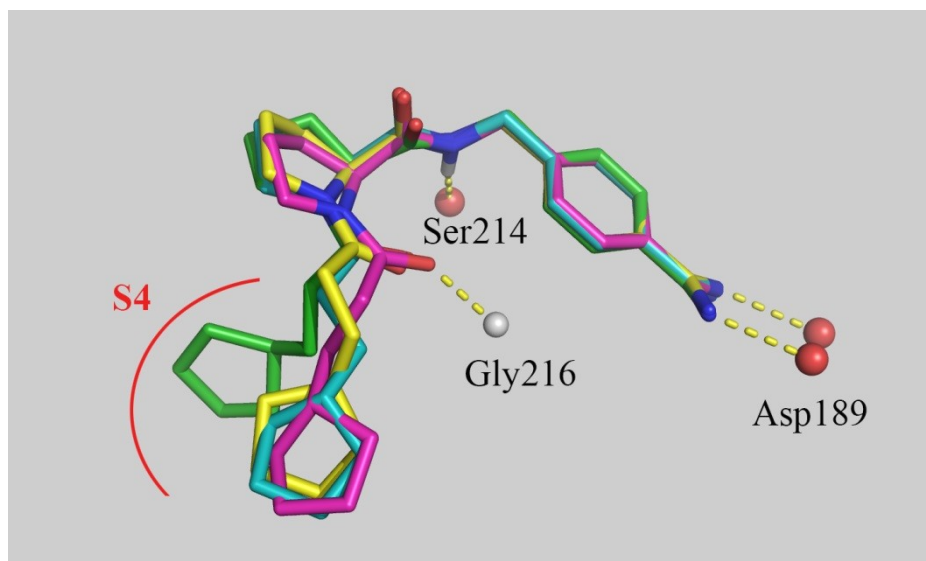


Figure 3. Results of cross-docking for the ligand from 2ZDN into the protein from 2ZDM. 4 different ligand poses are shown: the quasi-native pose (carbon atoms – in green color), the pose after docking with no moveable protein atoms (carbon atoms – in cyan color), the pose after docking with moveable protein atoms selected by Mark-PMA (purple-colored carbon atoms), and the pose after docking with moveable protein atoms chosen by hand (yellow-colored carbon atoms). Protein atoms involved in H-bonding with the ligand are shown as spheres. Nitrogen atoms are colored in blue, oxygen atoms – in red, hydrogen atoms – in white. For sake of clarity, most hydrogen atoms of the ligand are removed.

CONCLUSIONS

Three docking programs developed at Lomonosov Moscow State University are described in the present work: SOL, FLM and SOL-P. Their performance is based on the docking paradigm connecting docking with the global optimization problem: the ligand is bound near the global energy minimum of the protein-ligand complex. The first program, SOL, is used successfully for the computer aided structural based drug design during almost 15 years. The MMFF94 force field is used in SOL for the calculation of the energy of protein-ligand complexes and the genetic algorithm is used for the global optimization. The preliminary calculated grid of potentials of interactions of ligand probe atoms with the target protein is used in SOL and they are Coulomb, van der Waals interatomic interactions and desolvation potentials appeared from the simplified form of the implicit Generalized Born solvent model. The SOLGRID module generating the grid as well as the docking SOL module are parallelized and adapted for the supercomputer calculations. SOL is used for initial docking of native ligands into new targets and then for large ligand databases virtual screening.

FLM and SOL-P belong to the new generation of generalized docking programs designed for running on supercomputers. They use the MMFF94 force field both without any simplifications and fitting parameters. Their task is to find the whole spectrum of low energy minima for a given energy

function. FLM can perform long time on available computing resources until the found pool of low energy minima reaches the saturation, i.e. until the pool ceases to be updated. For the first time we investigated carefully spectra of low energy minima of several dozen protein-ligand complexes and checked the feasibility of the docking paradigm. Low energy minima sets found by FLM can be used as reference sets to compare different docking algorithms and energy functions. The quasi-docking procedure approaching quantum chemical docking is realized on the base of several thousand low energy minima found by FLM. It is shown that the PM7 quantum chemical semiempirical method together with the COSMO solvent model is one of the best candidates for energy calculations in the docking procedure.

The new TT-docking algorithm is realized in the SOL-P program. This algorithm is based on the recently developed so-called tensor train (TT) global optimization method which in its turn is based on the TT approximation of large multi-dimensional tensors. The main advantage of this TT-docking method is its ability to perform docking with a large number of degrees of freedom, i.e. to find low energy minima spectra on the energy surface with very large number of dimensions. This property of the TT docking algorithm opens up the possibility for docking molecules with a large number (> 20) of torsions and for docking flexible ligands into proteins with mobile atoms. In the TT-docking procedure all degrees of freedom, i.e. all variables describing ligand and protein

conformations, are treated equally and simultaneously during the global energy optimization process. Some examples of successful docking of ligands with a larger number of torsions, docking into the protein with moveable atoms as well as cross-docking are presented.

Finally, the supercomputer docking programs briefly described in this work open the road to higher accuracy of docking: to the higher positioning accuracy as well as to the high accuracy of the protein-ligand binding energy calculation. This will certainly result in higher effectiveness of the rational drug design.

ACKNOWLEDGEMENTS

The manuscript is presented at the 12th Asian Federation for Medicinal Chemistry (AFMC) International Symposium (AIMECS 2019), 08-11 September, 2019, Istanbul, Turkey. The work was financially supported by the Russian Science Foundation, Agreement No. 15-11-00025-П. The research is carried out using the equipment of the shared research facilities of HPC computing resources at Lomonosov Moscow State University, including the Lomonosov supercomputer (27,53).

REFERENCES

- Sulimov VB, Sulimov A V. Docking: Molecular modeling for drug discovery. Moscow: AINTELL; 2017. 348 (in Russian).
- Sadovnichii VA, Sulimov VB. Supercomputing technologies in medicine. In: Sadovnichii VA, Savin GI, Voevodin VV, editors. Supercomputing Technologies in Science. Moscow: Moscow University Publishing; 2009. p. 16–23.
- Sliwoski G, Kothiwale S, Meiler J, Lowe Jr. EW. Computational methods in drug discovery. Pharmacological reviews [Internet]. 2013;66(1):334–95. Available from: <https://www.ncbi.nlm.nih.gov/pubmed/24381236>.
- Sulimov VB, Kutov DC, Sulimov A V. Advances in docking. Current Medicinal Chemistry [Internet]. 2019;25(42):1–25. Available from: <http://www.eurekaselect.com/node/165105/article>.
- Pagadala NS, Syed K, Tuszynski J. Software for molecular docking: a review. Biophysical Reviews. 2017/05/17. 2017;9(2):91–102.
- Yuriev E, Holien J, Ramsland PA. Improvements, trends, and new ideas in molecular docking: 2012–2013 in review. Journal of Molecular Recognition. 2015/03/27. 2015;28(10):581–604.
- Berman HM, Westbrook J, Feng Z, Gilliland G, Bhat TN, Weissig H, et al. The Protein Data Bank. Nucleic Acids Research [Internet]. 1999/12/11. 2000;28(1):235–42. Available from: <https://www.ncbi.nlm.nih.gov/pubmed/10592235>.
- Allen WJ, Balius TE, Mukherjee S, Brozell SR, Moustakas DT, Lang PT, et al. DOCK 6: Impact of new features and current docking performance. Journal of Computational Chemistry [Internet]. 2015/04/29. 2015;36(15):1132–56. Available from: <https://www.ncbi.nlm.nih.gov/pubmed/25914306>.
- Brozell SR, Mukherjee S, Balius TE, Roe DR, Case DA, Rizzo RC. Evaluation of DOCK 6 as a pose generation and database enrichment tool. Journal of Computer-Aided Molecular Design [Internet]. 2012;26(6):749–73. Available from: <https://doi.org/10.1007/s10822-012-9565-y>.
- Trager RE, Giblock P, Soltani S, Upadhyay AA, Rekapalli B, Peterson YK. Docking optimization, variance and promiscuity for large-scale drug-like chemical space using high performance computing architectures. Drug Discovery Today [Internet]. 2016/06/30. 2016;21(10):1672–80. Available from: <http://www.sciencedirect.com/science/article/pii/S1359644616302410>.
- Sulimov AV, Kutov DC, Katkova EV, Kondakova OA, Sulimov VB. Search for approaches to improving the calculation accuracy of the protein-ligand binding energy by docking. Russian Chemical Bulletin [Internet]. 2017;66(10):1913–24. Available from: <https://doi.org/10.1007/s11172-017-1966-6>.
- Sulimov AV, Kutov DC, Oferkin IV, Katkova EV, Sulimov VB. Application of the docking program SOL for CSAR benchmark. Journal of Chemical Information and Modeling [Internet]. 2013/07/09. 2013;53(8):1946–56. Available from: <https://www.ncbi.nlm.nih.gov/pubmed/23829357>.
- Romanov AN, Kondakova OA, Grigoriev FV, Sulimov AV, Lushekina SV, Martynov YB, et al. The SOL docking package for computer-aided drug design. Vol. 9, Numerical Methods and Programming. 2008. p. 213–233 (in Russian).
- Oferkin IV, Katkova EV, Sulimov AV, Kutov DC, Sobolev SI, Voevodin VV, et al. Evaluation of docking target functions by the comprehensive investigation of protein-ligand energy minima. Advances in Bioinformatics [Internet]. 2015 [cited 2015 Dec 23];2015(Article ID 126858, 32 pages). Available from: <https://www.ncbi.nlm.nih.gov/pubmed/26693223>.
- Oferkin IV, Zheltkov DA, Tyrtshnikov EE, Sulimov AV, Kutov DC, Sulimov VB. Evaluation of the docking algorithm based on tensor train global optimization. Bulletin of the South Ural State University, Ser Mathematical Modelling, Programming & Computer Software [Internet]. 2015;8(4):83–99. Available from: <https://mmp.susu.ru/article/en/362>.
- Sulimov AV, Kutov DC, Sulimov VB. Parallel supercomputer docking program of the new generation: finding low energy minima spectrum. In: Voevodin V, Sobolev S, editors. 4th Russian Supercomputing Days, RuSCDays 2018. Cham: Springer International Publishing; 2019. p. 314–30. (Communications in Computer and Information Science; vol. 965).

17. Kutov DC, Sulimov AV, Sulimov VB. Supercomputer docking: Investigation of low energy minima of protein-ligand complexes. *Supercomputing Frontiers and Innovations* [Internet]. 2018;5(3):134-7. Available from: <http://superfri.org/superfri/article/view/248>.
18. Sulimov AV, Zheltkov DA, Oferkin IV, Kutov DC, Katkova EV, Tyrtshnikov EE, et al. Evaluation of the novel algorithm of flexible ligand docking with moveable target-protein atoms. *Computational and Structural Biotechnology Journal* [Internet]. 2017;15:275-85. Available from: <https://www.ncbi.nlm.nih.gov/pubmed/28377797>.
19. Sulimov AV, Zheltkov DA, Oferkin IV, Kutov DC, Katkova EV, Tyrtshnikov EE, et al. Tensor train global optimization: Application to docking in the configuration space with a large number of dimensions. In: Voevodin VV, Sobolev SI, editors. *3rd Russian Supercomputing Days, RuSCDays 2017* [Internet]. Cham: Springer International Publishing; 2017. p. 151-67. (Communications in Computer and Information Science; vol. 793). Available from: https://doi.org/10.1007/978-3-319-71255-0_12.
20. Sulimov V, Romanov A, Grigoriev F, Kondakova O, Sulimov A, Bryzgalov P, et al. Web-oriented system Keenbase for virtual screening and design of new ligands for biological macromolecules. Application for new drugs searches. In: *Saint-Petersburg international workshop on nanobiotechnologies*. Saint-Petersburg; 2006. p. 33-4.
21. Halgren TA. Merck molecular force field [Internet]. Vol. 17, *Journal of Computational Chemistry*. 1996. p. 490-641. Available from: [http://onlinelibrary.wiley.com/doi/10.1002/\(SICI\)1096-987X\(199604\)17:5/6%3C490::AID-JCC1%3E3.0.CO;2-P/abstract](http://onlinelibrary.wiley.com/doi/10.1002/(SICI)1096-987X(199604)17:5/6%3C490::AID-JCC1%3E3.0.CO;2-P/abstract).
22. Halgren TA. MMFF VII. Characterization of MMFF94, MMFF94s, and other widely available force fields for conformational energies and for intermolecular-interaction energies and geometries. *Journal of Computational Chemistry* [Internet]. 1999 May 1;20(7):730-48. Available from: [https://doi.org/10.1002/\(SICI\)1096-987X\(199905\)20:7%3C730::AID-JCC8%3E3.0.CO](https://doi.org/10.1002/(SICI)1096-987X(199905)20:7%3C730::AID-JCC8%3E3.0.CO).
23. Beachy MD, Chasman D, Murphy RB, Halgren TA, Friesner RA. Accurate ab Initio Quantum Chemical Determination of the Relative Energetics of Peptide Conformations and Assessment of Empirical Force Fields. *Journal of the American Chemical Society* [Internet]. 1997;119(25):5908-20. Available from: <http://dx.doi.org/10.1021/ja962310g>.
24. Forli S, Huey R, Pique ME, Sanner M, Goodsell DS, Olson AJ. Computational protein-ligand docking and virtual drug screening with the AutoDock suite. *Nature protocols* [Internet]. 2016;11(5):905-19. Available from: <http://www.ncbi.nlm.nih.gov/pmc/articles/PMC4868550/>.
25. Liebeschuetz JW, Cole JC, Korb O. Pose prediction and virtual screening performance of GOLD scoring functions in a standardized test. *J Comput Aided Mol Des* [Internet]. 2012/05/10. 2012;26(6):737-48. Available from: <https://www.ncbi.nlm.nih.gov/pubmed/22569591>.
26. Oferkin IV, Sulimov AV, Kondakova OA, Sulimov VB. Implementation of parallel computing for docking programs SOLGRID and SOL. *Noviye viychi*. Vol. 12, *Numerical Methods and Programming*. 2011. p. 9-23 (in Russian).
27. Voevodin VV, Antonov AS, Nikitenko DA, Shvets PA, Sobolev SI, Sidorov IY, et al. Supercomputer Lomonosov-2: Large scale, deep monitoring and fine analytics for the user community. *Supercomputing Frontiers and Innovations* [Internet]. 2019;6(2):4-11. Available from: <https://superfri.org/superfri/article/view/278>.
28. Damm-Ganamet KL, Smith RD, Dunbar Jr. JB, Stuckey JA, Carlson HA. CSAR Benchmark Exercise 2011-2012: Evaluation of Results from Docking and Relative Ranking of Blinded Congeneric Series,. *J Chem Inf and Model*. 2013;53:1853-70.
29. Sulimov VB, Romanov AN, Kondakova OA, Sinauridze EI, Butylin AA, Gribkova IV, et al. New thrombin inhibitors: Molecular design and experimental discovery. In: *5th Anniversary Congress of International Drug Discovery Science & Technology 2007, IDDST 2007, 7-13 November 2007*. Xi'an, China; 2007. p. 145.
30. Sinauridze EI, Romanov AN, Gribkova IV, Kondakova OA, Surov SS, Gorbatenko AS, et al. New synthetic thrombin inhibitors: Molecular design and experimental verification. *PLoS One* [Internet]. 2011/05/24. 2011;6(5):e19969. Available from: <https://www.ncbi.nlm.nih.gov/pubmed/21603576>.
31. Sulimov VB, Katkova EV, Oferkin IV, Sulimov AV, Romanov AN, Roschin AI, et al. Application of molecular modeling to urokinase inhibitors development. *BioMed Research International* [Internet]. 2014/06/27. 2014;2014:625176. Available from: <https://www.ncbi.nlm.nih.gov/pubmed/24967388>.
32. Beloglazova IB, Plekhanova OS, Katkova EV, Rysenkova KD, Stambol'skii DV, Sulimov VB, et al. Molecular modeling as a new approach to the development of urokinase inhibitors. *Bulletin of Experimental Biology and Medicine* [Internet]. 2015;158(5):700-4. Available from: <https://doi.org/10.1007/s10517-015-2839-3>.
33. Sulimov VB, Gribkova IV, Kochugaeva MP, Katkova EV, Sulimov AV, Kutov DC, et al. Application of molecular modeling to development of new factor Xa inhibitors. *BioMed Research International* [Internet]. 2015 [cited 2015 Oct 21];2015(Article ID 120802, 15 pages). Available from: <https://www.ncbi.nlm.nih.gov/pubmed/26484350>.
34. Ilin I, Lipets E, Sulimov A, Kutov D, Shikhaliev K, Potapov A, et al. New factor Xa inhibitors based on 1,2,3,4-tetrahydroquinoline developed by molecular modelling. *Journal of Molecular Graphics and Modelling* [Internet]. 2019;89:215-24. Available from: <http://www.sciencedirect.com/science/article/pii/S109326318305576>.
35. Byrd R, Lu P, Nocedal J, Zhu C. A Limited Memory Algorithm for Bound Constrained Optimization. *SIAM Journal on Scientific Computing* [Internet]. 1995;16(5):1190-208. Available from: <https://doi.org/10.1137/0916069>.

36. Zhu C, Byrd RH, Lu P, Nocedal J. Algorithm 778: L-BFGS-B: Fortran subroutines for large-scale bound-constrained optimization. *ACM Transactions on Mathematical Software*. 1997;23(4):550–60.
37. Sulimov VB, Mikhalev AY, Oferkin IV, Oseledets IV, Sulimov AV, Kutov DC, et al. Polarized continuum solvent model: Considerable acceleration with the multicharge matrix approximation. *International Journal of Applied Engineering Research*. 2015;10(24):44815–30.
38. Rezac J, Hobza P. Advanced Corrections of Hydrogen Bonding and Dispersion for Semiempirical Quantum Mechanical Methods. *J Chem Theory Comput* [Internet]. 2012/01/10. 2012;8(1):141–51. Available from: <https://www.ncbi.nlm.nih.gov/pubmed/26592877>.
39. Stewart JJ. Optimization of parameters for semiempirical methods VI: more modifications to the NDDO approximations and re-optimization of parameters. *J Mol Model* [Internet]. 2012/11/29. 2013;19(1):1–32. Available from: <https://www.ncbi.nlm.nih.gov/pubmed/23187683>.
40. Sulimov AV, Kutov DC, Katkova EV, Sulimov VB. Combined docking with classical force field and quantum chemical semiempirical method PM7. *Advances in Bioinformatics* [Internet]. 2017;2017(Article ID 7167691, 6 pages). Available from: <https://www.ncbi.nlm.nih.gov/pubmed/28191015>.
41. Sulimov AV, Kutov DC, Katkova EV, Ilin IS, Sulimov VB. New generation of docking programs: Supercomputer validation of force fields and quantum-chemical methods for docking. *Journal of Molecular Graphics and Modelling* [Internet]. 2017;78:139–47. Available from: <https://www.ncbi.nlm.nih.gov/pubmed/29055806>.
42. Klamt A, Schuurmann G. COSMO: a new approach to dielectric screening in solvents with explicit expressions for the screening energy and its gradient. *Journal of the Chemical Society, Perkin Transactions 2* [Internet]. 1993;(5):799–805. Available from: <http://dx.doi.org/10.1039/P29930000799>.
43. Stewart JJP. MOPAC2016 [Internet]. Colorado Springs, CO, USA: Stewart Computational Chemistry; 2016. Available from: <http://openmopac.net>.
44. Sulimov AV, Kutov DK, Il'in IS, Sulimov VB. Doking s kombinirovanniyim primeneniiev silovovo pola i kvantovohimicheskovo metoda. *Biomeditsinskaya himiya*. 2019;65(2):80–5 (in Russian).
45. Oseledets I, Tyrtysnikov E. Breaking the Curse of Dimensionality, Or How to Use SVD in Many Dimensions. *SIAM Journal on Scientific Computing* [Internet]. 2009;31(5):3744–59. Available from: <https://doi.org/10.1137/090748330>.
46. Oseledets I. Tensor-Train Decomposition. *SIAM Journal on Scientific Computing* [Internet]. 2011;33(5):2295–317. Available from: <https://doi.org/10.1137/090752286>.
47. Oseledets I, Tyrtysnikov E. TT-cross approximation for multidimensional arrays. *Linear Algebra and its Applications* [Internet]. 2010;432(1):70–88. Available from: <http://www.sciencedirect.com/science/article/pii/S0024379509003747>.
48. Goreinov S, Tyrtysnikov E. The maximal-volume concept in approximation by low-rank matrices. *Contemporary Mathematics*. 2001;268:47–51.
49. Zheltkov DA, Oferkin IV, Katkova EV, Sulimov AV, Sulimov VB, Tyrtysnikov EE. TTDock: a docking method based on tensor train decompositions [Internet]. Vol. 14, *Numerical Methods and Programming*. 2013. p. 279-291 (in Russian). Available from: http://num-meth.srcc.msu.ru/zhurnal/tom_2013/pdf/v14r131.pdf.
50. Hanwell MD, Curtis DE, Lonie DC, Vandermeersch T, Zurek E, Hutchison GR. Avogadro: an advanced semantic chemical editor, visualization, and analysis platform. *Journal of Cheminformatics* [Internet]. 2012;4(1):17. Available from: <https://doi.org/10.1186/1758-2946-4-17>.
51. Sulimov A, Kutov D, Ilin I, Zheltkov D, Tyrtysnikov E, Sulimov V. Supercomputer docking with a large number of degrees of freedom. *SAR and QSAR in Environmental Research* [Internet]. 2019 Oct 3;30(10):733–49. Available from: <https://www.tandfonline.com/doi/full/10.1080/1062936X.2019.1659412>.
52. Brandt T, Holzmann N, Muley L, Khayat M, Wegscheid-Gerlach C, Baum B, et al. Congeneric but still distinct: how closely related trypsin ligands exhibit different thermodynamic and structural properties. *Journal of molecular biology* [Internet]. 2011;405(5):1170–1187. Available from: <https://doi.org/10.1016/j.jmb.2010.11.038>.
53. Sadovnichy V, Tikhonravov A, Voevodin V, Opanasenko V. "Lomonosov": Supercomputing at Moscow State University. In: *Contemporary High Performance Computing: From Petascale toward Exascale*. Boca Raton, United States: Boca Raton, United States; 2013. p. 283–307.



A Turn-on Fluorescent Sensor For Cadmium Ion Detection In Aqueous Solutions

Ziya Aydin*  

*Vocational School of Technical Sciences, Karamanoglu Mehmetbey University, 70200 Karaman, Turkey.

Abstract: Fluorescent sensors have attracted an important interest due to their advantages such as high selectivity, rapid response, easy use, etc. In this study, a rhodamine based fluorescent sensor, RhDP, was synthesized, and used for selective detection of Cd²⁺ ions. The sensor responds to Cd²⁺ via the coordination induced fluorescence activation (CIFA) mechanism. RhDP gives a very fast and reversible fluorescence response to Cd²⁺ in the presence of the metal ions tested. The complex stoichiometry between RhDP and Cd²⁺ was found to be 1:1 and the binding constant was calculated as $2.70 \times 10^7 \text{ M}^{-1}$ in acetonitrile (ACN)/HEPES buffer (10 mM, pH: 7.05, v/v 1:1). The fluorescent detection limit of RhDP for Cd²⁺ was found to be 0.218 μM , which gave a marked sensitivity towards Cd²⁺.

Keywords: Fluorescence, Sensor, Cadmium, Rhodamine B, Turn-on.

Submitted: October 28, 2019. **Accepted:** December 27, 2019.

Cite this: Aydin Z. A Turn-on Fluorescent Sensor For Cadmium Ion Detection In Aqueous Solutions. JOTCSA. 2020;7(1):277-86.

DOI: <https://doi.org/10.18596/jotcsa.638912>.

***Corresponding author.** ziyaaydin@kmu.edu.tr; ziyaaydin@yahoo.com.

INTRODUCTION

Cadmium, which is one of the highly toxic heavy metals, is widely distributed in soil, water and crops, generated from volcanic eruption, the combustion of fossil fuels, Ni-Cd rechargeable batteries, fertilizers, paint pigments, etc., causing serious problems for human health (1-3). Cadmium ion (Cd²⁺) shows high affinity to sulfur, and it can interfere with metal ions such as Ca²⁺ and Zn²⁺ to replace in the binding sites of some enzymes (4, 5). It causes dysfunction of these enzymes, causing serious damage to the organs. Cadmium and cadmium compounds are category I carcinogens (6), and are known to be associated with cancer mortality, hepatic and renal damage, and cardiovascular disease (7-9). Thus, it is an essential point to develop detection methods for cadmium.

Several methods have been reported to detect Cd²⁺; however, these methods are generally

expensive and have complicated sample pre-treatment procedures and sophisticated synthetic procedure (10-13). As an alternative method, fluorescence spectroscopy requires easier procedures. In recent years, considerable effort has been dedicated towards the design and preparation of various colorimetric and fluorescent sensors for the detection of Cd²⁺ ions; however, they respond to Cd²⁺ by fluorescence quenching (14-16). Some organic molecules can also be used as turn-on fluorescent sensor for Cd²⁺ (17-19); however, many of them have some technical drawbacks. For example, some Cd²⁺-selective sensors also give response to Zn²⁺ ions because they are in the same group of the periodic table and have similar properties (20, 21). Some Cd²⁺ sensors have a poor detection limit (22) and complicated synthetic routes (23, 24). Thus, better turn-on fluorescent sensors should be developed for Cd²⁺ ions. Rhodamine-based sensors are believed to be the ideal platforms for turn-on fluorescent tools because of its excellent

photophysical properties (25). Since the report of Czarnik's Cu²⁺-sensor (26), various rhodamine-based turn-on fluorescent sensors have been reported for Hg²⁺ (27), Fe³⁺ (28), Cr³⁺ (29), Cu²⁺ (30), and Pd²⁺ (31). So far, a few rhodamine-based turn-on fluorescent sensors have been reported for Cd²⁺ (32-36). However, some of these sensors also have some technical drawbacks such as interference with other metal ions (36) and sensing to hydrogen ions (33). In this paper, a simple and reliable turn-on rhodamine based fluorescent sensor RhDP for Cd²⁺ has been introduced. The sensor exhibited good selectivity and sensitivity for Cd²⁺. The sensor gives response to Cd²⁺ very fast (<1 minute) and is stable even under pH 5.

EXPERIMENTAL

Materials and general methods

Rhodamine B base, 2,6-diacetylpyridine and dimethyl aspartate were purchased from TCI America. The solvents and the other chemicals used in the experiments were obtained commercially. The solution of Fe²⁺ and Fe³⁺ were prepared by dissolving in 0.1 M HCl. Unless otherwise stated, the stock solutions of the metal ions tested were prepared from chloride salts or nitrate salts of them in deionized water. A stock solution of RhDP (500 μM) was prepared in ACN and diluted to 20 μM with ACN/HEPES buffer (10 mM, pH: 7.05, v/v 1:1).

An NMR spectrometer (Bruker DRX-300) was used to record ¹H and ¹³C NMR spectra. A Perkin Elmer API 150EX mass spectrometer was used to perform ESI-MS analyses. A Perkin Elmer Lambda 25 spectrophotometer at 293 K was used to record UV-Vis spectra. Fluorescent intensities were collected with a Perkin-Elmer LS55 luminescence spectrometer at 293 K.

Synthesis of RhDP

Rhodamine B hydrazine was synthesized using the published method (37). Before RhDP was synthesized, the intermediate product (1) was prepared and the synthesis of 1 was explained below.

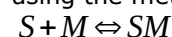
Synthesis of 1 : Rhodamine B hydrazine (1 mmol, 0.556 g) and 2,6-diacetylpyridine (1 mmol, 0.162 g) were dissolved and mixed in boiling ethanol. The mixture was then refluxed for 5 hours. The solution was then cooled and allowed to stand at room temperature. After the solvent was evaporated under reduced pressure, the crude product was obtained. The crude product was then purified by silica gel column chromatography using CH₃OH/CH₂Cl₂ (1:20, v/v) as eluent to obtain 0.405 g of **1** (yield, 56%). ¹H NMR (CDCl₃, 300 MHz δ(ppm): 8.72 (d, 1 H), 8.08 (d, 1 H), 7.78–7.67

(m, 2 H), 7.62–7.53 (m, 2H), 7.23 (d, 1 H), 6.54–6.46 (m, 4H), 6.21 (d, 2 H), 3.63 (m, 8 H), 2.70 (s, 3H), 1.91 (s, 3H), 1.21 (t, 12H); ¹³C NMR (CDCl₃, 75 MHz δ(ppm): 168.8, 154.3, 153.3, 152.6, 150.1, 148.3, 147.8, 145.7, 137.7, 133.8, 129.6, 128.1, 127.4, 124.5, 123.2, 119.9, 118.9, 108.1, 107.097.7, 66.5, 51.7, 44.3, 21.7, 12.7; ESI-MS: found: *m/z* = 602.1 [M+H]⁺, calcd for C₃₇H₃₉N₅O₃ = 601.2.

Synthesis of RhDP : 1 (0.670 mmol, 0.405 g) and dimethyl aspartate (0.670 mmol, 0,076 g) were dissolved in ethanol (15 mL). The mixture was then refluxed overnight. The solvent was evaporated under vacuum and the crude product was purified by alumina gel column using CH₂Cl₂ to CH₂Cl₂/MeOH as eluent to afford RhDP as a yellow solid (0.115 g, yield, 23%). ¹H NMR (CDCl₃, 300 MHz δ(ppm): 8.82 (d, 1 H), 8.14 (d, 1 H), 7.78–7.67 (m, 2 H), 7.62–7.53 (m, 2H), 7.23 (d, 1 H), 6.54–6.46 (m, 4H), 6.21 (d, 2 H), 3.82 (s, 6H) 3.63 (m, 8 H), 3.01 (m, 1H), 2.70 (s, 3H), 2.58 (d, 2H) 1.91 (s, 3H), 1.21 (t, 12H); ¹³C NMR (CDCl₃, 75 MHz δ(ppm): 158.8, 154.3, 153.3, 152.6, 150.1, 148.3, 147.8, 145.7, 137.7, 133.8, 129.6, 128.1, 127.4, 124.5, 123.2, 119.9, 118.9, 108.1, 107.097.7, 66.5, 54.6, 51.7, 44.3, 41.6, 36.1, 21.7, 12.7; ESI-MS: found: *m/z* = 745.2 [M+H]⁺, calcd for C₄₃H₄₈N₆O₈ = 744.3.

Binding studies

The binding constant between RhDP and Cd²⁺ was determined with the absorption values at 557 nm using the method explained below.



Where S = sensor, M = Cd²⁺ and SM = RhDP + Cd²⁺

The complex apparent binding constant is given by

$$K = \frac{[SM]}{[S][M]}$$

Here, the concentrations at equilibrium.

$$F_c = \frac{(A_u - A_m)}{(A_u - A_c)} = K = \frac{[SM]}{[S]}$$

F_c is the fraction of S that formed a complex, [SM] is concentration at equilibrium, [S] is initial concentration. A_u; A_m; and A_c are the absorbance (at a chosen wavelength) of solutions of S only (before Cd²⁺ was added); S and SM mixture (somewhere in the middle of titration); and SM only (at the end of titration) respectively. The concentration of free Cd²⁺ at equilibrium, [M]_e, is found with the following identity.

$$[M]_e = [M]_0 - [SM]_e = [M]_0 - F_c [S]_0$$

$$K = \frac{F_c}{1 - F_c} \times \frac{1}{[M]_{eq}}$$

Quantum yield

Quantum yields of RhDP and RhDP + Cd²⁺ were calculated using the method reported (38).

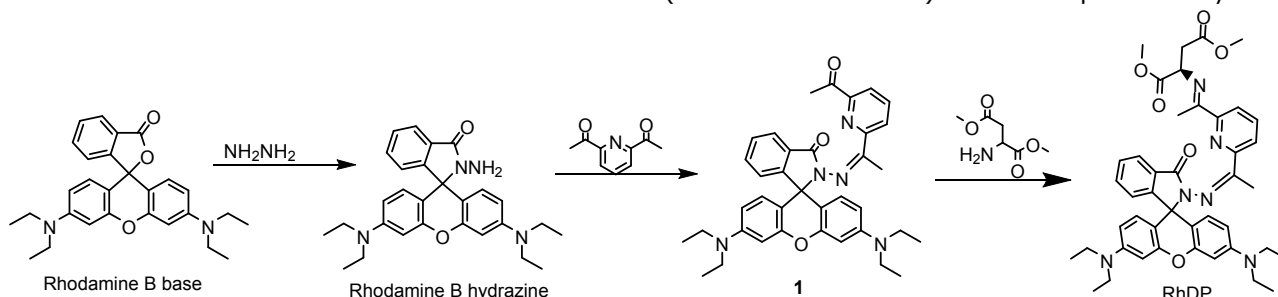
$$\phi = \phi_R \left(\frac{\text{Grad}}{\text{Grad}_R} \right) \left(\frac{\eta^2}{\eta_r^2} \right)$$

$$\Phi_{\text{RhDP}} = 0.0187, \Phi_{\text{RhDP}+\text{Cd}^{2+}} = 0.219$$

RESULTS and DISCUSSION

The strategy for the development of RhDP is as follows: 1) Rhodamine B was chosen as a fluorophore due to its excellent photophysical properties (39). 2) Rhodamine B was reacted with

hydrazine to lower the sensitivity of the rhodamine part to pH and be suitable for the next step. 3) Rhodamine B hydrazine was first reacted with 2,6-diacetyl pyridine and then reacted with dimethyl aspartate to obtain the binding part for Cd^{2+} . The binding part consists of three nitrogen and three oxygen atoms to afford one six-membered ring and four five-membered rings. The sensor, RhDP, was synthesized in a three step procedure (the synthesis of RhDP was explained in the experimental part) with overall yield of 23% (Scheme 1). The sensor was characterized by NMR (^{13}C NMR and ^1H NMR) and mass spectrometry.



Scheme 1: Synthesis of RhDP.

The absorption spectral changes of RhDP after coordination with Cd^{2+} in ACN/HEPES buffer (10 mM, pH: 7.05, v/v 1:1) were investigated at first. The absorption spectra were recorded at approximately 5 minutes after the addition of each Cd^{2+} concentration. RhDP is a colorless compound showing very weak absorption ($\epsilon = 7.6 \times 10^3 \text{ M}^{-1} \text{ cm}^{-1}$) in the 450-650 nm region; indicating that RhDP was dominantly in the formation of the spirocyclic form (40). Upon addition of Cd^{2+} to the colorless solution of RhDP, it instantaneously turned to pink (see inset in Figure 1a) with an absorption band appearing at 557 nm ($\epsilon = 3.15 \times$

$10^5 \text{ M}^{-1} \text{ cm}^{-1}$) and growing in intensity with the gradual addition of Cd^{2+} (Figure 1a), which implies that the rhodamine spirocyclic ring was under ring-opening process (41) as a result of Cd^{2+} binding. In order to examine the selectivity of RhDP to Cd^{2+} , the absorption spectra of RhDP with various metal ions Cr^{3+} , Cu^{2+} , Na^+ , Hg^{2+} , Mg^{2+} , Ca^{2+} , Fe^{3+} , Zn^{2+} , Ag^+ , Pb^{2+} , K^+ , Co^{2+} , Fe^{2+} , Mn^{2+} and Ni^{2+} were collected. As shown in Figure 1b, only Cd^{2+} gave a large response to RhDP while other metal ions showed little change in maximum UV-Vis absorption peak (only Cu^{2+} and Co^{2+} give response to the sensor).

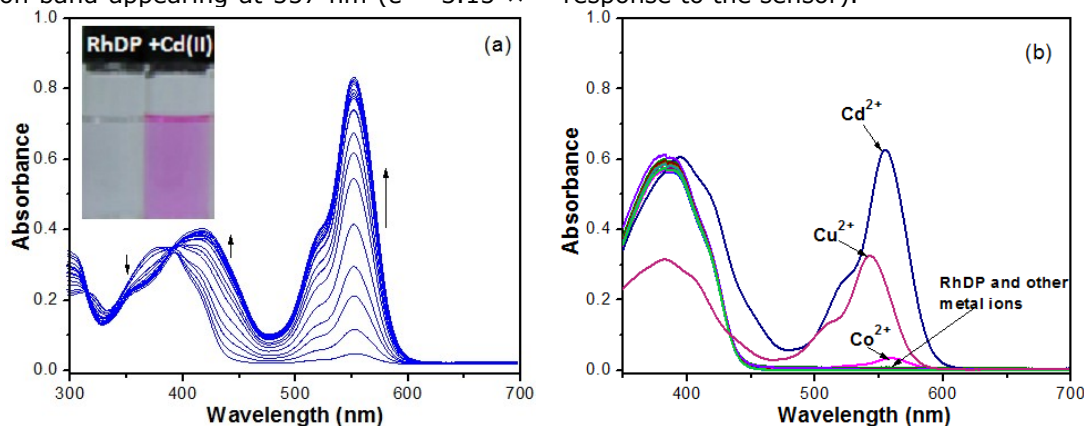


Figure 1: (a) Absorption spectra of 20 μM RhDP with gradual addition of CdCl_2 (0, 2, 4, 6, 8, 10, 12, 14, 16, 18, 20, 25, 30, 35, 40 μM respectively) in ACN/HEPES buffer (10 mM, pH: 7.05, v/v 1:1); (b) Absorption spectra of RhDP (20 μM) with various metal ions (20 μM for Cd^{2+} , Cu^{2+} , Ni^{2+} , Mn^{2+} , Hg^{2+} , Zn^{2+} , Ag^+ , Pb^{2+} , Fe^{3+} , Co^{2+} , Fe^{2+} , Cu^+ and Cr^{3+} ; 100 μM for Ca^{2+} , Mg^{2+} , K^+ and Na^+)

Before performing fluorescent experiments for RhDP, the time evolution of RhDP, the response of the RhDP to 1 equivalent of Cd^{2+} and their stability in ACN/HEPES buffer (10 mM, pH: 7.05, v/v 1:1)

were studied. As seen in Figure 2, the interaction of RhDP with Cd^{2+} was completed in less than 5 minutes, and it was stable for 15 hours. RhDP itself was stable in aqueous solution for 8h (emission at

591 nm). The results showed that the coordination of Cd^{2+} to RhDP also increased the stability of the sensor.

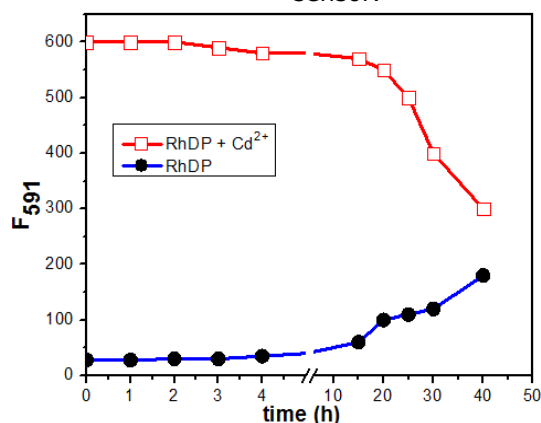


Figure 2: Time evolution for RhDP (20 μM) and RhDP+ Cd^{2+} (20 μM).

To examine the fluorescent response to Cd^{2+} , a solution of RhDP in ACN/HEPES buffer (10 mM, pH: 7.05, v/v 1:1) was titrated with various concentrations of Cd^{2+} and monitored with a fluorometer by excitation at 530 nm. The sensor ($\Phi=0.0187$) showed a very weak fluorescent emission at 580 nm. Upon the addition of Cd^{2+} to the RhDP solution, a large increase in fluorescence was observed at 591 nm, which is attributed to the ring opening induced by the complexation of Cd^{2+} (Figure 3a). The changes in the fluorescent properties of RhDP as a result of addition of the various metal

ions were tested at 591 nm (excitation at 530 nm). As seen in Figure 3b and blue bars in Figure 4b, only Cd^{2+} gave a great response to RhDP while other metal ions showed little change in maximum fluorescent intensity peak (similar as that observed by UV-Vis, only Cu^{2+} and Co^{2+} showed a minor enhancement in fluorescence under these conditions.). The emission intensity enhancement at 591 nm ($\Phi=0.219$) is greater than 40-fold with 1.0 equivalent of Cd^{2+} , which was red-shifted about 11 nm compared with that of RhDP, suggesting that RhDP is a great turn-on fluorescent sensor for Cd^{2+} .

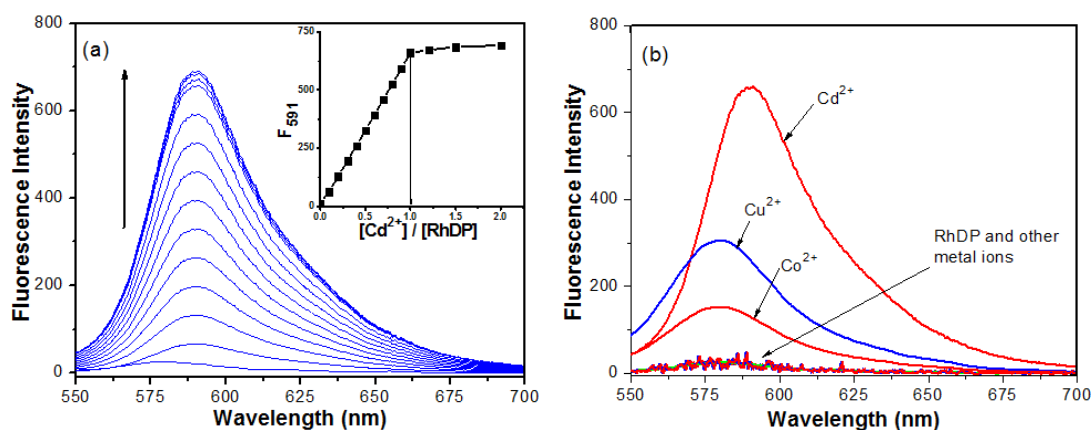


Figure 3: (a) Fluorescence intensities of 20 μM RhDP with gradual addition of CdCl_2 (0, 2, 4, 6, 8, 10, 12, 14, 16, 18, 20, 25, 30, 40 μM respectively) in ACN/HEPES buffer (10 mM, pH: 7.05, v/v 1:1); (b) Fluorescence spectra of RhDP (20 μM) with various metal ions (20 μM for Cd^{2+} , Cu^{2+} , Ni^{2+} , Mn^{2+} , Hg^{2+} , Zn^{2+} , Ag^+ , Pb^{2+} , Fe^{3+} , Co^{2+} , Cu^+ , Fe^{2+} and Cr^{3+} ; 100 μM for Ca^{2+} , Mg^{2+} , Na^+ and K^+).

Rhodamine-based sensors also give response to hydrogen ions (37, 41). To clarify whether the sensor is in the closed-form in ACN/HEPES buffer (10 mM, pH: 7.05, v/v 1:1), the stability of the sensor at different pH values was investigated and monitored by absorption spectra. The pH of the solutions was adjusted by adding HCl (0.1 M) into the solutions. The absorption of RhDP at different pH values was plotted in Figure 4a. The sensor is stable even under pH 5.5.

The detection of the target cation in the presence of other metal ions in real sample is an important assay. Competitive experiments were performed to confirm the high selectivity of the detection system. First, the metal ions such as Cr^{3+} , Cu^{2+} , Na^+ , Hg^{2+} , Mg^{2+} , Ca^{2+} , Fe^{3+} , Zn^{2+} , Ag^+ , Pb^{2+} , K^+ , Co^{2+} , Fe^{2+} , Mn^{2+} and Ni^{2+} were pre-incubated with RhDP. As expected, no remarkable change was observed (blue bars in Figure 4b). However, the

addition of 1 equivalent of Cd^{2+} to each of them caused fluorescence enhancement (red bars in Figure 4b). These results showed that none of the

metal ions tested affected the sensing properties of RhDP to Cd^{2+} .

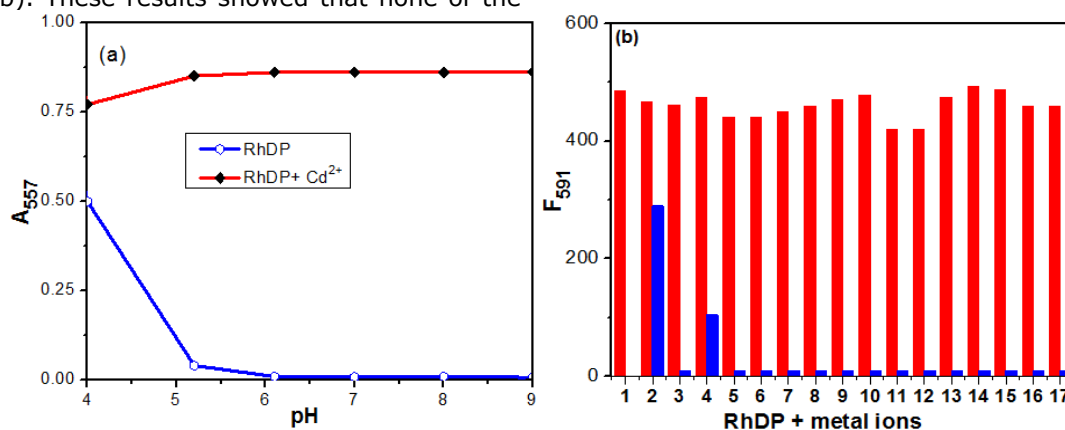


Figure 4: (a) Variation of absorption values (557 nm) of RhDP (20 μM) and RhDP+ Cd^{2+} (20 μM) at various pH values. (b) Fluorescence intensities of RhDP with various metal ions (blue bars) and the subsequent addition of Cd^{2+} (red bars): 1, Cd^{2+} ; 2, Cu^{2+} ; 3, Zn^{2+} ; 4, Co^{2+} ; 5, Cr^{3+} ; 6, Ni^{2+} ; 7, Hg^{2+} ; 8, Mn^{2+} ; 9, Pb^{2+} ; 10, Ag^{+} ; 11, Cu^{+} ; 12, Fe^{3+} ; 13, K^{+} ; 14, Na^{+} ; 15, Mg^{2+} ; 16, Ca^{2+} ; 17, Fe^{2+} .

In order to confirm the binding stoichiometry between RhDP and Cd^{2+} , Job's plot and absorption/fluorescent titration spectra were carried out. As shown in Figure 5a (Job's plot), RhDP/ Cd^{2+} molar fractions represented a maximum absorption peak (at 557 nm) when it was close to 0.5, which indicated that the binding between RhDP and Cd^{2+} was in 1:1 stoichiometry. Typical UV-Vis titration and fluorescent intensity spectra for RhDP with Cd^{2+} were shown in Figure 3a (see inset in the

Figure) and Figure 5b. As seen in the Figures, the RhDP/ Cd^{2+} molar ratio (for both absorption and fluorescent results) reached a plateau when the concentration of Cd^{2+} and an equivalent amount of RhDP was close to 1:1, suggesting the formation of a 1:1 RhDP- Cd^{2+} complex. The binding constant between Cd^{2+} and RhDP was determined by a previously reported method (42) with absorption values at 557 nm and was determined to be $2.70 \times 10^7 \text{ M}^{-1}$.

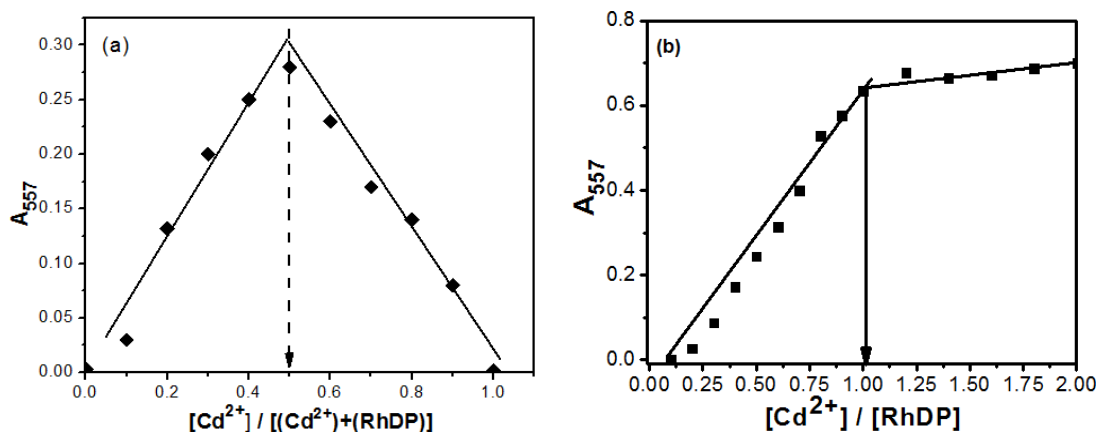


Figure 5: (a) Job's plot (b) Titration of 20 μM RhDP with increasing concentrations of CdCl_2 (0, 2, 4, 6, 8, 10, 12, 14, 16, 18, 20, 25, 30, 35, 40 μM respectively) in ACN/HEPES buffer (10 mM, pH: 7.05).

Furthermore, the reversibility of the binding between RhDP and Cd^{2+} was examined. The complex solution of the sensor and Cd^{2+} was treated with a solution of EDTA (5.0 equivalent).

As seen in Figure 6, the fluorescence signals of RhDP- Cd^{2+} disappeared, which indicated that the binding RhDP and Cd^{2+} is reversible.

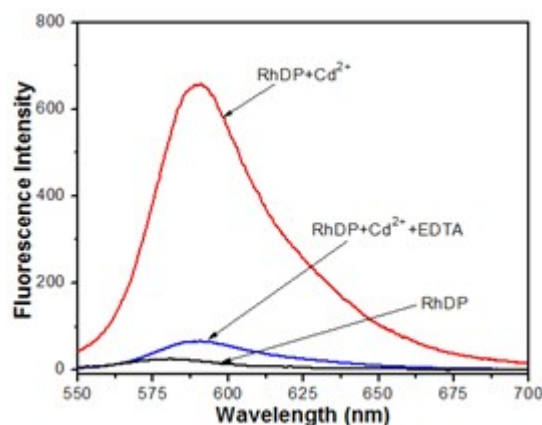
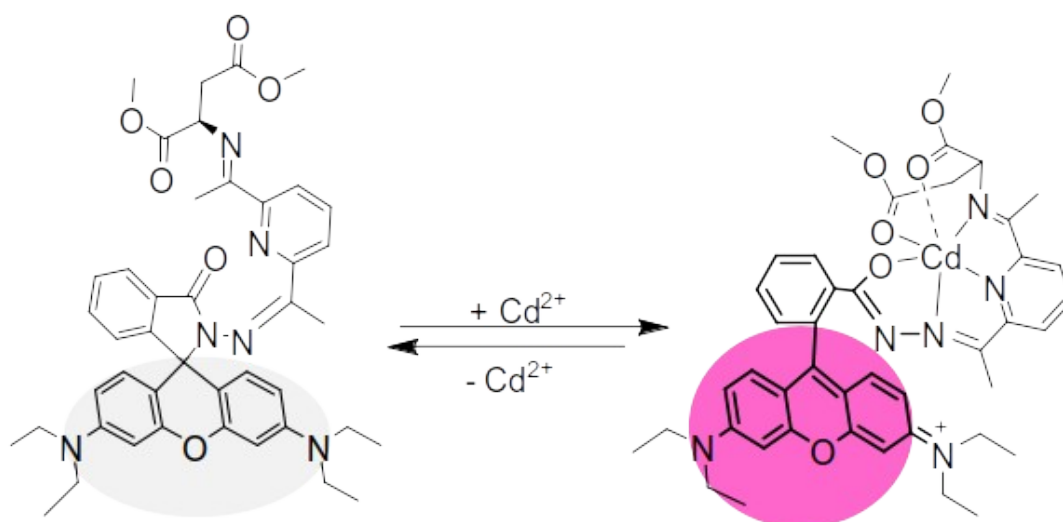


Figure 6: Fluorescence emissions showing reversibility of RhDP (20 μM) to Cd^{2+} ions by EDTA.

From the above results RhDP coordinates with Cd^{2+} in a reversible 1:1 binding mode. The proposed 1:1 binding mode of RhDP- Cd^{2+} is presented in Scheme 2.



Scheme 2: Proposed reversible binding mechanism between RhDP and Cd^{2+} . The structure on the left is ring-closed form and is very weakly fluorescent. The structure on the right is ring-opened form and is strongly fluorescent.

Moreover, the linear concentration range and the fluorescent detection limit of RhDP were obtained. The range of fluorescent intensity (at 591 nm) was linearly dependent on the concentration of Cd^{2+} in

the range from 0 to 20 μM ($R^2 = 0.998$). The fluorescent detection limit was calculated to be 0.218 μM based on $3\sigma/k$ (Figure 7).

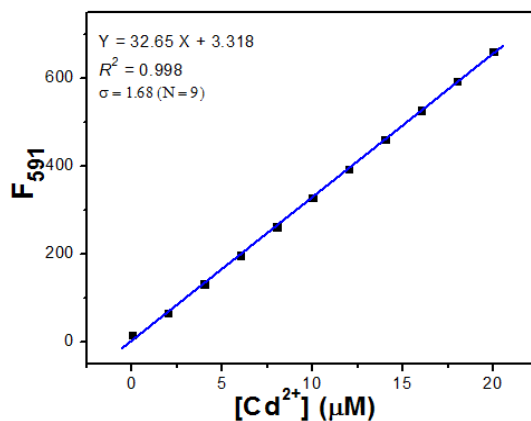


Figure 7: Linear relationship between fluorescent intensity and Cd²⁺ concentration (0–20 μM) Limit of detection (LOD) of RhDP towards Cd⁺ by fluorescent method.

In summary, a new turn-on rhodamine based fluorescent sensor RhDP was designed and synthesized for selective detection of Cd²⁺ ions in aqueous solutions. The sensor showed an excellently selective fluorescence enhancement for Cd²⁺ over other metal ions tested with a colour change and reversible response. The complex stoichiometry between RhDP and Cd²⁺ was found to be 1:1 and the binding constant was calculated as $2.70 \times 10^7 \text{ M}^{-1}$ ($\log K = 7.43$) in ACN/HEPES buffer (10 mM, pH: 7.05, v/v 1:1). The fluorescent detection limit of RhDP for Cd²⁺ was found to be 0.218 μM, which gave a marked sensitivity towards Cd²⁺.

REFERENCES

- Wang C, Fang Y, Peng S, Ma D, Zhao J. Synthesis of novel chelating agents and their effect on cadmium decorporation. *Chemical Research in Toxicology*. 1999;12(4):331-4.
- Williams C, David D. The effect of superphosphate on the cadmium content of soils and plants. *Soil Research*. 1973;11(1):43-56.
- Salviano Mendes AM, Duda GP, Araujo do Nascimento CW, Silva MO. Bioavailability of cadmium and lead in a soil amended with phosphorus fertilizers. *Scientia Agricola*. 2006;63(4):328-32.
- Prozialeck WC, Edwards JR, Woods JM. The vascular endothelium as a target of cadmium toxicity. *Life Sciences*. 2006;79(16):1493-506.
- Varriale A, Staiano M, Rossi M, D'Auria S. High-affinity binding of cadmium ions by mouse metallothionein prompting the design of a reversed-displacement protein-based fluorescence biosensor for cadmium detection. *Analytical Chemistry*. 2007;79(15):5760-2.
- Can IAFRo. IARC monographs on the evaluation of the carcinogenic risks to humans: beryllium, cadmium, mercury, and exposures in the glass manufacturing industry: World Health Organization; 1993.
- McFarland C, Bendell-Young L, Guglielmo C, Williams T. Kidney, liver and bone cadmium content in the Western Sandpiper in relation to migration. *Journal of Environmental Monitoring*. 2002;4(5):791-5.
- Goyer RA, Liu J, Waalkes MP. Cadmium and cancer of prostate and testis. *Biometals*. 2004;17(5):555-8.
- Satarug S, Baker JR, Urbenjapol S, Haswell-Elkins M, Reilly PE, Williams DJ, et al. A global perspective on cadmium pollution and toxicity in non-occupationally exposed population. *Toxicology Letters*. 2003;137(1-2):65-83.
- Ye Q-y, Li Y, Jiang Y, Yan X-p. Determination of trace cadmium in rice by flow injection on-line filterless precipitation– dissolution preconcentration coupled with flame atomic absorption spectrometry. *Journal of Agricultural Food Chemistry*. 2003;51(8):2111-4.
- Pyle SM, Nocerino JM, Deming SN, Palasota JA, Palasota JM, Miller EL, et al. Comparison of AAS, ICP-AES, PSA, and XRF in determining lead and cadmium in soil. *Environmental Science Technology*. 1995;30(1):204-13.
- Dolan SP, Nortrup DA, Bolger PM, Capar SG. Analysis of dietary supplements for arsenic, cadmium, mercury, and lead using inductively coupled plasma mass spectrometry. *Journal of Agricultural Food Chemistry*. 2003;51(5):1307-12.
- Bakker E, Pretsch E. Potentiometric sensors for trace-level analysis. *Trends in Analytical Chemistry*. 2005;24(3):199-207.

14. Prabhakaran D, Yuehong M, Nanjo H, Matsunaga H. Naked-eye cadmium sensor: using chromoionophore arrays of Langmuir–Blodgett molecular assemblies. *Analytical Chemistry*. 2007;79(11):4056-65.
15. Zhu Y-F, Wang Y-S, Zhou B, Yu J-H, Peng L-L, Huang Y-Q, et al. A multifunctional fluorescent aptamer probe for highly sensitive and selective detection of cadmium(II). *Analytical Bioanalytical Chemistry*. 2017;409(21):4951-8.
16. Choi M, Kim M, Lee KD, Han K-N, Yoon I-A, Chung H-J, et al. A new reverse PET chemosensor and its chelatoselective aromatic cadmium. *Organic Letters*. 2001;3(22):3455-7.
17. Zhang Y, Zhang Z, Yin D, Li J, Xie R, Yang W. Turn-on fluorescent InP nanoprobe for detection of cadmium ions with high selectivity and sensitivity. *ACS Applied Materials Interfaces*. 2013;5(19):9709-13.
18. Shim S, Tae J. Rhodamine Cyclen-based fluorescent chemosensor for the detection of Cd²⁺. *Bulletin of the Korean Chemical Society*. 2011;32:2928-32.
19. Kim HN, Ren WX, Kim JS, Yoon J. Fluorescent and colorimetric sensors for detection of lead, cadmium, and mercury ions. *Chemical Society Reviews*. 2012;41(8):3210-44.
20. Nolan EM, Ryu JW, Jaworski J, Feazell RP, Sheng M, Lippard SJ. Zinspy sensors with enhanced dynamic range for imaging neuronal cell zinc uptake and mobilization. *Journal of the American Chemical Society*. 2006;128(48):15517-28.
21. Komatsu K, Kikuchi K, Kojima H, Urano Y, Nagano T. Selective zinc sensor molecules with various affinities for Zn²⁺, revealing dynamics and regional distribution of synaptically released Zn²⁺ in hippocampal slices. *Journal of the American Chemical Society*. 2005;127(29):10197-204.
22. Gunnlaugsson T, Lee TC, Parkesh R. Highly selective fluorescent chemosensors for cadmium in water. *Tetrahedron*. 2004;60(49):11239-49.
23. Xue L, Li G, Liu Q, Wang H, Liu C, Ding X, et al. Ratiometric fluorescent sensor based on inhibition of resonance for detection of cadmium in aqueous solution and living cells. *Inorganic Chemistry*. 2011;50(8):3680-90.
24. Xue L, Liu C, Jiang H. Highly sensitive and selective fluorescent sensor for distinguishing cadmium from zinc ions in aqueous media. *Organic Letters*. 2009;11(7):1655-8.
25. Chen X, Pradhan T, Wang F, Kim JS, Yoon J. Fluorescent chemosensors based on spiroring-opening of xanthenes and related derivatives. *Chemical Reviews*. 2011;112(3):1910-56.
26. Dujols V, Ford F, Czarnik AW. A long-wavelength fluorescent chemodosimeter selective for Cu(II) ion in water. *Journal of the American Chemical Society*. 1997;119(31):7386-7.
27. Shiraishi Y, Sumiya S, Kohno Y, Hirai T. A rhodamine–cyclen conjugate as a highly sensitive and selective fluorescent chemosensor for Hg(II). *The Journal of Organic Chemistry*. 2008;73(21):8571-4.
28. Bhalla V, Sharma N, Kumar N, Kumar M. Rhodamine based fluorescence turn-on chemosensor for nanomolar detection of Fe³⁺ ions. *Sensors Actuators B: Chemical*. 2013;178:228-32.
29. Weerasinghe AJ, Schmiesing C, Sinn E. Highly sensitive and selective reversible sensor for the detection of Cr³⁺. *Tetrahedron Letters*. 2009;50(46):6407-10.
30. Jiao Y, Zhou L, He H, Yin J, Gao Q, Wei J, et al. A novel rhodamine B-based “off-on” fluorescent sensor for selective recognition of copper(II) ions. *Talanta*. 2018;184:143-8.
31. Adak AK, Purkait R, Manna SK, Ghosh BC, Pathak S, Sinha C. Fluorescence sensing and intracellular imaging of Pd²⁺ ions by a novel coumarinyl-rhodamine Schiff base. *New Journal of Chemistry*. 2019;43(9):3899-906.
32. Goswami S, Aich K, Das S, Das AK, Manna A, Halder S. A highly selective and sensitive probe for colorimetric and fluorogenic detection of Cd²⁺ in aqueous media. *Analyst*. 2013;138(6):1903-7.
33. Aich K, Goswami S, Das S, Mukhopadhyay CD, Quah CK, Fun H-K. Cd²⁺ triggered the FRET “ON”: a new molecular switch for the ratiometric detection of Cd²⁺ with live-cell imaging and bound X-ray structure. *Inorganic Chemistry*. 2015;54(15):7309-15.
34. Maniyazagan M, Mariadasse R, Jeyakanthan J, Lokanath N, Naveen S, Premkumar K, et al. Rhodamine based “turn-on” molecular switch FRET–sensor for cadmium and sulfide ions and live cell imaging study. *Sensors Actuators B: Chemical*. 2017;238:565-77.
35. Sakthivel P, Sekar K, Sivaraman G, Singaravadivel S. Rhodamine diaminomaleonitrile

conjugate as a novel colorimetric fluorescent sensor for recognition of Cd²⁺ ion. *Journal of Fluorescence*. 2017;27(3):1109-15.

36. Soibinet M, Souchon V, Leray I, Valeur BJ. Rhod-5N as a fluorescent molecular sensor of cadmium(II) ion. *Journal of Fluorescence*. 2008;18(6):1077.

37. Aydin Z, Wei Y, Guo M. An "off-on" optical sensor for mercury ion detection in aqueous solution and living cells. *Inorganic Chemistry Communications*. 2014;50:84-7.

38. Taylor D, Demas J. Light intensity measurements I: Large area bolometers with microwatt sensitivities and absolute calibration of the Rhodamine B quantum counter. *Analytical Chemistry*. 1979;51(6):712-7.

39. Kim HN, Lee MH, Kim HJ, Kim JS, Yoon J. A new trend in rhodamine-based chemosensors: application of spirolactam ring-opening to sensing ions. *Chemical Society Reviews*. 2008;37(8):1465-72.

40. Wei Y, Aydin Z, Zhang Y, Liu Z, Guo M. A turn-on fluorescent sensor for imaging labile Fe³⁺ in live neuronal cells at subcellular resolution. *ChemBioChem*. 2012;13(11):1569-73.

41. Aydin Z, Wei Y, Guo M. A highly selective rhodamine based turn-on optical sensor for Fe³⁺. *Inorganic Chemistry Communications*. 2012;20:93-6.

42. Guo M, Perez C, Wei Y, Rapoza E, Su G, Bou-Abdallah F, et al. Iron-binding properties of plant phenolics and cranberry's bio-effects. *Dalton Transactions*. 2007(43):4951-61.



The Investigation of the Effect of Mineral Oils which Have Different Specifications on The Performance of Palm- and Tallow-Based Soap Recipes

Esra Gül*  , Aslı Özge Avcı Tuna  , Özlem Esen  

Evyap Sabun, Yağ ve Gliserin San. Tic. A.Ş., 34957, İstanbul, Turkey.

Abstract: In this work, three different types of mineral oils, with the same amount (1% as a ratio), have been added to two different soap recipes from animal origin oils and vegetable-derived fatty acids that have the same rate of foaming agent and similar critical specification values. The pH/conductivity, foaming performance, hardness, and pellet tests were applied to the soaps obtained; and the results were analyzed by comparing the effects of different specifications of mineral oil. The result of this study, the effect of the addition of mineral oils on the soap samples were clarified and characterized by advanced research.

Keywords: Soap, mineral oils, pH, conductivity, foam performance.

Submitted: May 27, 2019. **Accepted:** January 15, 2020.

Cite this: Gül E, Avcı Tuna A, Esen Ö. The Investigation of the Effect of Mineral Oils which Have Different Specifications on The Performance of Palm and Tallow Based Soap Recipes. JOTCSA. 2020; 7(1): 287-94.

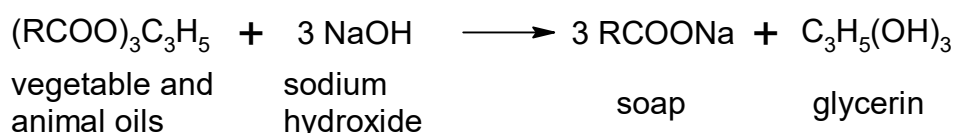
DOI: <https://doi.org/10.18596/jotcsa.570449>.

***Corresponding author. E-mail:** esgul@evyap.com.tr.

INTRODUCTION

Soap is a product obtained from the chemical reactions of directly vegetable and animal oils or the chemical reactions of fatty acids obtained from these oils with alkaline hydroxides (1, 2). The saponification processes used in soap formulas in

the industry for many years are based on a simple neutralization system. In this type of process, saponification occurs by mixing the vegetable and animal oils with the appropriate amount of alkaline substances and exposing them to appropriate heat. The natural saponification reactions are given below (2-4).

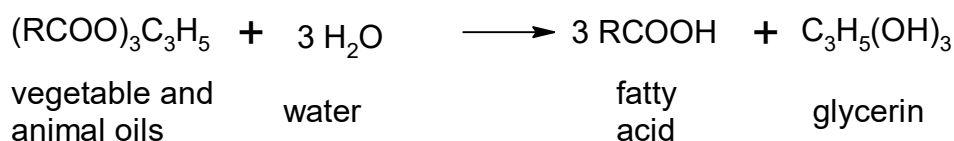


Since soaps are both the alkaline metal salts of fatty acids and the surfactant material, they are used as cleaning agents. Natural fats and oils hydrolyzed as fatty acids are aliphatic monocarboxylic acids (5). Oleic, stearic, palmitic, myristic, and lauric acids are mostly used as fatty acids (6). The basic process of soap making has

not changed since 2000 years. In this method, the solid oils or liquid oils are saponified with an alkali, and then the soap is removed by adding salt to the mixture. Major changes in production; pre-treatment of solid oils or liquid oils and making the prepared soap usable. Industrial processes such as hydrolysis, solvent extraction of oils,

hydrogenation, liquid-liquid extraction have led to the preparation of better-quality raw materials. Besides, batch manufacturing has been replaced by continuous processes (7-14). Fatty acid

saponification mechanisms were given in two reactions below (2,3).
Hydrolysis part;



Saponification part;

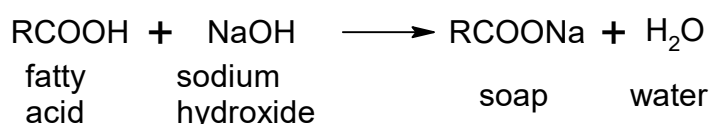


Table 1. Viscosity and density values of various mineral oils.

	Trade Name	INCI Name	Viscosity (cPs)	Density (g/cm ³)
Mineral Oil 1	Mineral Oil Light	white mineral oil (petroleum)	11.20	0.82
Mineral Oil 2	Mineral Oil Medium	white mineral oil (petroleum)	45.60	0.85
Mineral Oil 3	Mineral Oil Heavy	white mineral oil (petroleum)	132.00	0.87

Table 2. Critical spec values of soap formulas.

SOAP BASE	Vegetable Oil Acids 9010 78 TFM	Animal Oil 9010 78 TFM
Total Fatty Acid Matter, % Min	78.00 min.	78.50 min
Free Fatty Acid (as Oleic), %	1.50 max.	1.50 max.
Free Alkali (as NaOH), %	Absent	absent
Chlorides (as NaCl),%	0.45 – 1.05	1.00 max.
Glycerin,%	1.00 max.	1.00 max.
Unsaponifiable Matter,%	1.00 max.	1.00 max.
Volatile Matter (105 °C), %	12.00 – 14.50	15.00 max.

Mineral oils are clear, colorless, and oily liquids that are by-products of the distillation of petroleum (15). Mineral oils are natural materials obtained from various sources. Oil is a mixture of liquid hydrocarbons and other chemical compounds. These are waxes, paraffin, sulfur derivatives, organic aromatic compounds, solid components, etc. (16). Mineral oil is the major source of our liquid fuels and petrochemicals. It consists of long straight-chain alkanes and is contaminated by compounds containing sulfur, nitrogen, and metals, mostly as heavy heterocyclic aromatics and as metalloporphyrin-type materials. Viscous properties of mineral oils are important for technological processes. Maintenance of characteristics of pavements or other compounded

products depends on their viscoelastic properties and mechanical strength; the latter is most likely related to the viscoelasticity of material.

In cosmetics, mineral oil helps reduce water loss from a person's skin, helping keep the skin moisturized. It is also inert, which makes it less likely to cause a skin reaction. According to one recent study, mineral oil is preferable for many different skin types, including a baby's sensitive skin. The purified type of mineral oils, considering cosmetic grade, have been using in products like baby oil and cold creams (17). Mineral oil is an inert, chemically stable ingredient, with a long history of safe use in common topical applications. The Food Additives (FDA) regulations, the

Cosmetic Ingredient Review (CIR) and the Cosmetics Directive of the European Union allow the use of mineral oil in cosmetics and personal care products with no listed restrictions (17). This study presents mineral oils effect in soap products since there is no research to investigate the effect of mineral oils in this area.

White mineral oil (petroleum) a highly refined petroleum mineral oil consisting of a complex combination of hydrocarbons obtained from the intensive treatment of a petroleum fraction with sulfuric acid and oleum, or by hydrogenation, or by a combination of hydrogenation and acid treatment. Additional washing and treating steps may be included in the processing operation. It consists of saturated hydrocarbons having carbon numbers predominantly in the range of C15 through C50 (18). In this study, three mineral oils, white mineral oils (petroleum), that have different viscosity value, was used to investigate the effect of viscosity of mineral oils on a soap. Mineral oil 1, Mineral oil 2 and Mineral oil 3 have different viscosity 11.20, 45.60 and 132 cPs, respectively.

Three different mineral oils (Table 2), with the same amount, have been added to two different soap formulas from animal origin oils and vegetable-derived fatty acids (Table 1) that have the same rate of foaming agent and similar critical specification values. The pH/conductivity, foam performance, hardness and pellet (mush) tests were applied to the eight hand soaps obtained; and the results were analyzed by comparing the effects of different specifications of the mineral oil. The result of this study, the effect of the addition of mineral oils on the eight soap samples were clarified and characterized by advanced research analysis.

MATERIALS AND METHODS

Materials and Characterization

All mineral oils were obtained from Sonneborn and used as received. Soaps were obtained from Evyap Sabun Malaysia Sdn. Bhd as two forms; produced with animal origin oils and vegetable-derived fatty acids. Four soap samples were obtained from animal origin oil, in which three of them contain %1 of three different mineral oils, as one is blank. The same procedure was applied to the soap samples obtained from vegetable-derived fatty acids.

Foaming Test Method:

0.4 g of soap sample was planed and put into a beaker. 1000 mL of distilled water was added on it

and homogenized at 3600 rpm for 5 min. After 5 min, water was discharged into 3 measuring cylinders with 50 mL capacity. Each of the measuring cylinders was turned in a rotation tool for 30 seconds for finding a foam value. Then the first value of foam is marked. After 15 min and 30 min, the second value and third value of foam are marked, respectively.

To determine the foaming performance of soaps, the foaming test method was applied to soap samples.

Pellet (Mush) Test Method:

The soap weight without a fork and with a fork (dry weight) was measured. Mush part of the soap was determined that is marked with a knife as from fork part. The soap was put into the beaker and distilled water was filled up the mark and waited for 2 hours at 25 °C. After 2 hours, the water was drained and waited for 5 min. After 5 min, the weight with mush is measured. Then the mush part is cleaned and again the soap is weighed. The following calculations were applied:

weight with mush (g) - weight without mush (g) = weight of mush (g)

Weight of mush without water (g) = dry weight (g) - weight without mush (g)

water uptake (g) = weight with mush (g) - dry weight (g)

Hardness Test:

Hardness analysis was performed by using the LTCM-100 Chatillian Metek instrument to measure the hardness value of soap samples.

pH and conductivity measurement:

Different concentrations of soap solutions were prepared as 1%, 5% and 10% in water to determine the pH and conductivity of soap samples. The pH values were measured from solutions by using a 780 pH meter Metrohm with a glass electrode. The conductivity measurements were performed on a 905 Titrande Metrohm conductivity meter with a glass electrode at 25 °C.

RESULTS AND DISCUSSION

Figure 1 shows the conductivity changing graphs. It has been obtained that different concentrations of three different mineral oils, which were added to two different soap forms obtained from fatty acids of *vegetable* oils and directly from animal oil give different results.

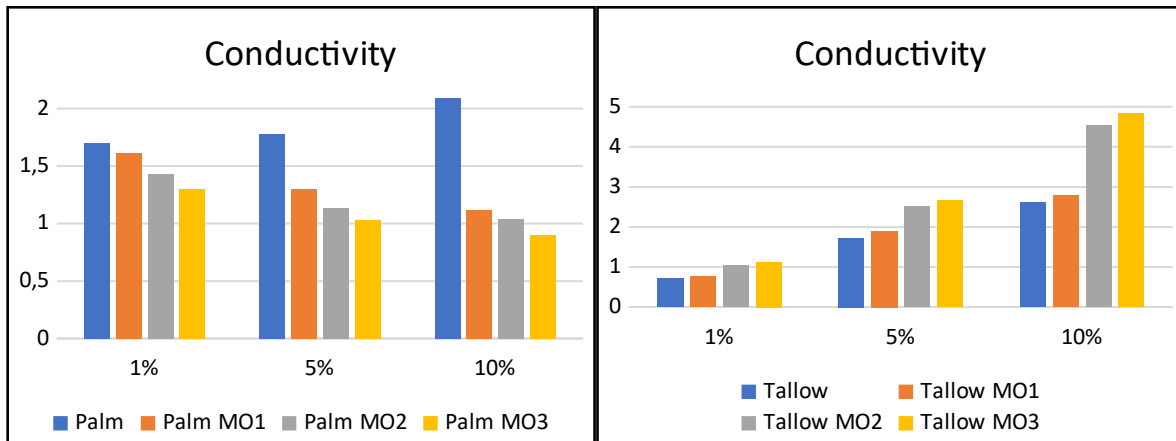


Figure 1. Variation graph on the conductivity of 3 different mineral oils based on palm and tallow at different concentrations.

In this part of the study, the effects of mineral oil on the conductivity of soap were investigated. The electrical conductivity is a magnitude that describes the ability of a material or solution to conduct an electric current. The electrical conductivity of a solution depends on the number and mobility of ions and charged particles present in the solution (19). The soaps obtained from fatty acids of vegetable oils had to decrease of conductivity with the addition of mineral oils. On the other hand, the increase in the conductivity of

the soap was measured with the addition of mineral oils in soaps obtained from animal oils. It is thought that this may change depending on the movement of fatty acids and Na⁺ ions in the content of soaps.

Although differences in conductivity measurements were determined, there was no difference in pH values. This shows that mineral oils do not affect the pH values of the soap. The graph of pH and conductivity values are given in Figure 2.

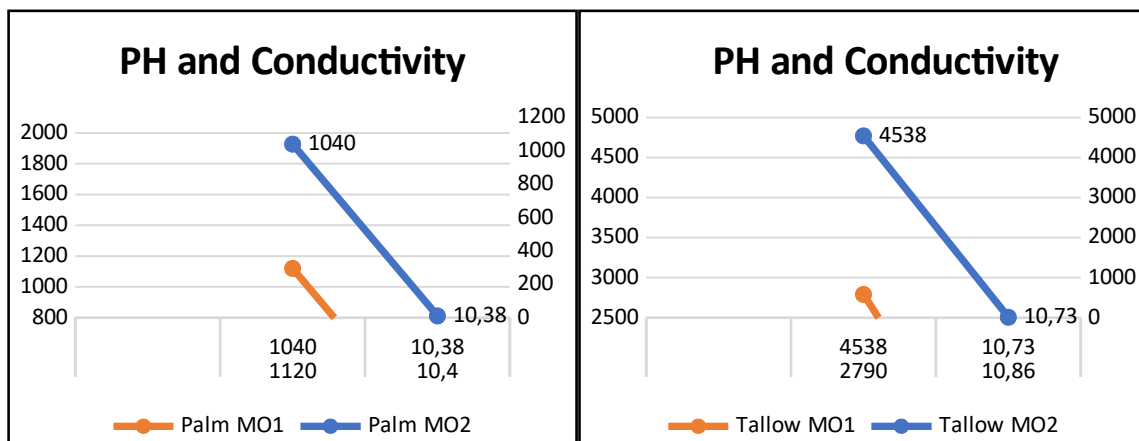


Figure 2. Graphs of change in conductivity and pH on 3 different mineral oils based on palm and tallow at 25 °C.

In the second part of the study, the foam performance of vegetable oils' fatty acids soaps and animal oils' soaps, were evaluated by "foam volume measurement" after adding different

mineral oils with different specifications. The graphs of the measurement results are given in Figure 3. The X-axis shows the foam volume in percent and the Y-axis shows the time axis.

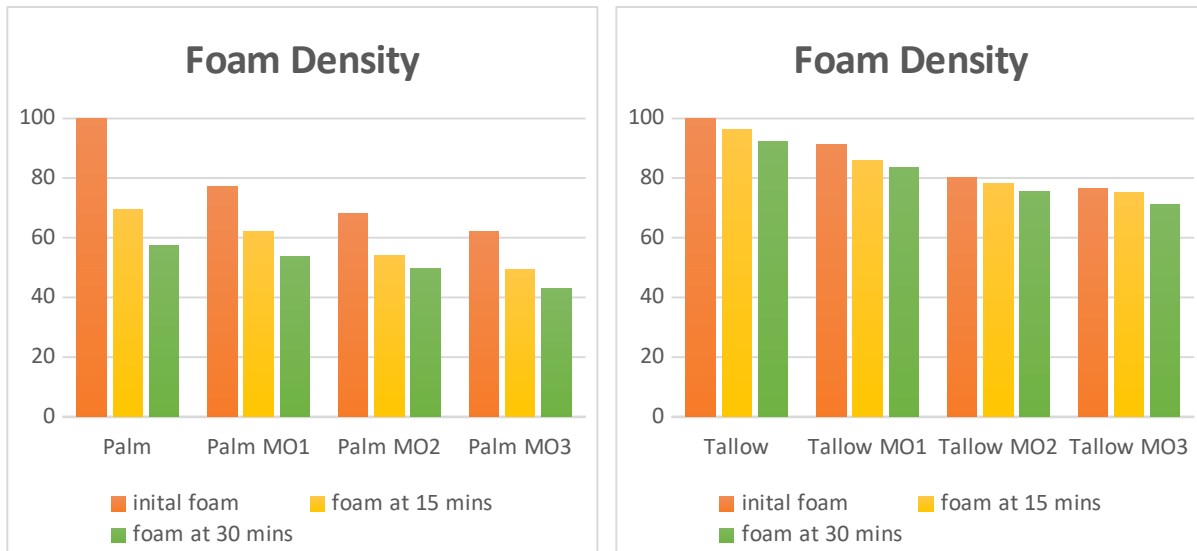


Figure 3. Foam volume values of 3 different mineral oils based on palm and tallow.

The results show that 1% of mineral oils 1, 2 and 3 adding to the vegetable-based soap recipe, the measure of foam volume decreased by 20%, 25%, and 40%, respectively.

In animal-derived recipes, when the effect of 1% of mineral oils adding on the foam was examined, it was observed that it was reduced by a maximum of 24%. As a result of the studies, it was seen that mineral oils have negatively affected the foam performance of soap in both soaps. However, this effect is higher based on Palm.

When mineral oils are compared by themselves, it is observed that primarily mineral oil 3 has the most negative effect than the others on both animal and vegetable-based foam.

With the addition of mineral oil, a reduction in the amount of foam in both soap formulations was observed. It was determined that this decrease is related to the viscosity of mineral oils. The viscosity values of mineral oils are given in Table 2. When the data in Table 2 were taken together with the soap foam performance test of the soap,

it was revealed that the mineral oil had a structural effect on the foam. As a result of the study, it was observed that mineral oils caused a decrease in the amount of foam linearly from the low viscosity value to the high viscosity by the addition of soap.

In the third part of the study, hardness values were measured and evaluated after the addition of mineral oils in 3 different specs to 2 formula prescriptions which are in the form of animal oils and vegetable-derived fatty acids at 25 °C.

In animal-based formulas, it was observed that all three types of mineral oils decreased the hardness of soap, while all mineral oils increased the hardness by creating an opposite effect on the palm. The viscosity and density values of mineral oils are given in Table 2.

The evaluation of hardness changes of plant-based and animal-based formulas, together with % pellet changes, indicating softening of the soap and residue, were added to the studies and plotted in Figure 4.

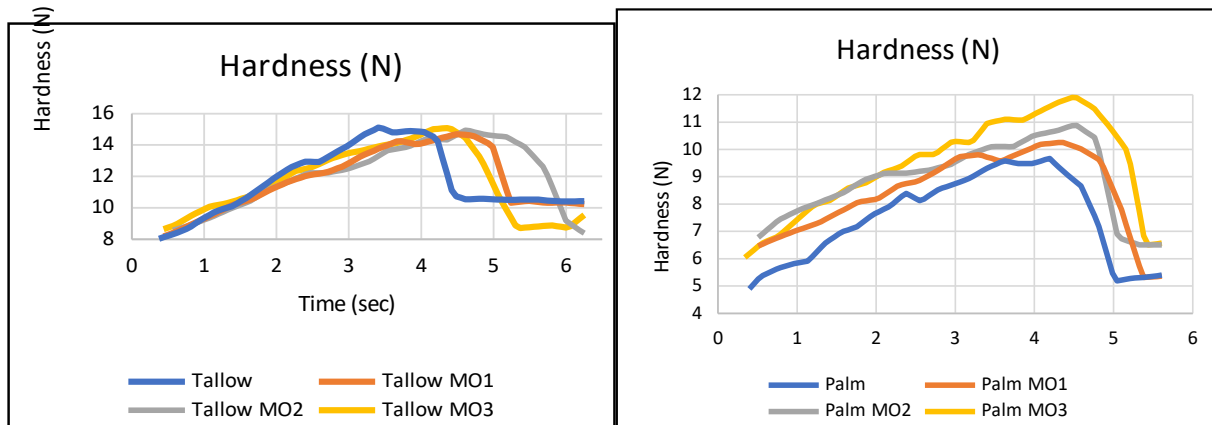


Figure 4. Hardness graphs of soaps produced with 3 different mineral oils on the base of Palm and Tallow at 25°C

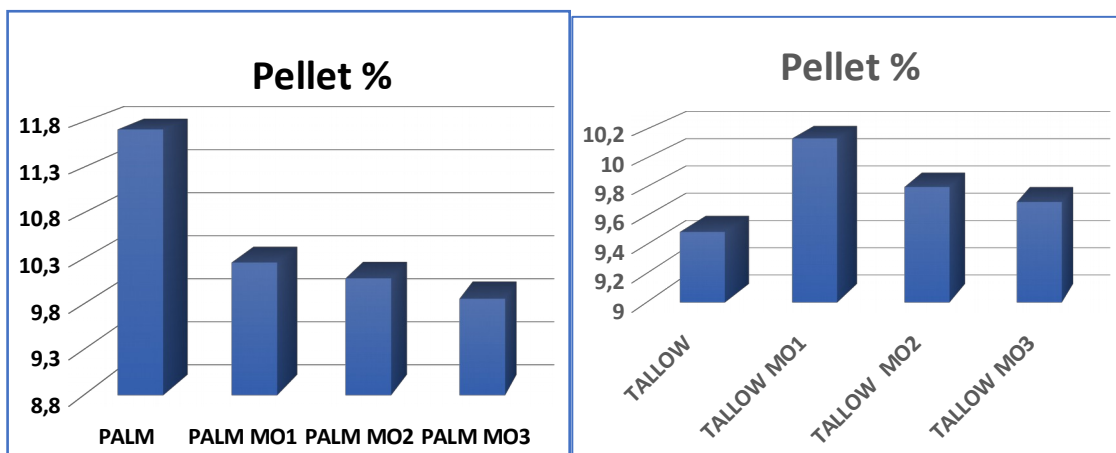


Figure 5. Pellet (%) change graph of soaps produced with 3 different mineral oil based on Palm and Tallow at 25°C.

According to the measured results, the addition of mineral oils in plant-based reduced the amount of pellet; the addition of mineral oils in animal origin prescriptions increased the amount of pellet formation.

These results also support the hardness values of soaps of the same formulas. The harder the soap, the less the formation of the soap pellets.

CONCLUSION

Consequently, this study results showed the following:

- No significant difference was found by the addition of mineral oils at the pH of all soaps. This shows that the soap base and mineral oil do not affect the pH value of the soap.
- At the vegetable-derived fatty acid soap formulations, it was observed that the conductivity decreases by the addition of any kind of mineral oils to the soap, while the conductivity of the soap increased with the addition of mineral oils to animal-derived soaps.

- Although there was no difference in pH values, differences in conductivity measurements were determined. This is thought to be due to the movement of the fatty acids and Na⁺ ions in the content of soaps.
- When the effects of the performance of foaming evaluated with different specs of mineral oils addition to both vegetable-derived fatty acid soaps and animal oils soaps both had a reduction of foaming. In the same study, it was determined that the foam performance of especially vegetable origin recipes were affected more from mineral oils in a negative way compared to animal-based recipes.
- It was measured that, with the addition of mineral oils that cause a decrease in the amount of foam, from viscosity low mineral oil to viscosity high mineral oil in correlation.
- It was measured that mineral oils with different specs make vegetable-derived fatty acid soaps harder but animal oil-based soaps softer.
- As a result of hardness increase the pellet % of palm soap had a decrease and as a result of softness animal oil-based soaps had an increase at pellet percentage.

In conclusion, these findings have shown that %1 of mineral oil 3 adding has decreased foam volume 40%. In the future, Mineral oil 3 can be considered as a defoaming agent for the soap-based detergent industry.

REFERENCES

1. TSE Sabun Türk Standardı , [cited 2018 Nov 3], Available from: <https://intweb.tse.org.tr/standard/standard/Standard.aspx?081118051115108051104119110104055047105102120088111043113104073088066122074112099075071049107075>
2. Spitz L. Soap Manufacturing technology. London, United Kingdom Academic Press and AOCS Press, Second edition; 2018.
3. Schumann K., Siekmann K. Soaps. Ullman's Encyclopedia of Industrial Chemistry. 1993, A(249) : 247-266.
4. O'Connor S., Rudkowska I., Chapter Two - Dietary Fatty Acids and the Metabolic Syndrome: A Personalized Nutrition Approach. Advances in Food and Nutrition Research. 2019, 87, 43-146.
5. Menaa F., Bouzid Menaa B., Kahn B.A., Menaa A., Chapter 2 - Trans Fats and Risks of Cardiovascular Diseases: Facts or Artifacts. Handbook of Lipids in Human Function, 2016, 21-38.
6. Sabun ve Deterjan Endüstrileri, Bölüm II, 2019. Available from: http://webcache.googleusercontent.com/search?q=cache:sqBvxybA0NQJ:content.lms.sabis.sakarya.edu.tr/Uploads/65467/49523/b%25C3%25B6%25C3%25BCm-%25C4%25B1%25C4%25B1_sabun_ve_deterjan_k%25C4%25B1sa.doc+&cd=1&hl=tr&ct=clnk&gl=tr
7. Hall N., Implications of Soap Structure for Formulation and User Properties. Soap Manufacturing Technology (Second Edition). 2016,1-33 p.
8. Hill M., Moaddel T., Soap Structure and Phase Behavior. Soap Manufacturing Technology. 2016, 35-54 p.
9. Alpar S.R., Organik Sınai Kimya, İstanbul Üniversitesi Kimya Fakültesi Yayınları, İstanbul, 1969.
10. Alpar S.R., Hakdiyen M.İ., Bigat T. Sınai Kimya Analiz Metodları, İstanbul Üniversitesi Kimya Fakültesi Yayınları, İstanbul, 1971.
11. Bektaşoğlu S.Y. İğeme Ürün Profili. İğeme, 1995, 4, 1-20 p.
12. DPT. Kimya Sanayinin Genel Değerlendirilmesi ve Yatırım Alanları Özel İhtisas Alt Komisyon Raporu, Devlet Planlama Teşkilatı, 1991.
13. Koç, N., Köpük ve Köpürme prensipleri, Available from: http://www.kmo.org.tr/resimler/ekler/de0e671163cd540_ek.pdf?dergi=68
14. Douguet M., Picard C., Savary G., Merlaud F., Loubat-Bouleuc F., Grisel M. Spreading properties of cosmetic emollients: Use of synthetic skinsurface to elucidate structural effect. Colloids and Surfaces B: Biointerfaces , 2017, 154, 307-314 p.
15. The Editors of Encyclopaedia Britannica, Mineral oil [Internet]. Encyclopædia Britannica Encyclopædia Britannica inc., 2019 [cited 2019 Nov 27]. Available from: <https://www.britannica.com/technology/mineral-oil>
16. Prof. Dr.Alexander Ya. Malkin, Prof. Dr.Avraam I Isayev, Applications of Rheology, Rheology Concepts, Methods, and Applications (Second Edition), 2012. Chapter 6, 365-420 p. Available from: <https://doi.org/10.1016/B978-1-895198-49-2.50011-6>
17. Mineral oil [Internet]. 2020 ChemicalSafetyFacts.org. [cited 2019 Nov 27]. Available from: <https://www.chemicalsafetyfacts.org/mineral-oil/>
18. Cosmetics - CosIng, Ingredient: PARAFFINUM LIQUIDUM [Internet], European Commission, Internal Market, Industry, Entrepreneurship and SMEs, Sectors, Cosmetics, CosIng, [cited 2019 Nov 27]. Available from: https://ec.europa.eu/growth/tools-databases/cosing/index.cfm?fuseaction=search.details_v2&id=35850
19. Taherian R., The Theory of Electrical Conductivity. Electrical Conductivity in Polymer-Based Composites. Experiments, Modelling, and Applications, Plastics Design Library. 2019, 1-18 p.



Biosorption Studies of Mushrooms for Two Typical Dyes

Ayfer YILDIRIM^{1*}  , Hilal ACAY²  

¹Vocational Higher School of Health Services, Mardin Artuklu University, Mardin, Turkey

²Department of Nutrition and Dietetics, Faculty of Health, Mardin Artuklu University, Mardin, Turkey

Abstract: This study investigated the adsorption behaviour of two cationic dyes, methylene blue (MB) and malachite green (MG) onto *Pleurotus ostreatus*, *Armillaria tabescens*, and *Morchella conica* mushrooms. The effects of contact time, initial dye concentration, and solution pH (3-11) were also determined. The adsorption on all mushrooms attained equilibrium within 120 min for both MB and MG. To evaluate the experimental kinetics data, the pseudo-first-order, pseudo-second-order, and intraparticle diffusion kinetics equations were utilised. The pseudo-first-order kinetic model demonstrated a good fit with all adsorption kinetics. The Langmuir and Freundlich isotherm models were used to analyse the mechanism of the adsorption isotherm. The adsorption equilibrium isotherm was in a good agreement with the Freundlich model. Thermodynamic parameters such as ΔH enthalpy variation, ΔS entropy variation, and ΔG free Gibbs energy variation were calculated at 303-323 K. The results suggested that the *Pleurotus ostreatus* mushroom was the most suitable adsorbent for both cationic dyes' removal.

Keywords: Mushroom, biosorption, methylene blue, malachite green, thermodynamic parameters.

Submitted: June 21, 2019. **Accepted:** January 19, 2020.

Cite this: Yildirim A, Acay H. Biosorption Studies of Mushrooms for Two Typical Dyes. JOTCSA. 2020; 7(1): 295-306.

DOI: <https://doi.org/10.18596/jotcsa.581007>.

***Corresponding author. E-mail:** ayferyildirim@artuklu.edu.tr. **Tel:** +90 482 213 4002/7261

INTRODUCTION

Dyes that are used in the food, textiles, paper, plastics, cosmetics, pharmaceuticals, and other industries generally have carcinogenic, mutagenic, and teratogenic properties. This is why they can cause serious environmental problems (1,2).

Among the techniques used to remove dye molecules from wastewater, adsorption has been recognised as the most effective one as it is proven to be practical and low-cost and have high efficiency (3). However, it has been reported that most sufficient adsorbents such as activated carbon are costly in overcoming the pollution problems of dyes. Thus, the high cost of commercial adsorbents has encouraged researchers to investigate non-toxic, low-price, biodegradable, and environment-friendly alternative biosorbent materials (4). In general, these materials include natural biosorbents derived from waste materials from industries and agriculture. White rot fungi are the most commonly

used organisms in biological treatment studies in the field of waste and environmental biotechnology (5). Among them, the Basidiomycetes group takes a great part in the organic compound oxidation of very different molecular structures with various enzymes synthesised mainly by the laccase enzyme, which increases because of intensive industrial activity and environmental annihilation and pollution (6). These mushrooms draw great attention with their properties and have been used in many biotechnological studies. The most commonly used white fungi species include *Phanerochaete chrysosporium*, *Coriolus versicolor*, and *Trametes versicolor* as well as *Funalia trogii*, *Pleurotus ostreatus*, *P. sajor-caju* and *P. eryngii*, (7,8). It has been reported in the studies in the literature that these mushrooms have been widely used all over the world to eliminate the color of textile wastewaters (9-11).

Pleurotus ostreatus (M1) and *Armillaria tabescens* (M2), which are the mushroom species used in the present study, are white-rot fungi and in the

basidiomycetes group while *Morchella conica* (M3), the other species used in this study, is not white-rot fungi and in the ascomycetes group. To the best of our knowledge, no study has been reported on the adsorption behaviours of Methylene blue (MB) and Malachite green (MG), both cationic dyes, by these three edible fungi (M1, M2, and M3). The influence of kinetics, contact time, pH and initial dye concentration on the adsorption capacity was evaluated and discussed. By using the Freundlich and Langmuir isotherms, the equilibrium data were analysed and characteristic parameters were determined.

MATERIALS AND METHODS

Preparation of the biosorbent

The M1, M2 and M3 mushrooms used in this study were obtained from the province of Mardin in Turkey between April-May 2016. The mushrooms were identified according to Phillips (1994) using ecological, macroscopic and microscopic data. The mushrooms were dried at room temperature for four days. The dried mushroom samples were pulverised in a mixer to be used in the experimental studies.

Preparation of the adsorbate

MB was purchased from Merck while MG was purchased from Sigma. The other reagents used were of analytical grade and all solutions were prepared with distilled water.

Characterisation methods

The characterisation of the mushrooms was achieved by differential scanning calorimetry (DSC) measurements that were performed on a TA Instruments DSC250 with a heating rate of 10 °C min⁻¹ under nitrogen atmosphere and Fourier-transform infrared (FTIR) spectra which were recorded on ALPHA Bruker spectrometer with a Platinum-ATR accessory (ZnSe crystal).

Kinetic and equilibrium biosorption studies

1000 mg L⁻¹ of the dyes were prepared in distilled water to obtain stock solutions and, by using the stock solutions, the required concentrations were achieved with dilution. The current pH was adjusted by 0.1 N HCl and 0.1 N NaOH solutions.

To investigate the kinetics of the biosorption ability of the three fungal biosorbents on the MB and MG dyes, batch experiments were carried out typically, using 50 mg biomasses, 50 ml of dye solutions (25-75 mg L⁻¹) in 100 mL glass flask with an agitation speed of 120 rpm (GFL 1083 model thermostatted shaker) at natural pH at 303 K for certain times (30, 60, 90, 120, 150, 180, 240 min). The dyes' concentration in aqueous solution was measured at a max wavelength of 632 (MB) and 617 (MG) nm using PG T80+ Model UV-Visible spectrophotometer.

The concentration retained in the fungal biomasses phase was calculated by the following equation:

$$q = (C_0 - C_e) V / m$$

Where q is the amount of the dye adsorbed per unit weight of the biosorbent (mg g⁻¹), C_0 is the initial concentration of the dye (mg L⁻¹), C_e is the concentration of the dye in solution at equilibrium time (mg L⁻¹), V is the solution volume (L) and m is the weight of the mushrooms (g).

RESULTS AND DISCUSSION

Characterisation of mushrooms

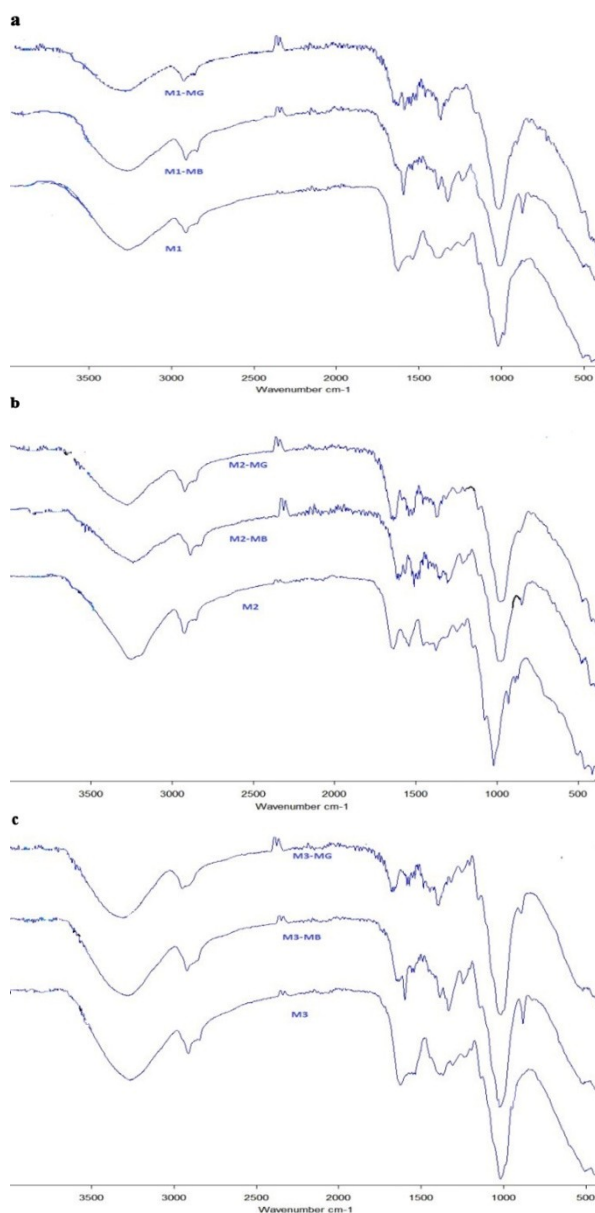


Figure 1. FTIR spectra of M1, M2, M3 and MB, MG loaded a:M1 b:M2 c:M3.

The chemical structures of the mushrooms were confirmed by determining the functional groups in their structures using FTIR spectroscopic analysis (Fig.1a-c.). The FTIR spectra of the mushrooms were found to demonstrate characteristic amine absorption peak around 1600 cm⁻¹. The C-H stretch peak around 2900 cm⁻¹ and broad peaks at 3500-3100 cm⁻¹ are attributed to N-H and OH-O stretching. Besides, the amide I peak (1700-1600

cm^{-1}) is known to provide information about the C=O stretching of amide groups (Fig. 1a-c.) (12,13). According to Figure 1a-c, the peak at 1633.93 cm^{-1} (M1), 1635.93 cm^{-1} (M2) and 1635.65 cm^{-1} (M3) is typical of a C-N and N-H deformations that shifted to 1597.25 cm^{-1} , 1636.48 cm^{-1} and 1633.36 cm^{-1} after MB adsorption and shifted to 1635.45 cm^{-1} , 1646.60 cm^{-1} and 1647.09 cm^{-1} after MG adsorption.

The presence of peaks at 1393.69 cm^{-1} , 1326.11 cm^{-1} (M1), 1374.93 cm^{-1} , 1339.26 cm^{-1} (M2) and 1374.58 cm^{-1} , 1317.73 cm^{-1} (M3) is attributed to COO^- vibration in carboxylates that shifted to 1386.11 cm^{-1} , 1328.78 cm^{-1} ; 1386.99 cm^{-1} , 1338.17 cm^{-1} ; 1386.49 cm^{-1} , 1333.90 cm^{-1} and increased after the adsorption of MB and shifted to 1395.97 cm^{-1} , 1339.18 cm^{-1} ; 1396.16 cm^{-1} , 1339.38 ; 1396.43 cm^{-1} , 1339.60 cm^{-1} after MG adsorption which indicated the presence of MB and MG molecules adsorbed (C=C of the alkyl R-). The peaks observed at 1028.70 cm^{-1} (M1), 1021.50 cm^{-1} (M2) and 1026.94 cm^{-1} (M3) cm^{-1} are attributed to the C-O stretching of alcohol and carboxylic acids that shifted to 1017.76 cm^{-1} , 1006.14 cm^{-1} and 1026.94 cm^{-1} after the adsorption of MB and shifted to 1008.46 cm^{-1} , 1020.71 cm^{-1} and 1012.88 cm^{-1} after the adsorption of MG dye molecules (14-18).

The peak at 899.82 cm^{-1} (M2) shifted to 884.09 cm^{-1} after MB adsorption and shifted to 878.72 cm^{-1} after MG adsorption while new peaks at 883.66 cm^{-1} (M1) and 884.52 cm^{-1} (M3) were formed after the adsorption of MB at 885.14 cm^{-1} (M1), 867.01 cm^{-1} (M3) after the adsorption of MG belongs to the C-H out of plane bending vibration of an aromatic ring (Fig. 1a-c.) (19-21).

The change and shift in the intensity of the characteristic peaks in the hybrid spectra after adsorption could also be evidence of interactions between the functional groups of the mushrooms and dye molecules (22).

Figure 2 shows the DSC measurements which determined the thermal behaviour of the mushrooms. The samples were heated from $-50 \text{ }^\circ\text{C}$ to $250 \text{ }^\circ\text{C}$ at a heating rate of $10 \text{ }^\circ\text{C}/\text{min}$ under an inert atmosphere of nitrogen. There was an endothermic peak of each mushrooms appearing at $92.39 \text{ }^\circ\text{C}$ (M1), 82.56 and $143.80 \text{ }^\circ\text{C}$ (M2) and $92.32 \text{ }^\circ\text{C}$ (M3) while enthalpy was 236.36 J/g (M1), 169.39 and 4.1701 J/g (M2) and 268.51 J/g (M3), respectively. The endothermic process mainly contained hydrogen bond dissociation and water loss. Thus, the endothermic peak of M2 presented the highest value due to slow water loss, increasing thermal stability. This may be caused by the fact that M2 is from a different

group of species and has a different chemical composition and physical properties (such as density) (23,24).

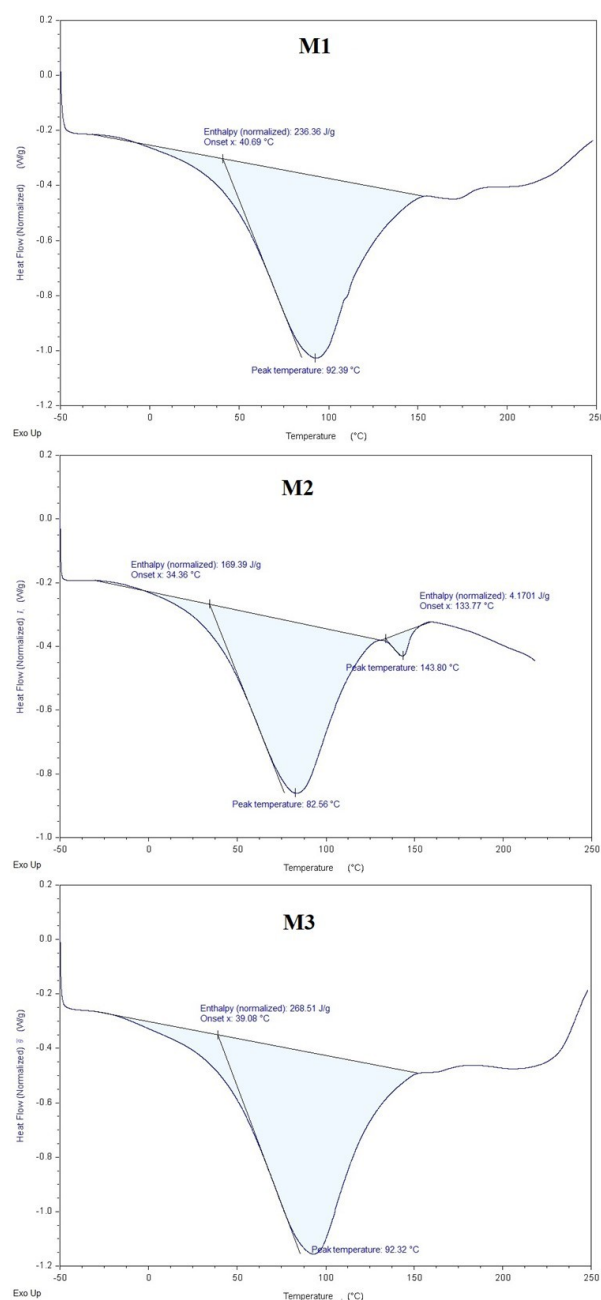


Figure 2. The DSC plots for the mushrooms investigated.

The effect of contact time

The adsorption capacity of two cationic dyes increased with contact time and reached equilibrium about 240 min with a fixed $V=50 \text{ mL}$, $C_0=25, 50, 75 \text{ mg L}^{-1}$, $m=0.01 \text{ g}$ and $r=120 \text{ rpm}$ (Fig.3a,b).

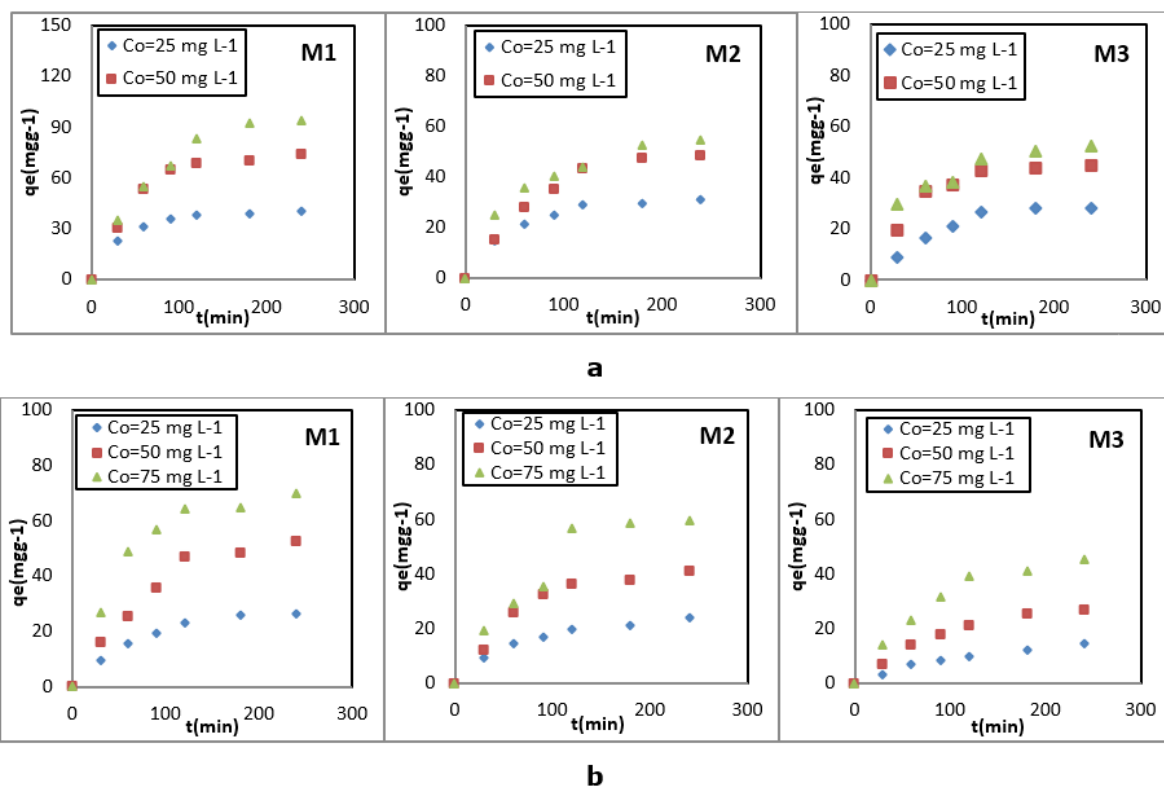


Figure 3. Effect of contact time on the adsorption of **a:** MB, **b:** MG onto M1, M2, M3.

According to Figure 3a-b, the q_e was (for $Co=25, 50, 75 \text{ mg L}^{-1}$) 38.48, 68.77 and 82.81 mg g^{-1} for M1; 28.96, 43.20, 43.90 mg g^{-1} for M2 and 26.63, 36.45, 38.47 mg g^{-1} for M3 with the adsorption of MB while it was 23.10, 47.02, 64.13 mg g^{-1} for M1, 19.80, 36.17, 56.80 mg g^{-1} for M2 and 9.98, 20.92, 39.28 mg g^{-1} for M3 with the adsorption of MG respectively. This result suggests that M1 is a more appropriate adsorbent than M2 and M3 ($M1 > M2 > M3$) for the effective removal of both MB and MG dyes. Besides, Table 4 shows the comparison of the adsorption capacities of MB and MG cationic dyes onto M1, M2, M3 with the biosorbents in the literature.

Effect of pH

pH can significantly affect the adsorption process. To study the influence of pH on the adsorption capacity of the mushrooms, experiments were performed under the pH range from 3 to 11. It was found that the adsorption amount of MB increased with increasing pH from 3 to 11 while MG adsorption increased rapidly at a low pH value (3-6) and increased further in the range of pH from 6 to 12 (Fig. 4a,b). At a low pH (in acidic media), repulsion activities occurred greatly between cationic dyes (MB, MG) ions and positively charged groups on the surface of the mushrooms. On the contrary, with increasing pH, electrostatic attractions between cationic dye ions and negatively charged sites on mushrooms' surface were enhanced both cationic dyes adsorption (25-28). These results indicate that the adsorption of MG is more influenced by pH change than the adsorption of MB on the surface of mushrooms.

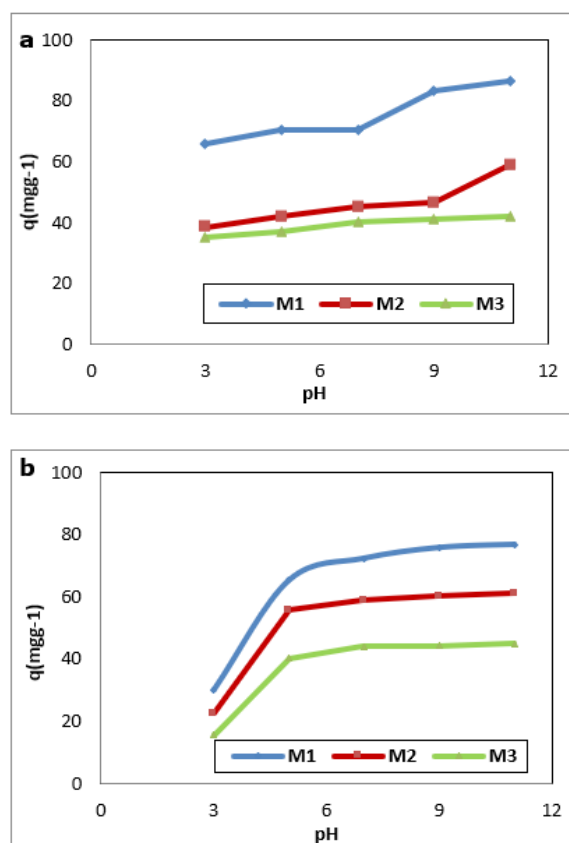


Figure 4. Effect of pH on the adsorption **a:**MB, **b:**MG on the M1, M2, M3.

Evaluation of biosorption kinetics

Two kinetic models, namely pseudo-first-order equation and pseudo-second-order equation were used to investigate the adsorption kinetic

behaviors of MB and MG onto three mushrooms. To estimate the suitability of the models, it is necessary to introduce the correlation coefficient ($R \sim 1$). The higher R^2 value indicates a more applicable model to the kinetics of dye adsorption.

The pseudo-first-order kinetic model is expressed by the equation 1 (29):

$$\log(q_e - q_t) = \log(q_e) - k_1 t \quad (1)$$

where q_e and q_t refer to the amount of MB and MG adsorbed (mg g^{-1}) at equilibrium and at any time t (min), respectively, and k_1 is the equilibrium rate constant of pseudo-first-order (min^{-1}).

k_1 is the equilibrium rate constant of pseudo-first-order model which was calculated by the slope and intercept of the plot of $\log(q_e - q_t)$ versus t (Fig. 5a,b).

The pseudo-second-order model which is expressed by equation 2 (30):

$$t/q_t = 1/k_2 q_e^2 + t/q_e \quad (2)$$

Where, k_2 is the equilibrium rate constant of pseudo-second-order ($\text{g mg}^{-1} \text{min}^{-1}$) which can be determined by the slope and intercept of the plot of t/q_t versus t (Fig. 6a,b).

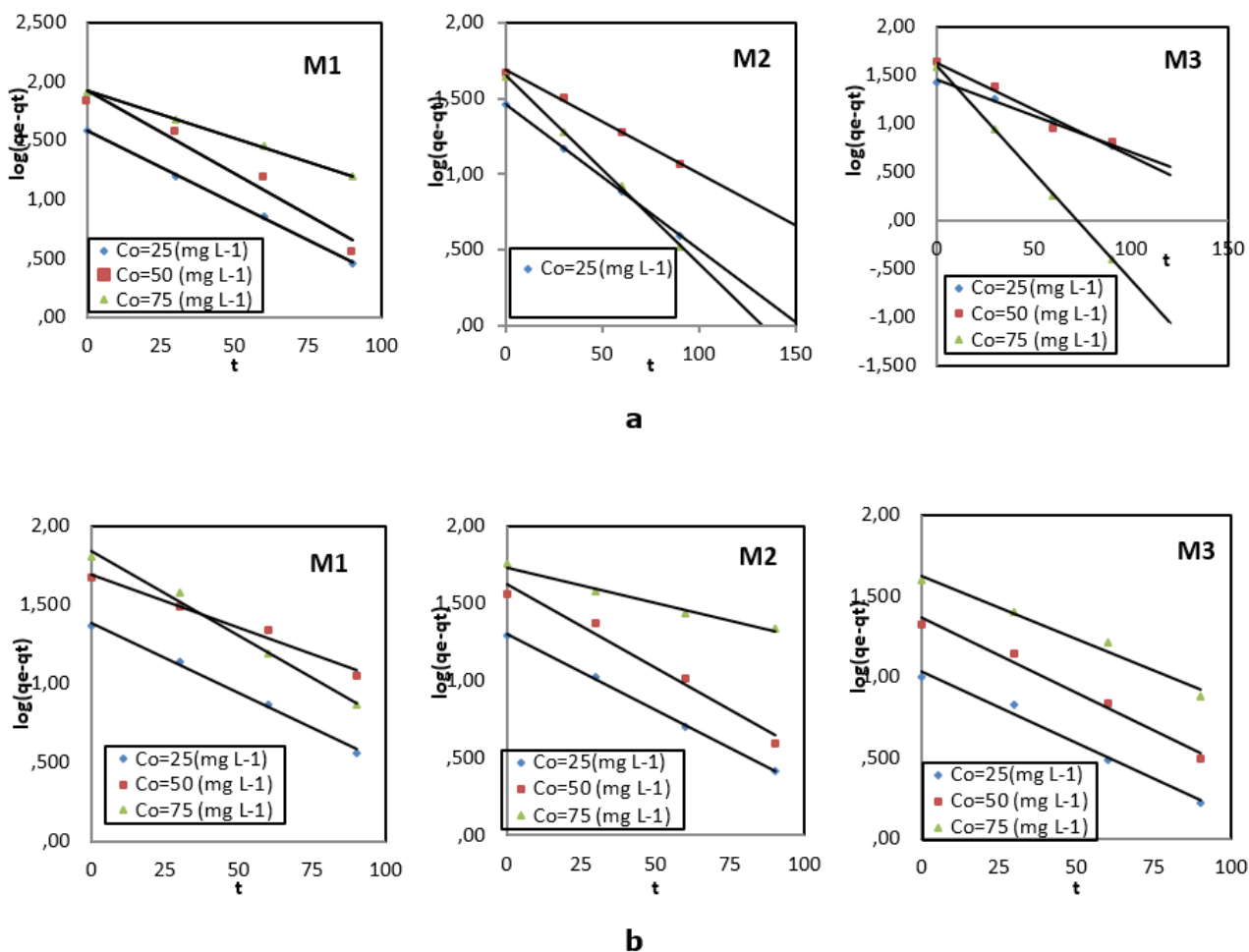


Figure 5. Plots for the pseudo-first-order kinetic model a:MB adsorption, b:MG adsorption.

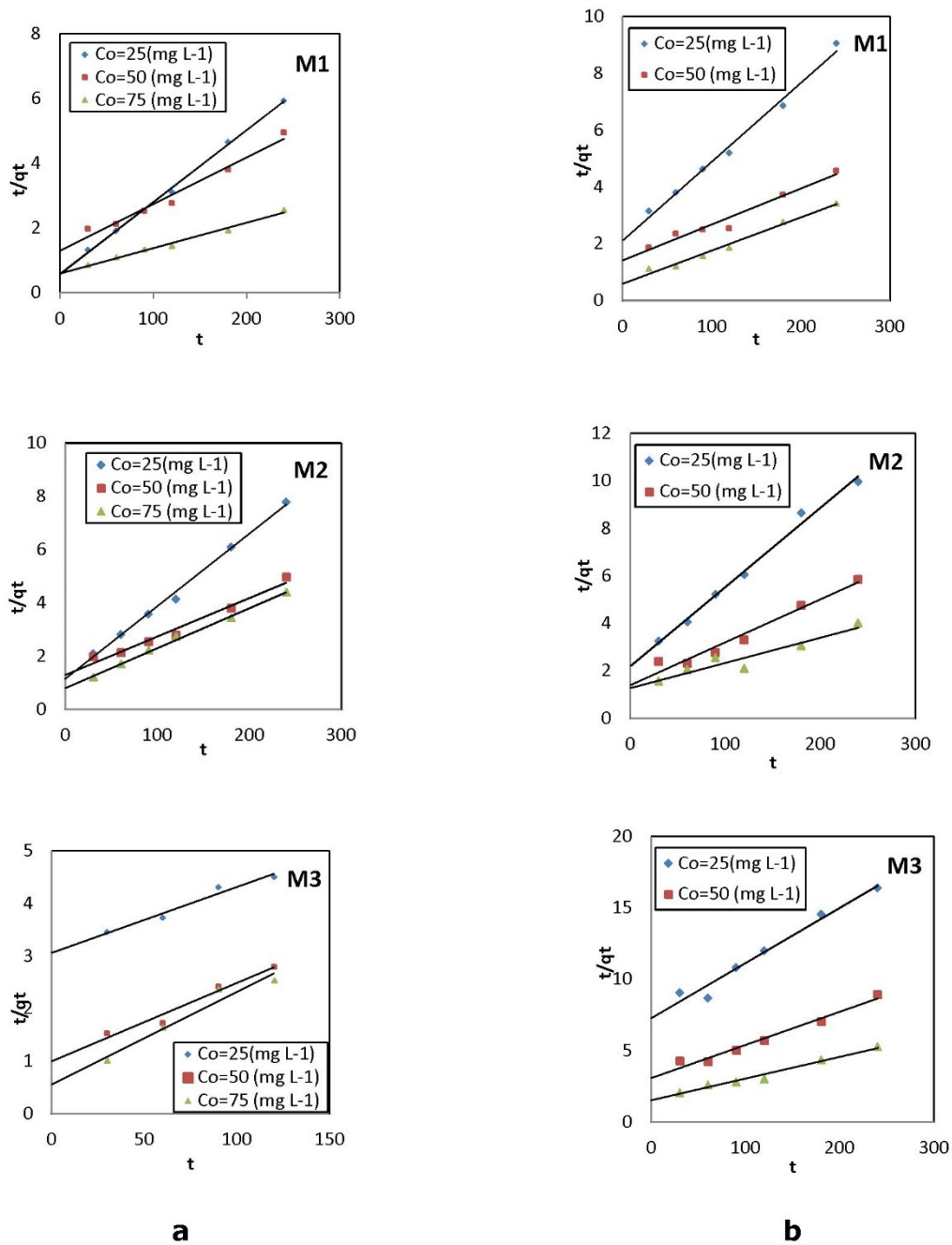


Figure 6. Plots for the pseudo-second-order kinetic model a:MB adsorption b:MG adsorption.

Table 1. Parameters for pseudo-first and second-order kinetic models

Dye	Adsorbent	C ₀ (mg L ⁻¹)	q _{e,exp} (mg g ⁻¹)	Pseudo-first			Pseudo-second		
				q _{e,c} (mg g ⁻¹)	k ₁ (min ⁻¹)	R ²	q _{e,c} (mg g ⁻¹)	k ₂ (g mg ⁻¹ min ⁻¹)	R ²
MB	M1	25	38.48	38.26	0.0286	0.999	44.84	1.7379	0.990
		50	68.77	71.98	0.0334	0.998	54.35	2.1119	0.995
		75	82.81	83.37	0.0184	0.999	126.58	1.6750	0.988
	M2	25	28.96	28.85	0.0221	0.999	36.63	0.8669	0.995
		50	47.05	48.38	0.0292	0.998	54.35	2.1119	0.995
		75	43.90	44.52	0.0286	0.999	66.67	1.2279	0.991
	M3	25	26.63	28.14	0.0170	0.992	80.00	0.3259	0.962
		50	43.66	47.11	0.0269	0.992	71.43	0.9747	0.969
		75	38.47	39.25	0.0511	0.999	42.55	3.7092	0.998
MG	M1	25	23.10	24.13	0.0205	0.996	36.10	0.4684	0.990
		50	47.02	49.07	0.0154	0.981	79.37	0.7039	0.959
		75	64.13	69.25	0.0246	0.991	86.21	16.4069	0.984
	M2	25	19.80	20.22	0.0228	0.999	30.03	0.4523	0.991
		50	36.17	41.94	0.0249	0.984	55.56	0.7068	0.963
		75	56.80	54.31	0.0106	0.985	94.34	0.7780	0.903
	M3	25	9.98	10.79	0.0205	0.987	25.91	0.1367	0.970
		50	20.92	23.26	0.0214	0.982	43.29	0.3201	0.972
		75	39.28	41.64	0.0177	0.980	65.36	0.6468	0.978

Table 1 summarises the suitable results obtained from the two models. It can be seen from the results that the correlation coefficients of the pseudo-first-order model are higher than the pseudo-second-order. Thus, the pseudo-first-order-model was adopted to describe the process. Besides, the experimental adsorption capacities of two dyes onto mushrooms were closer to pseudo-first-order values. This result indicates that the number of free sites was significantly higher than the number of adsorbed dye molecules and reveals that the adsorption between dyes and biosorbents was physisorption which leads to a slow adsorption process. Furthermore, the pseudo-first-order model shows the effect of adsorption at the solid-liquid interface, indicating that the mushrooms had a certain affinity to the dye molecules (31).

Evaluation of biosorption isotherms

Two isotherm models namely, Freundlich and Langmuir, were used to identify the adsorption equilibrium. The equation for the Freundlich and Langmuir models predicated as in the Eqs.3 and 4:

$$\ln q_e = \ln K_F + (1/n_F) \ln C_e \quad (3)$$

$$C_e/q_e = 1/bq_m + C_e/q_m \quad (4)$$

where C_e is the equilibrium concentration (mg L⁻¹), q_e is the adsorption amount (mg g⁻¹) at equilibrium, q_m is the theoretical maximum adsorption capacity (mg g⁻¹) and b is Langmuir constant representing the enthalpy of sorption while K_F and n_F are the Freundlich constants related to the biosorption capacity (mg g⁻¹) and biosorption intensity or heterogeneity of the adsorbent, respectively. According to the Langmuir isotherm model, all the adsorption sites were the same and dynamically equivalent due to the monolayer adsorption. In the case of the Freundlich isotherm model, the adsorption caused by a heterogeneous mechanism. The calculated parameters of both models are summarized in Table 2 and it can be seen that the Freundlich isotherm model is well fitted with the biosorption of all mushrooms onto two dye processes because of their high R² values. Furthermore, the 1/n values which were in a range of 0-1 indicated favourability of the adsorption of the mushrooms onto the MB and MG dyes. The equilibrium isotherms are presented in Figure 7.

Table 2. Parameters for the Langmuir and Freundlich isotherm models

Dye	Mushroom	T (K)	Freundlich			Langmuir		
			K_F	n	R^2	q_m	b	R^2
MB	M1	303	9.34	1.76	0.9888	114.94	0.04	0.9818
		313	7.23	1.86	0.9868	87.72	0.04	0.9454
		323	5.87	1.86	0.9932	69.93	0.04	0.9931
	M2	303	5.71	1.62	0.9919	102.04	0.03	0.9715
		313	9.35	1.27	0.9972	142.86	0.01	0.9788
		323	2.59	1.43	0.9952	86.96	0.02	0.9715
	M3	303	2.75	1.29	0.9929	144.93	0.01	0.9089
		313	1.68	1.21	0.9928	80.65	0.01	0.9721
		323	1.34	1.20	0.9906	53.48	0.02	0.9727
MG	M1	303	2.51	1.25	0.9983	163.93	0.01	0.9614
		313	3.51	1.51	0.9977	69.93	0.06	0.9722
		323	2.48	1.44	0.9942	28.41	0.06	0.9744
	M2	303	2.03	1.21	0.9810	166.67	0.01	0.9799
		313	2.36	1.37	0.9870	100.00	0.01	0.9836
		323	1.86	1.43	0.9929	65.79	0.02	0.9927
	M3	303	1.87	1.23	0.9977	144.93	0.01	0.9727
		313	1.79	1.36	0.9906	77.52	0.01	0.9823
		323	1.50	1.40	0.9974	61.73	0.01	0.9781

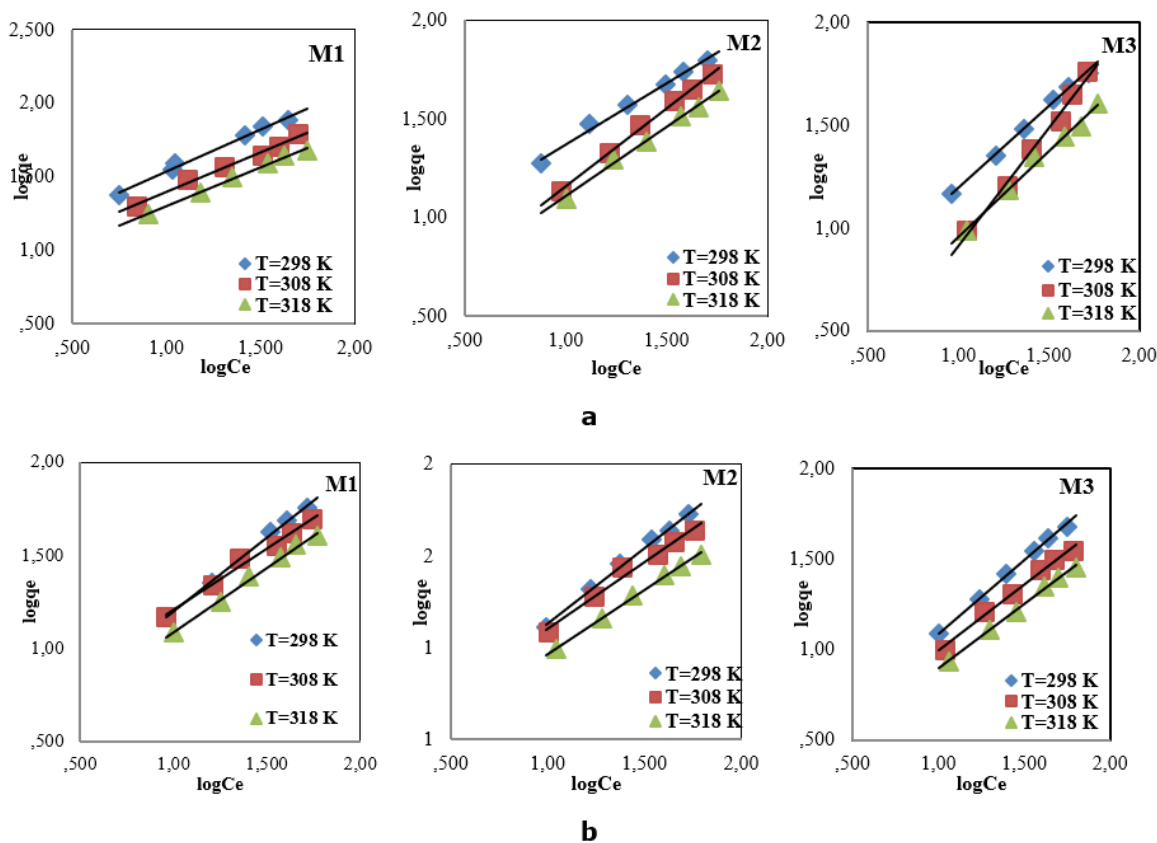


Figure 7. The plot of the Freundlich isotherm model **a:** MB, **b:** MG.

Besides, as shown in Table 2, theoretical adsorption capacity, q_m , decreased with increasing temperature remarking that the adsorptions of M1, M2, M3 on the MB and MG are favorable at lower temperatures. Also, the maximum adsorption capacities (Table 2) of M1, M2, M3 were determined as 82.81, 47.40 and 43.90 mg g^{-1} for

MB and 64.13, 56.80 and 39.28 mg g^{-1} for MG adsorption at 303 K, respectively. Similarly, in the study of Yan and Wang (2013), the q_m was found as 63.5 mg g^{-1} for the adsorption of methylene blue by the spent mushroom substrate (32).

Thermodynamics of biosorption

To investigate the nature of the biosorption process of both cationic dyes onto M1, M2, M3, thermodynamic studies were applied. In this study, the thermodynamic equilibrium constant K_0 for the biosorption process was carried out by plotting $\ln(Q_e/C_e)$ versus Q_e in the temperature range of 303–323 K. Besides, thermodynamic parameters such as ΔH^0 enthalpy change and ΔS^0 entropy change were calculated from Eq.5 that was based on the slope and intercept of the Van't Hoff plots ($\ln K_0$ vs $1/T$, not shown) and the values of ΔG^0 Gibbs free energy change was calculated using Eq.6 (33):

$$\ln K = \Delta S^0/R - \Delta H^0/R (1/T) \quad (5)$$

$$\Delta G^0 = -RT \ln K_0 \quad (6)$$

where K_0 is the equilibrium constant, T is the solution temperature (K) and R is the gas constant ($8.314 \text{ J mol}^{-1} \text{ K}^{-1}$).

The related parameters are presented in Table 3. As can be seen from the table, the negative values of ΔG^0 show that the adsorption of two cationic dyes onto the mushrooms is spontaneous and feasible. The negative value of change in enthalpy (ΔH^0) indicates that the adsorption was an exothermic process. Since all values of ΔH^0 are smaller than 40 kJ/mol, the adsorption of MB and MG onto M1, M2 and M3 was a physisorption process. Furthermore, the positive value of change in entropy (ΔS^0) indicates the increasing randomness while negative value (MG adsorption of M2, M3) proves that the randomness of the solid/solution interface decreased during the adsorption process

Table 3. Thermodynamic parameters for MB, MG dyes on M1, M2, M3.

Dye	Mushroom	T (K)	$\Delta G(\text{kJ/mol})$	$\Delta H(\text{kJ/mol})$	$\Delta S(\text{kJ/molK})$
MB	M1	303	-24.82	-23.16	3.49
		313	-22.97		
		323	-24.97		
	M2	303	-24.75	-8.88	54.32
		313	-27.13		
		323	-25.76		
	M3	303	-26.57	-16.04	36.2
		313	-28.31		
		323	-27.24		
MG	M1	303	-24.57	-0.5	79.47
		313	-25.38		
		323	-26.16		
	M2	303	-26.85	-39.21	-60.01
		313	-25.67		
		323	-25.68		
	M3	303	-26.48	-38.12	-47.15
		313	-25.40		
		323	-25.53		

Table 4. Comparison of adsorption capacity of MB, MG dyes on M1, M2, M3 with other biosorbents.

Adsorbent	dye	Adsorption capacity (mg g^{-1})	Reference
Activated carbon	MG	57.03	(34)
<i>Luffa aegyptica peel</i>	MG	70.22	(35)
<i>Pleurotus ostreatus</i>	MG	32.35	(36)
<i>Trichoderma viride</i>	MB	201.50	(37)
<i>Carica papaya wood</i>	MG	52.63	(38)
	MB	32.25	
<i>Phellinus igniarius fungi</i>	MB	232.21	(39)
<i>Aspergillus fumigatus</i>	MB	125.07	(40)
<i>Corynebacterium glutamicum</i>	MB	207.30	(41)
M1 M2 M3	MB	82.81	This study
		43.90	
		38.47	
M1 M2 M3	MG	64.13	This study
		56.80	
		39.28	

CONCLUSIONS

In the present study, the M1, M2 and M3 mushrooms were used as adsorbents for the investigation of MB and MG adsorption. The maximum adsorption capacity of M1, M2, M3 was found as 82.81, 43.90 and 38.47 mg g^{-1} for the MB dye and 64.13, 56.80 and 39.28 mg g^{-1} for the MG dye, respectively. The adsorption capacity of both dyes was found to increase with increasing pH from 3 to 11. The kinetic data were well fitted to pseudo-first-order. The isotherm data were in good agreement with the Freundlich isotherm model. All the results showed that the adsorption was

exothermic. The studies in the literature also support the results of the present study by stating that the adsorption of MB and MG cationic dyes onto mushrooms is quite convenient.

REFERENCES

1. Wu J, Zhang T, Chen C, Feng L, Su X, Zhou L, Chen Y, Xia A, Wang X. Spent substrate of *Ganoderma lucidum* as a new bio-adsorbent for adsorption of three typical dye. *Bioresource Technology*. 2018; 266: 134–8.
2. Gao Y, Deng SQ, Jin X, Cai SL, Zheng SR, Zhang WG. The construction of amorphous metal-organic

- cage-based solid for rapid dye adsorption and time-dependent dye separation from water. *Chemical Engineering Journal*. 2019; 357: 129–39.
3. Molla A, Li Y, Mandal B, Gu Kang S, Hur SH, Chung JS. Selective adsorption of organic dyes on graphene oxide: Theoretical and experimental analysis. *Applied Surface Science*. 2019; 464: 170–7.
 4. Wang X, Jiang C, Hou B, Wang Y, Hao C, Wu JX. Carbon composite lignin-based adsorbents for the adsorption of dyes. *Chemosphere* 20. 2018; 6: 587-96.
 5. Yeşilada Ö. Decolorization of Crystal Violet by Fungi, *World Journal of Microbiology and Biotechnology*. 1995; 11: 601-2.
 6. Kunamneni A, Ghazi I, Camarero S, Ballesteros A, Plou FJ, Alcalde M. Decolorization of synthetic dyes by laccase immobilized on epoxyactivated carriers. *Process Biochemistry*. 2008; 43(2): 169-78.
 7. Wesenberg D, Buchon F, Agathos SN. Degradation of Dye Containing Textile Effluent by Agaric White - Rot Fungus *Clitocybula dusenii*. *Biotechnology Letters*. 2002; 24: 989-93.
 8. Stainer RY, Adelberg EA, Ingraham J. *The Microbial World* Prentice Hall. Inc. Englewood Cliffs. New Jersey. 1976; 105-18.
 9. Jaspers CJ, Penninck MJ. Adsorption Effects On the Decolorization of a Craftblach Plant Effluent by *Phanerochaete chrysosporium*. *Biotechnology Letters*. 1996; 11(18): 1257-60.
 10. Couto SR, Ravela I, Munos MR, Sanroman A. Ligninolytic Enzyme Production and The Ability of Decolourisation of Poly R-478 in Packed Bed Bioreactors by *Phanerochaete chrysosporium*. *Bioprocess Engineering*. 2000; 23: 287-93.
 11. Wang Y, Yu J. Adsorption and Degradation of Synthetic Dyes on the Mycelium of *Trametes versicolor*. *Water Science Technology*. 1998; 4-5(38): 233-8.
 12. Poverenov E, Arnon-Rips H, Zaitsev Y, Bar V, Danay O, Horev B, Bilbao-Sainz C, McHugh T, Rodo V. Potential of chitosan from mushroom waste to enhance quality and storability of fresh-cut melons. *Food Chemistry*. 2018; 268: 233–41.
 13. Kurt A, Gençlelep H. Enrichment of meat emulsion with mushroom (*Agaricus bisporus*) powder: Impact on rheological and structural characteristics. *Journal of Food Engineering*. 2018; 237: 128–36.
 14. Sewu DD, Boakye P, Jung H, Woo SH. Synergistic dye adsorption by biochar from co-pyrolysis of spent mushroom substrate and *Saccharina japonica*. *Bioresource Technology*. 2017; 244: 1142–9.
 15. Kariuki Z, Kiptoo J, Onyanch D. Biosorption studies of lead and copper using rogers mushroom biomass '*Lepiota hystrix*'. *South african journal of chemical engineering*. 2017; 23: 62-70.
 16. Kamasonlian S, Balomajumder C, Chand S, Suresh S. Biosorption of Cd(II) and As(III) ions from aqueous solution by tea waste biomass. *Afr. J. Environ. Sci. Technol*. 2011; 5(1):1-7.
 17. Negm NA, Wahed MGAE, Hassan ARA, Kana MTHA. Feasibility of metal adsorption using brown algae and fungi: Effect of biosorbents structure on adsorption isotherm and kinetics *Journal of Molecular Liquids*. 2018; 264: 292–305.
 18. Auta M, Hameed BH. Chitosan-clay composite as highly effective and low cost adsorbent for batch and fixed-bed adsorption of methylene blue. *Chemical Engineering Journal*. 2014; 237: 352-61.
 19. Karadirek Ş, Okay H. Statistical modeling of activated carbon production from spent mushroom compost. *Journal of Industrial and Engineering Chemistry*. 2018; 63: 340–7.
 20. Hu S, Hsieh Y. Preparation of Activated Carbon and Silica Particles from Rice Straw. *ACS Sustain, Chem. Eng*. 2014; 2(4): 726.
 21. Mahmoud ME, Nabil GM, El-Mallah NM, Bassiouny HI, Kumar S, Abdel-Fattah TM. Kinetics, isotherm, and thermodynamic studies of the adsorption of reactive red 195 A dye from water by modified Switchgrass Biochar adsorbent. *J. Ind. Eng. Chem.* 2016; (37) 156. <https://doi.org/10.1016/j.jiec.2016.03.020>.
 22. Budnyak TM, Aminzadeh S, Pylypchuk IV, Sternik D, Tertykh VA, Lindström ME, Sevastyanova O. Methylene Blue dye sorption by hybrid materials from technical lignins. *Journal of Environmental Chemical Engineering*. 2018; 6: 4997–5007.
 23. Zahira A, Aslam Z, Kamal MS, Ahmad W, Abbas A, Shawabk RA. Development of novel cross-linked chitosan for the removal of anionic Congo red dye. *Journal of Molecular Liquids*. 2017; 244: 211–8.
 24. Singh S, Gaikwad KK, Lee M, Lee YS. Thermally buffered corrugated packaging for preserving the postharvest freshness of mushrooms (*Agaricus bisporus*). *Journal of Food Engineering*. 2018; 216: 11-9.
 25. Tong DS, Wu CW, Adebajo MO, Jin GC, Yu WH, Ji SF, Zhou CH. Adsorption of methylene blue from aqueous solution onto porous cellulose derived carbon/montmorillonite nanocomposites. *Applied Clay Science*. 2018; 161(1): 256-64.

26. Auta M, Hameed BH. Chitosan–clay composite as highly effective and low-cost adsorbent for batch and fixed-bed adsorption of methylene blue. *Chemical Engineering Journal*. 2014; 237: 352–61.
27. Liu X, Lee DJ. Thermodynamic parameters for adsorption equilibrium of heavy metals and dyes from wastewaters. *Bioresource Technology*. 2014; 160: 24–31.
28. Ishmaturrehmi R, Mustafa I. Methylene blue removal from water using H₂SO₄ crosslinked magnetic chitosan nanocomposite beads. *Microchemical Journal*. 2019; 144: 397–402.
29. Ho YS, McKay G. Review of second-order models for adsorption systems, *Chem. Eng. J.* 1998; 70: 115–24. <https://doi.org/10.1016/j.jhazmat.2005.12.043>.
30. Ho YS, McKay G. Pseudo-second order model for sorption processes, *Process Biochem.* 1999; 34: 451–65, [https://doi.org/10.1016/S0032-9592\(98\)00112-5](https://doi.org/10.1016/S0032-9592(98)00112-5).
31. Ai T, Jianga X, Liu Q, Lv L, Wu H. Daptomycin adsorption on magnetic ultra-fine wood-based biochars from water: Kinetics, isotherms, and mechanism studies. *Bioresource Technology*. 2019; 273: 8–15.
32. Yan T, Wang L. Adsorptive Removal of Methylene blue from Aqueous Solution by spent mushroom substrate: Equilibrium, Kinetics, and Thermodynamics. *BioResources*. 2013; 8(3): 4722-34.
33. Wong S, Tumari HH, Ngadi N, Mohamed NB, Hassan O, Mat R, Amin NAS. Adsorption of anionic dyes on spent tea leaves modified with polyethyleneimine (PEI-STL). *Journal of Cleaner Production*. 2019; 206: 394-406.
34. Rahman IA, Saad B, Shaidan, Sya Rizal E S . Adsorption characteristics of malachite green on activated carbon derived from rice husks produced by chemical–thermal process. *Bioresource Technology*. 2005; 96(14):1578-83.
35. Mashkooor F, Nasar A. Preparation, characterization and adsorption studies of the chemically modified *Luffa aegyptiaca* peel as a potential adsorbent for the removal of malachite green from aqueous solution. *Journal of Molecular Liquids*. 2019; 274:315–27.
36. Chen Z, Deng H, Chen C, Yang Y, Xu H. Biosorption of malachite green from aqueous solutions by *Pleurotus ostreatus* using Taguchi method. *Journal of Environmental Health Science & Engineering*. 2014; 12: 63.
37. Saeed A, Iqbal M, Zafar S I. Immobilization of *Trichoderma viride* for enhanced methylene blue biosorption: Batch and column studies. *Journal of Hazardous Materials*. 2009; 168(1): 406-15.
38. Rangabhashiyam S, Lata S, Balasubramanian P. Biosorption characteristics of methylene blue and malachite green from simulated wastewater onto *Carica papaya* wood biosorbent. *Surfaces and Interfaces*. 2018; 10: 197-215.
39. Maurya N S, Mittal A K, Cornel P, Rother E. Biosorption of dyes using dead macro fungi: Effect of dye structure, ionic strength and pH. *Bioresource Technology*. 2006; (7)3:512-21.
40. Abdallah R, Taha S. Biosorption of methylene blue from aqueous solution by nonviable *Aspergillus fumigatus*. *Chemical Engineering Journal*. 2012; 195–196, 69-76.
41. Vijayaraghavan K, Won S W, Mao J, Yun Y-S. Chemical modification of *Corynebacterium glutamicum* to improve methylene blue biosorption. *Chemical Engineering Journal*. 2008; 145(1): 1-6.



Removal of Pb²⁺ Ions from Aqueous Medium by Using Chitosan-Diatomite Composite: Equilibrium, Kinetic, and Thermodynamic Studies

Zeynep Mine ŞENOL^{1*}  , Selçuk ŞİMŞEK²  

¹Cumhuriyet University, Zara Vocational School, Department of Food Technology, 58140 Sivas, Turkey.

²Cumhuriyet University, Faculty of Science, Department of Chemistry, 58140 Sivas, Turkey.

Abstract: In this study, a novel, low-cost, natural, and highly effective adsorbent, chitosan (Ch) - diatomite (D) composite was synthesized. Ch-D composite was tested as an effective and alternative adsorbent for the removal of Pb²⁺ ions. The Ch-D composite was characterized by FT-IR, SEM-EDX and PZC analyses. The adsorption process of Pb²⁺ ions onto Ch-D as initial lead concentration, solution pH, temperature, contact time and recovery was investigated. From the adsorption process results, it has been observed that the highest removal efficiency is approximately 95% at a contact time of 4-hour, initial Pb²⁺ concentration of 500 mg L⁻¹ and agitation speed of 150 rpm at natural pH 4.0. The maximum Pb²⁺ adsorption capacity from the Langmuir model was found as 0.154 mol kg⁻¹ at 25 °C. Besides, adsorption kinetics was also explained with pseudo-first-order models. Adsorption thermodynamics have shown that Pb²⁺ adsorption onto Ch-D is possible, spontaneous and exothermic. Ch-D composite can become an alternative adsorbent for the treatment of lead ions in the wastewater.

Keywords: Diatomite, chitosan, composite, adsorption, lead.

Submitted: October 18, 2019. **Accepted:** January 19, 2020.

Cite this: Şenol Z, Şimşek S. Removal of Pb²⁺ Ions from Aqueous Medium by Using Chitosan-Diatomite Composite: Equilibrium, Kinetic, and Thermodynamic Studies. JOTCSA. 2020; 7(1): 307-18.

DOI: <https://doi.org/10.18596/jotcsa.634590>.

***Corresponding author.** E-mail: msenol@cumhuriyet.edu.tr.

INTRODUCTION

Industrial wastewater causes heavy metal pollutions in the environment. Nowadays, the removal of heavy metals and pollutions from wastewater is very important (1). Heavy metals and pollutants cause health problems in living organisms. Among these heavy metals, lead is an inhibitor of metabolic poison and enzyme, and it can damage the central nervous system and accumulate in the bones, brain, kidney, and muscles in humans (2). It is very important to remove these heavy metal pollutants from industrial wastewater.

Various methods have been used for removal and recovery of metal industry wastewater such as reverse osmosis, ion exchange, chemical precipitation, adsorption and membrane filtration (3). Among these methods, adsorption is the most preferred method for the removal of heavy metal pollutions from industrial wastewater. Adsorption has the advantages of low cost, high selectivity, environment-friendly, reusable adsorbent design, and easy usability.

Diatomite is a fine sedimentary rock of biogenetic origin with SiO₂.nH₂O formula that is mainly composed of the siliceous skeletal remains of diatoms (4). Diatomite has unique physicochemical

properties, such as highly developed mesoporosity and/or macroporosity, hydrophobia, charge, solubility, ion exchange, acidity and high adsorptive capabilities (5). So, it is used as an effective adsorbent in the removal of heavy metal pollutants and toxic organic pollutants from industrial wastewater (6).

Chitosan is one of the most important natural polymers in nature. It is often used in the structure of many composite materials. Chitosan is used as an effective adsorbent in the removal of heavy metal ions due to their hydrophilicity, biodegradability, non-toxicity, and has hydroxyl and a large number of amino groups (7).

The literature review shows that many studies have been conducted about the removal of lead. A series of recent studies; Fan et al., (8) chitosan/graphene oxide composite, Senol et al., (9) chitosan/vermiculite composite, Sun et al., (10) chitosan/cellulose composite, Gupta et al., (11) chitosan/hydroxyapatite composite, Titom et al., (12) chitosan/clay composite have examined for removal of lead ions by adsorption. However, there is no reported study on the use of chitosan-diatomite composite in the removal of lead ions.

Chitosan can be dissolved under acidic conditions, although it does not have a solubility in alkaline and neutral media. So, this condition limits the use of chitosan as an adsorbent. But it can be possible to use chitosan as an adsorbent with generated composites. A new approach is therefore needed for a useful, cost-effective, water-insoluble, non-toxic, and natural polymer/mineral adsorbent. Within this scope, Ch-D composite was synthesized using chitosan (Ch) biopolymer and diatomite (D) mineral. Thus, the practicality of use for chitosan was provided. The adsorbent properties of Ch-D composite for the removal of lead ion from aqueous medium were investigated. The characterizations of the newly synthesized adsorbent were performed by FTIR, SEM-EDX, and point of zero charge (PZC) analyses. Adsorption properties were investigated for lead ions from aqueous solution. The effect of solution pH, initial Pb^{2+} concentration, temperature, contact time and recovery on adsorption were considered and optimum conditions were determined.

MATERIALS AND METHODS

Chemicals and Devices

In this study, medium molecular weight chitosan (Ch) (Sigma-Aldrich, Germany) was preferred. The natural diatomite was supplied from Akmin Mining (Ankara). $Pb(NO_3)_2$, 4-(2-pyridylazo) resorcinol (PAR) and other chemicals were achieved from Merck (Germany). Double-distilled water used in

all dilutions and experiments. The lead concentration was determined using a UV-vis spectrophotometer (SHIMADZU, 160 A model, Japan).

Characterization techniques

Ch, D, and Ch-D were characterized by FT-IR and SEM-EDX analysis. FT-IR spectra of Ch-D and its components were recorded in a Perkin Elmer 400 spectrometer. SEM images and EDX compositional data of Ch-D composite and its components were obtained with a Leo 440 Computer Controlled Digital System.

Synthesis of Ch-D Composite

To synthesize about 4 g of Ch-D composite, 2 g of chitosan and 2 g of diatomite were mixed in a 5% (v/v) acetic acid solution for 2 hours until a homogeneous mixture was obtained. Then a solution of epichlorohydrin (ECH) was added and stirred. The mixture was then added dropwise to the sodium tripolyphosphate (NaTPP) solution to form composite beads. The resulting beads were washed with double-distilled water until the conductivity of the wash water reached approximately the conductivity of double-distilled water. The samples dried in the oven at 40 °C were ground and stored in closed containers for later use.

UV-Vis spectrophotometric method

The concentration of Pb^{2+} ions was determined by measuring the UV-Vis spectrophotometric method of the complex formed by PAR (13). PAR was used as a complex-forming reagent for the determination of Pb^{2+} in the supernatants. A solution of 3.5×10^{-3} mol L^{-1} of PAR in 0.7 mol L^{-1} of Tris/HCl at pH 8–9 was prepared. A 50 μL fraction of supernatant was added onto 3 mL of the reagent and the absorbance of the formed metal complex was measured at $\lambda = 518.5$ nm for Pb^{2+} .

Batch adsorption procedure

The adsorption of Pb^{2+} ions onto Ch-D composite adsorbent was investigated in batch adsorption experiments. The stock solution of Pb^{2+} (1000 mg L^{-1}) was prepared using double-distilled water. The adsorbent-solution systems were equilibrated with 500 mg L^{-1} (2.4×10^{-3} mol L^{-1}) Pb^{2+} concentration at natural pH 4.0, for 24 h at 25 °C in 10 mL polypropylene tubes containing 10 mL of Pb^{2+} solution. Pb^{2+} ion concentration was determined by the absorbance measurement. The batch adsorption conditions are given in Table 1. Adsorption% and Q (mol kg^{-1}) were calculated with Eq. 1 and Eq. 2.

$$\text{Adsorption \%} = \left[\frac{C_i - C_f}{C_i} \right] \times 100 \quad \text{Eq. 1}$$

$$Q = \left[\frac{C_i - C_f}{m} \right] \times V \quad \text{Eq. 2}$$

Where, C_i is the initial concentration (mg L^{-1}), m refers to the adsorbent mass (g), C_f is equilibrium concentration (mg L^{-1}), and V is the solution volume (L).

Table 1. Batch adsorption experiment conditions for Pb^{2+} adsorption onto Ch-D

Experiment	Solution pH	Initial Pb^{2+} conc. (mg L^{-1})	Contact time (min)	Temperature ($^{\circ}\text{C}$)
Effect of pH	1.0-5.0	500	1440	25
Effect of concentration	4.0	50-800	1440	25
Effect of time	4.0	500	2-1440	25
Effect of temperature	4.0	500	1440	5, 25, 40
Desorption	4.0	500	1440	25

Desorption experiments

Desorption studies were performed for adsorbent recovery and re-use in adsorption processes. In this study, dilute 0.1 mol L^{-1} HCl, 0.1 mol L^{-1} NaOH, 0.1 mol L^{-1} HNO_3 and 0.1 mol L^{-1} ethyl alcohol solutions were used for desorption of the Pb^{2+} ions from the surface of the Ch-D. To determine the recovery property of the adsorbent, the experiments were repeated three times with the same adsorbent for the adsorbent/desorption cycle. At the end of each experiment, the solutions were centrifuged at 5000 rpm for 10 minutes to ensure liquid-solid separation and the amount of Pb^{2+} ions in the equilibrium solution was determined by UV-Vis spectrophotometric method. % Desorption was calculated with Eq. 3.

$$\text{Desorption \%} = \frac{Q_{des}}{Q_{ads}} \times 100 \quad \text{Eq. 3}$$

In the equation, Q_{des} is the desorbed amount of adsorbate (mol kg^{-1}), and Q_{ads} is the adsorbed amount of adsorbate (mol kg^{-1}).

Equilibrium isotherm studies

The adsorption isotherms are very useful to describe the interaction between the adsorbate and the adsorbent. The adsorption of Pb^{2+} ions onto Ch-D was modeled using the Langmuir, Freundlich, and Dubinin-Radushkevich (D-R) isotherm models (14, 15). The Langmuir, Freundlich, and Dubinin-Radushkevich (D-R) isotherm equations are expressed below (Eq. 4, Eq. 5 and Eq. 6, respectively).

$$Q = \frac{X_L K_L C_e}{1 + K_L C_e} \quad \text{Eq. 4}$$

$$Q = K_F C_e^n \quad \text{Eq. 5}$$

$$Q_e = Q_{DR} e^{-K_{DR} \varepsilon^2} \quad \text{Eq. 6}$$

where Q (mol kg^{-1}) is the amount of adsorbed metal ions, X_L is the maximum adsorption capacity, K_L is the parameter for Langmuir isotherm and C_e is the equilibrium concentration (mol L^{-1}) and K_F : Freundlich constant, β : adsorbent surface heterogeneity. X_{DR} is a measure of adsorption capacity, K_{DR} is the activity coefficient ($\text{mol}^2 \text{K J}^2$) and ε is the Polanyi potential, R is the ideal gas constant ($8.314 \text{ J mol}^{-1} \text{ K}^{-1}$) and T is the absolute temperature (K). The Polanyi potential (ε) is expressed by Eq. 7:

$$\varepsilon = RT \ln \left(1 + \frac{1}{C_e} \right) \quad \text{Eq. 7}$$

The adsorption energy (E) is expressed by the following Eq. 8:

$$E_{DR} = (2 K_{DR})^{-0.5} \quad \text{Eq. 8}$$

If the adsorption energy is $8 < E < 16 \text{ kJ mol}^{-1}$, the adsorption is physically controlled and $E < 8 \text{ kJ mol}^{-1}$ indicates that the adsorption proceeds physically (16, 17).

Kinetics studies

The three most commonly used kinetics models were used to evaluate the contact time dependence of the adsorption process (18, 19). The adsorption kinetics of Pb^{2+} ions onto Ch-D were described by pseudo-first-order (PFO),

pseudo-second-order (PSO) and intraparticle diffusion (IPD) kinetic models equations (Eq. 9, Eq. 10 and Eq. 11, respectively).

$$Q_t = Q_e [1 - e^{-k_1 t}] \quad \text{Eq. 9}$$

$$Q_t = \frac{t}{\left[\frac{1}{k_2 Q_e^2} \right] + \left[\frac{t}{Q_e} \right]} \quad \text{Eq. 10}$$

$$Q_t = k_i t^{0.5} \quad \text{Eq. 11}$$

where Q_t (mol kg⁻¹) is the lead adsorbed amount at time t (min), Q_e (mol kg⁻¹) is the adsorbed amount at equilibrium, k_1 , k_2 and k_i is the rate constant of the PFO (min⁻¹), the PSO model (mol⁻¹ kg min⁻¹) and the intra-IPD (mol⁻¹ kg min^{-0.5}) model, respectively.

Thermodynamic studies

Thermodynamic parameters are used to explain the effect of the temperature on the adsorption. Enthalpy and entropy (ΔH^0 and ΔS^0) are obtained from $\ln K_D$ against the $1/T$ graph. The slope ($-\Delta H^0/R$) and y -intercept ($\Delta S^0/R$) of the data plotted as $\ln K_D$ against the $1/T$ graph. The free Gibbs energy (ΔG^0) is calculated from Equation 15. ΔH^0 , ΔS^0 , and ΔG^0 were calculated using the following equations:

$$K_D = \frac{Q}{C_e} \quad \text{Eq.12}$$

$$\Delta G = -RT \ln K_D \quad \text{Eq.13}$$

$$\ln K_D = \frac{\Delta S^0}{R} - \frac{\Delta H^0}{RT} \quad \text{Eq.14}$$

$$\Delta G^0 = \Delta H^0 - T \Delta S^0 \quad \text{Eq.15}$$

RESULTS AND DISCUSSION

FT-IR analysis

The FT-IR spectra of the D, Ch and Ch-D composite are given in Figure 1. When the FT-IR spectrum of the diatomite was examined, it is observed that the absorption peak at 1103, 1015 cm⁻¹ showed the -Si-O-Si- vibration, the peak at 913 cm⁻¹ showed the Si-O stretching, the peak at 796 and 694 cm⁻¹ showed the SiO-H vibration, and the peaks at 537 and 469 cm⁻¹ showed the Si-O-Si bonding vibration (20-22). Additionally, the wide peak between the wavelengths of 1640-3600 cm⁻¹ is assigned to the H-O-H and OH groups. In the FT-IR spectra of chitosan, bands between 3290-3350 cm⁻¹ are associated with the OH and NH groups and 2864 cm⁻¹ is observed the characteristic Ch peak. Peaks corresponding to the 1650 and 1575 cm⁻¹ wavenumbers correspond to amide C-O and amide N-H groups, 1070 cm⁻¹ attributed to the C-O bond which are characteristic peaks for Ch (23). When the FT-IR spectrum of Ch-D composite is examined, it is seen that it is different from both spectra. The spectrum of Ch-D composite is observed in the characteristic peaks of both Ch and D.

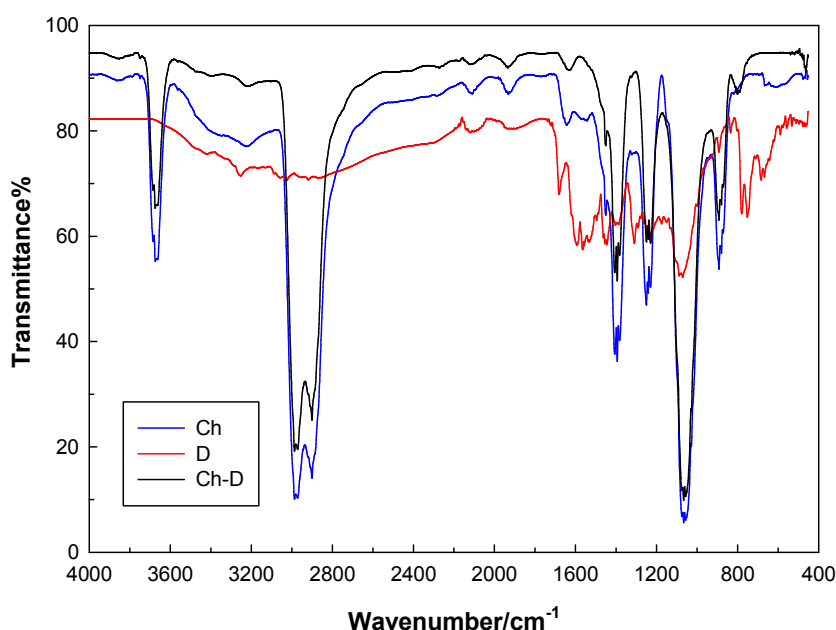


Figure 1. FT-IR spectra of Ch, D, and Ch-D.

When the FT-IR spectrum before and after Pb^{2+} adsorption was examined, peak intensities increased (Figure 2). Although the location of the peaks after Pb^{2+} adsorption did not change, peak

intensity increased after Pb^{2+} adsorption. Changes in FT-IR spectra obtained before/after Pb^{2+} adsorption on Ch-D were considered as evidence for Pb^{2+} adsorption.

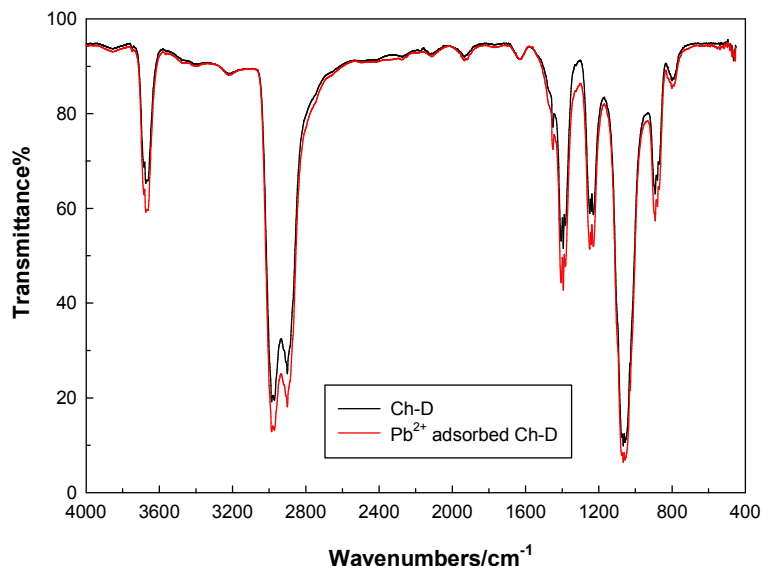


Figure 2. FT-IR spectra before and after adsorption.

SEM-EDX analysis

Microphotographs of Ch, D, and Ch-D are shown in Figure 3. The microphotograph of diatomite shows diatoms that generally have cylindrical, sheet-like shapes, and a porous structure (24). Microphotograph of Ch-D shows a structure having the structure of both Ch and D. EDX results of Ch, D, and Ch-D in Figure 3. EDX techniques show that the Ch mainly consists of C (52.8%), O (36.6%), N(10.6%) the D consists of O (53.7%) and Si

(46.3%). The C, O, Si and N contents of Ch-D are the evidence of the presence of Ch and D.

Scanning electron microphotographs of Ch-D, before and after adsorption were shown in Figure 4. After adsorption, Pb^{2+} ions were coated on the surface of the chitosan–diatomite. Changes in SEM images obtained before/after Pb^{2+} adsorption on Ch-D were considered as evidence for Pb^{2+} adsorption. On the other hand, the Pb content in EDX spectra of Ch-D is evidence of adsorption of Pb^{2+} onto Ch-D.

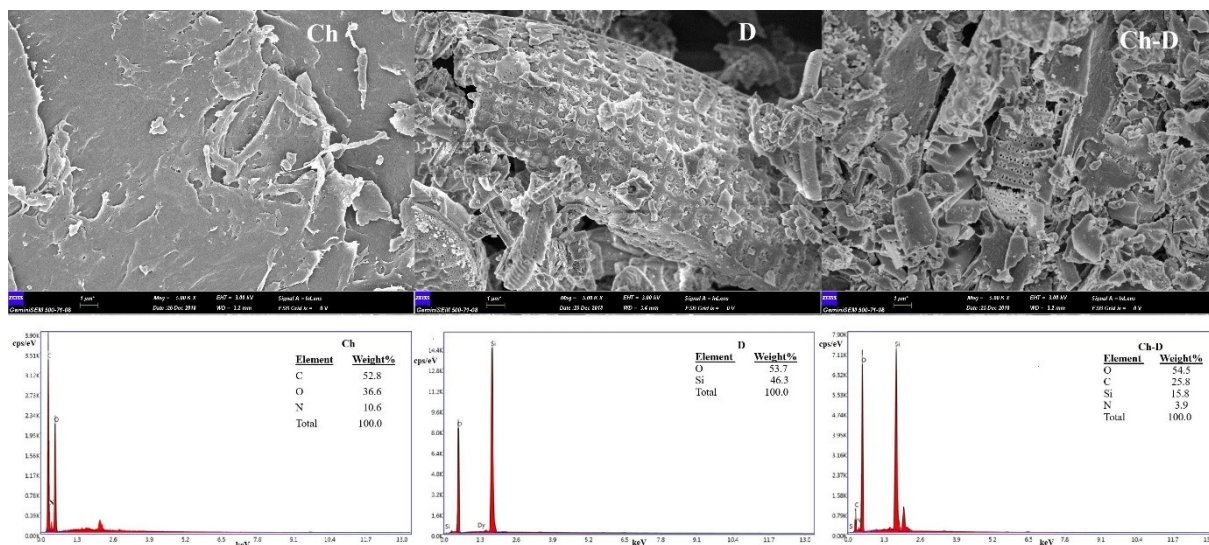


Figure 3. Scanning electron microphotographs of Ch, D, and Ch-D and EDX results of Ch, D, and Ch-D.

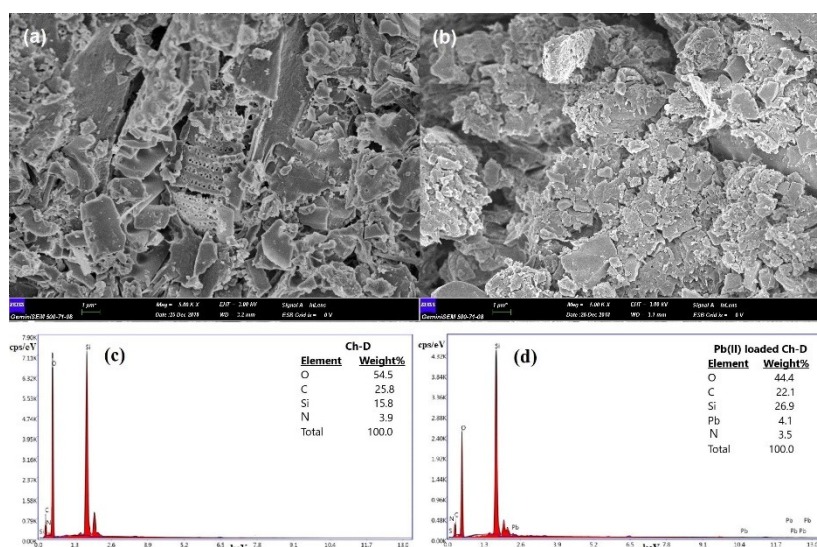


Figure 4. Scanning electron microphotographs of Ch-D (a) and Pb^{2+} adsorbed Ch-D (b) and EDX results of Ch-D (c) and Pb^{2+} loaded Ch-D (d).

Effect of pH

The adsorption mechanism is related to the physicochemical interactions of the species in solution. At high acidic pHs, metal cations and hydrogen ions compete for binding to active sites, resulting in less adsorption of the metal. At high basic pH values, soluble hydroxide complexes of metal ions are formed, so the adsorption is reduced.

To investigate the pH effect, adsorption studies were carried out at different pHs at constant Pb^{2+}

ion concentration and results are presented in Figure 5. According to Figure 5, the percentage of the adsorption rate increased from 5% to 61% with increasing pH values from 1.0 to 4.0, respectively. The maximum adsorption rate was found as 61% at pH 4.0, which was the natural pH of the Pb^{2+} solution and was found to be the pH at which the adsorption was highest. Therefore, all adsorption experiments were performed at the natural pH of the Pb^{2+} ion. Pb^{2+} ions can precipitate at alkaline pHs as hydroxides. So, pHs beyond 5.0 were not studied.

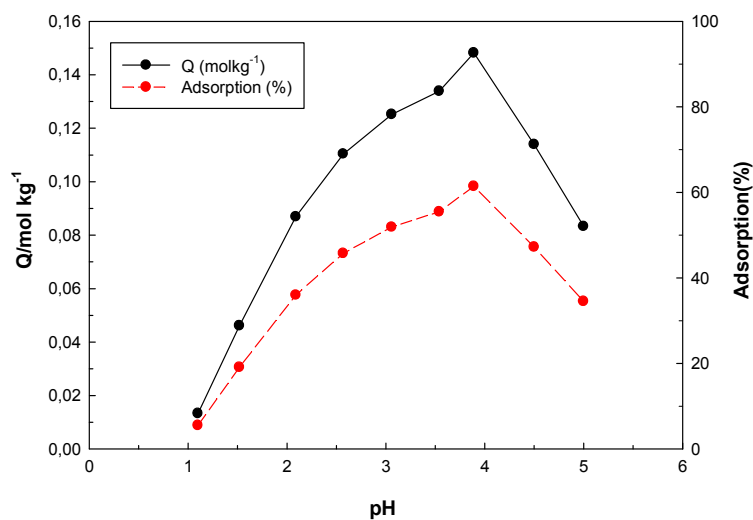


Figure 5. Effect of pH on adsorption of Pb^{2+} onto Ch-D (at 25°C; adsorbent dose:100 mg; C_0 :500 mg L⁻¹).

To determine the point of zero charge (PZC) values of Ch-D composite, 100 mg Ch-D was held in solutions in the pH = 1.0-12.0 range by NaOH and HCl at 25 °C for 24 h and the equilibrium pH was

measured. The results are given in Figure 6. The surface charge of the Ch-D composite adsorbent was found to be positively charged, under pH 4.63 and negatively charged above pH 4.63 (25).

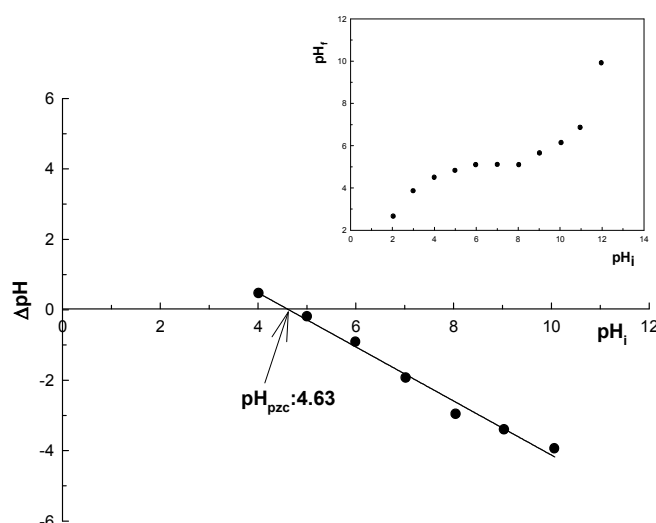


Figure 6. PZC plots of the Ch-D composite.

Adsorption isotherms

The harmony of the Langmuir, Freundlich, and Dubinin-Radushkevich isotherm models was presented in Figure 5 and Table 2, with the parameters used in the isotherms. The maximum adsorption capacity was calculated to be 0.154 mol

kg⁻¹ from the Langmuir isotherm model. Pb^{2+} adsorption onto Ch-D fitted well the Freundlich model. The Freundlich parameter n indicates the degree of heterogeneity of the surface and the E_{DR} value found in the D-R model indicates that the adsorption process is chemical.

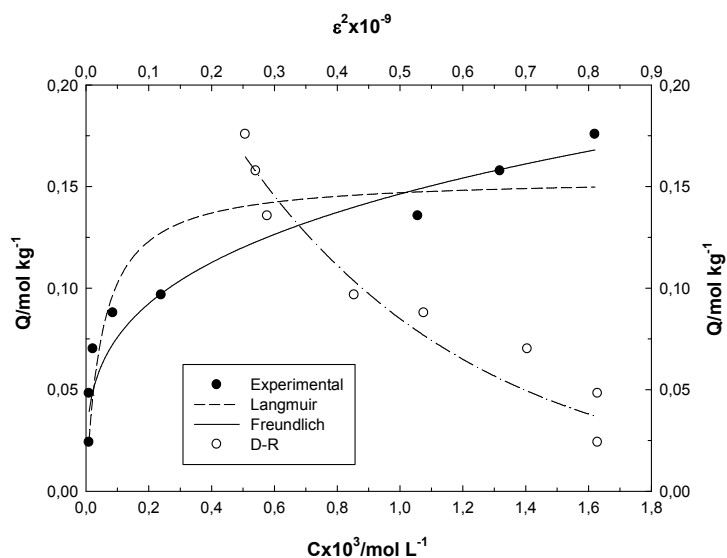


Figure 7. Langmuir, Freundlich, and D-R isotherm plot for the adsorption of Pb^{2+} onto Ch-D (at 25 °C; adsorbent dose: 100 mg; C_0 : 50-800 mg L⁻¹).

Table 2. Adsorption isotherm parameters.

	Langmuir		Freundlich		D-R
$X_L/mol\ kg^{-1}$	0.154	K_f	1.06	X_{DR}	0.326
$K_L/L\ mol^{-1}$	19570	β	0.286	$-K_{DR} \times 10^6$	2.69
R^2	0.882	R^2	0.927	R^2	0.932
				$E/kJ\ mol^{-1}$	13.6

Standard Deviation 0.053 mol kg⁻¹, Standard Error 0.018 mol kg⁻¹

Adsorption kinetics

Adsorption data for kinetics studies were performed in the time range of 2-1440 min. The adsorption kinetics of Pb^{2+} onto Ch-D composite were presented in Figure 8 and Table 3. From the

regression coefficient (R^2) and the harmony of theoretically calculated Q_t and experimental Q_e values, it was concluded that the PFO model was a suitable model for the adsorption kinetics of Pb^{2+} ions on the Ch-D composite adsorbent.

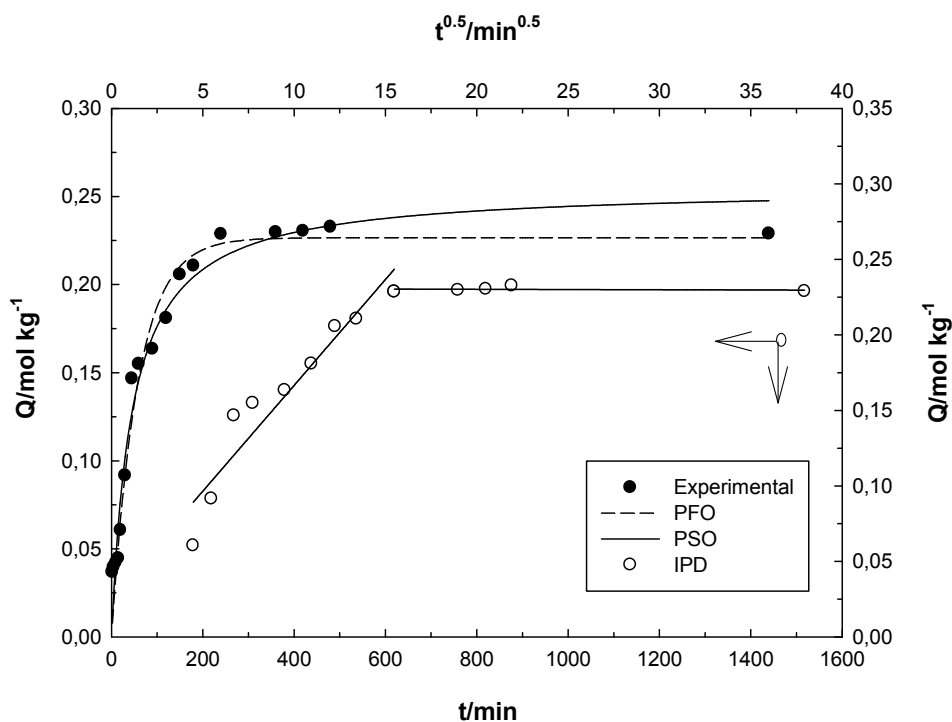


Figure 8. Compatibility of Pb^{2+} adsorption kinetics to PFO, PSO and IPD models (at 25°C; adsorbent dose:300 mg; C_0 :500 mg L⁻¹).

Table 3. Adsorption kinetic parameters.

Pb^{2+}	$(k_1, k_2, k_i) \times 10^3$	R^2	Q_t	Q_e	$H \times 10^3$
PFO	57.5	0.972	0.228	0.227	3.97
PSO	58.1	0.971	0.228	0.313	5.69
IPD	25.7	0.905	-	-	-

Standard Deviation 0.078 mol kg⁻¹, Standard Error 0.019 mol kg⁻¹

Adsorption thermodynamics

To explain the thermodynamic behavior of Pb^{2+} ions adsorption onto the Ch-D composite, it was studied at temperatures of 5 °C, 25 °C, and 40 °C and Figure 9 was obtained. In Figure 9 ($\ln K_D - 1/T$) the values of ΔH^0 and ΔS^0 were calculated from the slope of the graph and the cut-off, respectively.

Adsorption enthalpy was found negative. ΔH^0 was calculated as -11.3 kJ mol⁻¹ showed that the adsorption process was exothermic. ΔS^0 was calculated as 2.29 J mol⁻¹ K⁻¹. The free energy value was found as -12.0 kJ mol⁻¹ at 25 °C. The negative free energy value indicated that spontaneous adsorption was possible.

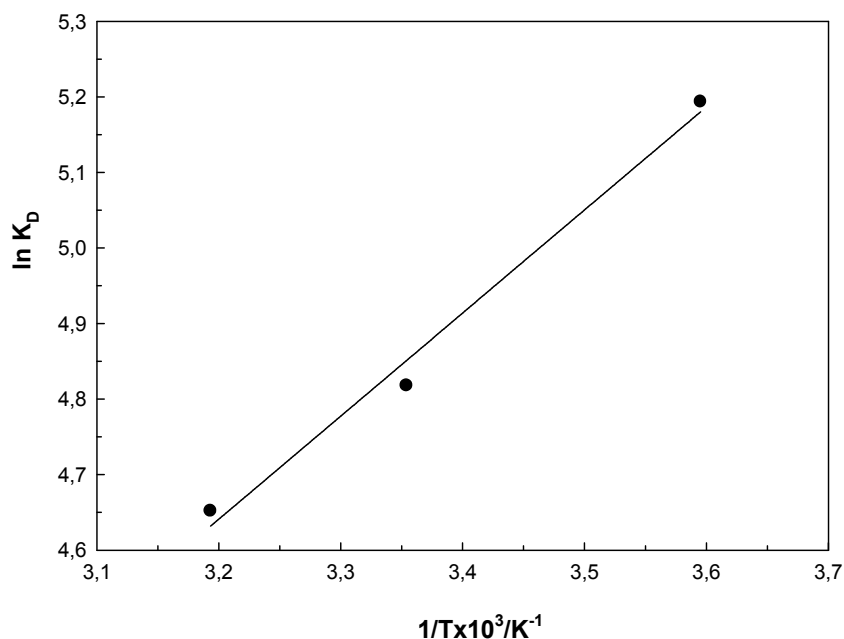


Figure 9. Effect of temperature on the adsorption. (at 5°C, 25°C, 40°C; adsorbent dose:100 mg; C_0 :500 mg L⁻¹)

Desorption

Reusability investigated the desorption ability for Pb²⁺ ions onto Ch-D composite. The Ch-D composite was regenerated using HCl, NaOH, HNO₃, and ethyl alcohol. The obtained Pb²⁺

removal efficiency for three times is plotted in Figure 10. The maximum recovery percentage for Pb²⁺ ions onto Ch-D was achieved with HCl (89%). The minimum recovery percentage for Pb²⁺ ions onto Ch-D was achieved with ethyl alcohol (11%).

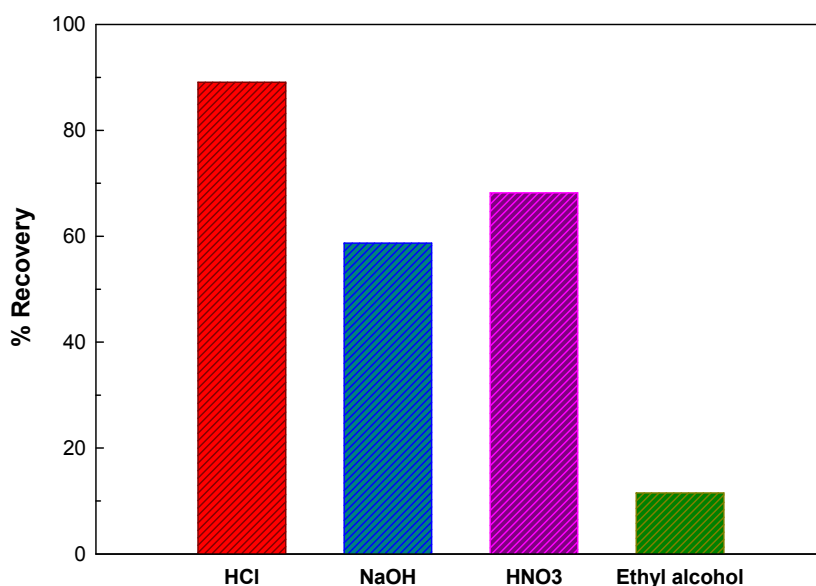


Figure 10. Recovery percents of HCl, NaOH, HNO₃ and ethyl alcohol for the desorption of Pb²⁺ onto Ch-D (at 25°C; adsorbent dose:100 mg; C_0 :500 mg L⁻¹).

Comparison of results with literature

A comparison has been made between the chitosan composites adsorbents reported in the literature for the adsorption Pb^{2+} . The maximum adsorption capacity obtained from the Langmuir model was

used for the comparison of different chitosan composite adsorbents. As can be seen in Table 4, the maximum adsorption capacity of chitosan-diatomite composite adsorbent ($0.154 \text{ mol kg}^{-1}$) was higher than that of various chitosan composite adsorbents.

Table 4. Comparison of Pb^{2+} adsorption on the chitosan-diatomite composite with other chitosan composite adsorbents.

Adsorbent	$X_L/\text{mol kg}^{-1}$	Reference
Chitosan-graphene oxide	0.372	(8)
Chitosan-vermiculite	0.598	(9)
Chitosan-cellulose	0.130	(10)
Chitosan-hydroxyapatite	0.058	(11)
Chitosan-clay	0.156	(12)
Chitosan-sand	0.060	(26)
Chitosan-bentonite	0.382	(27)
Chitosan-diatomite	0.154	(This study)

CONCLUSIONS

In this investigation, Ch-D composite can be used as an effective, alternative adsorbent for the removal of Pb^{2+} ions. Optimal conditions of the study for the adsorption were determined and were selected as pH:4.0, m:100 mg, t:24 h, and T:25 °C. The Freundlich model was found to be the better fit to the experimental data. The maximum adsorption capacity was found to be $0.154 \text{ mol kg}^{-1}$ from the Langmuir isotherm model. Adsorption thermodynamics indicated that the adsorption process was exothermic, possible and spontaneous. Ch-D composite adsorbent had a well adsorption-desorption ability for Pb^{2+} ions. Ch-D composite can use as an effective and alternative adsorbent in the removal of lead pollutants from industrial wastewater.

ACKNOWLEDGMENT

This study was presented as an oral presentation at the 31st National Chemistry Congress.

The present study (Project no: ZARA004) was supported by the Cumhuriyet University Scientific Research Projects Commission. The authors strongly declare that no scientific and/or financial conflicts of interest exist with other people or institutions.

REFERENCES

- Paulino AT, Minasse FAS, Guilherme MR, Reis AV, Muniz EC, Nozaki J. Novel adsorbent based on silk worm chrysalides for removal of heavy metals from wastewaters. *Journal of colloid and interface science* 2006;301(2):479-87.
- Fu F, Wang Q. Removal of heavy metal ions from wastewaters: A review. *Journal of environmental management*. 2011;92(3):407-18.
- Benito Y, Ruiz ML. Reverse osmosis applied to metal finishing wastewater. *Desalination*. 2002; 142(3):229-34.
- Al-Degs Y, Khraisheh MAM, Tutunji MF. Sorption of lead ions on diatomite and manganese oxides modified diatomite. *Water Research*. 2001;35(15):3724-8.
- Deng L, Du P, Yu W, Yuan P, Annabi-Bergaya F, Liu D, Zhou J. Novel hierarchically porous allophane/diatomite nanocomposite for benzene adsorption. *Applied Clay Science*. 2019;168:155-63.
- Şenol ZM, Arslan DS, Şimşek S. Preparation and characterization of a novel diatomite-based composite and investigation of its adsorption properties for uranyl ions. *Journal of Radioanalytical and Nuclear Chemistry*. 2019;321(3):791-803.
- Vakili M, Deng S, Liu D, Li T, Yu, G. Preparation of aminated cross-linked chitosan beads for efficient adsorption of hexavalent chromium. *International journal of biological macromolecules*. 2019;139:352-60.
- Fan L, Luo C, Sun M, Li X, Qiu H. Highly selective adsorption of lead ions by water-dispersible magnetic chitosan/graphene oxide composites. *Colloids and Surfaces B: Biointerfaces*. 2013;103:523-9.

9. Senol ZM. Kitosan-Vermikülit Kompoziti Kullanılarak Sulu Çözeltilerden Etkin Kurşun Giderimi: Denge, Kinetik ve Termodinamik Çalışmalar, Academic Platform Journal of Engineering and Science. 2020;8(1):15-21.
10. Sun X, Peng B, Ji Y, Chen J, Li D. Chitosan(chitin)/cellulose composite biosorbents prepared using ionic liquid for heavy metal ions adsorption. AICHE Journal. 2009;55(8):2062-2069.
11. Gupta N, Kushwaha AK, Chattopadhyaya MC. Adsorptive removal of Pb²⁺, Co²⁺ and Ni²⁺ by hydroxyapatite/chitosan composite from aqueous solution. Journal of the Taiwan Institute of Chemical Engineers, 2012;43(1):125-31.
12. Tirtom VN, Dinçer A, Becerik S, Aydemir T, Çeli A. Comparative adsorption of Ni(II) and Cd(II) ions on epichlorohydrin crosslinked chitosan-clay composite beads in aqueous solution. Chemical Engineering Journal, 2012;197:379-86.
13. Senol ZM, Gül ÜD, Şimşek S. Assessment of Pb²⁺ removal capacity of lichen (Evernia prunastri): application of adsorption kinetic, isotherm models. and thermodynamics. Environmental Science and Pollution Research. 2019;26(26):27002-13.
14. Langmuir J. The adsorption of gases on plane surfaces of glass, mica and platinum I. Journal of the American Chemical Society. 1918;40:1361-1403.
15. Helfferich F. Ion exchange. McGraw Hill. New York. 1962;166.
16. Dubinin MM. The potential theory of adsorption of gases and vapors for adsorbents with energetically non-uniform surface. Chemical Reviews. 1960; 60:235-66.
17. Hobson JP. Physical adsorption isotherms extending from ultra-high vacuum to vapor pressure. The Journal of physical chemistry. 1969;73:2720-7.
18. Cui X, Hao H, Zhang C, He Z, Yang X. Science of the total environment capacity and mechanisms of ammonium and cadmium sorption on different wetland-plant derived biochars. Science of the Total Environment. 2016;539:566-75.
19. Inyang M, Gao B, Ding W, Pullammanappallil P, Zimmerman AR, Cao X. Enhanced Lead sorption by biochar derived from anaerobically digested sugarcane bagasse. Separation Science and Technology. 2011;46:1950-6.
20. Sharma P, Tomar R. Synthesis and application of an analogue of mesolite for the removal of uranium (VI), thorium (IV), and europium (III) from aqueous waste. Microporous and Mesoporous Materials, 2008;116 (1-3):641-52.
21. Sheng G, Hu J, Wang X. Sorption properties of Th (IV) on the raw diatomite—effects of contact time, pH, ionic strength and temperature. Applied Radiation and Isotopes, 2008; 66(10):1313-20.
22. Khraisheh MA, Al-degs YS, Mcminn WA. Remediation of wastewater containing heavy metals using raw and modified diatomite. Chemical Engineering Journal. 2004;99(2):177-84.
23. Pawlak A, Mucha M. Thermogravimetric and FTIR studies of chitosan blends. Thermochemica Acta. 2003;396(1-2):153-66.
24. Sprynskyy M, Kovalchuk I, Buszewski B. The separation of uranium ions by natural and modified diatomite from aqueous solution. Journal of Hazardous Materials. 2010; 181(1-3):700-7.
25. Čerović LS, Milonjić SK, Todorovi, MB, Trtanj MI, Pogožhev YS, Blagoveschenskii Y, Levashov EA. Point of zero charge of different carbides. Colloids and Surfaces A: Physicochemical and Engineering Aspects. 2007;297(1-3):1-6.
26. Ngah WW, Teong L, Hanafiah M. Adsorption of dyes and heavy metal ions by chitosan composites: A review. Carbohydrate Polymers, 2011;83(4):1446-56.
27. Ska DK. Chitosan as an effective low-cost sorbent of heavy metal complexes with the polyaspartic acid. Chemical Engineering Journal, 2011;173:520-9.



Antibiotic Susceptibility of *Klebsiella pneumoniae* Strains Isolated from Clinical Samples

Ahmet Ozan OZGEN¹  , Ozan Emre EYUPOGLU²  

¹Istanbul Medipol University, School of Pharmacy, 34810, Beykoz-Istanbul/ Turkey.

²Istanbul Medipol University, School of Pharmacy, Biochemistry Department, 34810, Beykoz-Istanbul/ Turkey.

Abstract: Antibiotic resistance in bacteria has become a worrying phenomenon in today's world. *K. pneumoniae* is a member of the *Enterobacteriaceae* family, which causes nosocomial infections as an opportunistic pathogen but inherently harboured as a part of the natural human microbiota. Carbapenem resistance of *K. pneumoniae* was a rare occurrence up to ten years ago, but in recent years many types of carbapenemase producing *K. pneumoniae* have become common. This retrospective study aims analysing susceptibility to various antibiotics, commonly used in treatment against *K. pneumoniae* strains isolated by using conventional methods from various infection sites. Antibiotic susceptibility tests were performed by using an automated system, the VITEK 2 Compact ®. In this study, 502 *K. pneumoniae* strains isolated from patients that treated at various services of a university hospital with 515-bed capacity were examined. When compared to the data available with studies of recent years in Turkey, especially in intensive care and inpatient services, the resistance of *K. pneumoniae* strains to antibiotics against most to carbapenems is rapidly increasing in the degree of high concern. Therefore, in all hospitals, antibiotic management policies should be implemented with a multidisciplinary approach.

Keywords: *Enterobacteriaceae*, *Klebsiella pneumoniae*, Drug Resistance, Bacterial, Retrospective Studies.

Submitted: October 20, 2019. **Accepted:** January 21, 2020.

Cite this: Ozgen A, Eyupoglu O. Antibiotic Susceptibility of *Klebsiella pneumoniae* Strains Isolated from Clinical Samples. JOTCSA. 2020; 7(1): 319-30.

DOI: <https://doi.org/10.18596/jotcsa.635088>.

***Corresponding author.** E-mail: oeeyupoglu@medipol.edu.tr, Tel: +905385882070.

INTRODUCTION

Increasing resistance of bacteria is reported with each passing day. This global threat now requires the implementation of antibiotic management policies in all hospitals. In antibiotic management, there are packages of measures aimed at improving the quality of anti-infective therapy with regulations on dosage, method of administration, and duration of treatment. While the best possible treatment is configured for each patient individually, resistance development is minimised and costs are reduced considering public health (1). Many international guidelines have defined the

structural requirements and basic strategies of antibiotic management (2). However, for example in the USA, there is a legal requirement for antibiotic management only since 2017. In Germany, the Infection Protection Law was amended in 2011 and necessary measures were taken to rationalise antibiotic consumption by hospitals (1). Also in Turkey, there is a legal penalty for antibiotic sale without a proper prescription only since 2017 (3).

The genus name of *Klebsiella* comes from the German scientist Edwin Klebs (1834-1913) who discovered them. It is a genus of bacteria that is

often isolated from health facilities such as hospitals, nursing homes, and long-term treatment centers. The capsules of *Klebsiella* species are responsible for the mucoid appearance of bacterial colonies and the increased virulence of the microorganism *in vivo*. The most commonly isolated forms of these bacteria are *Klebsiella oxytoca* and *Klebsiella pneumoniae*, which cause nosocomial or community-acquired lobar pneumonia. Symptoms vary according to which part of the body is affected by the bacteria. Besides, these symptoms are the same regardless of which bacteria are the causes. For example, a *Klebsiella*-induced pneumonia patient and a patient suffering from pneumonia for another reason have the same symptoms as high fever, chills, chest pain, and difficulty of breathing (4).

Although *K. pneumoniae* is a bacterium that is resistant to many antibiotics, it is reported that *K. pneumoniae* has a natural resistance to ampicillin (4). Mostly cephalosporin and aminoglycoside antibiotics were chosen for the treatment of the infections caused by it, but *K. pneumoniae* isolates have developed resistance to cephalosporin by the production of extended-spectrum beta-lactamase (ESBL) enzymes and limited their use. Therefore, carbapenems are now preferred (5). With the introduction of carbapenems, resistance to these antibiotics has been reported too. Determining the appropriate treatment protocol for *K. pneumoniae* isolates and analysing the resistance status to prevent the development of resistance has become essential. High mortality rates have been seen in infections caused by *K. pneumoniae* strains resistant to carbapenems, especially septicemia. Most of these infections occur asymptomatic and the risk of comorbidity increases by previous surgeries, invasive devices and apparatuses and colonies commonly found in the body (6).

Although it is a rare phenotype in many geographical regions, carbapenem resistance of *K. pneumoniae* was first reported in 1983. Then carbapenemase-producing *K. pneumoniae* (primarily in Greece) emerged and shown that they were producing Metallo-beta-lactamase (7). *K. pneumoniae carbapenemase* (KpC), a new family of enzymes, were first identified in the USA and caused epidemics, mainly in New York. Carbapenemase-producing *Enterobacteriaceae* members are susceptible only to polymyxins and tigecycline, so they pose a serious threat in hospitals and should be carefully monitored for carbapenem resistance (8).

In this study, 502 *K. pneumoniae* isolates were examined which have been taken from the various clinical specimens. The isolates were transferred by medical personnel to the medical microbiology

laboratory of a university hospital. Data were listed in the Microsoft Excel spreadsheets considering their susceptibility to antibiotics.

The aim of this retrospective study is analysing susceptibility to various antibiotics, commonly used in treatment, against *K. pneumoniae* strains isolated from various infection sites.

MATERIALS AND METHODS

Between 15.08.2017 and 10.11.2018, 502 microorganisms isolated from various regions of a university hospital were analysed retrospectively, considering patients' records. The study was approved by the ethics committee of İstanbul Medipol University.

Collection Of Isolates

K. pneumoniae culture samples were provided to a university hospital's clinical microbiology laboratory from over 33 separate outpatient clinics and inpatient wards; MacConkey and blood agar cultivation was carried out by microbiologists and samples were incubated at 37 °C for 17-24 hours. For the objectives of this research, only the cultures that tested positive for *K. pneumoniae* were included in the study. VITEK 2 Compact® (Biomerieux, France), for the identification of species of isolated microorganisms, an automated bacterial identification system, and common conventional methods have been used.

Susceptibility testing

All susceptibility testing was performed in a clinical microbiology laboratory. Antibiotic susceptibility of the isolated strains to 16 antibiotics (Amikacin, Ampicillin, Ampicillin-Sulbactam, Imipenem, Meropenem, Levofloxacin, Ciprofloxacin, Fosfomycin, Nitrofurantoin, Amoxicillin-Clavulanic Acid, Piperacillin-Tazobactam, Trimethoprim-Sulfamethoxazole, Cefotaxime, Cefepime) were tested. The method was coordinated with VITEK 2 Compact® (France, Biomerieux) automated antibiotic susceptibility testing system. Antimicrobial susceptibility of the isolates was examined by considering the recommendations of the European Antimicrobial Susceptibility Testing Committee (EUCAST) (9).

Data organisation & Statistical analysis

The data was imported into Microsoft Excel (Microsoft, Inc., U.S.A.) spreadsheet file and all-important patient identifiers were properly and securely discarded. The patients' data were classified according to type of clinic that they have been treated, nationality, sex, and age, microorganisms were classified according to the regions on patients they were colonised and antibiotic conditions were examined but not all

antimicrobials were tested against each isolate. In the study group, patients between 10 and 60 years of age were included in the sample in order to avoid inconsistency in the analysis results of age-related risk factors (10,11). Descriptive statistical analysis of isolates was performed using the program Prism (software version 8.3.0 (538); GraphPad Software, LLC). T-tests (two-tailed), Chi-square (and Fisher's exact) tests were used to assess any significant differences among the groups. A probability value of (P) <0.05 was considered statistically significant.

Comparison of materials and methods used in various studies

While analysing, regional differences in antibiotic susceptibilities should be considered as a result of antibiotics that used commonly in that region. Risk factors that play a role in the development of infections such as microbiota status, age, sex, postoperative status, implant and chronic diseases of the patients should be considered. When necessary, these patients should be excluded from the study sample in order not to cause meaninglessness in the study and thus to reduce reliability (10,11). Also, in studies involving large patient groups, separate studies should be conducted on the effects of risk factors on infection and bacterial resistance. Patients admitted to an institute as a tourist, especially in retrospective analysis, should be excluded from the research sampling when necessary, especially patients who cannot be treated in their own country because they are likely to have infections caused by bacteria with multiple drug resistance.

Many systems have been tried for continuous optimisation of treatment protocols, especially in the fight against nosocomial infections. However, in these studies, ones that placed the retrospective analysis method at the center, we encounter inconsistent results due to the risk factors mentioned. For example, systems such as the global anti-microbial resistance surveillance system (GLASS) have the disadvantage that they present too much data to a small staff to analyse, while not allowing them to validate results because of the distance from the environment where the data is

obtained. The abundance of data distorts the study results and makes the analysis difficult. Single-center working groups should be formed and regional results should be combined (1).

Various programs (IBM SPSS, Stata, PSPP) are used for performing statistical analyses in clinical studies. Although statistical analyses can be performed manually by using the proper formulae for observed data (12). The program Prism was used in this study, and proper formulae were chosen according to literature sources that interest this study (13–15).

Clinical and statistical significance in medicine differs from each other. Statistical significance is making predictions about the population, which are based on the sample size of the patients, with clinical data gathered. So every statistically significant finding may not be clinically relevant, likewise for every clinically finding is subjected to the same situation. Considering this, various methods should be used to eliminate mistakes in clinical results and data should be organised in the best way possible for statistical analyses (16). For example, results obtained with automation systems such as VITEK 2 Compact and MALDI-TOF MS (e.g., carbapenem inactivation method (CIM) for Carbapenem resistance) should be provided manually at the center where the work is performed.

According to the data obtained in the centers where the studies are conducted, treatment protocols should be coordinated and implemented especially for the empirical treatment. The results of the studies should be compared according to the effectiveness of the treatments. Thus, another method can be obtained to validate the results of the studies (1).

RESULTS

The university hospital, which is the center of the study, accepts patients from many countries as shown in Figure 1. Thus, antibiotic resistance in different countries, Turkey is composed of comparisons with the data.

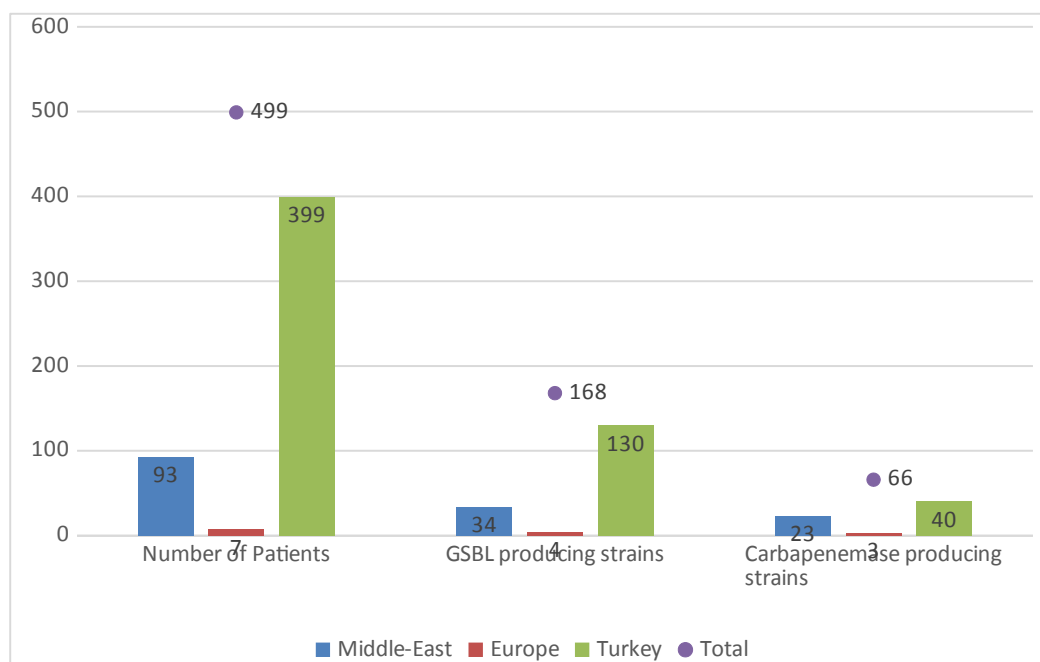


Figure 1: Patients sorted by their country.

As shown in Table 1, there is only one strain that does not express any beta-lactamase and probably this result was obtained due to an error; because *K. pneumoniae* has a natural resistance to ampicillin (4). In *K. pneumoniae*, resistance to beta-lactam group antibiotics is of concern. In addition, Cefepim, a member of 4th generation cephalosporins, has superiority over 3rd generation Cefotaxime as expected. All ESBL

positive strains are considered resistant to cefotaxime and other third-generation cephalosporins (17). Clinical use of carbapenems for Turkey is still effective in the treatment of *K. pneumoniae* infection. However, in order to prevent the development of resistance to this group of antibiotics in the future, particular attention should be paid to its use in the treatment of empirical therapy.

Table 1: Antibiotic susceptibility and total sample numbers of strains that were isolated*

Antibiotic	Resistant Strains	Susceptible strains	Total
Amikacin	34	383	417
Ampicillin*	222	1	223
Ampicillin-Sulbactam	121	101	222
Imipenem	64	437	501
Meropenem	88	414	502
Levofloxacin	146	356	502
Ciprofloxacin	168	334	502
Fosfomycin	12	85	97

Nitrofurantoin	52	123	175
Amoxicillin-Clavulanic Acid	169	159	328
Piperacillin-Tazobactam	120	208	328
Trimethoprim-Sulfamethoxazole	160	168	328
Cefotaxime	224	193	417
Cefepime	133	284	417

#P<0,0001 (Chi-square), * Ampicillin is not included because of *K. pneumoniae*'s natural resistance.

The higher smoking addiction in men than in women and the consequence of chronic pulmonary diseases such as COPD; It can be said that strains

isolated from pulmonary infections in men cause more resistance as seen in Figure 2 (18).

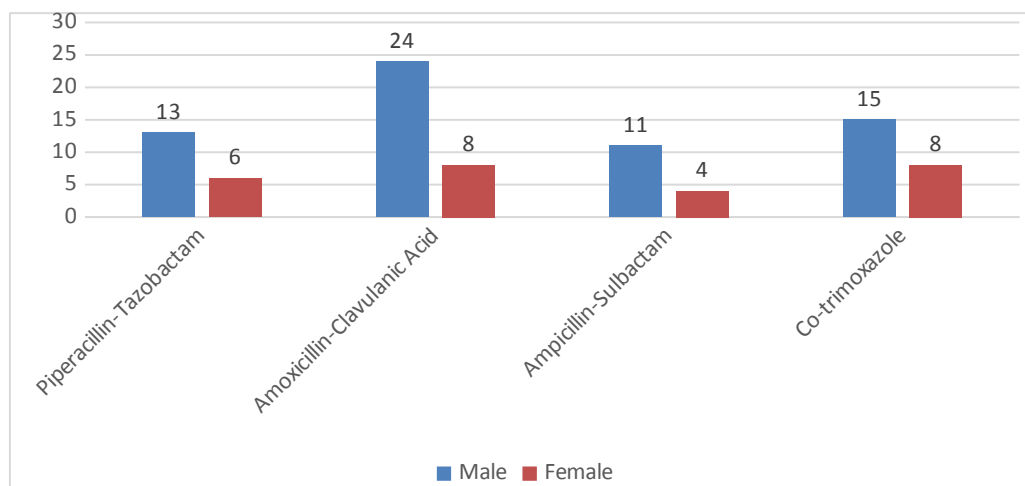


Figure 2: Gender distribution of antibiotic resistance of strains isolated from tracheal aspirate and bronchoalveolar lavage cultures, P=0.0261 (T-test).

Women are more prone to urinary tract infections due to their biological structure (19). Therefore, women are exposed to bacterial profiles more resistant than males because they use more

antibiotics against infection. Likewise, the distribution of efficacy of strains isolated from urinary tract infections against broad-spectrum fluoroquinolone antibiotics and phosphomycin was seen with high resistance in females (Figure 3).

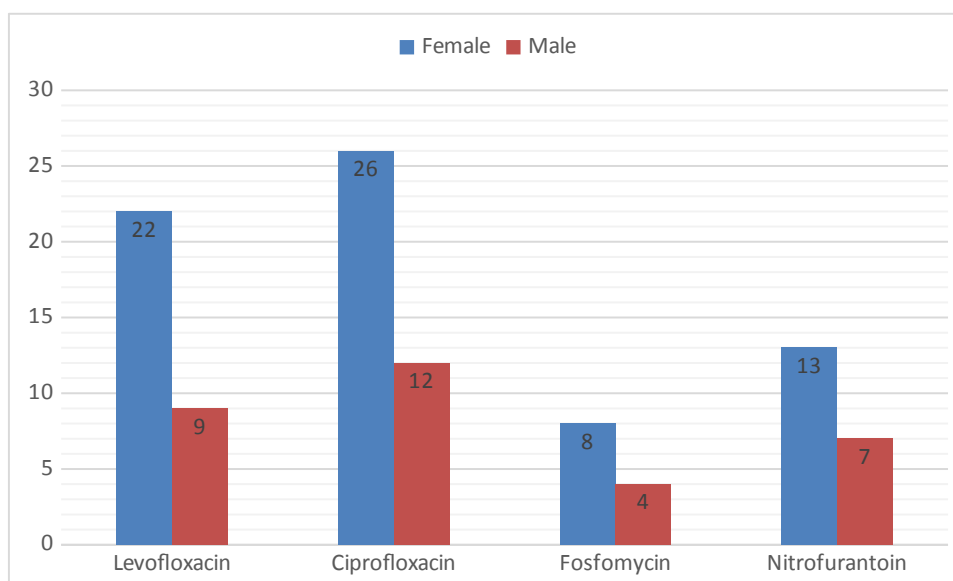


Figure 3: Resistance Distribution According to Gender in Urinary Tract Infections, $P = 0.0341$ (T-test).

DISCUSSION AND CONCLUSION

Today, due to the unnecessary and widespread use of antibiotics, gram-negative rods with multidrug resistance are reported all over the world. In recent years, the treatment of strains that become hypervirulent by producing ESBL (oxacylanase, high-level AmpC Beta-Lactamase, Carbapenemase) has become a major problem due to the multiple resistance strains encountered in intensive care patients (20).

In a multi-center study conducted in our country, "Meropenem Yearly Susceptibility Test Information Collection" 2007 data, 40.5% of *K. pneumoniae* strains were found to be ESBL positive (21). Different results have been observed in different regional studies conducted in our country. ESBL rates in *K. pneumoniae* strains were found to be 42% in another study and 74% in another study (22). According to another study conducted between 2007 and 2008, 41 *K. pneumoniae* strains produced 24% ESBL (23). In this study, it can be stated that 33% of ESBL producing strains were detected.

Although it varies according to the region it is isolated, carbapenem resistance has started to be seen more frequently in our country. In a study that was conducted with 2903 strains isolated, Samasti *et al.* reported that carbapenem resistance of *K. pneumoniae* was found to be 3.13% (24). In another study conducted in 2014, they reported imipenem resistance to blood cultures as 47% and meropenem resistance as 45% (22). In this study, 13% of resistance was determined against carbapenems.

While analysing, regional differences in antibiotic conditions and the difference between the number of samples studied can be considered as the reason for the differences between susceptibility rates.

For further studies, susceptibility results should be provided by performing disc diffusion tests in the comparative analysis sections (e.g. analysing sex-related factors on susceptibility), the zone radius should be used instead of positive/negative results. Besides, sample numbers should be equal. This will improve statistical significance.

Amoxicillin-Clavulanic Acid, in Turkey, is a common antibiotic used as an empirical treatment choice for community-acquired infections. Data gathered in this study shows that this choice of treatment is still partially effective against *K. pneumoniae* with a rate of 48.5%.

Almost all of the studies in different geographies around the world show that the development of resistance to antibiotics is developing at an alarming rate. Therefore, to keep up with the bacteria in the fight against antibiotic resistance, sufficient personnel and resources need to be mobilised, but on the contrary, we see that some firms have terminated the budgets allocated for antibiotic research and even countries such as the USA are trying to implement national antibiotic management policies more recently (25).

ESBL production rates of *E.coli*, *K. pneumoniae* and other gram-negative enteric bacteria, which are expensive and difficult to treat, should be monitored by each center. In the treatment of infections preferred broad-spectrum beta-lactam

antibiotics should be used with caution. Inpatients should be isolated and surveillance studies should be performed in hospital departments at risk.

Identification of organisms causing nosocomial infections, conducting in vitro antibiotic susceptibility tests and rational use of antibiotics may increase the chance of treatment success, prevent the spread of resistant nosocomial infections and reduce treatment costs. Therefore, antibiotic management policies should be implemented in all hospitals with a multidisciplinary approach.

ACKNOWLEDGEMENT

The authors would like to thank Dr. Betül GİRAY for her help in supplying research materials and Ph.D. Meltem Ezgi DURGUN for her help in statistical data analysis. We also appreciate the support from the management of Clinical Microbiology Laboratory, Medipol University Hospital.

REFERENCES

1. Sirijatuphat R, Sripanidkulchai K, Boonyasiri A, Rattanaumpawan P, Supapueng O, Kiratisin P, et al. Implementation of global antimicrobial resistance surveillance system (GLASS) in patients with bacteremia. PLOS ONE. 2018 Oct;13(1):e0190132.
2. Leung E, Weil DE, Raviglione M, Nakatani H. The WHO policy package to combat antimicrobial resistance. Bull World Health Organ. 2011 May;89:390–2.
3. Reçetesiz ilaç satılmıyor [Internet]. CNN Türk. [cited 2020 Jan 20]. Available from: <https://www.cnntrk.com/turkiye/recetesiz-ilac-satilmiyor>
4. Murray PR. Aerobic Fermentative Gram-Negative Rods. In: Basic Medical Microbiology. Philadelphia, USA: Elsevier; 2018. p. 85–9.
5. Paterson DL. Resistance in gram-negative bacteria: Enterobacteriaceae. Am J Infect Control. 2006 Jun 1;34(5, Supplement):S20–8.
6. Bassetti M, Giacobbe DR, Giamarellou H, Viscoli C, Daikos GL, Dimopoulos G, et al. Management of KPC-producing *Klebsiella pneumoniae* infections. Clin Microbiol Infect. 2018 Feb;24(2):133–44.
7. Giakkoupi P, Xanthaki A, Kanelopoulou M, Vlahaki A, Miriagou V, Kontou S, et al. VIM-1 Metallo-β-Lactamase-Producing *Klebsiella*

pneumoniae Strains in Greek Hospitals. J Clin Microbiol. 2003 Aug 1;41(8):3893–6.

8. Pereira EC, Shaw KM, Vagnone PMS, Harper J, Lynfield R. A review of multidrug-resistant Enterobacteriaceae. Minn Med. 2011 Oct;94(10):44–8.
9. Leclercq R, Cantón R, Brown DFJ, Giske CG, Heisig P, MacGowan AP, et al. EUCAST expert rules in antimicrobial susceptibility testing. Clin Microbiol Infect. 2013 Feb 1;19(2):141–60.
10. Liu C, Guo J. Hypervirulent *Klebsiella pneumoniae* (hypermucoviscous and aerobactin positive) infection over 6 years in the elderly in China: antimicrobial resistance patterns, molecular epidemiology and risk factor. Ann Clin Microbiol Antimicrob. 2019 Jan 21;18(1):4.
11. Dasgupta S, Das S, Chawan NS, Hazra A. Nosocomial infections in the intensive care unit: Incidence, risk factors, outcome and associated pathogens in a public tertiary teaching hospital of Eastern India. Indian J Crit Care Med Peer-Rev Off Publ Indian Soc Crit Care Med. 2015 Jan;19(1):14–20.
12. Taitt CR, Leski TA, Erwin DP, Odundo EA, Kipkemoi NC, Ndonge JN, et al. Antimicrobial resistance of *Klebsiella pneumoniae* stool isolates circulating in Kenya. Butaye P, editor. PLOS ONE. 2017 Jun 2;12(6):e0178880.
13. Moghnieh R, Estaitieh N, Mugharbil A, Jisr T, Abdallah DI, Ziade F, et al. Third generation cephalosporin resistant Enterobacteriaceae and multidrug resistant gram-negative bacteria causing bacteremia in febrile neutropenia adult cancer patients in Lebanon, broad spectrum antibiotics use as a major risk factor, and correlation with poor prognosis. Front Cell Infect Microbiol [Internet]. 2015 Feb 12 [cited 2020 Jan 19];5. Available from: <http://journal.frontiersin.org/Article/10.3389/fcimb.2015.00011/abstract>
14. Shao Y, Lu R, Yang Y, Xu Q, Wang B, Ye G. Antibiotic resistance of *Helicobacter pylori* to 16 antibiotics in clinical patients. J Clin Lab Anal. 2018 May;32(4):e22339.
15. Liu D-S, Wang Y-H, Zeng Z-R, Zhang Z-Y, Lu H, Xu J-M, et al. Primary antibiotic resistance of *Helicobacter pylori* in Chinese patients: a multiregion prospective 7-year study. Clin Microbiol Infect. 2018 Jul;24(7):780.e5-780.e8.
16. Sainani KL. Clinical Versus Statistical Significance. PM&R. 2012;4(6):442–5.

17. Aykan ŞB, Çiftci İH. Türkiye’de İdrar Kültürlerinden İzole Edilen Escherichia coli Suşlarının Antibiyotiklere Direnç Durumu: Bir Meta-Analiz. :16.

18. Hardin M, Foreman M, Dransfield MT, Hansel N, Han MK, Cho MH, et al. Sex-specific features of emphysema among current and former smokers with COPD. Eur Respir J. 2016 Jan 1;47(1):104–12.

19. Fethers KA, Fairley CK, Hocking JS, Gurrin LC, Bradshaw CS. Sexual Risk Factors and Bacterial Vaginosis: A Systematic Review and Meta-Analysis. Clin Infect Dis. 2008 Dec 1;47(11):1426–35.

20. Balıkçı H, Açıkgöz ZC, Güvenman S, Çel N, Özdem B. Escherichia coli ve Klebsiella spp. İzolatlarında Plazmid Kaynaklı AmpC Beta-Laktamaz Üretimini Araştırılması. MİKROBİYOLOJİ Bül. :13.

21. Eraksoy H, Basustaoglu A, Korten V, Kurt H, Ozturk R, Ulusoy S, et al. Susceptibility of Bacterial Isolates From Turkey - A Report From the Meropenem Yearly Susceptibility Test Information Collection (MYSTIC) Program. J Chemother. 2007 Dec 1;19(6):650–7.

22. Kahraman EP, Karakeçe E, Erdoğan F, Uluyurt H, Köroğlu M, Çiftci İH. Klebsiella pneumoniae izolatlarının antibiyotiklere direnç durumlarının değerlendirilmesi. Ortadoğu Tıp Derg. 2017 Mar 2;9(1):12–8.

23. Al-Muhtaseb M, Kaygusuz A. Kan kültürlerinden izole edilen Escherichia coli ve Klebsiella pneumoniae suşlarında genişletilmiş spektrumlu betalaktamaz (GSBL) sıklığı. ANKEM Dergi. 2008;22(4):175–82.

24. Samasti M, Koçoğlu ME, Davarci İ, Vahaboğlu H, Çaşkurlu H. Investigation of Carbapenemase Genes and Clonal Relationship in Carbapenem Resistant *Klebsiella pneumoniae* Strains. Bezmialem Sci. 2019 Jul 26;7(3):186–90.

25. Darby L. Antibiotic-Resistant Plagues Are Coming and We’re Wildly Unprepared [Internet]. [cited 2019 Oct 20]. Available from: <https://www.gq.com/story/antibiotic-resistant-plagues-are-coming>



Antibiotic Susceptibility of *Klebsiella pneumoniae* Strains Isolated from Clinical Samples

Ahmet Ozan OZGEN¹, Ozan Emre EYUPOGLU²

¹Istanbul Medipol University, School of Pharmacy, 34810, Beykoz-Istanbul/ Turkey

²Istanbul Medipol University, School of Pharmacy, Biochemistry Department, 34810, Beykoz-Istanbul/ Turkey

SUPPLEMENTARY INFORMATION

- 1) Ethical council's decision
- 2) Decision form



T.C.
İSTANBUL MEDİPOL ÜNİVERSİTESİ
Girişimsel Olmayan Klinik Araştırmalar Etik Kurulu Başkanlığı

E-İmzalıdır

Sayı : 10840098-604.01.01-E.53649
Konu : Etik Kurulu Kararı

21/12/2018

Sayın Ahmet Ozan ÖZGEN

Üniversitemiz Girişimsel Olmayan Klinik Araştırmalar Etik Kuruluna yapmış olduğunuz "Klinik örneklerden izole edilen Klebsiella pneumoniae suşlarının antibiyotik duyarlılıkları" isimli başvurunuz incelenmiş olup etik kurulu kararı ekte sunulmuştur.

Bilgilerinize rica ederim.

Prof. Dr. Hanefi ÖZBEK
Girişimsel Olmayan Klinik Araştırmalar
Etik Kurulu Başkanı

Ek:
-Karar Formu (2 sayfa)

Bu belge 5070 sayılı e-İmza Kanununa göre Prof. Dr. Hanefi ÖZBEK tarafından 21.12.2018 tarihinde e-imzalanmıştır. Evrağınızı <https://ebys.medipol.edu.tr/e-imza> linkinden F8838D57XC kodu ile doğrulayabilirsiniz.

İstanbul Medipol Üniversitesi

Kavacak Mah. Ekinciler Cad. No.19 Kavacak Kavşağı - Beykoz
34810 İstanbul

Tel: 444 85 44
İnternet: www.medipol.edu.tr
Ayrıntılı Bilgi İçin : [bilgi@medipol.edu.tr](mailto: bilgi@medipol.edu.tr)

İSTANBUL MEDİPOL ÜNİVERSİTESİ
GİRİŞİMSEL OLMAYAN KLİNİK ARAŞTIRMALAR
ETİK KURULU KARAR FORMU

BAŞVURU BİLGİLERİ	ARAŞTIRMANIN AÇIK ADI	Klinik örneklerden izole edilen Klebsiella pneumoniae suşlarının antibiyotik duyarlılıkları			
	KOORDİNATÖR/SORUMLU ARAŞTIRMACI UNVANI/ADI/SOYADI	Ahmet Ozan ÖZGEN			
	KOORDİNATÖR/SORUMLU ARAŞTIRMACININ UZMANLIK ALANI	Öğrenci			
	KOORDİNATÖR/SORUMLU ARAŞTIRMACININ BULUNDUĞU MERKEZ	İstanbul			
	DESTEKLEYİCİ	-			
	ARAŞTIRMAYA KATILAN MERKEZLER	TEK MERKEZ <input type="checkbox"/>	ÇOK MERKEZLİ <input checked="" type="checkbox"/>	ULUSAL <input checked="" type="checkbox"/>	ULUSLARARASI <input type="checkbox"/>

**İSTANBUL MEDİPOL ÜNİVERSİTESİ
GİRİŞİMSEL OLMAYAN KLİNİK ARAŞTIRMALAR
ETİK KURULU KARAR FORMU**

Değerlendirilen Belgeler	Belge Adı	Tarihi	Versiyon Numarası	Dili
	ARAŞTIRMA PROTOKOLÜ/PLANI			Türkçe <input type="checkbox"/> İngilizce <input type="checkbox"/> Diğer <input type="checkbox"/>
	BİLGİLENDİRİLMİŞ GÖNÜLLÜ OLUR FORMU			Türkçe <input checked="" type="checkbox"/> İngilizce <input type="checkbox"/> Diğer <input type="checkbox"/>
Karar Bilgileri	Karar No: 764		Tarih: 19/12/2018	
	Yukarıda bilgileri verilen Girişimsel Olmayan Klinik Araştırmalar Etik Kurulu başvuru dosyası ile ilgili belgeler araştırmanın gerekeçe, amaç, yaklaşım ve yöntemleri dikkate alınarak incelenmiş ve araştırmanın etik ve bilimsel yönden uygun olduğuna "oybirliği" ile karar verilmiştir.			

İSTANBUL MEDİPOL ÜNİVERSİTESİ GİRİŞİMSEL OLMAYAN KLİNİK ARAŞTIRMALAR ETİK KURULU	
BAŞKANIN UNVANI / ADI / SOYADI	Prof. Dr. Hanefi ÖZBEK

Unvanı/Adı/Soyadı	Uzmanlık Alanı	Kurumu	Cinsiyet		Araştırma ile ilişki		Katılım *		İmza
			E <input checked="" type="checkbox"/>	K <input type="checkbox"/>	E <input type="checkbox"/>	H <input checked="" type="checkbox"/>	E <input checked="" type="checkbox"/>	H <input type="checkbox"/>	
Prof. Dr. Şeref DEMİRAYAK	Eczacılık	İstanbul Medipol Üniversitesi	E <input checked="" type="checkbox"/>	K <input type="checkbox"/>	E <input type="checkbox"/>	H <input checked="" type="checkbox"/>	E <input checked="" type="checkbox"/>	H <input type="checkbox"/>	
Prof. Dr. Hanefi ÖZBEK	Farmakoloji	İstanbul Medipol Üniversitesi	E <input checked="" type="checkbox"/>	K <input type="checkbox"/>	E <input type="checkbox"/>	H <input checked="" type="checkbox"/>	E <input checked="" type="checkbox"/>	H <input type="checkbox"/>	
Doç. Dr. İlkur KESKİN	Histoloji ve Embriyoloji	İstanbul Medipol Üniversitesi	E <input type="checkbox"/>	K <input checked="" type="checkbox"/>	E <input type="checkbox"/>	H <input checked="" type="checkbox"/>	E <input checked="" type="checkbox"/>	H <input type="checkbox"/>	
Dr. Öğr. Üyesi Devrim TARAKCI	Ergoterapi	İstanbul Medipol Üniversitesi	E <input checked="" type="checkbox"/>	K <input type="checkbox"/>	E <input type="checkbox"/>	H <input checked="" type="checkbox"/>	E <input type="checkbox"/>	H <input checked="" type="checkbox"/>	
Dr. Öğr. Üyesi Sibel DOĞAN	Psiko-onkoloji	İstanbul Medipol Üniversitesi	E <input type="checkbox"/>	K <input checked="" type="checkbox"/>	E <input type="checkbox"/>	H <input checked="" type="checkbox"/>	E <input checked="" type="checkbox"/>	H <input type="checkbox"/>	
Dr. Öğr. Üyesi Mehmet Hikmet ÜÇİŞİK	Biyoteknoloji	İstanbul Medipol Üniversitesi	E <input checked="" type="checkbox"/>	K <input type="checkbox"/>	E <input type="checkbox"/>	H <input checked="" type="checkbox"/>	E <input checked="" type="checkbox"/>	H <input type="checkbox"/>	
Dr. Öğr. Üyesi Keziban OLCAY	Endodonti	İstanbul Medipol Üniversitesi	E <input type="checkbox"/>	K <input checked="" type="checkbox"/>	E <input type="checkbox"/>	H <input checked="" type="checkbox"/>	E <input checked="" type="checkbox"/>	H <input type="checkbox"/>	

* :Toplantıda Bulunma